NASA Conference Publication 2121

Proceedings of the Aero-Optics Symposium on Electromagnetic Wave Propagation from Aircraft

April 1980

NASA
National Aeronautics and Space Administration

NASA Conference Publication 2121

Proceedings of the Aero-Optics Symposium on Electromagnetic Wave Propagation from Aircraft

Sponsored by Air Force Weapons Laboratory
and
NASA-Ames Research Center

Held at
Ames Research Center, Moffett Field, California
August 14-15, 1979

NASA
National Aeronautics and
Space Administration

Ames Research Center
Moffett Field, California 94035

FOREWORD

The interaction of radiation and turbulent fluid motions is a problem area of interest in many areas of natural science. In recent years, coherent radiation propagation through a turbulent gaseous medium has become important in airborne astronomical observations, guidance and control sensors, narrow band airborne photography, and high energy laser propagation technology. In order to further the understanding of the effect of turbulence on coherent radiation, a basic research program known as the Aero-Optics Program was jointly sponsored by the NASA-Ames Research Center, the Air Force Weapons Laboratory and the Air Force Flight Dynamics Laboratory. Turbulence typical of that found in aerodynamic applications, including atmospheric turbulence, has been investigated by both aerodynamic instrumentation and direct optical quality measurement techniques.

The basic experimental program consisted of a series of four wind-tunnel tests using models that produced turbulent boundary layers, shear layers and flow about a three-dimensional surface. The wind-tunnel data established trends of optical degradation with flow Mach number, Reynolds number and type of flow field. These trends were verified in full-scale flight tests using the same instrumentation as in the wind-tunnel tests.

Another aspect of the program was an experimental investigation of the mechanical jitter which results from aerodynamically-induced disturbances on the aircraft structure and optical elements. The problem was initially investigated in a series of both small and large scale wind tunnel tests, with emphasis on windowless optical enclosures and multi-directional pointing. Flight tests were again used to substantiate the load predictions and the pointing stability analysis.

During the course of the Aero-Optics Program, aerodynamicists, physicists, opticians and instrumentation engineers were involved in data acquisition and analysis. As a result of their efforts, an extensive data base was established. This data base provides insight into the causes and magnitudes of expected optical degradation produced by aerodynamically generated turbulence. Further, the measurement techniques developed in this program are available to investigate any of a wide class of flow geometries in the future. In order to make this information available to interested government and industry personnel, the USAF/NASA Aero-Optics Symposium was held and the bound proceedings published herein.

TABLE OF CONTENTS

TURBULENT TWO-DIMENSIONAL JET FLOW AND ITS EFFECT ON LASER BEAM DEGRADATION

By

G. D. Catalano
G. F. Cudahy
J. T. Van Kuren
H. E. Wright

I ABSTRACT

A laser beam traversing turbulence undergoes an intensity reduction which is correlated with the statistical behavior at refractive index perturbations. The analytical relation predicts degradation as a function of beam diameter, path length, wave number and wave structure function. Refractive index perturbations are approximated via the equations of state, using temperature and velocity perturbations. An experiment was conducted in which visible wavelength lasers traversed a well-documented two-dimensional jet. Temperature perturbations vary from 0.25 to 1.80 ^{o}K and velocity fluctuations range from 9.2 to 30.8 m/sec. Measured central spot intensities are as low as 18% of the undisturbed beam, depending on jet Mach number, beam position relative to the jet exit and wavelength. The average difference between theory and experiment is two percent in terms of far field intensity.

To supplement the flow field information, a laser Doppler velocimeter is developed to measure both mean and fluctuating velocities. A photon correlator is used as a signal processor.

II INTRODUCTION

The effect that the turbulent flow field of a high subsonic Mach number two-dimensional jet shear layer produces on a coherent light beam is not precisely known. The refractive index perturbations cause a decrease in the central spot intensity of the beam in the far field because the total energy is spread over a larger area than in the unperturbed case. Furthermore, the long-time average at the mean location of the central spot is decreased by beam wandering. Numerous theoretical

and experimental efforts have been presented concerning the propagation of laser beams through natural atmospheric turbulence; however, in the atmosphere the absolute intensities of the velocity, temperature and pressure perturbations are relatively low; the beam path lengths are usually long; and the turbulence scales are quite large compared to beam diameter.[1-6] Recently, lasers have been used for wind tunnel diagnostics and in certain applications involving propagation out of aircraft in which case the beams must pass through boundary layers and free shear layers.

There are numerous examples in fluid flow problems where the local turbulence intensities are very high. One of the few methods capable of obtaining meaningful measurements in a very high turbulence environment is a laser Doppler velocimeter used in conjunction with a frequency shifting device. However, it is still the notable case that very little information exists for fluid flow problems where the local turbulence intensities exceed 30%. Thus, the need exists to develop a system that can perform reliably in the high turbulence environment.

The present study was an attempt to correlate the degradation of the far field central spot intensity formed by a collimated coherent light beam traversing the high intensity turbulence of a shear layer. In addition an attempt was made to measure the spreading of the energy over a larger area in the far field (termed broadening), and the motion of the beam in the far field (called wandering).

It was necessary to design an experiment that would approximate in a controlled manner the turbulent shear layer that exists over an open cavity normal to a uniform high velocity stream. A two-dimensional jet

with a well designed settling chamber and subsonic nozzle was fabricated. This set-up also provided double shear layers for added sensitivity. The uniform velocity core-flow could be varied with Mach numbers ranging from 0.4 to 0.8 to emphasize the compressible regime. To determine if wave length and beam size relative to turbulence scale were important, two laser frequencies were used and three beam sizes were tried at each frequency. The beam traversed the turbulent jet successively at 25, 50 and 75 nozzle widths downstream from the nozzle exit.

Since the first published account of the use of a laser Doppler velocimeter (LDV) appeared in 1964, much effort has been devoted to the LDV's development. A nonintrusive fluid diagnostic technique such as laser velocimetry allows for greater flexibility in the type measurements that can be made in a given flow situation.

In the past, the common techniques for signal analysis and information retrieval have often required relatively high powered lasers and sophisticated electronics. In addition the two most common processing schemes (i.e. (1) counter and (2) tracker) each required the inclusion of a light scattering marker in the flow. A recent advance in data acquisition utilizing the laser Doppler velocimeter technique involves the use of a photon correlator. Photon counting techniques offer improved system sensitivity by allowing velocity measurements to be made even when there are insufficient signal photons available to define the classical scattering signal.

In order to examine the effect(s) of high turbulence levels and/or high mean velocities, the LDV setup is used to monitor the velocity field of a compressed air jet. The data obtained from the LDV is compared to hot-wire anemometer data when appropriate.

III SUMMARY

A summary of the significant results obtained in this experiment will now be given.

This investigation correlated the degradation of the far field central spot intensity formed by a collimated coherent light beam traversing high intensity turbulence with the statistical behavior of the turbulence generated refractive index perturbations causing the degradation. Since refractive index perturbations could not be readily measured a method to approximate these perturbations, via the equation of state, using velocity and temperature perturbations was developed. The turbulence quantities measured were path length, velocity correlation function and temperature correlation function. The path length had a minimum at the 25 cm test station. The rms velocity perturbations had a maximum of 30.8 m/sec at the 25 cm test station at 0.8 Mach and on an axis minimum of 9.2 m/sec at the 75 cm test station at 0.4 Mach. The corrected temperature perturbations had a maximum of 1.89 ^{o}K and minimum of 0.25 ^{o}K at the above respective test stations and nozzle exit flow conditions.

The actual far field central spot intensities were measured. The 4416 Å, 50 mm beam traversing the 25 cm test station when the nozzle exit velocity was 0.8 Mach had an intensity of 18 percent of the reference intensity. At the 75 cm test station, with 0.4 Mach nozzle exit velocity the 6328 Å, 11.0 mm laser beam had a far field central spot intensity of 100 percent of the reference intensity.

The results of the experimentally measured central spot degraded intensities were compared with the analytically predicted, using

experimentally determined turbulence characteristics, central spot intensities. For the same laser beams traversing statistically identical flow fields, the greatest difference between experimentally-measured and analytically-predicted degraded, far-field, central-spot intensities was 8.2 percent. The average difference between the experimentally and analytically determined intensities for all test conditions was less than two percent. These results support the approximations used to arrive at the analytical expressions which predict the laser beam for far-field central spot intensity degradation caused by turbulent flow fields and yield confidence in the ability to accurately predict those degradations using readily measurable turbulent flow field statistical parameters.

It was found that the frequency shifting crystal oscillator was needed in order to determine both the local mean velocity and the local turbulence intensity in a highly turbulent portion of the flow. For example, the downstream decay of the mean velocity at the centerline of the jet was readily determined using the basic LDV without the frequency shifting device. Typically, the turbulence intensities at the centerline do not exceed 20% for the initial development region. Once the measuring volume was located in the mixing region, the turbulence served to damp the autocorrelation function so severely as to mask out the information needed to determine the mean and rms velocities.

Due to the sampling rate having an upper limit of 50 nanoseconds, high velocities create additional problems. Recalling that the Doppler shift is given by:

$$f_D = \frac{2U \sin (\theta/2)}{\lambda}$$

and if the largest shift detectable is less than 20 MHz then for very large velocities either the half angle between the intersecting beams

$(\theta/2)$ must be made very small or the wavelength of the laser light (λ) be increased. The first approach being much more practical than the latter. Reducing the angle however also reduces the spatial resolution, thus making the velocity field seem much larger than it really is and also smearing out the finer scale turbulent occurrences.

IV DATA DESCRIPTION

To document the reliability of the photon correlation laser Doppler velocimeter, measurements are made in the flow field of a turbulent jet exhausting into the atmosphere.

Mean velocities in the longitudinal direction are measured and similarity profiles are shown for varying downstream locations and different exit Mach numbers (Fig. 1). The profiles are compared to theoretical curves developed by Gortler and Tollmien.

The decay of the centerline mean velocity with downstream displacement is also shown (Fig. 2) for different Mach numbers, and compared to data obtained by use of a hot-wire anemometer (Fig. 3).

Finally, an exit velocity profile using the LDV is compared to a profile obtained by using a hot-wire anemometer (Fig. 4). Note the difference in the flow widths.

Turbulence Characteristics Used to Predict Laser Beam Degradation

The refractive index perturbations which have the major effect on the laser beam degradation of this investigation were caused by turbulence induced density variations in the active medium through which the laser beam propagates. These density variations were not amenable to direct measurement, thus the equation of state was used to determine turbulent density variations via other readily measurable turbulence quantities. It was determined that velocity and temperature perturbations could be

transformed into density and, subsequently, refractive index perturbations. Since the frequency response of the temperature measuring device was insufficient for the temperature field to be measured, a method was developed to correct the temperature measurements obtained with this device.

The measurement and recording of instantaneous turbulent flow field characteristics for the entire flow field area of interest for a given experimental configuration of investigation were not possible. Statistical characterization of the turbulent flow field was, therefore, resorted to, and the prediction of the laser beam degradation was then necessarily limited to average degradation.

The turbulence parameters used to predict the laser beam degradation were the spatial temperature correlation function, spatial velocity correlation function, and the path length of turbulence field thickness associated with each correlation function. The correlation functions actually measured were temporal correlation functions. These functions and Taylor's hypothesis were used to approximate the spatial correlation functions.

Figure 5 shows examples of velocity correlation functions as they appeared on the display element of the correlator and the spectrum display. The frequency response of the constant temperature anemometer was sufficient to measure the highest frequency component of the turbulent velocity field.

Figure 6 shows examples of temperature correlation functions. Two similar functions with different correlator display time bases are shown in Fig 7(a). As discussed earlier, the frequency response of the constant current anemometer system used to measure the temperature perturbations of the turbulent field of this study was insufficient for many of

the flow conditions experienced.

Table I lists the rms velocity perturbations, rms measured temperature perturbations, temperature correction factors, corrected rms temperature perturbations, thickness of turbulence field each of these measurements represents, and mean velocity of the flow field for each of these measurements. The Mach number and downstream test station of each set of parameters is also given.

Predicted Versus Measured Unperturbed Laser Beam Far Field Spot Profiles

In order to compare the unperturbed beam intensity profile actually detected with that which would be analytically predicted, Eq. 1 was numerically integrated with T_τ set equal to unity. This yielded the far field spot in the focal plane of the far field forming lens. Figures 7a, b, c, d, e and f show the photographs of the test beam spots as projected on the opal glass measured by the TV camera and portrayed on the oscilloscope. Figures 8 a and b show the analytically predicted beam spots. As can be seen from the photographs and plots, the predicted and measured beam spots agree quite closely for four of the six test beams.

Solution of the Laser Beam Degradation Equations

Equation 2 in combination with Eqs. 3, 4, 5, and 6 is not amenable to exact solution; thus, numerical techniques were resorted to in the endeavor to solve these equations. Simpson's Rule was used to integrate numerically the equations with "Ar" of 0.125 mm. In order to utilize conveniently the temperature and velocity correlation functions in the numerical integrations, the correlation functions were digitized values using a least squares fit subroutine.

The solution of Eq. 2 using Eqs. 3 and 5 for T_τ took about 50 times more computer time than the solution using Eqs. 5 and 6. The results of the numerical integration of these equations are shown in Table II. Solutions were obtained for measured input laser beam diameters and input laser beam diameters which would yield the far field spot diameters measured.

Predicted Versus Measured Turbulent Refractive Index Induced Laser Beam Degradations

Examples of the degraded far field laser beam spots as recorded on the oscilloscope are shown in Figure 9. These photographs show the long term average degraded laser beam spots as measured by the TV camera in the regular scan mode. Since these examples show little motion of the far field spot, it is apparent that any motion which contributes to the overall degradation occurs at a frequency equal to or higher than the reciprocal of the integration time of the TV camera system. This frequency of motion will be discussed further when the results of the far field measurements using the TV camera in a single line scan mode are presented. Figure 10 shows the percentages of the detected long term average central spot intensities for all laser beams, test locations and Mach numbers. Table II lists these same data along with the solution of Eq. 2 using Eqs. 3, 4, 5, and 6 for T_τ. Figure 11 shows in graphical form the detected far field spot intensities versus those predicted by the solution of Eq. 2 using Eq. 3 for T_τ with input beam diameters which would yield the far field spot diameters measured.

Laser Beam Far Field Spot Broadening and Wandering

With the TV camera in the single line scan mode, the detection system was able to detect motions with a frequency of up to 3000 Hz. Examples were made of several measurements of the beam spots with the TV camera in

the single line scan mode, and with several detected spots superimposed. The area of maximum brightness closely coincided, in most cases, to the long term average central spot intensity detected with a TV camera in regular scan. Thus, this maximum intensity was taken as the intensity remaining after degradation by broadening alone. The percentage of this maximum which yields the long term average intensity was taken as the intensity remaining after degradation by beam motion (or wandering) alone. A laboratory schematic of the test configuration is shown in Figure 12.

Bibliography

1. Hufnagle, R. E. and N. R. Stanley. "Modulation Transfer Function Associated with Image Transmission Through Turbulent Media." Journal of the Optical Society of America, Vol. 54, Number 1, 1964.

2. Lutomirski, R. F., R. E. Huschke, W. C. Meecham and H. T. Yura. "Degradation of Laser Systems by Atmospheric Turbulence." The Rand Corporation, R-1171-ARPA/RC, June 1973.

3. Lutomirski, R. F., A. R. Shapiro and H. T. Yura. "Experiments on Turbulence Effects in Laser Propagation." The Rand Corporation, WN-7063-ARPA, September 1970.

4. Lutomirski, R. F. and H. T. Yura. "On the Mutual Coherence Function of an Optical Wave in a Turbulent Atmosphere." The Rand Corporation, RM-6266-ARPA, July 1970.

5. Sutton, G. W. "Effect of Turbulent Fluctuations in an Optically Active Fluid Medium." AIAA Journal. Volume 7, Number 9, September 1969.

6. Tatarski, V. I. Wave Propagation in Turbulent Medium. New York: McGraw-Hill Book Company, 1961.

LIST OF EQUATIONS

$$\frac{I(s)}{I_o(o)} = \hat{I}(s) = \frac{\int_o^S e^{-\frac{r^2}{2R^2}} T_\tau J_o\left(\frac{2\pi rs}{F\lambda}\right) rdr}{\int_o^S e^{-r^2/2R^2}\, rdr.} \tag{1}$$

$$\hat{I}(o) = \frac{\int_o^S e^{-r^2/2R^2} T_\tau rdr}{\int_o^S e^{-r^2/2R^2}\, rdr} \tag{2}$$

$$T_\tau = \exp\left[-4k^2(79 \times 10^{-6})^2 X\right. \tag{3}$$

$$\sum_{i=1}^{N} \left[\frac{\Delta L_i}{\bar{\Theta}_i^4} \int_o^\infty \left\{\frac{\rho_i^2 \bar{\Theta}_i^2}{2} \left[B_{ui}^2(y) - B_{ui}^2\left(\sqrt{r^2+y^2}\right)\right]\right.\right.$$

$$\left.\left. + \bar{P}_i^2\left[B_{\theta i}(y) - B_{\theta i}\left(\sqrt{r^2+y^2}\right)\right]\right\} dy\right]\Big]$$

$$T_\tau = \exp\left[-4k^2(79 \times 10^{-6})^2 X\right. \tag{4}$$

$$\sum_{i=1}^{N} \frac{\Delta L_i}{\bar{\Theta}_i^4} \int_o^\infty \left\{\frac{\rho_i^2 \bar{\Theta}_i^2}{2} \left[B_{ui}^2\left(\sqrt{r^2+y^2}\right) - B_{ui}^2(y)\right.\right.$$

$$\left. + 2B_{ui}(o)\left(B_{ui}(y) - B_{ui}\left(\sqrt{r^2+y^2}\right)\right)\right]$$

$$\left. + \bar{P}_i^2\left[B_{\theta i}(y) - B_{\theta i}\left(\sqrt{r^2+y^2}\right)\right]\right\} dy\Big]$$

$$T_\tau = \exp\left[-2.91k^2 r(79 \times 10^{-6})^2 X\right. \tag{5}$$

$$\sum_{i=1}^{N} \left[\frac{\Delta L_i}{\bar{\Theta}_i^4} \left\{\frac{\rho_i^2}{2} \bar{\Theta}_i^2 \left[B_{ui}^2(o) - B_{ui}^2(r)\right]\right.\right.$$

$$\left.\left. + \bar{P}_i^2\left[B_{\theta i}(o) - B_{\theta i}(r)\right]\right\}\right]$$

$$T_\tau = \exp\left[-2.91k^2 r(79 \times 10^{-6})^2 X\right. \tag{6}$$

$$\sum_{i=1}^{N} \left[\frac{\Delta L_i}{\bar{\Theta}_i^4} \left\{\frac{\rho_i^2}{2} \bar{\Theta}_i^2 \left[B_{ui}^2(o) + B_{ui}^2(r)\right.\right.\right.$$

$$\left.\left.\left. - 2B_{ui}(o)\, B_{ui}(r)\right] + \bar{P}_i^2\left[B_{\theta i}(o) - B_{\theta i}(r)\right]\right\}\right]$$

TABLE I

TURBULENCE PARAMETERS

LOCATION TEST STATION	y (cm)	MACH NO.	u (m/sec)	θ_s (°K)	$\sqrt{m}$	θ (°K)	ΔL (cm)	$\bar{U}$ (m/sec)
25	0	0.8	24.0	1.23	1.4	1.72	0.5	156.
25	0.5	0.8	26.4	1.31	1.4	1.83	1.0	147.
25	1.0	0.8	29.0	1.35	1.4	1.89	1.0	133.
25	1.5	0.8	30.8	1.29	1.4	1.81	1.0	114.
25	2.0	0.8	30.4	1.23	1.3	1.60	1.5	91.8
25	3.0	0.8	25.6	1.09	1.1	1.20	2.0	54.0
25	4.0	0.8	17.6	0.87	1.15	1.00	2.0	27.0
25	5.0	0.8	8.0	0.44	1.1	0.48	2.0	12.4
50	0	0.8	18.4	0.88	1.3	1.15	1.0	112.
50	1.0	0.8	19.6	0.93	1.4	1.31	2.0	107.
50	2.0	0.8	21.0	0.91	1.2	1.10	2.0	92.6
50	3.0	0.8	22.2	0.83	1.1	0.92	2.0	77.8
50	4.0	0.8	21.4	0.72	1.1	0.79	2.0	63.4
50	5.0	0.8	19.6	0.62	1.05	0.65	2.0	51.2
50	6.0	0.8	17.4	0.53	1.05	0.55	3.0	38.6
50	8.0	0.8	11.4	0.36	1.0	0.36	4.0	19.4
50	10.0	0.8	5.8	0.26	1.0	0.26	4.0	16.1
75	0	0.8	16.6	0.61	1.0	0.61	2.0	87.6
75	2.0	0.8	17.8	0.62	1.0	0.62	4.0	78.9
75	4.0	0.8	18.4	0.57	1.0	0.57	4.0	65.0
75	6.0	0.8	17.4	0.48	1.0	0.48	4.0	50.8
75	8.0	0.8	15.2	0.38	1.0	0.38	4.0	36.0
75	10.0	0.8	12.7	0.29	1.0	0.29	6.0	25.6
25	0	0.6	19.6	0.77	1.46	1.12	0.5	119.
25	0.5	0.6	21.0	0.81	1.09	1.0	1.0	112.
25	1.0	0.6	23.0	0.82	1.3	1.06	1.0	99.4
25	1.5	0.6	23.6	0.79	1.3	1.02	1.0	85.8
25	2.0	0.6	23.0	0.72	1.1	0.79	1.5	70.8
25	3.0	0.6	20.0	0.62	1.05	0.65	2.0	43.1
25	4.0	0.6	13.6	0.26	1.1	0.29	2.0	21.6
25	5.0	0.6	6.8	0.17	1.0	0.17	2.0	8.6

TABLE I

(Continued)

LOCATION TEST STATION	y (cm)	MACH NO.	u (m/sec)	θ_s (°K)	$\sqrt{m}$	θ (°K)	ΔL (cm)	$\overline{U}$ (m/sec)
50	0	0.6	15.4	0.54	1.05	0.56	1.0	84.4
50	1.0	0.6	16.6	0.56	1.05	0.58	2.0	81.8
50	2.0	0.6	17.6	0.56	1.0	0.56	2.0	73.2
50	3.0	0.6	17.2	0.50	1.0	0.50	2.0	61.8
50	4.0	0.6	16.4	0.44	1.05	0.46	2.0	50.1
50	5.0	0.6	15.6	0.37	1.0	0.37	2.0	39.4
50	6.0	0.6	13.7	0.31	1.0	0.31	3.0	29.2
50	8.0	0.6	9.5	0.21	1.0	0.21	5.0	16.4
75	0	0.6	12.8	0.38	1.05	0.40	2.0	61.6
75	2.0	0.6	13.4	0.39	1.0	0.39	4.0	56.4
75	4.0	0.6	13.6	0.34	1.0	0.34	4.0	47.6
75	6.0	0.6	12.8	0.28	1.0	0.28	6.0	36.4
75	10.0	0.6	9.5	0.17	1.0	0.17	10.0	17.8
25	0	0.4	13.8	0.43	1.1	0.47	0.5	81.6
25	0.5	0.4	15.2	0.43	1.2	0.51	1.0	76.6
25	1.0	0.4	15.8	0.43	1.2	0.51	1.0	68.4
25	1.5	0.4	16.2	0.41	1.2	0.49	1.0	58.2
25	2.0	0.4	15.8	0.38	1.05	0.4	1.5	48.0
25	3.0	0.4	13.0	0.31	1.05	0.33	2.0	29.6
25	4.0	0.4	9.6	0.23	1.1	0.25	2.0	16.5
25	5.0	0.4	5.0	0.17	1.0	0.17	2.0	7.3
50	0	0.4	11.0	0.29	1.1	0.32	1.0	60.8
50	1.0	0.4	11.8	0.30	1.1	0.33	2.0	57.5
50	2.0	0.4	12.4	0.30	1.0	0.30	3.0	49.6
50	4.0	0.4	11.6	0.23	1.0	0.23	4.0	35.1
50	6.0	0.4	9.4	0.23	1.0	0.23	6.0	21.4
75	0	0.4	9.2	0.25	1.0	0.25	2.0	41.1
75	2.0	0.4	9.6	0.24	1.0	0.24	4.0	39.2
75	4.0	0.4	8.8	0.23	1.1	0.25	4.0	31.8
75	6.0	0.4	8.8	0.20	1.05	0.21	6.0	26.4
75	10.0	0.4	6.3	0.16	1.0	0.16	10.0	13.6

TABLE II

MEASURED AND CALCULATED LASER BEAM DEGRADED INTENSITIES

λ (A°)	LASER BEAM SIZE (mm)	MACH NO.	TEST STATION (cm)	MEASURED INTENSITY (%)	CALCULATED INTENSITY (%) EQ. 3	EQ. 4	EQ. 5	EQ. 6
6328	50.0	0.4	25	93	92.8	91.6	89.4	92.7
6328	26.8	0.4	25	94	93.6	92.9	91.1	94.2
6328	11.0	0.4	25	98	96.9	97.3	96.8	98.4
4416	50-0	0.4	25	90	85.8	83.7	79.7	85.8
4416	26.0	0.4	25	92	87.6	86.4	83.2	88.8
4416	12.3	0.4	25	97	92.9	93.7	92.4	96.0
44.6	21.0	0.4	25	92	88.8	88.2	85.5	90.7
4416	10.8	0.4	25	97	93.9	94.8	93.8	96.9
6328	50.0	0.6	25	70	72.8	69.9	63.6	74.5
6328	26.8	0.6	25	76	75.8	74.3	69.0	79.4
6328	11.0	0.6	25	86	87.7	89.7	87.6	94.0
4416	50.0	0.6	25	56	53.1	49.8	42.9	56.8
4416	26.0	0.6	25	63	58.1	56.8	50.0	64.9
4416	12.3	0.6	25	79	74.2	77.5	73.6	85.9
4416	21.0	0.6	25	63	61.6	61.6	55.4	70.2
4416	10.8	0.6	25	79	77.3	81.1	77.8	88.9
6328	50.0	0.8	25	34	40.6	38.2	31.2	45.2
6328	26.8	0.8	25	45	46.0	45.2	38.7	53.6
6328	11.0	0.8	25	67	69.1	73.5	69.9	83.2
4416	50.0	0.8	25	18	18.6	18.6	14.7	26.1
4416	26.0	0.8	25	25	24.2	25.7	21.3	35.4
4416	12.3	0.8	25	48	45.4	51.5	46.9	65.9
4416	21.0	0.8	25	25	28.4	30.8	26.2	42.0
4416	10.8	0.8	25	48	50.4	57.2	52.9	71.6
6328	50.0	0.4	50	96	95.3	95.9	94.8	97.3
6328	26.8	0.4	50	97	96.0	96.7	95.8	97.9
6328	11.0	0.4	50	98	98.4	98.9	98.6	99.5
4416	50.0	0.4	50	94	90.7	91.9	89.7	94.6
4416	26.0	0.4	50	95	92.1	93.5	91.7	95.9
4416	12.3	0.4	50	98	96.2	97.3	96.7	98.6
4416	21.0	0.4	50	95	93.0	94.5	93.0	96.6
4416	10.8	0.4	50	98	96.8	97.8	97.3	98.9
6328	50.0	0.6	50	83	83.6	85.8	82.4	91.5
6328	26.8	0.6	50	86	86.0	88.3	85.5	93.3
6328	11.0	0.6	50	95	94.1	96.0	95.0	98.3
4416	50.0	0.6	50	78	69.8	73.6	68.1	83.6

TABLE II

(Continued)

λ_o (A)	LASER BEAM SIZE (mm)	MACH NO.	TEST STATION (cm)	MEASURED INTENSITY (%)	CALCULATED INTENSITY (%) EQ. 3	EQ. 4	EQ. 5	EQ. 6
4416	26.0	0.6	50	81	74.2	78.4	73.8	87.2
4416	12.3	0.6	50	89	86.6	90.6	88.4	95.6
4416	21.0	0.6	50	81	77.1	81.5	77.4	89.5
4416	10.8	0.6	50	89	88.7	92.4	90.6	96.6
6328	50.0	0.8	50	60	60.7	63.4	57.8	72.8
6328	26.8	0.8	50	68	65.6	69.0	64.2	78.0
6328	11.0	0.8	50	85	83.9	87.8	86.1	93.3
4416	50.0	0.8	50	41	38.2	42.1	36.2	54.6
4416	26.0	0.8	50	51	45.2	50.2	44.8	62.9
4416	12.3	0.8	50	72	67.3	74.0	78.8	84.5
4416	21.0	0.8	50	51	50.0	55.6	50.7	68.2
4416	10.8	0.8	50	72	7.15	78.0	75.3	87.6
6328	50.0	0.4	75	97	96.9	97.5	97.0	98.2
6328	26.8	0.4	75	98	97.4	97.9	97.6	98.6
6328	11.0	0.4	75	100	99.0	99.3	99.3	99.6
4416	50.0	0.4	75	98	93.8	95.0	94.1	96.4
4416	26.0	0.4	75	97	94.9	96.0	95.3	97.2
4416	12.3	0.4	75	99	97.7	98.4	98.2	99.0
4416	2.10	0.4	75	97	95.6	96.6	96.1	97.7
4416	10.8	0.4	75	99	98.1	98.7	98.6	99.2
6328	50.0	0.6	75	91	90.6	92.7	90.8	95.9
6328	26.8	0.6	75	92	92.0	94.0	92.5	96.8
6328	11.0	0.6	75	98	96.9	98.0	97.6	99.2
4416	50.0	0.6	75	83	81.8	85.7	82.3	91.9
4416	26.0	0.6	75	87	84.8	88.5	85.7	93.7
4416	12.3	0.6	75	94	92.7	95.2	94.1	97.9
4416	21.0	0.6	75	87	86.7	90.2	87.8	94.8
4416	10.8	0.6	75	94	9319	96.2	95.3	98.3
6328	26.8	0.8	75	80	78.6	84.0	79.9	91.6
6328	50.0	0.8	75	74	75.0	80.1	75.7	89.3
6328	11.0	0.8	75	90	91.1	94.6	93.1	97.8
4416	50.0	0.8	75	57	56.6	65.3	58.1	79.8
4416	26.0	0.8	75	65	62.7	71.4	65.2	84.2
4416	12.3	0.8	75	81	80.4	87.4	84.2	94.5
4416	21.0	0.8	75	65	66.9	75.4	69.8	87.0
4416	10.8	0.8	75	81	83.3	89.7	87.1	95.7

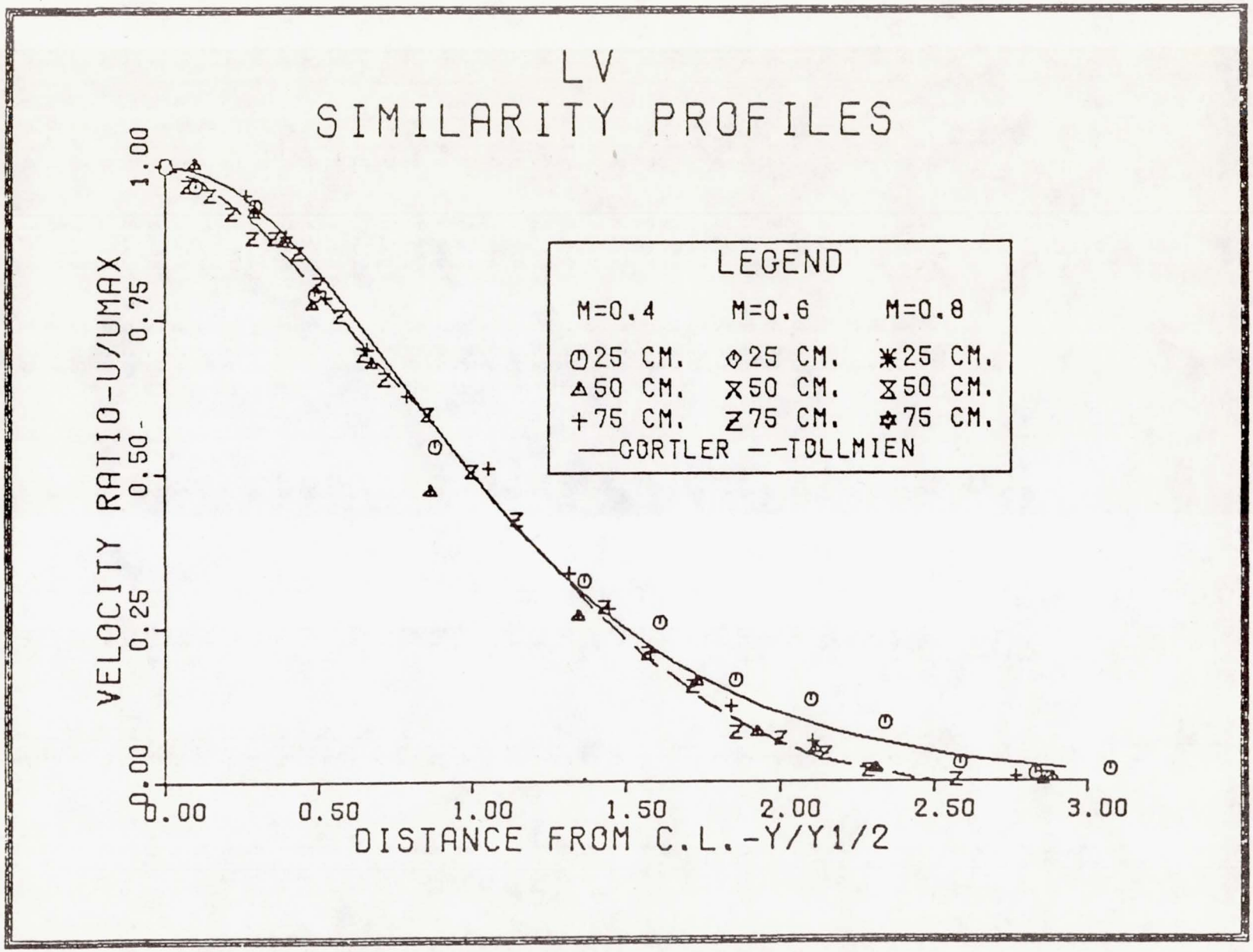

FIG. 1 LV MEAN VELOCITY SIMILARITY PROFILES.

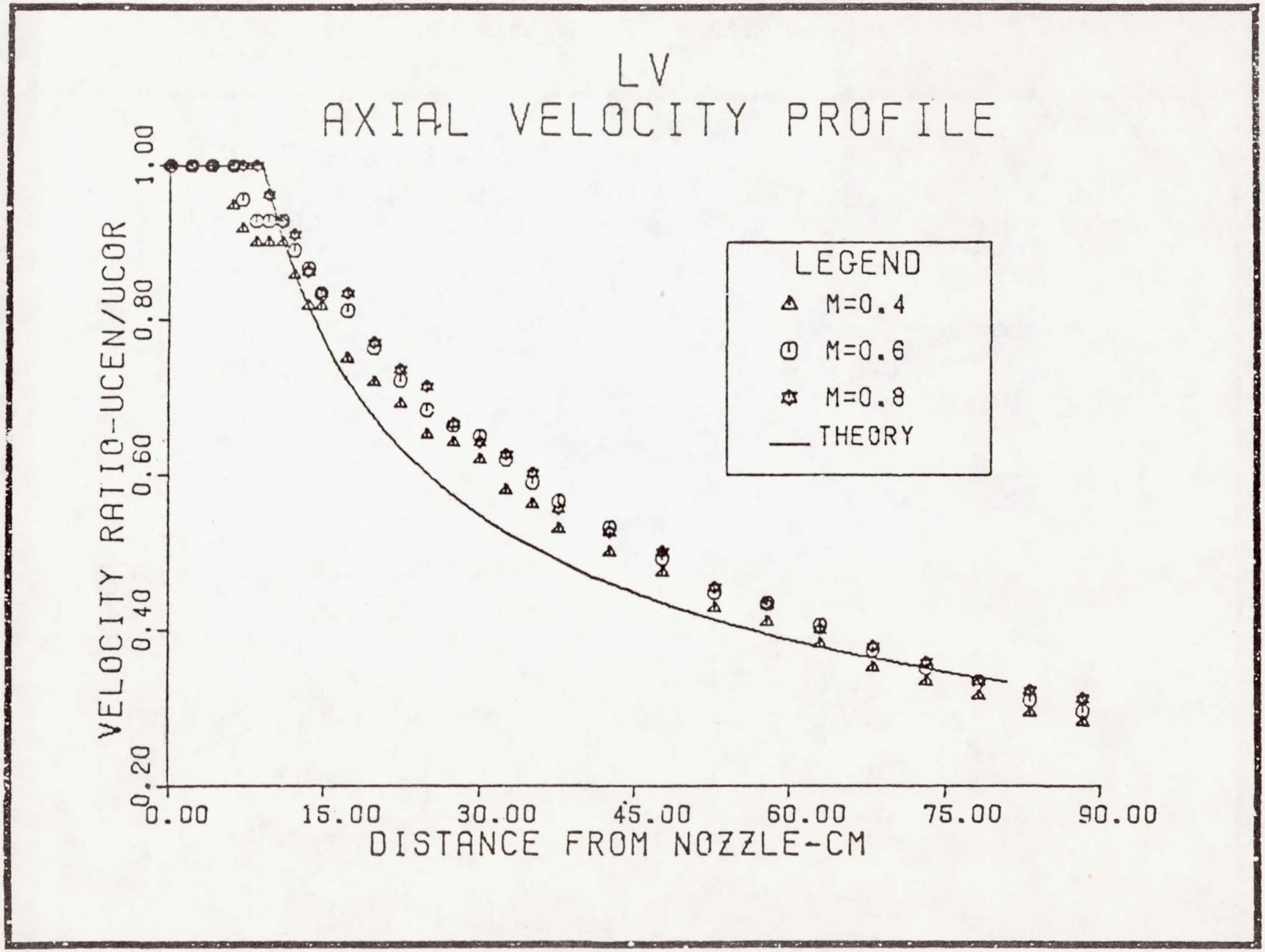

FIG. 2 LV AXIAL VELOCITY PROFILE.

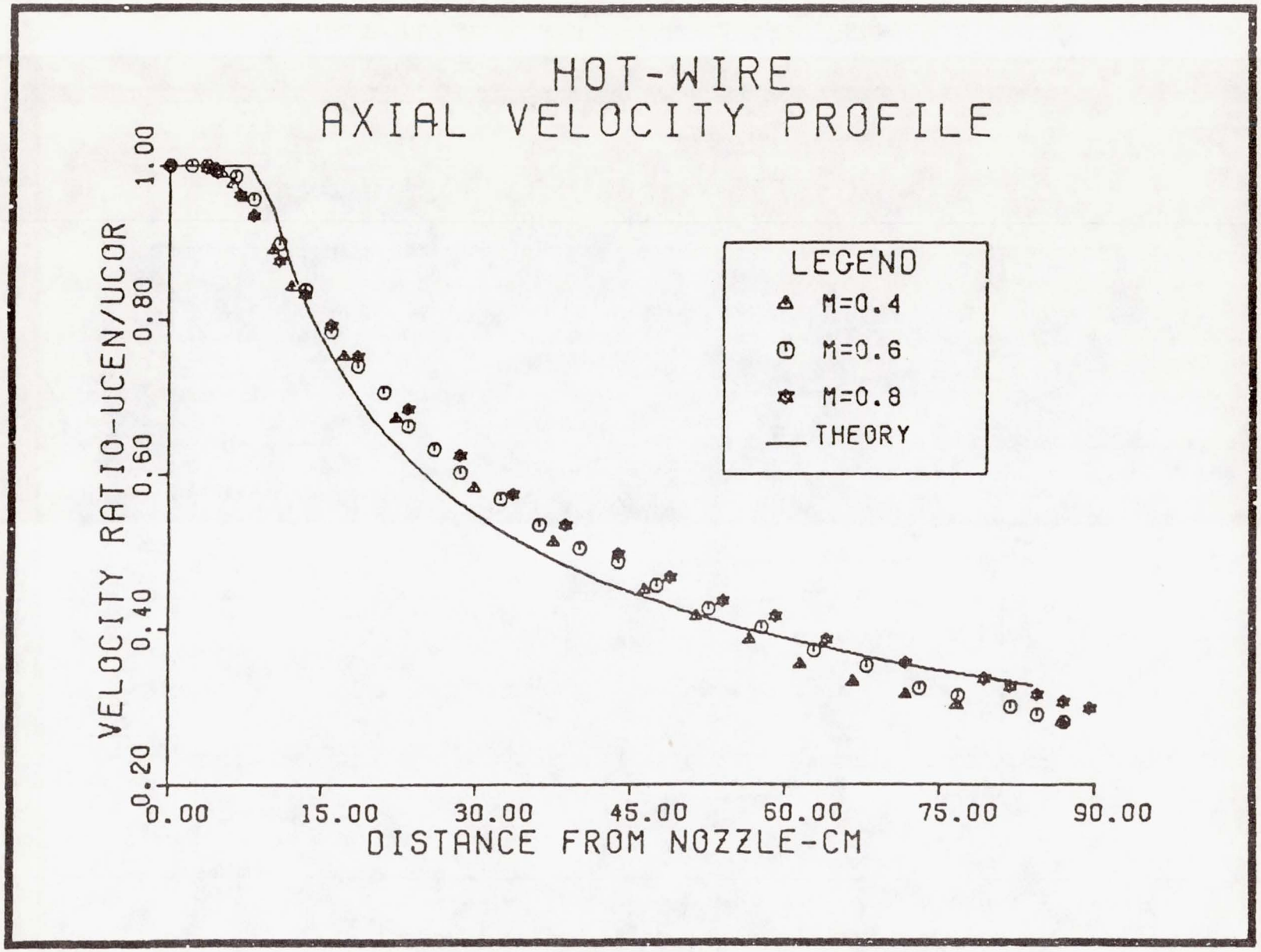

FIG. 3 HOT WIRE AXIAL VELOCITY PROFILE.

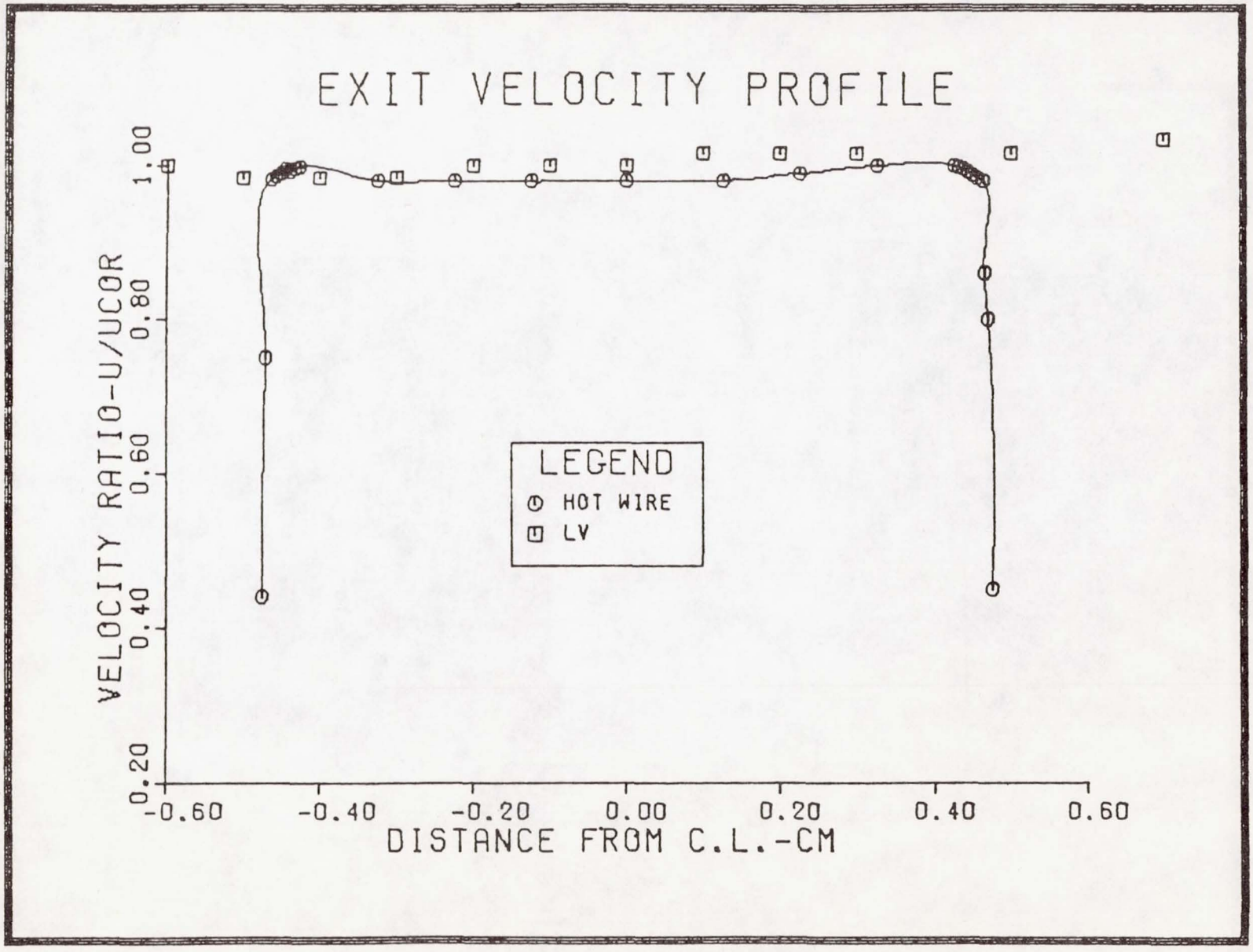

FIG. 4 HOT WIRE AND LV NOZZLE EXIT PROFILE.

Figure 5 - Velocity Correlation Functions.

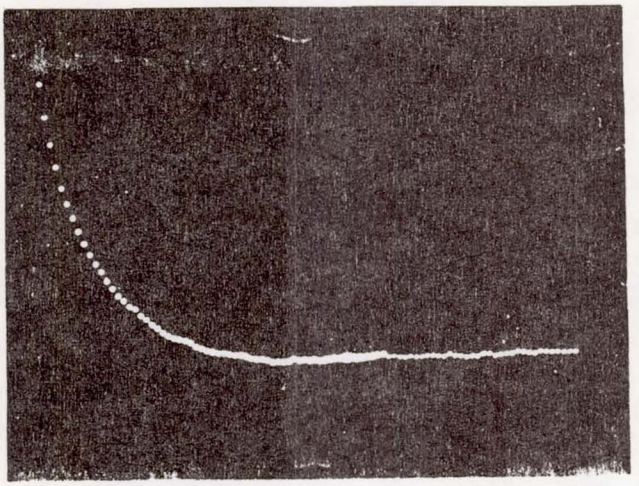

(a) Mach 0.6 50 cm Station Y=0 cm

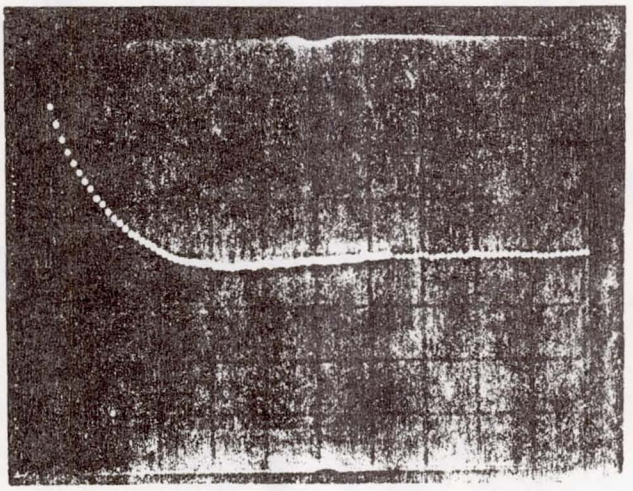

(b) Mach 0.4 24 cm Station Y=1.5 cm

Figure 6 - Temperature Correlation Functions.

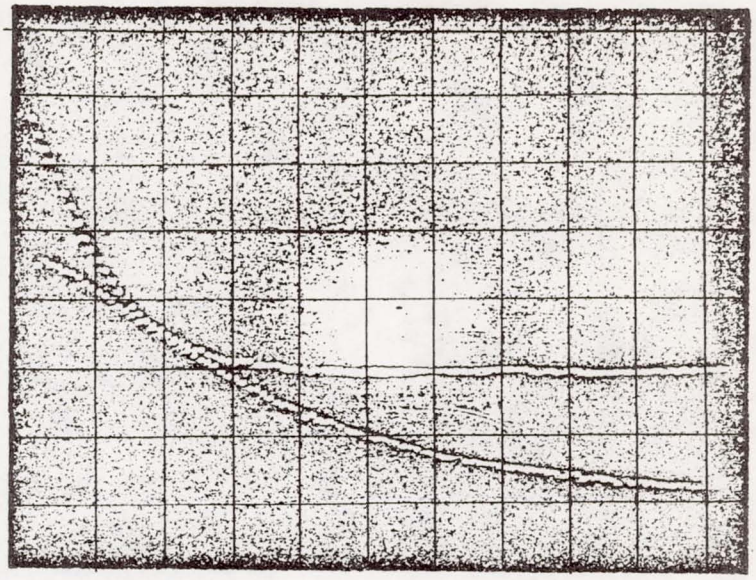

(a) 0.6 Mach, 50 cm Test Station, y = 0

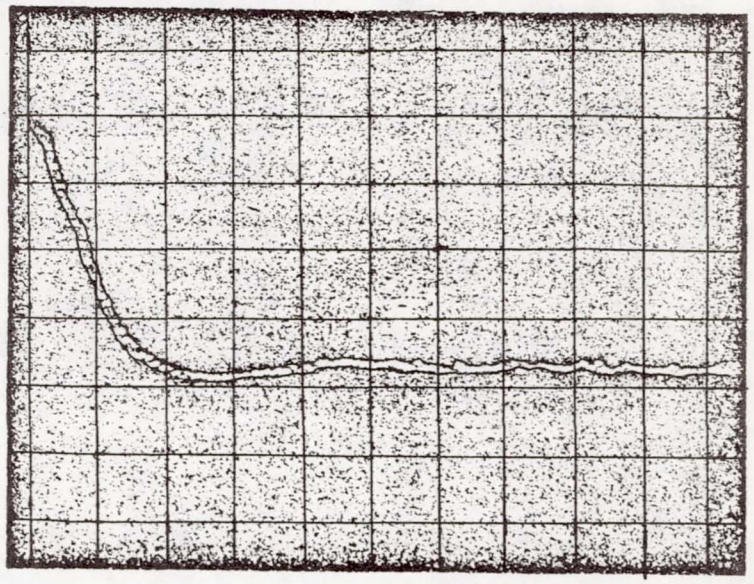

(b) 0.4 Mach, 25 cm Test Station, y = 1.5 cm

Figure 7 - Measured Beam Images.

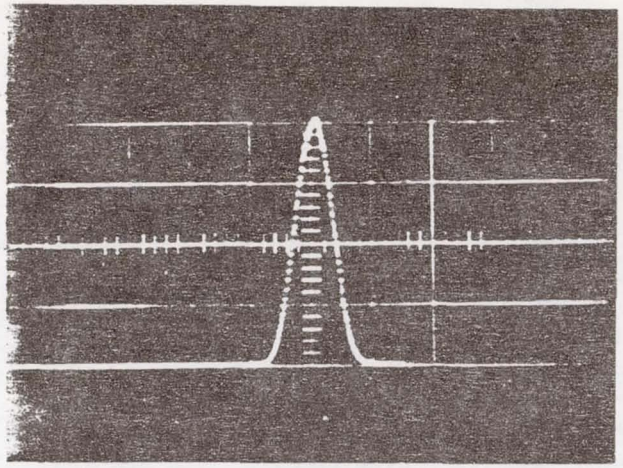

(a) 50.0 mm Beam, 6328 Å

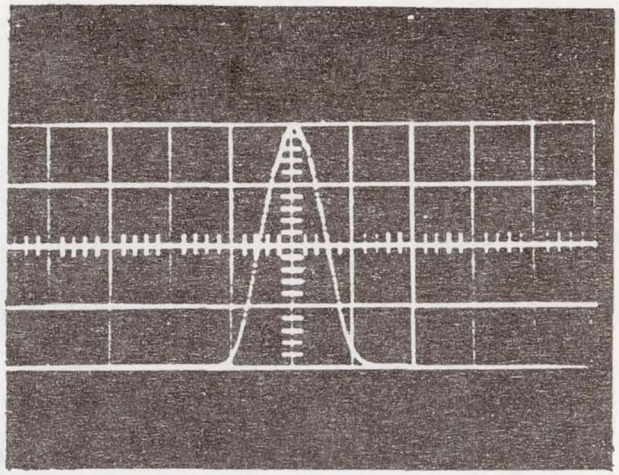

(b) 26.8 mm Beam, 6328 Å

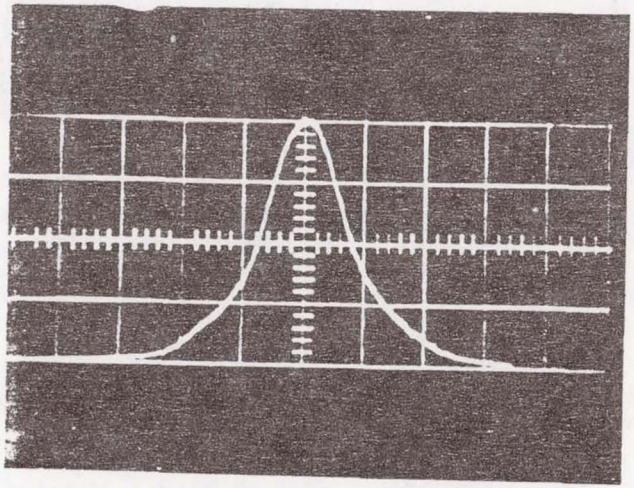

(c) 11.0 mm Beam, 6328 Å

Figure 7 - Measured Beam Images (Cont'd).

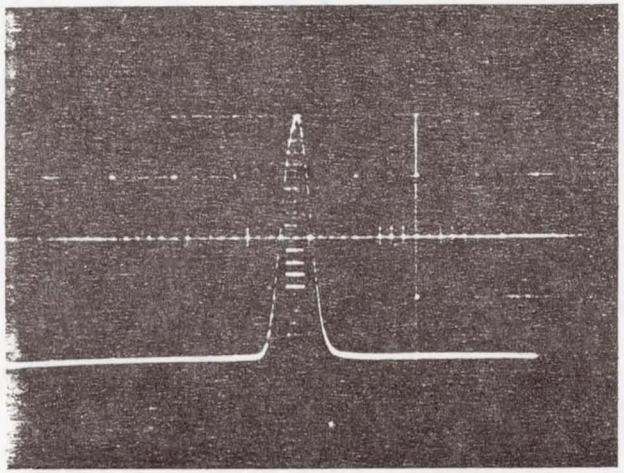

(d) 50.0 mm Beam, 4416 Å

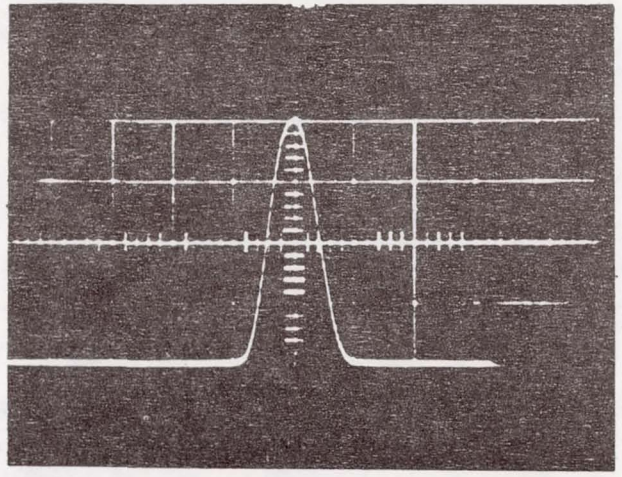

(e) 26.0 mm Beam, 4416 Å

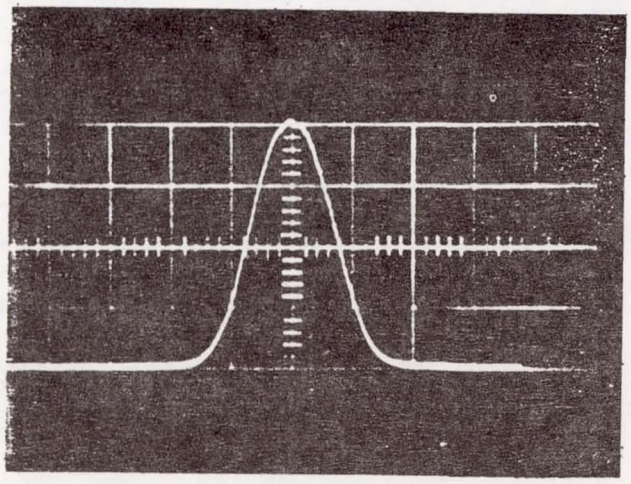

(f) 12.3 mm Beam, 4416 Å

Figure 8 - Calculated Beam Image.

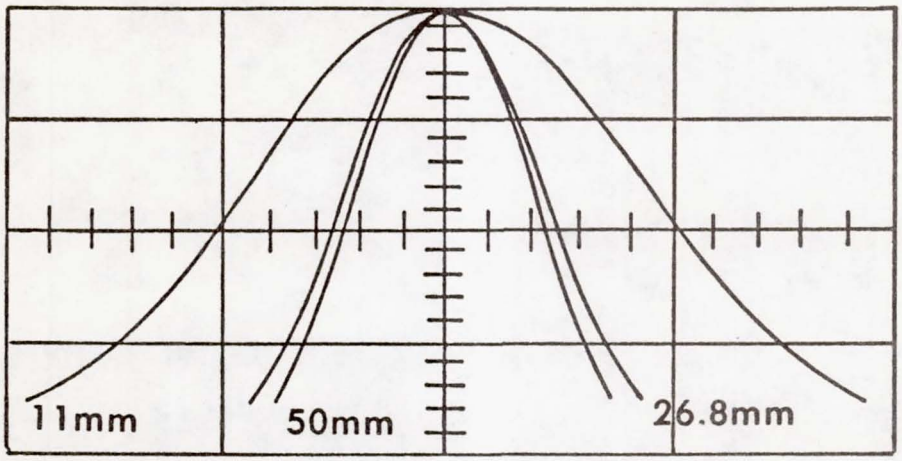

(a) 6328 Å

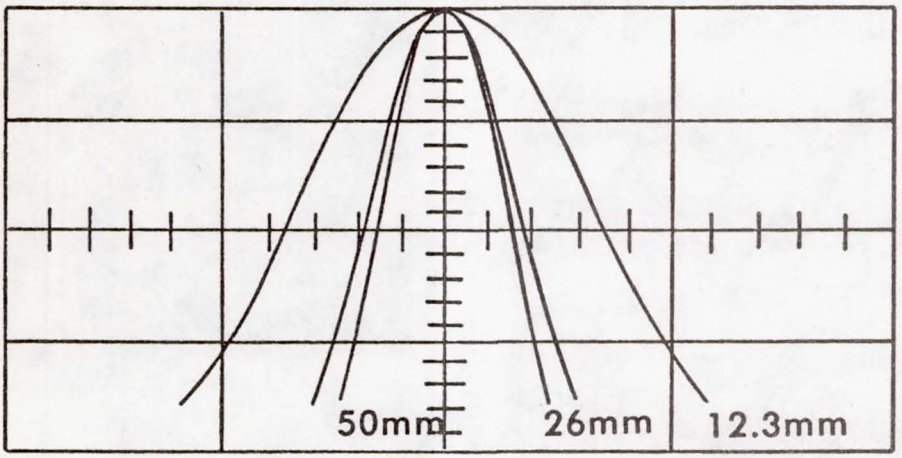

(b) 4416 Å

Figure 9 - Degraded Beam Images.

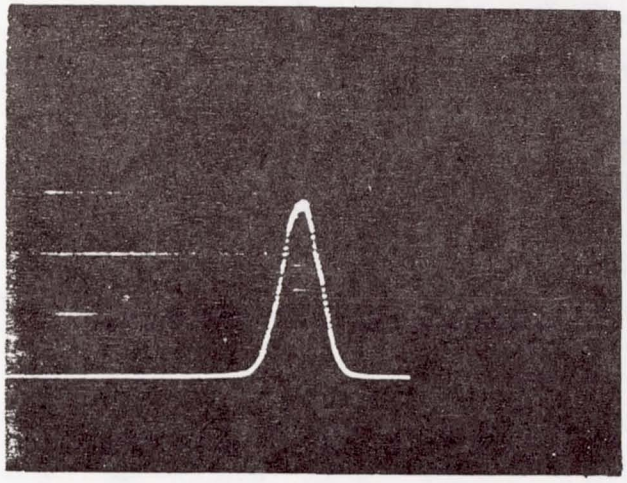

(a) 50.0 mm Beam, 6328 Å
Mach 0.6, 25 cm Station

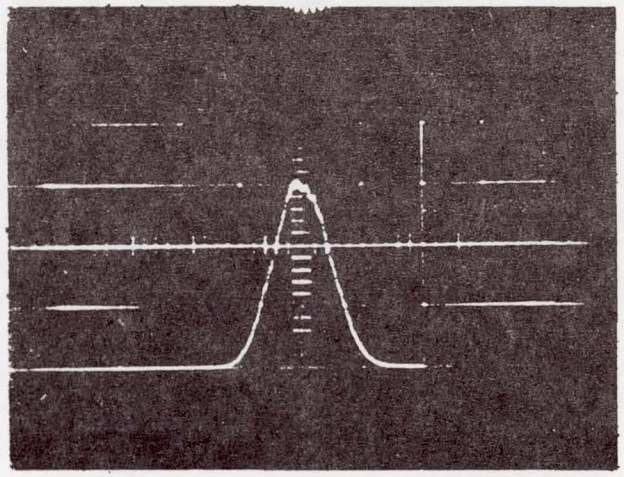

(b) 26.8 mm Beam, 6328 Å
Mach 0.6, 25 cm Station

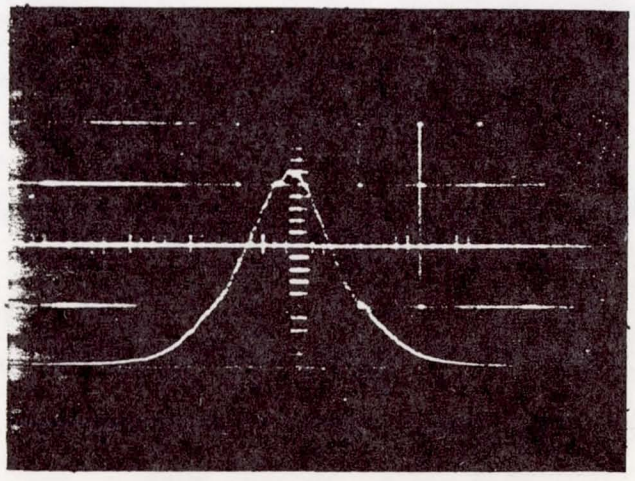

(c) 11.0 mm Beam, 6328 Å
Mach 0.8 50 cm Station

Figure 9 - Degraded Beam Images (Cont'd).

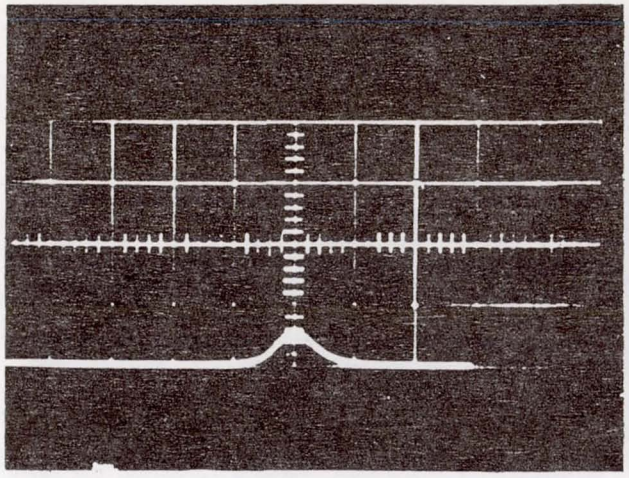

(d) 50.0 mm Beam, 4416 Å
Mach 0.8, 25 cm Station

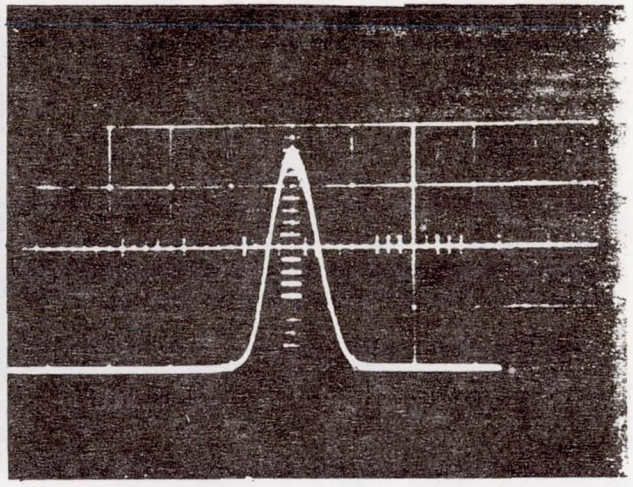

(e) 26.0 mm Beam, 4416 Å
Mach 0.6, 75 cm Station

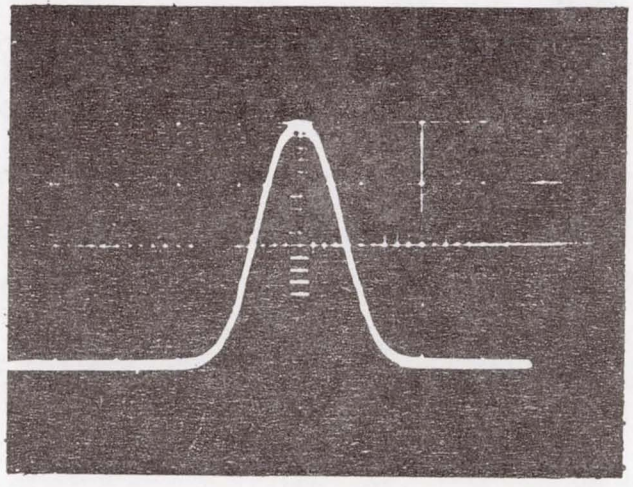

(f) 12.3 mm Beam, 4416 Å
Mach 0.4, 50 cm Station

Figure 10 - Average Degraded Intensities.

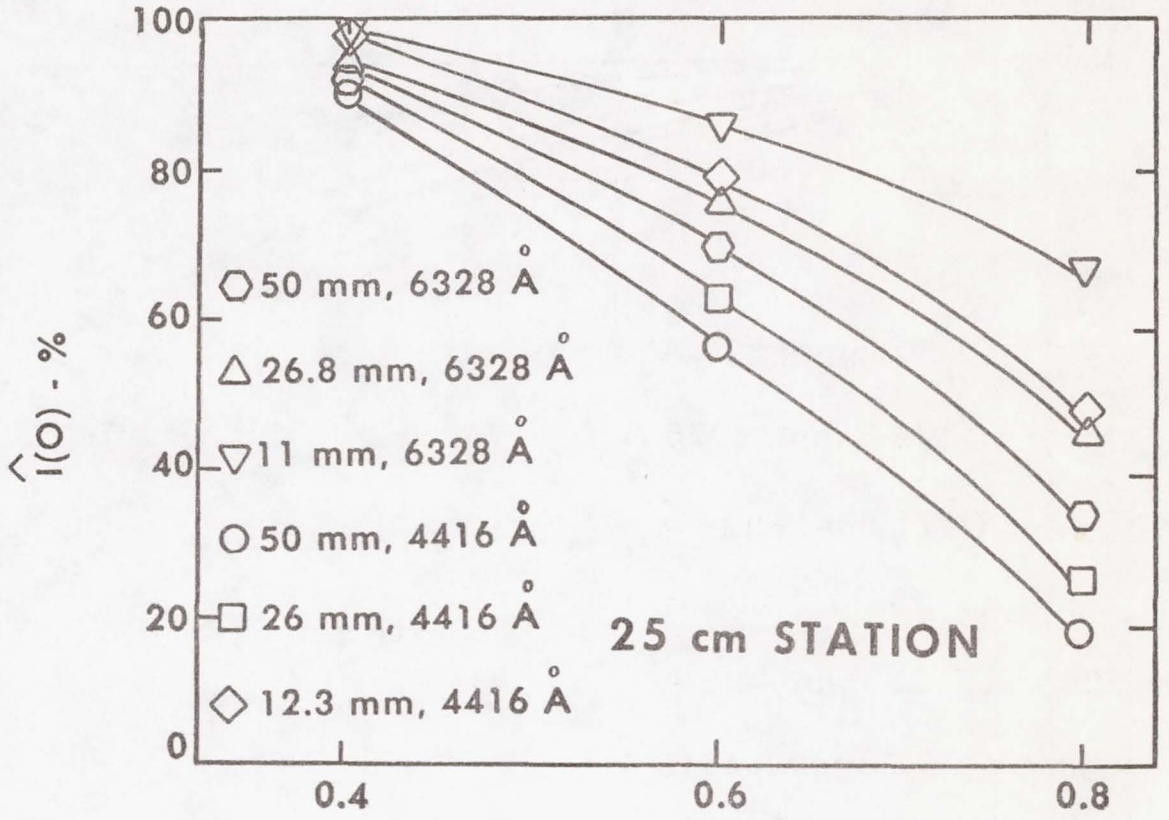

Figure 10 - Average Degraded Intensities.

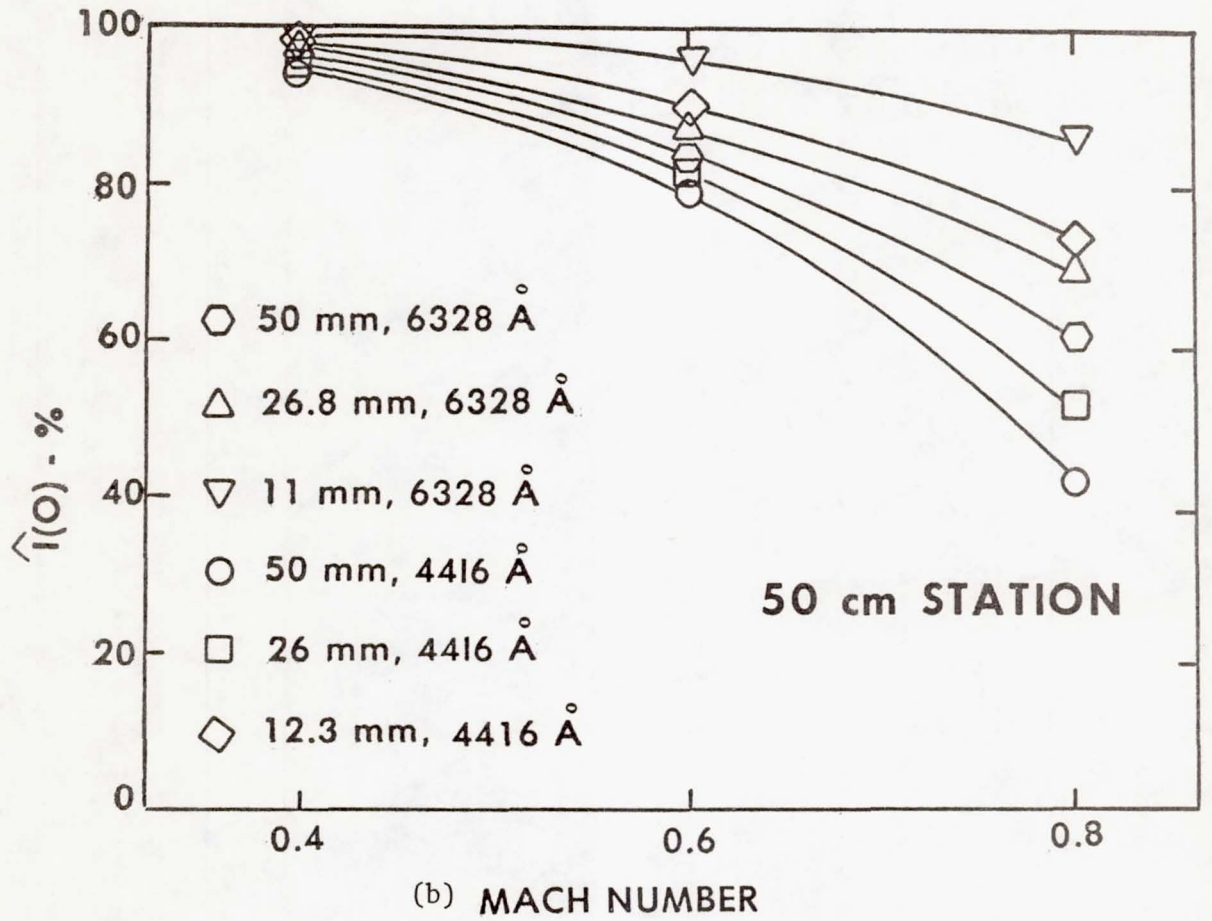

Figure 10 - Average Degraded Intensities (Cont'd).

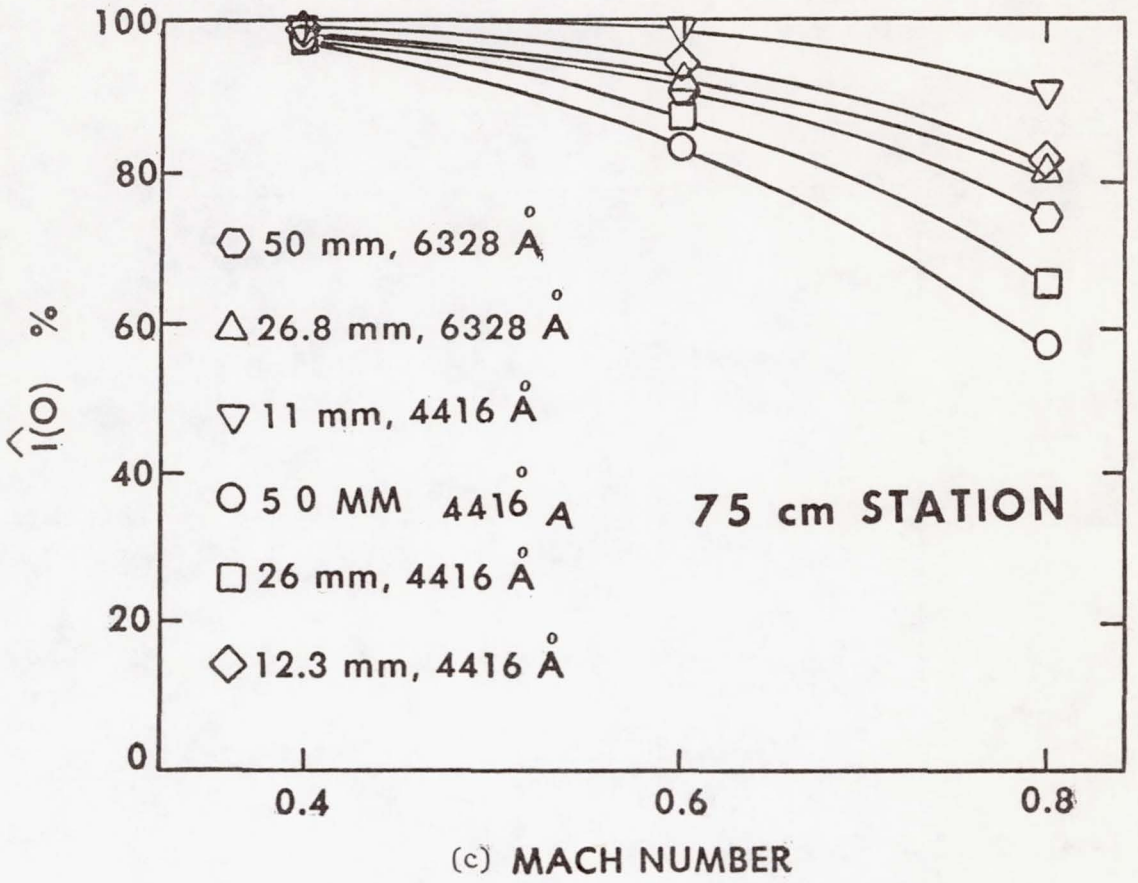

Figure 11 - Far-field Spot Intensities.

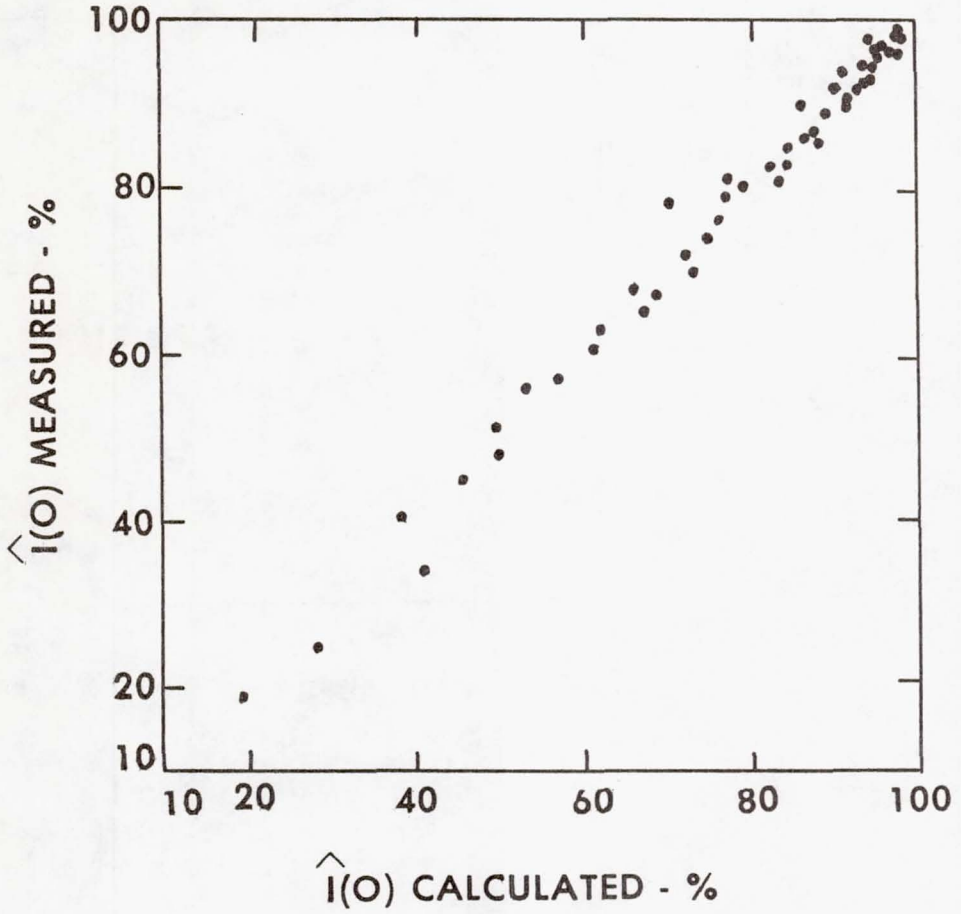

Figure 12 - Laboratory Schematic.

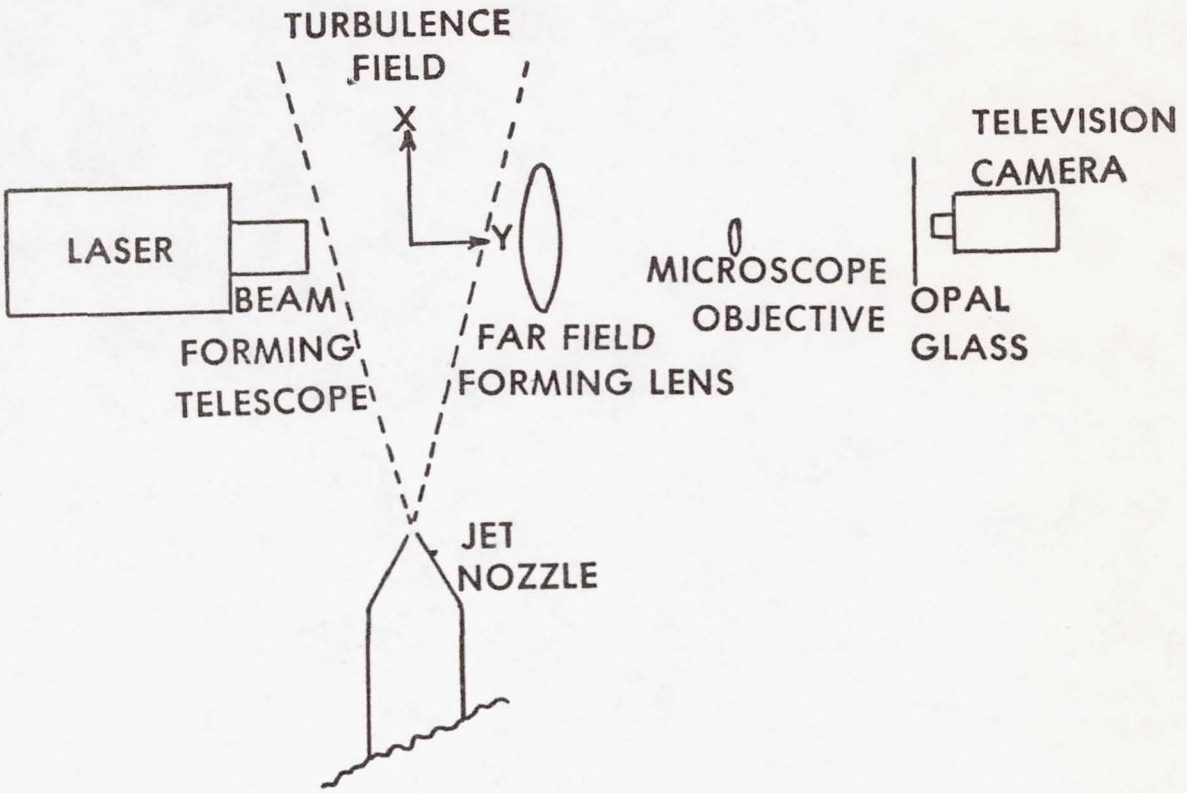

OVERVIEW OF 6-X 6-FOOT WIND TUNNEL AERO-OPTICS TESTS

Donald A. Buell
Ames Research Center

SUMMARY

The paper describes the splitter-plate arrangement used in tests in the 6-x 6-Foot Wind Tunnel and how it was configured to study boundary layers, both heated and unheated, shear layers over a cavity, separated flows behind spoilers, accelerated flows around a turret, and a turret wake. The flows are characterized by examples of the steady-state pressures and of velocity profiles through the various types of flow layers. An introduction to the instrumentation used by other authors is included.

INTRODUCTION

A series of wind-tunnel tests was conducted as a cooperative program between NASA, the Air Force Weapons Laboratory, the Air Force Flight Dynamics Laboratory (AFFDL), and their contractors over a period of 4 years. The goal was to simulate flows representative of the airflow around an airplane, to measure the characteristics of optical wave propagation through the flow, to quantify the aerodynamic disturbances that distort the optical beam, and to confirm assumed relationships between aerodynamics and optics. The 6-x 6-Foot Wind Tunnel was selected because it permitted the use of models large enough to give a reasonable resolution with existing instrumentation. It also provided transonic flow, controllable Reynolds number, and less optical distortion than other Ames facilities.

This paper is an overview of the tests, with descriptions of the models and the steady-state flow characteristics of each model. In ensuing papers, Mr. Raman will describe the dynamic pressures which he measured in the flow and on the model surfaces; Capt. Wade Bailey will describe optical measurements that he and others from the Air Force Weapons Laboratory made by passing laser beams through the flows; Dr. Trollinger will describe his interferometry; Drs. William Rose and Dennis Johnson will describe the dynamic density characteristics inferred from their measurements with hot wires and a laser doppler velocimeter; and Dr. August Verhoff will compare optical degradations computed from the density characteristics with the degradations observed. The author is indebted to Mr. Raman for the boundary-layer profile data presented herein and to Maj. John Otten for his efforts in organizing and coordinating the test program. The basic model was

designed and built by McDonnell-Douglas Corporation under contract to the Air Force Weapons Laboratory. Later modifications were made in NASA shops at Ames Research Center.

Many of the tests (with pins, fences, and a cavity) have been reported in reference 1, and figures from that reference have been used where relevant. Later tests with a turret model have not been reported elsewhere and are described in somewhat more detail. The turret model was a small-scale replica of the "coelostat" model on which loads have been measured both at NASA and AFFDL. The "coelostat" loads data will be discussed in later papers on the large-scale aero-optics tests. This particular turret configuration was not selected because of its attributes but rather because of the availability of the model from AFFDL and the availability of comparison data.

SYMBOLS

C_p	static-pressure coefficient, $\frac{\bar{p} - \bar{p}_\infty}{q}$
$\dot{m}$	mass flow of air injected into cavity, kg/sec
M	free-stream Mach number at a station 97 cm downstream from the plate leading edge
M_L	time-averaged local Mach number at arbitrary point in the flow
p	static pressure at point of measurement, N/m^2
p_T	total pressure at point of measurement, N/m^2
p_∞	free-stream static pressure where M is defined, N/m^2
p_{T_∞}	free-stream total pressure where M is defined, N/m^2
q	free-stream dynamic pressure, $1/2\rho_\infty V_\infty^2$, N/m^2
R	free-stream Reynolds number per meter, $\frac{\rho_\infty V_\infty}{\mu_\infty}$
R_{EP}	component parallel to splitter plate of distance from center of turret to external probe, cm
V_∞	free-stream velocity where M is defined, m/sec
x	coordinate in downstream direction (figs. 2 and 6), cm
y	coordinate in cross-stream direction parallel to plate (figs. 2 and 6), cm
z	distance from surface of plate, cm
θ	azimuth angle, when θ_{Cp} and θ_{EP} are equal, deg
θ_{CP}	azimuth angle of turret cavity and cavity probe (fig. 7), deg
θ_{EP}	azimuth angle between stream direction and R_{EP} (fig. 6), deg
μ_∞	free-stream viscosity where M is defined, kg/m-sec
ρ_∞	free-stream density where M is defined, kg/m^3
$\bar{(\ )}$	time-averaged quantity

MODELS

Splitter Plate

Figure 1 shows the splitter plate used to isolate the modelled flows from the wind-tunnel boundary layer. The flows of interest were examined in the region between the return mirror and the plate. A window in the plate permitted laser beams to be passed through the pylon and the flow to the mirror and back to the instrumentation outside the wind tunnel.

In preliminary entries, the mirror was not used; instead, a splitter plate was attached to both wind-tunnel walls, and the beam was passed across the entire wind tunnel. However, it was found that the free-stream introduced enough unwanted disturbances to make the optical signal/noise ratio marginal, and the mirror was then added.

Pin/Fence/Cavity Models

Figure 2 is a view of the splitter plate from the center of the wind tunnel in two of many configurations. The figure also shows the probe supports for holding hot wires, pressures probes, etc. One of the supports was remotely adjustable in x and z, while the other was manually adjustable in 3 dimensions. The turbulence-generating pins were intended to thicken the boundary layer and improve the probing resolution. Other arrangements of pins were used in preliminary tests and are the subject of reference 2. The seeding pins were the means of adding particles to the flow to enhance the signal to a laser doppler velocimeter and were left in for most of the tests. Porous spoilers of various sizes and porosities could be attached ahead of the test volume. A cube-shaped cavity could also be installed in place of the window. A glass bottom in the cavity allowed a laser beam to be passed through the shear layer. It was also possible to change the front wall of the cavity to a porous wall for the purpose of injecting air into the cavity.

Cavity flow is an essential part of the simulation because it is often desirable to omit windows in the optical system being simulated. The power levels of projected high-energy lasers are such that window materials generally absorb enough energy to induce significant index of refraction variations. This, in turn, causes serious degradation in far-field intensity. Fences have proven to be an effective means of inhibiting cavity resonance. Hence, it was deemed useful to simulate the shear flows from cavities and fences, both separately and in combination. The various model configurations are described in table 1. Fence details are sketched in figures 3 and 4.

Heated Model

Figure 5 shows the splitter plate with a heated copper plate installed upstream of the test volume. It was possible to maintain the plate

temperature about 50°C above the total temperature of the wind tunnel to simulate a heat leak from an aircraft. However, the amount of energy added by this means was small relative to that in the nearby airstream, and only a few of the configurations were tested in combination with the heated plate.

Turret Model

Figures 6 and 7 show details of the turret and fairing mounted on the plate, and figure 8 is a photograph of the turret configuration. For these tests, the "external" probe support was made remotely adjustable in 3 directions, necessitating the opening of a large cavity in the downstream portion of the pylon. The fence is not intended to affect the flow around the turret, but only to protect the wiring in the pylon cavity. The turret azimuth could be controlled remotely, and a probe support in the turret was also remotely adjustable along an imaginary optical beam emanating from the turret cavity. It should be noted that no optical measurements were actually made with the turret configuration, except for interferometer studies by Dr. Trollinger. In order to cover the mechanism, the turret and fairing were mounted on a thin plate bolted on top of the aft 2/3 of the original splitter plate.

The fairing used in some of the tests with the turret was intended to reattach the flow downstream of the turret and to move the shock waves off of the turret surface. Coordinates of the fairing are given in table 2. A gap of about 0.16 cm existed between the fairing and turret.

INSTRUMENTATION

Optical measurements were under the direction of the Air Force Weapons Laboratory and consisted of sending laser beams of various wave lengths and diameters through the flow to detectors. Both line-spread function and modulation transfer function were evaluated with fast-scanning devices that minimized vibration interference.

Instruments for determining aerodynamic characteristics of the flows included hot wires, operated at both high and low over-heats, and pressure transducers, both dynamic and steady-state. These devices were operated in pairs or in greater multiples to obtain correlations from which scale lengths could be deduced and statistical averages could be determined. The pin, fence, and cavity flows were also probed with a laser-doppler velocimeter, which measured particle velocity, and with various forms of interferometry. Details of these measurements are reported elsewhere in this conference paper. Preliminary results from the hot wires and laser-doppler velocimeter have been reported in reference 3.

The flows were also probed with a multiple-tube total-pressure rake and by a 5-hole hemisphere-head directional probe similar to that described in reference 4. In addition, steady-state pressure taps and high-response pressure transducers were distributed about the plate and turret surfaces. All of the aerodynamic instrumentation except the directional probe are described in greater detail in reference 1.

The directional probe measured mean pressures at the intersection of the hemisphere surface with the axis of symmetry and on 4 equally-spaced rays from the center of the hemisphere and 45° from the axis. The probe was calibrated in a 5-cm jet at Mach numbers from 0.3 to 1.5 to give angle of attack, angle of sideslip, local Mach number, local total pressure, and derived parameters. The probe was recalibrated at zero flow angle in the 6-x 6-Foot Wind Tunnel. Figure 9 shows how the Mach number indicated by a ratio of pressures on the probe varies with true Mach number. Its sensitivity to such parameters as Mach number was limited but marginally usable at supersonic speeds. The calibration was checked at a high flow angle over the entire range of Mach numbers in the 6-x 6-Foot Wind Tunnel. The results are shown in figure 10. Errors are generally less than 5 percent except at M = 1.2. These results were obtained with curve fits of the parameter versus indicated flow angle and indicated Mach number. It is recognized that in the wake there would be an additional error of unknown magnitude due to fluctuation of the pressures being measured.

TESTS

The tests of the pin, fence, cavity, and heated plate models were performed in three wind-tunnel entries at free-stream Mach numbers from 0.6 to 0.9 and Reynolds numbers of 6.6 and 9.8 million/m (2 and 3 million/ft). Tests of the turret model in a separate entry were performed at free-stream Mach numbers from 0.62 to 1.49 at a Reynolds number of about 4.9 million/m (1.5 million/ft) and at Mach numbers from 0.62 to 0.95 at Reynolds numbers of 9.8 million/m (3 million/ft). For calibrations of the directional probe, the Mach number range was extended to 0.4 and 1.7 at the lower Reynolds number.

Model configurations 3 through 6 were investigated with a rake and surface static pressures only. Optical measurements were made on all other models except the turret. Selected models were chosen for an additional detailed probing of the flow, and these are indicated in table 1.

The total temperature of the wind tunnel varied from 290° to 305° K.

RESULTS

The results to be presented here consist only of steady-state pressures measured on the models, on the total-pressure rake, and on the directional probe. The presentation is intended to characterize the various flows simulated in the tests.

Plate Pressures

Figures 11 through 18 show pressure coefficients for the pin model, the fence model, and the cavity model with and without a small fence, for both high and low subsonic speeds. The data are taken from reference 1, which has additional data for these and other models. The test volume which was the object of both optical and aerodynamic probing lies between $x = 0$ and $x = 20$ cm.

The pressure data indicate a high speed flow over the pin area near the leading edge, a deceleration in front of the return mirror, some asymmetry in the tunnel flow as the plate pushed the air towards the opposite side, and a little asymmetry across the plate in the y direction, probably due to the concentration of the seeding pins at the center of the plate. None of these factors was thought to significantly detract from the objectives of the test. The fences are seen to cause considerable disturbance, and the cavity pressures indicate an appreciable gradient in the z direction. Reynolds number effects were typically negligible.

It should be noted here that the solid-wall cavity resonated in a depth mode at the low Mach number and in a fore-aft mode at the high Mach number. When the upstream cavity wall was made porous to permit air injection from a plenum next to the cavity wall, the acoustical absorption was sufficient to inhibit resonance even without air injection. The thick boundary layer approaching the cavity is thought to have also contributed to this result. Despite the dynamic air movement induced by the resonance, the steady-state pressures were not appreciably affected by the resonance, and the data of figures 15 and 16 are reasonably representative of either case.

Turret Pressures

Figures 19 through 23 present steady-state pressure coefficients over the turret and on the plate beside the turret. The turret cavity azimuth was 120°, at which angle the static-pressure taps in the turret were approximately streamwise. The figures show that there was little pressure recovery on the downstream side of the turret at high Mach numbers. Even the plate pressures in figures 20 and 22 indicate the presence of a sizable wake at a Mach number of 0.95. The main effect of the fairing appears to be increased velocities over and beside the turret except in the cutout region between the turret and fairing.

Boundary-Layer Profiles

Figures 24 through 26 show velocities calculated from pressure measurements in the pin, fence, and cavity boundary layers. One can see in figure 24 that the 2 cm boundary layer without pins was tripled in thickness by either the turbulence pins or seeding pins and that the combination (model 1) yielded a layer 8 cm thick. While not duplicating the profile of a naturally occurring boundary layer, this layer was thick and repeatable and was the subject of extensive measurements. Reference 1 shows that Mach number, Reynolds number, and fore-aft position had only minor effects on the profile. Figure 25 shows the large fence shear layer which proved to be detrimental to optical propagation. The mirror is seen to have negligible effect. Figure 26 shows profiles over the cavity which are little affected by resonance (model 14 to model 8) and are actually fairly close to the profiles of model 3, which also had seeding pins but no cavity. The effects of fence height and porosity are evident. Both model 13 and 14 were probed extensively.

Figures 27 and 28 show rake measurements upstream and downstream of the turret. Although no attempt was made to calculate velocities, it is apparent that the approaching boundary layer was similar to previous models without pins. Figure 28 indicates that the wake enlarged abruptly as Mach number was increased. Hot wire measurements in the wake have led to calculated values of optical degradation that were very large under some conditions.

A more relevant picture of the velocity distribution around the turret was given by measurements with the directional probe. This probe was positioned not only at different heights above the plate, but also at different radii from the center of the turret along the line of sight from the turret cavity. Figures 29 through 31 are representative of the magnitude and direction of the Mach number vector at one height above the plate. A large lateral spread of the wake is evident from these data at the higher Mach numbers.

Figures 32 through 35 show the absolute magnitude of the Mach number vectors at different heights above the plate. It is apparent that the wake at an azimuth angle of 150° and a Mach number of 0.95 was much larger than at the other conditions. Even the 90° azimuth position shows a disturbed region of accelerated flow at the higher Mach number which helps to make the higher Mach numbers a special problem in optical propagation. Mach number effects are summarized for one height in figures 36 and 37. The latter figures also illustrate the small Reynolds number effect. A similarly small effect of the fairing is shown in figures 38 and 39.

Figures 40 through 43 give local density data for conditions comparable to the Mach number data shown previously. Density gradients were again most troublesome at the higher Mach number. Both the local mean density and Mach number distributions are required to convert the hot wire readings to density fluctuations, as will be discussed in Dr. Rose's paper.

CONCLUDING REMARKS

This paper has described a series of models which created various flow disturbances in transonic wind-tunnel tests and provided a vehicle for exploring the relationship between aerodynamics and optical propagation. The paper has presented characterizations of the disturbed flows by means of steady-state pressure data and derived parameters measured on the surface, on a rake, and on a directional probe. The flows included thickened boundary layers, shear layers over a cavity and behind porous spoilers, accelerated flow around a turret, and a turret wake. Detailed optical and aerodynamic measurements made in the flows are presented in subsequent papers.

REFERENCES

1. Buell, Donald A.: Aerodynamic Properties of a Flat Plate With Cavity for Optical-Propagation Studies. NASA TM-78487, January 1979.

2. Otten, L. J.; and Van Kuren, J. T.: Artificial Thickening of Transonic Boundary Layers. AIAA Paper 76-51, 1976.

3. Johnson, D. A.; and Rose, W. C.: Turbulence Measurements in a Transonic Boundary Layer and Free-Shear Flow Using Laser Velocimetry and Hot-Wire Anemometry Techniques. AIAA Paper 76-399, July 1976.

4. Armistead, Katharine H.; and Webb, Lannie, D.: Flight Calibration Tests of a Nose-Boom-Mounted Fixed Hemispherical Flow-Direction Sensor. NASA TN D-7461, October 1973.

TABLE 1.- MODEL CONFIGURATIONS

No.	Seed pins	Turbulence-generating pins	Return mirror	Fence height, cm	Fence porosity	Fence hole diameter, cm	Cavity	Cavity wall porosity	Cavity wall hole diameter, cm	Step height cm	Probe measure-ment
1	X	X	X	-	-	-	-	-	-	-	X
2	X	-	X	5.1	0.49	0.37	-	-	-	-	X
3	X	-	X	-	-	-	-	-	-	-	-
4	X	-	-	-	-	-	-	-	-	-	-
5	X	-	-	5.1	0.49	0.37	-	-	-	-	-
6	X	X	-	-	-	-	-	-	-	-	-
7	X	-	X	5.1	0.53	0.95	-	-	-	-	-
8	X	-	X	-	-	-	X	0	-	-	X
9	X	-	X	2.3	0.38	0.24 slits	X	0	-	-	-
10	X	-	X	2.3	0.38	0.52	X	0	-	-	-
11	X	-	X	4.6	0.38	0.52	X	0	-	-	X
12	X	-	X	4.6	0.58	0.99	X	0	-	-	-
13	X	-	X	2.3	0.58	0.99	X	0	-	-	X
14	X	-	X	-	-	-	X	0.49(Upst)	0.32	-	X
15	X	-	X	-	-	-	X	-	0.64slot	-	-
16	X	-	X	2.3	0.58	0.99	X	0.49(Upst)	0.32	-	-
18	-	-	X	-	-	-	-	-	-	0.64	-
19	-	-	X	-	-	-	-	-	-	-	-
20	-	X	X	-	-	-	-	-	-	-	-
21	-	X	X	-	-	-	-	-	-	0.64	-
Turret	-	-	-	4.6*	0.58*	0.99*	Fig.7	0.35	0.16		X

* Fence downstream of turret

TABLE 2.- TURRET - FAIRING COORDINATES

	Upper Surface		Lower Surface	
x, cm	y, cm	z, cm	y, cm	z, cm
-0.23	0.00	4.65		
0.00	0.00	4.83	0.00	4.52
0.00	0.23	4.75		
0.00	0.36	4.52		
1.37	0.00	5.00	0.00	4.39
1.37	0.28	4.98		
1.37	0.56	4.83		
1.37	0.69	4.37		
3.56	0.00	5.08	0.00	3.51
3.56	0.28	5.05	0.48	3.48
3.56	0.56	5.00	0.94	3.40
3.56	0.84	4.85		
3.56	1.07	4.67		
3.56	1.27	4.39		
3.56	1.35	4.11		
3.56	1.37	3.84		
3.56	1.35	3.56		
3.56	1.35	3.38		
4.67	0.00	5.03	0.00	2.57
4.67	0.28	5.00	0.41	2.54
4.67	0.56	4.98	0.79	2.49
4.67	0.84	4.91	1.17	2.41
4.67	1.12	4.80	1.55	2.29
4.67	1.42	4.65		
4.67	1.70	4.37		
4.67	1.80	4.11		
4.67	1.88	3.84		
4.67	1.91	3.56		
4.67	1.91	3.28		
4.67	1.85	3.00		
4.67	1.80	2.72		
4.67	1.80	2.44		
5.82	0.00	4.93	0.00	0.99
5.82	0.28	4.93	0.25	0.99
5.82	0.56	4.88	0.51	0.97
5.82	0.84	4.83	0.76	0.89
5.82	1.12	4.72	1.02	0.81
5.82	1.42	4.60	1.27	0.71
5.82	1.70	4.42	1.50	0.61
5.82	1.98	4.19	1.70	0.46
5.82	2.23	3.84	1.91	0.30
5.82	2.39	3.56		
5.82	2.46	3.28		
5.82	2.51	3.00		
5.82	2.54	2.72		
5.82	2.67	2.13		
5.82	2.82	1.85		
5.82	2.97	1.57		
5.82	3.15	1.30		
5.82	3.33	1.02		

TABLE 2.- Continued

Upper Surface			Upper Surface		
x, cm	y, cm	z, cm	x, cm	y, cm	z, cm
5.82(cont.)	3.56	0.74	13.72	0.00	3.61
5.82	3.81	0.46	13.72	0.51	3.56
5.82	4.19	0.00	13.72	1.02	3.48
			13.72	1.55	3.33
6.93	0.00	4.80	13.72	2.06	3.07
6.93	0.28	4.80	13.72	2.57	2.72
6.93	0.56	4.75	13.72	3.07	2.21
6.93	0.84	4.70	13.72	3.58	1.52
6.93	1.12	4.62	13.72	4.09	0.81
6.93	1.42	4.50	13.72	4.62	0.23
6.93	1.70	4.39	13.72	4.83	0.00
6.93	1.98	4.24			
6.93	2.26	4.04	16.54	0.00	3.02
6.93	2.46	3.84	16.54	0.43	3.00
6.93	2.69	3.56	16.54	0.94	2.90
6.93	2.84	3.28	16.54	1.40	2.77
6.93	2.97	3.00	16.54	1.85	2.57
6.93	3.05	2.72	16.54	2.34	2.26
6.93	3.15	2.44	16.54	2.79	1.85
6.93	3.28	2.13	16.54	3.25	1.27
6.93	3.43	1.85	16.54	3.73	0.69
6.93	3.61	1.57	16.54	4.34	0.00
6.93	3.78	1.30			
6.93	4.01	1.02	19.35	0.00	2.41
6.93	4.24	0.74	19.35	0.41	2.39
6.93	4.52	0.41	19.35	0.82	2.31
6.93	4.88	0.00	19.35	1.22	2.21
			19.35	1.63	2.03
8.08	0.00	4.65	19.35	2.01	1.80
8.08	0.56	4.57	19.35	2.41	1.50
8.08	1.12	4.42	19.35	2.82	1.04
8.08	1.70	4.22	19.35	3.23	0.58
8.08	2.26	3.89	19.35	3.73	0.00
8.08	2.82	3.43			
8.08	3.38	2.79	22.17	0.00	1.65
8.08	3.96	1.88	22.17	0.33	1.63
8.08	4.52	0.99	22.17	0.66	1.60
8.08	5.08	0.30	22.17	0.99	1.50
8.08	5.21	0.00	22.17	1.27	1.40
			22.17	1.63	1.24
10.90	0.00	4.17	22.17	1.96	1.04
10.90	0.53	4.14	22.17	2.29	0.74
10.90	1.09	4.01	22.17	2.62	0.41
10.90	1.63	3.81	22.17	3.00	0.00
10.90	2.18	3.53			
10.90	2.72	3.12	24.99	0.00	0.79
10.90	3.28	2.67	24.99	0.43	0.76
10.90	3.81	1.72	24.99	0.86	0.69
10.90	4.34	0.91	24.99	1.27	0.53
10.90	4.90	0.28	24.99	1.70	0.28
10.90	5.16	0.00	24.99	2.18	0.00
			27.33	0.00	0.00

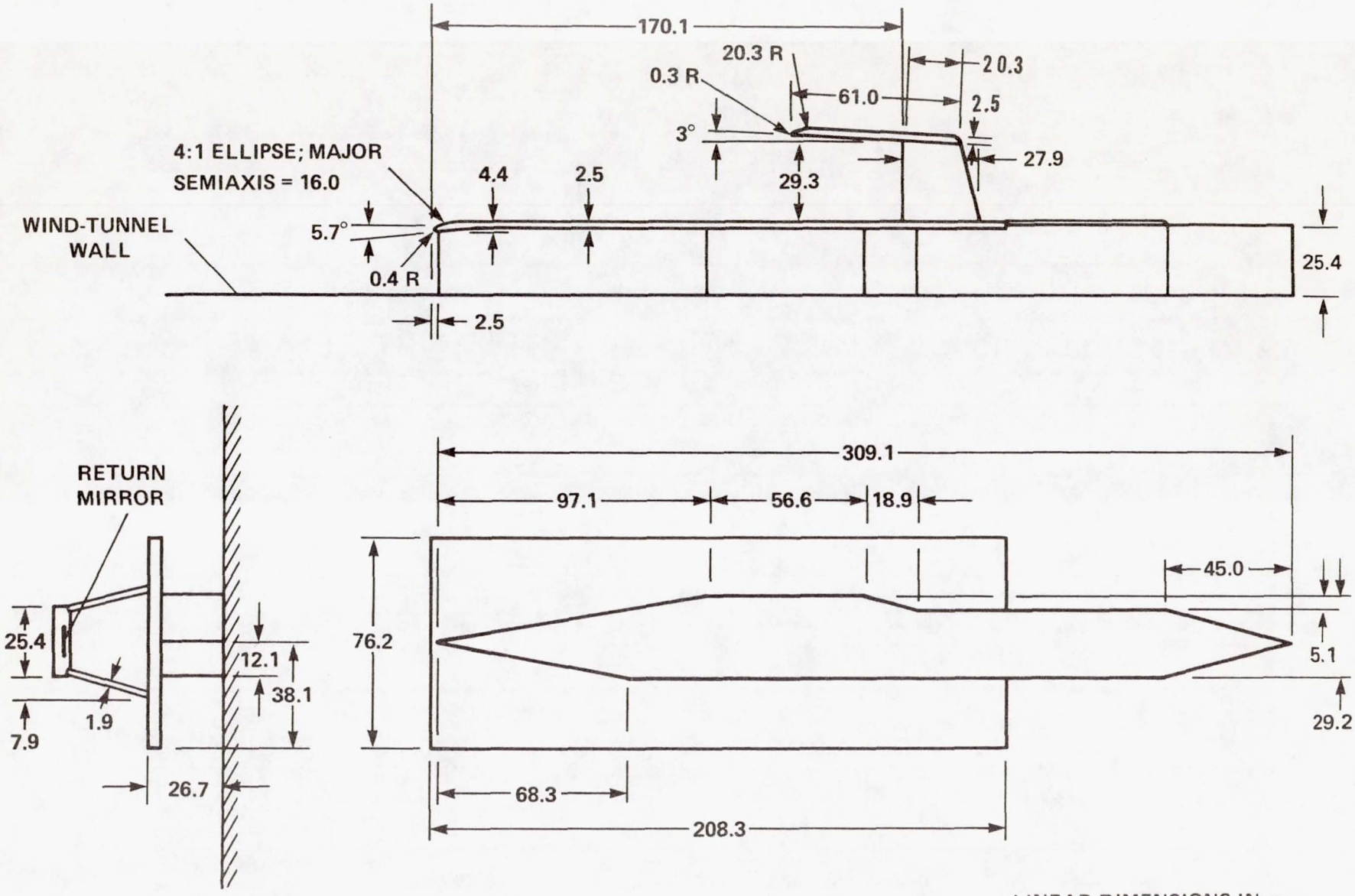

Figure 1.- Three-view drawing of the splitter plate with return mirror.

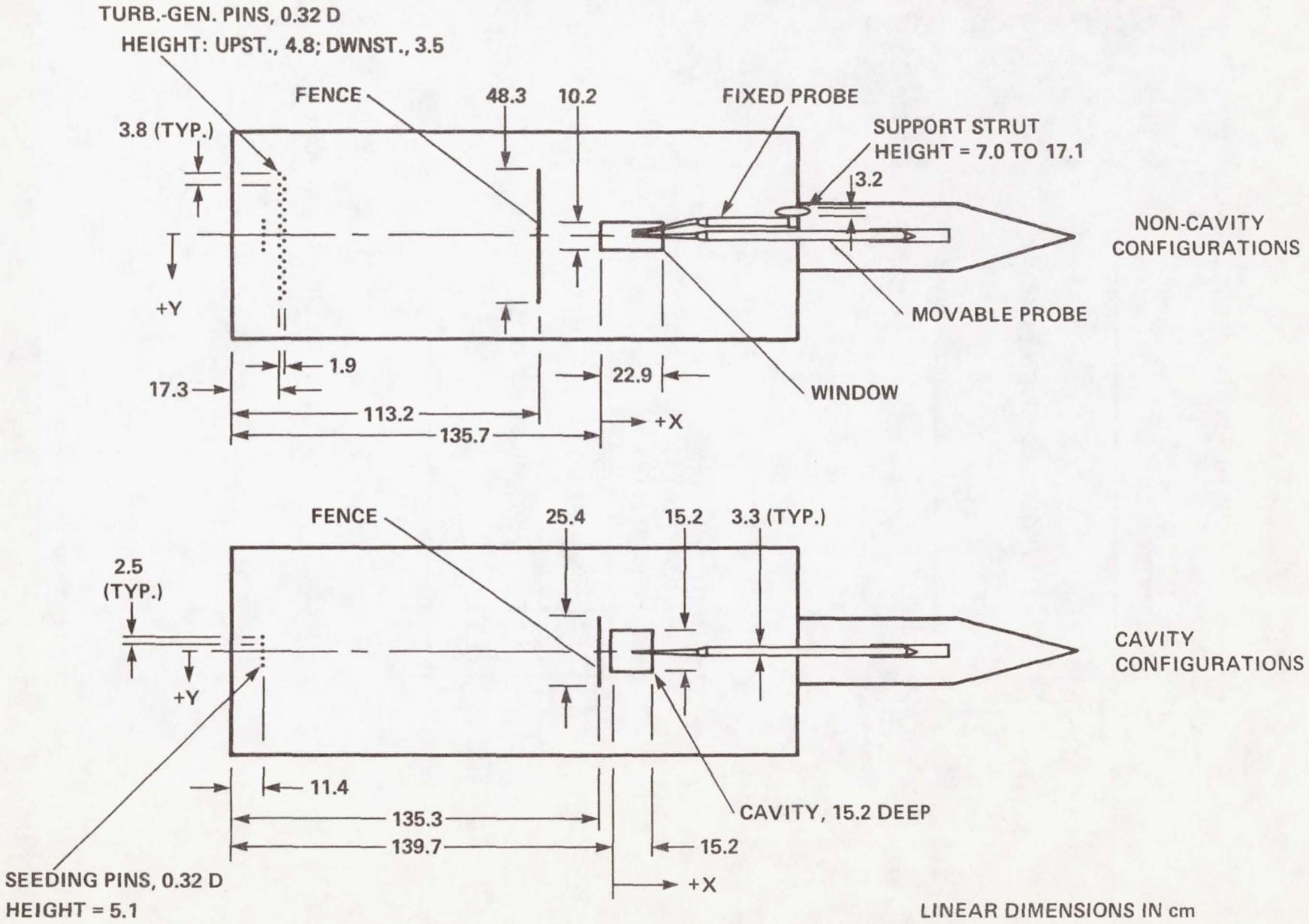

Figure 2.- Top views of the pin, fence, and cavity models (return mirror removed).

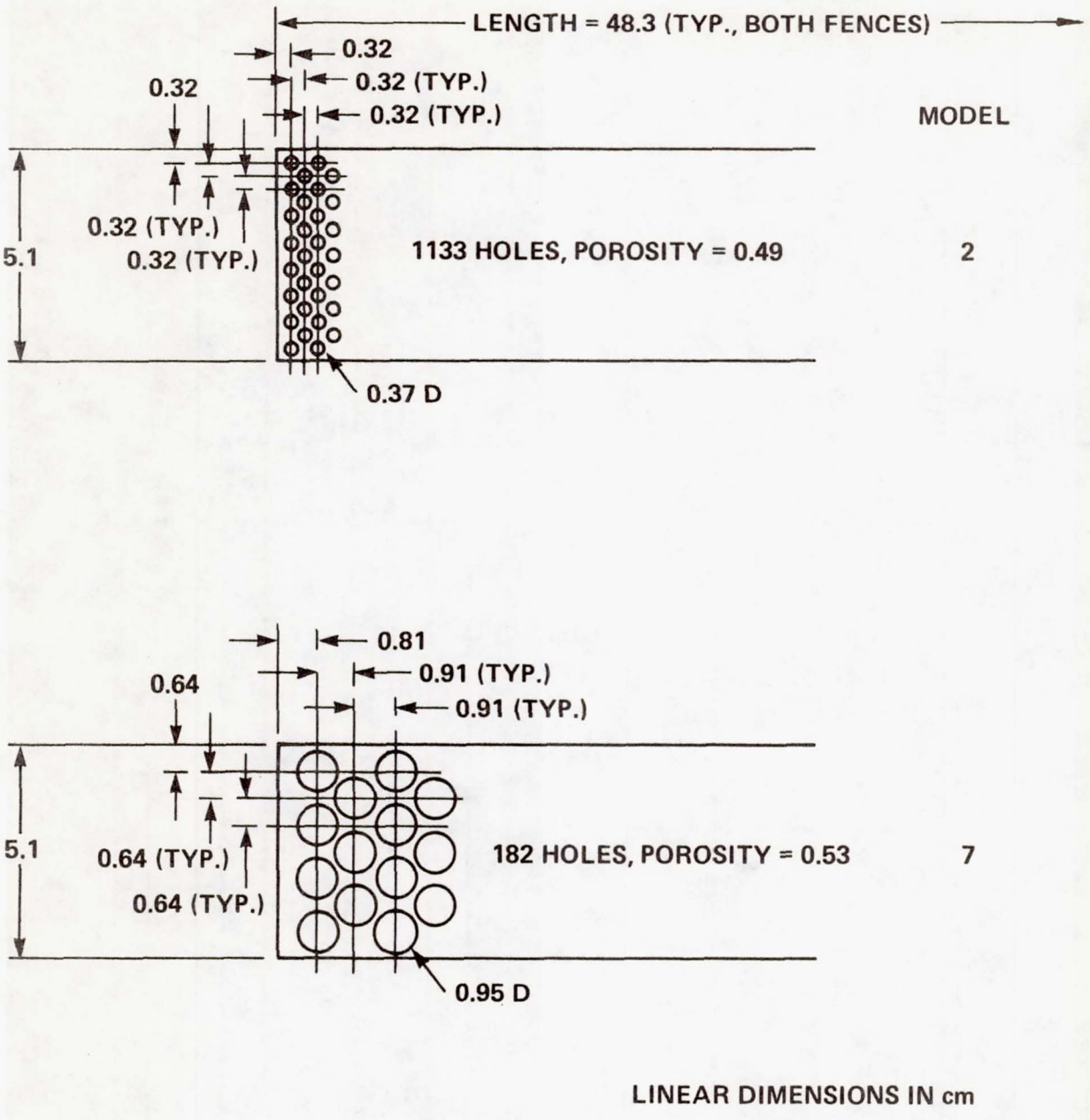

Figure 3.- Sketch of the no-cavity fences; thickness = 0.46 cm.

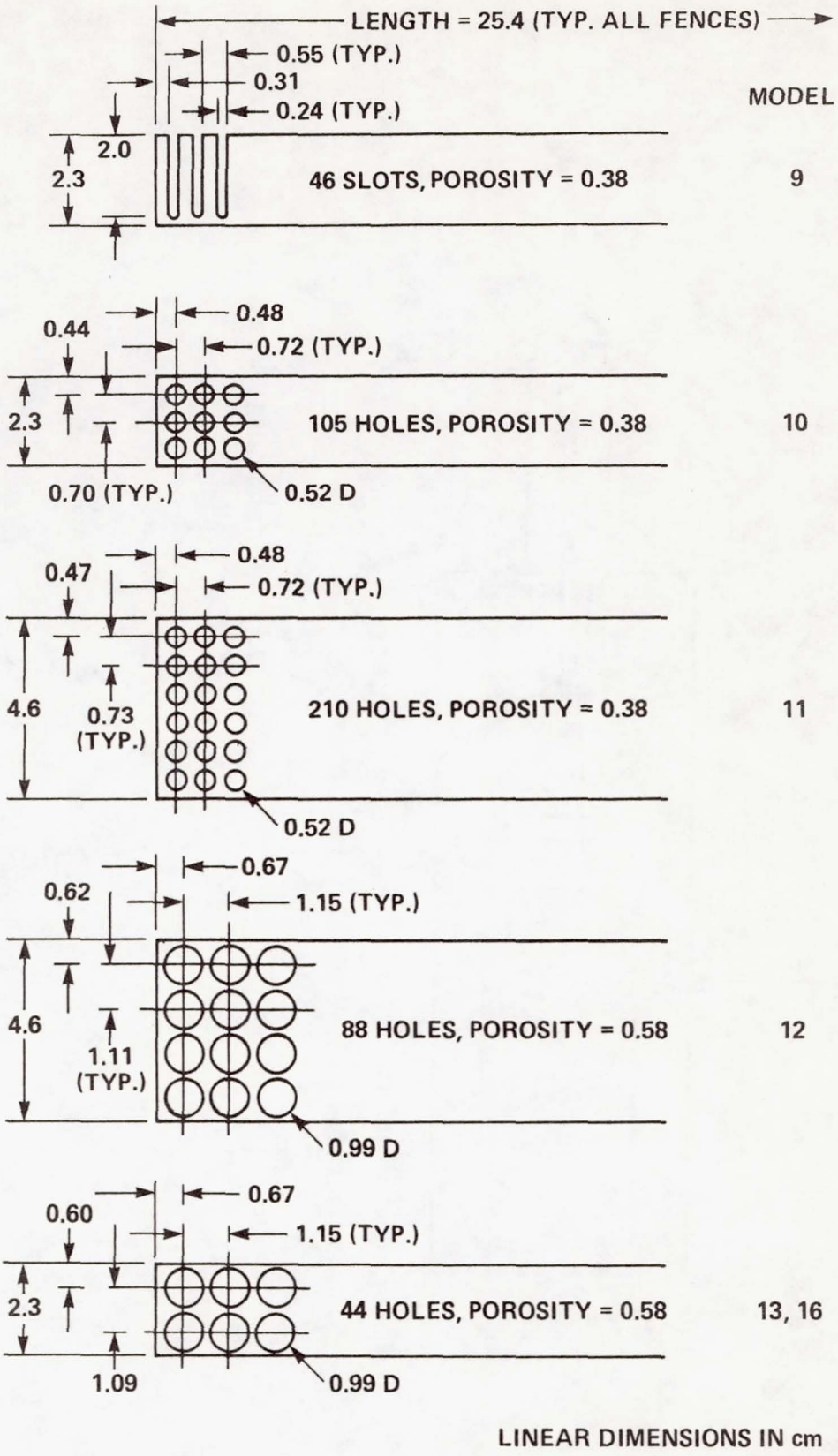

Figure 4.- Sketch of the cavity fences; thickness = 0.48 cm.

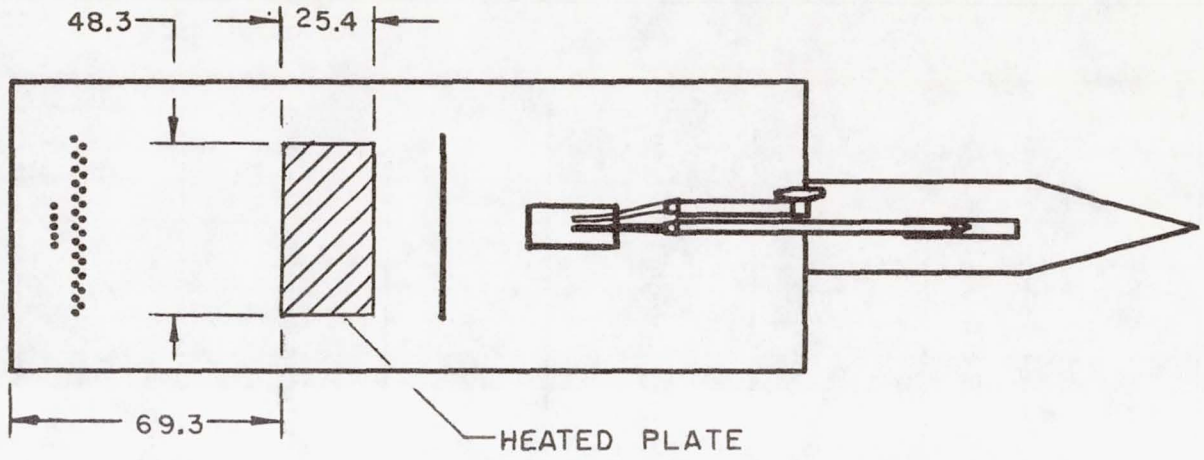

LINEAR DIMENSIONS IN cm

Figure 5.- Top view of the heated-plate model (return mirror removed).

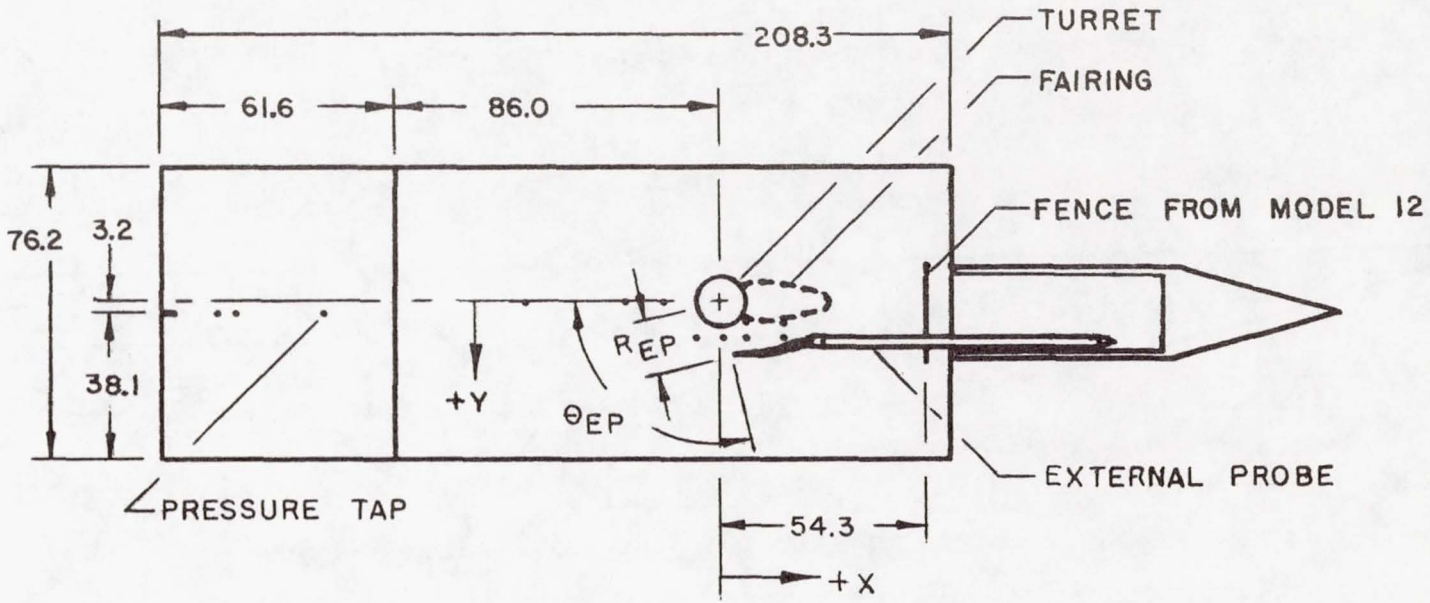

LINEAR DIMENSIONS IN cm

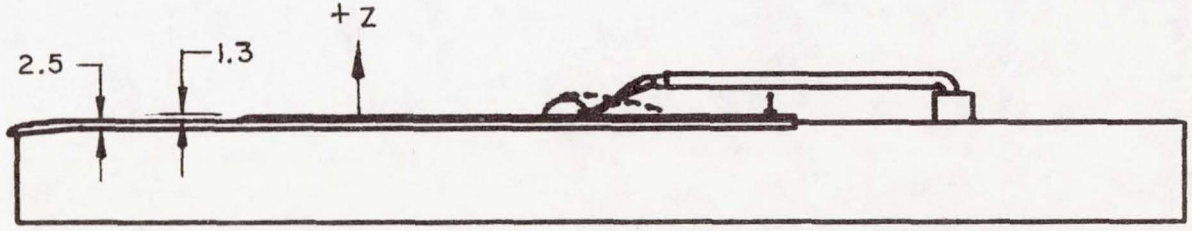

Figure 6.- Top and side views of the turret model.

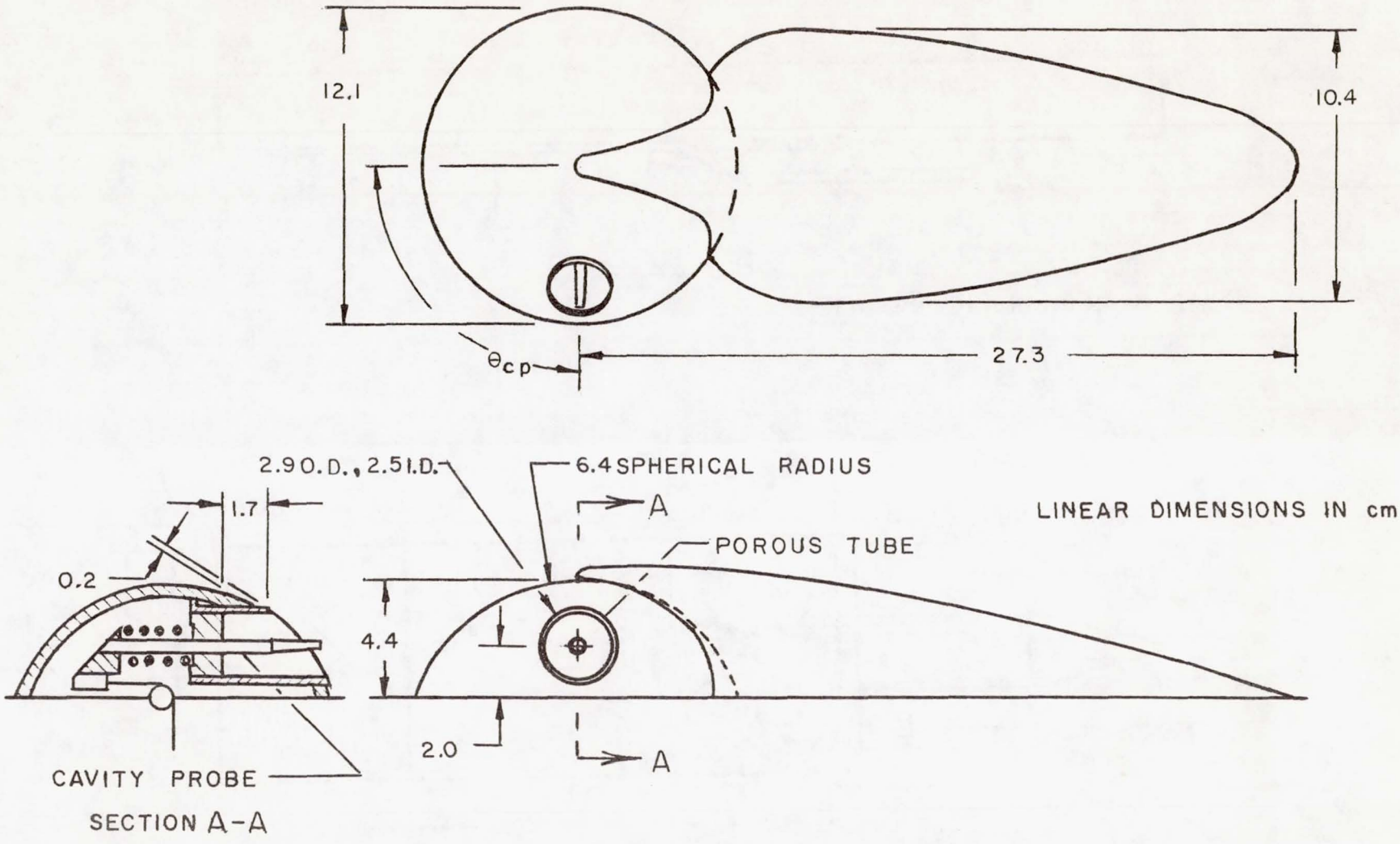

Figure 7.- Dimensions of the turret and fairing.

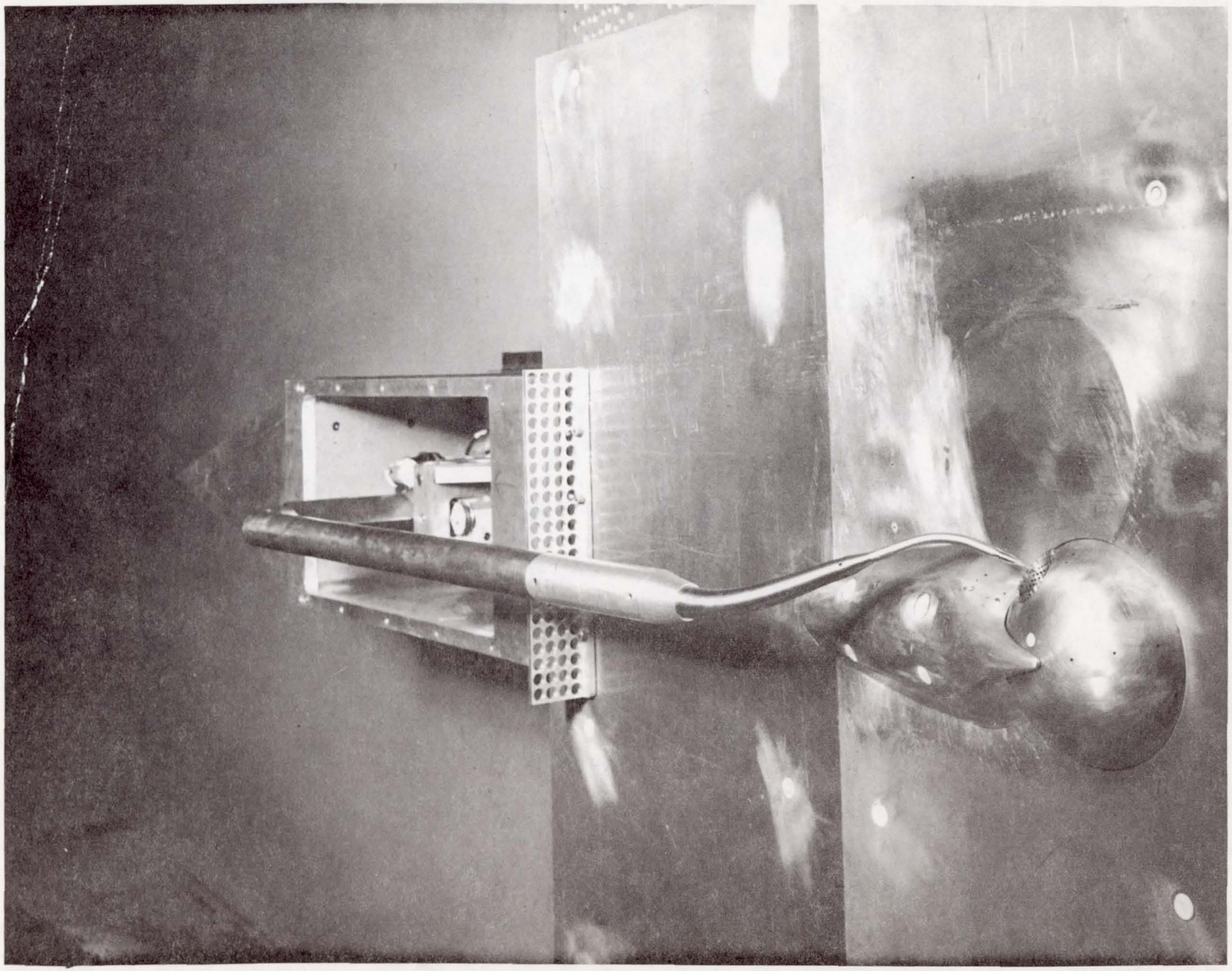

Figure 8.- Photograph of the turret and fairing with the external probe.

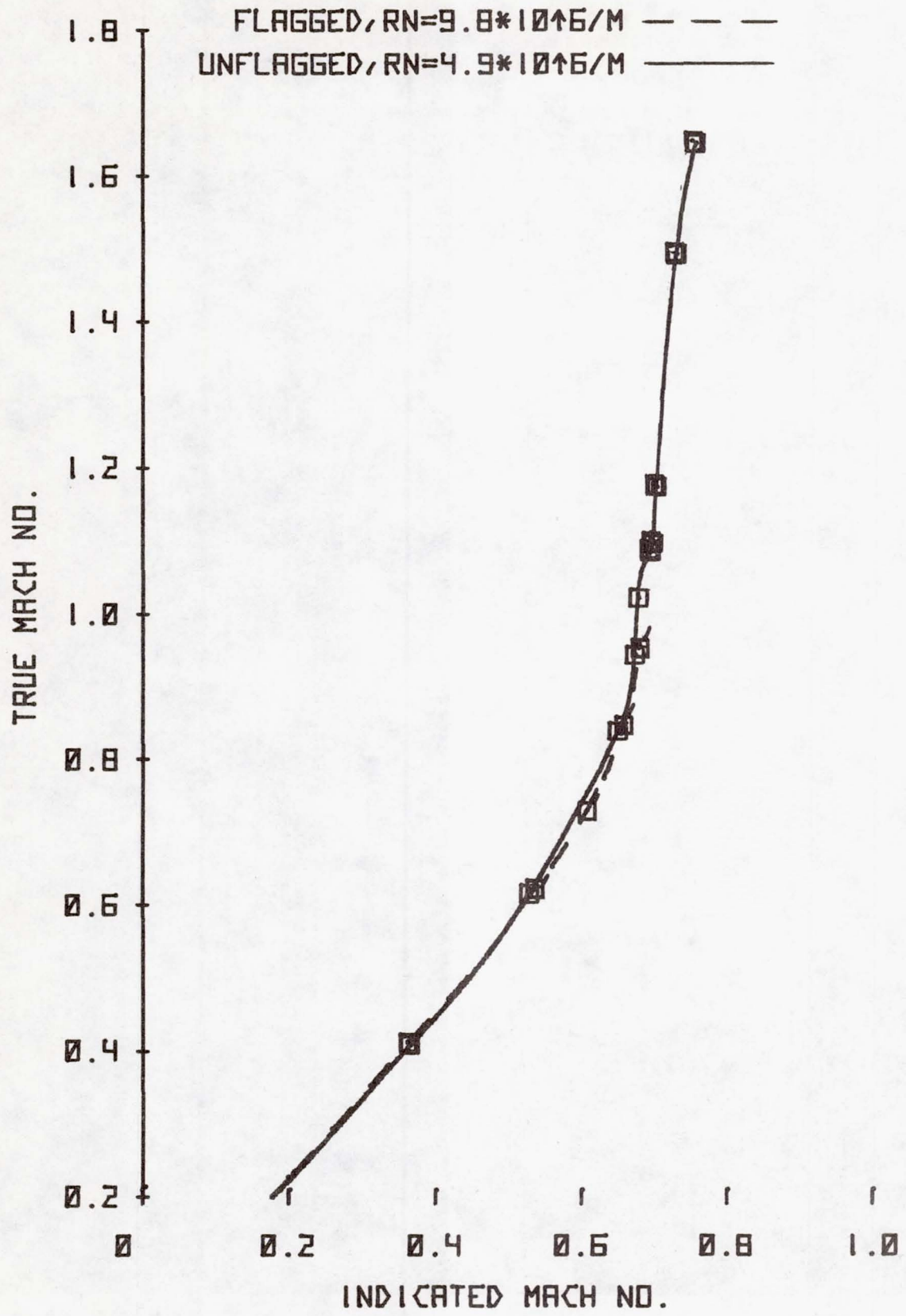

Figure 9.- Mach number calibration of the directional probe.

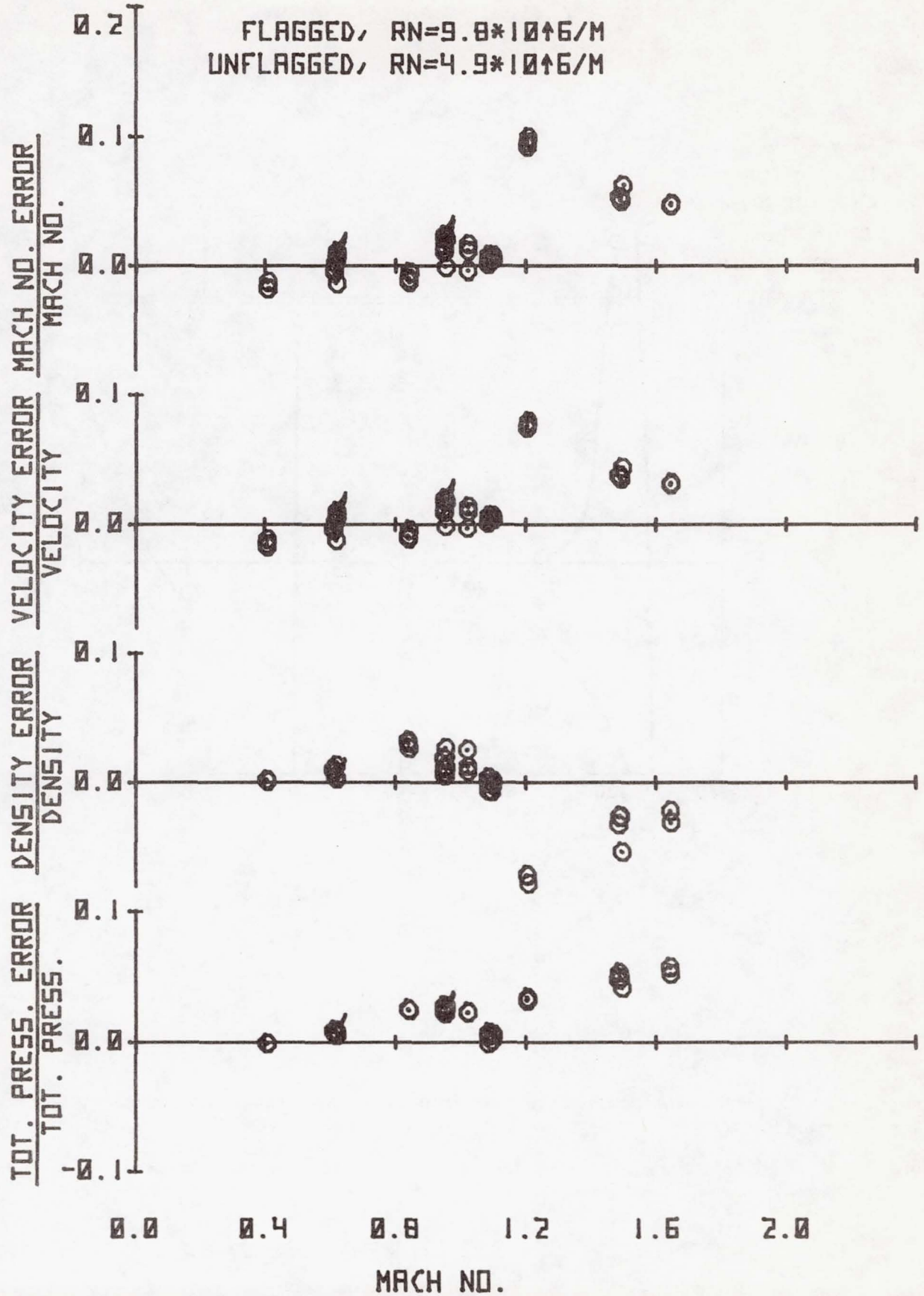

Figure 10.- Calibration errors of the directional probe at large flow angles; angle of attack = 8°, angle of sideslip = 28°.

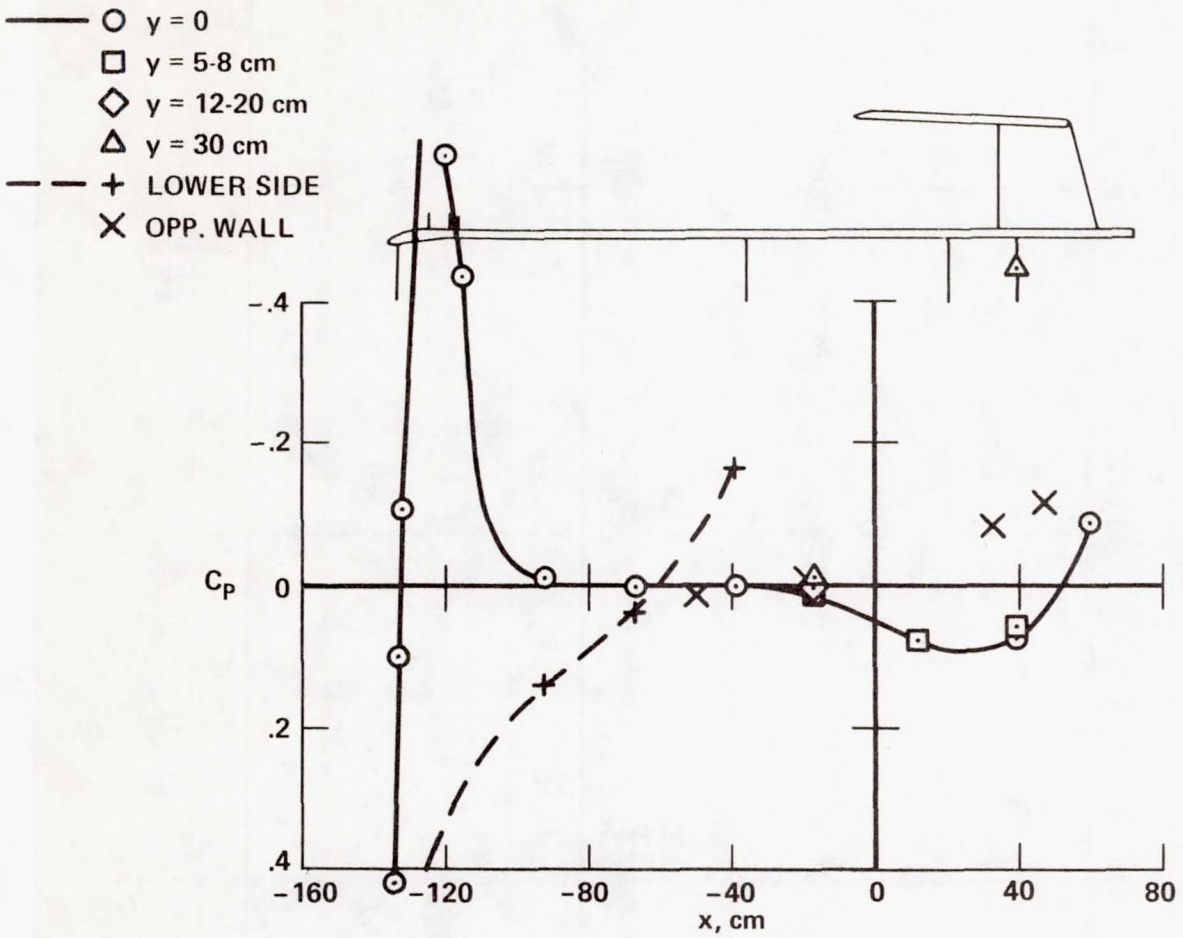

Figure 11.- Static-pressure coefficients on the plate and wall; pin model 1, M = 0.89, R = 9.8 million/m.

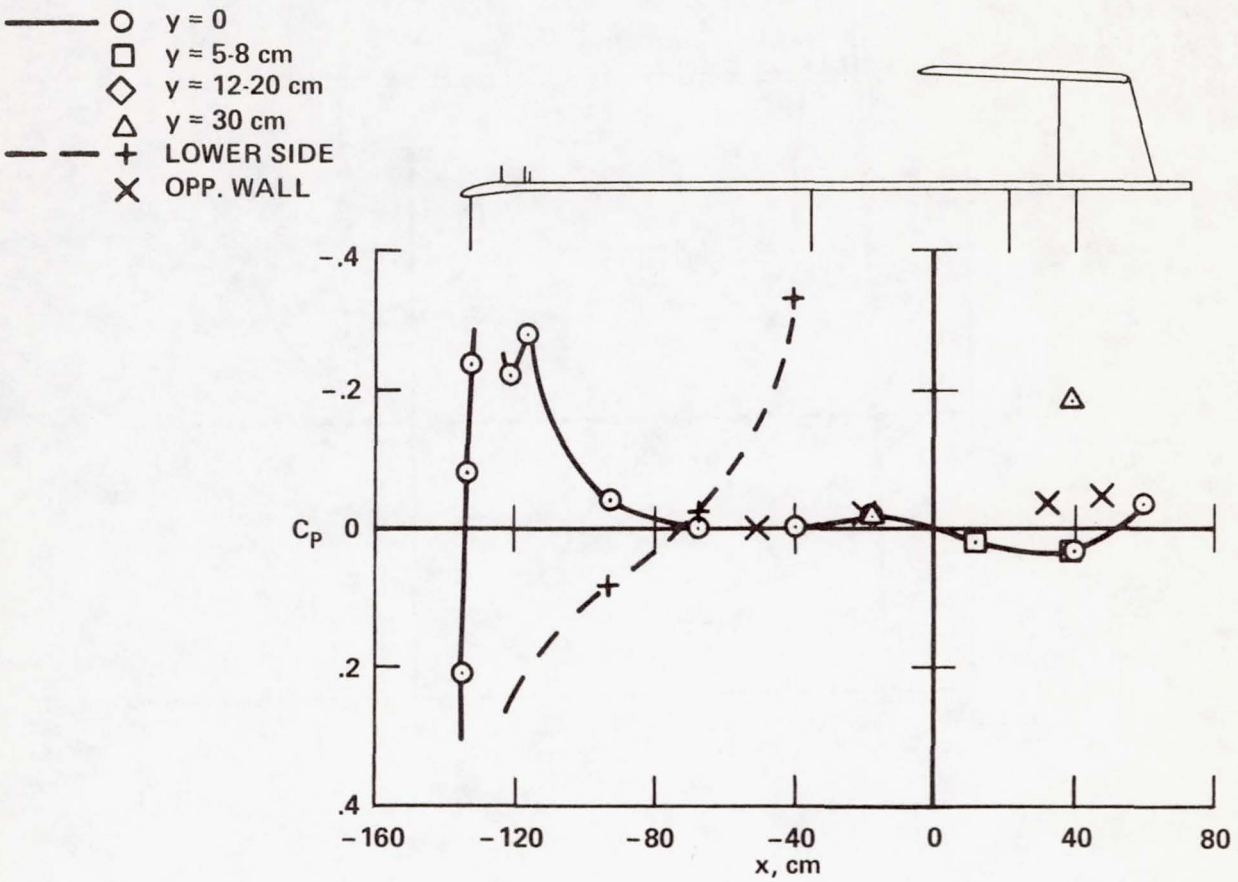

Figure 12.- Static-pressure coefficients on the plate and wall; pin model 1, M = 0.60, R = 9.8 million/m.

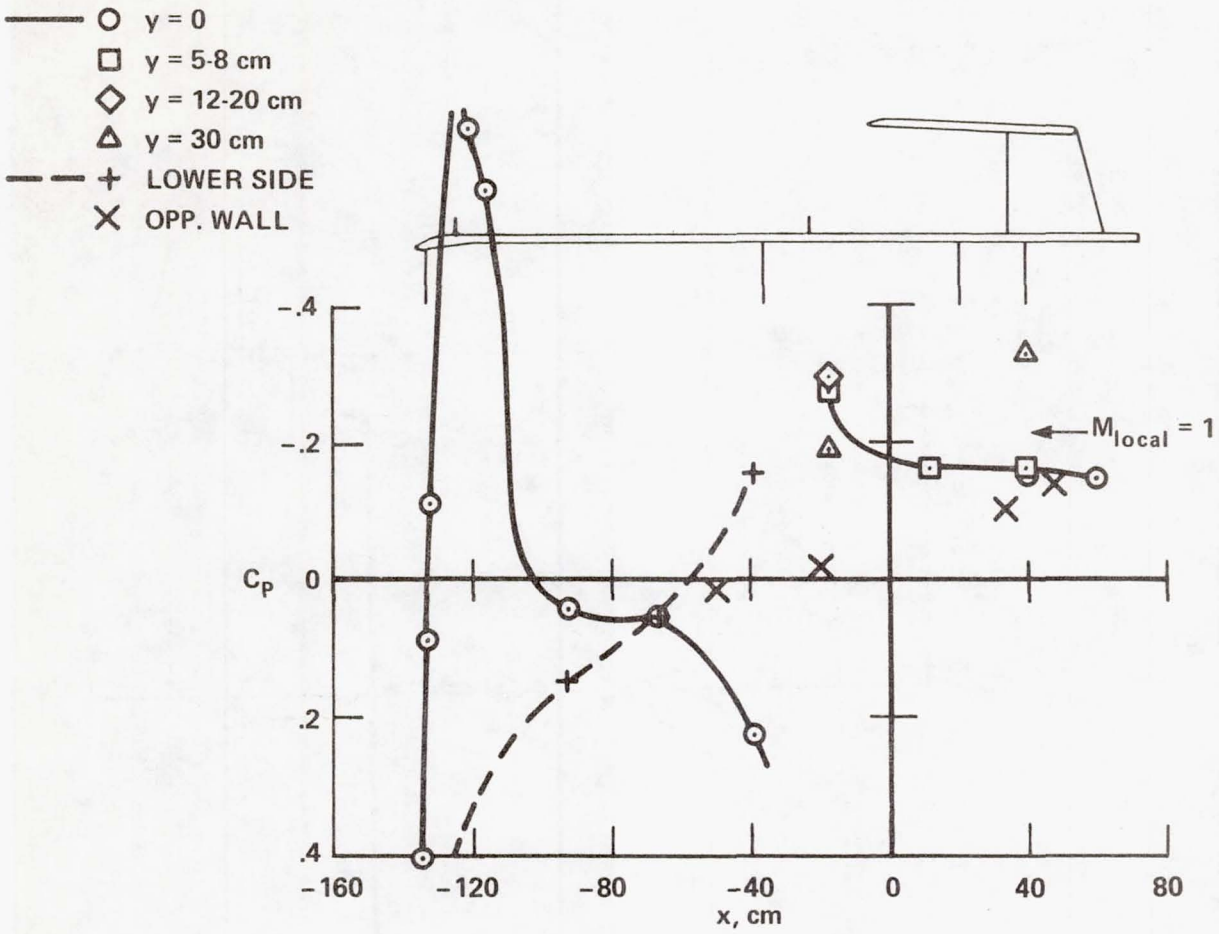

Figure 13.- Static-pressure coefficients on the plate and wall; fence model 2, M = 0.89, R = 9.8 million/m.

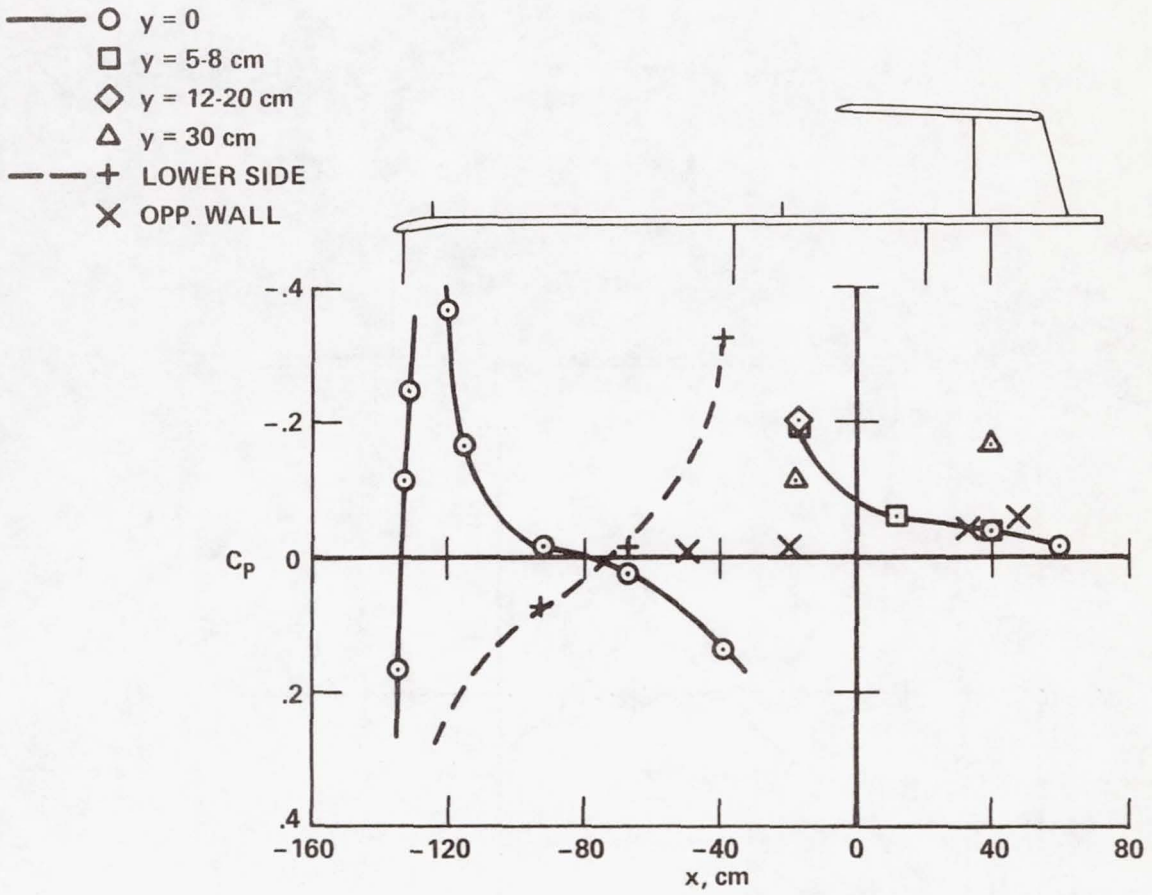

Figure 14.- Static-pressure coefficients on the plate and wall; fence model 2, M = 0.60, R = 9.8 million/m.

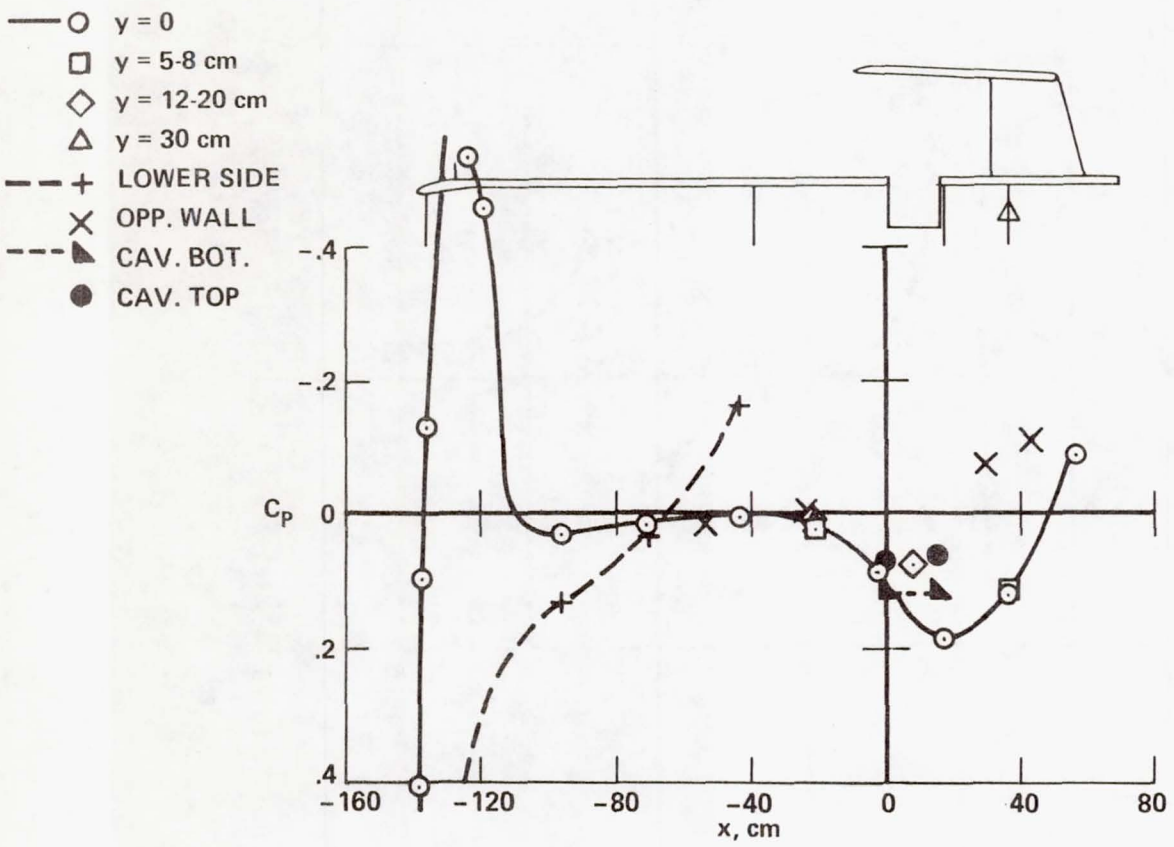

Figure 15.- Static-pressure coefficients on the plate, wall, and cavity; solid-wall cavity model 8, M = 0.89, R = 9.8 million/m.

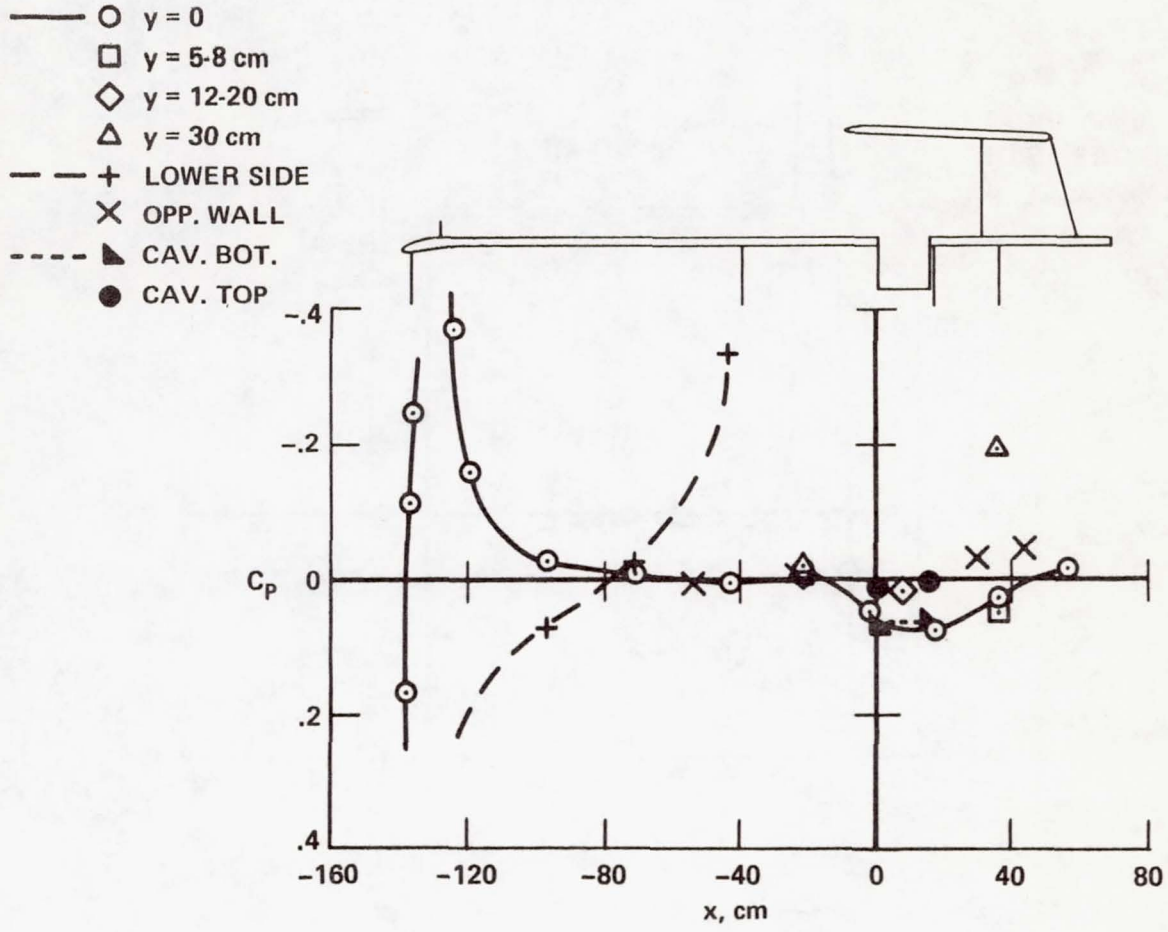

Figure 16.- Static-pressure coefficients on the plate, wall, and cavity; solid-wall cavity model 8, M = 0.60, R = 9.8 million/m.

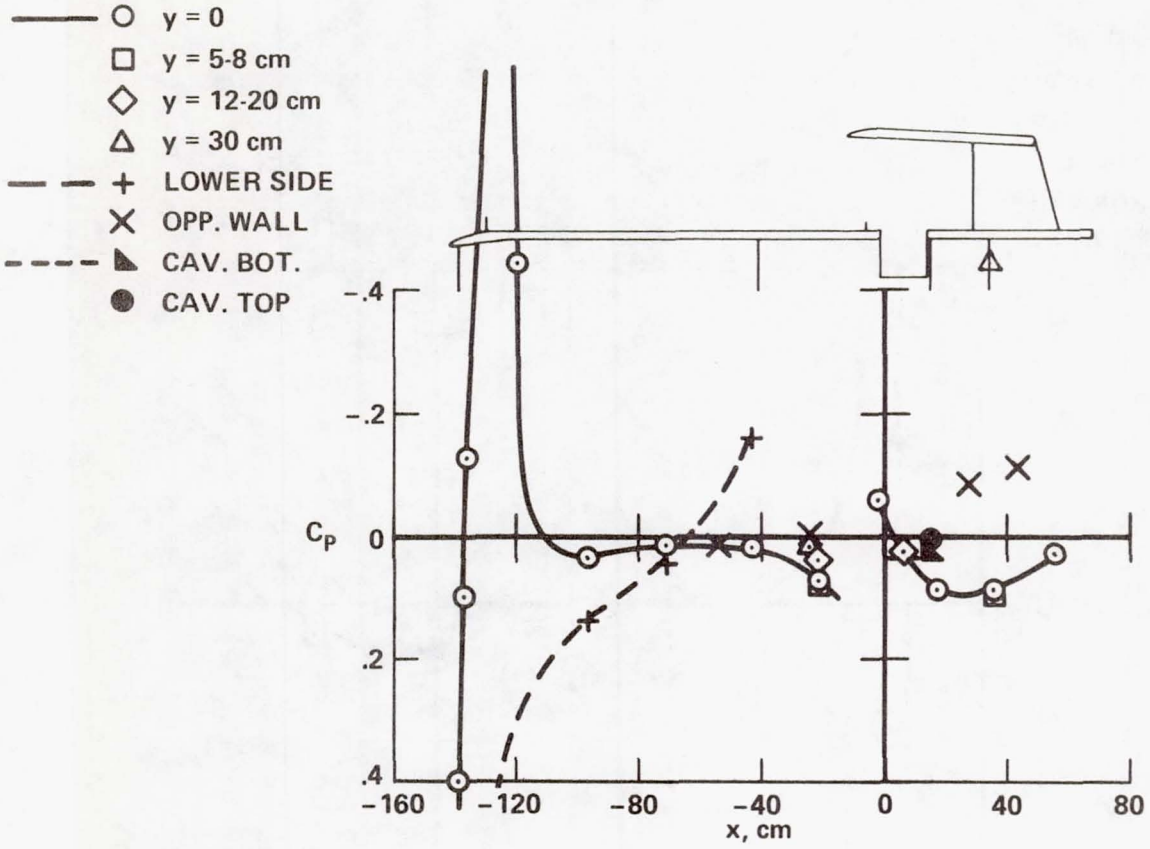

Figure 17.- Static-pressure coefficients on the plate, wall, and cavity; fence-cavity model 13, M = 0.89, R = 9.8 million/m.

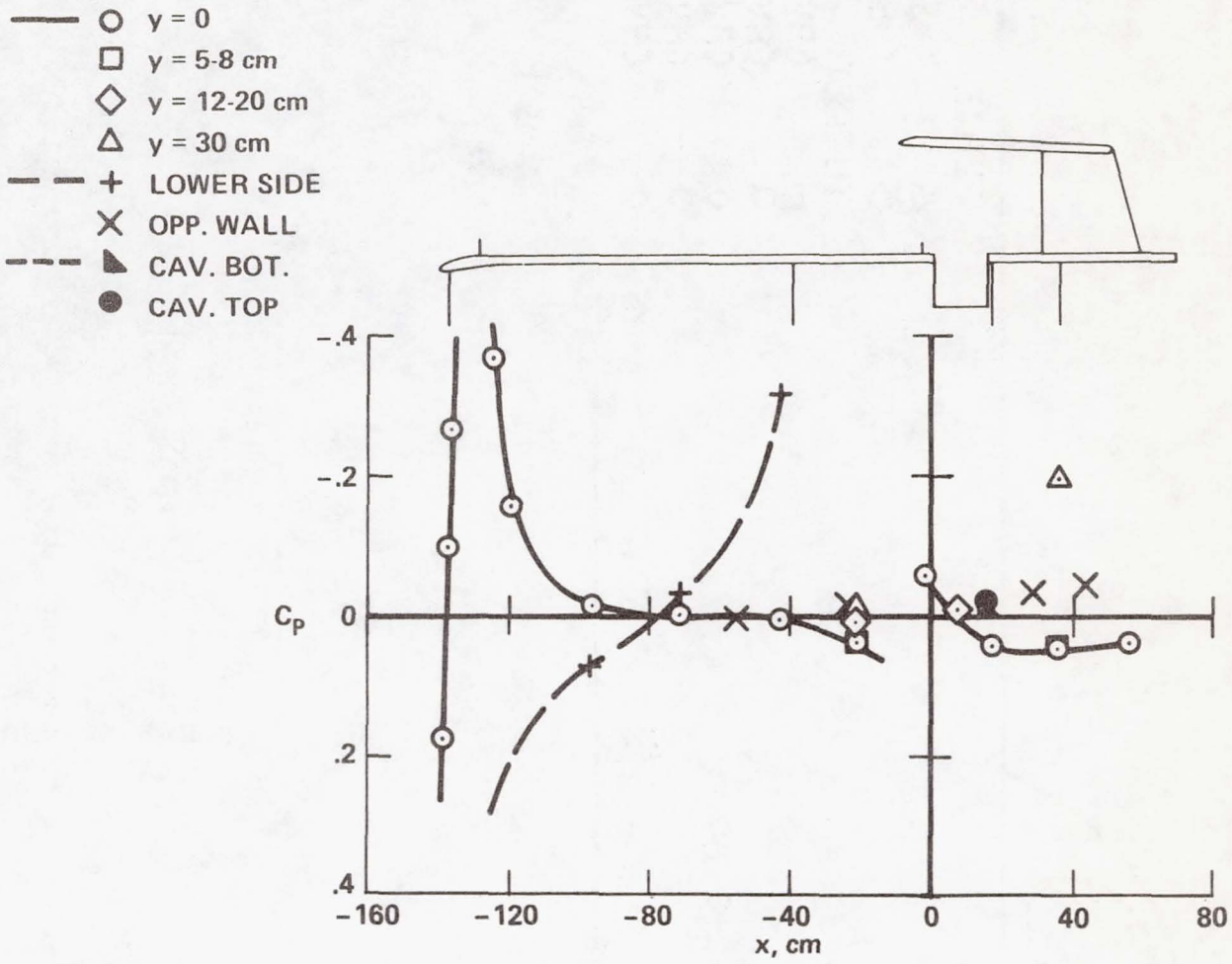

Figure 18.- Static-pressure coefficients on the plate, wall, and cavity; fence-cavity model 13, M = 0.60, R = 9.9 million/m.

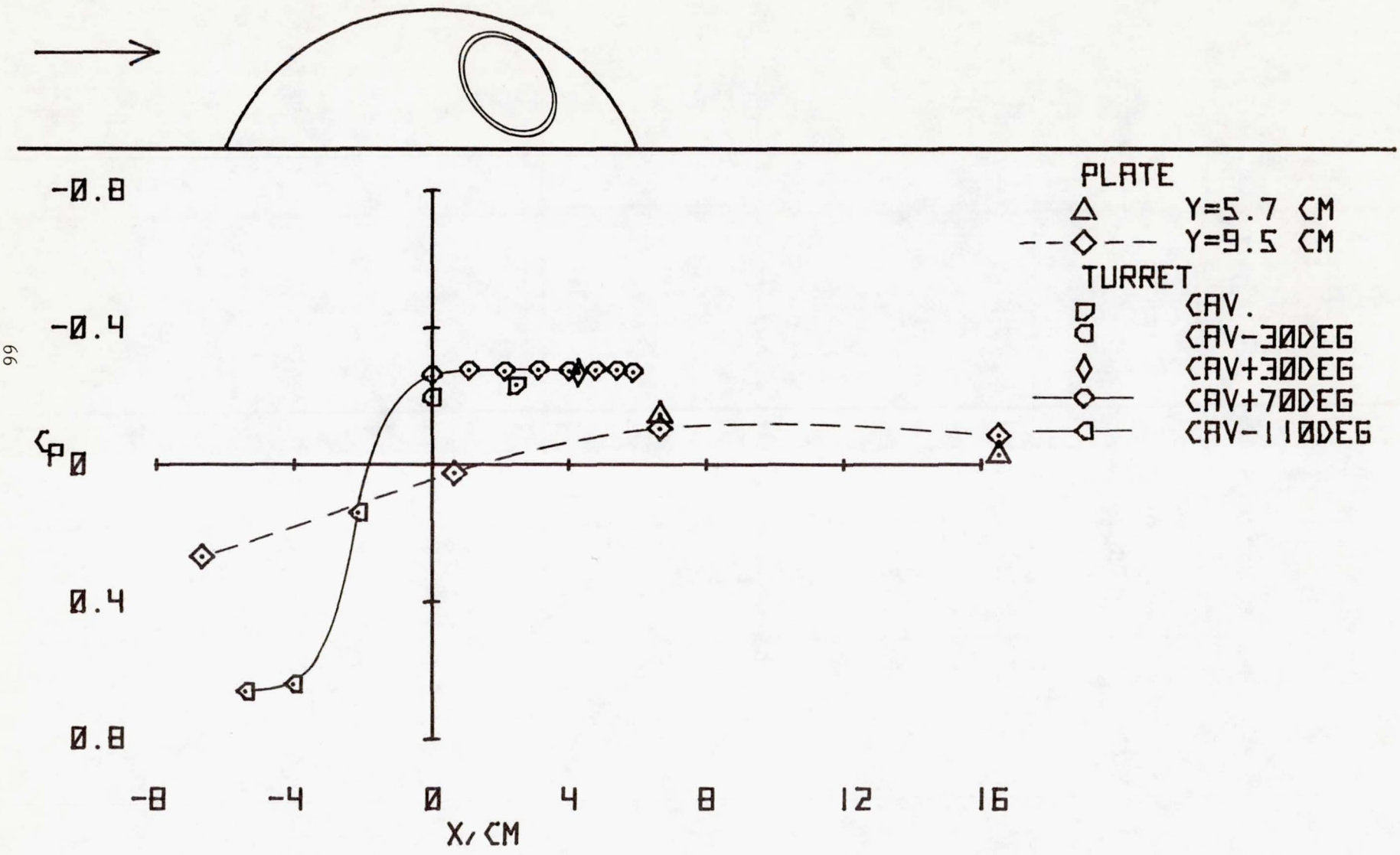

Figure 19.- Static-pressure coefficients on the turret and plate; M = 1.49, R = 4.8 million/m, $\theta = 120^{\circ}$.

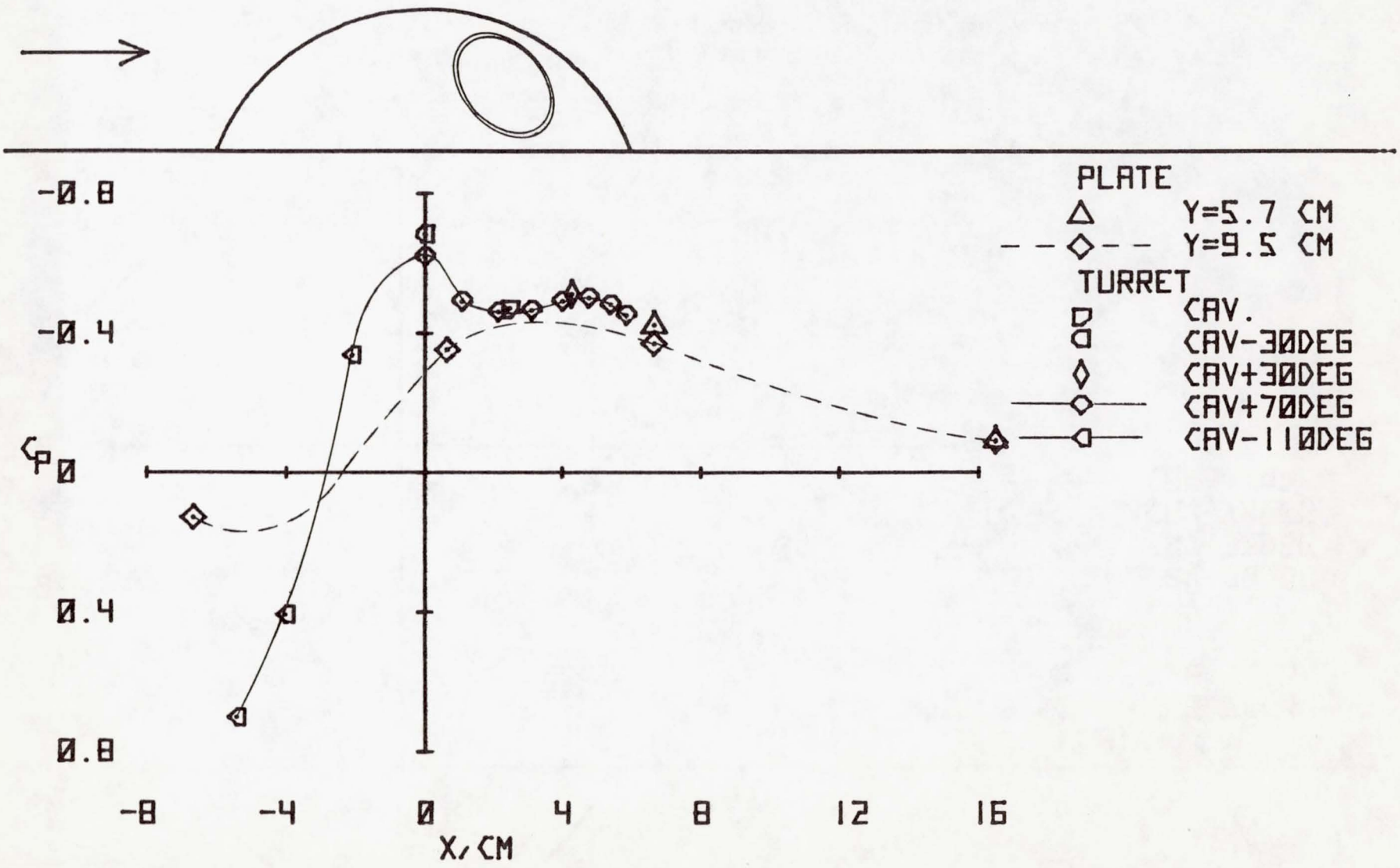

Figure 20.- Static-pressure coefficients on the turret and plate; M = 0.95, R = 4.9 million/m, $\theta = 120^{\circ}$.

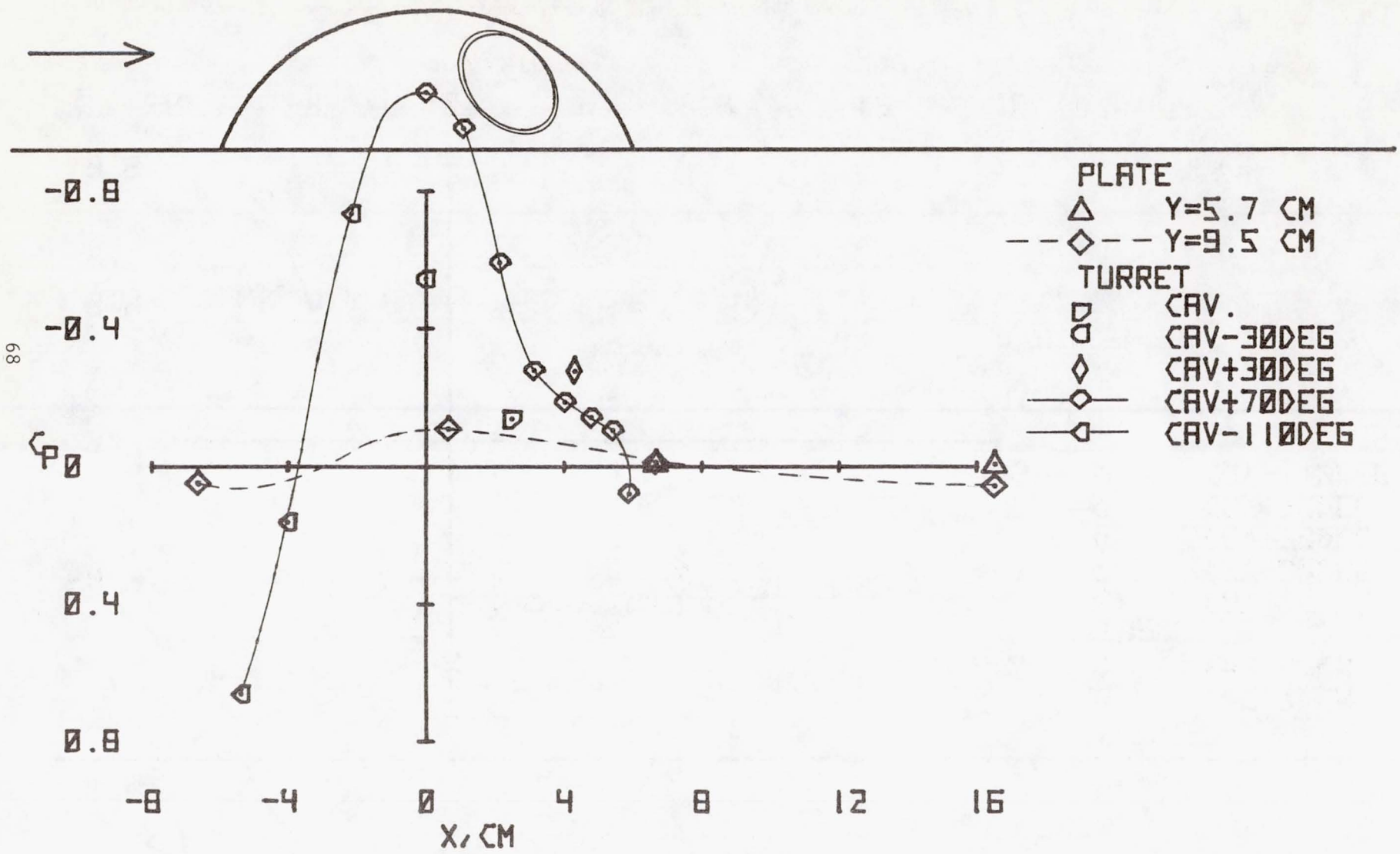

Figure 21.- Static-pressure coefficients on the turret and plate; M = 0.62, R = 5.0 million/m, $\theta = 120^{\circ}$.

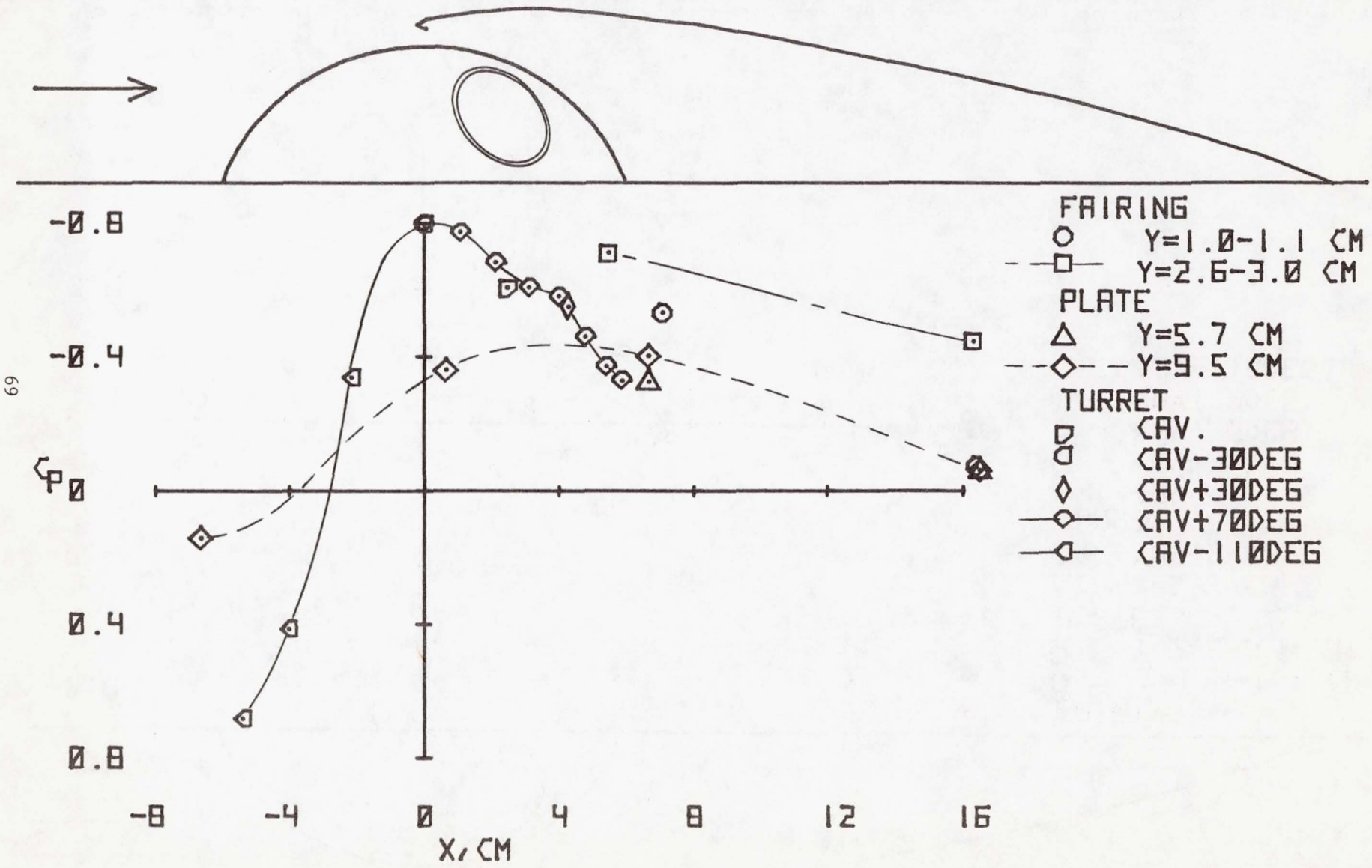

Figure 22.- Static-pressure coefficients on the turret, fairing, and plate; M = 0.95, R = 4.9 million/m, $\Theta = 120^{\circ}$.

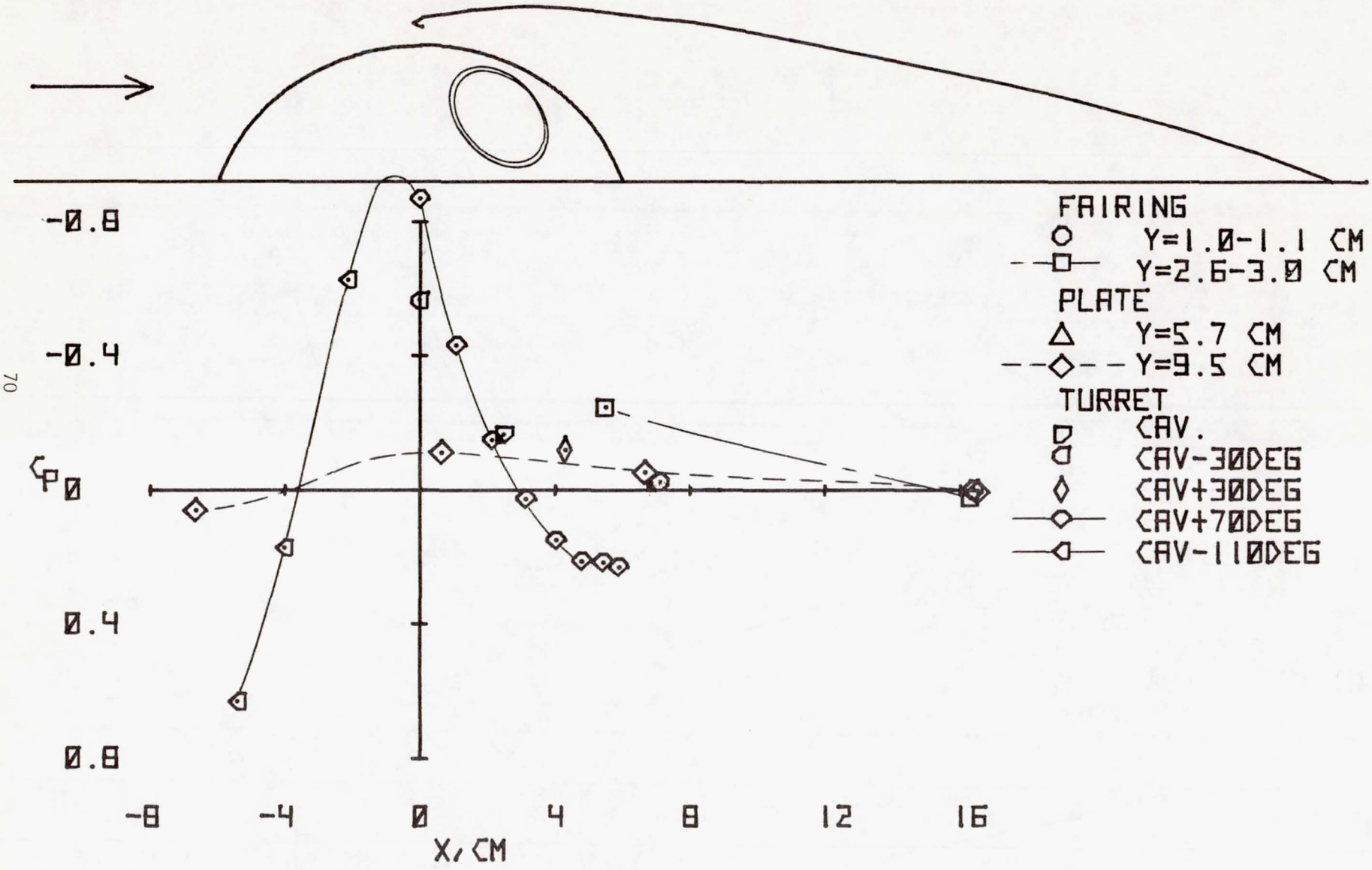

Figure 23.- Static-pressure coefficients on the turret, fairing, and plate; M = 0.62, R = 5.0 million/m, $\theta = 120^{\circ}$.

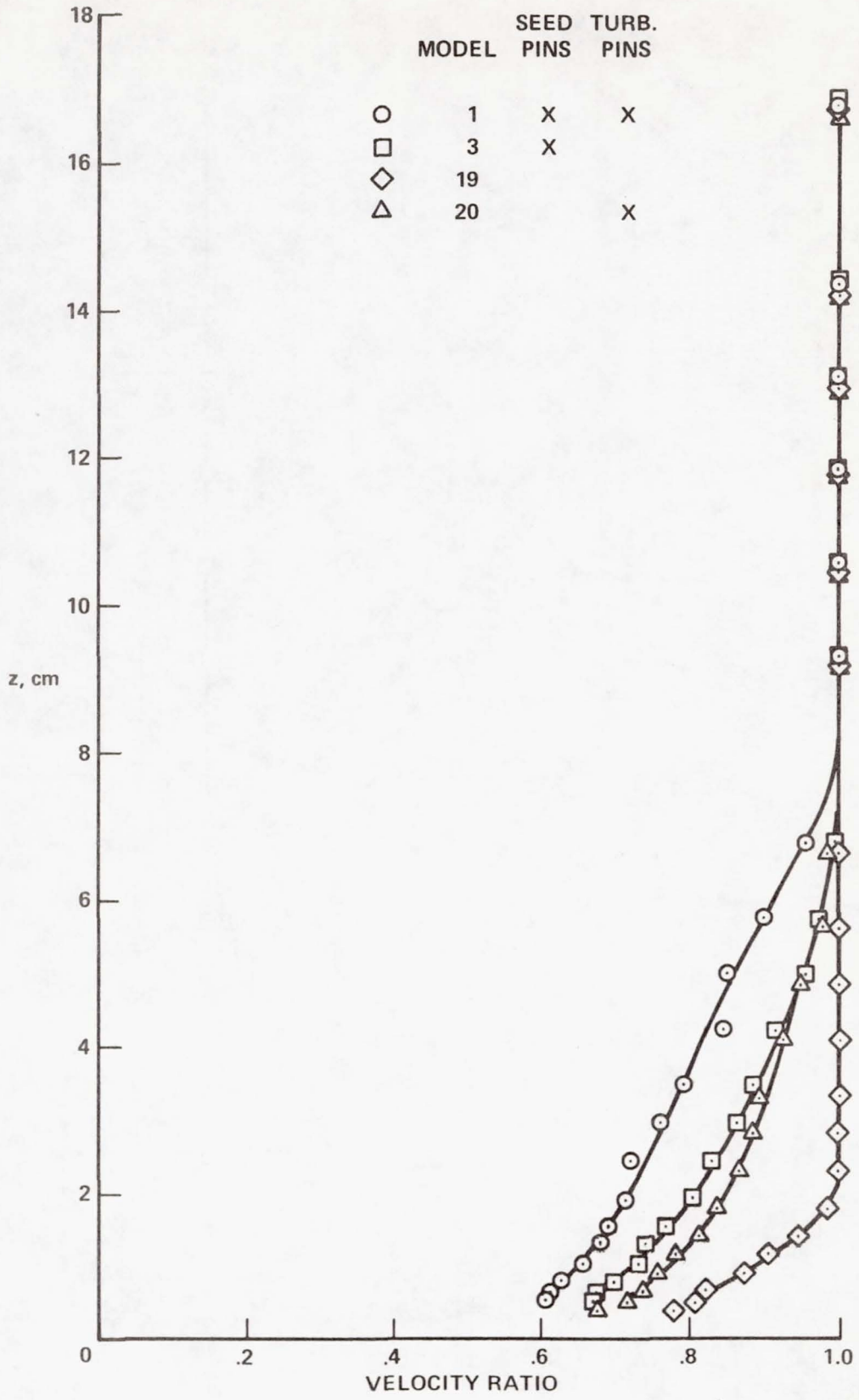

Figure 24.- Velocity profiles with and without pins; M = 0.60, R = 9.8 million/m, x = 21.6 cm, y = 0.

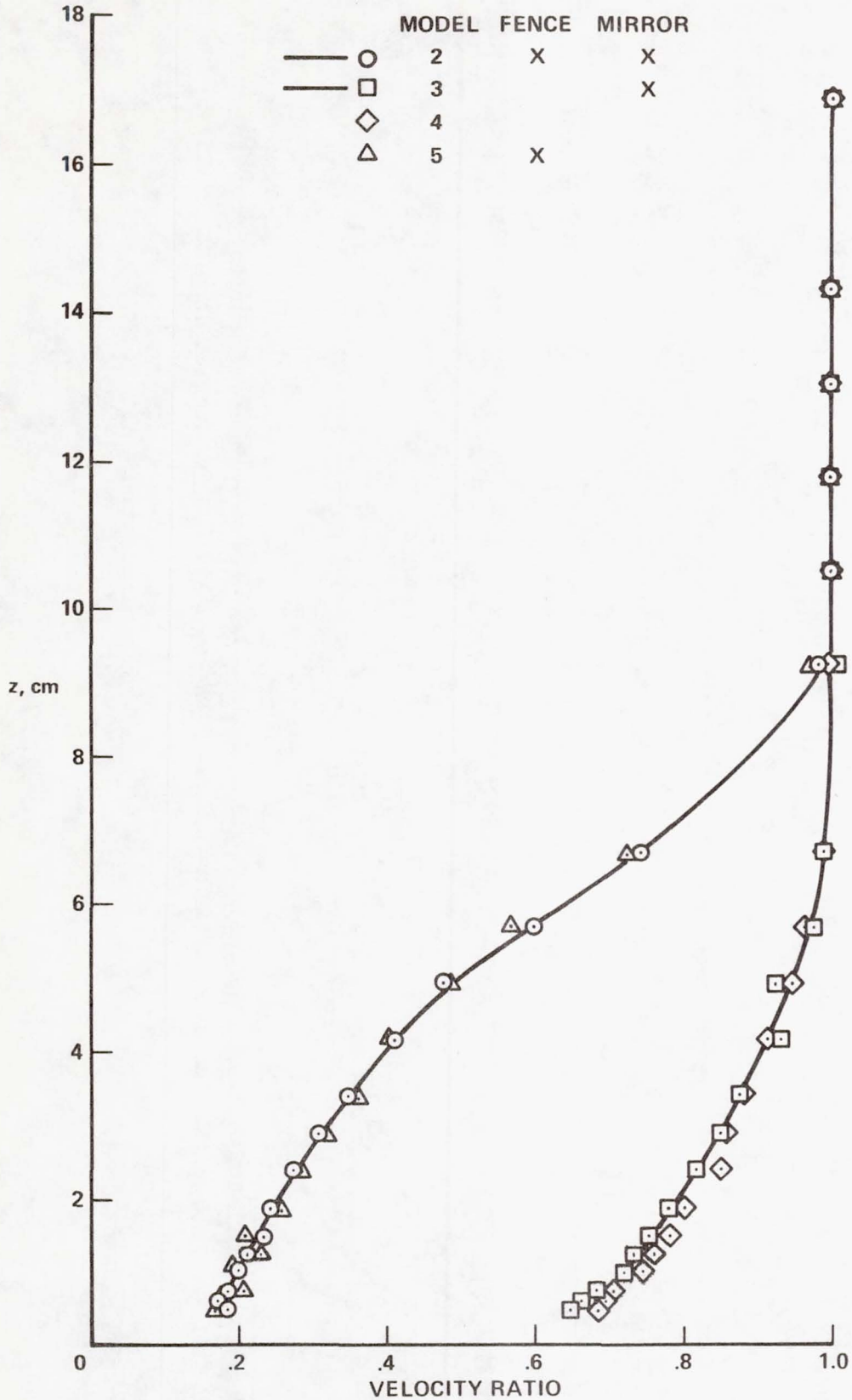

Figure 25.- Velocity profiles with and without fence and mirror; M = 0.60, R = 6.6 million/m, x = 11.4 cm, y = 0.

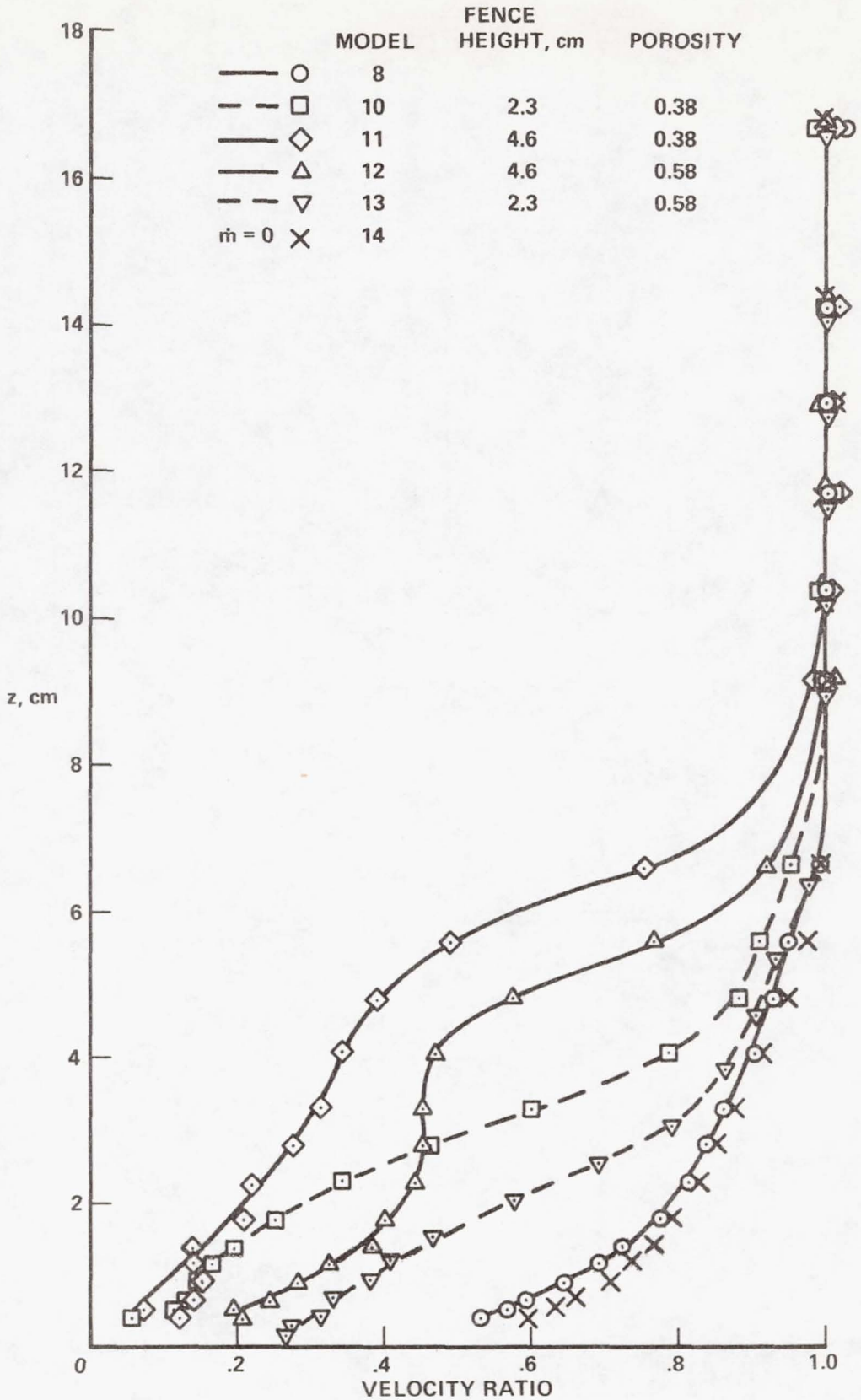

Figure 26.- Velocity profiles for cavity configurations; M = 0.60,R = 9.8 million/m, x = 7.6 cm, y = 0.1 cm.

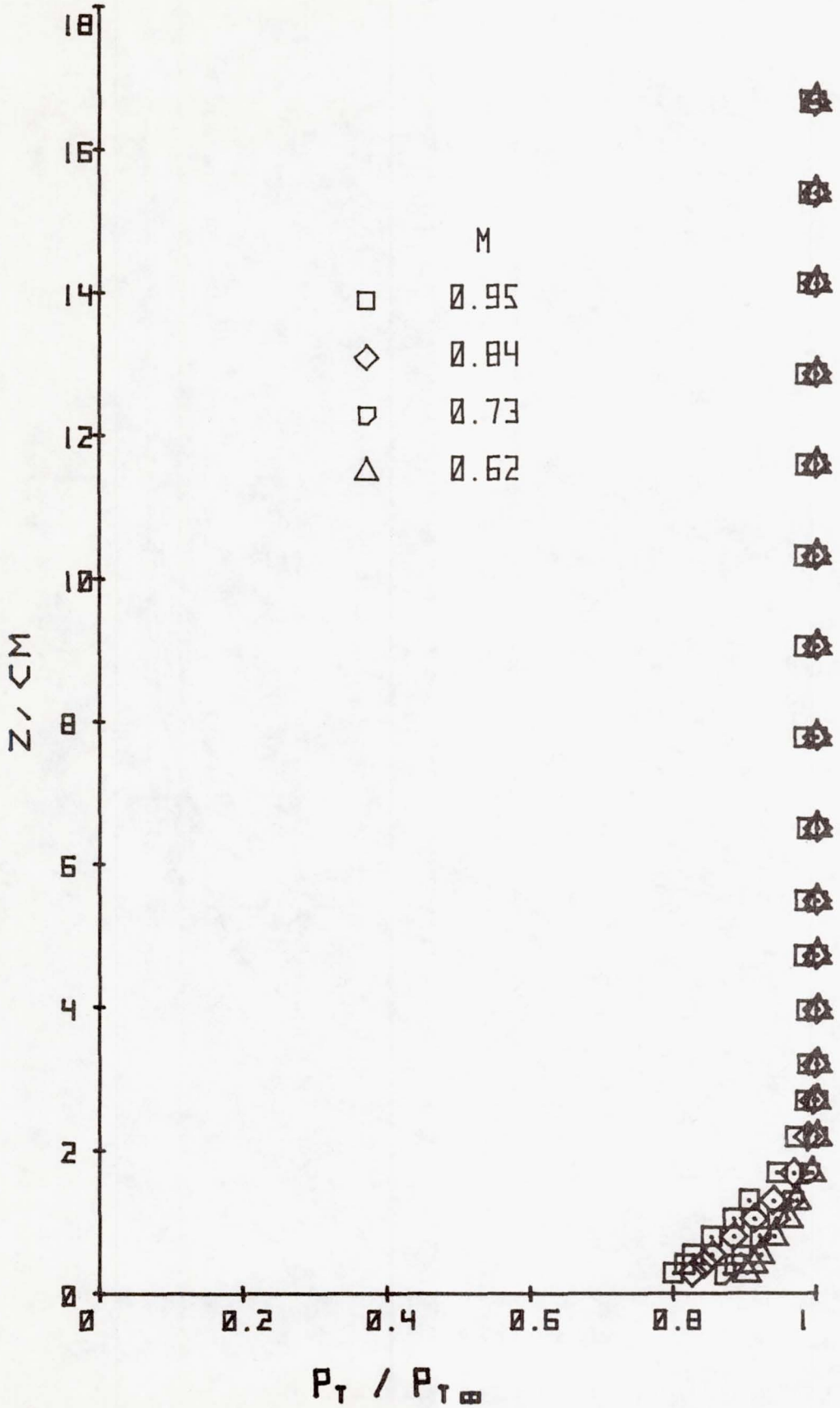

Figure 27.- Rake total pressures ahead of the turret; R = 9.9 million/m, x = -13.5 cm, y = 0, $\theta_{cp} = 150^{\circ}$.

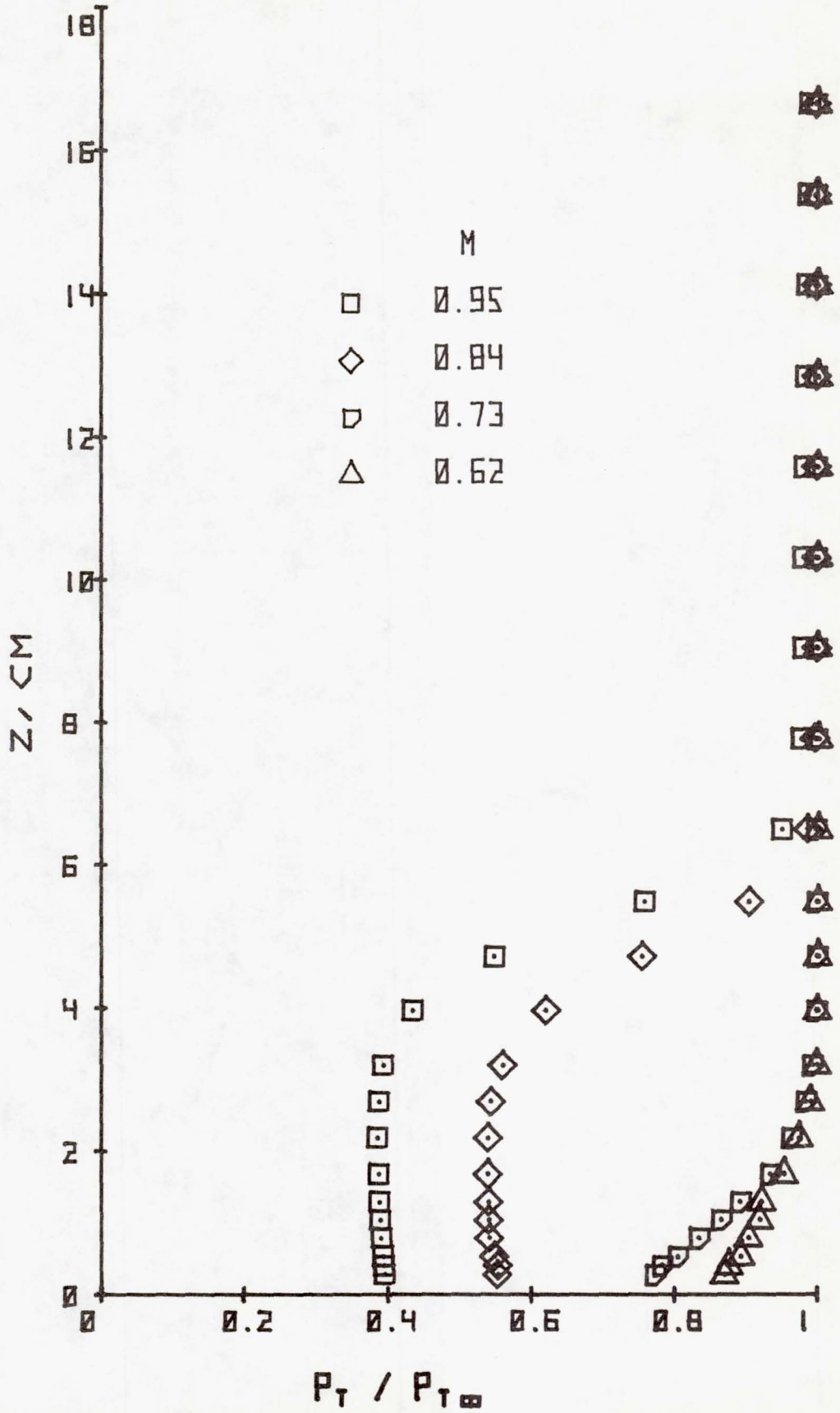

Figure 28.- Rake total pressures behind the turret; R = 9.9 million/m, x = 10.4 cm, y = 0, $\theta_{cp} = 150^{\circ}$.

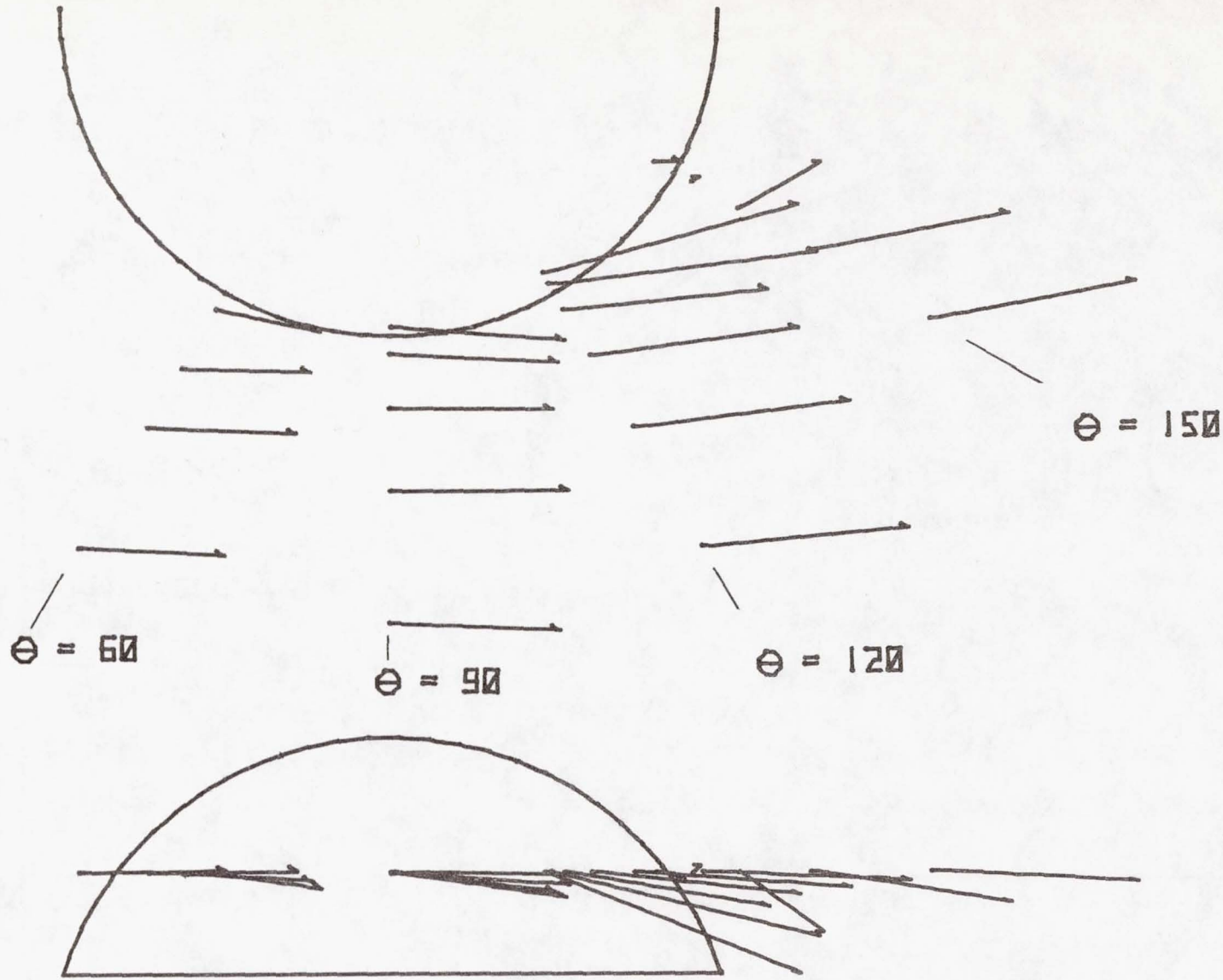

Figure 29.- Local Mach number vectors for various turret azimuths; M = 1.49, R = 4.8 million/m, z = 2.0 cm.

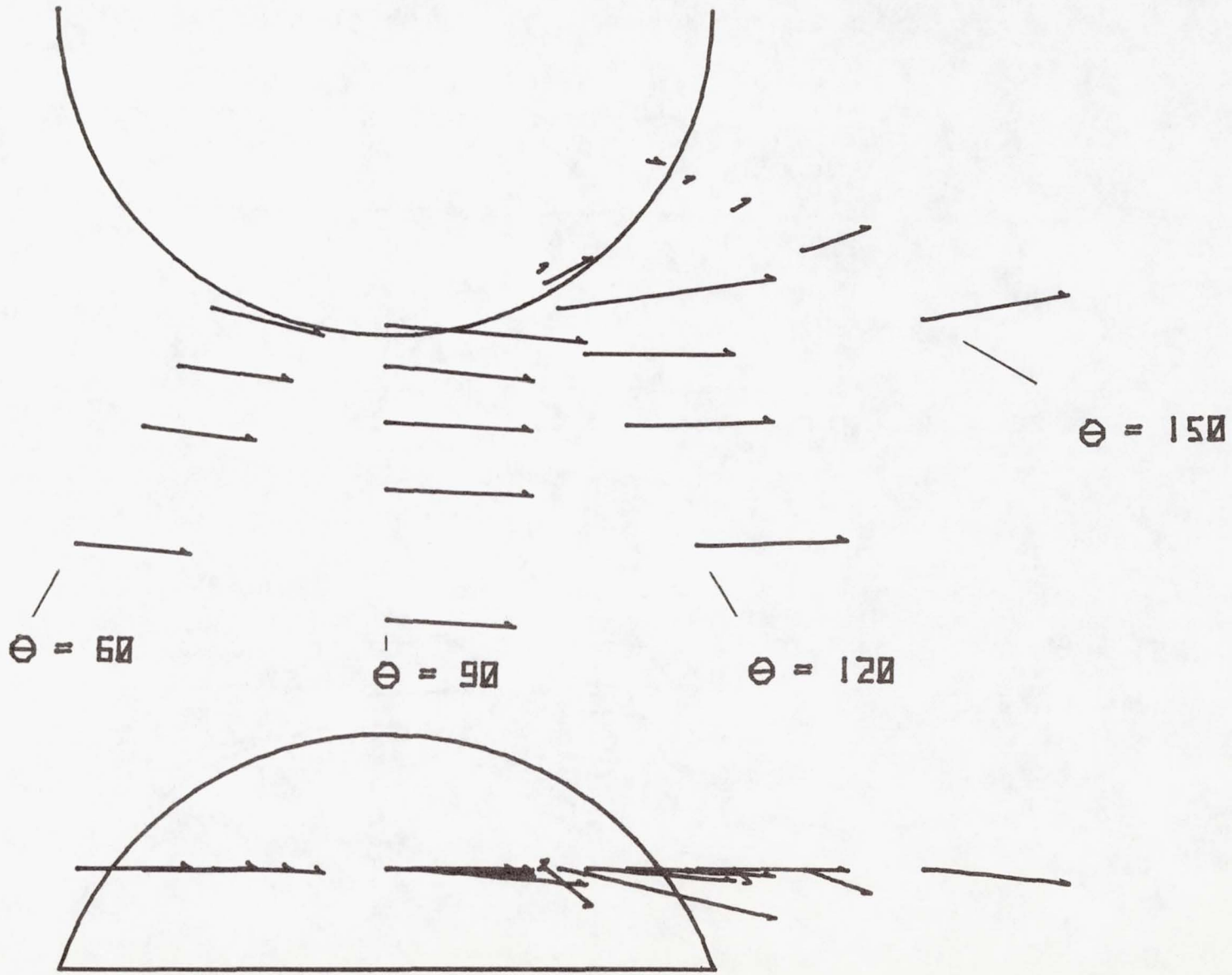

Figure 30.- Local Mach number vectors for various turret azimuths; M = 0.95, R = 4.9 million/m, z = 2.0 cm.

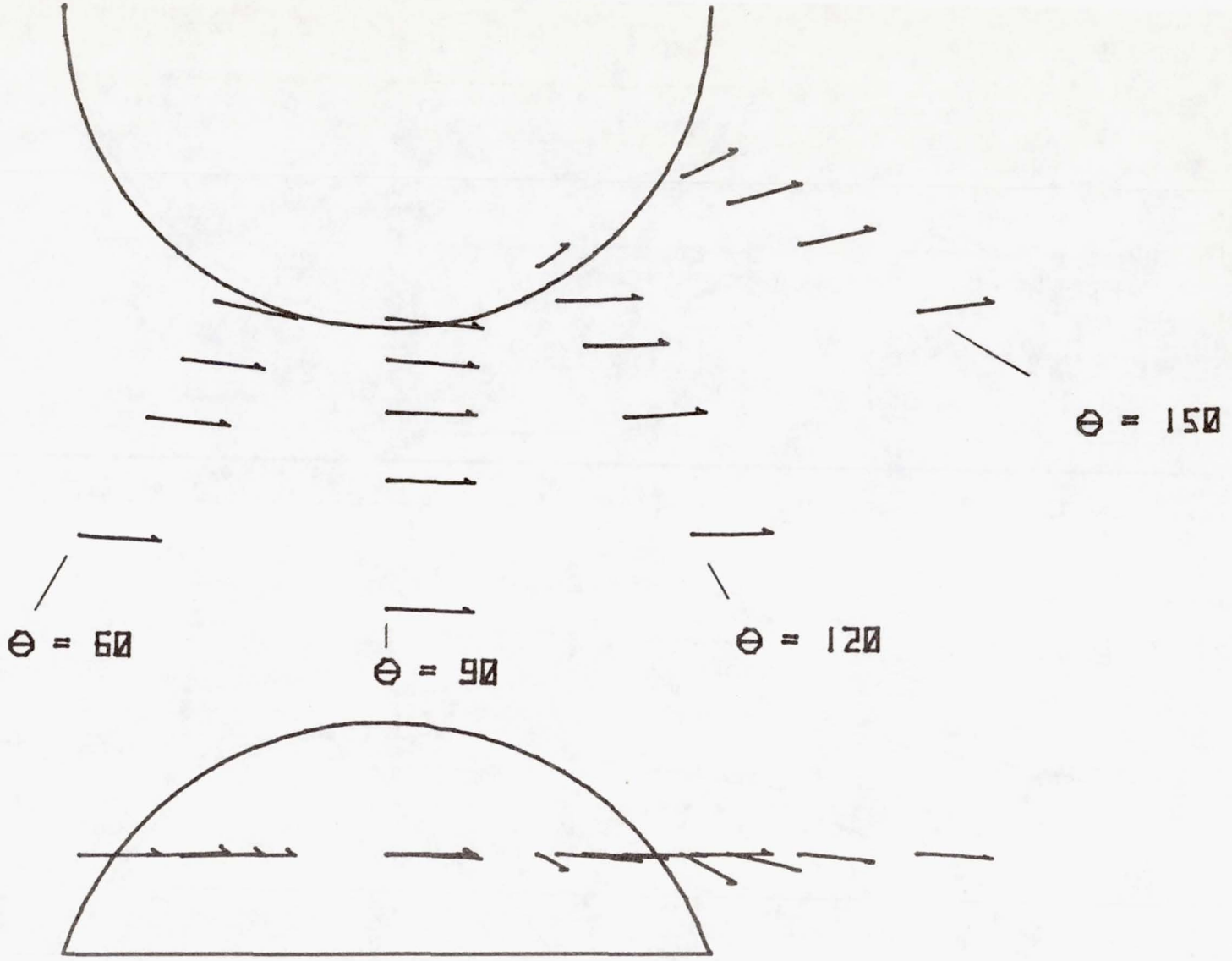

Figure 31.- Local Mach number vectors for various turret azimuths; M = 0.62, R = 5.0 million/m, z = 2.0 cm.

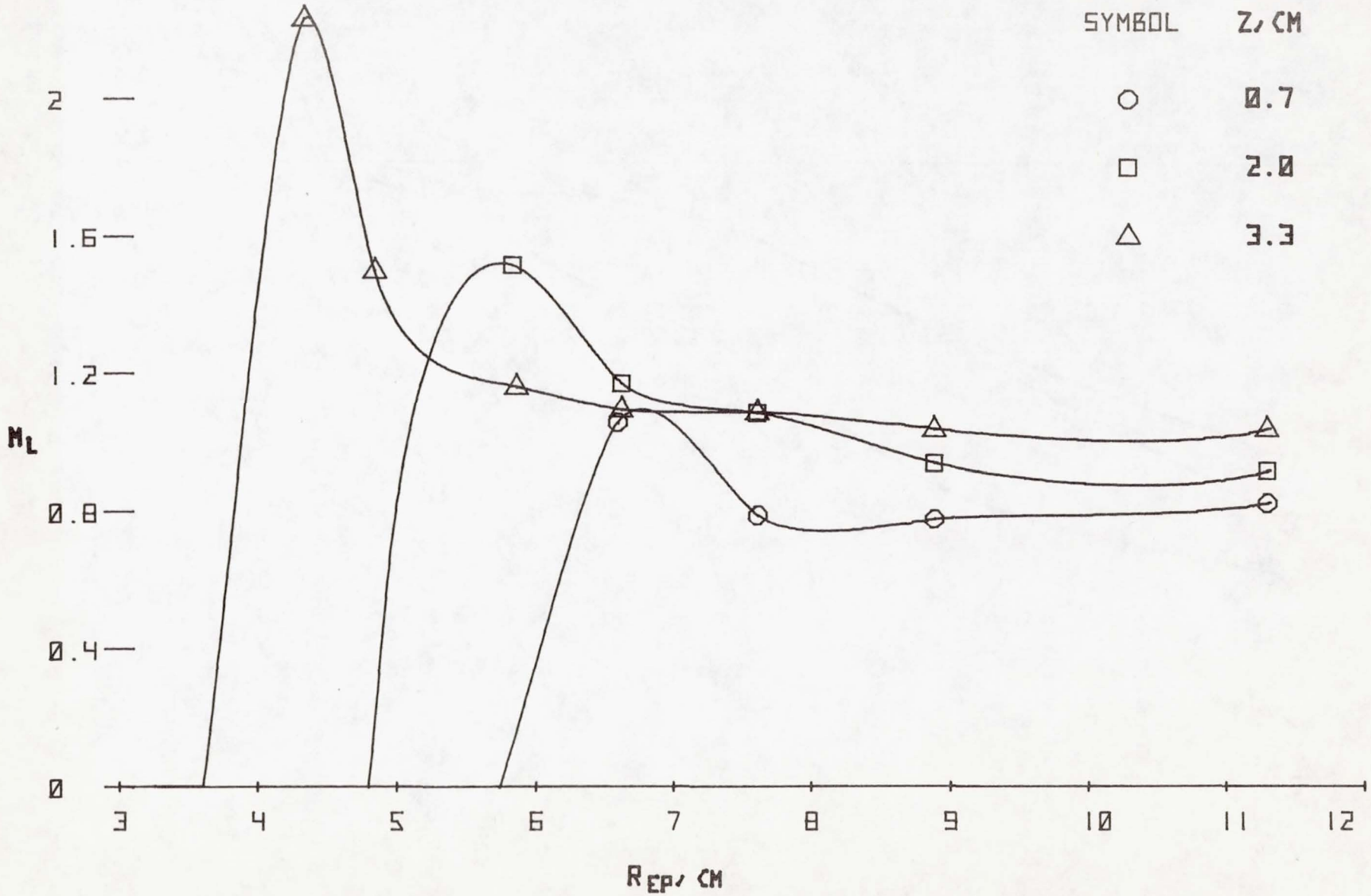

Figure 32.- Local Mach numbers along the line of sight from the turret cavity; M = 0.95, R = 9.8 million/m, $\theta = 90^{\circ}$.

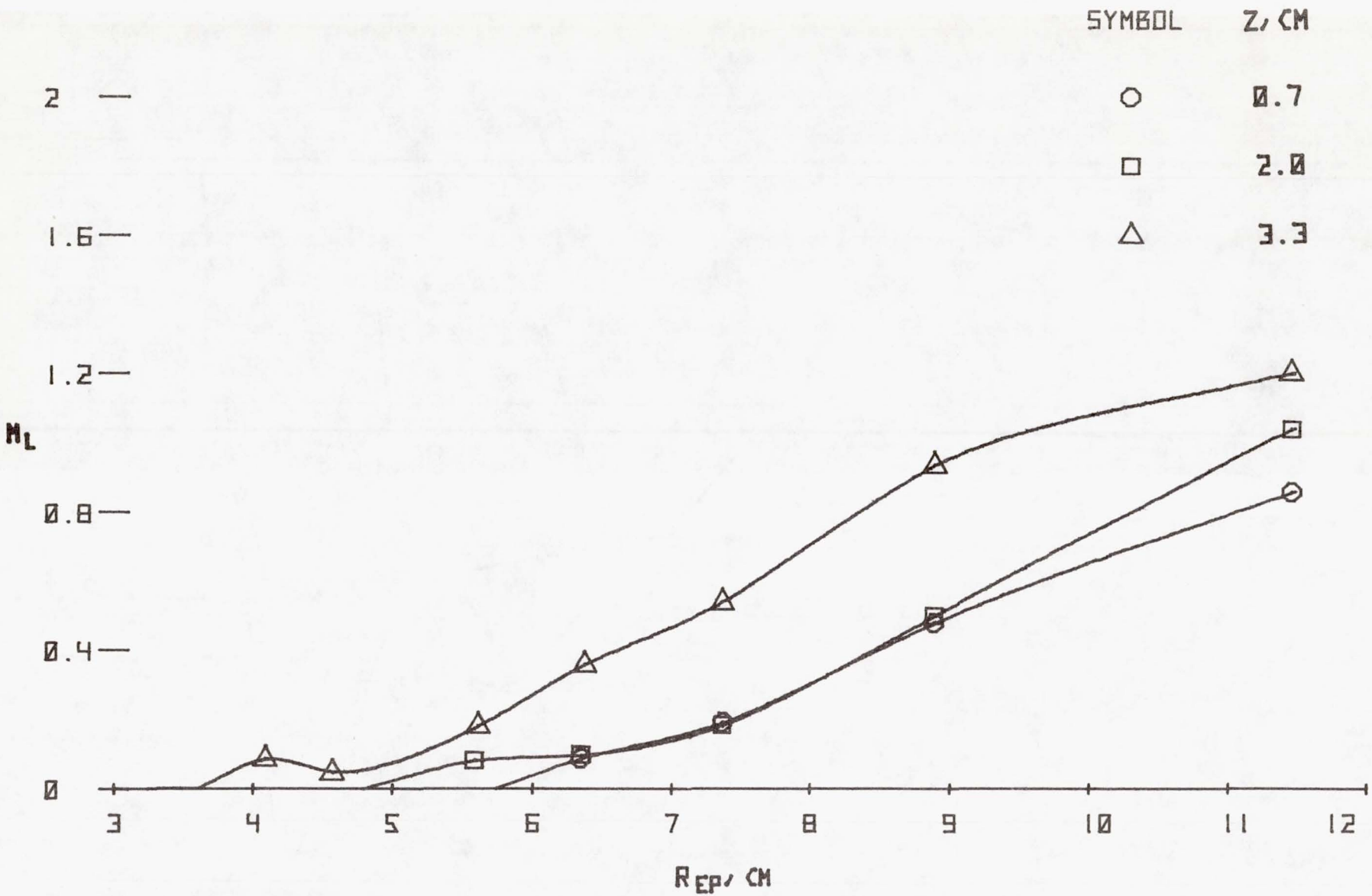

Figure 33.- Local Mach numbers along the line of sight from the turret cavity; M = 0.95, R = 9.8 million/m, $\theta = 150^{\circ}$.

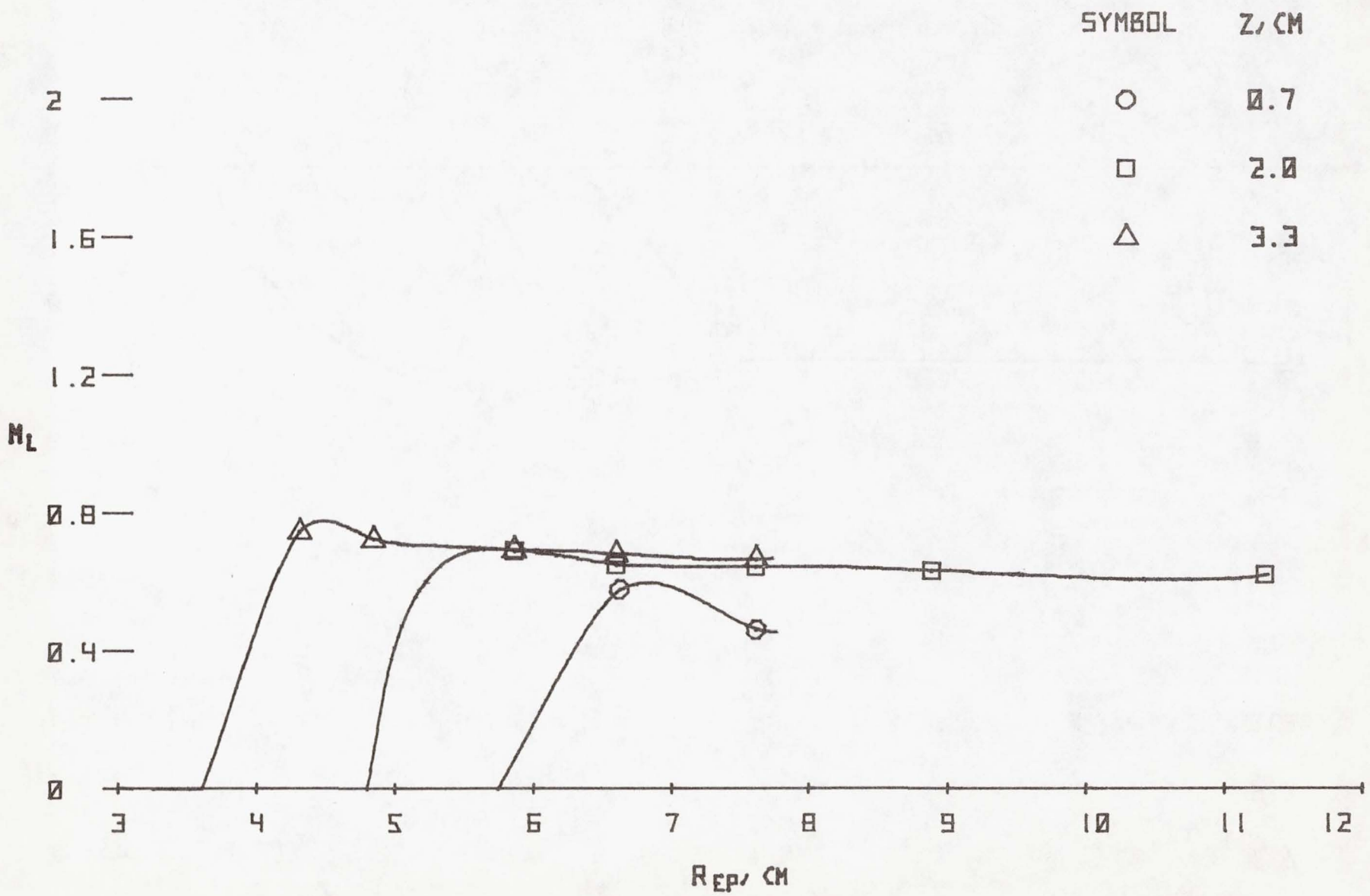

Figure 34.- Local Mach numbers along the line of sight from the turret cavity; M = 0.62, R = 10.0 million/m, $\theta = 90^{\circ}$.

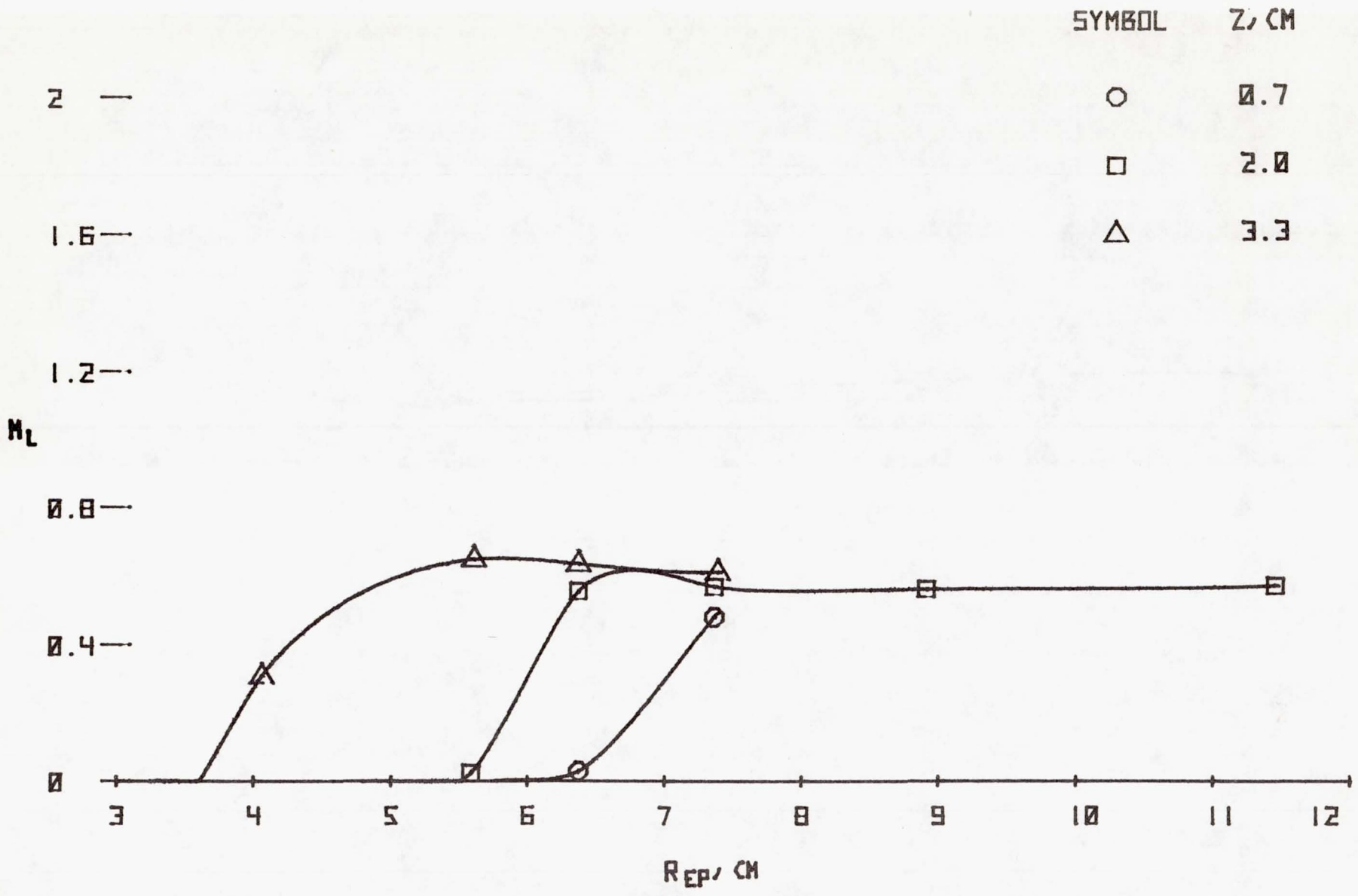

Figure 35.- Local Mach numbers along the line of sight from the turret cavity; M = 0.62, R = 10.0 million/m, $\theta = 150^{\circ}$.

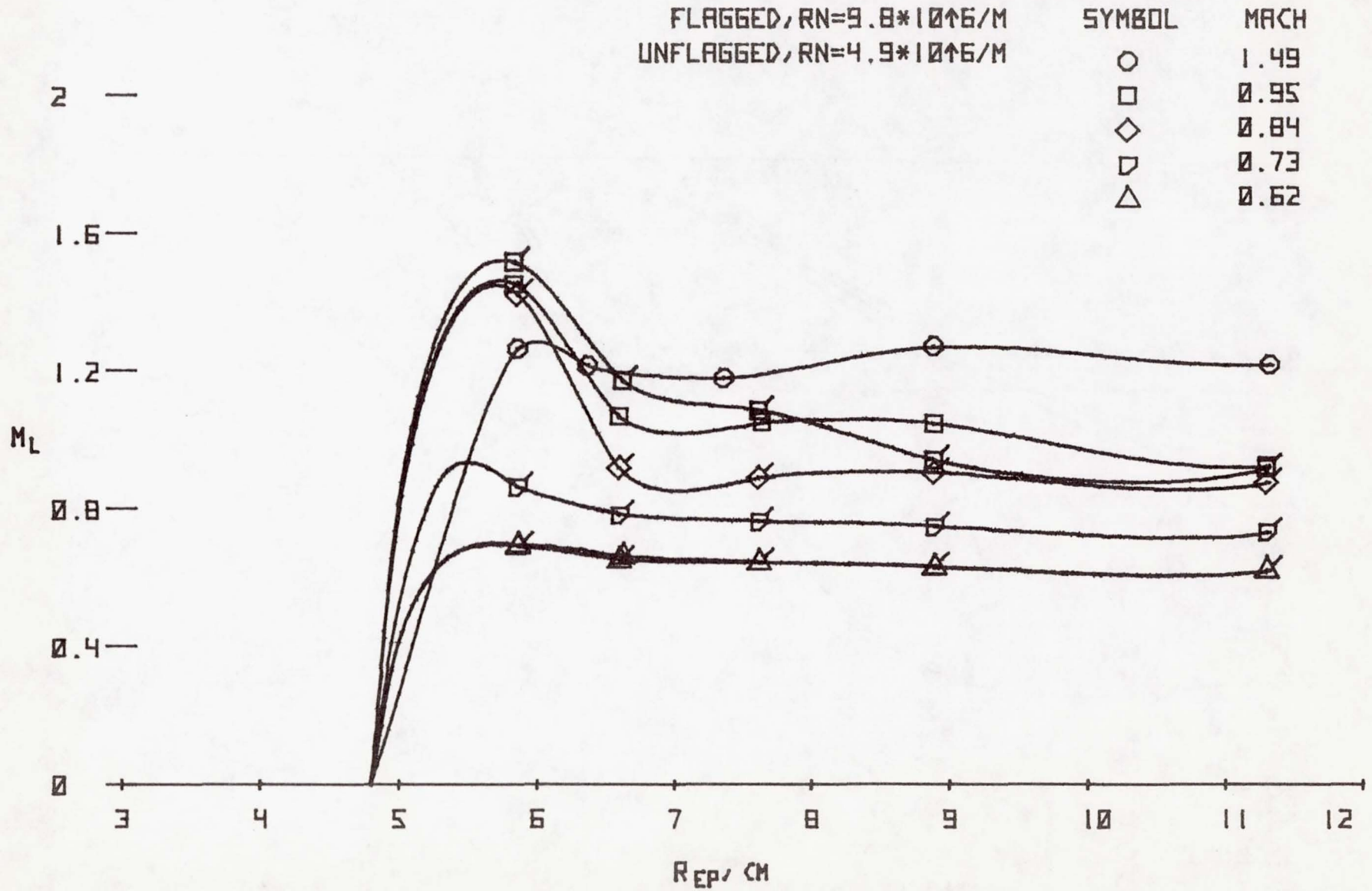

Figure 36.- Local Mach numbers along the line of sight from the turret cavity; $\theta = 90^{\circ}$, z = 2.0 cm.

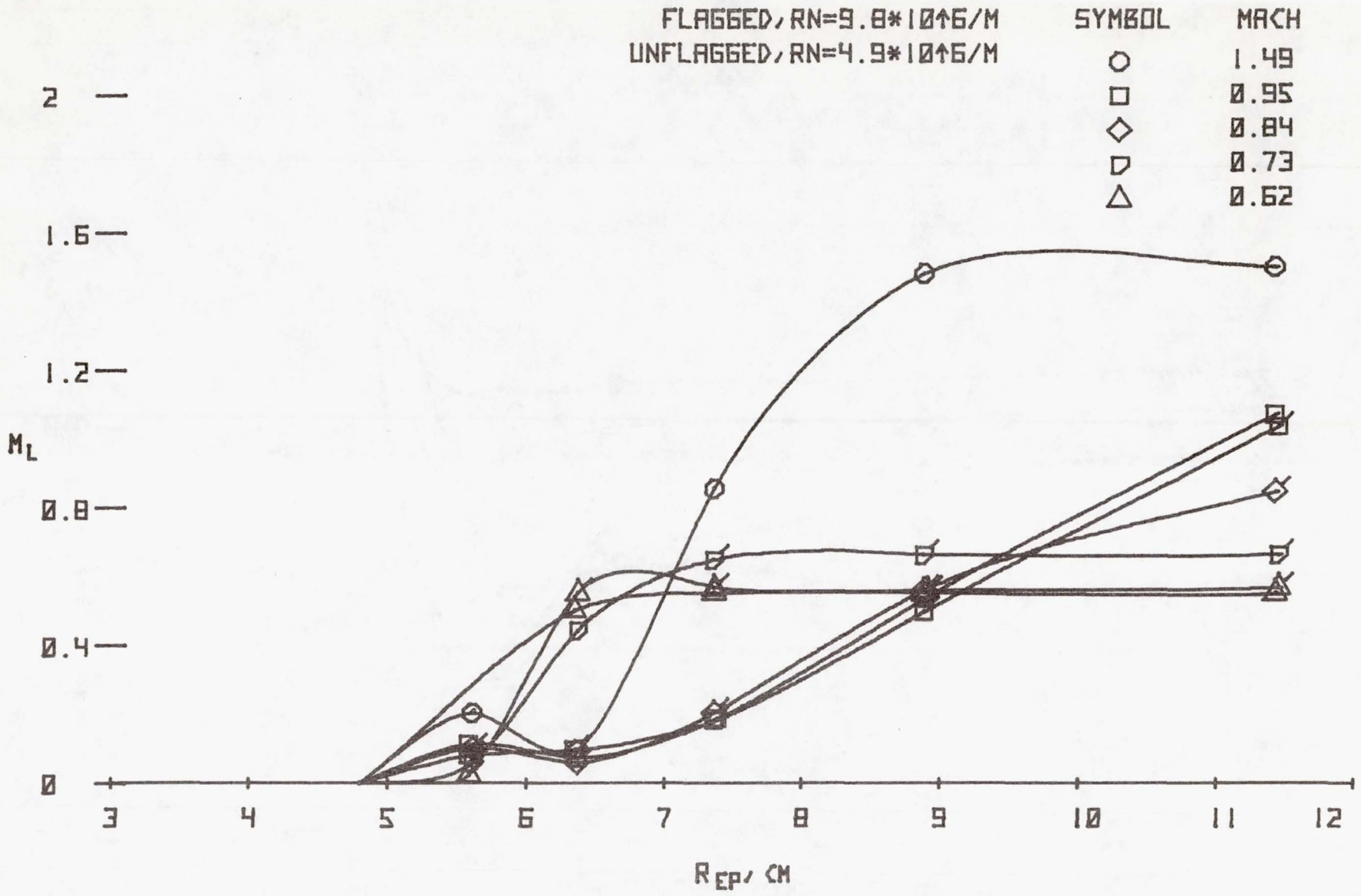

Figure 37.- Local Mach numbers along the line of sight from the turret cavity; $\theta = 150^{\circ}$, z = 2.0 cm.

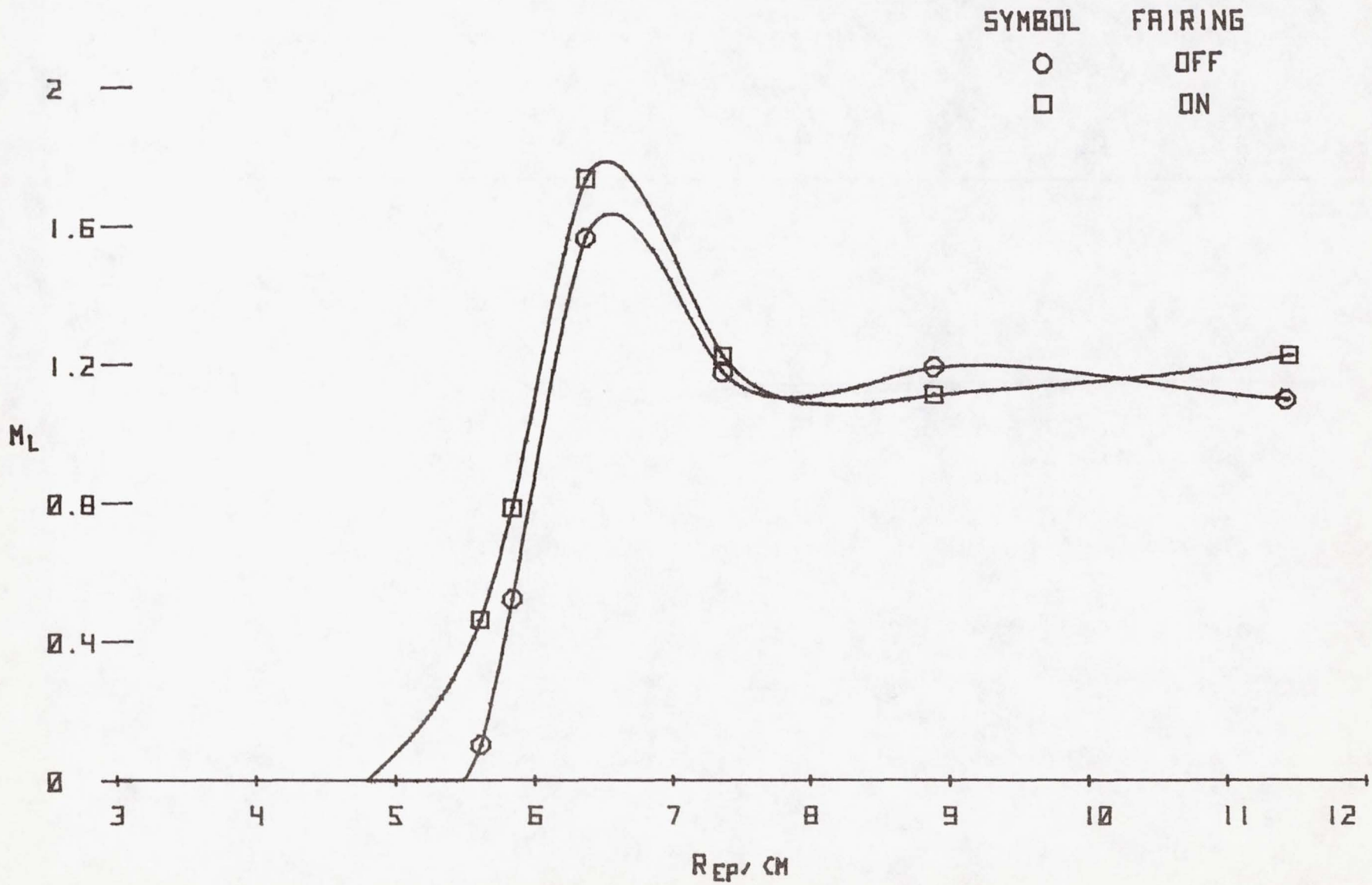

Figure 38.- Local Mach numbers along the line of sight from the turret cavity; M = 0.95, R = 9.8 million/m, $\theta = 120^{\circ}$, z = 2.0 cm.

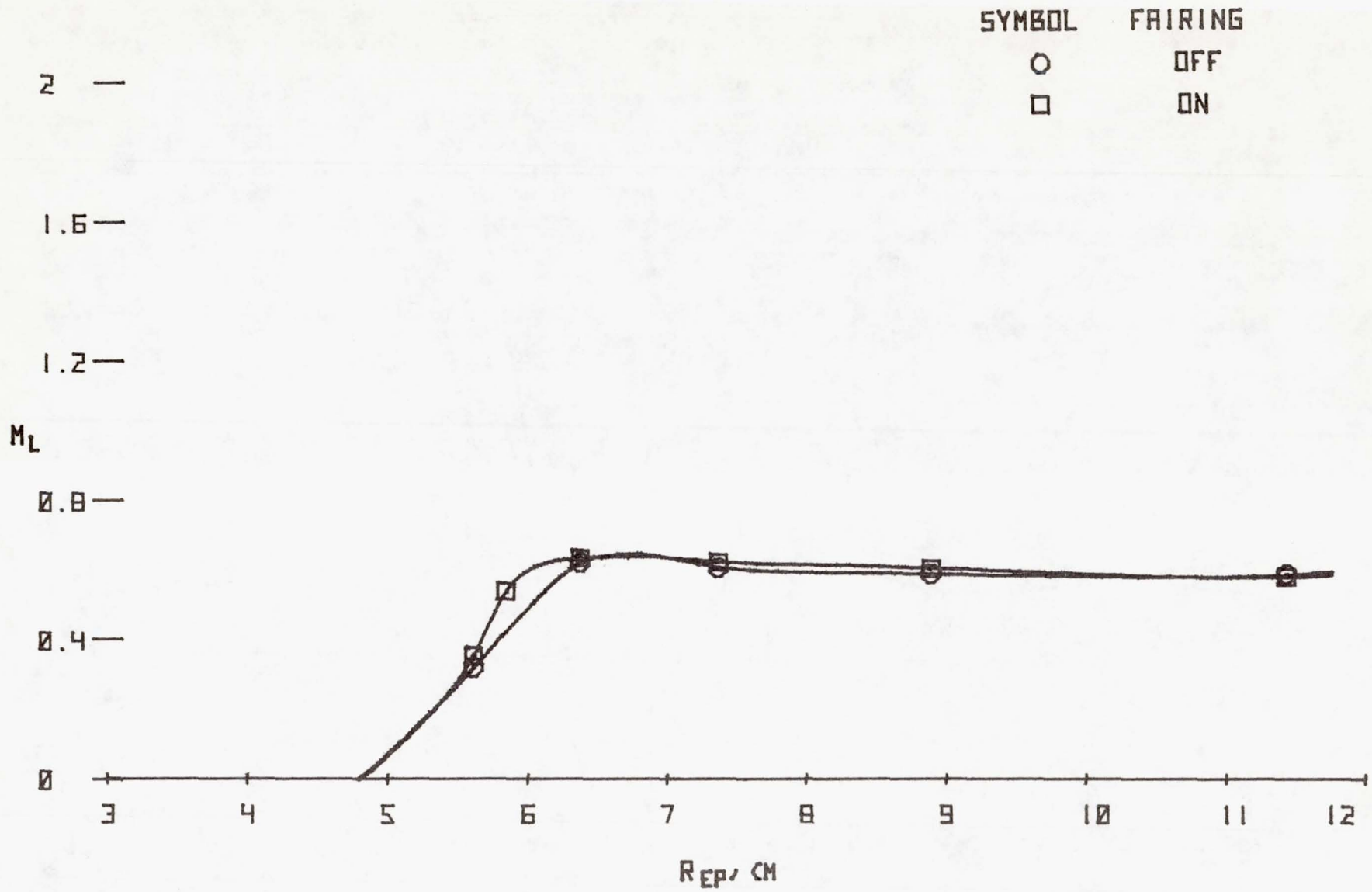

Figure 39.- Local Mach numbers along the line of sight from the turret cavity; M = 0.62, R = 10.0 million/m, $\theta = 120^{\circ}$, z = 2.0 cm.

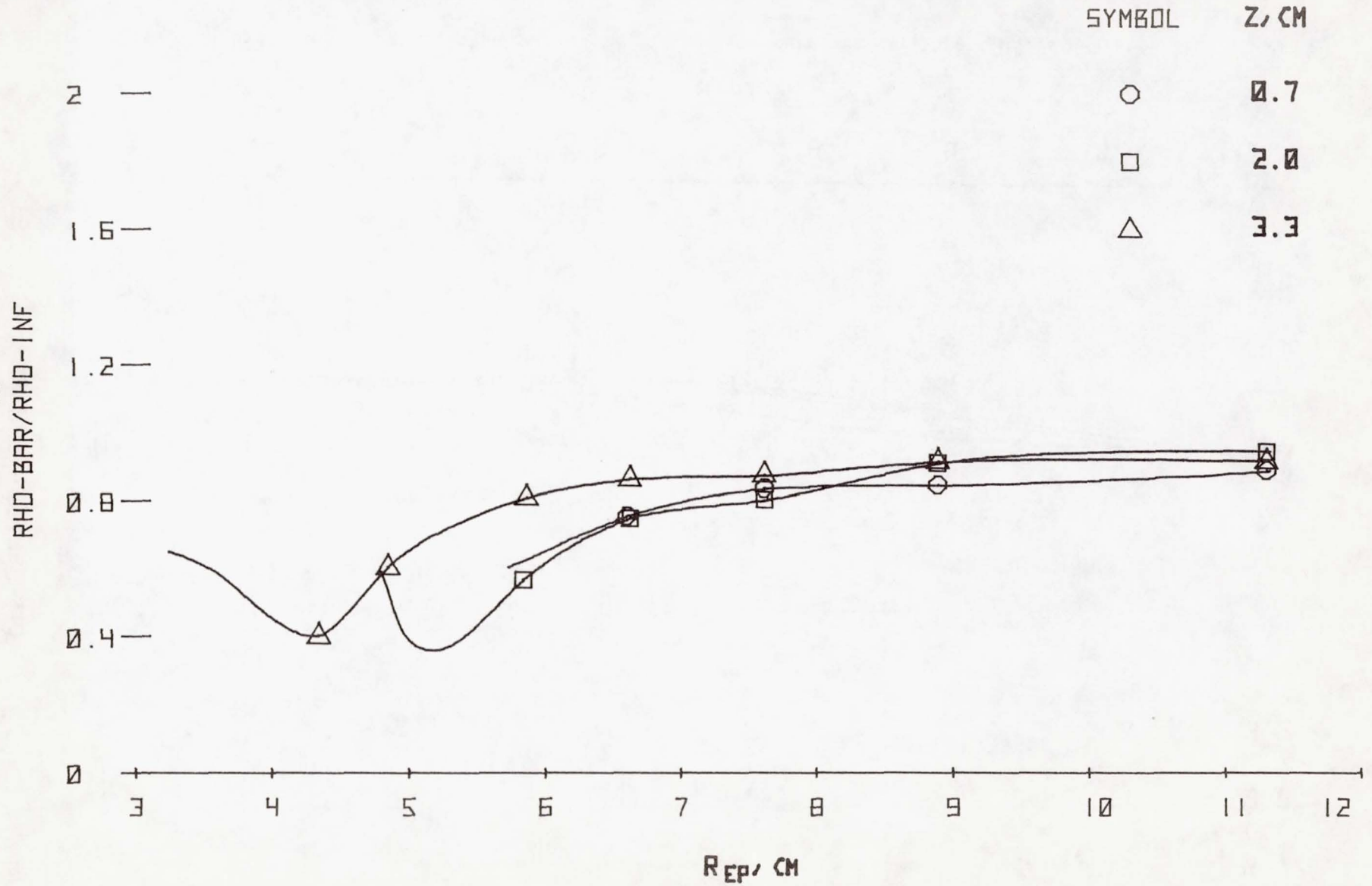

Figure 40.- Local density along the line of sight from the turret cavity; M = 0.95, R = 9.8 million/m, $\theta = 90^{\circ}$.

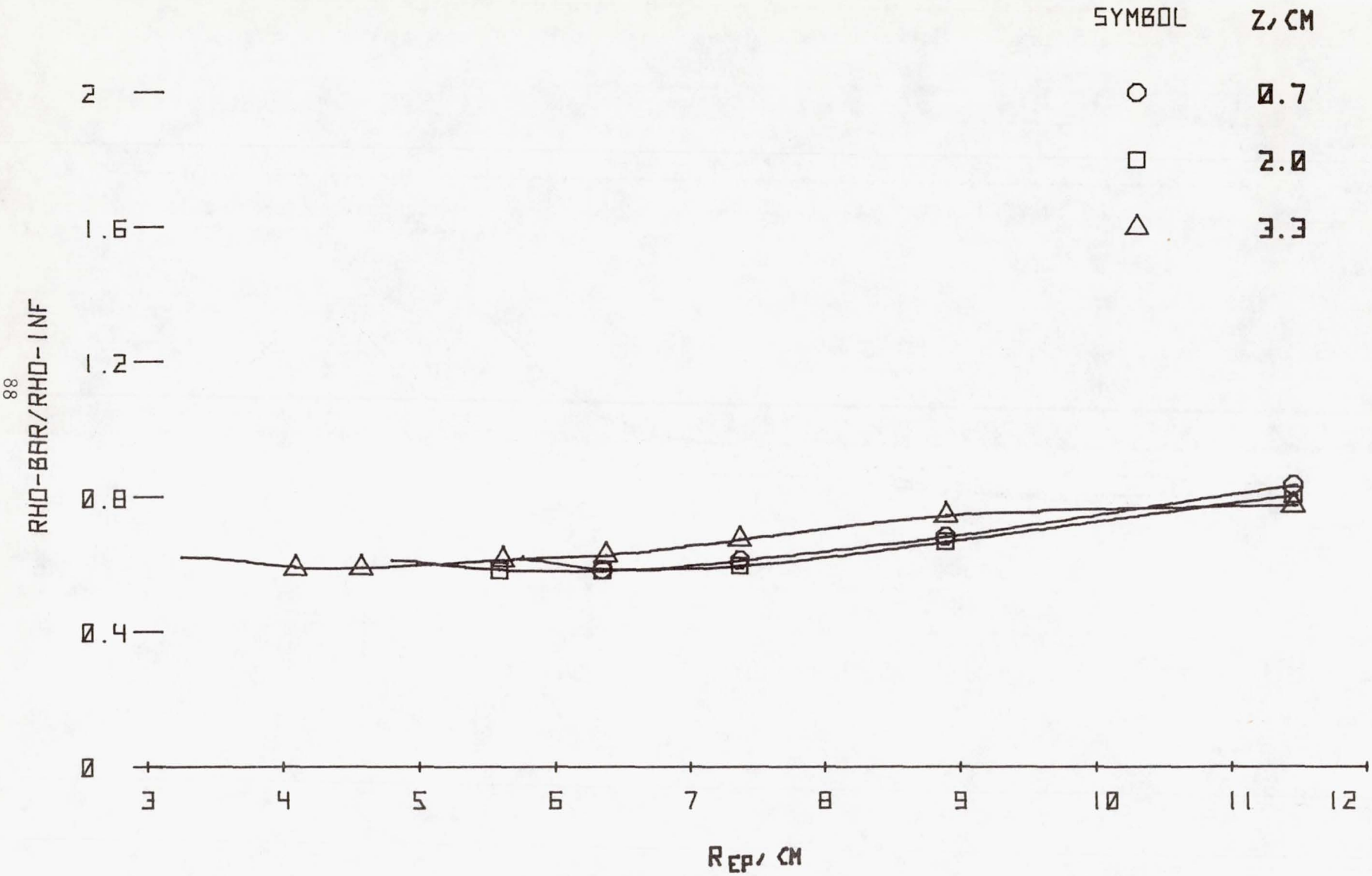

Figure 41.- Local density along the line of sight from the turret cavity; M = 0.95, R = 9.8 million/m, $\theta = 150^{\circ}$.

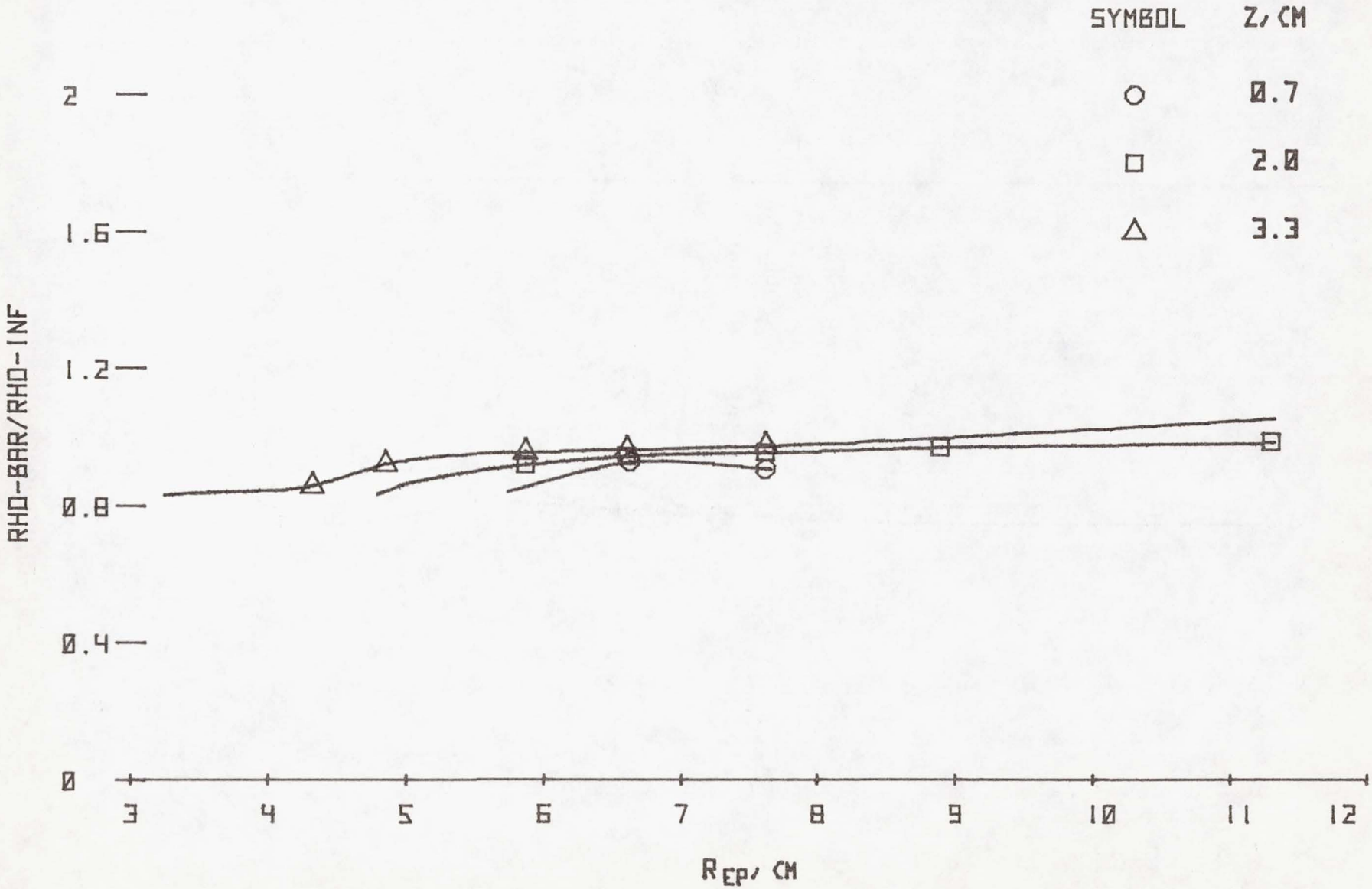

Figure 42.- Local density along the line of sight from the turret cavity; M = 0.62, R = 10.0 million/m, $\theta = 90^{\circ}$.

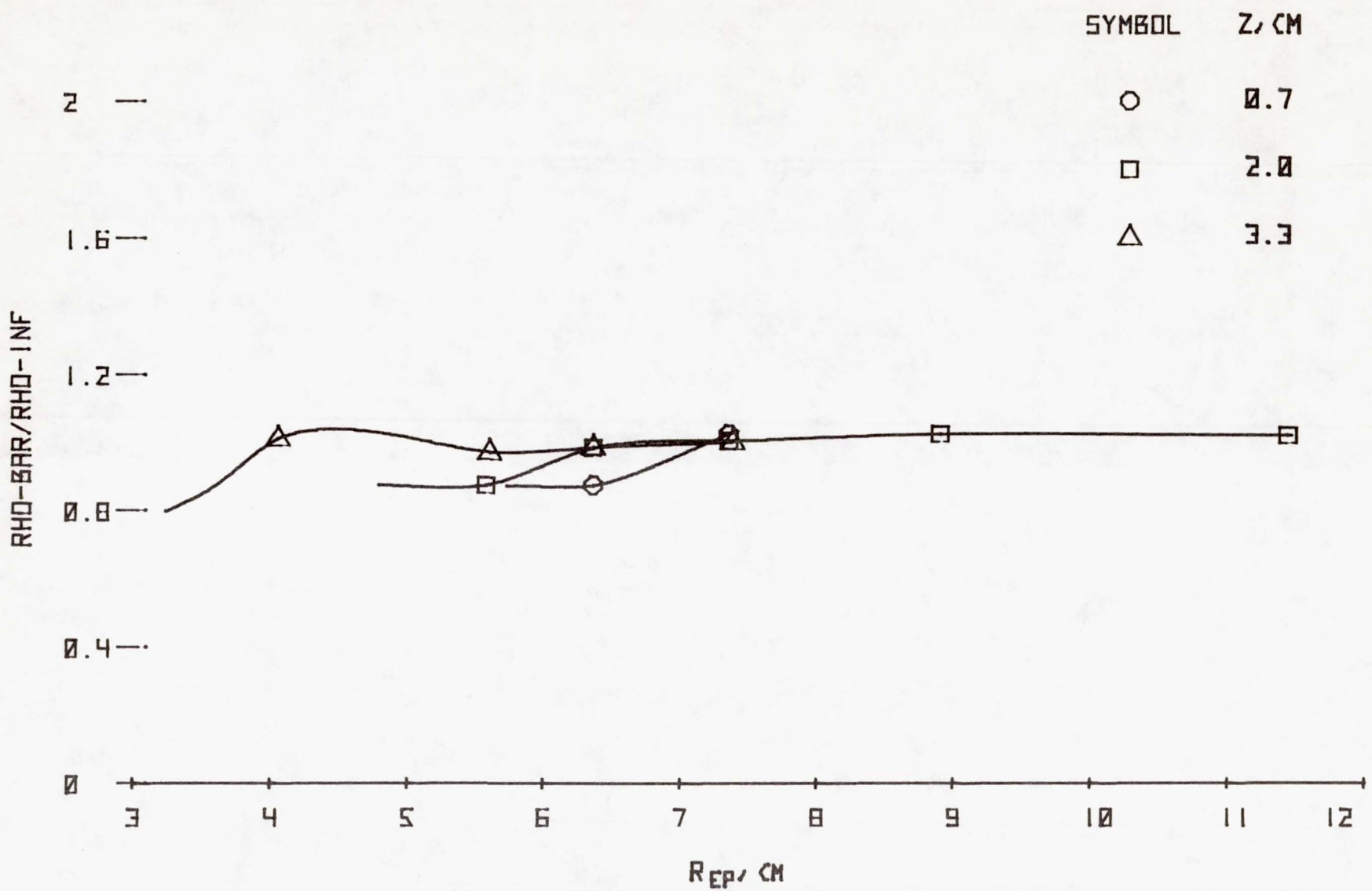

Figure 43.- Local density along the line of sight from the turret cavity; M = 0.62, R = 10.0 million/m, $\theta = 150^{\circ}$.

Pressure and Temperature Fields Associated with Aero-Optics Tests†

K.R.Raman
Raman Aeronautics, Inc.

Summary

This paper describes the experimental investigations carried out in the 6 x 6 ft Ames wind tunnel at Moffett Field, California, on four model configurations in the Aero-Optics series of tests, and presents the data obtained on the random pressures (static and total pressures) and total temperatures from these tests. In addition, the data for static pressure fluctuations on the Coelostat turret model are presented.

These measurements indicate that the random pressures and temperatures are negligible compared to their own mean (or steady state) values for the four models considered, thus allowing considerable simplification in the calculations to obtain the statistical properties of the density field. In the case of the Coelostat model tests these simplifications cannot be assumed a priori and require further investigation. Some correlation data obtained using two identical probes, are also presented here. From these correlation plots appropriate scale lengths can be determined.

Symbols

M	Free-stream Mach number
p	Static pressure, N/m^2
$\tilde{p}$	RMS value of static pressure, N/m^2
p_T	Total pressure, N/m^2
$\tilde{p}_T$	RMS value of total pressure, N/m^2
PSD	Power spectral density, $(N/m^2)^2$
q	Dynamic pressure, N/m^2
Re/m	Reynolds number per meter, 1/L
RMS	Root mean square value of parameter under consideration
T_T	Total temperature, ^oK
$\tilde{T}_T$	RMS value of total temperature, ^oK
ΔT	Surface temperature increase of splitter plate, ^oK
$\vec{U}_\infty$	Free-stream velocity, m/sec
$\vec{X}$	Position vector, (x,y,z), L
θ	Angular orientation of cavity in the Coelostat turret model, deg
τ	Time delay, sec.

Subscripts and Superscripts

∞	Free-stream conditions
$\sim$	RMS value of the parameter
$-$	Steady state value of the parameter considered
l	Local conditions

† This reported work was carried out under contract NAS 2-9920 funded by NASA/Ames Research Center, Moffett Field, CA.

Introduction

A laser beam from an Airborne Laser Laboratory (ALL) degrades in its performance as it passes through the aerodynamic flow field shrouding the aircraft. This performance degradation is directly dependent on the refractive index variations in time and space in the media. The refractive index itself is related to the local density, a parameter not readily amenable to direct measurements. In order to obtain the density field data indirectly one needs the measurements of all the pertient aerodynamic flow field parameters, namely, pressure (static and total pressures), temperature and velocity in the selected regions of interest. In this series of tests several experimenters participated, each contributing in his own field of expertise, and through the combined efforts a considerable amount of knowledge has been gained. The data concerning the pressure and temperature field will be discussed in this paper. Using the results from this experimental investigation along with some additional measurements of their own regarding the velocity field (using a Laser Doppler velocimeter) and the mass flux data acquired with the use of hotwire anemometry, an assessment of the density field was made by Rose and Johnson in their paper entitled "Unsteady Density and Velocity Measurements".

In addition, the information regarding scale lengths along the look direction of the pointing and tracking systems is required in order to determine the Strehl ratio along the optical path.

Experimental Facility

The wind-tunnel test facility and all the model configurations used in these tests are described fully by Buell in his paper "Overview of 6 x 6 ft Wind-tunnel Aero-Optics Tests" and in Ref.1. These tests were carried out with the following wind-tunnel test section flow conditions:

$$0.50 < \text{free-stream Mach number}, (M_\infty) < 1.00$$

$$6 \times 10^6 < \text{Reynolds number/meter} < 10^7$$

$$290^\circ \text{ K} < \text{total temperature of test stream} < 310^\circ \text{ K}$$

In fig. 1 the four models that were considered in this investigation are sketched with all significant components identified in order to point out the differences between each of the models tested.

Instrumentation

A rake consisting of 20 total pressure tubes and 2 static pressure tubes spanning 17 cm normal to the splitter plate was used to obtain the steady velocity profiles in the regions of interest. The surface static pressure†

† Static pressures being constant through the boundary layer (verified by our measurements) is the reason for using surface static pressures in calculations.

and free-stream total temperature data were necessary in these velocity calculations from the rake pressure data.

A specially designed " multi-probe " was used to measure steady and unsteady components of static pressures, total pressures and total temperatures in the region between the splitter plate and the return mirror and in regions above the cubical cavity opening. In fig.2 details of the multi-probe are schematically illustrated. The probe contains several components, all of them labelled in the sketch and briefly described in the figure itself. Two differential pressure sensors, *I* and *II*, monitor the fluctuations in total pressures and static pressures about their local mean pressures. The electrical leads are omitted in this illustration to avoid confusion. Tube AA (sensing the total pressure) is connected to a 4 meter long small capillary tubing (diam= 0.5 mm) in order to damp all the unsteady components before it is branched into two tubes. One of the branches is connected to A'A' and thus becomes the reference pressure for sensor *I*; the other branch is connected to an appropriate sensor for obtaining the steady state total pressure. Similar procedure is adopted for the static pressure sensor *II* to obtain the fluctuations about its local mean static pressures.

A hot-wire probe is mounted ahead of the total pressure opening(see fig.2). The bent prong tips are made of Nicoll wire and the 5 microns tungsten wire is welded to these tips. The hot-wire itself is located well ahead of the pressure port in order to avoid the wake influence from the hot-wire or the tips. The frequencies present behind the wire due to vortices (assuming a Strouhal number of 0.2) that are shed are well above the operating range of the sensor *I*. For temperature measurement the hot-wire is operated at low overheating ratio and in a constant current mode of operation. Appropriate compensation electronic circuitry was built to rectify for the inherent thermal lag in the hot-wire anemometer and thus the signals from the wire itself are valid up to 10 KHz in these tests.

All required signal conditioning electronics, amplifiers for various sensors, power supplies for excitation voltages etc are standard procedure and will not be discussed in this paper. Similarly, the use of tape recorders, RMS modules, Correlators etc will not be considered here. All through the data acquisition and data analysis phases, proper calibration of the electronic units needs to be carefully made and proper records of the gains, zero offsets etc are to be kept. In all this bookkeeping of the above described electronic units, the HP-9830 desk computer has been programmed and relied on.

Results and Discussion.

The velocity profiles for models 1 and 13 are presented in fig. 3 and 4 for free-stream Mach numbers equal to 0.60 and 0.89 and Reynolds number/meter equal to 9.8×10^6. The combination of turbulence generating pins and seeding pins in model 1 and the seeding pins alone in model 13 yield comparable boundary-layer thicknesses satisfying the power law profile with $7 \leq n \leq 9$. Thus the seeding pins alone are sufficient to generate the necessary thick

boundary layer for the series of tests considered here.

The splitter plate surface temperature was elevated above the adiabatic wall temperature by 44° - 56° K (through heating the plate) in order to increase the total temperature fluctuations in the boundary layer and thereby bring about an increase in density fluctuations adjacent to the plate. The effects on the optics performance could then be examined. However, heating the plate did not greatly affect the velocity profiles or the unsteady pressures, so the addition of heat in these tests was inadeqate to bring about the anticipated effects.

In figures 5(a) and 5(b) the normalized pressures, namely the ratios of RMS static pressure to the mean free-stream static pressure, $\tilde{p} / \bar{p}_{\infty}$, and the RMS total pressure to the mean free-stream total pressure, $\tilde{p}_T / \bar{p}_{T\infty}$, are given for model 1, M_{∞}=0.60 and M_{∞}=0.89 respectively. Similar data are presented in figures 6,7 and 8 for models 2,13 and 14. From these we note that the normalized pressures satisfy

$$0.007 < \tilde{p} / \bar{p}_{\infty} < 0.020 \qquad \text{and} \qquad 0.020 < \tilde{p}_T / \bar{p}_{T\infty} < 0.080$$

The measurement of unsteady total temperature as obtained by hot-wire anemometer in a constant current operation are given in figures 9,10,11 and 12 for M_{∞}=0.60 and M_{∞}=0.89 for all the four models considered. The essential features to observe from these measurements are

i) the surface heat addition to the splitter plate did not greatly influence the ratios of the RMS total temperatures to the free-stream total temperatures, $\tilde{T}_T / \bar{T}_{T\infty}$, and

ii) the ratio of $\tilde{T}_T / \bar{T}_{T\infty}$ in all cases considered is less than 1 %.

Using two identical multi-probes as illustrated in figure 13, and varying the separation distance between these two probes (in our investigation the normal distance to the splitter plate was varied), various cross-correlation functions were obtained. From these the scale lengths were extracted for each of the flow parameters under investigation.

In figs. 14(a), (b), and (c) the cross-correlation functions are given for static pressure, total pressure and total temperature respectively for model 1, M_{∞} = 0.89. Similar plots are given for model 13, M_{∞} = 0.89, in figs. 15(a), (b), and (c). The correlation scale lengths obtained for static pressure in general are greater than that for total pressures or total temperatures. The solid curves in these correlation plots were obtained by assuming an exponential form for the decay with increasing d and using a least square fit analysis. From this analysis the integral scale lengths are deduced. Further, if the hot-wire frequency range could be improved beyond 10 kHz, the scale length obtained from the total temperatures is expected to be comparable to the scale lengths obtained for total pressures (the pressure sensor frequency range is beyond 20 kHz).

During these tests the cross correlation functions involving fluctuations of static pressures, p, mass flux , ρu, total pressure, p_T , and total temperatures, T_T, were observed. The results indicate these correlations to be nearly zero; that is, $\overline{p(\rho u)}$, $\overline{pp_T}$,$\overline{pT_T}$ and $\overline{p_T T_T}$ are nearly zero. Thus the influence of these quantities in their contribution to RMS density values could be ignored.

In figure 16,the ratio of RMS static pressures to the local steady static pressures on the Coelostat turret model is plotted as a function of X distance. As can be seen in this case, the $\tilde{p}/\overline{p_1}$ can be as large as 8% and can play a major role in the RMS density calculations. In figure 16 the pressure data are indicated by A,B,C,D and E and correspond to sensors on the turret itself(A,B & C) and on the splitter plate (D & E). These are designated in order to present data of the power spectral analyses in figures17 and 18 corresponding to these sensors. The pressure ports A and C are located on each side of the pressure sensor B in the cavity itself. Pressure sensors D and E are located downstream of the turret model.

In figures17 and 18 the frequency content of the unsteady pressures corresponding to the sensors A to E (as given in figure 16) are presented. These power spectral density analyses were carried out at Ames Research Center using an existing Hybrid Spectral Analyzer program. In these plots the power spectral density peaks appearing at 1 kHz are due to the wind tunnel itself while the peaks at 500 Hz are due to flow associated with the Coelostat Turret model. Sensor C located on one side of the cavity does not show the peak at 500 Hz while the sensor A on the other side of the cavity shows the peak in the spectral plots. The influence of these peak signals downstream of the turret model is apparent from the results given in figure 18. As expected there is a high degree of coherence between the pressures between A,B,D and E sensors and slightly lower coherence value whenever sensor C was involved.

Reference

1. Buell,Donald A. Aerodynamic Properties of a Flat Plate with Cavity for Optical-Propagation Studies. Jan 1979. NASA Tech.Memo. 78487.

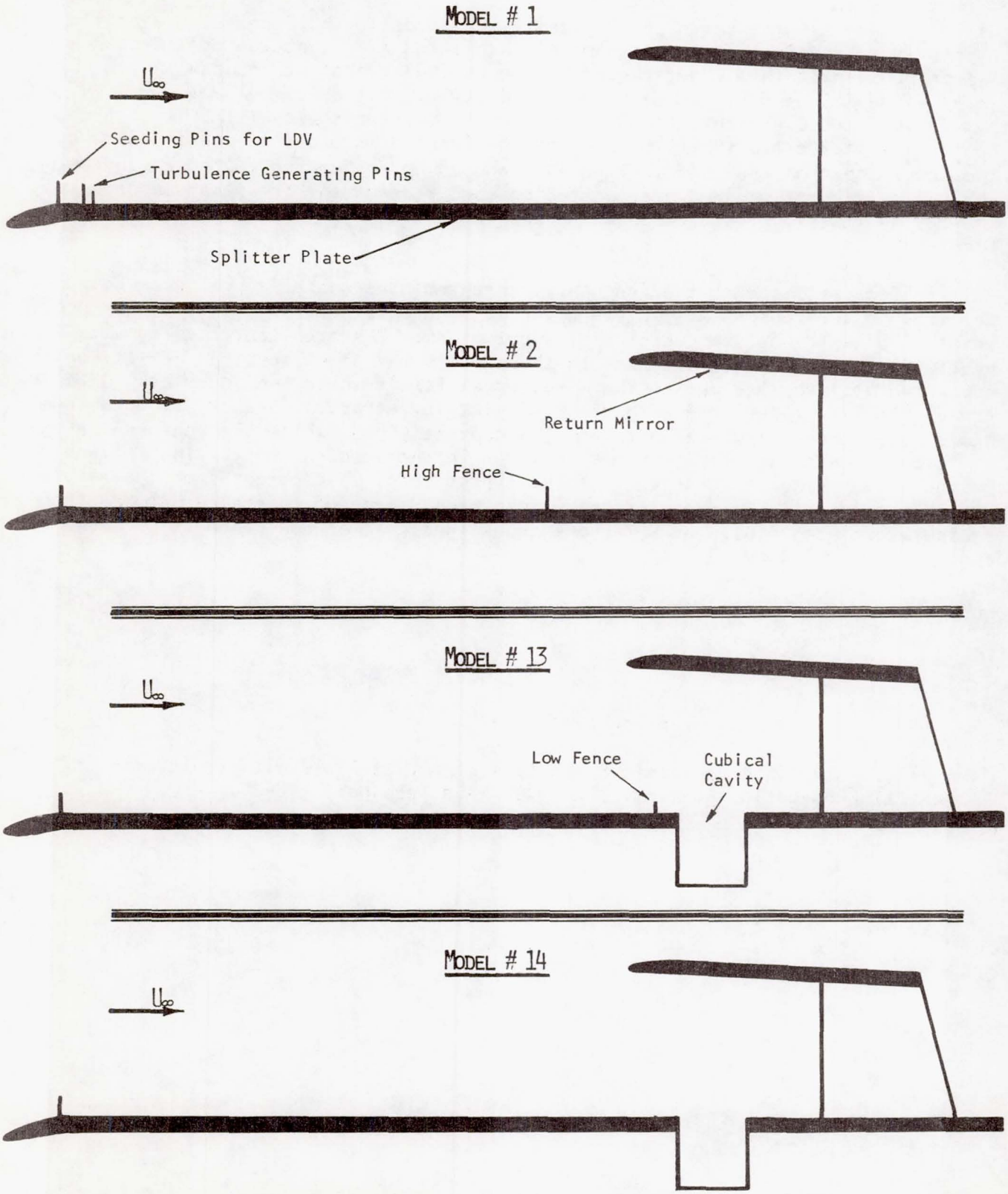

Figure 1. Sketch of the Four Selected Models Tested in 6x6 Foot Wind Tunnel.

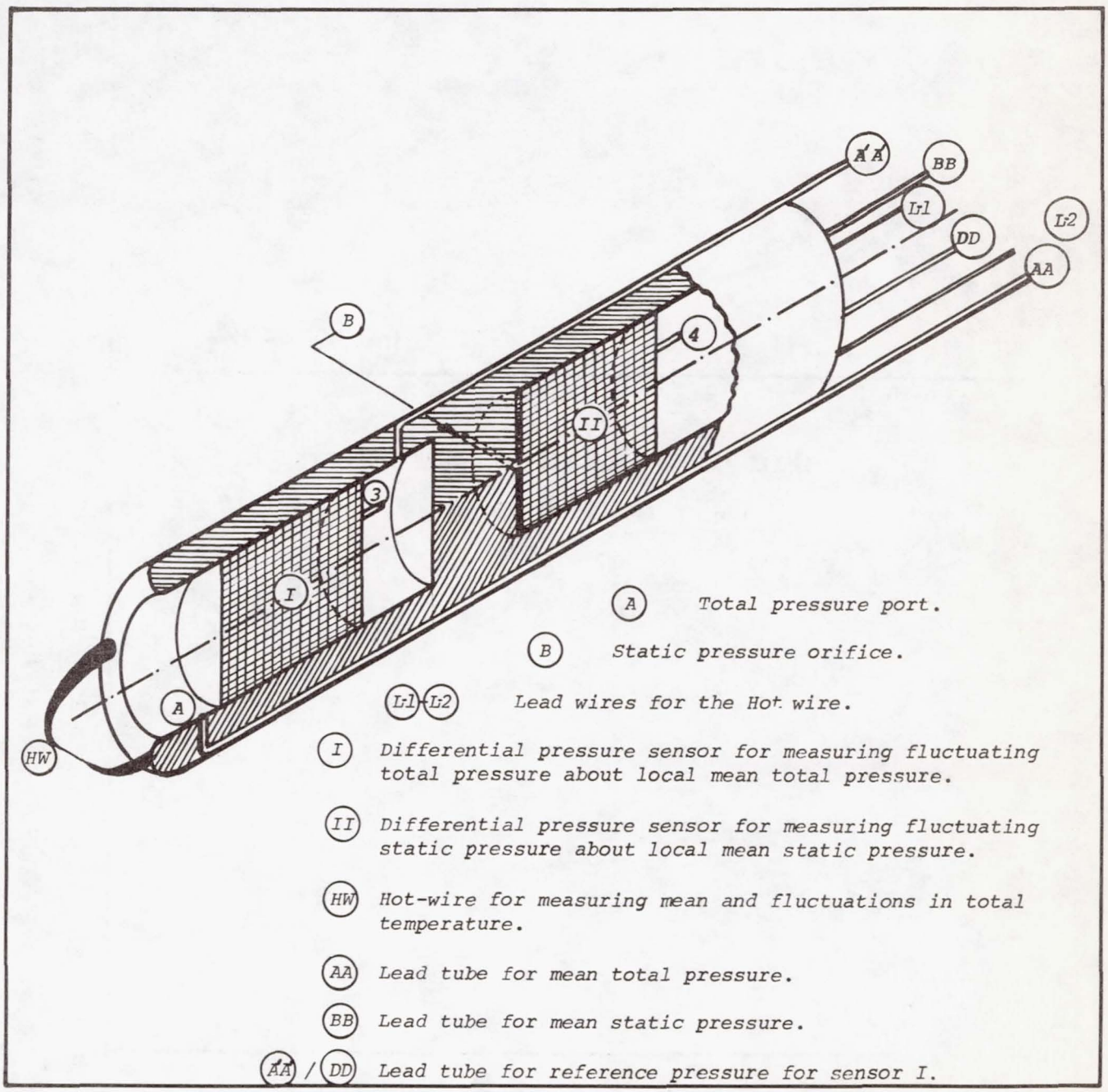

Figure 2. *Details of the Multi-probe Schematically Illustrated.*

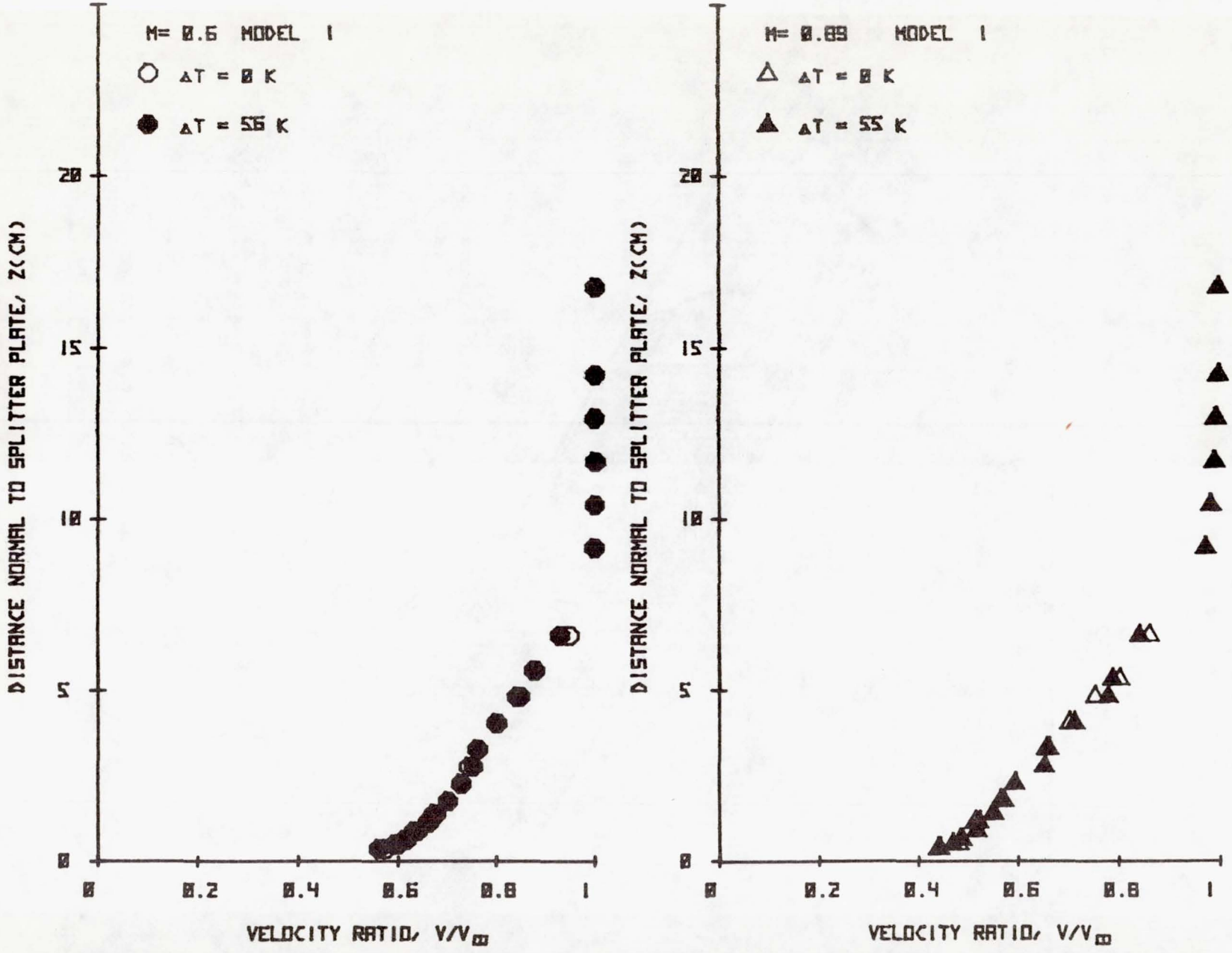

Figure 3. Velocity Profiles for Model 1 for Free-stream Mach Number 0.60 and 0.89.

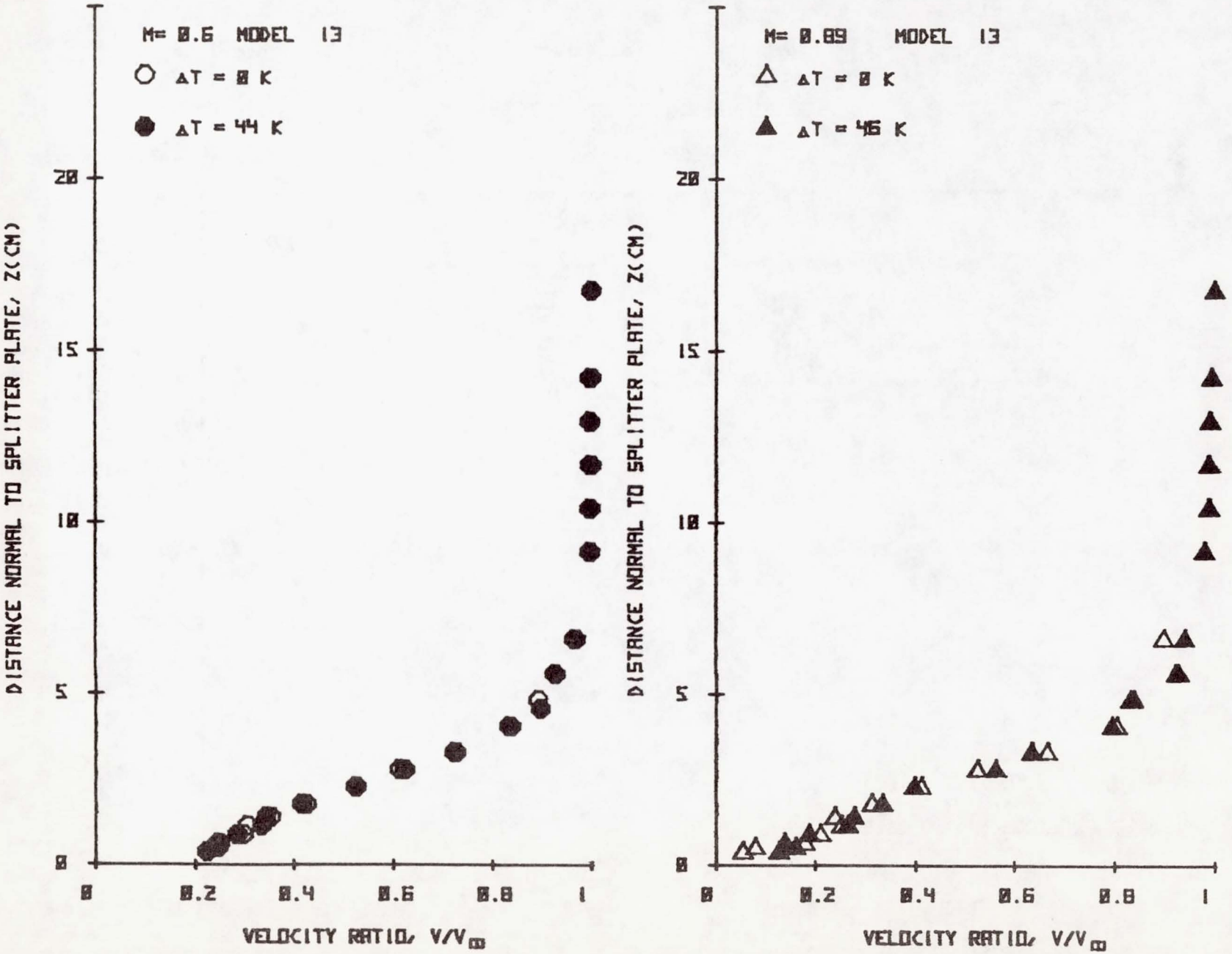

Figure 4. Velocity Profiles for Model 13 for Free-stream Mach Numbers 0.60 and 0.89.

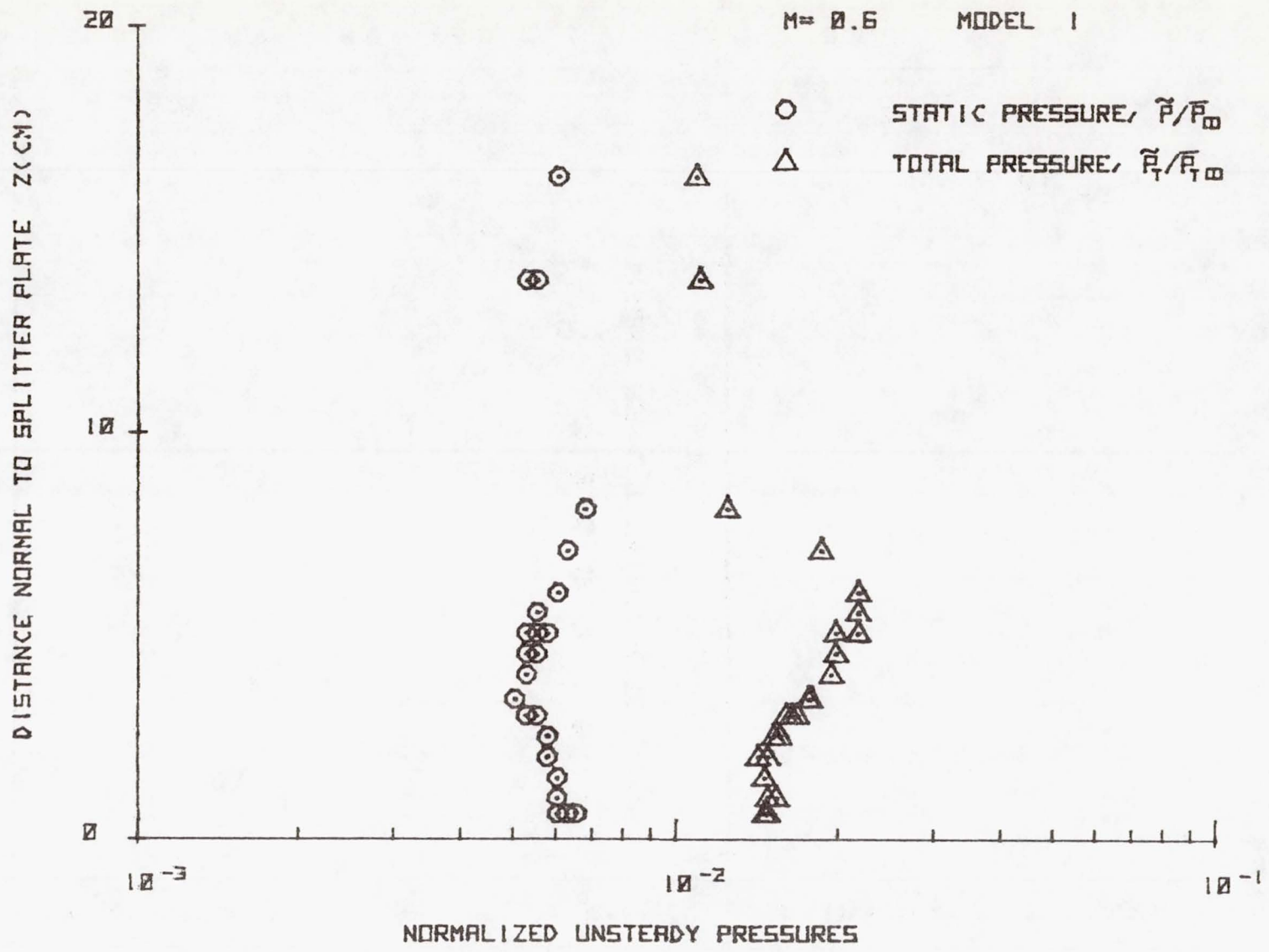

Figure 5(a). Normalized Unsteady Pressures for Model 1, M_∞=0.60.

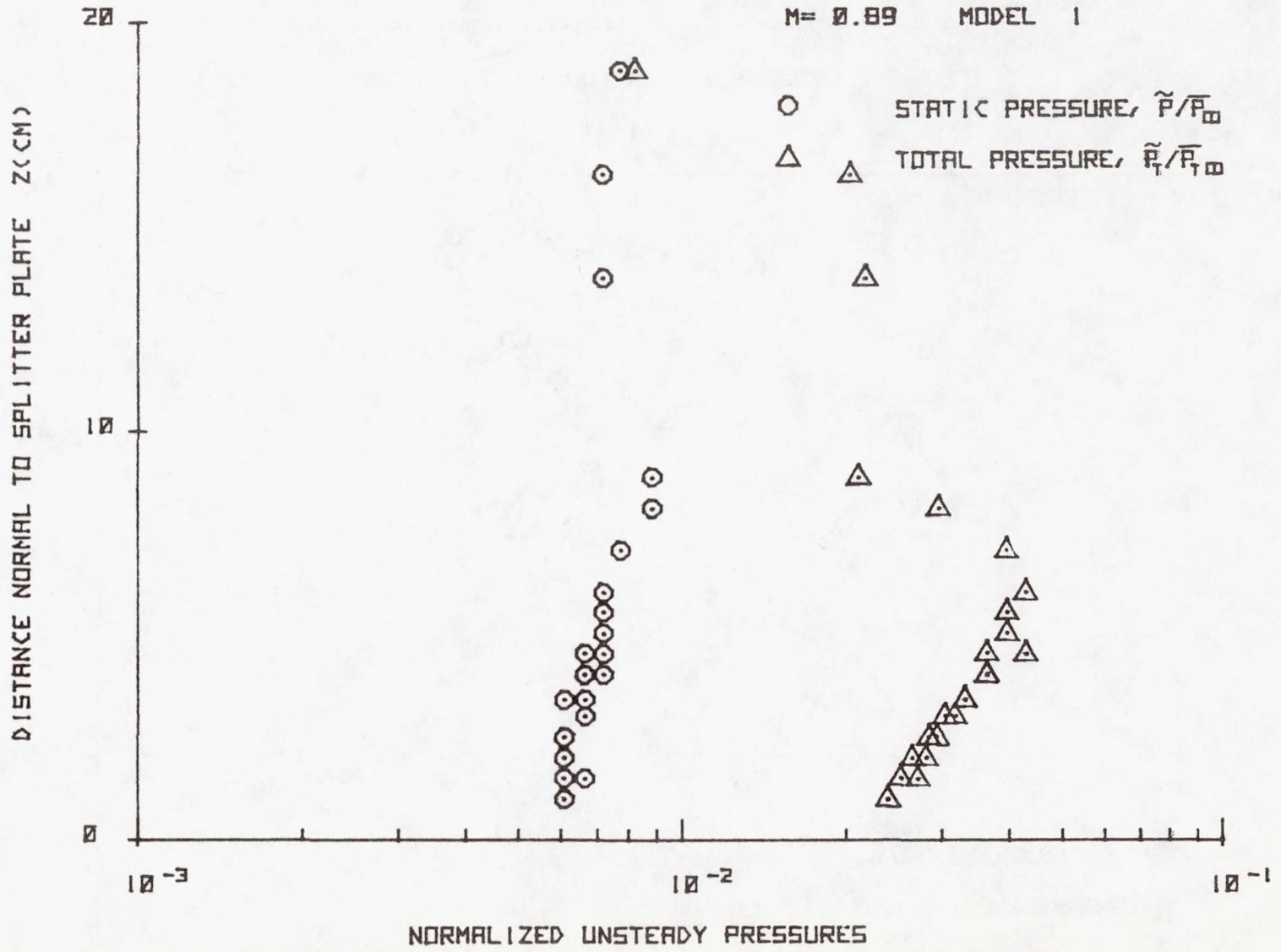

Figure 5(b). Normalized Unsteady Pressures for Model 1, M_∞ =0.89.

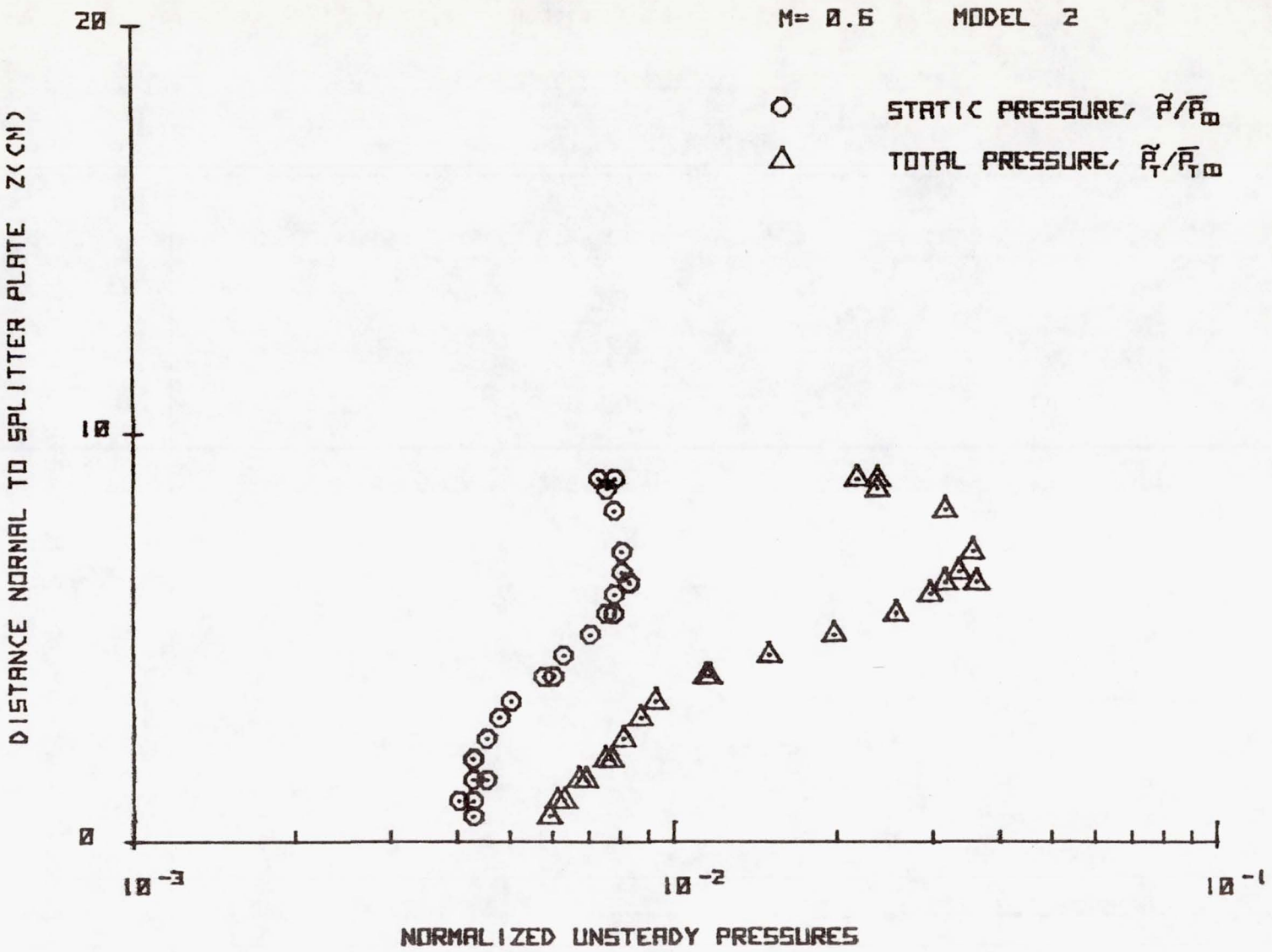

Figure 6(a). Normalized Unsteady Pressures for Model 2, M_∞=0.60.

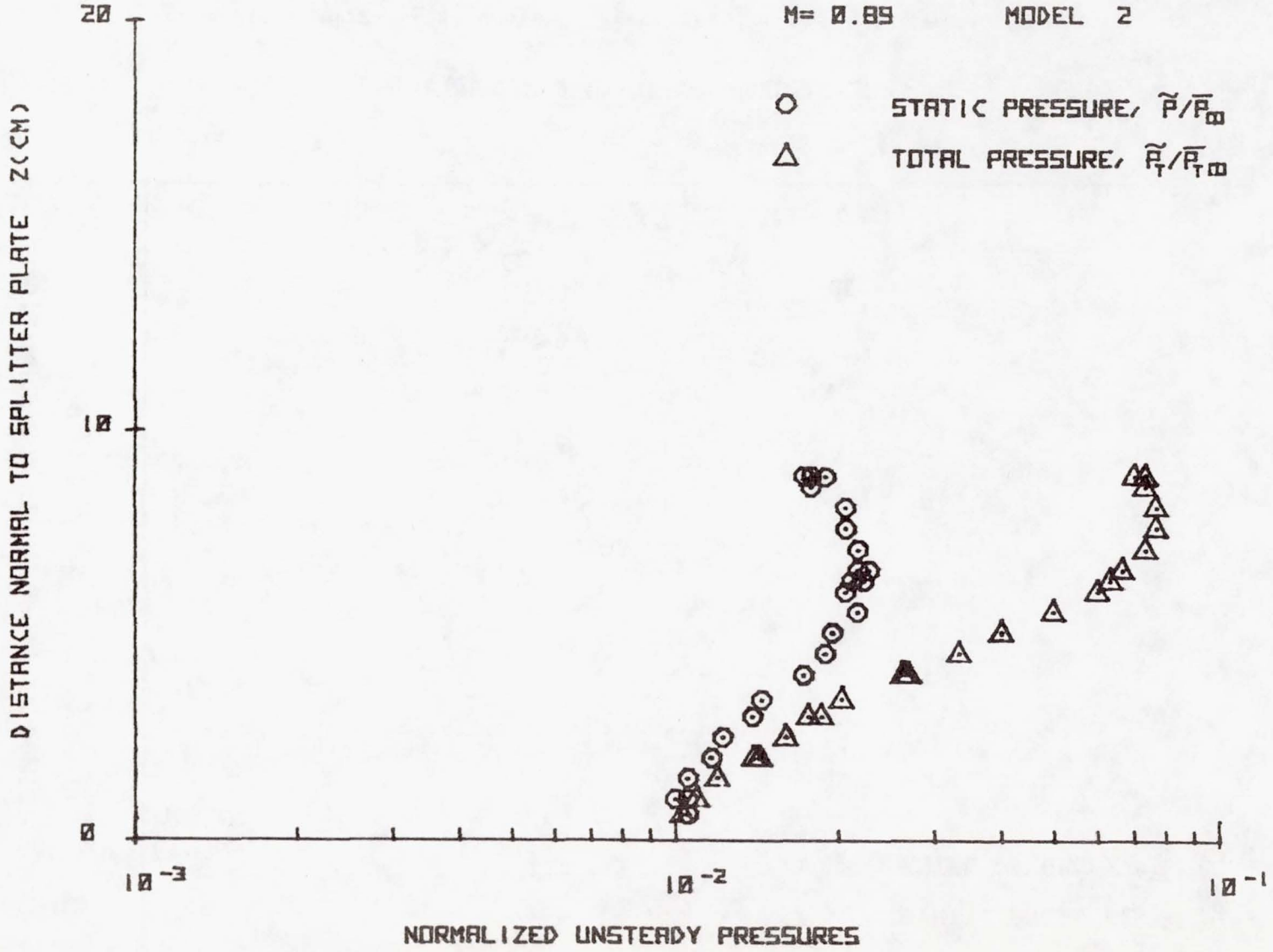

Figure 6(b). Normalized Unsteady Pressures for Model 2, M_∞=0.89.

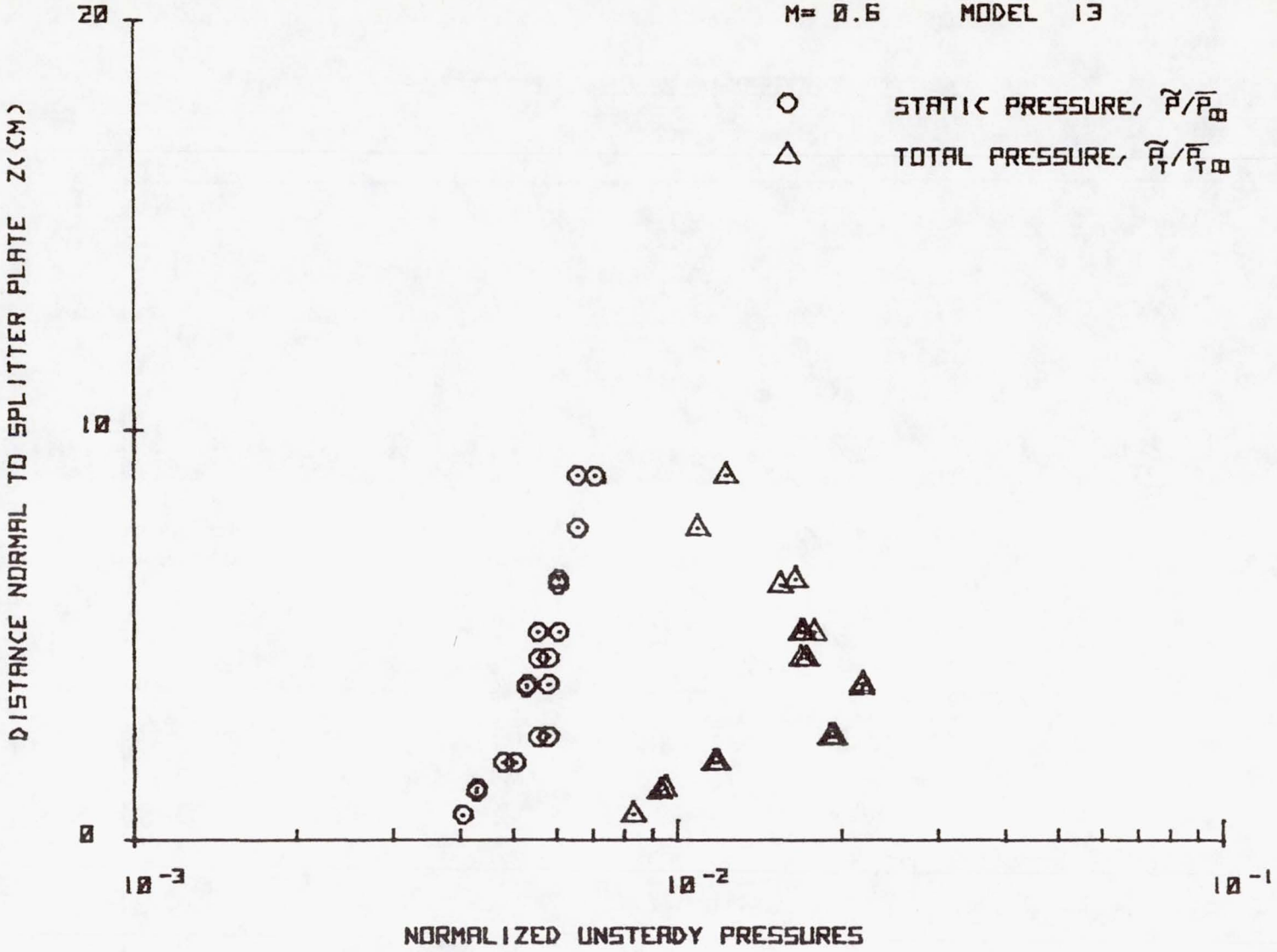

Figure 7(a). Normalized Unsteady Pressures for Model 13, M_∞ =0.60.

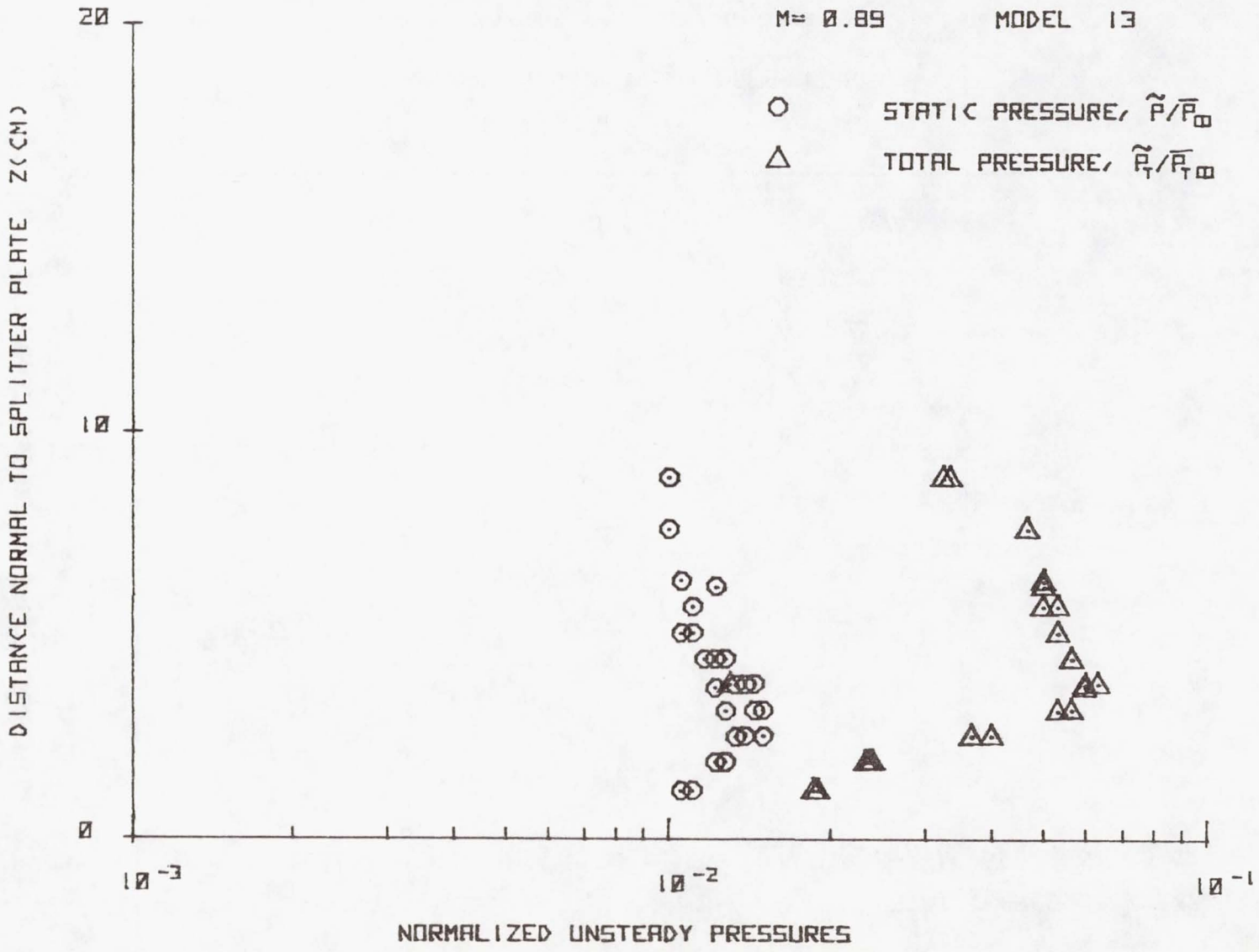

Figure 7(b). Normalized Unsteady Pressures for Model 13, M_∞ =0.89.

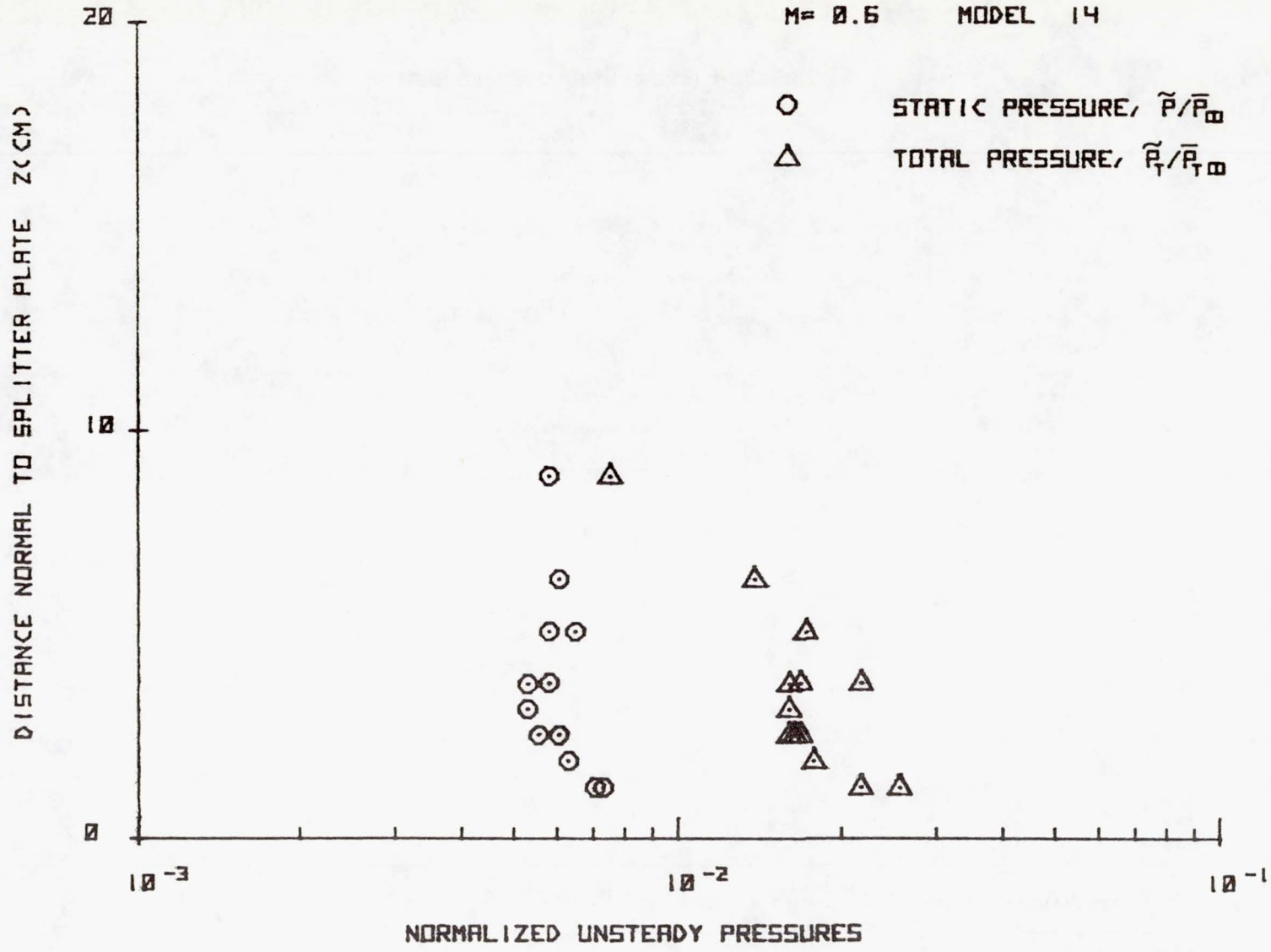

Figure 8(a). Normalized Unsteady Pressures for Model 14, M_∞ =0.60.

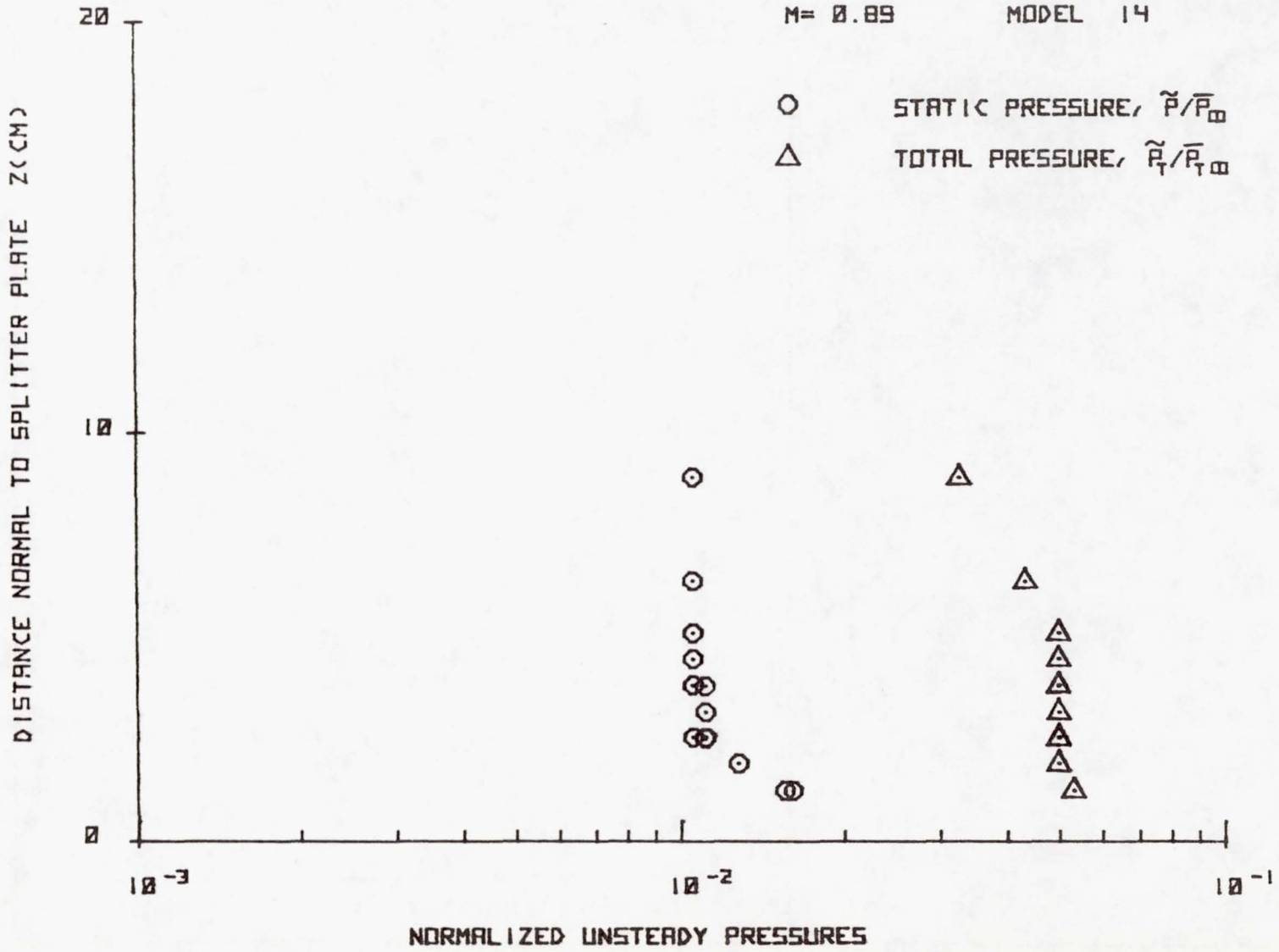

Figure 8(b). Normalized Unsteady Pressures for Model 14, M_∞= 0.89

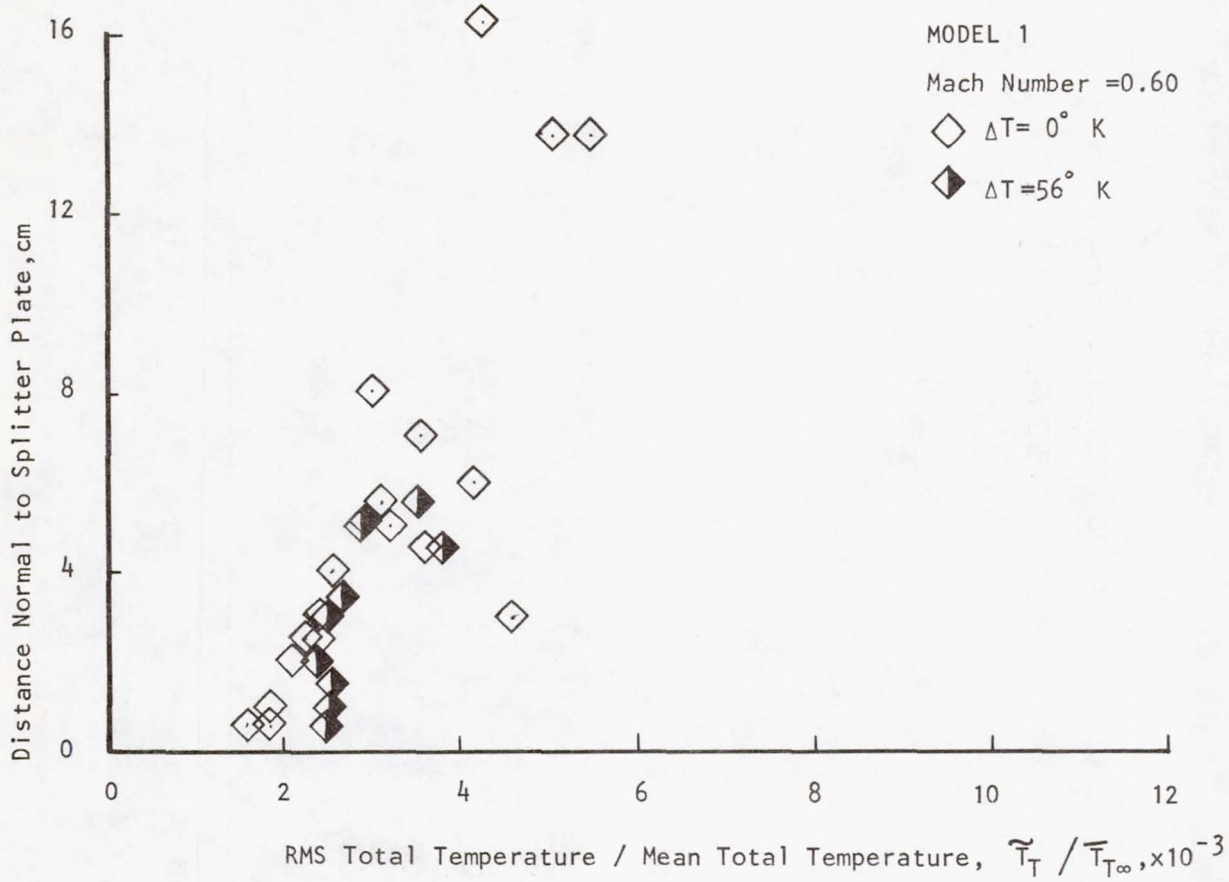

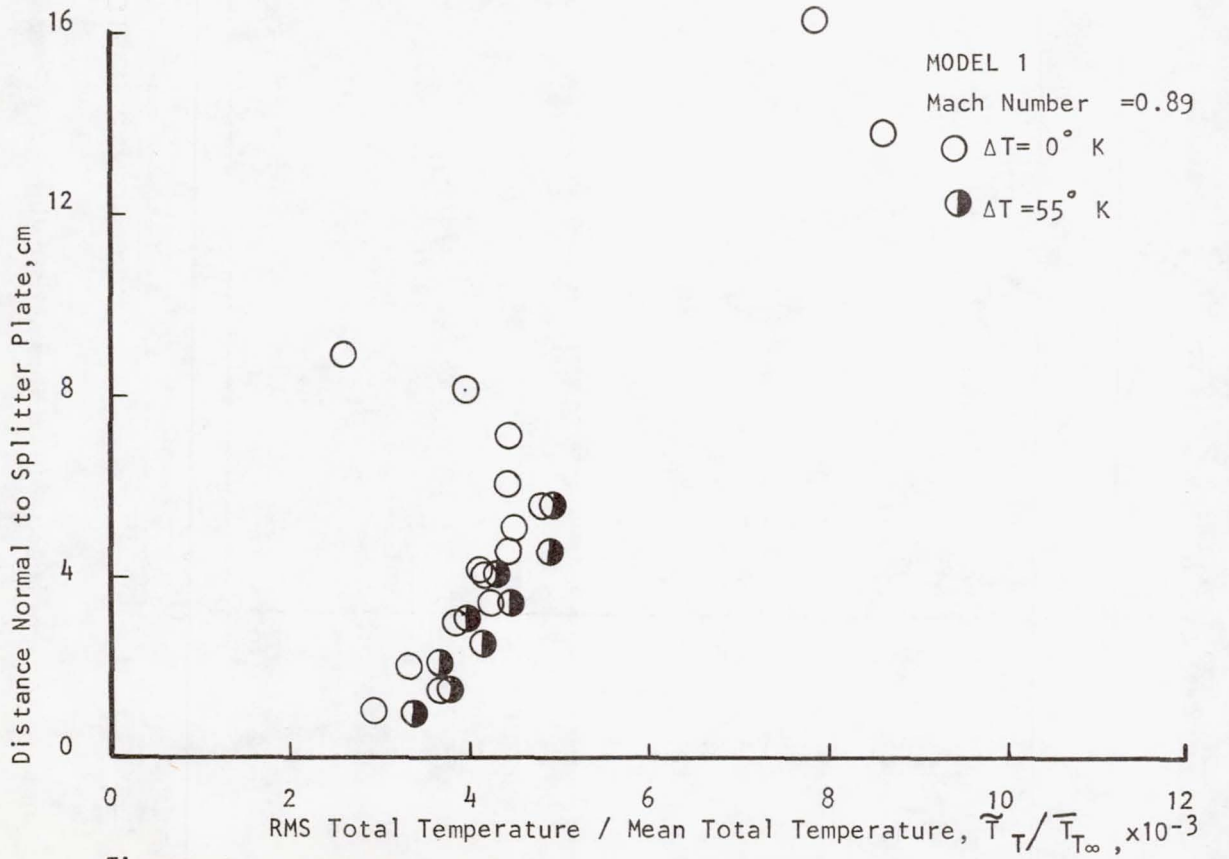

Figure 9 . Normalized Unsteady Total Temperatures for Model 1.

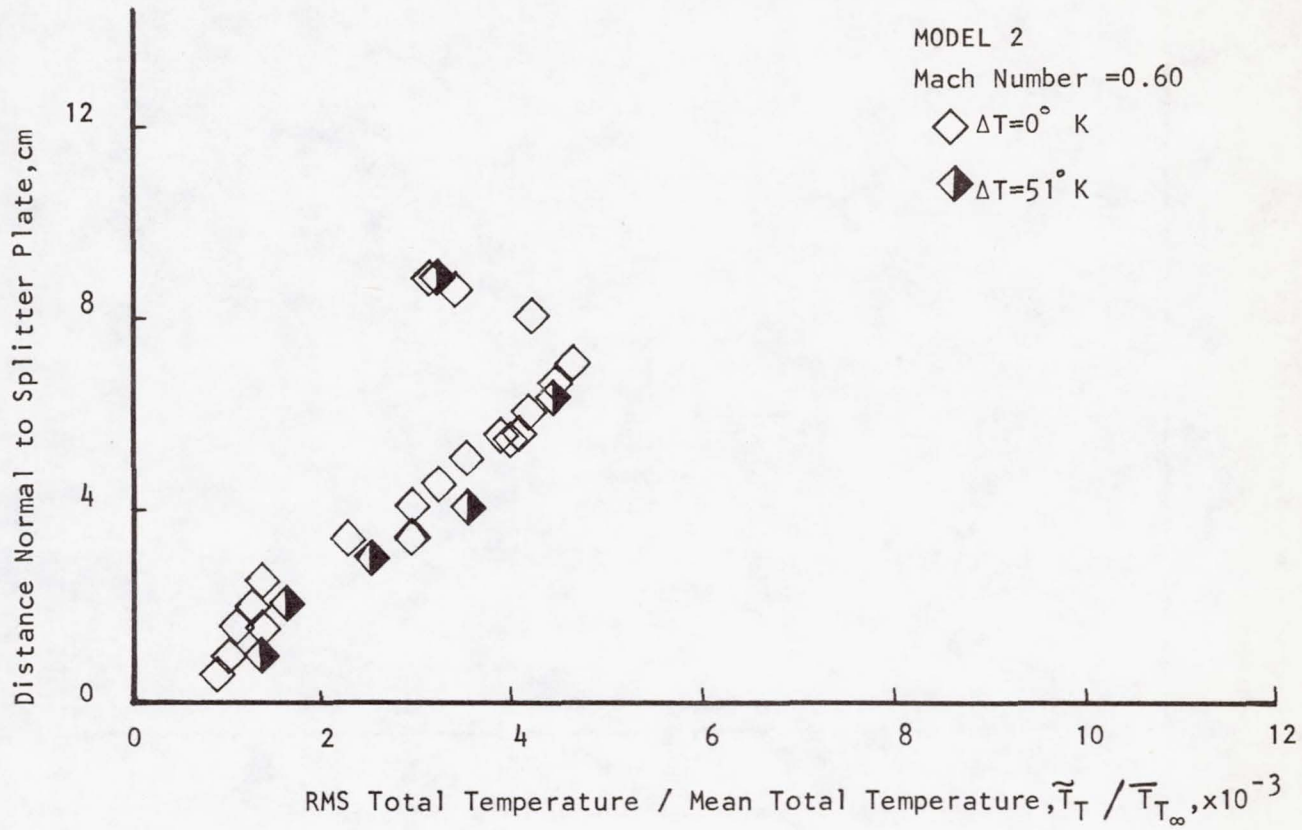

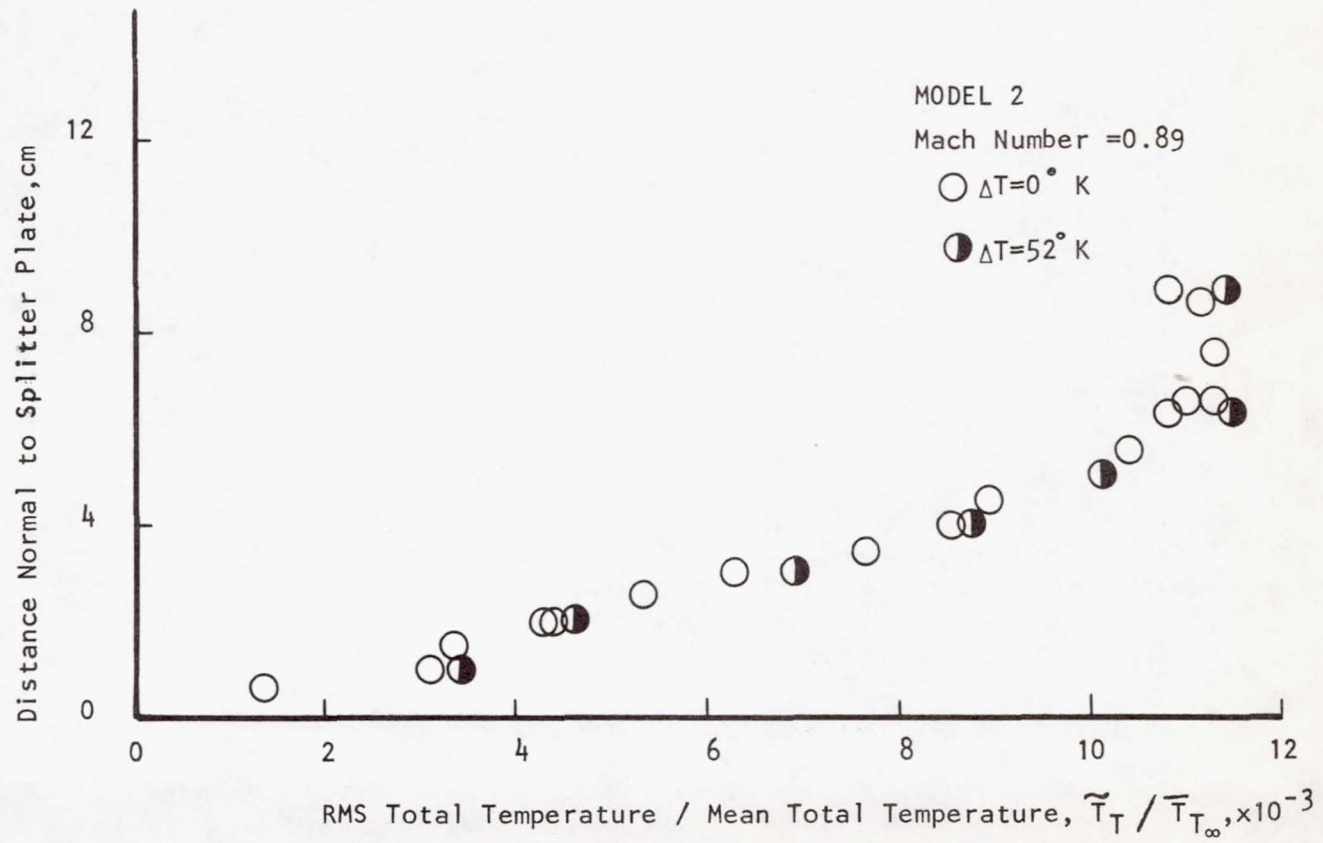

Figure 10 . Normalized Unsteady Total Temperatures for Model 2.

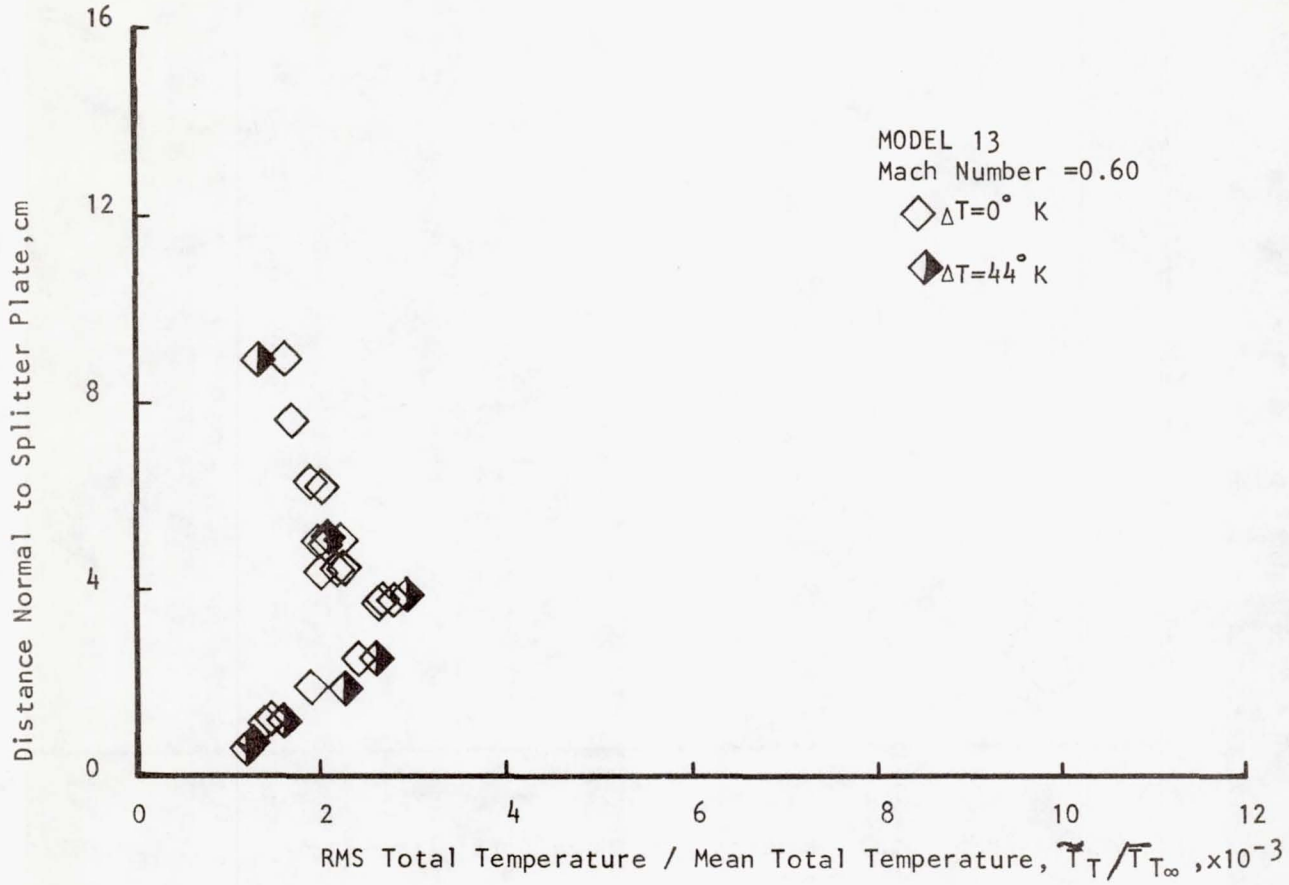

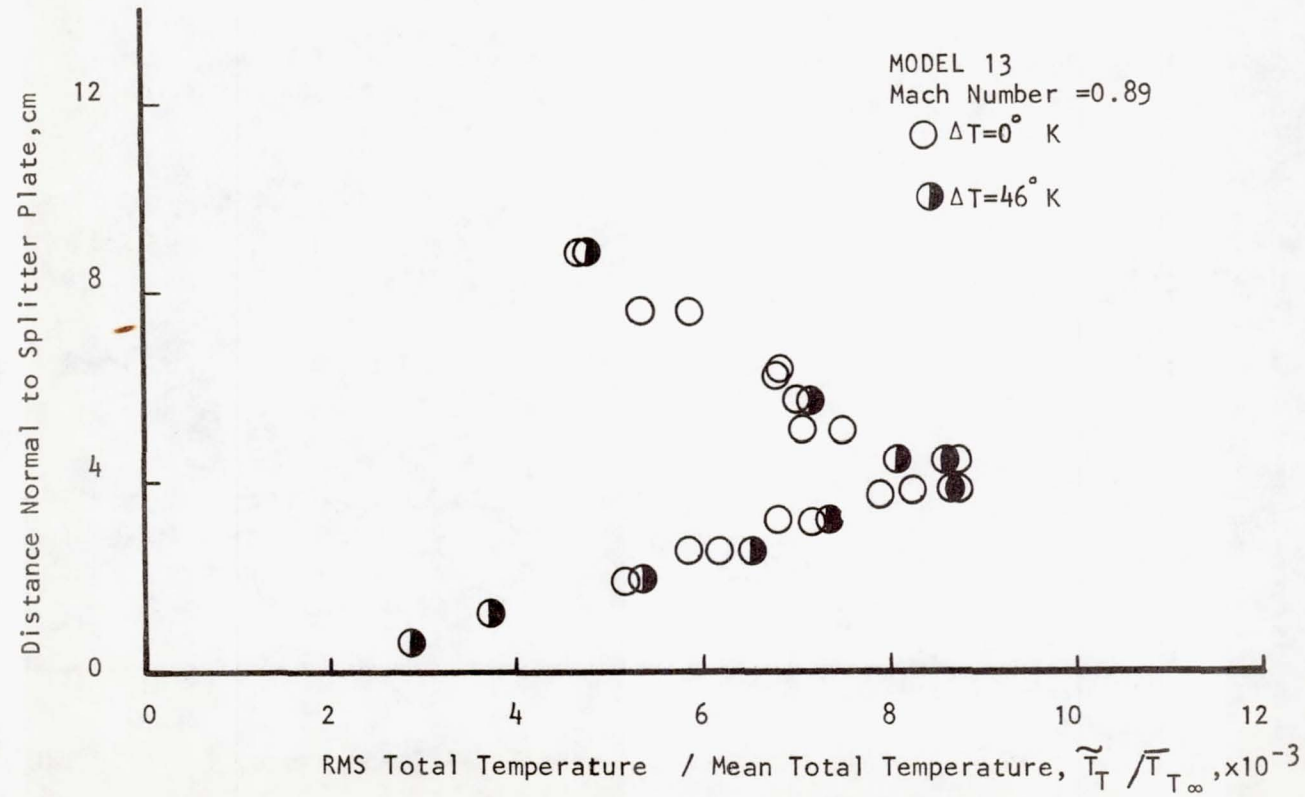

Figure 11. Normalized Unsteady Total Temperatures for Model 13.

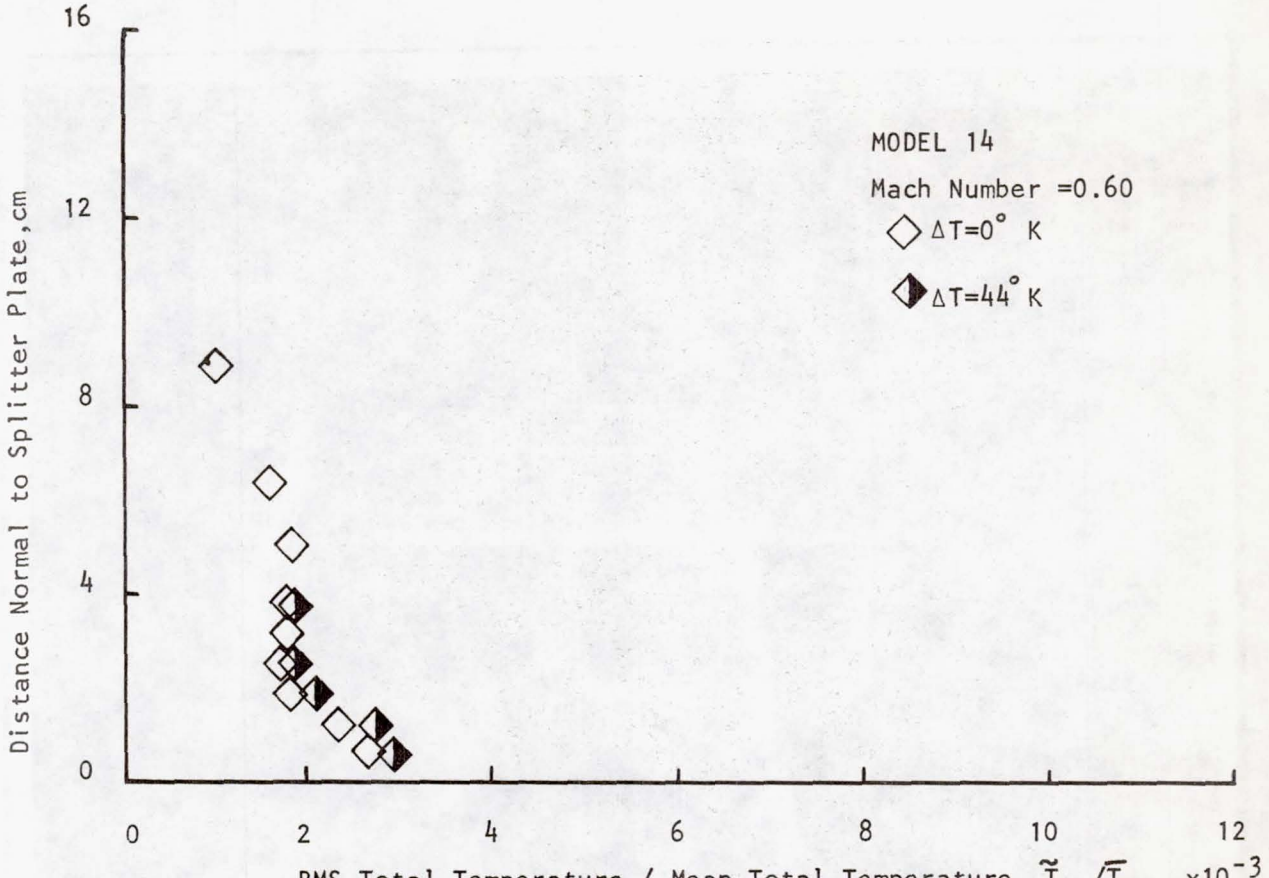

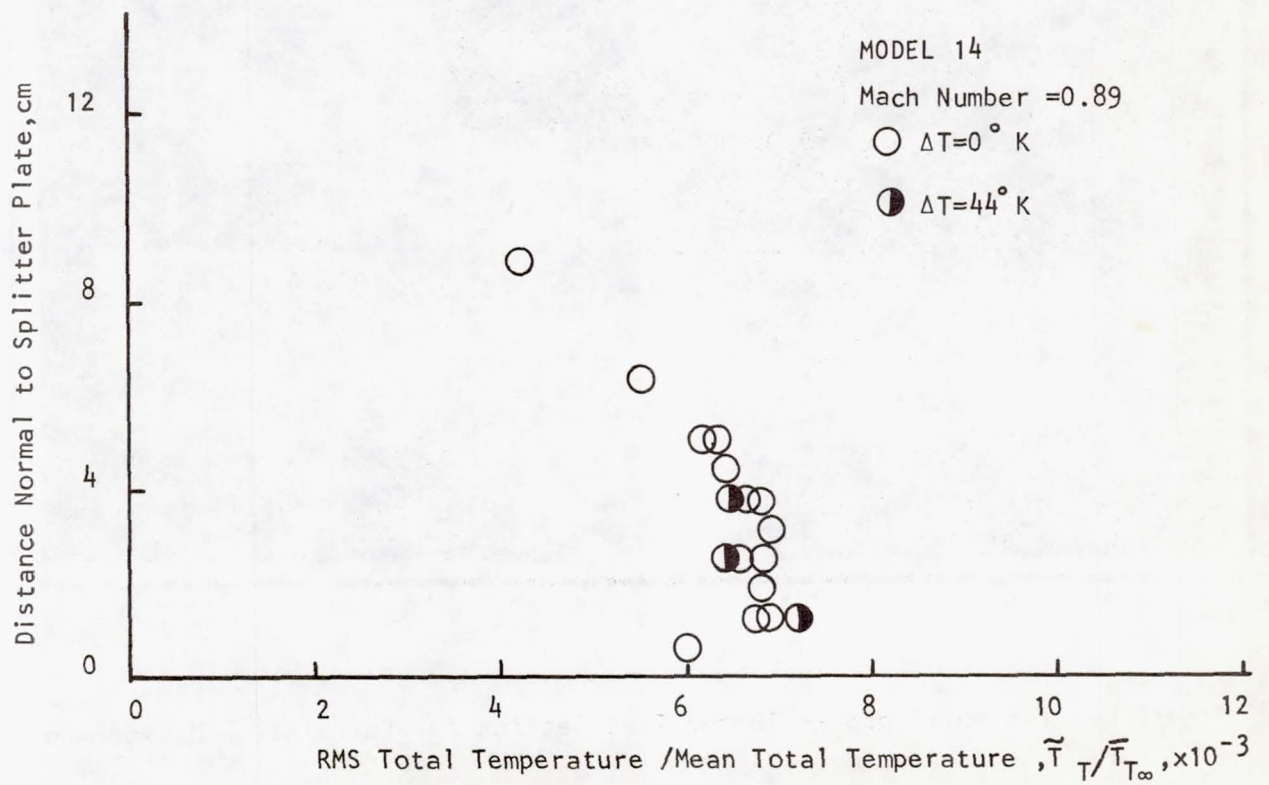

Figure 12. Normalized Unsteady Total Temperatures for Model 14.

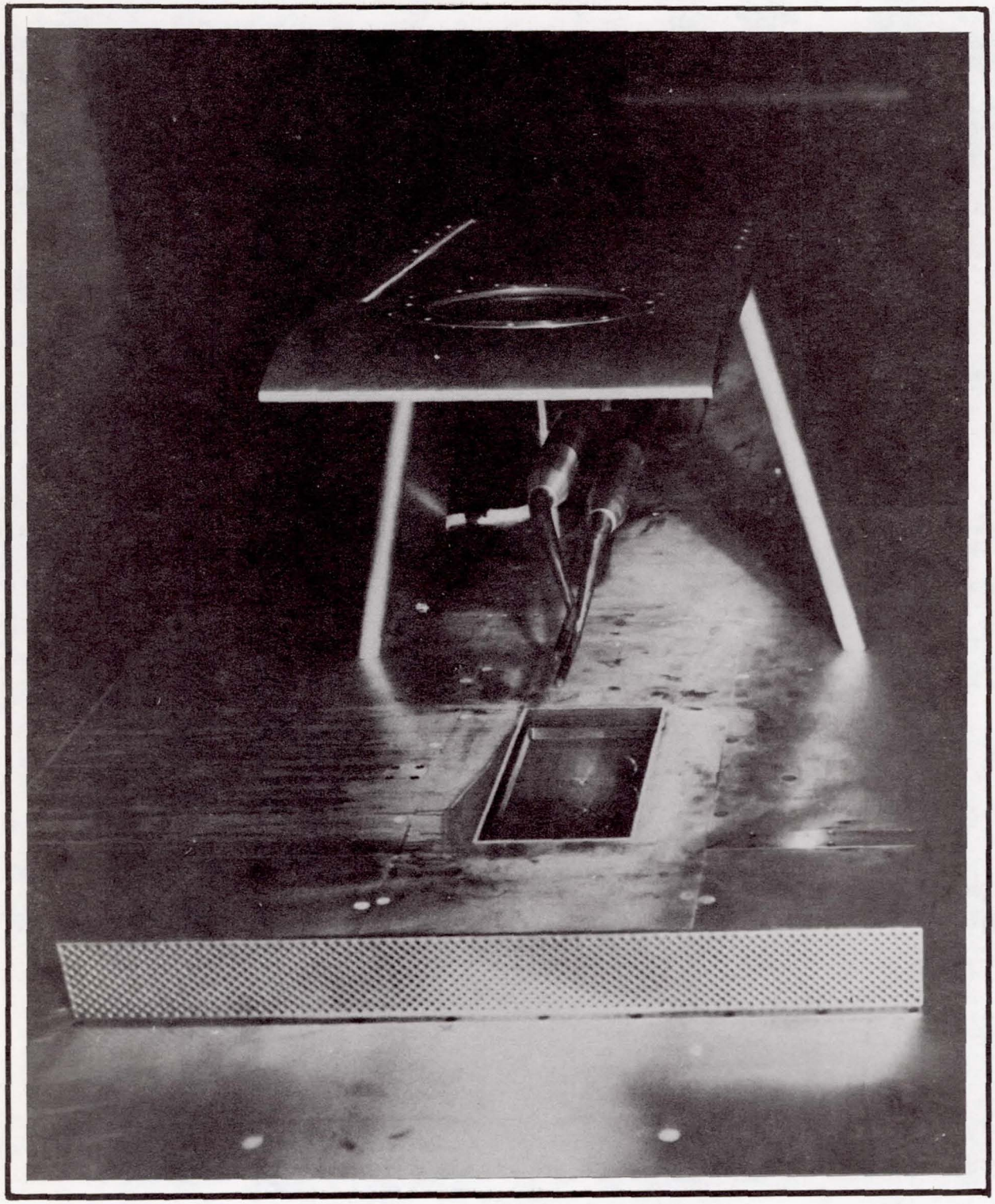

Figure 13. Two Multi-probes in the Test Section for Correlation Measurements.

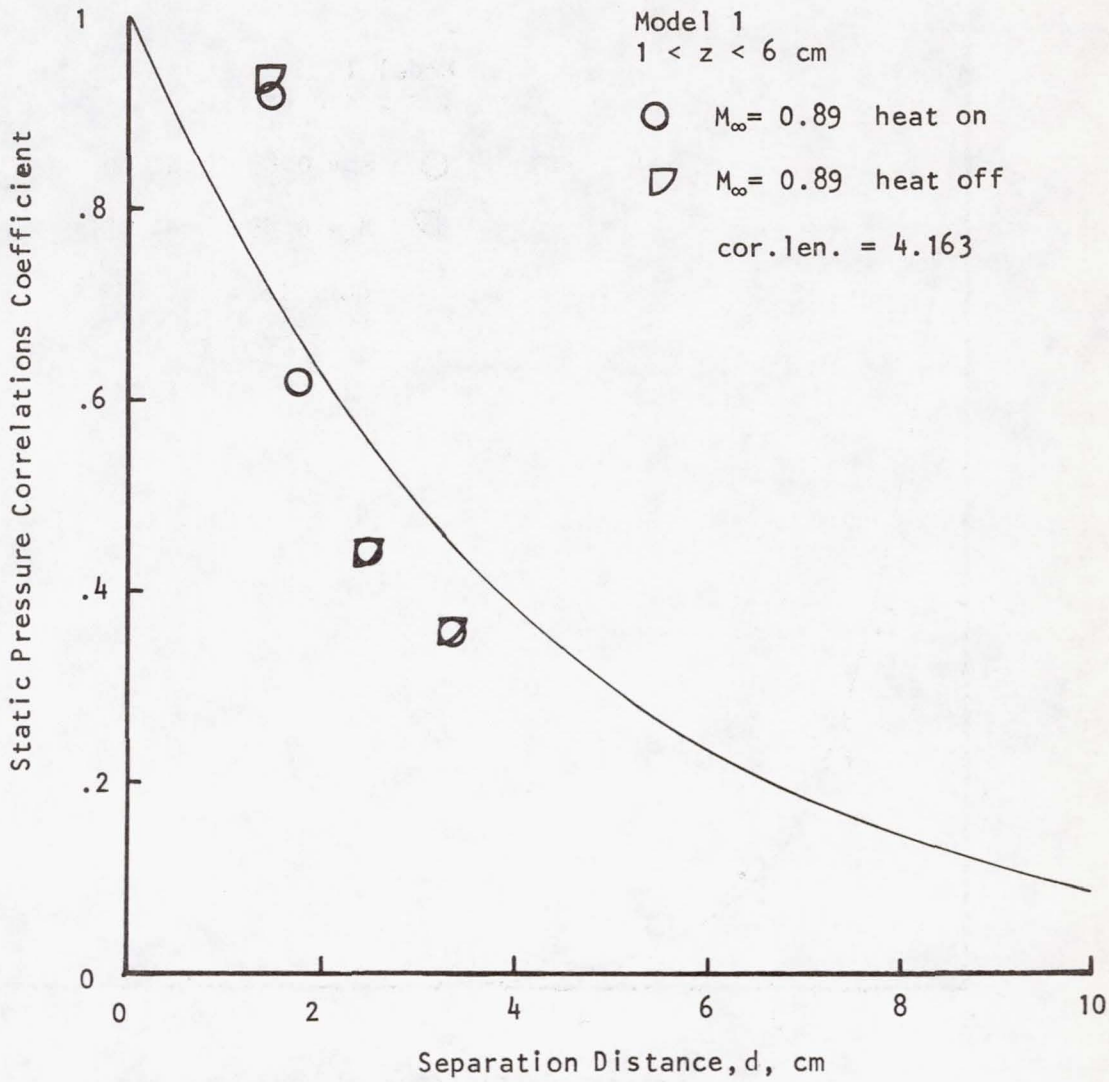

Figure 14(a). Static Pressure Correlation Coefficient versus Separation Distance for Model 1.

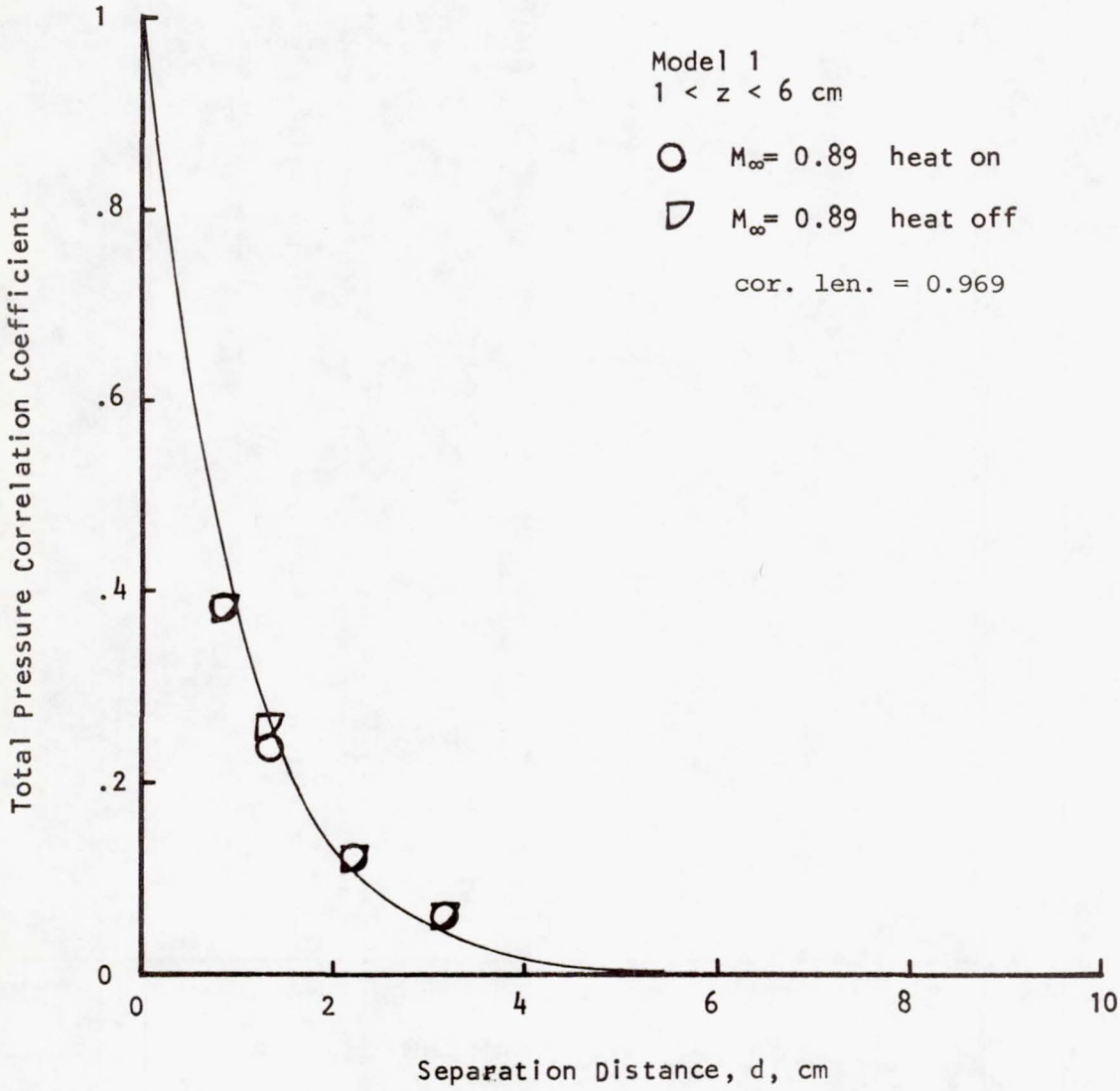

Figure 14(b). Total Pressure Correlation Coefficient versus Separation Distance for Model 1.

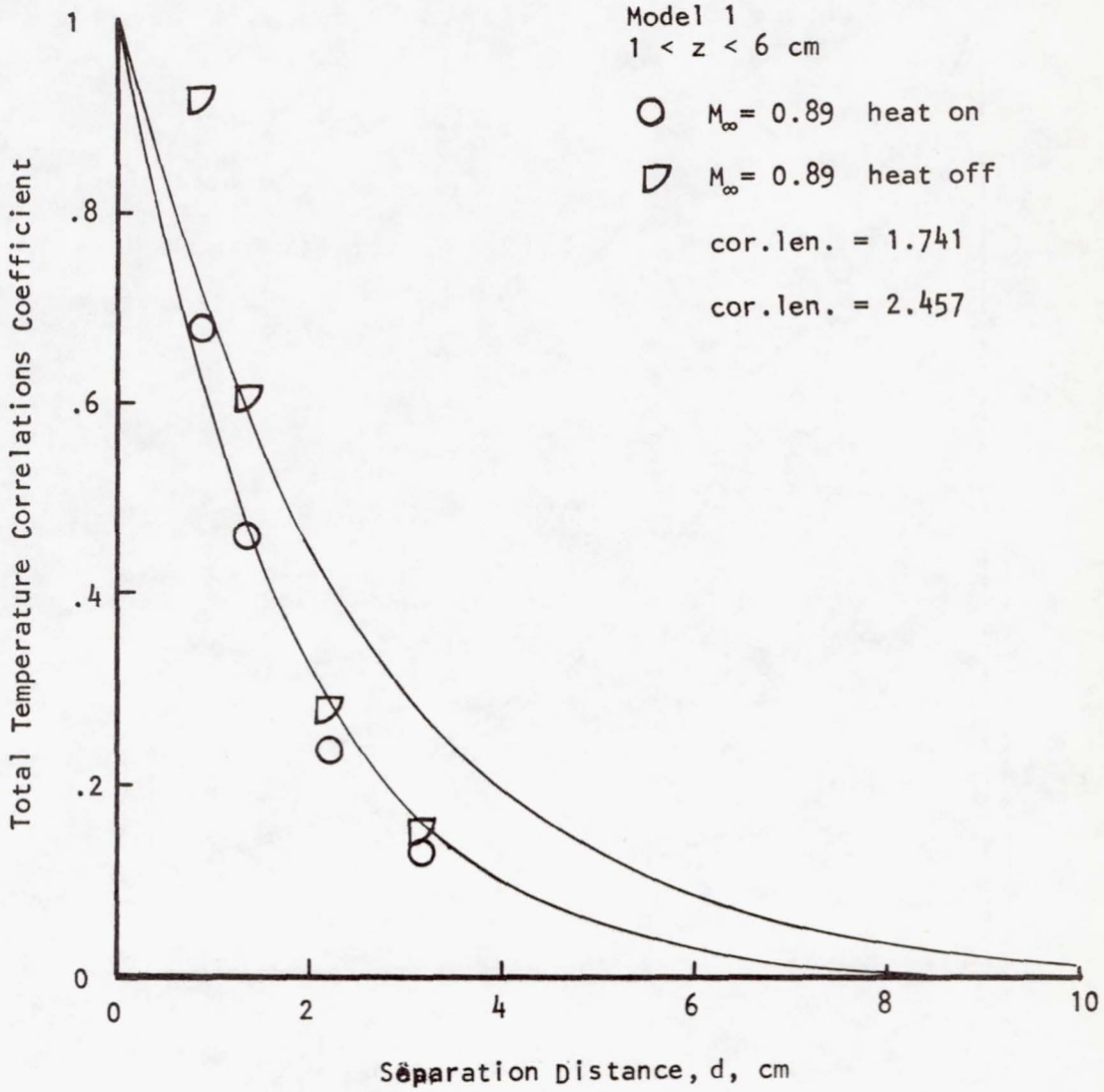

Figure 14(c). Total Temperature Correlation Coefficient versus Separation Distance for Model 1.

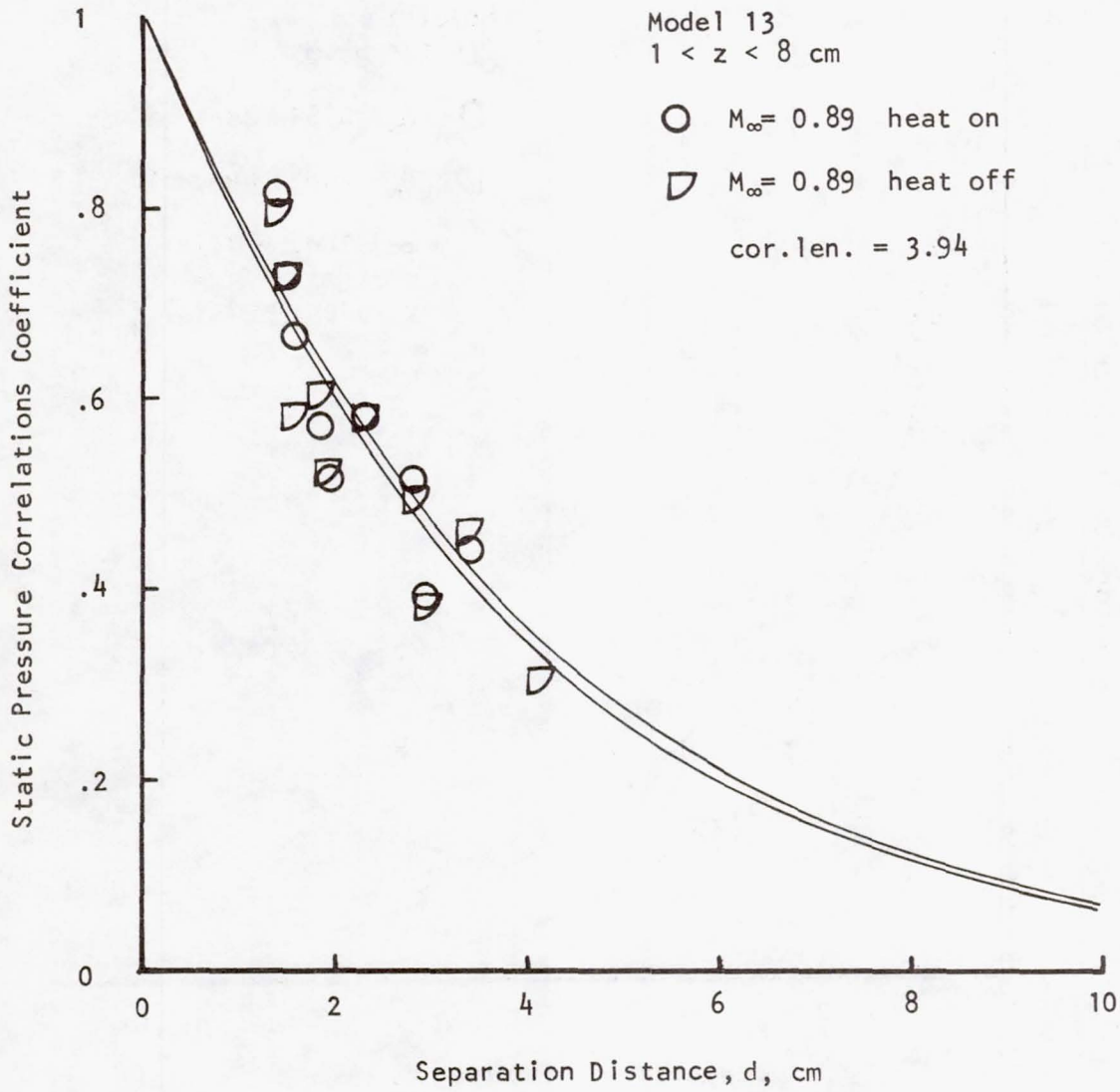

Figure 15(a). Static Pressure Correlation Coefficient versus Separation Distance for Model 13.

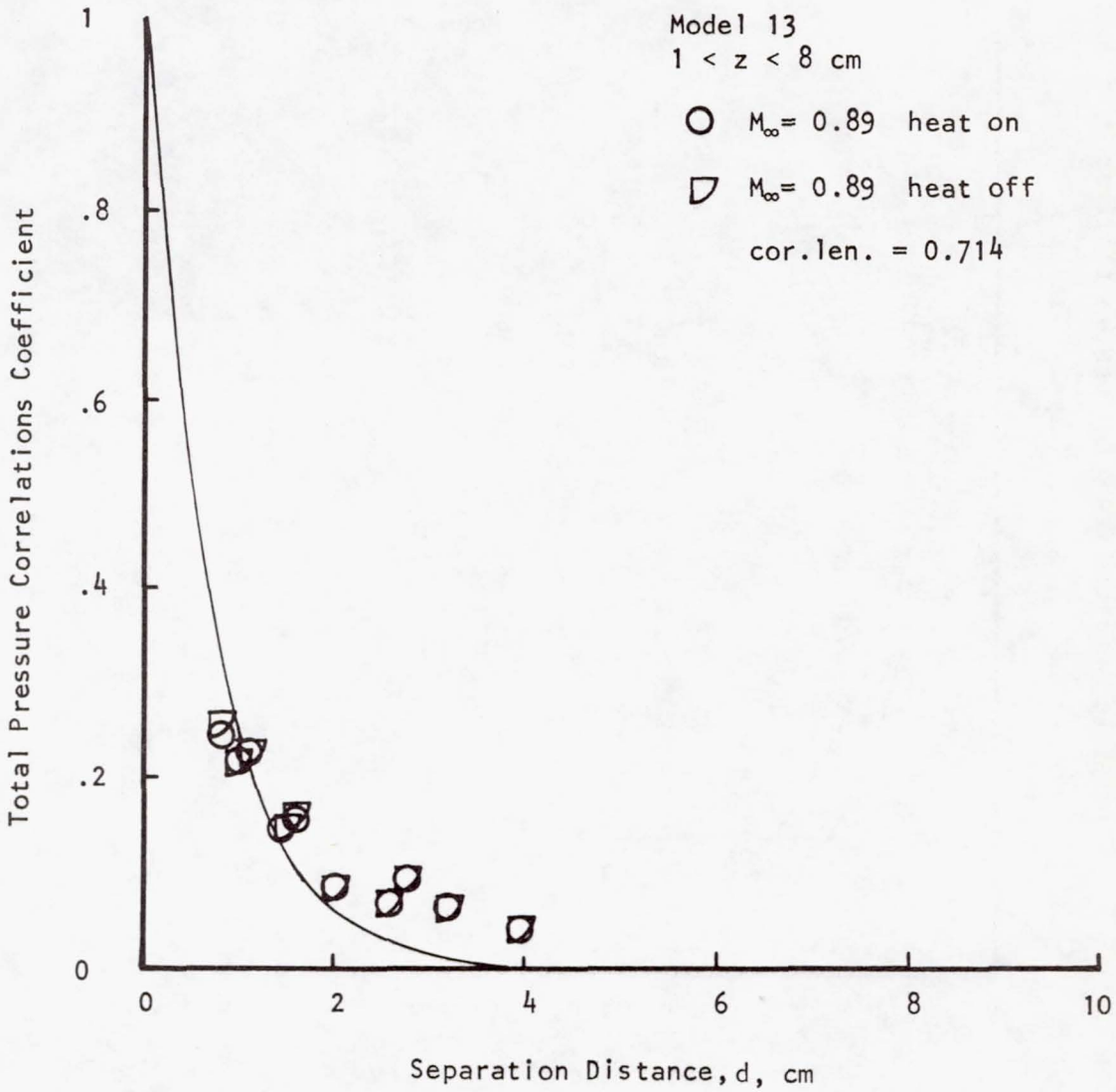

Figure 15(b). Total Pressure Correlation Coefficient versus Separation Distance for Model 13.

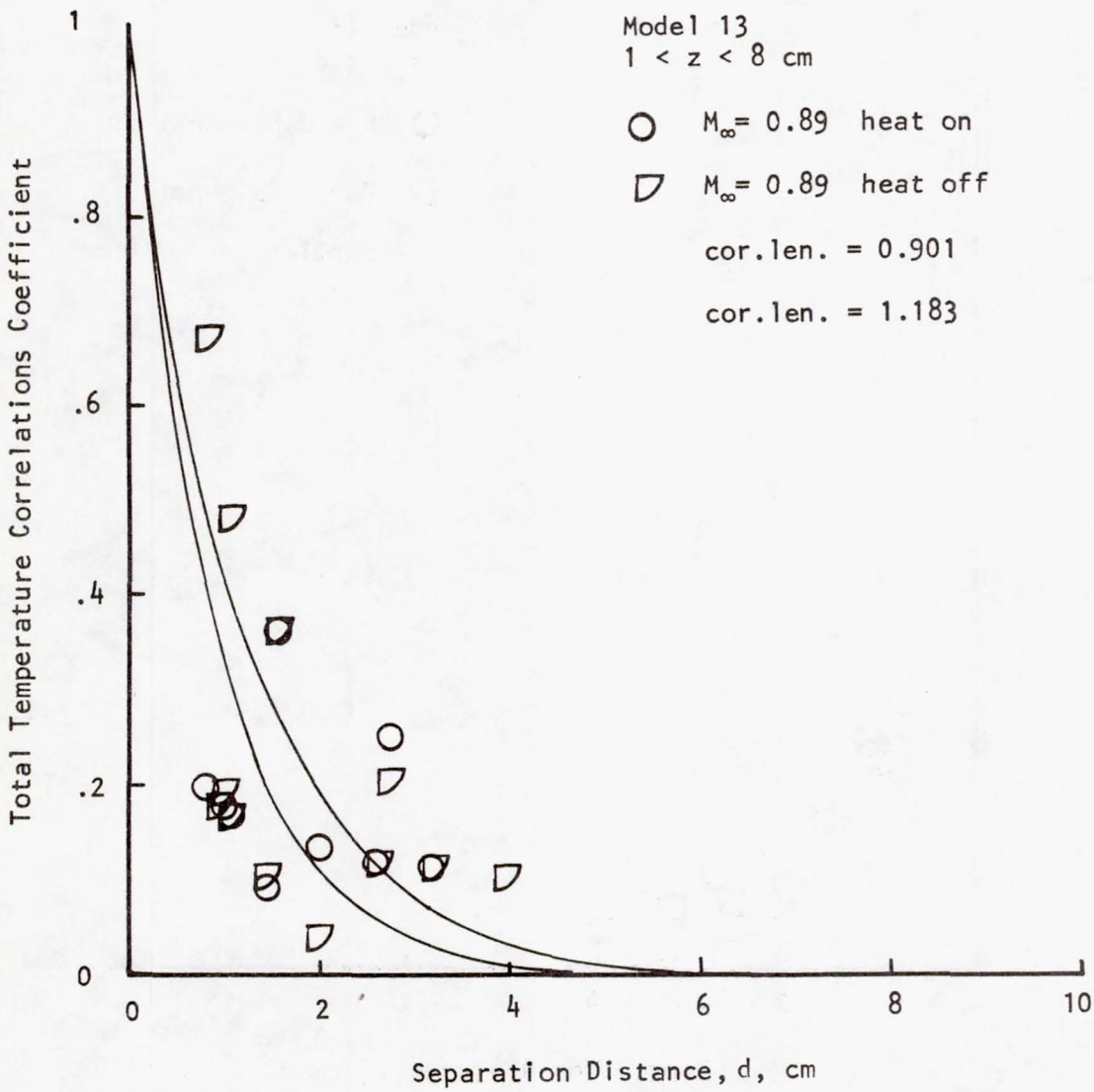

Figure 15 (c). Total Temperature Correlation Coefficient versus Separation Distance for Model 13.

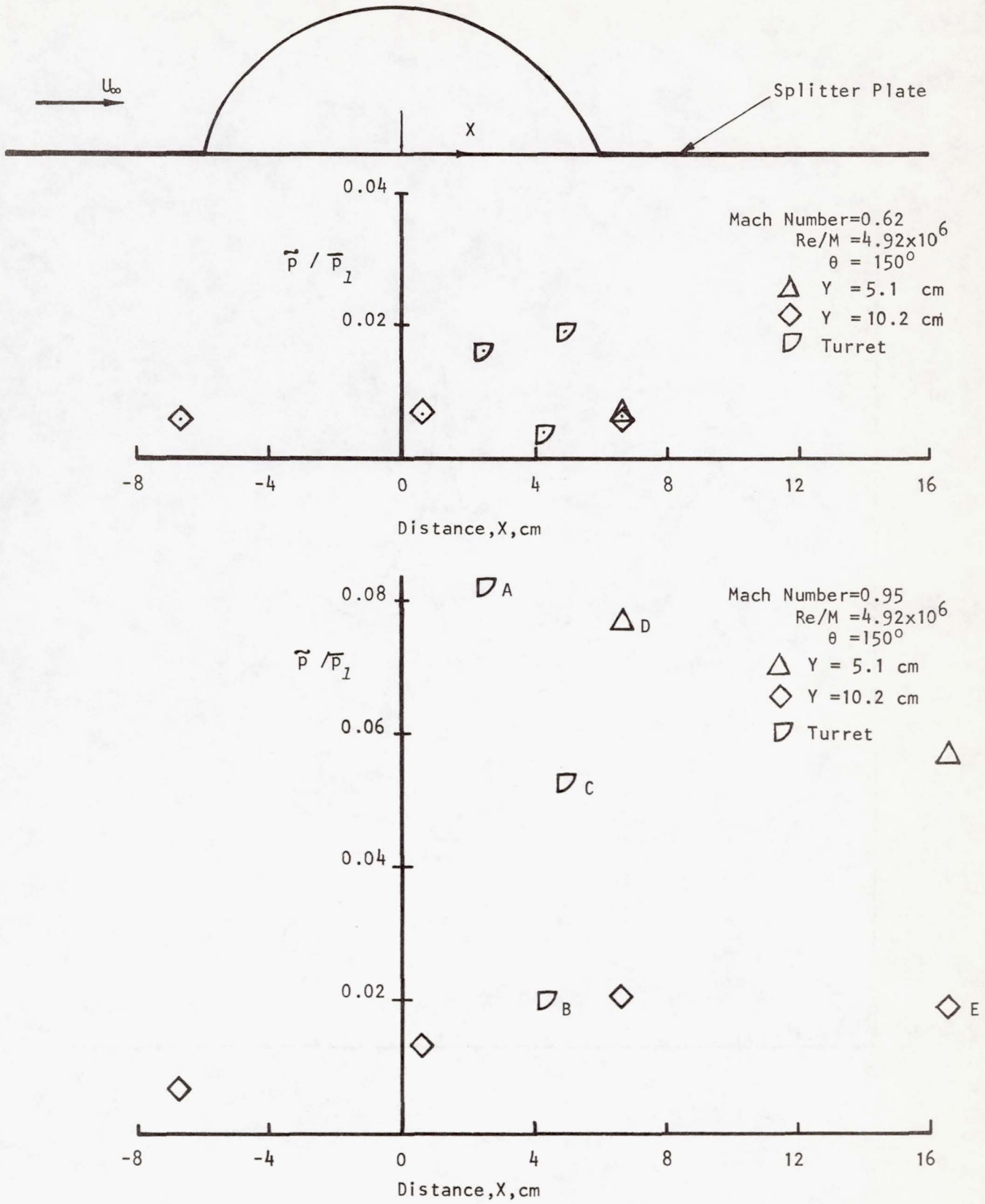

Figure 16. Normalized Unsteady Static Pressures on Coelostat Turret Model.

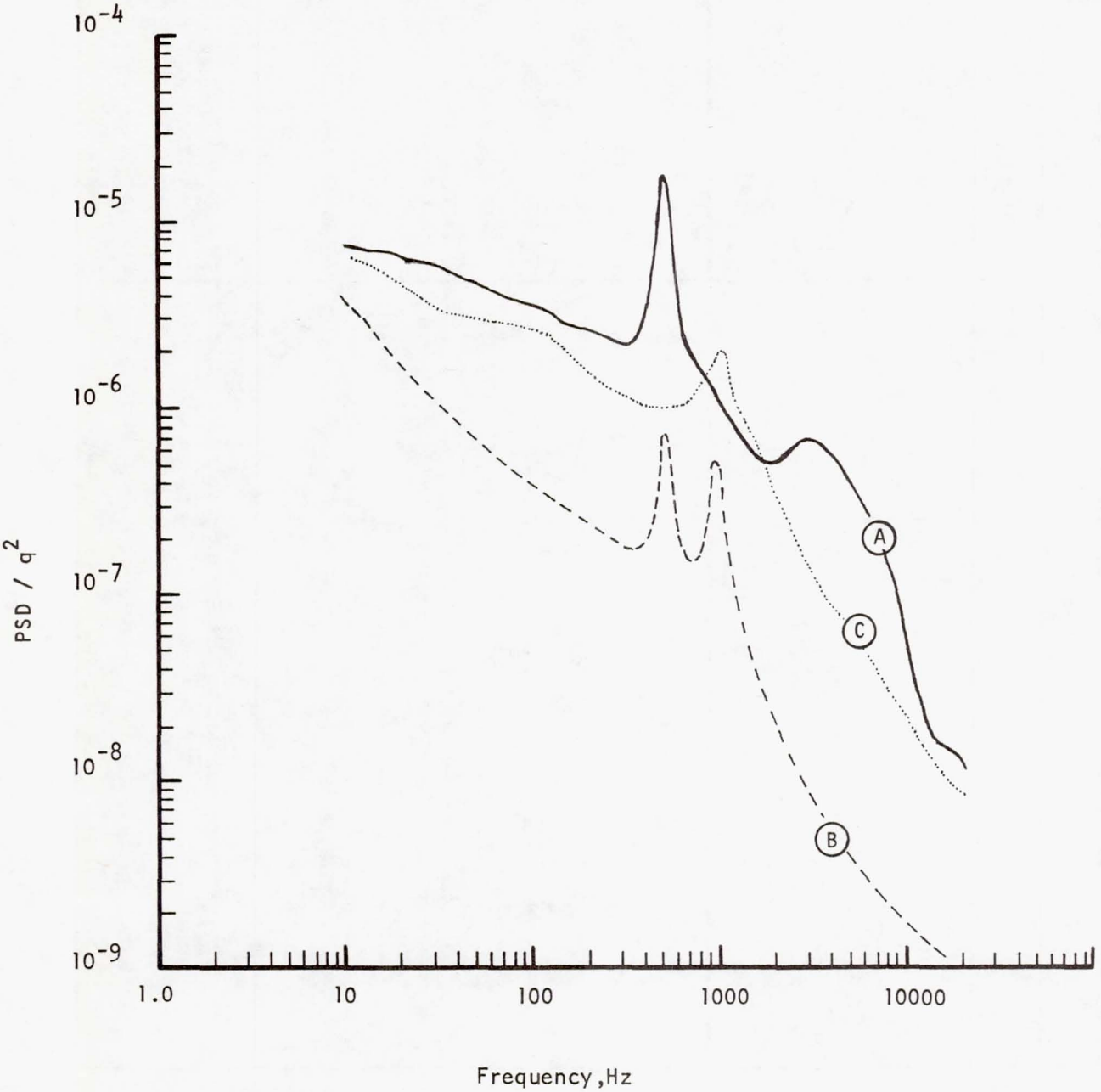

Figure 17. Power Spectral Density of Pressures from the Coelostat Turret Model Tests.

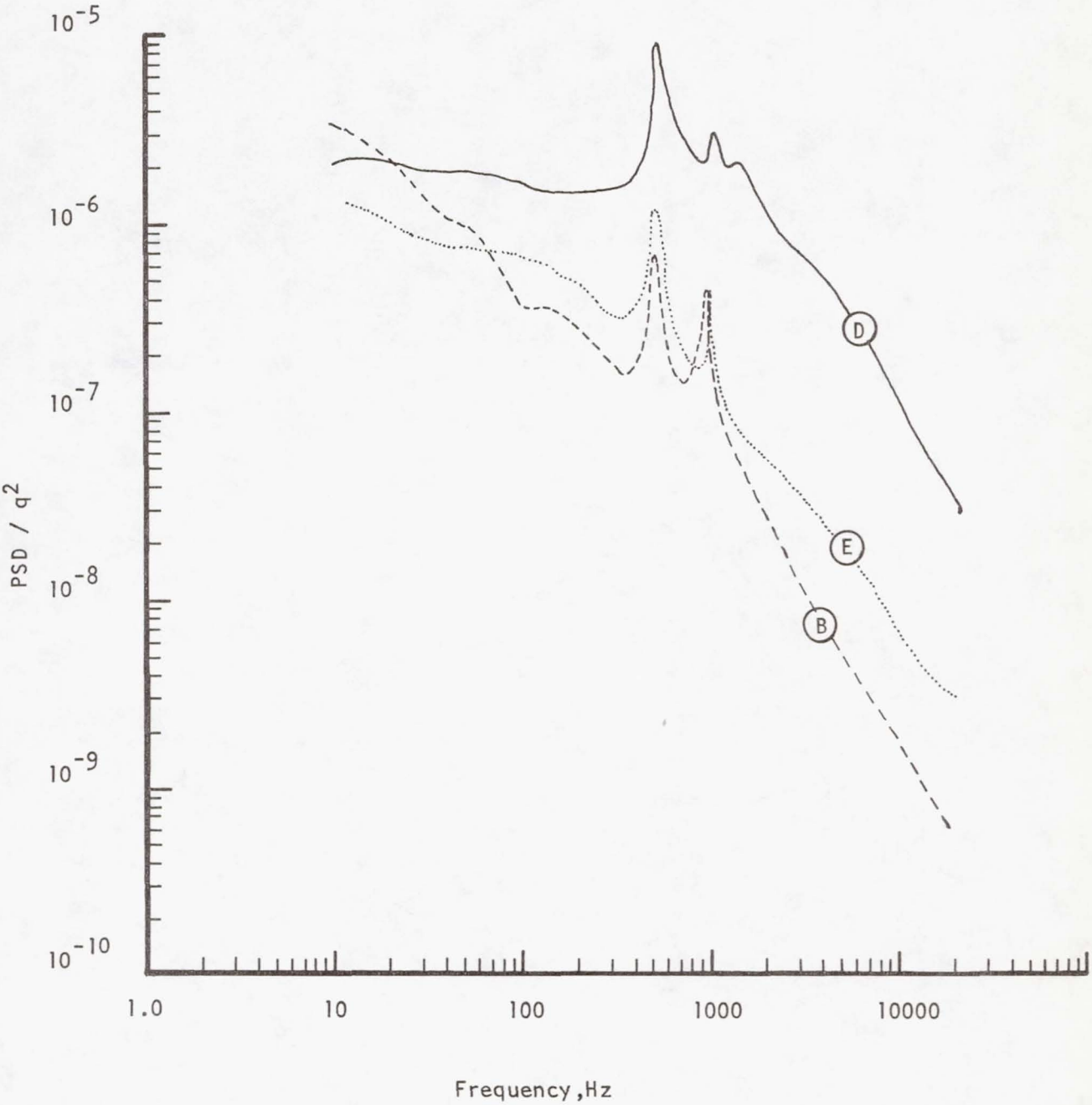

Figure 18. Power Spectral Density of Pressures from the Coelostat Turret Model Tests.

Line Spread Instrumentation for Propagation Measurements

Wade H. Bailey Jr., Captain, USAF
Air Force Weapons Laboratory/LRO
Kirtland AFB, NM 87117

Abstract

The Air Force Weapons Laboratory (AFWL) has been involved in the study of laser propagation from airborne platforms. A Line Spread Device (LSD) capable of yielding direct measure of a laser beam's Line Spread Function (LSF) was developed and employed in propagation tests conducted in a wind tunnel by AFWL to examine optimal acoustical suppression techniques for laser cavities exposed to simulated aircraft aerodynamic environments. Measurements were made on various aerodynamic fences and cavity air injection techniques that affect the LSF of a propagating laser. Using the quiescent tunnel as a control, the relative effect of each technique on laser beam quality was determined. The optical instrument employed enabled the comparison of relative beam intensity for each fence or mass injection. It was found that fence height had little effect on beam quality but fence porosity had a marked effect, i.e., 58% porosity alleviated cavity resonance and degraded the beam the least. Mass injection had little effect on the beam LSF. The use of a direct LSF measuring device proved to be a viable means of determining aerodynamic "seeing" qualities of flow fields. It could also be applied to static atmospheric "seeing" measurements through various gases and pollutants.

Introduction

An important aspect of the Air Force High Energy Laser Program is the examination of propagation effects associated with operating a laser from an airborne platform. This program studies in detail how the atmosphere would effect laser propagation, and, in particular, how the atmosphere would effect laser propagation in a dynamic situation, i.e., aerodynamic interference in the form of turbulent boundary layers, regions of separation, shock waves and other aerodynamic parameters associated with a possible airborne laser system. In conducting propagation measurements, large transonic wind tunnels were used to simulate conditions that could confront possible laser aircraft which may be employed in future weapons systems.

In order to quantify the optical performance of the numerous laser turret and aircraft models a device was required to measure laser beam quality as it was transmitted from these models into the surrounding flow field. Thus a device capable of direct measurement of the line spread function of coherent light evolved. The first generation Line Spread Device (LSD) was used in a wind tunnel test in April of 1975. An improved LSD instrument was planned for use in the follow-on wind tunnel test scheduled for July 1976. This latter series utilized the NASA Ames Research Center 6 x 6 foot transonic wind tunnel located at Moffett Field, California. The purpose of these tests was to develop cavity quieting techniques which permit efficient transmission of a laser beam from this exposed cavity into the surrounding flow field.

1453 received August 30, 1977. This paper was presented at the SPIE Seminar on Laser Technology for the Atmospheric Sciences, August 25-26, 1977, San Diego, California, and appears in SPIE Proceedings Volume 125.

Line Spread Device

The Line Spread Device (LSD) was conceived as a simple instrument capable of measuring directly the optical quality of a laser beam after it has been propagated through an optically distorted medium. In theory, sweeping the focal spot of a coherent light source across a slit that is narrower than the focal spot, and detecting the intensity of the light as it traverses the slit yields an integrated slice of the Airy Disc. This is referred to as the Line Spread Function (LSF) of the beam and is illustrated in Figure 1.

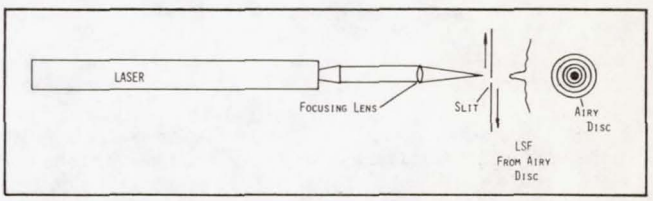

Figure 1. Principle of line spread function.

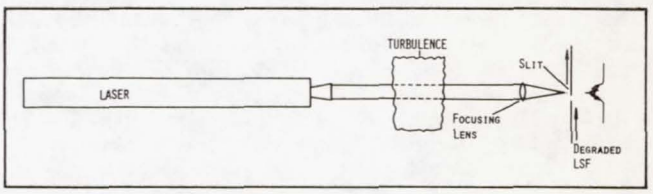

Figure 2. Output of optical disturbances.

Distortion of the line spread function occurs when the beam encounters an optically distorted medium, e.g., turbulence (see Figure 2). A measure of beam degradation can be made by comparing the undistorted LSF to the distorted LSF. Beam quality can then be expressed using various methods. The first method would be a simple intensity ratio determined directly from the LSF. A simple beam quality figure of merit is then the ratio of the intensity of a distorted LSF(I) to an undistorted LSF intensity (I_o). A second method would be to take the undistorted LSF and distorted LSF together and perform a Fast Fourier Transform which would produce a Modulation Transfer Function (MTF) of each. Taking the volume under each MTF and ratioing them as in the intensity method, a Strehl ratio can be determined. Phase tilt information can also be determined from the distorted beam as the tilt can cause lateral displacement of the LSF from a predetermined center line.

The line spread device used in the July 1976 wind tunnel test was relatively simple in construction and was composed entirely of off-the-shelf equipment. The optical components utilized in the LSD were of the highest quality. Figure 3 details the LSD as configured for the test. A 50 milliwatt helium-neon laser, Spectra-Physics model 125/250, was the source laser. A Spectra-Physics 2.5 centimeter collimator containing a microscope objective lens and a pinhole was used to spatially filter

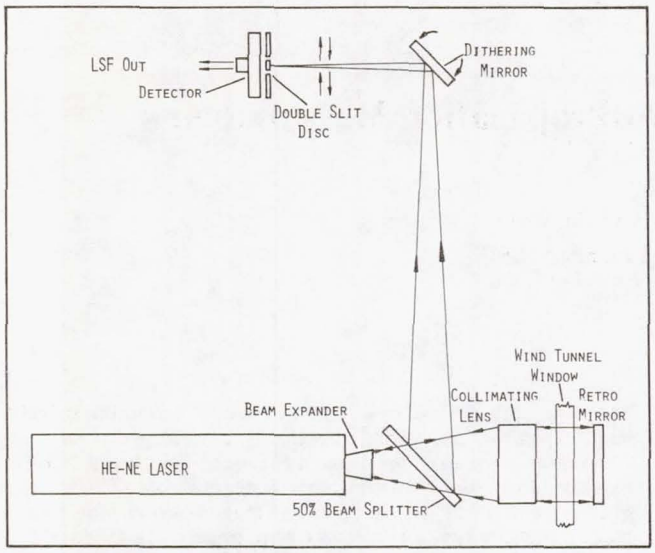

Figure 3. Line spread device configuration.

the beam. The beam exited the pinhole and expanded through a 7.6 x 5 x 1.5 centimeter 50% beam splitter for 6328 Å wavelength light. The beam continued its expansion until it encountered a 10.2 cm lens. This lens was the compound collimating lens of a Tropel Model 280 laser collimator. The laser beam now collimated at 10.2 cm passed through an 11 cm diameter iris capable of stopping down to 0.5 cm diameter. The collimated beam then traversed the flow field being studied. A retro-mirror immersed in the flow field returned the beam back along its original path. Results from the wind tunnel test of April 1975 indicated that when the laser beam was allowed to pass completely across the six-foot test section of the wind tunnel and sampled on the opposite side of the tunnel, the inherent optical degradation of the wind tunnel flow overshadowed any model-induced degradation. The placement of a retro-mirror in the flow shortened the beam path in the wind tunnel and thus permitted the effects of the various models to be discerned.

The beam returned from the retro-mirror, impinged the beam splitter, and was turned towards another mirror. This mirror was dithering at 60 Hertz and was controlled in amplitude by a General Scanning Model AX-100 motor control. Frequency was controlled by a Wavetek model 144 sweep generator. The dither mirror was oriented so as to turn the beam 90° and sweep the focused beam in a back-and-forth motion across a pair of 2 micron slits separated by 400 microns. The disc containing the slits was positioned directly over a photovoltaic detector which measured the line spread function of the laser beam. The complete line spread device as shown in Figure 3 was enclosed in a cardboard housing. A cardboard tube was constructed to enclose the beam as it exited the LSD housing until it entered the wind tunnel. The enclosures were employed to minimize the effects of the ambient room turbulence on the measurements.

LSF Data Acquisition System

As the focused beam was swept across the slits, the beam intensity was detected by a United Technology photovoltaic PIN-10 detector. The frequency response of the detector was enhanced by a bias circuit. The signal then went through a PAR amplifier Model 110 via triaxial cabling. The amplified signal was monitored on an oscilloscope which served to control signal level into the tape recorder. When proper voltage levels were achieved the signal was placed on a Bell and Howell 14 track tape recorder Model M-14G. IRIG B time was also recorded from a Datametrics time code generator.

Experimental Setup

The experimental objective was to determine the optically degrading effect on a laser beam that might occur as it propagated from an open cavity on an aircraft in flight. Figure 4 shows the

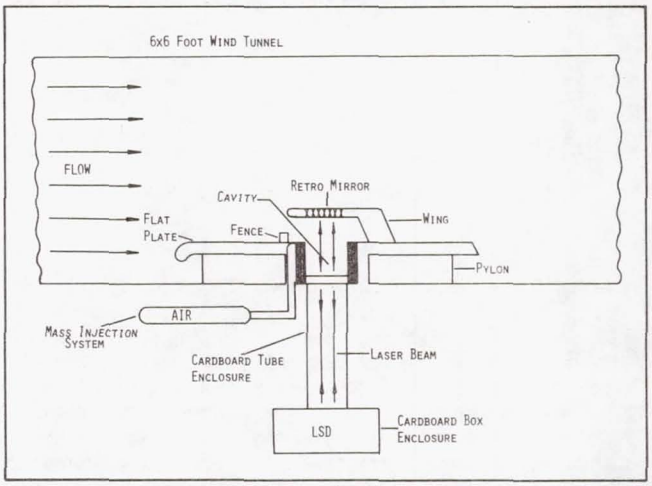

Figure 4. Top view of wind tunnel model configuration.

experimental setup. A splitter plate (3 m x 1.2 m) was mounted on a 25 centimeter pylon and placed on the side wall of the NASA Ames 6 x 6 foot transonic wind tunnel test section. A 6 inch cubical cavity was set into this plate. The bottom of the cavity (towards the wall) was constructed of high optical quality quartz. A "wing" was mounted on the plate to provide a mount for a return mirror which was 12 inches from the surface of the plate. Thus, an open cavity immersed in a high speed flow from which a laser could be propagated was simulated in the wind tunnel. This open cavity laser wind tunnel model was designed to simulate aircraft-induced effects.

The problems associated with airborne laser operation through an open cavity involve both acoustical and optical effects. The former are generated within the cavity and induce jitter within optical components. Optical effects are due mainly to the aerodynamic shear layer at the cavity exit. Methods to alleviate these effects were employed in this test. Metal bars referred to as "fences" were placed on the flat plate upstream of the cavity in an effort to suppress cavity acoustical noise. The fence heights ranged from 2.3 cm to 5.1 cm, which were one and two times the existing boundary layer height on the flat plate. Each fence varied in porosity, i.e., holes were drilled in the fences to permit mass flux through the fence. A method of injecting high pressure air into the cavity from the front wall was tried as an alternate means of quieting the cavity. As each technique was tested, the LSD made measurements of the LSF. Mach number was varied from M = 0.6 to M = 0.89 and Reynolds number was adjusted to either $R_e = 2 \times 10^6$ per foot or $R_e = 3 \times 10^6$ per foot. These aerodynamic parameters were varied for each cavity suppression technique tested. Table 1 presents a listing of techniques and parameters tested with the LSD in this experiment for which an LSF was obtained.

The procedure in obtaining the LSF was first to calibrate the LSF signal for apertures ranging from 2 cm to 8 cm at one centimeter intervals. These calibrations were accomplished with the wind tunnel sealed and no air flowing. All calibrations were recorded on analog tape. Gain settings of the oscilloscopes and amplifiers were noted for each aperture calibration. An example of a two centimeter calibration can be seen in Figure 5. At the completion of the calibration series the wind tunnel was activated and allowed to stabilize at a particular Mach number and Reynolds number. At each aerodynamic condition, LSF data was recorded on tape. As each aperture was scanned during the

Table 1. Wind Tunnel Model Configurations and the Aerodynamic Parameters Varied on Each

Model Configuration	Aperture Scan (cm)	Reynolds No.	Mach Number
Flat plate, no cavity	2, 4, 6, 8	2×10^6 3×10^6	.6, .7, .8, .9
Flat plate, cavity, fence: 5.1 cm high 49% porosity	2, 4, 6, 8	2×10^6 3×10^6	.6, .7, .8, .9
Flat plate, cavity, porous upstream cavity wall	2, 5, 8	3×10^6	.6, .7, .8, .9
Flat plate, cavity, fence: 2.3 cm high 58% porosity, porous upstream cavity wall, air injection into cavity	5, 7	3×10^6	.7, .9
Flat plate, cavity, fence: 2.3 cm high 58% porosity	2, 5, 7	2×10^6 3×10^6	.6, .7, .9
Flat plate, cavity, fence: 4.6 cm high 58% porosity	2, 5, 7	2×10^6 3×10^6	.6, .7, .9

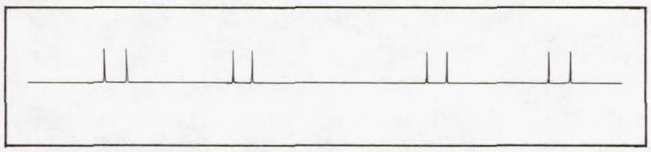

Figure 5. Example of LSF calibration 2 cm aperture.

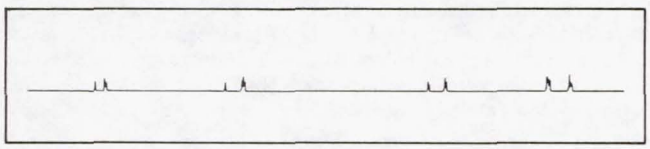

Figure 6. Example of LSF after traversing an optically degraded flow field 5 cm aperture.

run, the oscilloscope and amplifier settings were repeated as dictated by the calibration runs. The LSF of a degraded beam is shown in Figure 6 after it experienced an active flow field. When the wind tunnel was stopped for a configuration change, an additional calibration run was accomplished.

Discussion

The reduction of the data was to utilize the recorded line spread function in conjunction with a Tektronic DPO 1221 system. Strehl ratios were calculated by employing programs developed for the Tektronix system. In particular, 10 to 100 distorted LSFs for a test run were centered according to area in relation to a predetermined coordinate system thus producing an average LSF. (It is known that by centering the LSFs and averaging, phase tilt information is lost; however, due to the vibrational environment of a wind tunnel, jitter of the beam cannot be separated from the motion of the optics or jitter induced by the flow field.) With the average LSF, a Fast Fourier Transfer can be performed using the Tektronix to produce a modulation transfer function (MTF) of the beam. By comparing the peak MTF of the calibration signal for a particular aperture and the MTF of the degraded signal, one can obtain a Strehl ratio. This data reduction has merits because it permits comparison of this data to other data taken on previous tests by other methods. A quick and simple form of data reduction can be applied by taking the average peak intensity of the LSFs and making a ratio of the calibration intensity, i.e., I/I_{cal}.

Results

During the experiment it was discovered that jitter due to the vibrating optics, especially the retro-mirror in the wind tunnel, was introduced into the measurements thereby spreading the beam but not affecting peak intensity. The only method viable for use in data reduction was an intensity ratio of averaged test points to its corresponding calibration run. The data tape was placed on strip charts for each configuration tested. The calibration runs were also placed on strip charts. Samples of these are shown in Figures 5 and 6. From the strip charts an average peak intensity for each case was determined by using a Hewlett-Packard plot package. An average intensity of each case was tabulated using 40 LSFs and compared to the calibration case. These intensity ratios for each cavity suppression technique were plotted and trends were scrutinized to determine the technique that degraded the beam the least. Figures 7 through 10 show the results in comparison form. From the trends in the LSF data it was determined that 2.2 cm, 58% porosity fence was the best optically and that mass injection had little effect on better "seeing." Reynolds number increase degraded optical seeing as well as an increase in Mach number. Since this was the first time an attempt to measure the optical quality of cavity noise

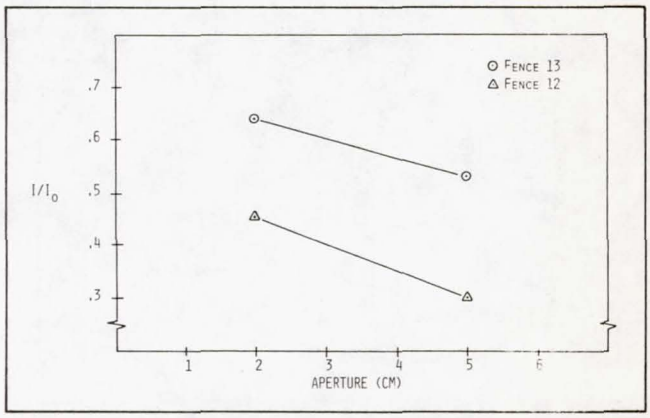

Figure 7. Comparison of two fences at M = 0.9 and $R_e = 2 \times 10^6$/ft. Fence 13: 58% porosity and 2.2 cm in height. Fence 12: 58% porosity and 4.5 cm in height.

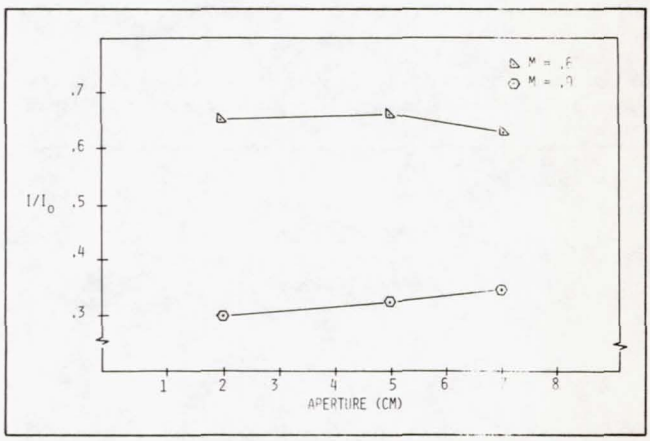

Figure 8. Comparison of Mach number dependence. Cavity model with Fence 13. $R_e = 3 \times 10^6$/ft.

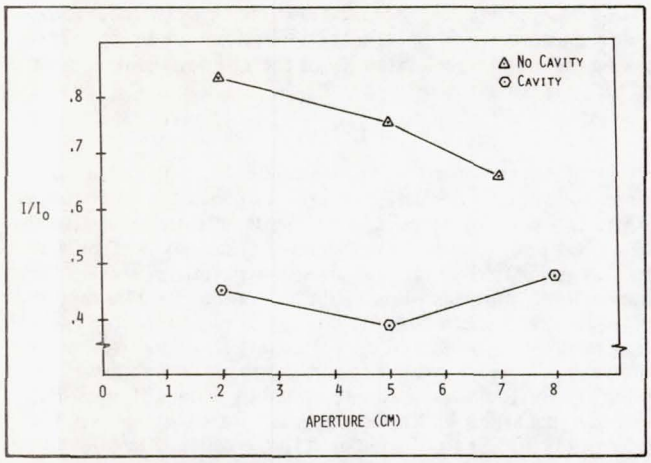

Figure 9. Comparison of flat plate with cavity and flat plate without cavity. M = 0.7 and $R_\theta = 3 \times 10^6$/ft.

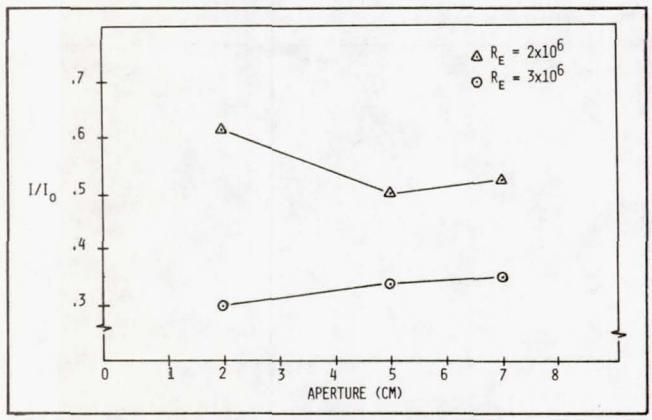

Figure 10. Comparison of Reynolds number dependence. Cavity model with Fence 13. M = 0.7.

suppression techniques was made, no earlier results are available for comparison.

Conclusion

It can be concluded from the data results shown in Figures 7 through 10 that the line spread device is an instrument capable of direct measurements of light transmission quality through various atmospheric media. The LSD configuration employed introduced errors through optical component jitter caused by the severe wind tunnel environment. The component jitter may explain anomalies in the graph, e.g., optical "seeing" improving with increased aperture. Another source of error may lie in quirks of wind tunnel operation, in that certain tunnel conditions could alter the optical qualities of the flow. The "wing" that housed the retro-mirror produced a Venturi effect that was not anticipated. This effect may have "smoothed" the flow at high Mach numbers. The experiment as performed, and the LSD as configured, produced useful information pertinent to design of airborne laser optics.

Recommendations

The data as acquired by the LSD are applicable to many other areas of atmospheric transmission measurements to be made in the visible. The "seeing" quality of various gases and pollutants can be determined utilizing a line spread device. Additional work can be seen for this device and an improved model is being designed and fabricated by the author at this time. In order to alleviate the jitter experienced by the LSD in the severe vibrational environment of the wind tunnel, the new design will make use of a high speed rotating mirror. The high speed rotation will freeze any optical component jitter and maintain the integrity of the necessary constant velocity across the slit detector.

Acknowledgments

The author is deeply indebted to Major Keith G. Gilbert and Captain Richard J. Cook for their assistance in all aspects of the experimental work and theoretical considerations. Thanks is also due to Staff Sergeant Mark A. Cook for his unparalleled help in actual data acquisition. The author would like to express his gratitude to his wife, Cathy, Dr. David Depatie, and Airman Felix Ternate. Acknowledgment also is directed to MIT Lincoln Laboratory for use of unpublished MTF data contained in D. Kelsall memo dated 26 April 1977.

References

1. AFWL TR 76-271, "Airborne Laser Laboratory Cycle II: Low-Power Experiments."
2. Meyer-Arendt, J. R., *Introduction to Modern and Classical Optics*, Prentice Hall, New Jersey, 1972.

AERO-OPTICAL CHARACTERIZATION OF AIRCRAFT OPTICAL TURRETS BY HOLOGRAPHY, INTERFEROMETRY AND SHADOWGRAPH

J. D. Trolinger

Spectron Development Laboratories, Inc.
3303 Harbor Blvd., Suite G-3
Costa Mesa, Ca. 92626

ABSTRACT

A number of laser based instruments have been used to characterize the optical properties of a flow field combined with an aircraft window. Density variations in the aircraft boundary layer, turret wakes, and shock waves create distortion of an optical wavefront through associated refractive index variations. Such effects can be observed directly through optical flow visualization. This paper describes the application of holographic interferometry, wave shearing interferometry, and laser shadowgraph to observe and quantify such effects.

Examples of the results from five different wind-tunnel tests are presented. The examples show that such diagnostics have provided valuable qualitative and quantitative data. These include (1) wake dimensions, (2) optical strength of the flow field, (3) turbulence characterization, (4) shock location, and (5) direct observation of aero-optical effects.

1. INTRODUCTION

When optical systems are used in aircraft, it is often required to construct windows of high optical quality to provide optical access to the outside of the aircraft. In some cases, it is necessary to mount such windows in turrets so that the window location can be scanned and pointed in a wide range of directions. Such access to the outside may be required to project optical energy from the aircraft to the outside (such as a laser weapon system) or it may be used as a port to receive optical information (such as a reconnaissance port for a camera). In either case, regardless of the quality of the window and the optical system inside the aircraft, aberrations are introduced on the wave front by the atmosphere outside the aircraft. Such aberrations are associated with density variations in the atmosphere. Such variations exist in the free atmosphere because of temperature gradients and atmospheric turbulence and they also exist because of the perturbation of the atmosphere by the aircraft and the optical turret. A high quality optical system can be severely limited in resolution by such effects. Interfacing to the outside involves either the design of optical windows which introduce the least possible aberration or some type of active system which takes that aberration into account and corrects for it. Although it is probably not possible to entirely remove the effects of the aircraft, studies have provided methods to minimize such effects and determine under what conditions the effects are most severe. They can provide measurements for active optical systems to correct for such aberrations.

These types of studies fall generally under the category of aero-optics. Such studies have involved theoretical analysis and modeling, wind tunnel studies, and full-scale aircraft studies of turrets and optical windows. The approaches to the studies are made both from optics as well as aerodynamics points of view. The aerodynamic approach includes measurements with pitot tubes, hot wires and pressure gauges, laser velocimeters and computations from boundary layer theory.

Optical characteristics have been measured by propagating beams across and from within the turret to provide measures of the optical transfer functions or its related characteristics such as point spread function, modulation transfer function, or pupil function. These studies have included wave-shearing interferometers, holographic interferometry, Schlieren, shadowgraph, and direct measures of the point spread function.

By properly modeling of the flows, optical properties can be computed from aerodynamic measurements. Such computations are at best limited because the complexity of such flows places their understanding at the very state-of-the-art in aerodynamics. No aerodynamic measurement can guarantee the required optical information. This can only be derived from a beam projected from the turret.

2. BACKGROUND

During the summer of 1976, flow visualization holography was added to the Air Force Weapons Lab Measurement Capability as a diagnostic tool for studying the optical properties of windows and turrets.

With few exceptions, flow visualization had been excluded from the studies before 1976. Examining the flow over the turret by conventional flow visualization is practically impossible because of the geometrical properties of the turret. Much of the interesting flows lies in corners or against opaque surfaces of the model, making transillumination impossible. Propagation from within the turret is difficult because return mirrors must be mounted in the wind tunnel.

Holography at first met a great deal of skepticism and widespread feeling that it was not applicable to this problem in some of the locations of the test. The first holography including test was accomplished in the NASA-Ames 6x6 Supersonic Wind Tunnel. These tests were extremely successful producing the first diagnostic method which actually depicted directly the aerodynamics and the optic properties of the aircraft window in the same data. Since this test series, four more applications of holography have been conducted in test series which included an optical cavity model, an aircraft model and scaled turret models. The application of holography appears finally to have attained a certain respectability as a reliable method for providing some of the most useful and clearly definitive information to be acquired in such tests.

3. SUMMARY AND DISCUSSION OF THE METHODS USED

In five tests, we have employed a variety of holographic interferometry, conventional interferometry and shadowgraph, to study the optical effects of flow over a window cavity model, propagation from

a one-third scale turret model, the flow over a one-seventh scale F-15 turreted model, and flow over a one-third scale turreted model.

The problem of retrieving an optical wavefront which has passed through the flow field is illustrated in Figure 1. The various geometrical and window conditions have required reflecting from retroreflective material, replicated mirrors, or mirrors positioned in the tunnel. All of the methods shown have now been used successfully. Both the replicated mirror techniques and retroreflective techniques were developed during these studies.

Figure 2 illustrates the holography system which has evolved during the studies. For all holography studies so far, a pulsed ruby laser with pulse of duration 10^{-8} seconds possessing multiple pulse capabilities has been used. Typical output energies are 50 millijoules per pulse. The output from this laser is split into two waves -- a reference wave and an object wave. The reference wave is is passed through a series of mirrors which carry it over an optical path length which is equal to that traveled by the object wave. The object wave passes into the wind tunnel through the flow field of interest where it picks up the appropriate modulation caused by the flow field and is recorded in the hologram to be later analyzed through interferometry, Schlieren or shadowgraph.

In some cases, where it was neither possible to provide a mirror within the flow field nor to pass the light through the test chamber, the retroreflective material similar to that used on street signs was used to coat the model to return light antiparallel to the initial direction.

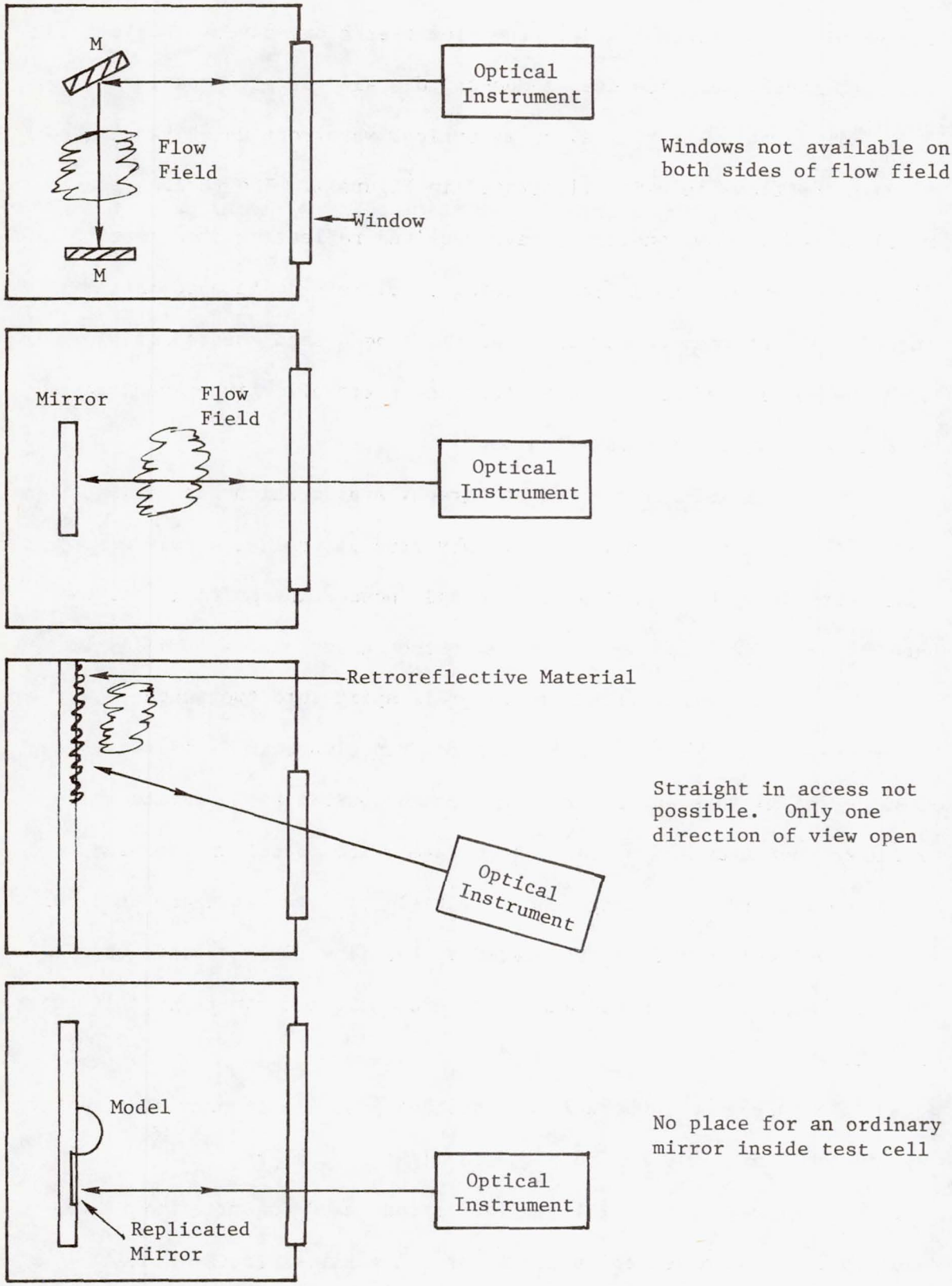

Figure 1. Retrieving the Wavefront with Limited Optical Access.

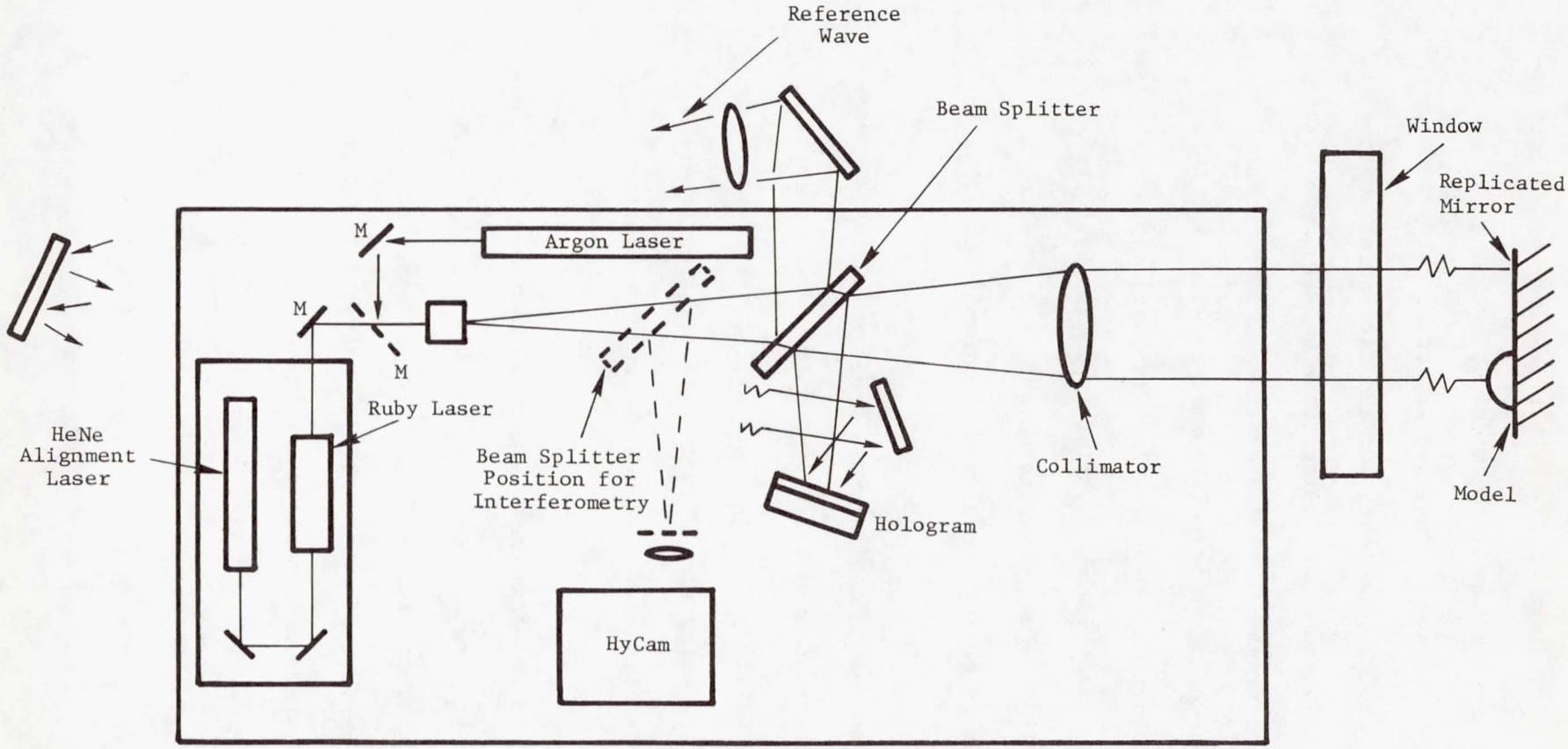

NOTE: Ruby Laser used for holography. Argon Laser used speed interferometry movies. Switching from one to the other required a five-minute alignment.

Figure 2. Holography/Interferometry Setup.

One particular advantage of the latter case is the ability to scan and cover quite large areas of the model by sweeping the beam over the area of the model and producing a number of holograms for any given condition. So far, in tests for the Air Force Weapons Lab, over 1,000 holograms have been made using these configurations.

The type of holography which has provided the most useful data has been double-pulsed hologram interferometry in which two pulses of light are produced during one laser flash lamp pulse producing two holograms on the same plate during a period separated by 50 to 100 microseconds. As will be shown, this technique is one of the most tractable methods for observing turbulent flow in a severe environmental condition.

The hologram stores an optical wave front in sufficient detail to allow its reconstruction at a later time. Therefore, when a wave front which has passed through a flow field of interest is recorded, it can be compared at a later time with a reference wave front to determine through interferometry how much the wave was distorted by the flow field.

In double-pulsed hologram interferometry, two wave fronts are recorded on the same hologram representing the optical system and flow field at two different times. When these two wave fronts are reconstructed, they produce (through interferometry) fringes which characterize changes which took place in the flow field in the time separating the passage of the two wave fronts through the flow field. This type of recording is especially useful in the viewing of turbulence since the flow can be compared with itself at two different

times. This can be done with time separation short enough so that vibrations and other common changes associated with wind tunnels do not affect the observation. Furthermore, since both wave fronts pass through the same optics and windows, the optical quality of such components is subtracted out and does not affect the observation of turbulence.

The first holographic study established the importance of turbulent flow and time-varying flow field conditions as a source of aberrations, and showed that inviscid flow effects were of almost negligible significance. This pointed to the need of a method to obtain more statistical data and to observe dynamic flow conditions.

During the summer of 1978, a high-speed wave shearing interferometry system which had been developed specifically for these studies was successfully put into operation and provided the required viewing of the dynamic flow cases. Briefly, the interferometer compares wave fronts which pass through the test chamber at slightly different positions in space and, therefore, provides a measure of density gradients in the flow field. Recordings were provided by a high-speeed camera which could be operated at rates up to 10,000 frames per second.

When it was realized that the holography data and the interferometry data were complimentary to each other, a configuration was devised to allow the operation of both systems with slight changes in the original setup. Finally, in the most recent tests, the holography system and the interferometry system evolved into devices which could cover a much larger field of view. The interferometry system was expanded to cover a 30 cm diameter field of view while the holography

system could produce coverage over a field of one meter in diameter by scanning.

4. EXAMPLES OF THE TYPES OF DATA PRODUCED

The purpose of this section is to provide illustrations of the types of data that have been produced in the studies carried out so far. Examples include several types of holographic interferometry, direct and indirect viewing and high-speed laser shadowgraph and interferometry.

Figure 3 illustrates holographic interferograms produced by propagating a beam from inside the turret through the flow field to a mirror located on the floor of a wind tunnel which returns the beam into the holocamera. In this type of interferogram only the time varying effects are observed. For example, a density increase or decrease which remains constant in the flow field or in the optical system is not observed, since it is recorded the same in both exposures. However, when a time varying density gradient such as a vortex in motion or a moving shock wave is present in the flow field, the two exposures record optical wavefronts which are different characterizing the two different states of the flow and which will interfere with each other, as seen in these figures. Vorticity is clearly evident in the flow field.

When the mirrors are vibrating during such a recording, a background set of linear fringes is produced. With no flow field

60°

M = .5 Cycle 3 (14D2)

No optical distortion in the turret wake would result in straight fringes here. Curvature in fringes measures twice the wavefront distortion since a double pass was made. Here, average distortion was less than $\lambda/10$.

90°

M = .5 Cycle 3 (16B1)

120°

M - .5 Cycle 3 (20C2)

At larger turret angles, this interferogram shows a significant ~ tenfold increase in distortion.

Figure 3a. Effect of Turret Position,

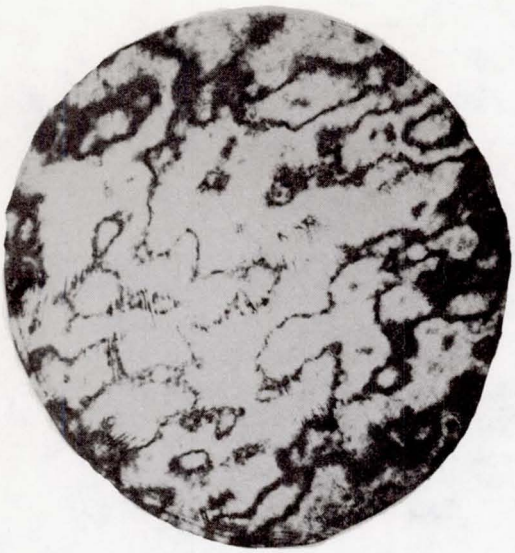

60°

At higher Mach No., distortion increased at all angles.

M = .75 Cycle 3 (15B2)

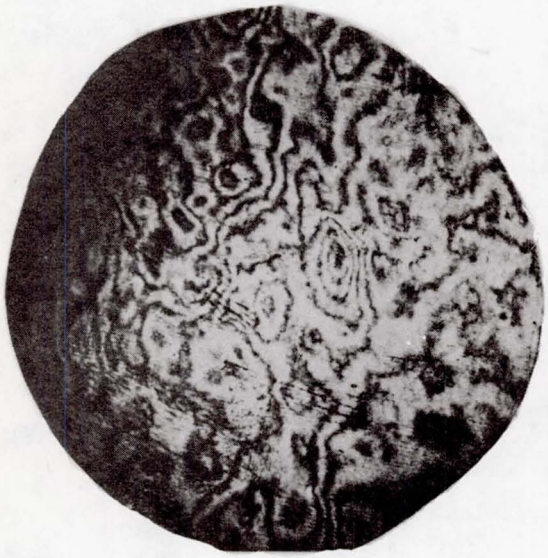

90°

Vorticity is not found to be totally random in nature. Therefore, material probe positioning will be extremely important.

M = .75 Cycle 3 (17C2)

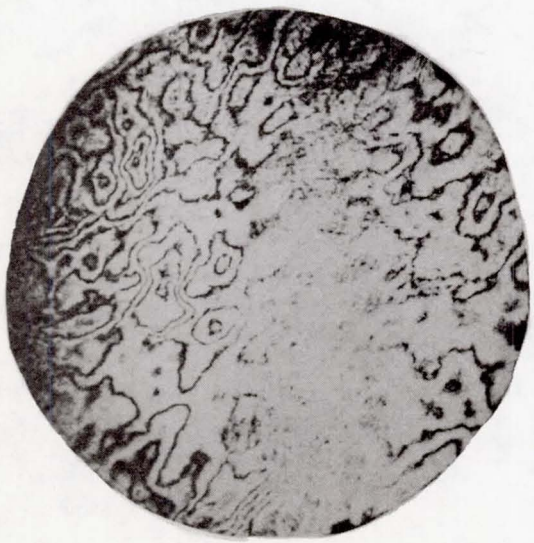

120°

The increased distortion at larger turret angles persisted.

M = .75 Cycle 2 (20A2)

Figure 3b. Effect of Turret Position and Mach No.

present these background fringes are linear. In these recordings it is clearly evident that the amount of turbulence and vorticity increases with Mach number and with increasing angle of the turret projection. The amount of distortion is seen to be quite severe when the turret is pointed beyond 90^{o} in the aft direction.

At Mach .5 when the turret is pointed in the forward direction, the optical strength of the flow field is less than one tenth wave distortion over most of the field, as can be seen from these pictures. At Mach .7 the amount of distortion exceeds one wave in much of the field. However, when the turret is pointed aft in the 120^{o} degree direction, the amount of distortion at Mach .5 is now somewhat greater than one wave and at Mach .7 the optical strength of the flow field has increased to nearly two waves in distortion over large areas.

These interferograms provide a very clear picture of how the aerodynamic flow field alters the modulation transfer function for the complete optical system. In principle, the modulation transfer function can be derived from interferograms such as those shown here. The problem here is that the unsteadiness of the flow field means that the modulation transfer function itself is varying and a more useful measurement would provide an average effect on the modulation transfer function. This can be acquired by taking many such interferograms since each presents the flow field at an instant.

In other tests the optics were not available to perform propagation measurements from the turret. Therefore, the flow field was observed from a different point of view. Recordings were made by

projecting an optical wavefront across the turret. This information is useful in addition to propagation measurements because it helps define another dimension of the flow field. The first such studies were made on a hemisphere turret mounted on a flat plate. The wavefront was returned by using a mirror which had been replicated onto the flat plate. The mirror became distorted and lost its optical quality when installed in the tunnel. Still, its quality was sufficient for wave shearing interferometry or for holographic interferometry. Figure 4 illustrates a holographic interferogram produced in this way. Here, the wake of the turret can be seen containing again turbulence and what appears to be a vortex structure. The wake dimensions can be determined and the optical strength of the wake can be determined from such a recording.

Figure 5 illustrates the appearance of wave-shearing interferograms produced from the replicated mirror using an Argon laser and a high-speed camera to make recordings up to 10,000 frames per second. In these cases the shock wave associated with the turret was displayed clearly. Turbulence created by the turret was observable and the dynamics of the flow could be quantified to some extent.

In larger scale tests it was not practical to replicate a mirror onto the surface of the splitter plate. Therefore, a technique which had been developed during these tests and using retroreflective material to reflect back the wavefront was used. Retroreflective material was placed on the splitter plate on which the

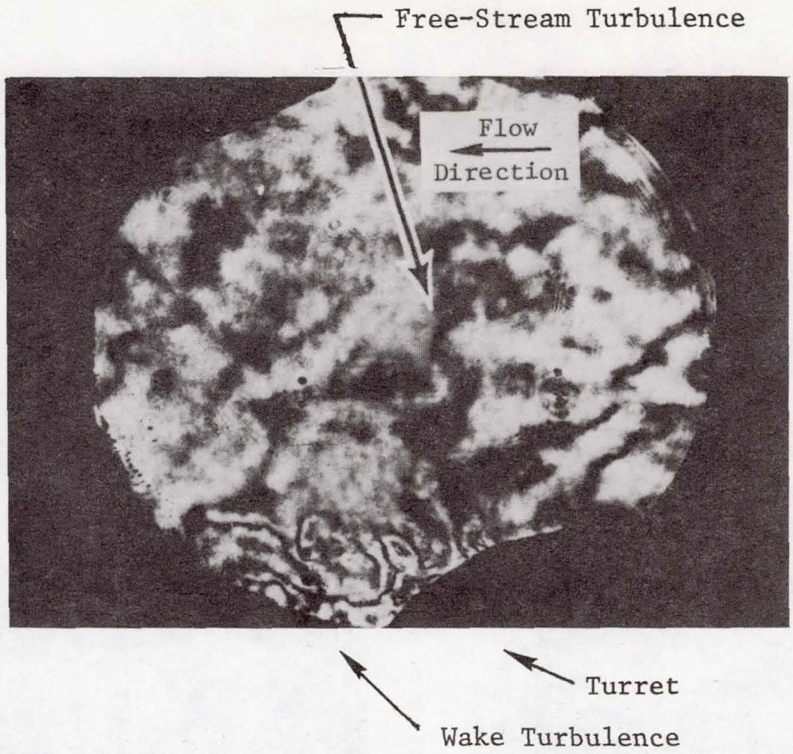

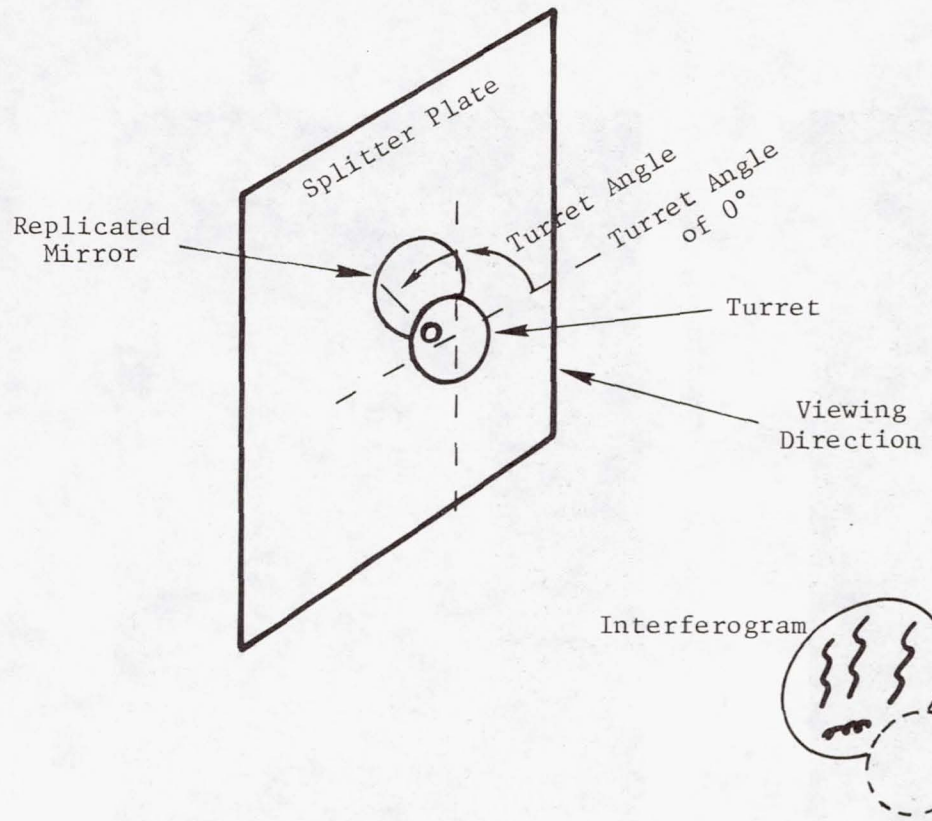

This view across the turret wake illustrates the extent and strength of the wake.

Figure 4. Holographic Interferogram Interpretation.

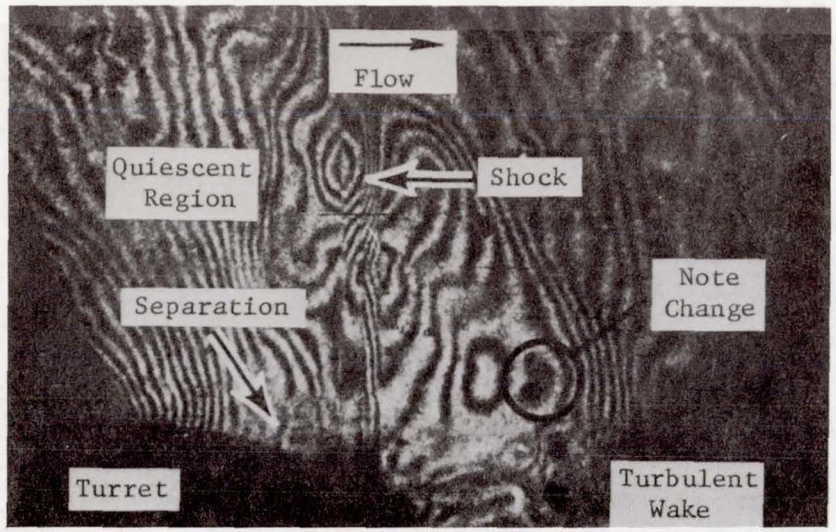

(a) t = 1.32 ms

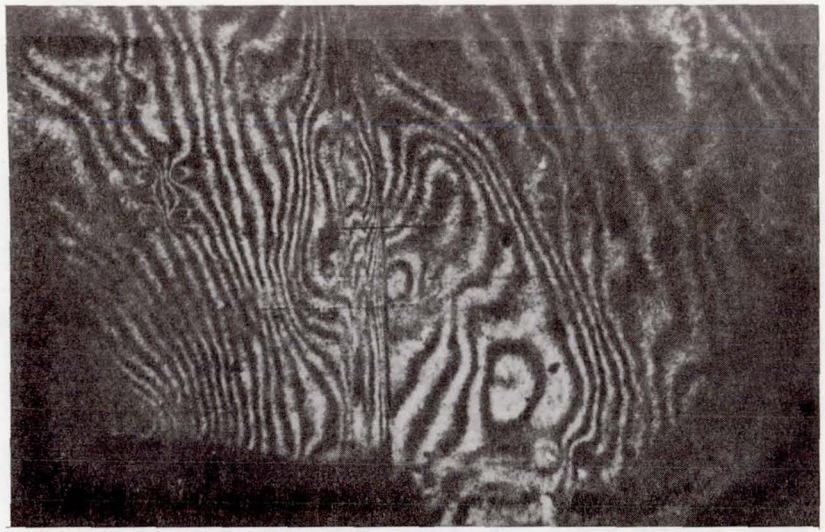

(b) t = 1.76 ms

The Shock waves were highly unstable, oscillating at 200 Hz or greater.

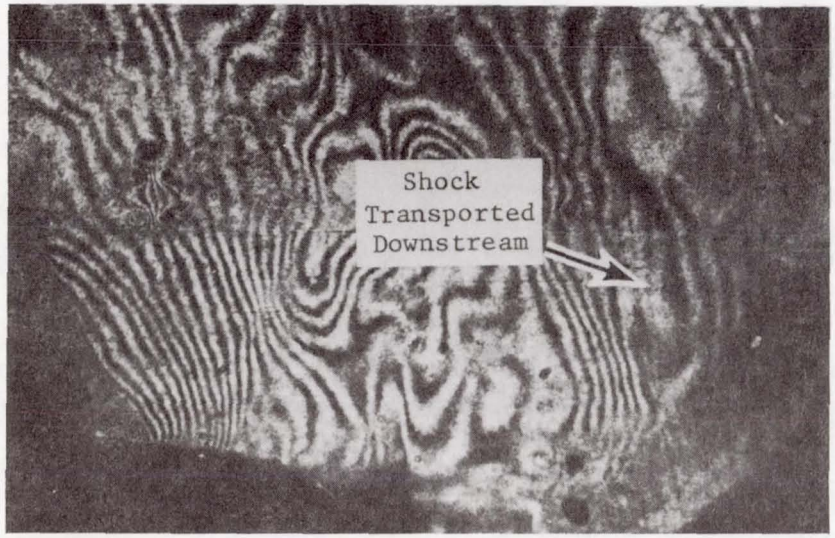

(c) t = 3.96 ms

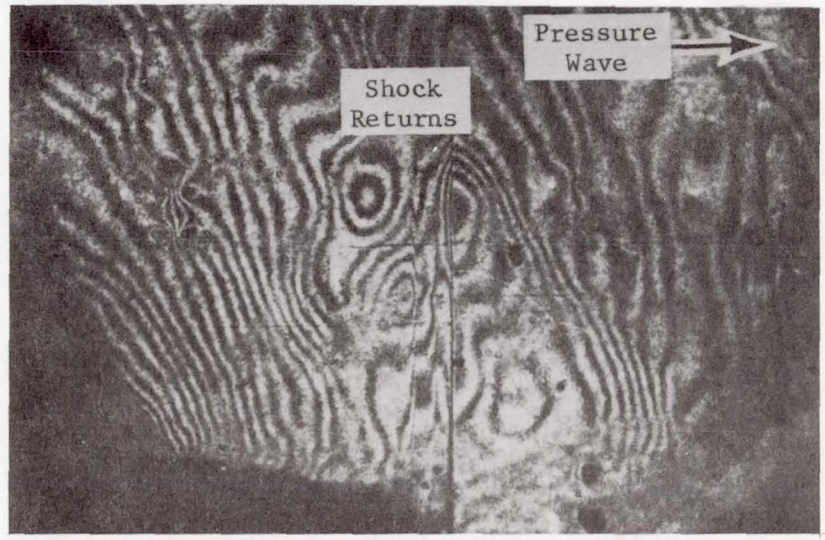

(d) t = 4.84 ms

Figure 5. Time Resolved Flow.

turret was mounted and was used to cover parts of the turret which presented a reasonable surface in the viewing direction. For this type of surface, the only type of holographic flow visualization which is applicable is double-pulsed hologram interferometry. Figure 6 illustrates typical results in such a case. To clarify the results, a photograph of the model itself has been superimposed on the reconstructed holographic interferogram. In this interferogram the effects, which are clearly observable, are the turbulent wake and its dimensions and characteristics of turbulence making up the wake. These pictures can provide a reasonable measure of the turbulence scale. The appearance of the flow away from the turret in the free stream of the test section is significantly different from that near the turret showing that the background wind-tunnel turbulence is sufficiently different in nature to allow the turret itself and its flow field to be characterized.

During these tests the wave-shearing interferometer which had been used in previous tests was also used. It was found, however, that the flow field was sufficiently slow that shadowgraph alone produced a reasonable picture of the flow field. This was especially fortunate in the 14-foot tunnel since the vibrational conditions in the location of this system were so severe that it was difficult to keep the interferometer aligned. The location of this system was on top of the 14-foot tunnel and projected through the top windows across the model in a vertical condition and was retroreflected from a mirror located in the floor of the wind tunnel.

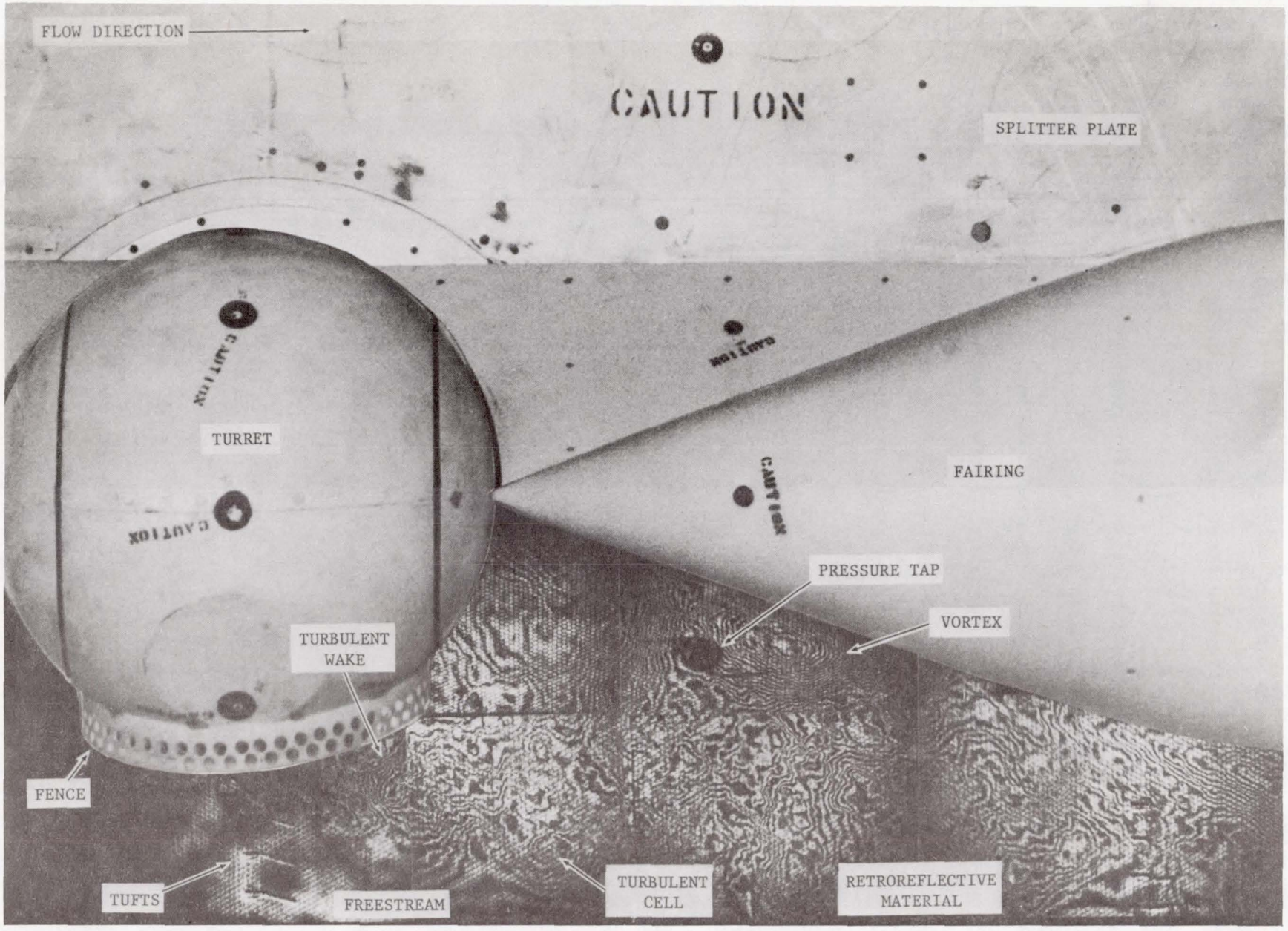

Figure 6. Double Pulsed Holographic Interferogram.

During this most recent test, nearly 500 holograms were made of the flow field across the turret viewing in a horizontal direction, while approximately 100 high-speed movies of the flow field looking across the turret from above were made. The data is still undergoing analysis and will be published in detail in a separate report.

5. SUMMARY OF RESULTS

5.1 Optical System Capabilities

During these tests a variety of optical system capabilities have been established and can now be considered available for use in future tests. Furthermore, a considerable amount of information is available in the data taken during the previous test. This data has not been fully exploited and a considerable amount of valuable information can still be derived from the holograms and movies recorded. The following kinds of information can be extracted from these data:

1) The wake, thickness and extent in space;
2) The structure of the wake, i.e., where it is turbulent, the type of turbulence, and the shape of the flow field;
3) The location of vortices and the determination of their strength;
4) An estimate of correlation lengths;
5) A measure of the optical distorting power of the flow field;

6) A location of shockwaves;

7) The effect of various turret angles, fence configurations, and fairing configurations;

8) A measure of the dynamic properties of the flow field; and

9) A clear depiction of the turbulent structure and its development in time.

5.2 Comparing Holographic Data with That from Pressure Taps and Hot Wires

When the desired result is to produce a turret which is optimized optically, the ultimate goal is to project a beam from the turret without distortion. Therefore, the direct measure of propagation and distortion by the flow field is the desired parameter to be measured. This can be done only with optical instruments such as holography, point-spread devices or interferometers. This information can be inferred by aerodynamic measurements if the flow is properly modeled and if the conversion of the aerodynamic parameters to optical parameters are completely understood. This also assumes that the probe itself does not improperly distort the flow field and that it fully characterizes the flow field. None of these assumptions can be automatically guaranteed. Flow visualization data puts serious doubt on the assumptions. Propagation through certain types of atmospheric turbulence is reasonably understood from an aerodynamics point of view. This is

the case, for example, through thin phase screens and through turbulence of a specific predetermined type. This is not what exists in general.

Optical instruments for probing the field around turrets are essentially non-intrusive and such measurements can be made with no perturbation to the flow field. The probing of a flow field with a material probe is especially intrusive at subsonic flow conditions and such measurements are always held in suspect where perturbation of the flow field is considered important. Quite commonly, such probes introduce distortions in the flow field of an optical nature which are of the same order as those present before the probe was introduced. Location of such probes in the flow field is also a critical factor.

Referring to Figure 6, we may draw a number of conclusions about the flow field for this particular case which is Mach .5. In general, such observations seem consistent with those made by other probes. Although a detailed analysis of this interferogram has not been carried out, a number of features can be immediately drawn simply by observing the picture. By observing the typical or average cell size in this interferogram, one can conclude that the correlation length that would be measured by a probe in this flow field would lie between .05 to .1 the diameter of the turret. A beam projected vertically downward at 90^{o} turret position would see an almost negligible distortion over the front half of the window. At .7 microns wavelength the distortion is less than one wave. Over the rear half of the turret, distortion at this wavelength could be in the order of about 5 waves or about a quarter wave at 10.6 microns. If this turret were tilted at 120^{o},

the distortion would be more serious even at 10.6 microns. The wake appears to be made up of a dynamic but partially coherent structure of vortices generated by the turret. Immediately behind the turret near the fairing appears a stationary vortex. Pressure taps which were mounted on the splitter plate would not likely see the same information shown in this interferogram, because one of these taps lay just outside the wake and the other tap lies in a region which is more quiescent. Also, these instruments measure information only at the surface of the splitter plate, while the interferogram measures an integrated quantity through the entire flow field. It is clear that the information that would be drawn from a material probe would depend extremely upon its position if moved about in this field. Therefore, we do not believe that an aerodynamic measurement with material probes can provide the kind of information illustrated in this figure.

Because the flow is not uniform, not random, and because it varies in all dimensions over the turret, a material probe would require traversing to all points in xyz for every turret configuration to provide the same information provided on one interferogram of a beam propagated from the turret! Even then the final conversion requires an accurate model of the flow field and light wave propagation through it.

6. CONCLUSIONS AND RECOMMENDATIONS

From the foregoing we conclude that:

(1) Holographic interferometry provides a powerful method for measuring the optical strength of flows over turrets.

(2) Complementary measurements can be made by propagating from the turret or passing the beam over the turret and reflecting from the model.

(3) Measurements which have been extracted from holographic data so far appear reasonably consistent with those extracted by aerodynamics and computations.

(4) The high-speed holographic interferometry and shadowgraph provide an insight to the dynamics of the flow field.

(5) Useful quantitative information can be derived from these data.

(6) The flow field can be understood from this type of data in ways which are not possible using material probes.

The techniques which have been developed so far are operational and can be used in future testing. However, a number of improvements are clearly needed. Such improvements appear to be within an easy reach of the present state of the art. These include a much higher data rate. It would be useful to record more data than has been recorded in the past to provide better statistical information. Such

can be accomplished with new Yag lasers which produce pulses of light at rates ten per second or greater. An on-line data display would be extremely useful in allowing quick looks at data during the test to allow concentrated efforts to be directed into certain types of data collection, such as now possible with thermo-plastic recording materials. Improved data interpretation is needed. It is not clear how to convert the displayed information into accurate numbers which can be compared with other instruments. Additional basic study is needed to understand how to model the turbulent flowfield in such a way that an optical interpretation can be made. Additional work is needed on previous data which has been taken. A great deal of this data has not been used to its fullest extent.

ACKNOWLEDGMENT

The work reported herein was conducted by Spectron Development Laboratories, Inc. while under contract to the Air Force Weapons Laboratories (AFWL). Much of the equipment as well as operations assistance was supplied by AFWL and NASA Ames Research Center. Captains Rich de Jonckheere and Wade Bailey worked directly with the holography team in all of the tests. Sargeant Harvey Childress of AFWL operated the high-speed camera in all of the interferometry and shadowgraph tests. The interferometer itself was a joint discovery found during preliminary mock-up tests by the author and Captain de Jonckheere. The author wishes to acknowledge the assistance of Fred Mason of Spectron, and Drs. Dennis Johnson and Ken Orloff and Mr. Don Buell

at NASA Ames who provided valuable assistance and equipment without which the results could not have been achieved.

UNSTEADY DENSITY AND VELOCITY MEASUREMENTS IN THE 6' x 6' WIND TUNNEL

by

William C. Rose
Rose Engineering and Research, Inc.
Incline Village, Nevada 89450

and

Dennis A. Johnson
NASA - Ames Research Center
Moffett Field, California 94035

SECTION I

INTRODUCTION

The propagation of coherent radiation through a gaseous turbulent flow medium is known to be affected by the intensity of the fluctuations in the index of refraction and the correlation volumes of the index throughout the flow medium. With aerodynamic instrumentation it is possible to measure the intensities and correlation volumes of the density fluctuations, and through the Gladstone-Dale relationship, the required index of refraction intensities and correlations. The degradation of beam quality as it traverses the turbulence is of interest to the propogation of high energy laser beams from airborne platforms out to distant targets, optical imaging, and other sensor performance.

Recent Air Force Weapons Laboratory (AFWL) research programs have established the correlation between directly measured beam degradation and the density fluctuation levels and spatial scales as measured by aerodynamic instrumentation. This demonstrated correlation is important since, in many instances, it may be easier to make the required aerodynamic measurements than to make meaningful measurements of loss in optical quality. Computer codes are available for transforming information concerning the density and velocity fields to optical propogation information.

Over the past five years, the AFWL, in cooperation with NASA's Ames Research Center and Air Force Flight Dynamics Laboratory (AFFDL),

has been conducting a continuing research program into the interaction of aerodynamics and optical performance. This program, known as the Aero-Optics Program, has produced significant results that further the understanding of aero-optical interaction.

Four major wind tunnel tests have been conducted in the NASA-Ames 6' x 6' wind tunnel: the first in the summer of 1975 and the second in the summer of 1976. A third test was completed in the fall of 1977. The first test served primarily as an introduction to the problems faced by both aerodynamicists and opticians. In the second test, both density fluctuation levels and their scales were obtained within the boundary layer and shear layer for several flow models. These aero-dynamically measured data appear to correlate well with the optical degradation data obtained for the same flow models. The third test investigated the effect of nonadiabatic wall temperature on optical degradation. A section of the model was heated to about 50°C above the adiabatic plate temperature to induce measurable total temperature fluctuations in the boundary layer.

As difficult and complex as these previous test programs appear to be, they have modeled only an ideal case of a beam looking normal to the plane of a two-dimensional shear layer representative of those occurring over open and closed port geometries. Presently conceived methods for beam exits involve the use of turrets and fairings which produce highly three-dimensional turbulent flow fields. The fourth test in the Aero-Optics Program was conducted in the fall of 1978. A small scale

(approx. 1/40) turret and fairing combination was mounted on the same plate as used in previous tests. The turret was a 12.7 cm ceolostat with a 2.5 cm aperture that could be remotely rotated from 60° to 150° in azimuth angle. Flow characteristics affecting optical performance were studied along imaginary beam paths of 60°, 90°, 120° and 150°.

All of the Aero-Optics tests were carried out over a range of Mach numbers between 0.6 and 0.9 with one set of data in A-O IV being obtained at M=1.5. The Reynolds numbers for these tests ranged between $6 \cdot 10^6$ and $12 \cdot 10^6$/m. Various thickness shear and boundary layers were generated so that the tunnel Reynolds number may not be as important as the shear-layer thickness Reynolds number, for example. The reader is referred to Reference 1 for further details of model geometry and flow configuration identification.

This report presents a brief summary of the results obtained in the four tests and the methods to obtain them. All of the information obtained in these tests has been presented in detail previously (see References 2, 3, and 4) and is, therefore, only summarized here.

SECTION II

INSTRUMENTATION AND DATA REDUCTION

Two proven systems for making the aerodynamic measurements necessary for inferring optical degradation due to a region of turbulent flow are the hot-wire anemometer and laser velocimeter. Their application and use in high subsonic and transonic flows has been discussed in detail in Reference 1. In order to present a description that can be read by those interested in fields other than aerodynamics, a brief description of the instrumentation and data reduction procedures used is given in this section. The discussion is included here since many of the concepts and techniques used in this report stemmed directly from the needs created by the Aero-Optics Program.

The laser velocimeter in its many forms is a nonintrusive optical device for measuring particle velocity in a moving stream. Successful measurements have been made in both water and air. When the particles are small enough, their velocity (and changes in velocity) are essentially the same as that of the fluid. Thus, the velocimeter is an instrument capable of making pure kinematic measurements, independent of the thermodynamic state of the fluid.

On the other hand, the hot-wire anemometer is an instrument that senses heat transfer from a fine wire; and thus it senses a combination of kinematic and thermodynamic flow properties. In a turbulent

compressible flow (i.e., $M \geq \approx 0.3$) all of the thermodynamic and kinematic flow properties can vary with time and space. The time variations are known as fluctuations and their long-time averages are characterized by the rms of the quantity. The spatial variations are generally complex, being strongly dependent on the history of the fluid prior to reaching the location of interest. A method of characterizing the large effects of spatial variations is that of correlation volume, which is essentially the volume in the fluid over which a turbulent burst or eddy retains its identity. Both rms values of the fluctuation levels of the fluid density and their correlation volumes affect optical degratation; hence, to characterize the optical effects, one must measure both properties of the flow.

Since there are no proven instruments for directly sensing fluid density or its time and spatial variations, other techniques must be employed to obtain information about the density. As noted above, the laser velocimeter can measure velocity fluctuations (u'). A very hot wire will measure the mass flux (product of density and velocity) fluctuations [$(\rho u)'$]. Another fluid parameter, the total temperature T_t, can also fluctuate and can be measured by an unheated wire sensor. The anemometers used for these two measurements (i.e., the electronics used to process the signals from the sensor wires) are a constant-temperature system for the mass flow and a constant-current system for the total temperature.

The interrelationship between the fluctuating variables in a compressible flow is not completely obvious; however, the thermal energy equation

$$T_t = T + u^2/2c_p \qquad (1)$$

constrains the way in which thermodynamic and kinematic variables may fluctuate. The logarithmic differential form of equation (1) involving the fluctuating quantities can be written as:

$$(1 + \frac{\gamma-1}{2}M^2)\frac{T_t'}{\bar{T}_t} = \frac{p'}{\bar{p}} - \frac{\rho'}{\bar{\rho}} + (\gamma-1)M^2\,\frac{u'}{\bar{u}} \qquad (2)$$

where the primed quantities are the real time fluctuations. Equation (2) is the basis for the aerodynamic data reduction employed throughout the Aero-Optics tests. The Mach number in (2) is that of the gas moving past the sensor while all of the barred quantities are the respective time averaged, local mean values. Since the fluctuating fluid density appears in equation (2) and cannot be measured directly, this relationship must be investigated to the fullest in order to use what can be measured to deduce information about the density, and, hence, the required optical information.

Some important implications of equation (2) are now discussed. If, somehow, the T_t' and p' terms are negligible compared to the others, then what remains is just

$$\frac{\rho'}{\bar{\rho}} = (\gamma-1)M^2\,\frac{u'}{\bar{u}} \qquad (3)$$

Thus, a knowledge of M^2, $\bar{\rho}$, and $u'/\bar{u}$ from a laser velocimeter would allow one to immediately obtain information about ρ'. The rms of the fluctuation at a point is the easiest quantity to obtain. The spatial scales or correlation volumes are more difficult to obtain since cross correlations of the output with various spatial separations of two sensing volumes would be required. To date, this has not been done, although, conceptually, it is possible given a high velocimeter data rate.

With respect to a hot-wire anemometer, the mass flux fluctuations do not appear in equation (2); however, the equation may be rewritten in either of two ways:

$$(1 + \frac{\gamma-1}{2}M^2)\frac{T_t'}{\bar{T}_t} = \frac{p'}{\bar{p}} - \frac{(\rho u)'}{\bar{\rho}\bar{u}} + [1 + (\gamma-1)M^2]\frac{u'}{\bar{u}} \qquad (4a)$$

or

$$(1 + \frac{\gamma-1}{2}M^2)\frac{T_t'}{\bar{T}_t} = \frac{p'}{\bar{p}} + (\gamma-1)M^2\frac{(\rho u)'}{\bar{\rho}\bar{u}} - [1 + (\gamma-1)M^2]\frac{\rho'}{\bar{\rho}} \qquad (4b)$$

Now consider a situation in which the p' term is negligible. Equations (4a) and (4b) provide a means of deducing either the u' term or ρ' term from direct measurements of T_t' and $(\rho u)'$. This is less restrictive than equation (3), since the presence of total temperature fluctuations can be accounted for in equation (4). If T_t' is significant, then a laser velocimeter alone cannot be used to infer the density fluctuations. If the p' term is significant, then an independent measurement of it is required to infer ρ' with either the hot-wire anemometer or the

laser velocimeter. The spatial scales can be easily obtained by the hot-wire anemometer, since the cross correlation of two analog signals with increasing separation distance is straightforward. All density scale sizes reported in the Aero-Optics test results were obtained by the hot-wire anemometer.

SECTION III

RESULTS

Measurements of the nondimensional velocity fluctuations from two configurations (see Buell, Ref. 1, for configuration identification) using the laser velocimeter and hot-wire anemometer are shown in Figure 1. The velocimeter data were obtained with and without artificial seeding and indicate slightly larger fluctuations near the boundary-layer edge with seeding. The hot-wire values were obtained using equation 4b with $T_t' = p' = 0$. The agreement between the independent systems is quite good up to turbulence levels of 25%. This type of agreement is typical of that obtained throughout the Aero-Optics program. The solid curves represent the best estimate between the two measurement systems. The density fluctuations are shown for three configurations in Figure 2 for the low and high Mach number cases. The boundary layer (2a) exhibits the usual shape of the fluctuation profile. Configuration 2, a large fence, produces nearly twice the fluctuation levels over a larger distance, producing a substantial optical degradation. Figure 3, a good fence ahead of the cavity, produces nearly boundary layer-like values except in the thin shear layer.

Correlation of two wires in the beam direction, Z, produces the integral scale lengths shown in Figure 3. Note in Figure 3b the decrease in scale size in the thin shear layer. This somewhat offsets

optical degradation caused by the increase in fluctuation level in that layer. All correlation data are best fit by an exponential curve rather than the Gausian assumed frequently.

Scaling the data to other Mach and Reynolds numbers is discussed in detail in Reference 3, however, the density fluctuation levels scale roughly as M^2 while Reynolds number effects the scale sizes and layer thicknesses in the usual way.

Heat addition to the boundary layer ahead of the measurement station was studied in Aero-Optics III. A section of the plate (see Ref. 1) was heated approximately 50°C above ambient which produced the change in total temperature profile shown in Figure 4. Little effect on velocity fluctuations was observed with the heat addition as can be seen in Figure 5. Density fluctuations, however, did increase by about 10-25% with heating (Figure 6). No effect on correlation length was observed with heat addition, indicating that the kinematics of the turbulence was not substantially altered by the amount of heating used here.

Results from the turret and fairing combination test (A-O IV) were typical of those shown in Figure 7 for a Mach number of 0.95. The rms velocity fluctuations, non-dimensionalized by their local mean value are shown in comparison to the mean Mach number distributions. Substantial velocity fluctuations are observed for the higher azimuth angles, although all the fluctuation data appear to be consistent with the presence of gradients in the mean flow. Some of these gradients are inviscidly generated (such as the supersonic "tongues" at 90° and

120°) and some viscously; however, no present means are available to distinguish between the fluctuations generated by various gradients. Fluctuations seen in the outer regions of these flows are probably caused by turbulence in the free shear layer associated with flow separation from the turret itself. Because the Mach numbers are observed to be much higher than the freestream, the potential for density fluctuations is quite large, since the mean density gradients will scale with the square of the local Mach number. The data at other Mach numbers all exhibit similar trends, however, for the lower Mach numbers, separation from the turret occurs at larger azimuth angles. In summary, the rather large values of density fluctuation appear to be the result of much higher Mach numbers than freestream and the violent turbulence in the flow as it separates from the turret.

A representative comparison of fairing on-fairing off rms density fluctuations shown in Figure 8 indicates essentially no effect at $M=0.62$ and a small effect at $M=0.95$. These data indicate that some slight improvement in optical quality can be expected with the addition of a fairing, although at $M=0.62$ its effect would be nil. Fairings are very useful in controlling pressure loads on turrets, but will not have first order effects on optical quality.

Scale sizes increase dramatically with increasing azimuth angle as shown in Figure 9 for a representative condition. Since both scale-sizes and fluctuation levels increase (total turbulence path length also increases) with azimuth angle, substantial optical degradation might be

expected. The Strehl ratio is shown in Figure 10 for the present data scaled up to a large turret in a flight environment. For shorter wave lengths, large degradations occur.

SECTION IV

CONCLUSIONS

1. State-of-the-art aerodynamic instrumentation and data interpretation methods allow the fluctuations in density and their spatial scales required to determine optical performance to be obtained in the most complex flows. In many cases it may be easier and/or more reliable to assess optical degradation due to an aerodynamic flow by aerodynamic measurements rather than direct optical techniques.

2. Wind tunnel testing at high subsonic and transonic Mach numbers usually produces wall conditions that are adiabatic, similar to those found in flight experiments. The amount of heat transfer from the surface that is required to produce observable increases in density fluctuations is at least an order of magnitude larger than that observed in flight.

3. The density fluctuations scale with a parameter that is essentially $q_\infty \ell_z/\delta$ **(the dynamic pressure times scale length divided by shear layer thickness).** Correlation of the wind tunnel data using this scaling is very good. This parameter can account for variations of Mach and Reynolds numbers as well as variations in ℓ_z/δ brought about by such things as strongly nonequilibrium turbulence behavior.

4. The loss in optical quality due to an aerodynamic fence is substantially larger than an attached boundary layer. The major source of this loss is the large density fluctuation level in the thin

shear layer that develops from the top of the fence. When a fence is present, its effect dominates any effect that the upstream boundary layer has on optical degradation.

5. For the small-scale turret and fairing combination, aerodynamic measurements of the fluctuation level and spatial scales of the density field have been made. Their effects on a coherent beam propagating through the flow have been made. Measurements were made around the turret at azimuth angles of 60°, 90°, 120° and 150° without the fairing and 60°, 90° and 120° with the fairing present. Considerable increases in density fluctuation level and scale size were observed with increasing azimuth angle, producing strong optical phase aberrations at the larger angles. Even for the 90° case, optical losses are observed to be higher than estimated on the basis of previous aero-optical investigations because the significant increase in Mach number over the flight Mach number around the turret was not considered previously. Attempts at scaling optical phase variance with aerodynamic parameters such as dynamic pressure were not successful. This was shown to result primarily from the nature of the flow causing the phase aberrations. For the turret, a large region of turbulent, separated flow exists which is only mildly influenced by Mach and Reynolds numbers and dynamic pressure; however, the large spatial scales arise almost uniquely as a result of the separation.

The addition of a fairing to the turret does little to aid in the optical quality, although fairings are quite useful in reducing aerodynamic loads on the surface and within the optical cavity of the aperture.

REFERENCES

1. Buell, D.A., "6' x 6' Wind Tunnel Aero-Optics Test Overview," Proceedings of the USAF/NASA Aero-Optics Symposium. August 14-15, 1979, NASA-Ames Research Center, Moffett Field, CA, Sept. 1979.
2. Johnson, D.A. and Rose, W.C., "Turbulence Measurements in a Transonic Boundary Layer and Free-Shear Flow Using Laser Velocimetry and Hot-Wire Anemometry Techniques," AIAA paper 76-399, San Diego, CA, 1976.
3. Rose, W.C., Measurements of Aerodynamic Parameters Affecting Optical Performance, AFWL TR-78-191, Air Force Weapons Laboratory, Kirtland AFB, NM, May 1979.
4. Rose, W.C., Optical Effects of Near-Field Turbulence About a Small-Scale Turret Model, AFWL TR-79-129, Air Force Weapons Laboratory, Kirtland AFB, NM, December 1979.

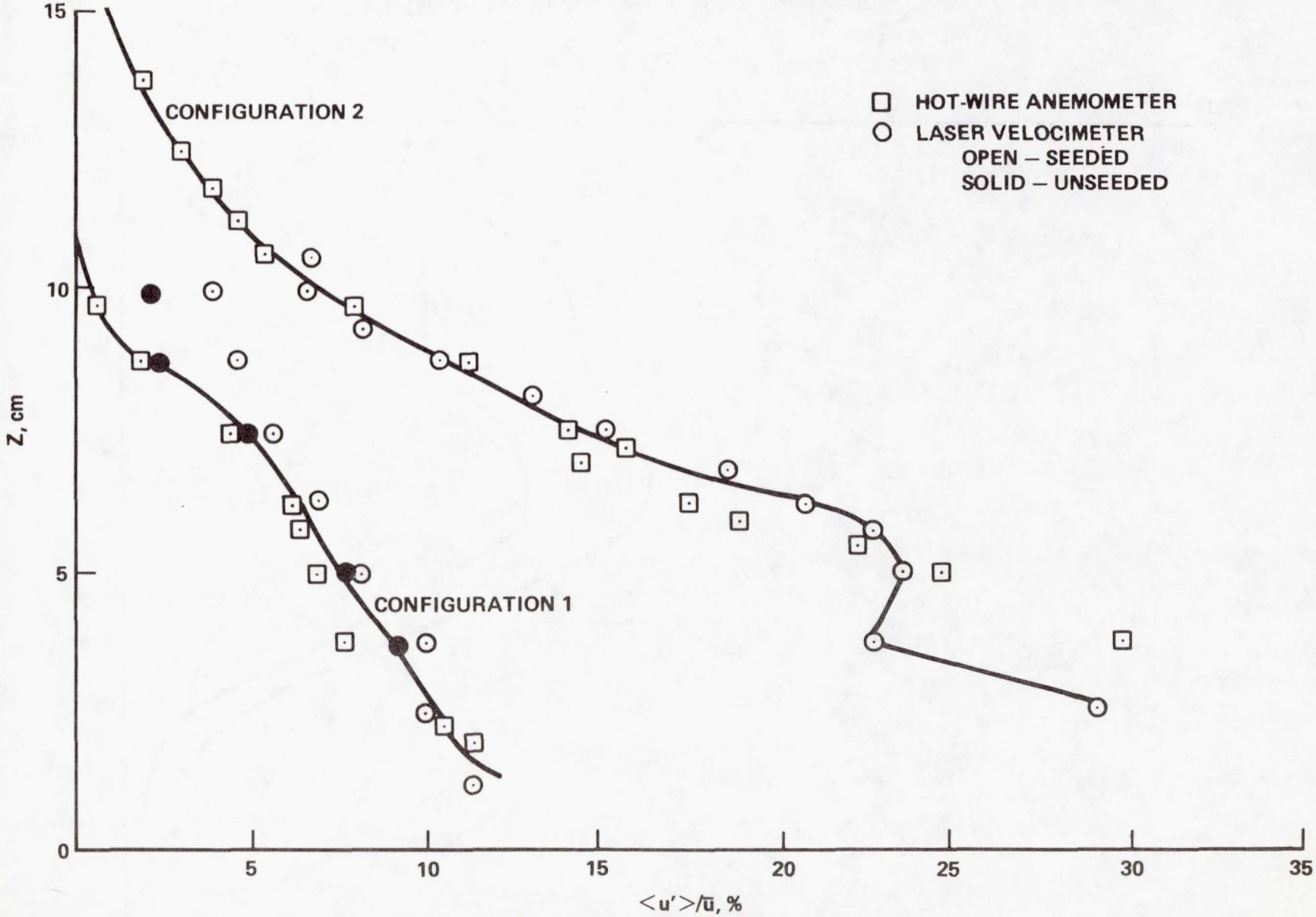

Figure 1. Velocity Fluctuations in Boundary and Shear Layers.

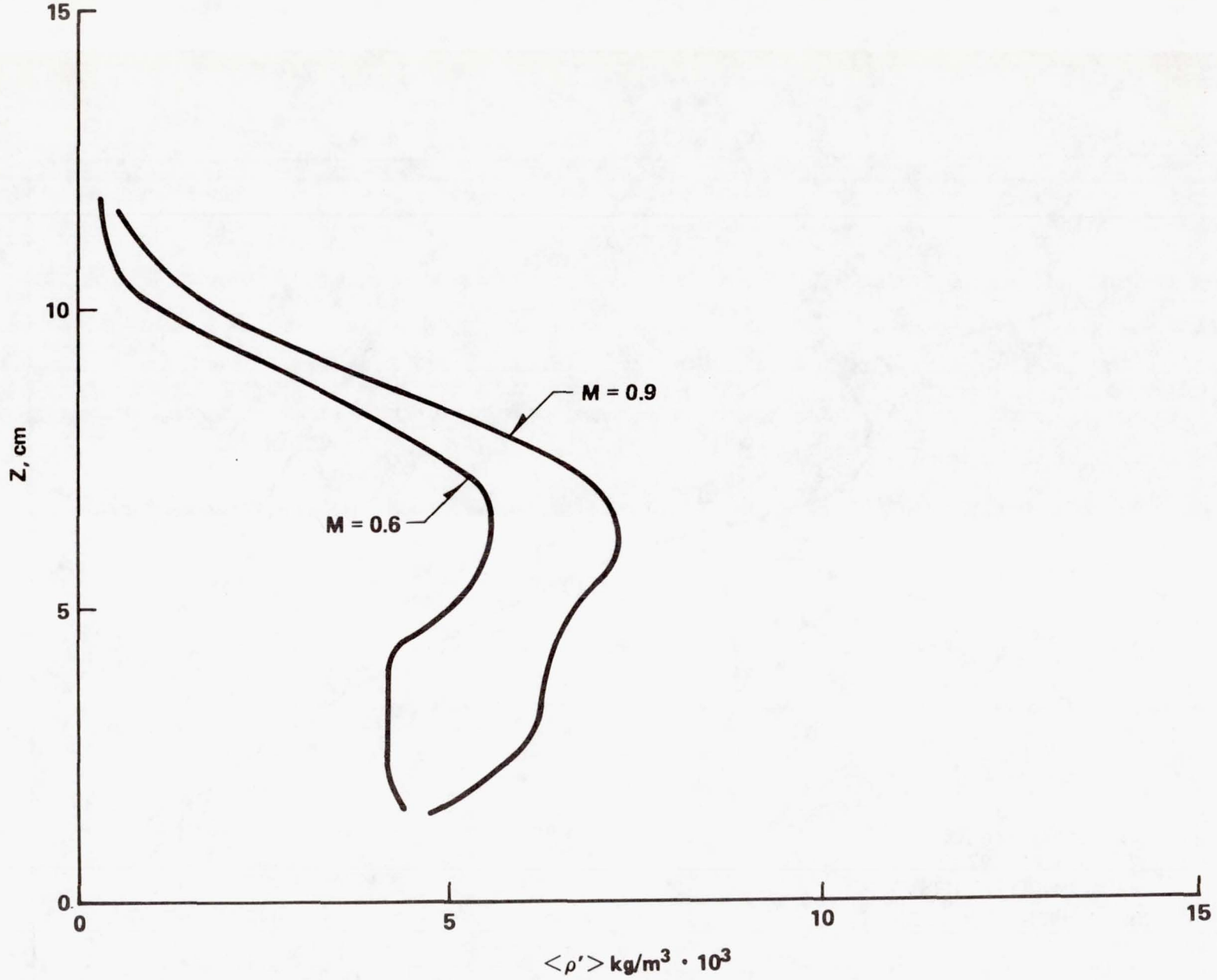

Figure 2. Density Fluctuations. a) Configuration 1.

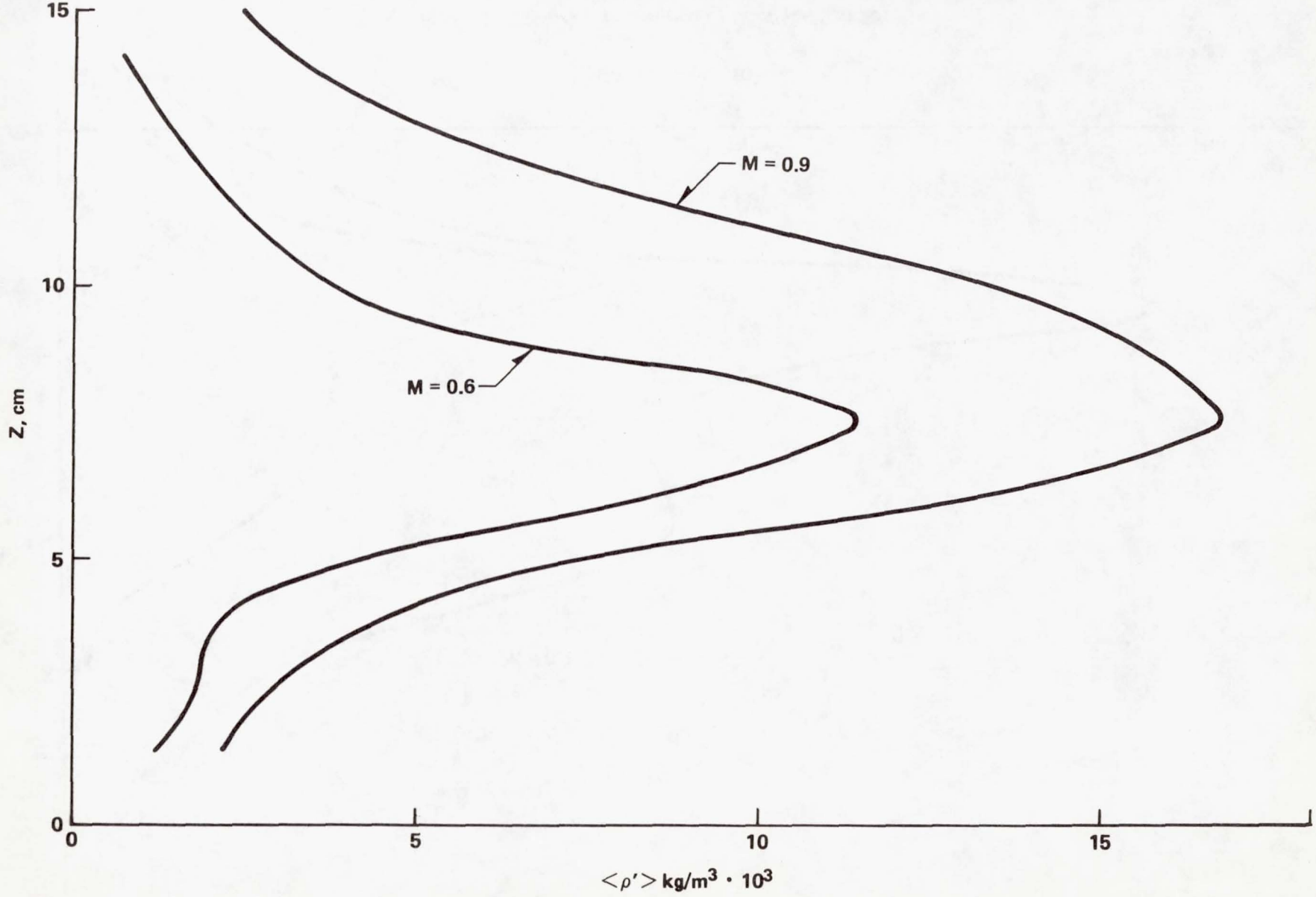

Figure 2. Density Fluctuations. b) Configuration 2.

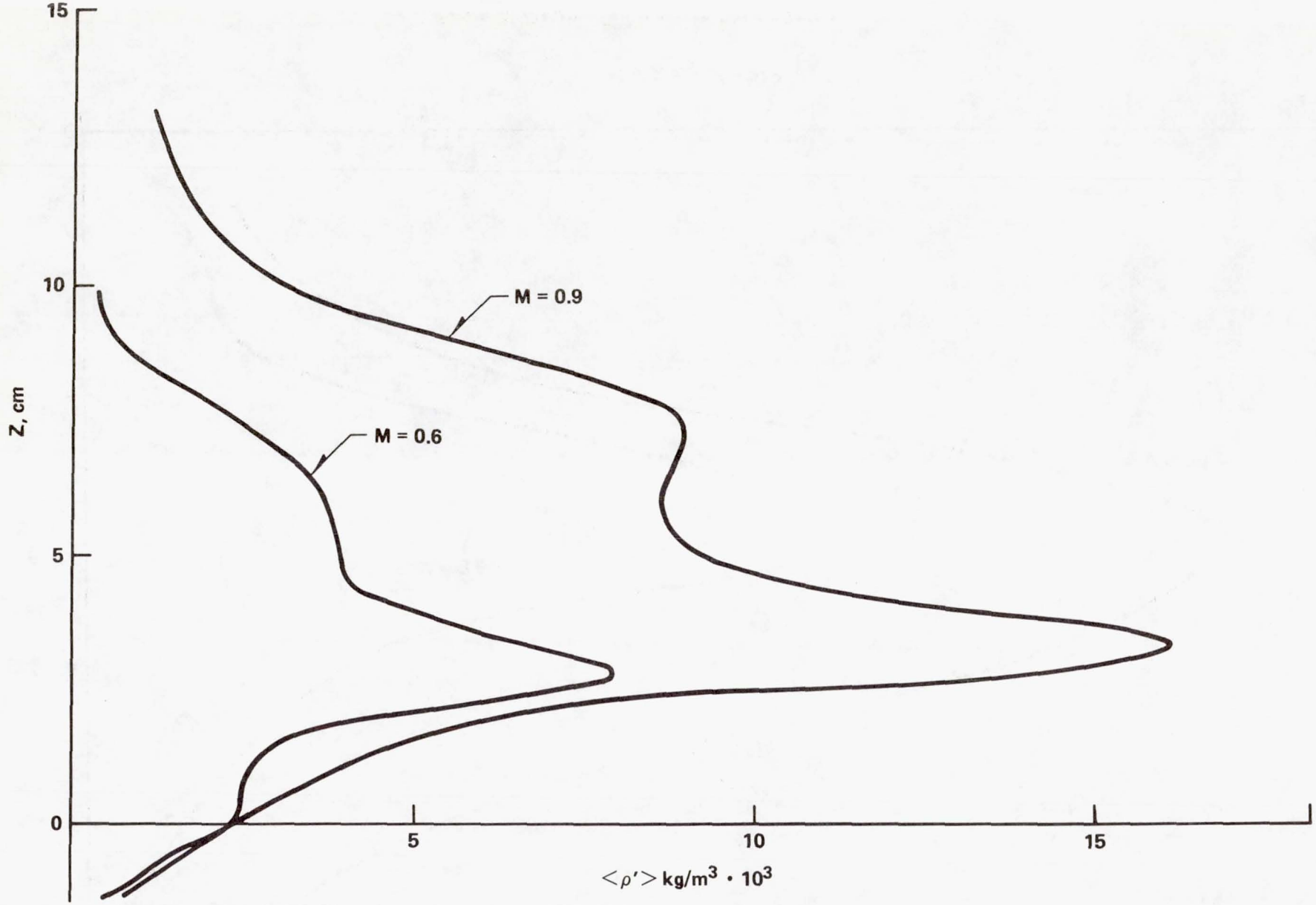

Figure 2. Density Fluctuations. c) Configuration 13.

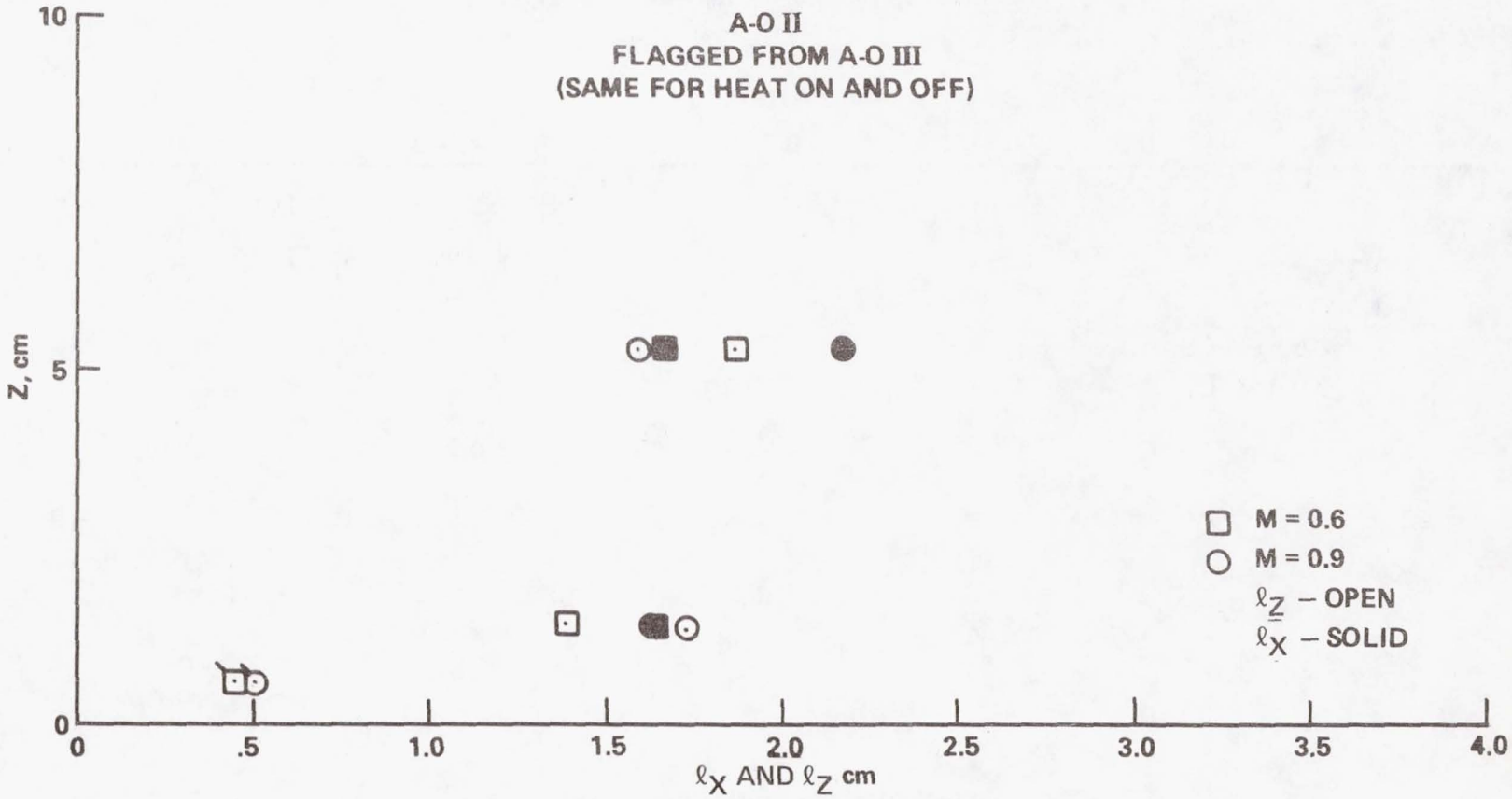

Figure 3. Correlation Lengths. a) Configuration 1.

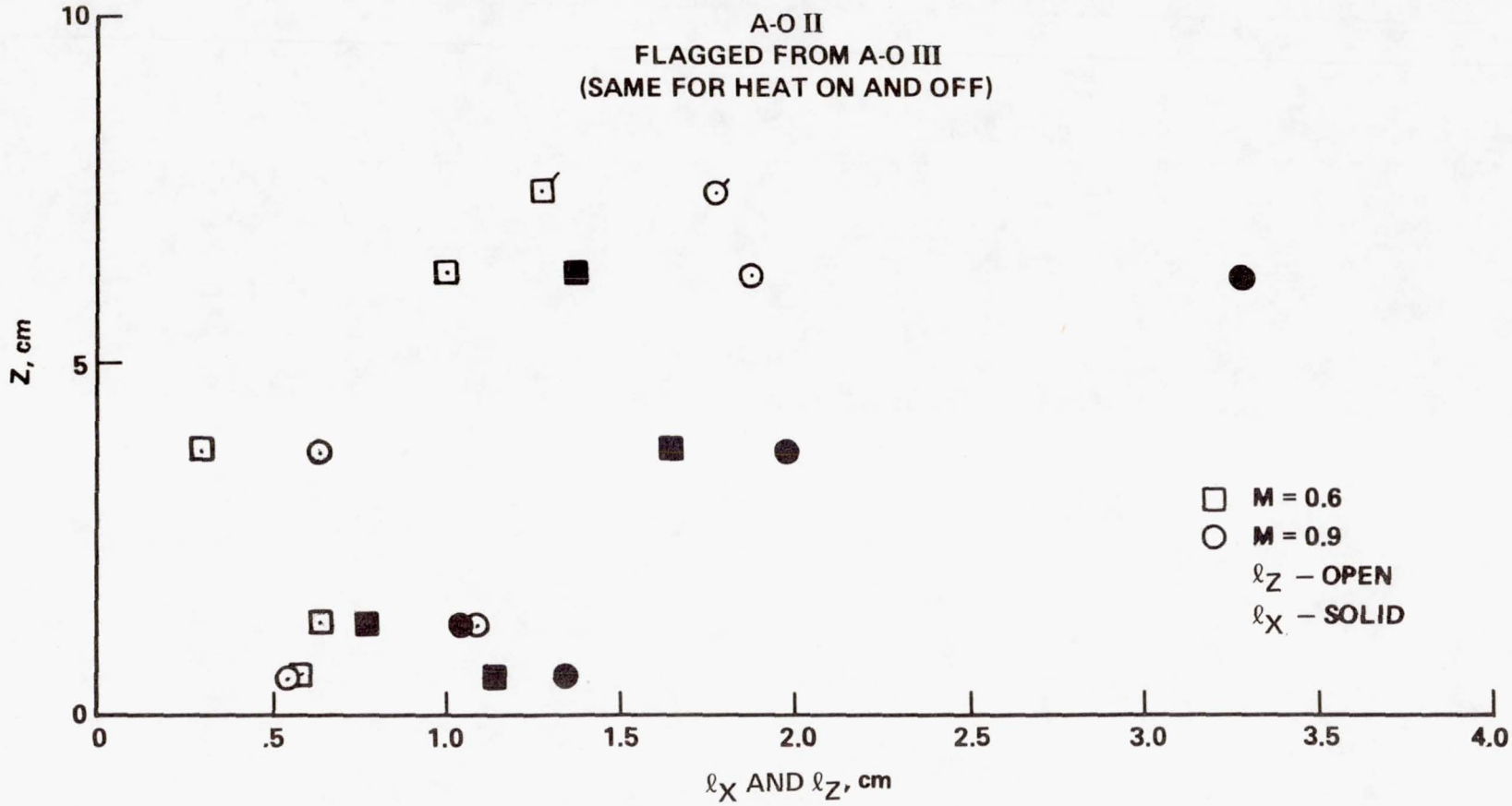

Figure 3. Correlation Lengths. b) Configuration 13.

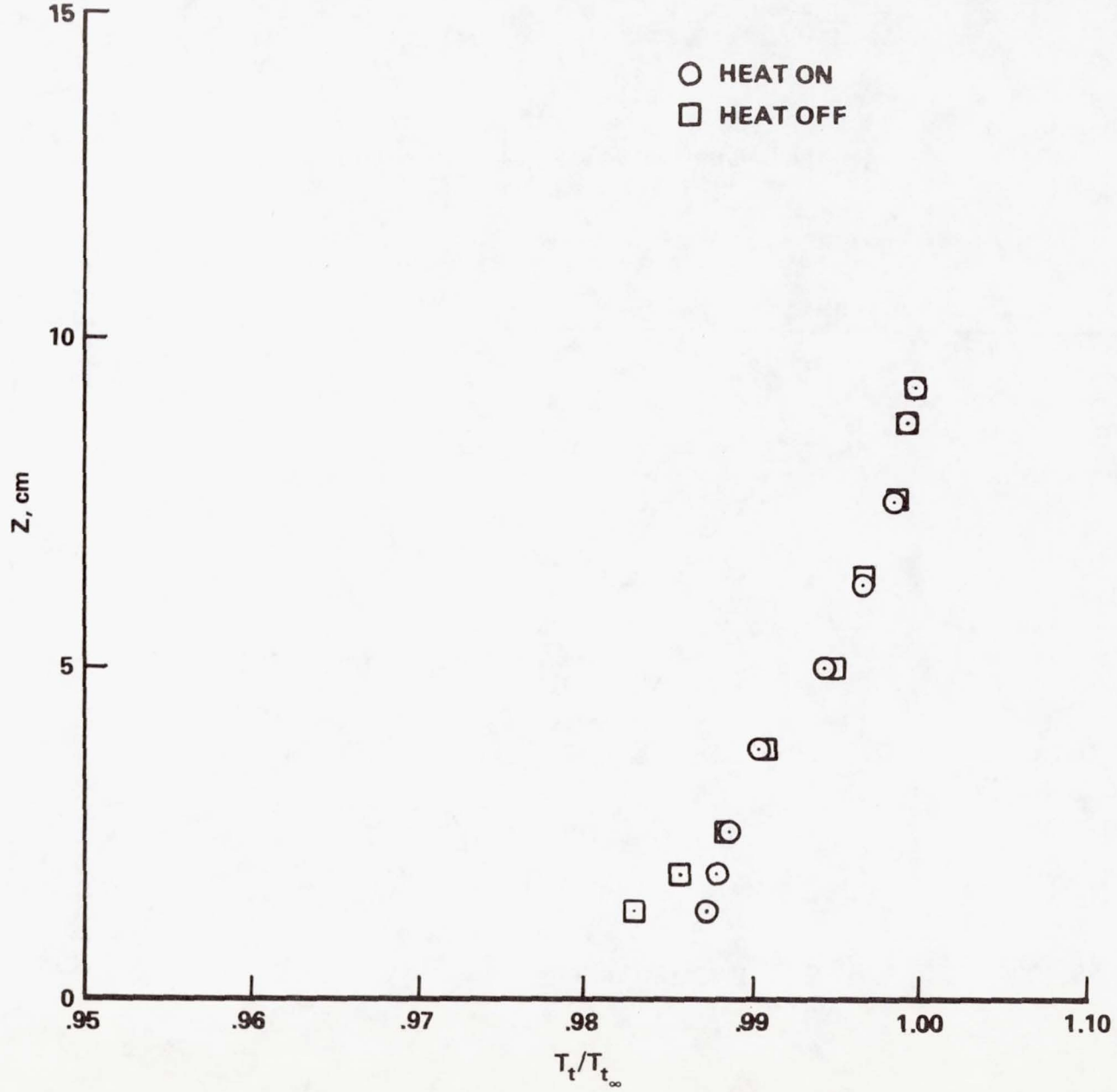

Figure 4. Total Temperature Profiles, Config. 1, M = 0.9.

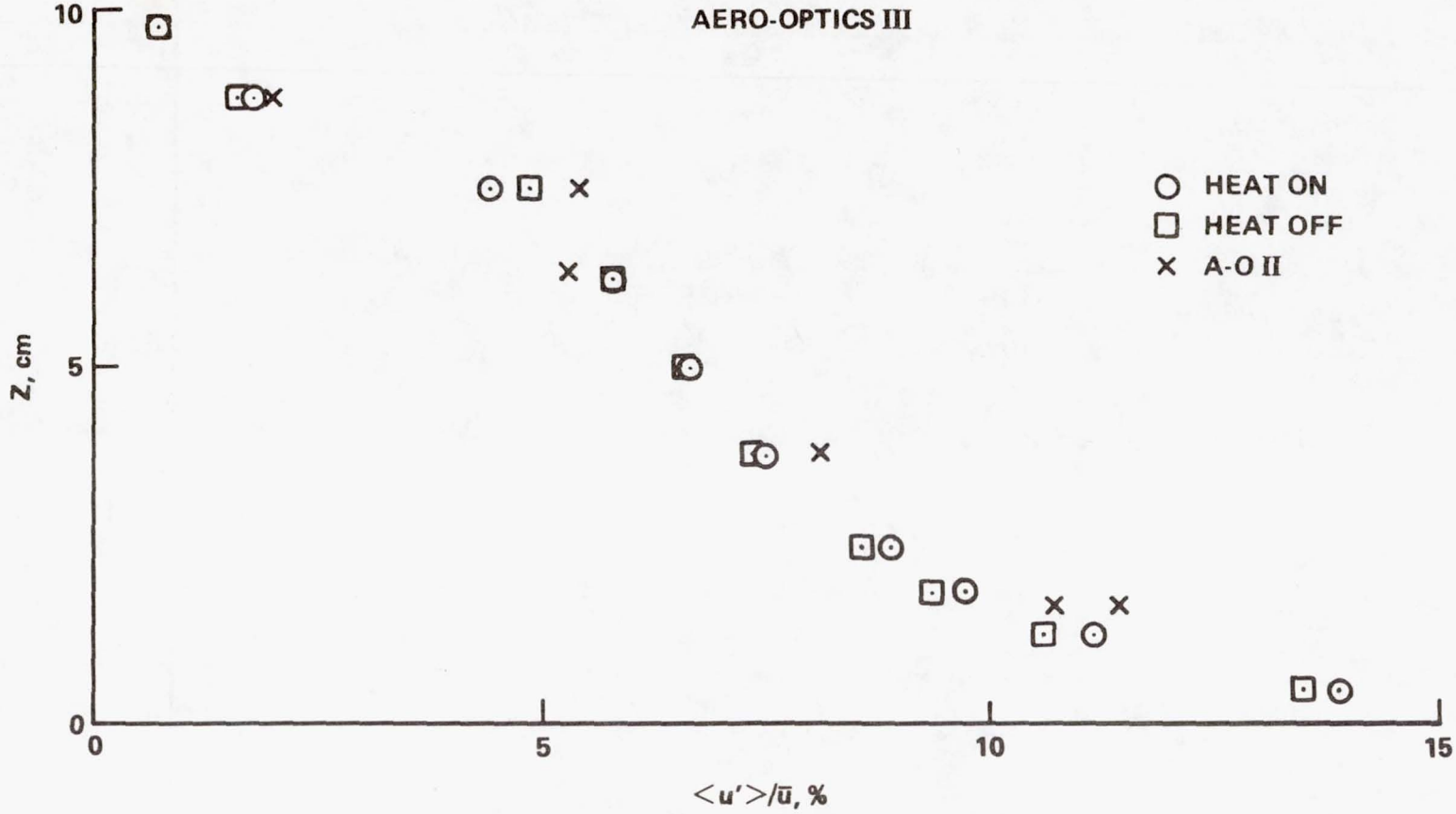

Figure 5. Velocity Fluctuations, Config. 1, M = 0.9.

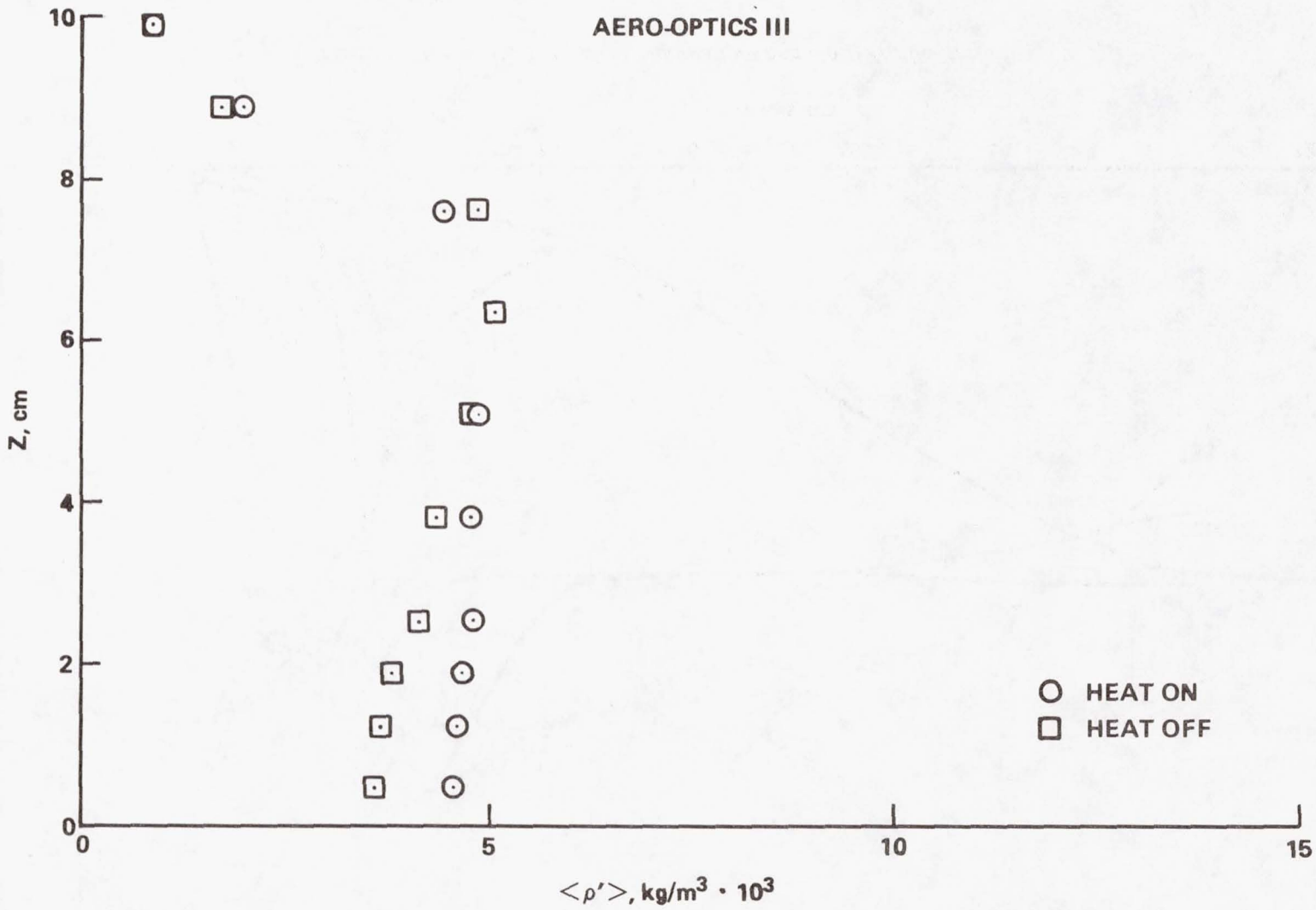

Figure 6. RMS Density Fluctuations, Config. 1, M = 0.9.

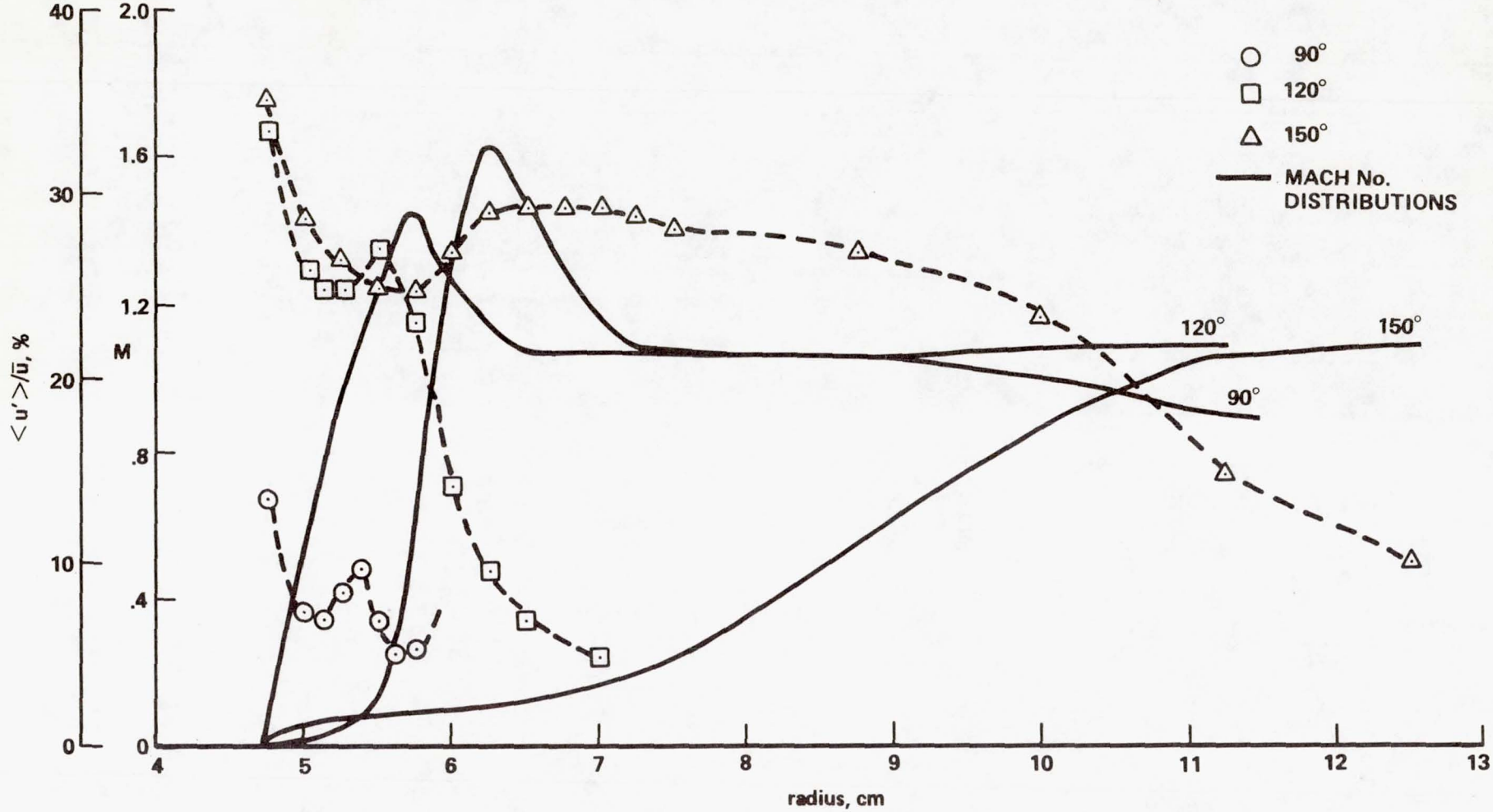

Figure 7. Kinematic (Velocity) Fluctuations and Mean Profiles from A-O IV.

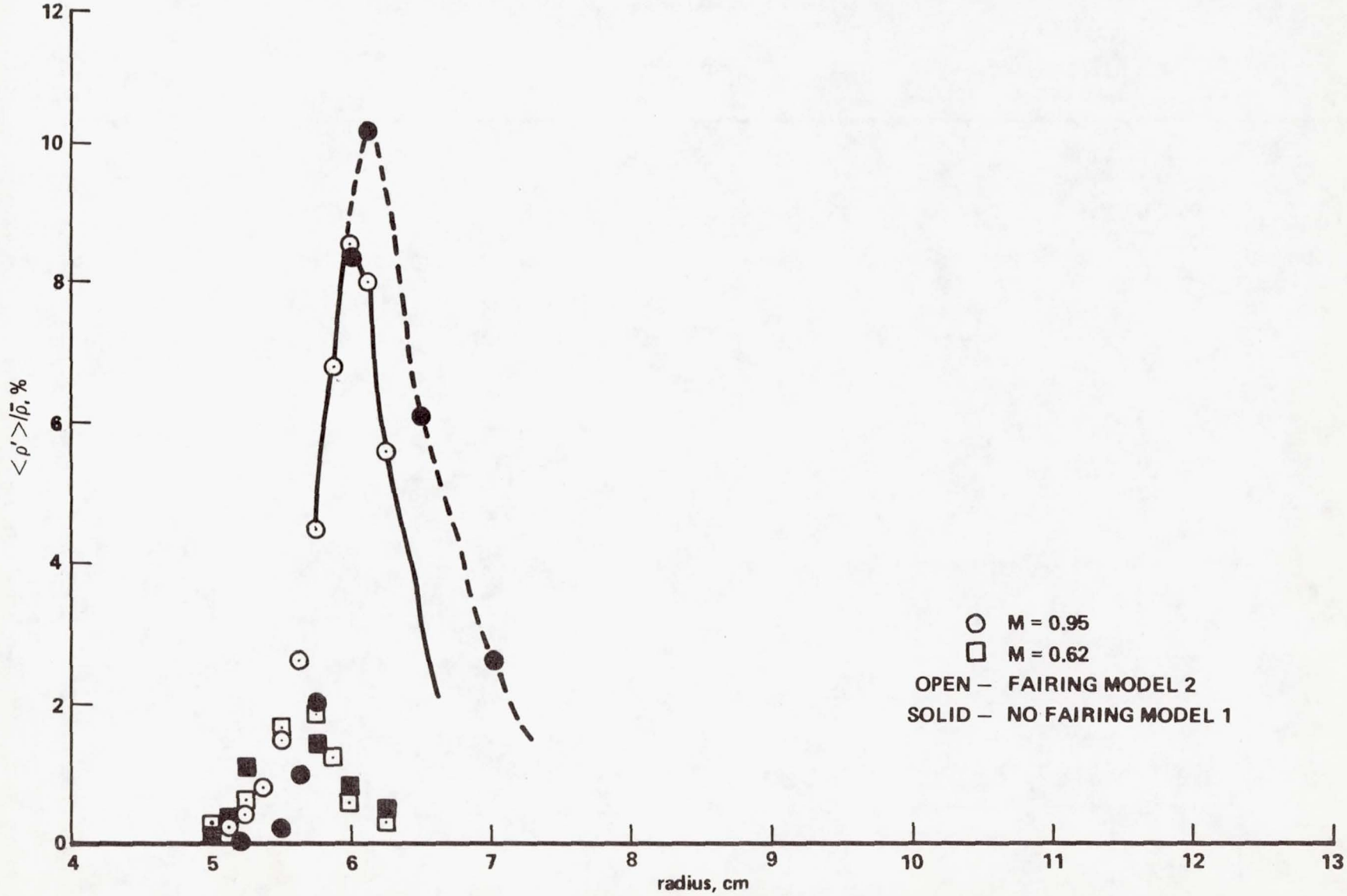

Figure 8. Effect of Fairing on Density Fluctuations at $\theta = 120°$.

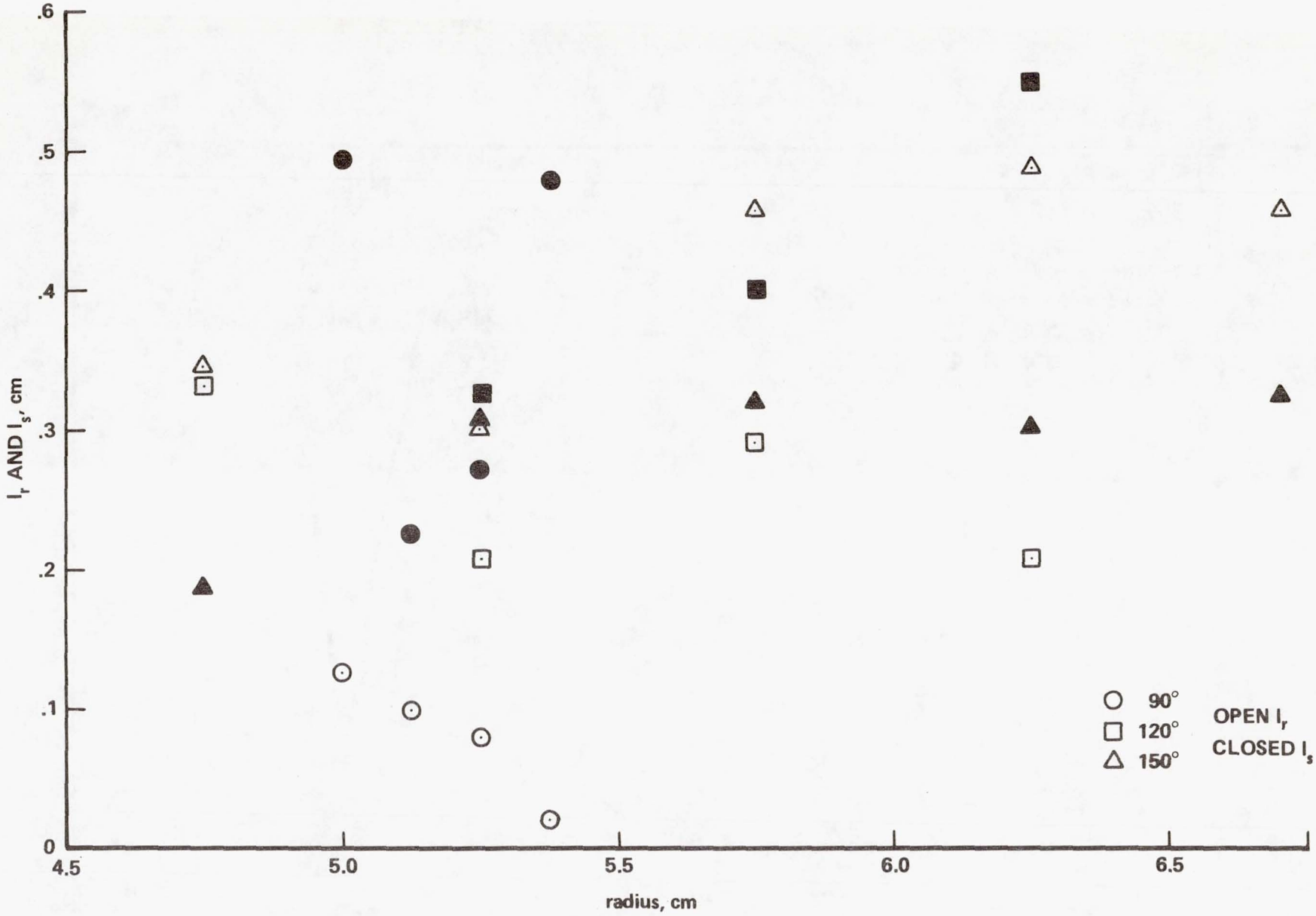

Figure 9. Effect of Azimuth Angle on Correlation Lengths.

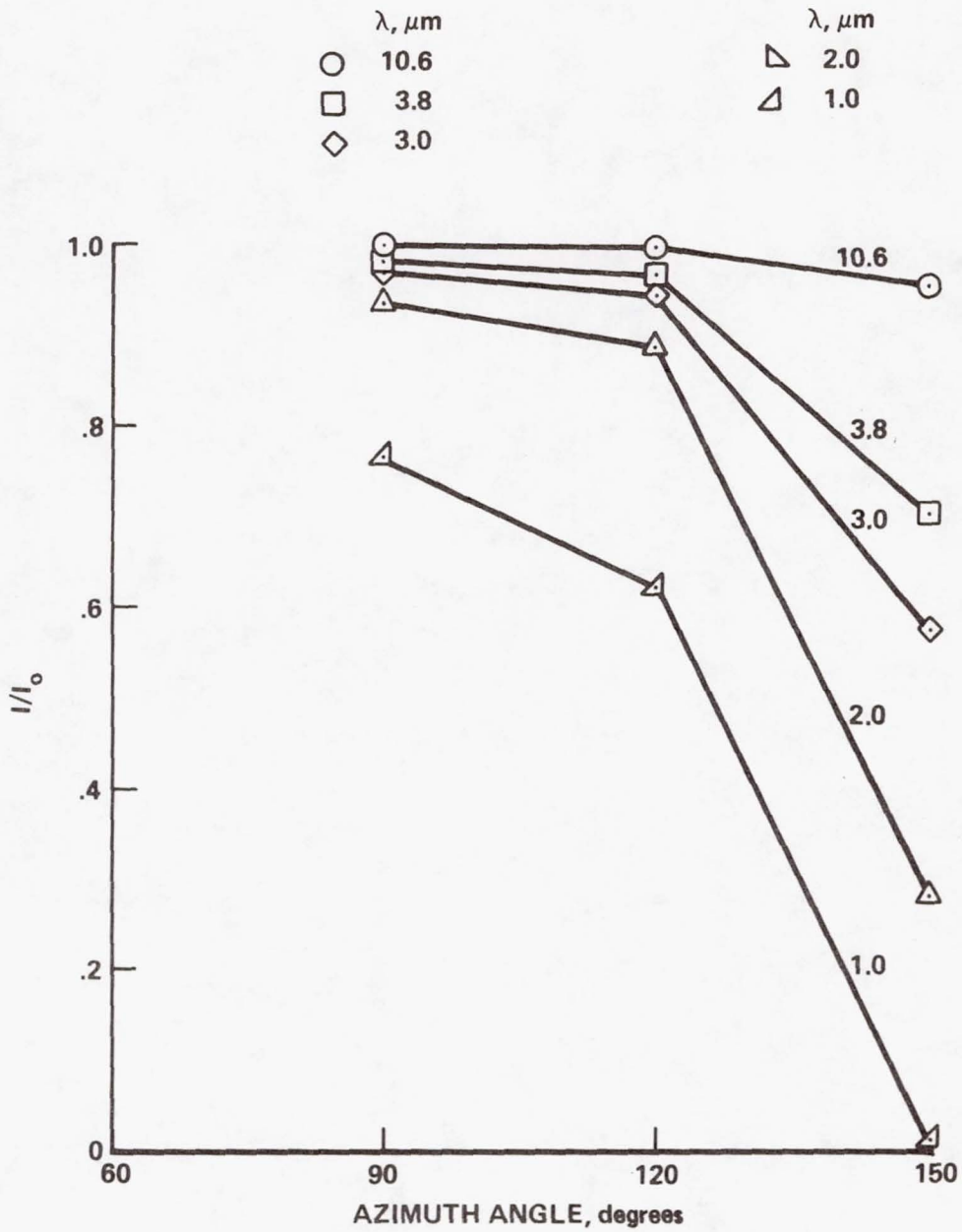

Figure 10. Effect of Wave Length on Optical Performance.

PREDICTION OF OPTICAL PROPAGATION LOSSES THROUGH TURBULENT BOUNDARY/SHEAR LAYERS

A. Verhoff

McDonnell Aircraft Company
McDonnell Douglas Corporation
P.O. Box 516, St. Louis, MO 63166

SUMMARY

A simplified mathematical model has been developed which predicts the optical propagation losses which occur when an optical beam of given wave length passes through a turbulent boundary layer or shear layer. The optical losses are predicted in terms of Line Spread Function (or Strehl Ratio) and Modulation Transfer Function by using experimentally determined values of layer thickness, streamwise, lateral and beamwise density fluctuation length scales, and distribution of the standard deviation of the density fluctuations through the turbulent layer.

The prediction model has been applied to the analysis of a number of selected cases of interest from the AFWL/NASA Series II Aerodynamic-Optical Interaction wind-tunnel investigation conducted in the NASA-Ames 1.83 x 1.83 meter (6 x 6 ft) wind tunnel during July and August 1976. Direct optical measurements were available for these cases and these data have been compared with the results predicted by the aerodynamic analysis.

INTRODUCTION

Airborne optical systems are susceptible to propagation losses when the aircraft is traveling at velocities at which compressibility effects are induced in the surrounding flow field. These losses are the result of changes in index of refraction within the flow field which are directly related to variations in air density due to compressibility. Losses incurred by the optical system may be attributed to two different sources. The first consists of the propagation losses produced when the optical beam passes through the viscous boundary or shear layers which exist very near the aircraft surface. Such viscous layers are typically turbulent with randomly fluctuating air density and require a statistical analysis of the aero-optical interaction effects. The second source of optical loss is the inviscid flow field surrounding the aircraft outside its thin viscous layer within which spatial density variations are steady (or only slowly varying with time). These phenomena are sketched schematically in Figure 1.

The purpose of this investigation was to develop a simple mathematical model which predicts the optical degradation which occurs when an optical beam passes through a turbulent boundary layer or shear layer as shown in Figure 1. This model is expressed in terms of aerodynamic variables associated with the turbulent layer, such as thickness and density correlation functions and length scales.

The prediction model has been applied to the analysis of a number of selected cases of interest from the AFWL/NASA Series II Aerodynamic-Optical Interaction wind-tunnel investigation conducted in the NASA-Ames 1.83 x 1.83 meter (6 X 6 ft) wind tunnel during July and August 1976. Direct optical measurements were available for these cases and these data have been compared with the results predicted by the aerodynamic analysis.

SYMBOL LIST

A - wave amplitude

B - function in Optical Transfer Function relation

D - aperture diameter

F - function proportional to error integral

G - pupil function

K - Gladstone-Dale constant

P - optical power

Q - function in Optical Transfer Function relation

R - density correlation function

S - Line Spread Function

T - averaging time

X - spatial frequency

a - longitudinal (streamwise) correlation length scale

b - lateral correlation length scale

c - normal (beamwise) correlation length scale

d - correlation function parameter $\sqrt{\left(\frac{x}{a}\right)^2 + \left(\frac{y}{b}\right)^2}$

e - exponential function

f - function in Optical Transfer Function relation

g - function in Optical Transfer Function relation

h - function in Optical Transfer Function relation

i - complex number ($\sqrt{-1}$)

k - wave number

r - radial coordinate $\sqrt{x^2 + y^2}$

t - time

u - argument of Optical Transfer Function

x - spatial coordinate (streamwise)

y - spatial coordinate (lateral)

z - spatial coordinate (beamwise)

α - approximation parameter

β - approximation parameter

δ - boundary/shear layer thickness

ζ - spatial coordinate (beamwise)

η - spatial coordinate (lateral)

λ - wave length

ξ - spatial coordinate (streamwise)

ρ - mass density

σ - density fluctuation scale factor

τ - Optical Transfer Function

Δ - wave phase

Σ - aperture area

Δ_m - mean component of wave phase

Δ_r - random component of wave phase

G_m - mean component of pupil function

Φ_{12} - covariance function of wave phase fluctuations

σ_1 - standard deviation of wave phase fluctuations

σ_2 - standard deviation of wave phase fluctuations

ρ_m - mean component of mass density

ρ_r - random component of mass density

ρ_r' - standard deviation of density fluctuations

$\bar{\tau}$ - time-averaged Optical Transfer Function

τ_o - diffraction limited Optical Transfer Function

$\bar{x}$ - normalized spatial frequency

$\bar{y}$ - normalized spatial frequency

$\bar{r}$ - normalized spatial frequency

S_L - Line Spread Strehl Ratio

$\dot{m}$ - mass injection rate

M_∞ - free stream Mach number

Re - Reynolds number per meter

ANALYSIS

Optical propagation losses through a flow field of varying index of refraction may be quantified by means of the Optical Transfer Function. This function is defined as the normalized two-dimensional Fourier transform of the focal plane image of a point source. The Optical Transfer Function may also be expressed directly as a function of the optical wave in the aperture plane. That is,

$$\tau(\bar{x},\bar{y},t) = \frac{1}{P}\int_{-\infty}^{\infty}\int G^{*}(\xi,\eta,t)\, G(\xi+x,\eta+y,t)\, d\xi\, d\eta$$

where the pupil function G is defined as

$$G(\xi,\eta,t) = \begin{cases} A(\xi,\eta,t)\, e^{ik\Delta(\xi,\eta,t)} & ;\ (\xi,\eta)\subset\Sigma \\ 0 & ;\ (\xi,\eta)\not\subset\Sigma \end{cases}$$

and the optical power is

$$P = \int_{-\infty}^{\infty}\int G^{*}(\xi,\eta,t)\, G(\xi,\eta,t)\, d\xi\, d\eta$$

The wave amplitude and phase are denoted by A and Δ while k is the wave number and Σ is the aperture area. Spatial coordinates in the aperture plane are (x,y) and (ξ,η) and an asterisk (*) denotes complex conjugate. Normalized spatial frequencies in the focal plane are $\bar{x}$ and $\bar{y}$. Since the turbulent flow through which the optical beam passes is random, both the amplitude and phase are dependent on the time t.

According to Tatarski (Reference 1) random amplitude effects can be considered negligible compared to random phase effects for the wave lengths λ and viscous layer thicknesses being considered in this analysis. Therefore, the above relations may be simplified to

$$G(\xi,\eta,t) = \begin{cases} A(\xi,\eta)\, e^{ik\Delta(\xi,\eta,t)} & ;\ (\xi,\eta)\subset\Sigma \\ 0 & ;\ (\xi,\eta)\not\subset\Sigma \end{cases}$$

and

$$P = \int_{-\infty}^{\infty}\int [A(\xi,\eta)]^2\, d\xi\, d\eta$$

As normally done in turbulent flow analyses, the pupil function G and phase Δ may be decomposed into mean and random components. That is,

$$\Delta(\xi,\eta,t) = \Delta_m(\xi,\eta) + \Delta_r(\xi,\eta,t) \tag{1}$$

and

$$G_m(\xi,\eta) = \begin{cases} A(\xi,\eta)\, e^{ik\Delta_m(\xi,\eta)}; & (\xi,\eta) \subset \Sigma \\ 0 \qquad\qquad\qquad\quad ; & (\xi,\eta) \not\subset \Sigma \end{cases} \tag{2}$$

The Optical Transfer Function then becomes

$$\tau(\bar{x},\bar{y},t) = \frac{1}{P}\int_{-\infty}^{\infty}\int G_m^*(\xi,\eta)G_m(\xi+x,\eta+y)e^{ik[\Delta_r(\xi+x,\eta+y,t) - \Delta_r(\xi,\eta,t)]}\, d\xi\, d\eta \tag{3}$$

Assuming a Gaussian joint probability density function for the random quantities $\Delta_r(\xi+x,\eta+y,t)$ and $\Delta_r(\xi,\eta,t)$, the expected value of τ may be written (Reference 2)

$$\langle\tau(\bar{x},\bar{y},t)\rangle = \frac{1}{P}\int_{-\infty}^{\infty}\int G_m^*(\xi,\eta)G_m(\xi+x,\eta+y)\, e^{-k^2[\frac{1}{2}(\sigma_1^2 + \sigma_2^2) - \Phi_{12}]}\, d\xi\, d\eta \tag{4}$$

where

$$\sigma_1^2 \equiv \langle\Delta_r(\xi+x,\eta+y,t)^2\rangle \tag{5}$$

$$\sigma_2^2 \equiv \langle\Delta_r(\xi,\eta,t)^2\rangle \tag{6}$$

and

$$\Phi_{12} \equiv \langle\Delta_r(\xi+x,\eta+y,t)\Delta_r(\xi,\eta,t)\rangle \tag{7}$$

This assumption is equivalent to approximating the quantity

$$e^{ik[\Delta_r(\xi+x,\eta+y,t) - \Delta_r(\xi,\eta,t)]}$$

in Equation (3) by the first and second moments of $\Delta_r(\xi+x,\eta+y,t)$ and $\Delta_r(\xi,\eta,t)$.

For steady mean flow conditions, the expected values of the above quantities in Equations (5), (6) and (7) may be replaced by time averages. That is,

$$\sigma_1^2 = \frac{1}{T}\int_0^T [\Delta_r(\xi+x,\eta+y,t)]^2 \, dt \tag{8}$$

$$\sigma_2^2 = \frac{1}{T}\int_0^T [\Delta_r(\xi,\eta,t)]^2 \, dt \tag{9}$$

and

$$\Phi_{12} = \frac{1}{T}\int_0^T \Delta_r(\xi,\eta,t)\,\Delta_r(\xi+x,\eta+y,t) \, dt \tag{10}$$

The instantaneous wave phase may be expressed in terms of the instantaneous density according to

$$\Delta(x,y,t) = K\int_0^\delta \rho(x,y,z,t) \, dz$$

where K is the Gladstone-Dale constant and δ denotes the turbulent boundary/shear layer thickness. In terms of mean and random density components

$$\Delta_m(x,y) = K\int_0^\delta \rho_m(x,y,z) \, dz \tag{11}$$

and

$$\Delta_r(x,y,t) = K\int_0^\delta \rho_r(x,y,z,t) \, dz \tag{12}$$

Using Equation (12) in Equation (10),

$$\Phi_{12} = \frac{K^2}{T}\int_0^T\int_0^\delta \rho_r(\xi,\eta,\zeta,t) \, d\zeta \int_0^\delta \rho_r(\xi+x,\eta+y,\zeta',t) \, d\zeta' \, dt$$

Since ζ and ζ' are independent

$$\Phi_{12} = \frac{K^2}{T}\int_0^T\int_0^\delta\int_0^\delta \rho_r(\xi,\eta,\zeta,t)\,\rho_r(\xi+x,\eta+y,\zeta',t) \, d\zeta' \, d\zeta \, dt$$

With the substitution $z = \zeta' - \zeta$, this expression becomes (after interchanging the time and spatial order of integration)

$$\Phi_{12} = \frac{K^2}{T}\int_0^{\delta}\int_{-\zeta}^{\delta-\zeta}\int_0^{T} \rho_r(\xi,\eta,\zeta,t)\ \rho_r(\xi+x,\eta+y,\zeta+z,t)\ dt\ dz\ d\zeta \qquad (13)$$

In a like manner, Equations (8) and (9) may be written

$$\sigma_1^2 = \frac{K^2}{T}\int_0^{\delta}\int_{-\zeta}^{\delta-\zeta}\int_0^{T} \rho_r(\xi+x,\eta+y,\zeta,t)\rho_r(\xi+x,\eta+y,\zeta+z,t)\ dt\ dz\ d\zeta \qquad (14)$$

$$\sigma_2^2 = \frac{K^2}{T}\int_0^{\delta}\int_{-\zeta}^{\delta-\zeta}\int_0^{T} \rho_r(\xi,\eta,\zeta,t)\ \rho_r(\xi,\eta,\zeta+z,t)\ dt\ dz\ d\zeta \qquad (15)$$

The time integrations in each of these expressions may be related to the density correlation function R and standard deviation of the random density fluctuations ρ_r'. That is,

$$\frac{1}{T}\int_0^{T} \rho_r(\xi,\eta,\zeta,t)\ \rho_r(\xi+x,\eta+y,\zeta+z,t)dt = [\rho_r'(\xi,\eta,\zeta)]^2 R(\xi,\eta,\zeta;x,y,z) \qquad (16)$$

$$\frac{1}{T}\int_0^{T} \rho_r(\xi+x,\eta+y,\zeta,t)\ \rho_r(\xi+x,\eta+y,\zeta+z,t)\ dt =$$

$$[\rho_r'(\xi+x,\eta+y,\zeta+z)]^2 R(\xi+x,\eta+y,\zeta+z;0,0,-z) \qquad (17)$$

$$\frac{1}{T}\int_0^{T} \rho_r(\xi,\eta,\zeta,t)\ \rho_r(\xi,\eta,\zeta+z,t)\ dt = [\rho_r'(\xi,\eta,\zeta)]^2 R(\xi,\eta,\zeta;0,0,z) \qquad (18)$$

Making use of the above results, the expected value or time-averaged value of the Optical Transfer Function (denoted now by $\bar{\tau}$) expressed in Equation (4) becomes

$$\overline{\tau(\bar{x},\bar{y})} = \frac{1}{P}\int\int_{-\infty}^{\infty} G_m^*(\xi,\eta)\, G_m(\xi+x,\eta+y)\, \exp\left\{-K^2k^2\delta^2 \int_0^1 \int_{-\zeta}^{1-\zeta} \right.$$

$$\left[\frac{1}{2}\rho_r'(\xi,\eta,\zeta)^2 R(\xi,\eta,\zeta;0,0,z) + \frac{1}{2}\rho_r'(\xi+x,\eta+y,\zeta+z)^2\right.$$

$$\left.\left. R(\xi+x,\eta+y,\zeta+z;0,0,-z) - \rho_r'(\xi,\eta,\zeta)^2 R(\xi,\eta,\zeta;x,y,z)\right] dz\, d\zeta\right\} d\xi\, d\eta \qquad (19)$$

In this relationship, spatial coordinates have been normalized by the boundary/shear layer thickness δ.

For the experimental conditions described in the next section, the following assumptions can be made:

- Flow is two-dimensional (no η dependence of mean flow properties or turbulence intensity and correlation functions)
- Variations of mean flow properties and turbulence quantities in the longitudinal flow direction (ξ) are negligible compared to those in the normal beamwise direction (ζ)
- Wave amplitude A is uniform in the aperture plane
- Density correlation functions may be approximated by

$$e^{-\sqrt{\left(\frac{x}{a}\right)^2 + \left(\frac{y}{b}\right)^2 + \left(\frac{z}{c}\right)^2}}$$

  where a, b and c denote correlation length scales in terms of boundary/shear layer thickness
- For given flow conditions, length scales a, b and c are constant

The exponential approximation for the density correlation function was chosen because it more nearly approximates the shape of experimentally measured results than, for instance, a Gaussian shape (Reference 3) while still providing a high degree of mathematical simplicity.

With the above approximations Equation (19) may be simplified to

$$\overline{\tau(\bar{x},\bar{y})} = \tau_o(\bar{r})\, \exp\left\{-\frac{1}{2}K^2k^2\delta^2 \int_0^1 \int_{-\zeta}^{1-\zeta} [\rho_r'(\zeta)^2 + \rho_r'(\zeta+z)^2]\, e^{-\left|\frac{z}{c}\right|} dz\, d\zeta \right.$$

$$\left. + K^2k^2\delta^2 \int_0^1 \rho_r'(\zeta)^2 \int_{-\zeta}^{1-\zeta} e^{-\sqrt{\left(\frac{x}{a}\right)^2+\left(\frac{y}{b}\right)^2+\left(\frac{z}{c}\right)^2}}\, dz\, d\zeta\right\} \qquad (20)$$

where τ_o is the diffraction limited Optical Transfer Function. For a circular aperture of diameter D

$$\tau_o(\bar{r}) = \begin{cases} \dfrac{2}{\pi}\left[\cos^{-1}\left(\dfrac{r\delta}{D}\right) - \left(\dfrac{r\delta}{D}\right)\sqrt{1-\left(\dfrac{r\delta}{D}\right)^2}\,\right] & ;\ 0 \leq r \leq D/\delta \\ 0 & ;\ r > D/\delta \end{cases}$$

where r is the radial location $\sqrt{x^2 + y^2}$ (normalized by δ) and $\bar{r}$ is the normalized spatial frequency.

In order to further simplify this analysis, the integrand $e^{-\sqrt{d^2 + \left(\frac{z}{c}\right)^2}}$ in Equation (20) where

$$d = \sqrt{\left(\frac{x}{a}\right)^2 + \left(\frac{y}{b}\right)^2}$$

will be approximated by $e^{-d}\, e^{-\alpha^2\left(\frac{z}{c}\right)^2 - \beta\left(\frac{z}{c}\right)}$. Both functions have the same value at $z = 0$ while the parameters α and β may be determined such that the approximation coincides with the integrand in value and slope at the value of z for half amplitude. That is,

$$\alpha^2 = [d^2 + \ln 2\ (\ln 2 + 2d)]^{-1/2} - [\ln 2 + 2d]^{-1}$$

and

$$\beta = \ln 2\ [\ln 2\ (\ln 2 + 2d)]^{-1/2} - \alpha^2\ [\ln 2\ (\ln 2 + 2d)]^{1/2}$$

The accuracy of this approximation is shown in Figure 2 for several values of d. With this simplification, the inner integrations in Equation (20) may be carried out with the result

$$\begin{aligned} \overline{\tau(\bar{x},\bar{y})} = \tau_o(\bar{r}) \exp\Bigg\{ & -K^2k^2\delta^2 c \int_0^1 \rho_r'(\zeta)^2\left(2 - e^{\frac{-\zeta}{c}} - e^{\frac{\zeta-1}{c}}\right) d\zeta \;+ \\ & K^2k^2\delta^2\frac{c}{\alpha}\, e^{\frac{1}{4}\left(\frac{\beta}{\alpha}\right)^2 - d} \int_0^1 \rho_r'(\zeta)^2\left[F\left(\frac{\alpha\zeta}{c} + \frac{1}{2}\frac{\beta}{\alpha}\right) + \right. \\ & \left. F\left(\frac{\alpha}{c} - \frac{\alpha\zeta}{c} + \frac{1}{2}\frac{\beta}{\alpha}\right) - 2F\left(\frac{1}{2}\frac{\beta}{\alpha}\right)\right] d\zeta \Bigg\} \end{aligned} \tag{21}$$

where F is proportional to the error function integral (Reference 4) and is defined as

$$F(z) = \int_0^z e^{-t^2}\, dt$$

A final simplification will be made with the assumption

$$\rho_r'(\zeta) = 4\sigma\zeta(1-\zeta) \tag{22}$$

where σ is a scale factor dependent on the flow conditions. This approximation does not destroy any fundamental variable dependency and any numerical error introduced after the integrations in Equation (21) are carried out should be within the experimental errors associated with the various fluid dynamic parameters. Specifically, the integrals in Equation (21) become

$$\int_0^1 \rho_r'(\zeta)^2 \left(2 - e^{-\zeta/c} - e^{\frac{\zeta-1}{c}}\right) d\zeta = 16\sigma^2 \left[\frac{1}{15} - 4c^3(12c^2 - 6c + 1) + 4c^3(12c^2 + 6c + 1)\, e^{-1/c}\right]$$

and

$$\int_0^1 \rho_r'(\zeta)^2 \left[F\left(\frac{\alpha\zeta}{c} + \frac{1}{2}\frac{\beta}{\alpha}\right) + F\left(\frac{\alpha}{c} - \frac{\alpha\zeta}{c} + \frac{1}{2}\frac{\beta}{\alpha}\right) - 2F\left(\frac{1}{2}\frac{\beta}{\alpha}\right)\right] d\zeta =$$

$$\sigma^2 \left\{ f \left(\frac{c}{\alpha}\right)^2 e^{-\left(\frac{\alpha}{c} + \frac{1}{2}\frac{\beta}{\alpha}\right)^2} - g\left(\frac{c}{\alpha}\right)^4 e^{-\frac{1}{4}\left(\frac{\beta}{\alpha}\right)^2} + \left[\frac{16}{15} + h\left(\frac{c}{\alpha}\right)^5\right]\left[F\left(\frac{\alpha}{c} + \frac{1}{2}\frac{\beta}{\alpha}\right) - F\left(\frac{1}{2}\frac{\beta}{\alpha}\right)\right]\right\}$$

where

$$f = \frac{8}{15} - \frac{4}{15}\left(1 + \frac{\beta}{c}\right)\left(\frac{c}{\alpha}\right)^2 + 4\left[\frac{8}{5} + \frac{11}{10}\left(\frac{\beta}{c}\right)^2 + \frac{1}{30}\left(\frac{\beta}{c}\right)^2\right]\left(\frac{c}{\alpha}\right)^4 + 2\left(\frac{\beta}{c}\right)^2\left(\frac{9}{5} + \frac{3}{10}\frac{\beta}{c}\right)\left(\frac{c}{\alpha}\right)^6 + \frac{1}{5}\left(\frac{\beta}{c}\right)^4\left(\frac{c}{\alpha}\right)^8$$

$$g = \frac{16}{3} + 8\left[\frac{4}{5} + \frac{5}{4}\frac{\beta}{c} + \frac{1}{6}\left(\frac{\beta}{c}\right)^2\right]\left(\frac{c}{\alpha}\right)^2 + 2\left(\frac{\beta}{c}\right)^2\left(\frac{9}{5} + \frac{1}{2}\frac{\beta}{c}\right)\left(\frac{c}{\alpha}\right)^4 + \frac{1}{5}\left(\frac{\beta}{c}\right)^4\left(\frac{c}{\alpha}\right)^6$$

and

$$h = 12 + 8\frac{\beta}{c} + 12\frac{\beta}{c}\left[1 + \frac{\beta}{c} + \frac{1}{9}\left(\frac{\beta}{c}\right)^2\right]\left(\frac{c}{\alpha}\right)^2 + 4\left(\frac{\beta}{c}\right)^3\left(1 + \frac{1}{4}\frac{\beta}{c}\right)\left(\frac{c}{\alpha}\right)^4 + \frac{1}{5}\left(\frac{\beta}{c}\right)^5\left(\frac{c}{\alpha}\right)^6$$

Defining

$$B = \frac{16}{15}c - 64c^4\left[12c^2 - 6c + 1 + \left(12c^2 + 6c + 1\right)e^{-1/c}\right]$$

and

$$Q = g\left(\frac{c}{\alpha}\right)^5 - f\left(\frac{c}{\alpha}\right)^3 e^{-\left(\frac{\alpha}{c}\right)^2 - \frac{\beta}{c}} - \frac{c}{\alpha}\left[\frac{16}{15} + h\left(\frac{c}{\alpha}\right)^5\right]\left[F\left(\frac{\alpha}{c} + \frac{1}{2}\frac{\beta}{\alpha}\right) - F\left(\frac{1}{2}\frac{\beta}{\alpha}\right)\right]e^{\frac{1}{4}\left(\frac{\beta}{\alpha}\right)^2}$$

then Equation (21) for the time-averaged Optical Transfer Function becomes

$$\overline{\tau(\bar{x},\bar{y})} = \tau_o(\bar{r})\ \exp\left\{-K^2k^2\delta^2\sigma^2\left[B + Q\,e^{-d}\right]\right\} \qquad (23)$$

where

$$d = \sqrt{\left(\frac{x}{a}\right)^2 + \left(\frac{y}{b}\right)^2}$$

Because $\bar{\tau}$ in Equation (23) is real and non-negative due to the assumptions underlying its derivation, $\bar{\tau}$ is identical to the Modulation Transfer Function. Another quantity useful in describing optical system performance is the Line Spread Function S, which is the one-dimensional Fourier Transform of the Optical Transfer Function. Considering only the case y = 0, $\bar{\tau}$ becomes an even function of x and, after normalization,

$$S(X) = \frac{3\pi}{4} \int_0^1 \cos(2\pi Xu)\ \bar{\tau}(u)\ du \tag{24}$$

where X represents spatial frequency and

$$\bar{\tau}(u) = \frac{2}{\pi} \left[\cos^{-1}u - u\sqrt{1-u^2}\right] \exp\left\{-K^2k^2\delta^2\sigma^2 \left[B + Q\,e^{-\frac{D}{\delta a}u}\right]\right\} \tag{25}$$

where

$$u = \frac{x\delta}{D} \tag{26}$$

The peak value of S (i.e., X = 0) is defined as the Line Spread Strehl Ratio S_L and depends only on the optical beam wave length and diameter and the fluid dynamic properties of the turbulent flow.

APPLICATION OF MATHEMATICAL PREDICTION MODEL TO EXPERIMENTAL TEST RESULTS

The effect of random density fluctuations on the propagation of an optical beam through a turbulent boundary or shear layer is described in general by Equation (19) in terms of density correlation functions and standard deviations. The test conditions existing during the AFWL Series II Aero-Optical wind-tunnel investigation in the NASA Ames 1.83 x 1.83 meter (6 x 6 ft) tunnel allow a number of simplifying assumptions resulting in the aerodynamic-optical interaction relationship given by Equation (25). A complete description of the aerodynamic test conditions, basic instrumentation and mean flow properties within the turbulent boundary/shear layer is given in Reference 5.

Both aerodynamic and optical data were obtained from the flat plate-cavity model shown schematically in Figure 3. The cavity was cubical in shape and measured 15.2 cm per side. The turbulent boundary layer which developed on the plate could be artificially thickened by either a set of pins (called V-K pins) or porous fences. Both devices were removable allowing for a clean plate configuration. The cavity was equipped with a bottom window and could also be covered by a flush window if desired.

Hot wire sensors were mounted on a movable probe which could be traversed in the normal (z) direction and on a stationary probe which could be fixed at several different normal locations. This arrangement allowed the measurement by NASA experimenters of fluctuation intensities and correlation functions within the turbulent layer. The hot wire sensors could also be inserted through the cavity walls for measurement within the cavity itself. Velocity fluctuation intensities and correlation functions were also measured independently in the turbulent layer and within the cavity by means of a Laser-Doppler Velocimeter shown in Figure 3. Optical measurements were obtained by AFWL experimenters by passing a He-Ne laser beam ($\lambda = .6328 \times 10^{-6}$ meters) through the cavity window(s) and reflecting it back through the cavity from the return mirror mounted in the free stream tunnel flow. The optical measurement equipment is not shown in Figure 3.

A summary of the many possible geometrical configurations which could be achieved by the wind-tunnel model is presented in Table 1. Nearly all of the configurations were tested at nominal free stream Mach numbers of 0.6, 0.7, 0.8 and 0.9 and nominal free stream Reynolds numbers of 6.6×10^6 and 9.8×10^6 per meter. Because the optical measurements could not be made simultaneously with the aerodynamic measurements because of instrumentation space limitations, each configuration was tested twice.

Five different configurations at nominal free stream Mach numbers of 0.6 and 0.9 and nominal free stream Reynolds number of 9.8×10^6 per meter were selected as being of particular interest. These configurations are denoted in the matrix in Table 1 by the AFWL designated configuration number. The mathematical prediction model was used to analyze these configurations. Aerodynamic data for these configurations were supplied by NASA (Reference 6) and are summarized in subsequent figures while the optical data were supplied by AFWL (Reference 7). A discussion of the mathematically predicted results using the aerodynamic data and the comparison of these results with direct optical measurements is presented below. The predicted results assume a perfectly correlated double pass from the return mirror through the turbulent layer.

Configuration #1

This configuration consisted of the flat plate with cavity covered and the V-K pins upstream to artificially thicken the turbulent boundary layer as sketched in Figure 4. The turbulent boundary-layer thickness showed little change with Mach number since for the most part the thickness is artificially induced by the V-K pins. The density fluctuation intensity level, however, does show an increase with Mach number.

Predicted Line Spread Strehl Ratios computed from Equation (24) using the aerodynamic data are shown in Figure 5. Optical measurements at several beam diameters are also shown for comparison and the agreement is reasonably good. Modulation Transfer Functions for several beam diameters were also predicted from the aerodynamic data using Equation (25). These results are shown in Figures 6, 7, and 8 along with direct optical measurements of the Modulation Transfer Function. The aerodynamic predictions show the expected decrease in optical beam quality with increasing Mach number and beam diameter while the optical measurements show the opposite trend with Mach number at the larger beam diameters. Line Spread Functions were computed from the optically measured Modulation Transfer Functions for this configuration using Equation (24) and compared with those predicted from the aerodynamic data. These results are shown in Figures 9, 10, and 11.

Configuration #8

This configuration consisted of the clean plate with the cavity open as sketched in Figure 12. A normal turbulent boundary layer developed along the plate which separated as a turbulent shear layer over the open cavity. The shear layer showed a significant increase in thickness and fluctuation intensity with Mach number as expected.

Line Spread Strehl Ratios predicted from the aerodynamic data are shown in Figure 13; direct optical measurements of Strehl Ratio for this configuration were not available. According to these results, the open cavity shear layer was better optically at the lower Mach number and worse at the higher Mach number than the thickened turbulent boundary-layer results shown in Figure 5. Modulation Transfer Functions for two beam diameters were predicted from the aerodynamic data and are compared with direct optical measurements in Figures 14 and 15. Both the aerodynamic predictions and optical measurements show the expected decrease in optical beam quality with increase in Mach number and beam diameter although they do not agree closely with each other.

Configuration #11

This configuration consisted of the plate with cavity open and a fence (4.6 cm height, 38% porosity) mounted upstream of the cavity as sketched in Figure 16. The cavity-fence arrangement produced a thinner turbulent shear layer over the open cavity than the clean plate with open cavity arrangement of Configuration #8. However, larger fluctuation intensities were induced by the fence. Both the shear layer thickness and fluctuation intensity increased substantially with Mach number.

Line Spread Strehl Ratios predicted from the aerodynamic data are shown in Figure 17; direct optical measurements for comparison were not available. Comparison of these results with those of Figure 13 show that the fence produced a higher level of optical degradation than the clean plate configuration. Modulation Transfer Functions for two beam diameters were predicted from the aerodynamic measurements and are compared with optical measurements in Figures 18 and 19. Although their agreement is not good, both the aerodynamically predicted results and optical measurements show the proper trend with beam diameter and Mach number.

Configuration #13

This configuration also consisted of the plate with cavity open and a fence (2.3 cm height, 58% porosity) mounted upstream of the cavity as sketched in Figure 20. This fence produced a thicker shear layer over the open cavity than the fence of Configuration #11 with about the same level of fluctuation intensity. Both the shear layer thickness and fluctuation intensity increased significantly with Mach number.

Line Spread Strehl Ratios predicted from the aerodynamic data are shown in Figure 21. Optical measurements of Strehl Ratio for several beam diameters are also shown for comparison. Agreement between the two is poor with the optical measurements showing improved performance with increasing beam diameter in contrast to the aerodynamic predictions. Based upon the aerodynamic prediction, the shorter fence of this configuration produced less optical degradation at low Mach numbers and more at high Mach numbers than the taller fence of Configuration #11. Modulation Transfer Functions for several beam diameters as predicted from the aerodynamic data are presented in Figures 22, 23 and 24 along with direct optical measurements for comparison. Both data sets show decreasing optical quality with increase in beam diameter and Mach number although only a weak Mach number dependence is evident from the optical measurements.

Configuration #14

This configuration consisted of the clean plate with cavity open and a porous cavity front wall for mass injection into the cavity as sketched in Figures 25 and 29. For the case of zero mass injection (Figure 25), the porous front wall acted as an acoustic damper and decreased the turbulent shear layer thickness over the cavity by a slight amount but caused an increase in fluctuation intensity as can be seen by referring to Figure 12. A nominal mass injection rate of .25 kg/sec (Figure 29) had little or no effect on the shear layer thickness or fluctuation intensity, although in either case both quantities increased significantly with Mach number.

Line Spread Strehl Ratios for the case of zero mass injection predicted from the aerodynamic measurements are shown in Figure 26 along with optically measured values for several beam diameters. Agreement is again poor with the optical measurements showing little change in degradation level with beam diameter. Based upon the aerodynamic predictions, the porous cavity front

wall caused some increase in optical degradation as can be seen from Figure 13 which corresponds to the case with solid cavity front wall. Results with mass injection shown in Figure 30 show some increase in beam quality over the zero mass injection case of Figure 26 with degradation levels approximately the same as the solid front wall case of Figure 13.

Modulation Transfer Functions for two beam diameters were predicted from the aerodynamic measurements and are compared with direct optical measurements in Figures 27 and 28 for the case of zero mass injection and Figures 31 and 32 for the mass injection case. Although their agreement is not close, both sets of measurements exhibit increasing optical degradation with increase in beam diameter and Mach number.

CONCLUSIONS

Qualitatively, the predictions based on the aerodynamic data consistently show for all of the cases analyzed the correct trend of increasing optical degradation with increase in Mach number (i.e., compressibility effect) and increase in beam diameter. However, for some of the cases the optical measurements show the opposite trends. Analysis of static pressure data has shown (Reference 5) that the return mirror mount located within the tunnel flow induced substantial longitudinal and beamwise pressure (and density) gradients in the tunnel flow between the return mirror and flat plate model. Such gradients undoubtedly have a detrimental effect on optical propagation through this region thereby adversely affecting the optical measurements. Other factors such as mechanical vibration of the optical instrumentation or flow induced vibration of the return mirror also affect the optical measurements and contribute to the differences between the measured and predicted results.

Quantitatively, the aerodynamic predictions and the optical measurements of Strehl Ratio show reasonably good agreement for the flat plate with thickened turbulent boundary layer (Configuration #1). However, the agreement is poor for the other two cases for which Strehl Ratio data were available, namely the open cavity with short boundary-layer fence (Configuration #13) and the open cavity with porous front wall and zero mass injection (Configuration #14). The Modulation Transfer Function comparisons show reasonably good agreement for only a few of the cases and primarily at the smallest beam diameters tested. In general, the optically measured Modulation Transfer Functions show considerably higher levels of optical degradation than those predicted from the aerodynamic measurements. Based upon the aerodynamic predictions, the most optically favorable configuration of those analyzed appears to be the clean plate with cavity open and mass injection (Configuration #14).

Because of the desirability of using a predictive method such as developed herein to assess the aerodynamic propagation losses through turbulent layers, it is recommended that further tests be conducted in which the experimental problems discussed above are eliminated. A more accurate evaluation of the mathematical prediction model can then be made.

REFERENCES

1. Tatarski, V. I., Wave Propagation in a Turbulent Medium, Dover, 1967.
2. Wolters, D. J., "Aerodynamic Effects on Airborne Optical Systems", McDonnell Aircraft Corp., MDC Report No. A2582, Dec. 1973.
3. Laufer, J., Private Communication.
4. Abramowitz, M. and Stegun, I. A., Handbook of Mathematical Functions, Dover, 1965.
5. Buell, D., "Aerodynamic Properties of a Flat Plate With Cavity for Optical-Propagation Studies", NASA TM-78487, June 1979.
6. Rose, W. C., Private Communication, 1977.
7. Bailey, W. H., Private Communication, 1977.

TABLE 1. SUMMARY OF GEOMETRICAL CONFIGURATIONS TESTED

	Clean plate	Turbulent boundary-layer thickener (V-K pins)	Boundary-layer fence A	Boundary-layer fence B	Boundary-layer fence C	Boundary-layer fence D	Boundary-layer fence E	Boundary-layer fence F	Boundary-layer fence G	Boundary-layer trip	Boundary-layer trip with V-K pins
Flat plate, cavity covered		1									
Flat plate, cavity open	8						13	11			
Flat plate, cavity open, porous cavity forward wall with mass injection	14										
Flat plate, cavity open, slotted cavity forward wall with mass injection											

FENCE DESCRIPTION

A - 38% Porosity, MCAIR Design
B - 58% Porosity, AFWL Design
C - 2.3 cm height, slotted
D - 2.3 cm height, 38% Porosity
E - 2.3 cm height, 58% Porosity
F - 4.6 cm height, 38% Porosity
G - 4.6 cm height, 58% Porosity

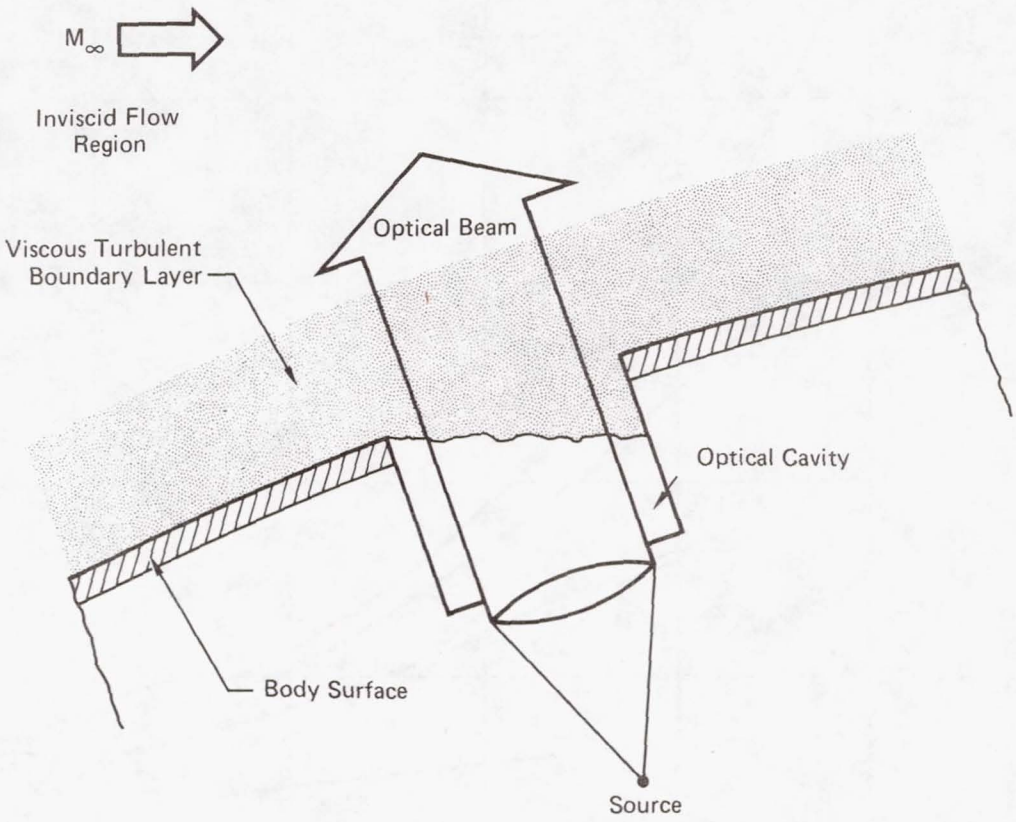

FIGURE 1
OPTICAL BEAM PROPAGATION THROUGH FLOW FIELD SURROUNDING A MOVING BODY.

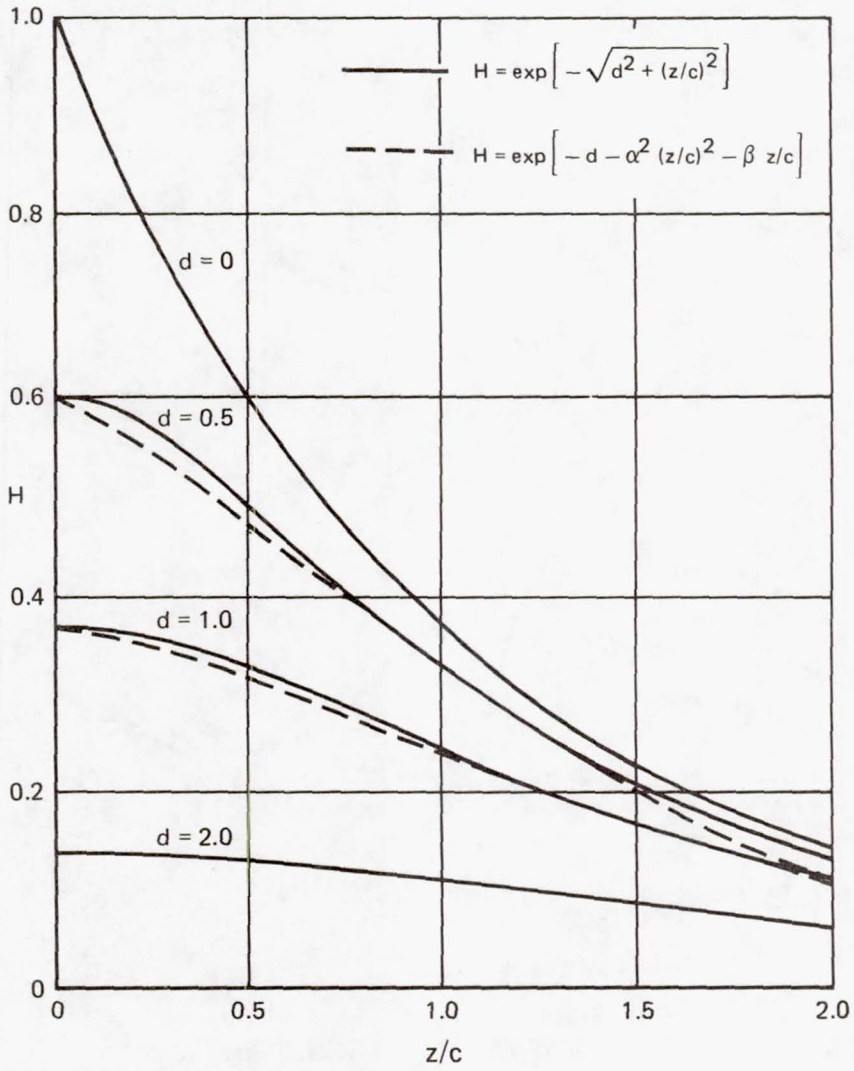

FIGURE 2
CORRELATION FUNCTION APPROXIMATION.

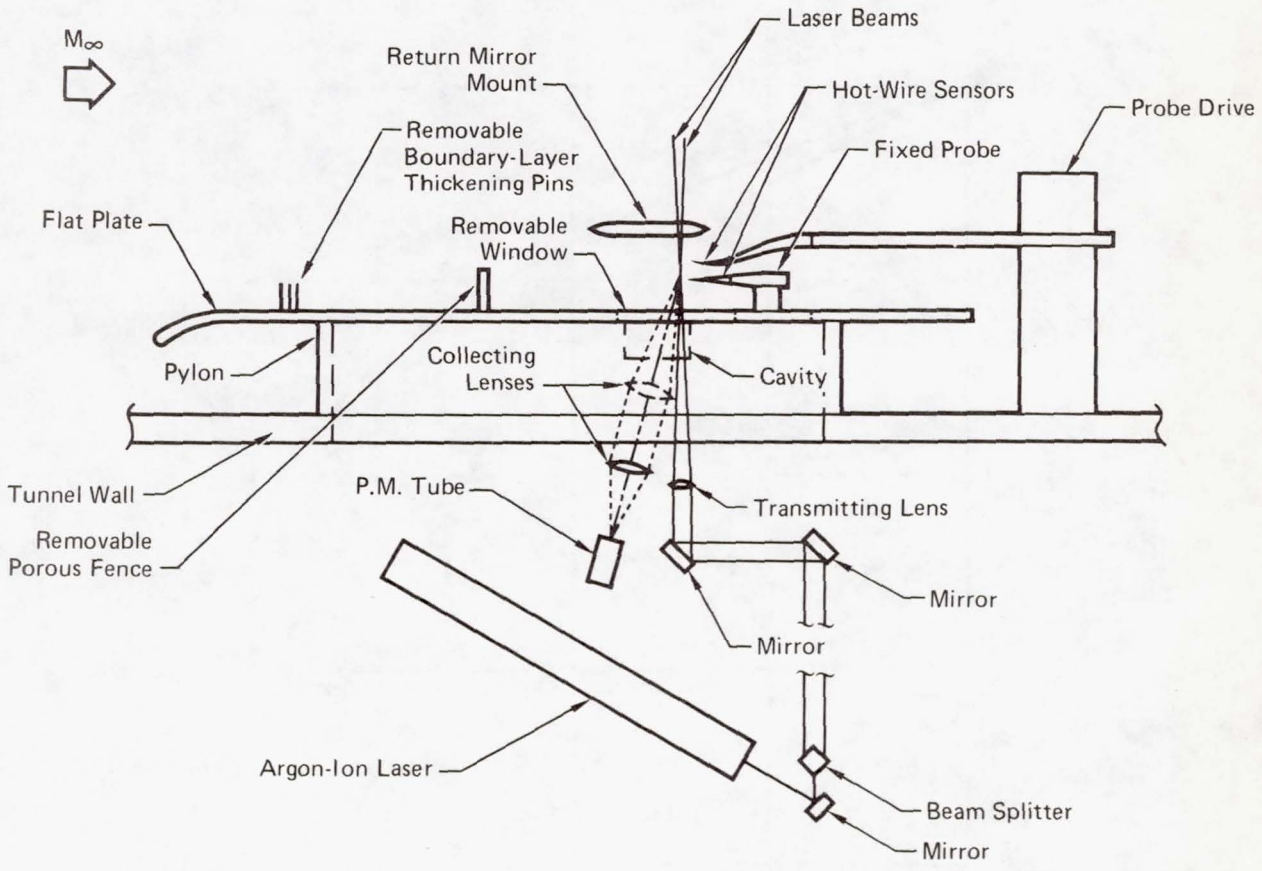

FIGURE 3
SCHEMATIC OF EXPERIMENTAL APPARATUS,
HOT-WIRE AND LDV SYSTEMS.

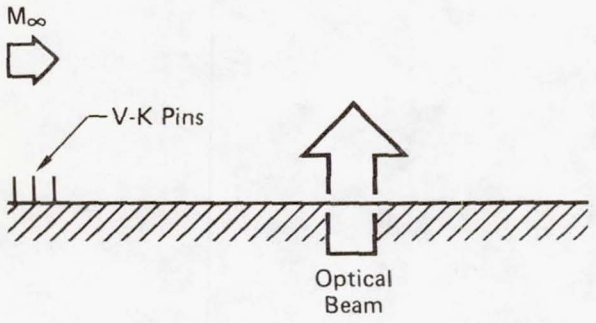

	○	□
M_∞	= 0.6	0.9
Re	= 9.8×10^6	9.8×10^6/meter
δ	= 10.8	11.2 cm
a	= 0.169	0.186
c	= 0.113	0.109
σ	= 0.0053	0.0073 kg/m^3

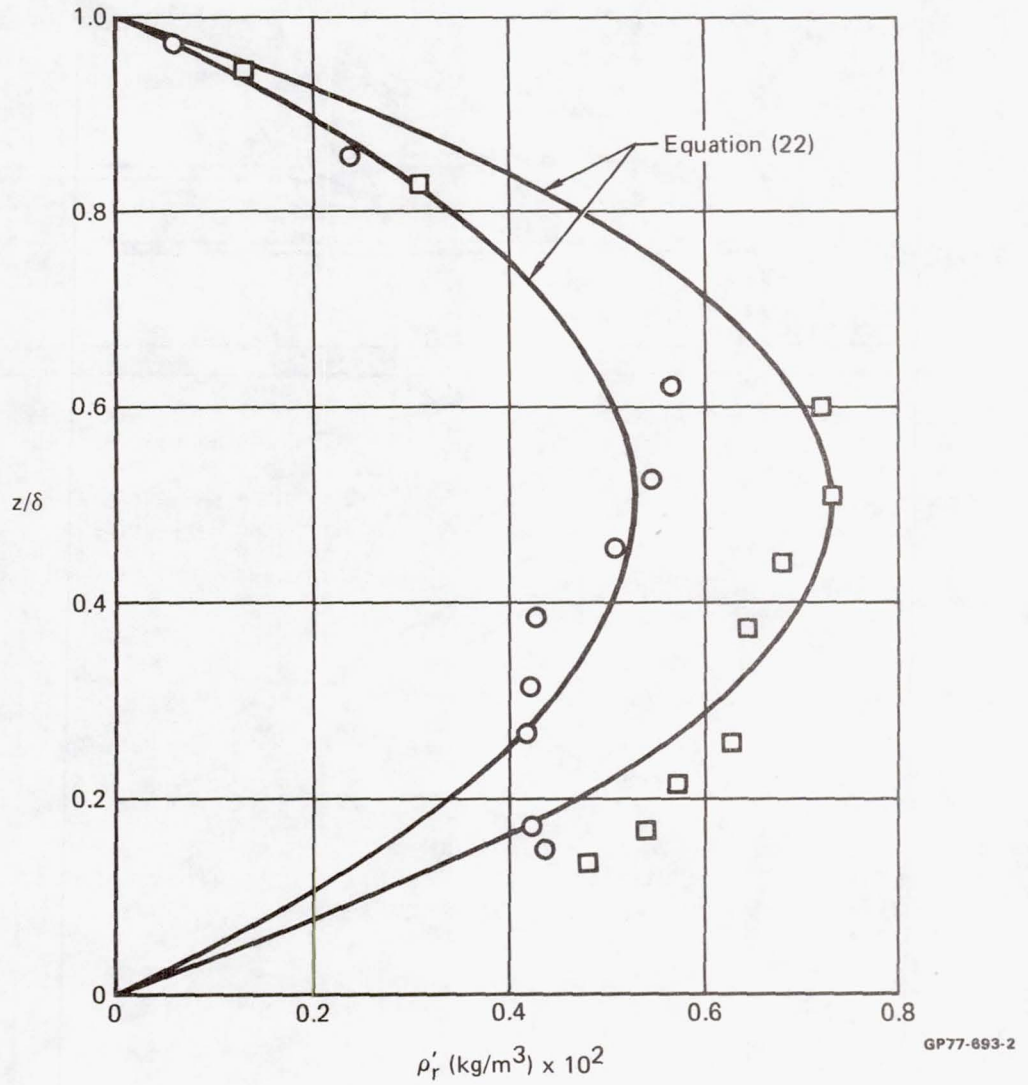

FIGURE 4
SUMMARY OF CONFIGURATION NO. 1 DATA.

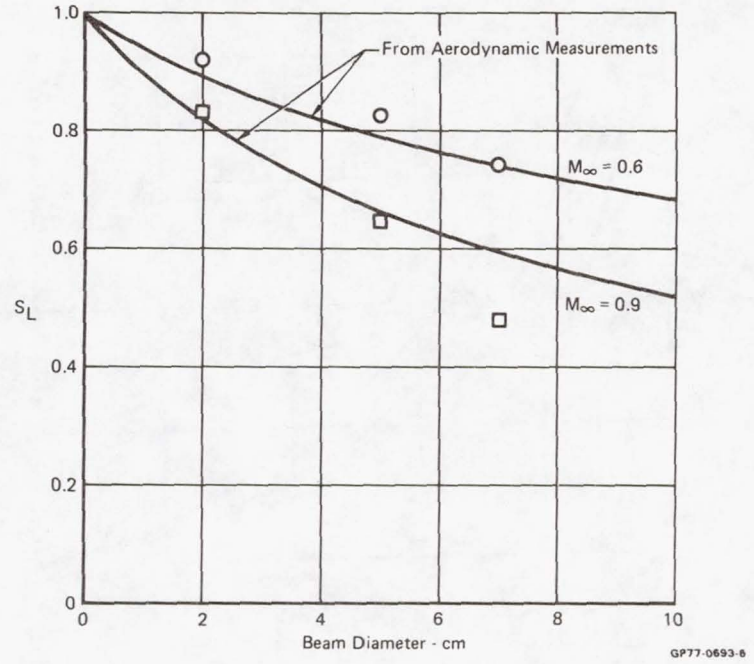

FIGURE 5
LINE SPREAD STREHL RATIO.
Configuration No. 1 - Re = 9.8×10^6/meter

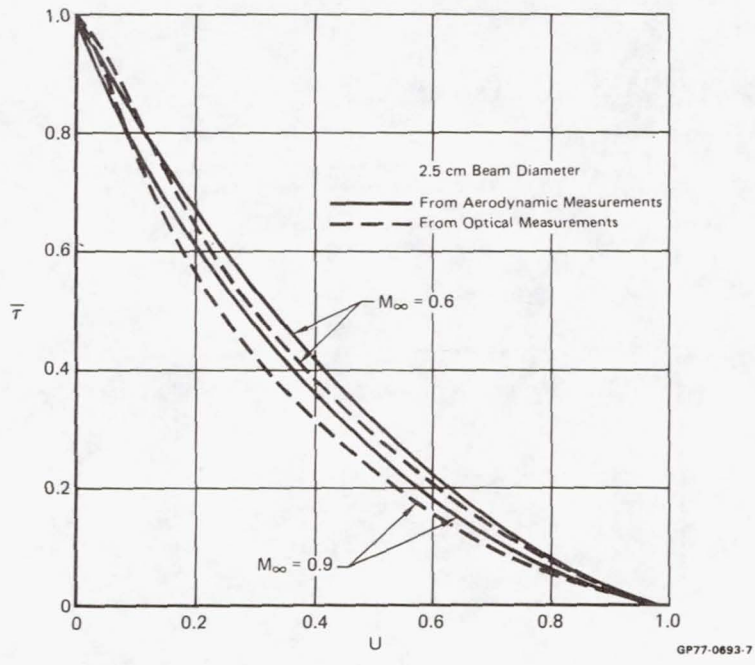

FIGURE 6
MODULATION TRANSFER FUNCTION.
Configuration No. 1 - Re = 9.8×10^6/meter

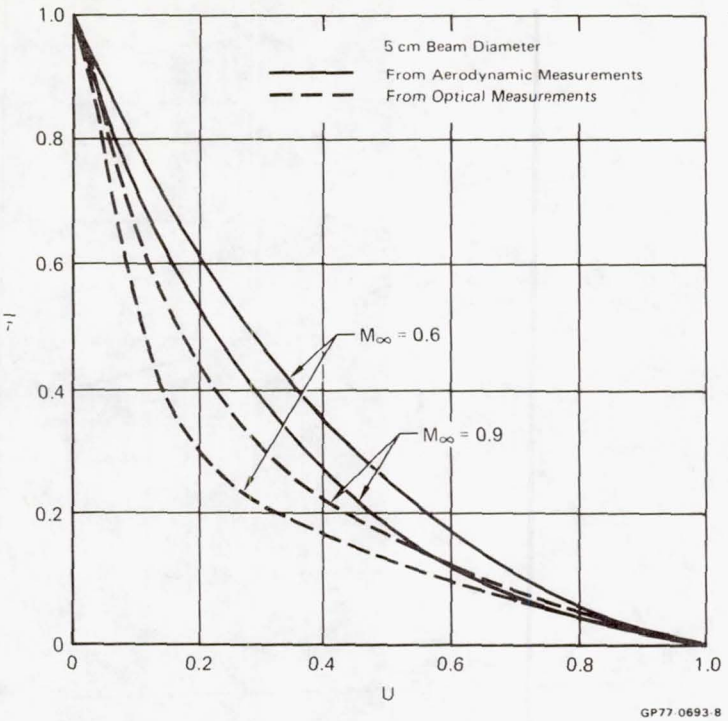

FIGURE 7
MODULATION TRANSFER FUNCTION.
Configuration No. 1 - Re = 9.8 x 10^6/meter

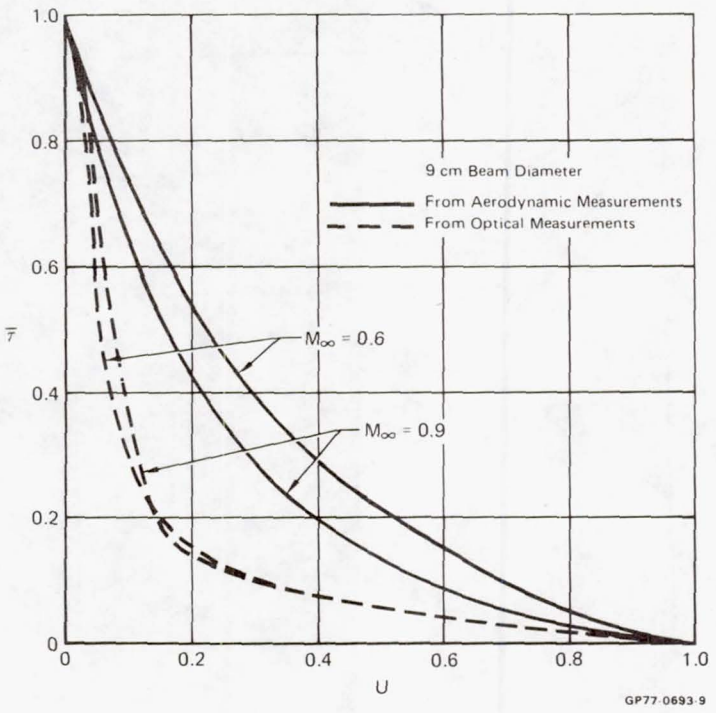

FIGURE 8
MODULATION TRANSFER FUNCTION.
Configuration No. 1 - Re = 9.8 x 10^6/meter

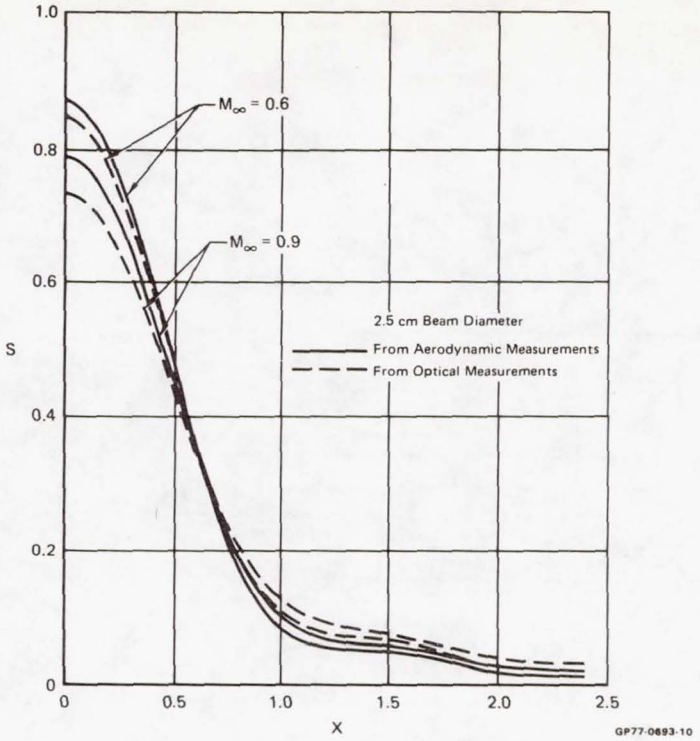

FIGURE 9
LINE SPREAD FUNCTION.
Configuration No. 1 - Re = 9.8 x 10^6/meter

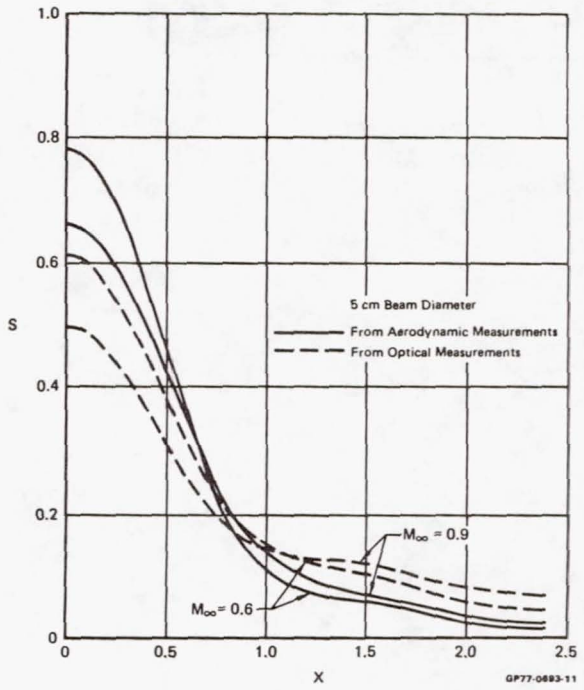

FIGURE 10
LINE SPREAD FUNCTION.
Configuration No. 1 - Re = 9.8 x 10^6/meter

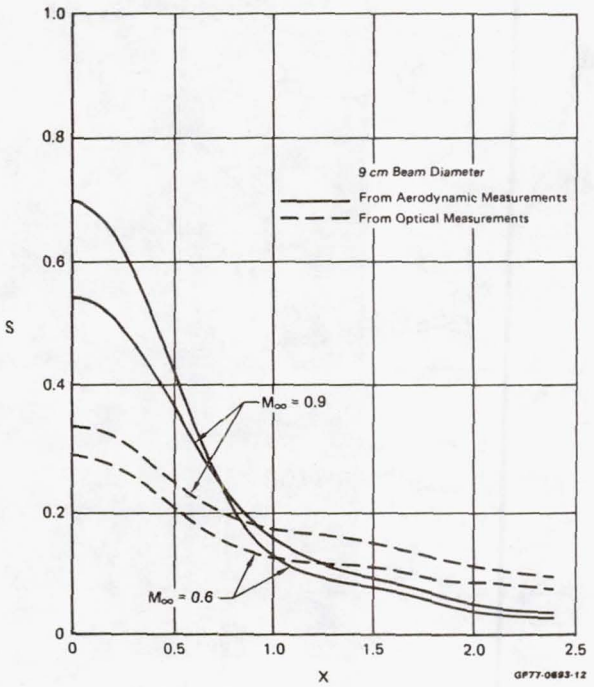

FIGURE 11
LINE SPREAD FUNCTION.
Configuration No. 1 - Re = 9.8 x 10^6/meter

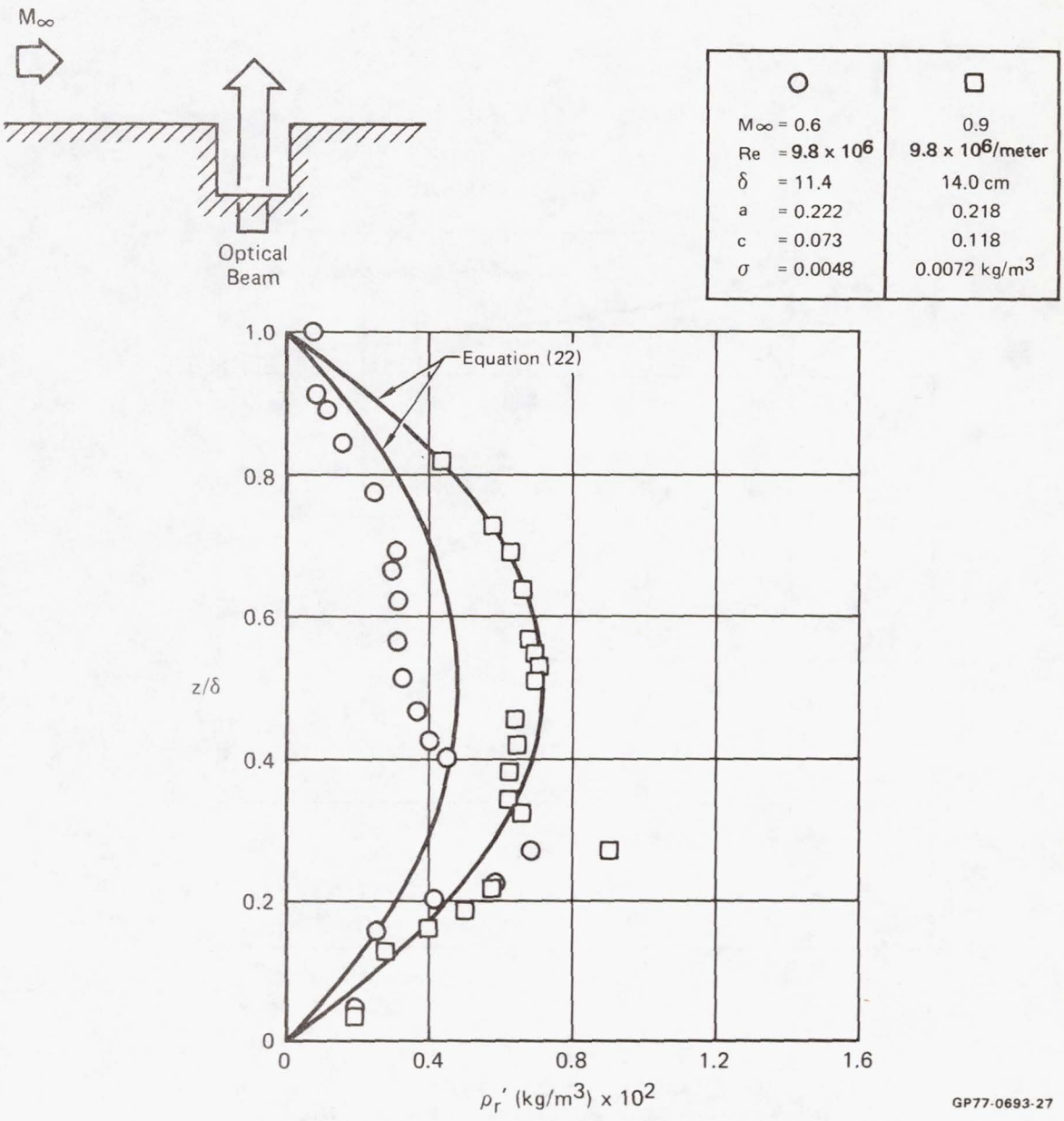

FIGURE 12
SUMMARY OF CONFIGURATION NO. 8 DATA.

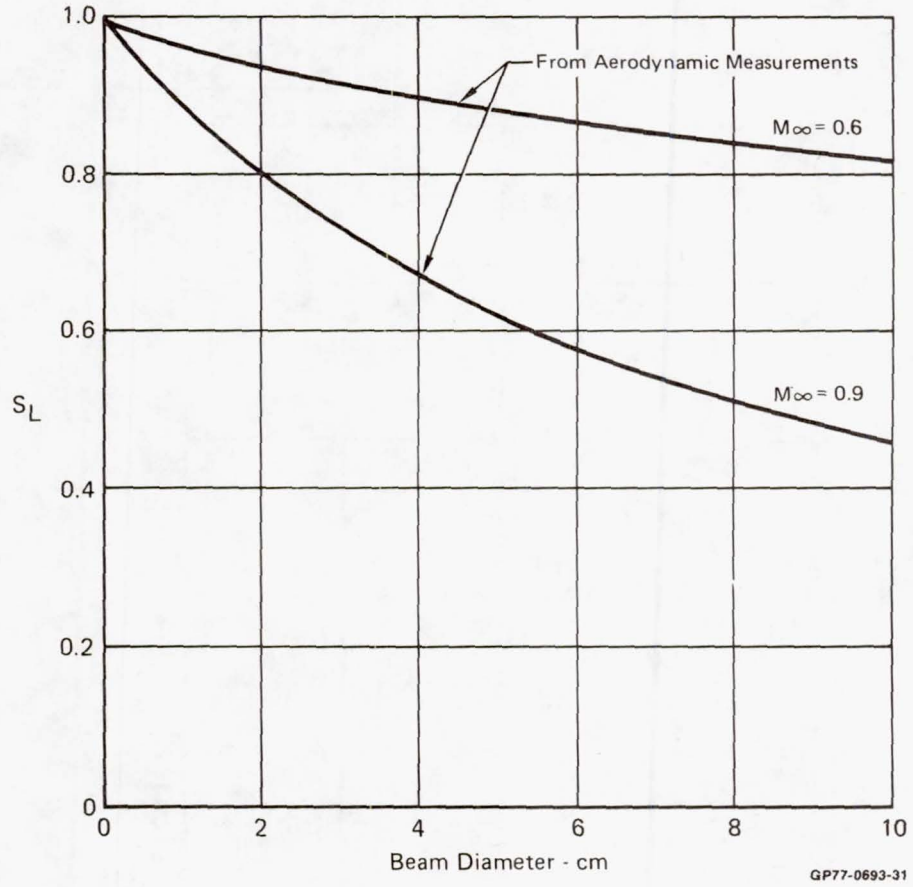

FIGURE 13
LINE SPREAD STREHL RATIO.
Configuration No. 8 - Re = 9.8 x 10^6/meter

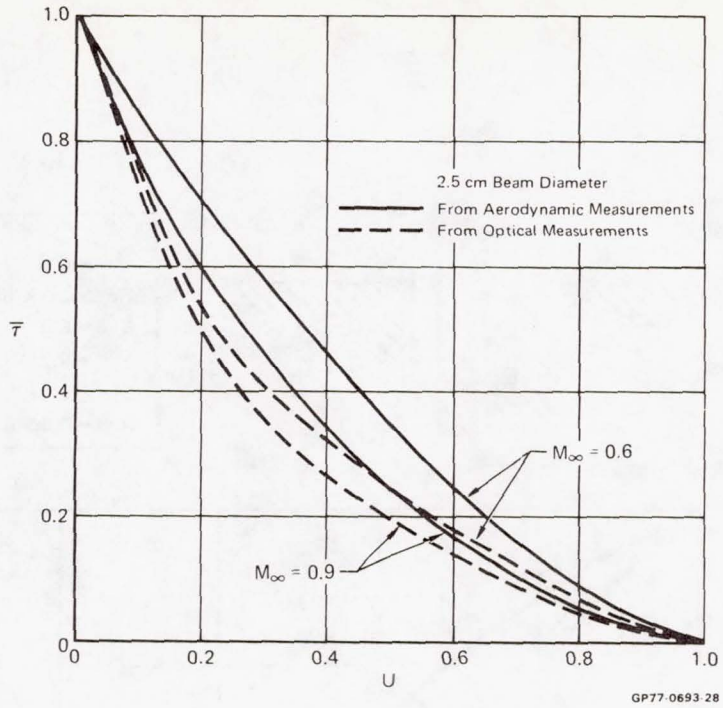

FIGURE 14
MODULATION TRANSFER FUNCTION.
Configuration No. 8 - Re = 9.8 x 10^6/meter

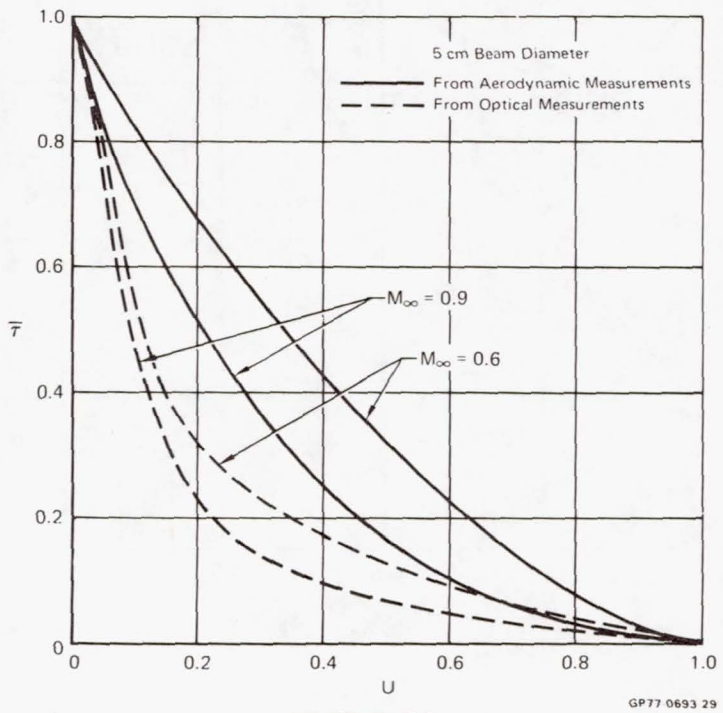

FIGURE 15
MODULATION TRANSFER FUNCTION.
Configuration No. 8 - Re = 9.8 x 10^6/meter

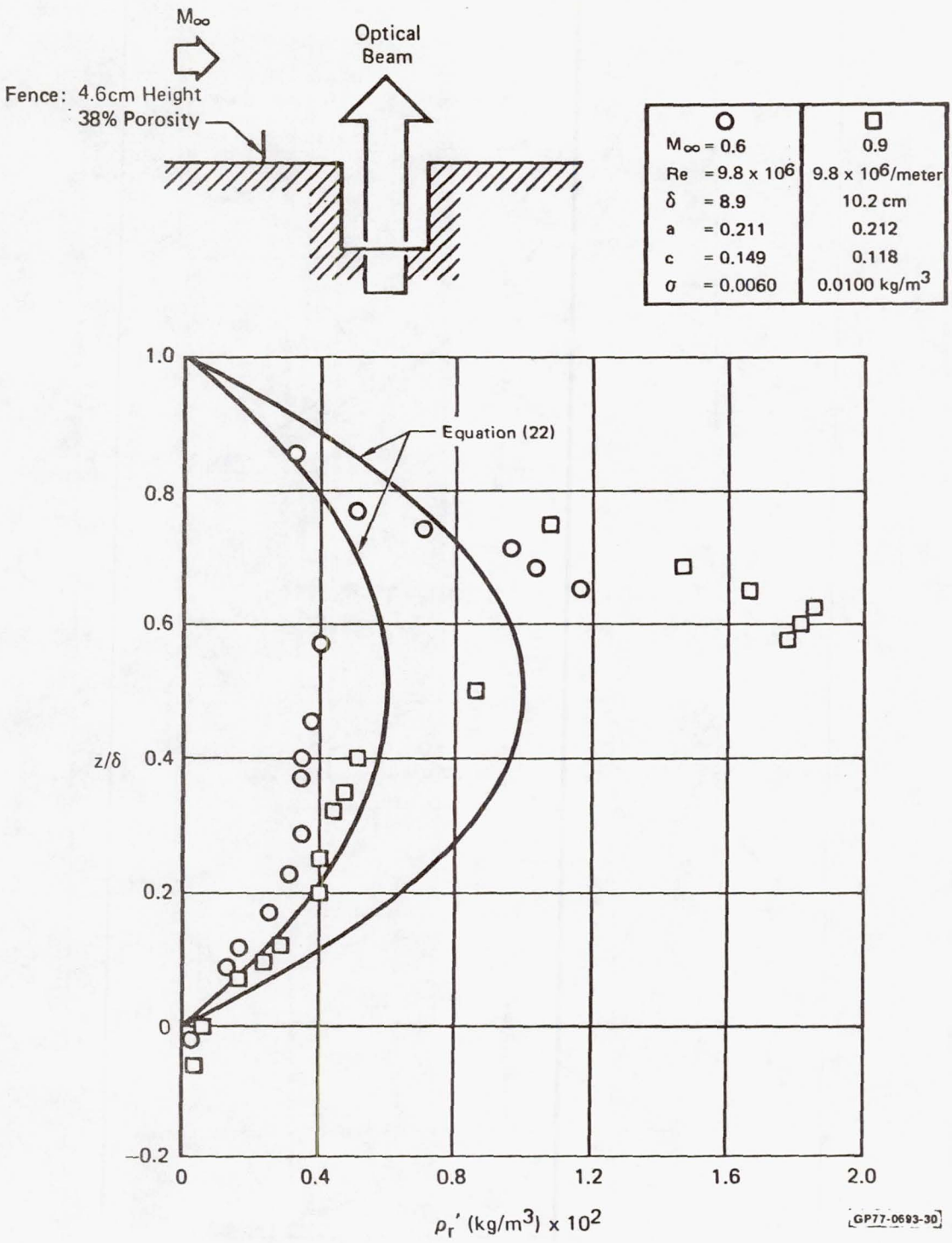

FIGURE 16
SUMMARY OF CONFIGURATION NO. 11 DATA.

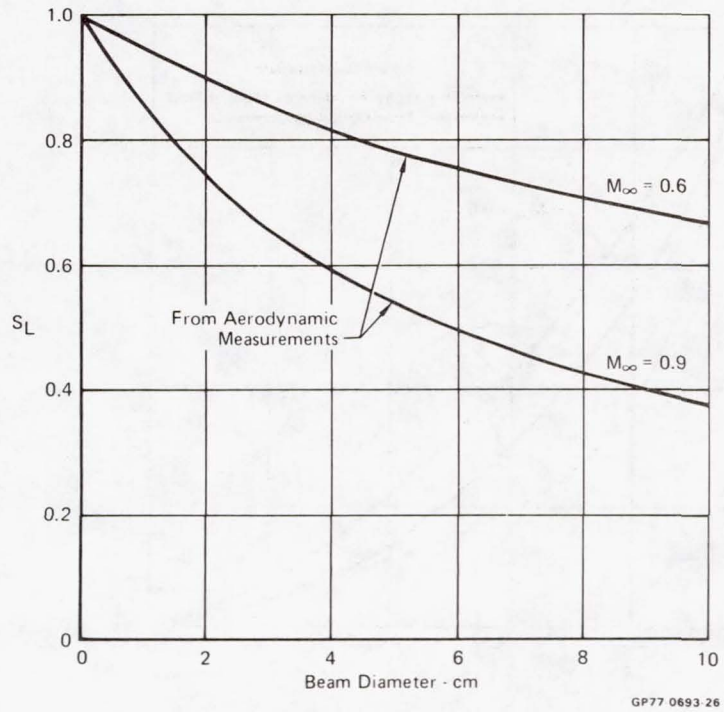

FIGURE 17
LINE SPREAD STREHL RATIO.
Configuration No. 11 - Re = 9.8×10^6/meter

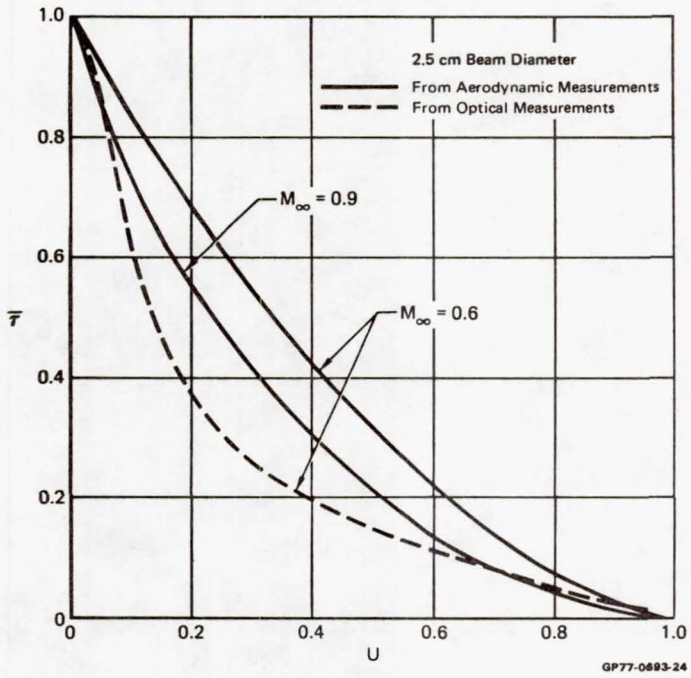

FIGURE 18
MODULATION TRANSFER FUNCTION.
Configuration No. 11 - Re = 9.8 x 10^6/meter

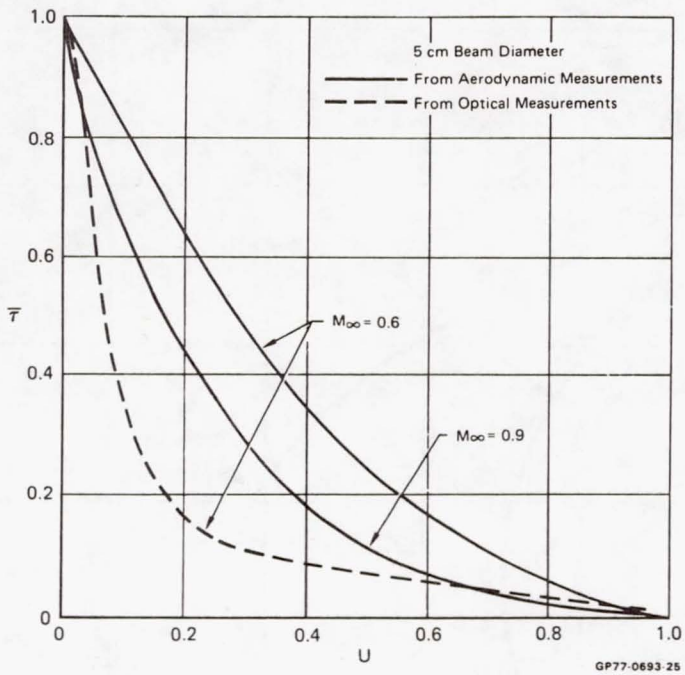

FIGURE 19
MODULATION TRANSFER FUNCTION.
Configuration No. 11 - Re = 9.8 x 10^6/meter

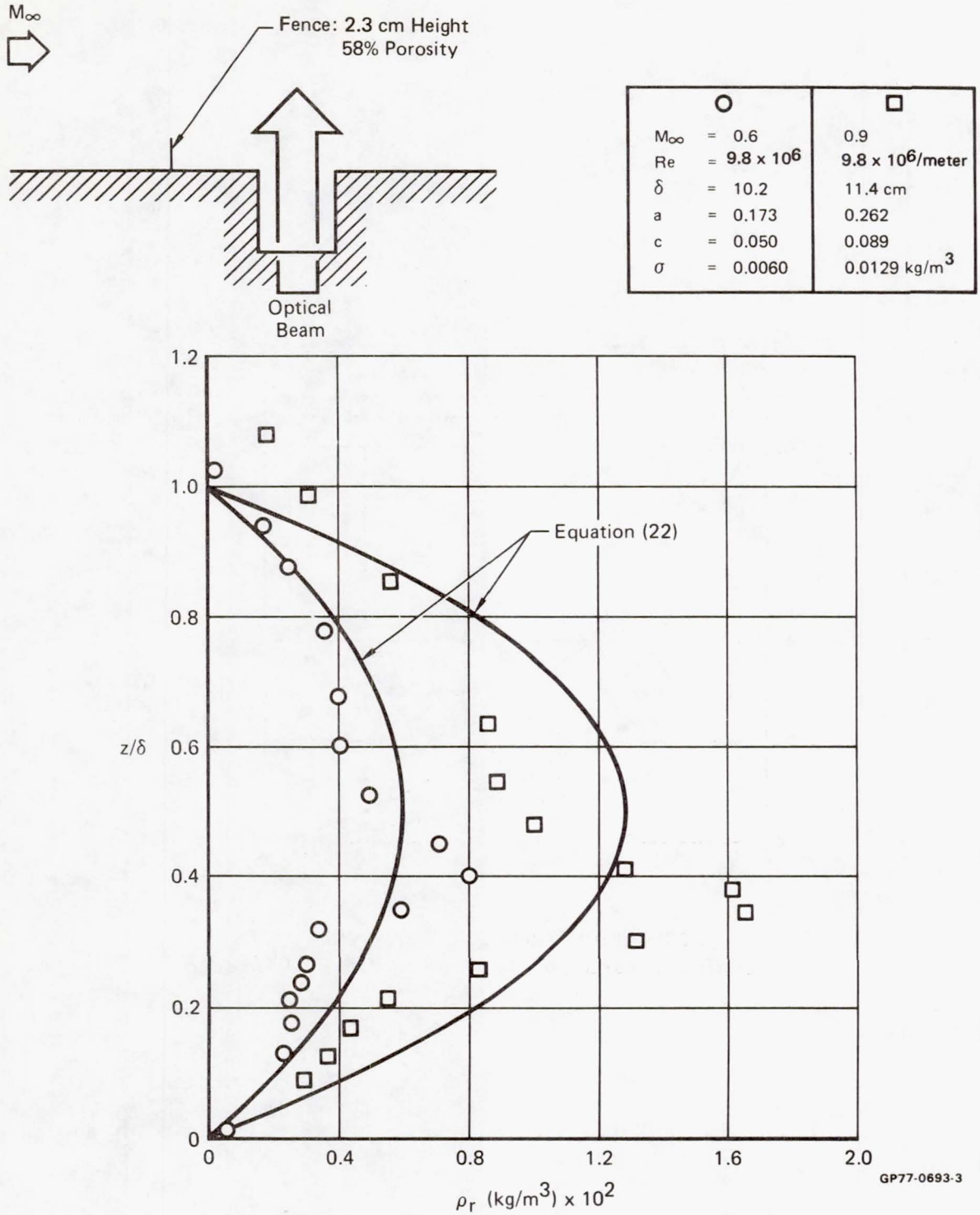

FIGURE 20
SUMMARY OF CONFIGURATION NO. 13 DATA.

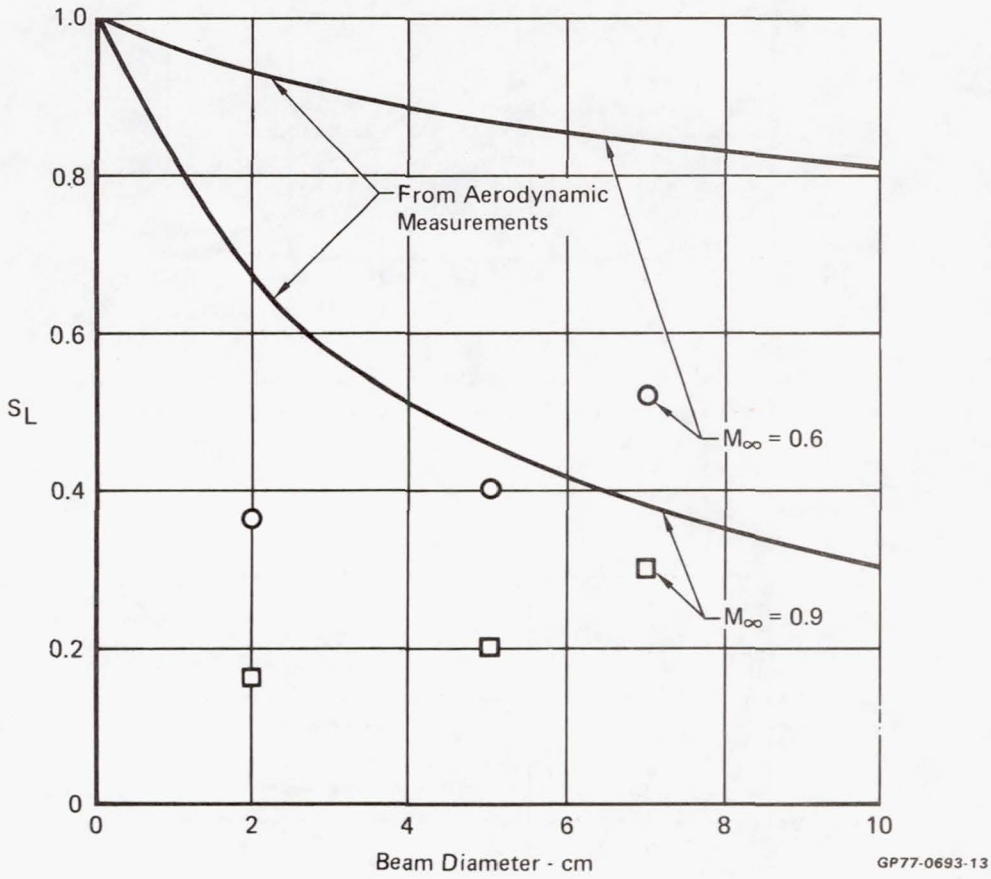

FIGURE 21
LINE SPREAD STREHL RATIO.
Configuration No. 13 - Re = 9.8 x 10^6/meter

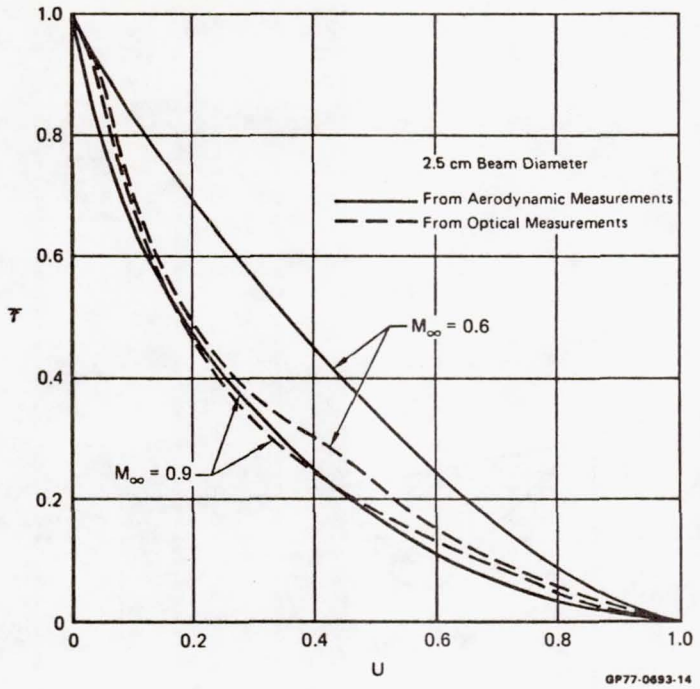

FIGURE 22
MODULATION TRANSFER FUNCTION.
Configuration No. 13 - Re = 9.8 x 10^6/meter

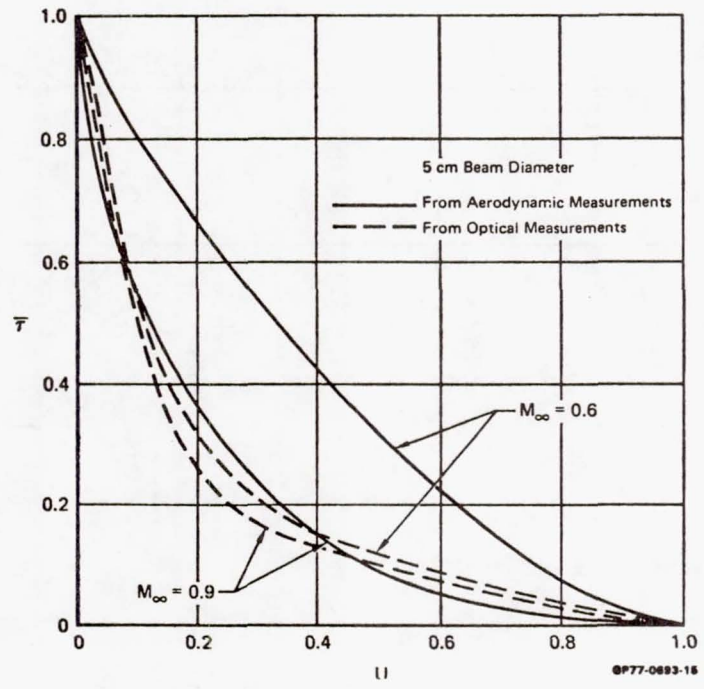

FIGURE 23
MODULATION TRANSFER FUNCTION.
Configuration No. 13 - Re = 9.8 x 10^6/meter

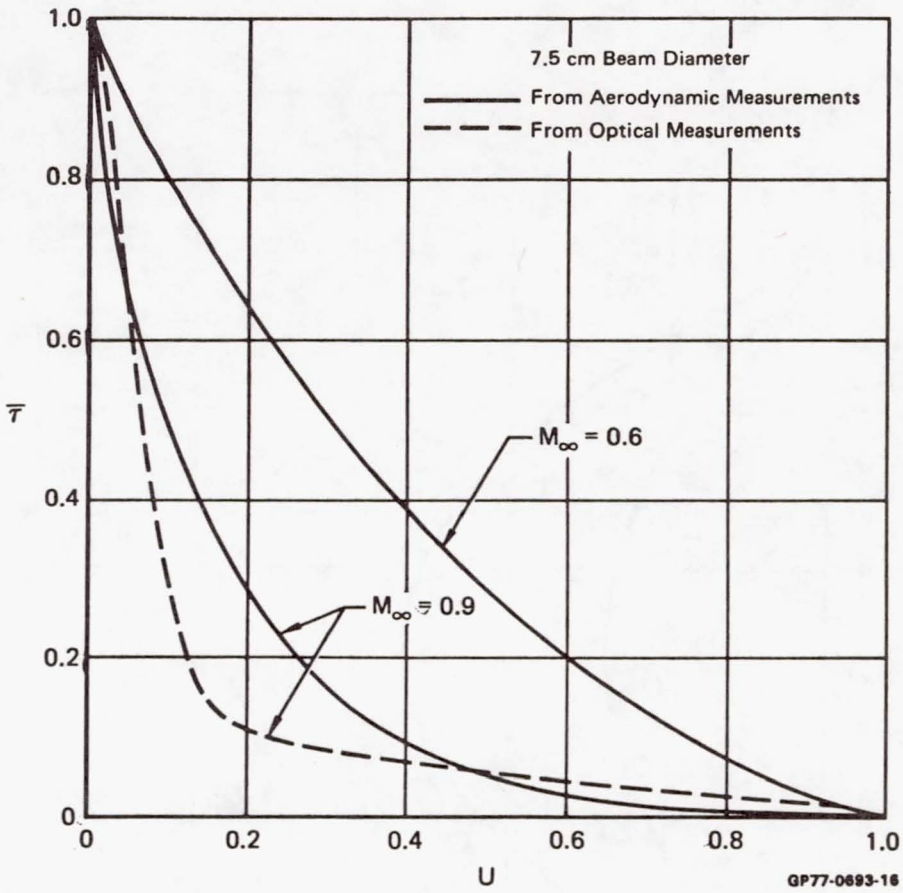

FIGURE 24
MODULATION TRANSFER FUNCTION.
Configuration No. 13 - Re = 9.8 x 10^6/meter

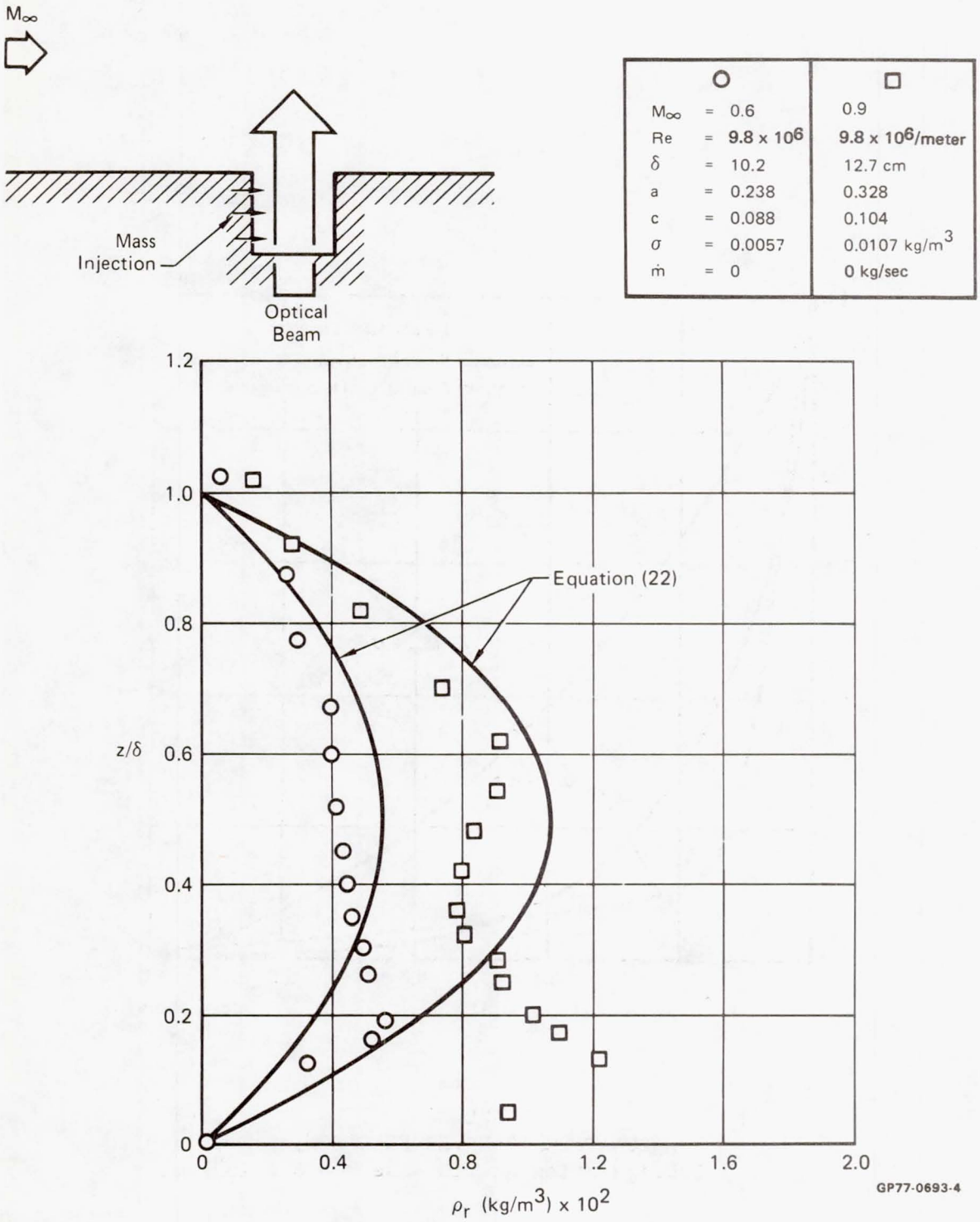

FIGURE 25
SUMMARY OF CONFIGURATION NO. 14 DATA.

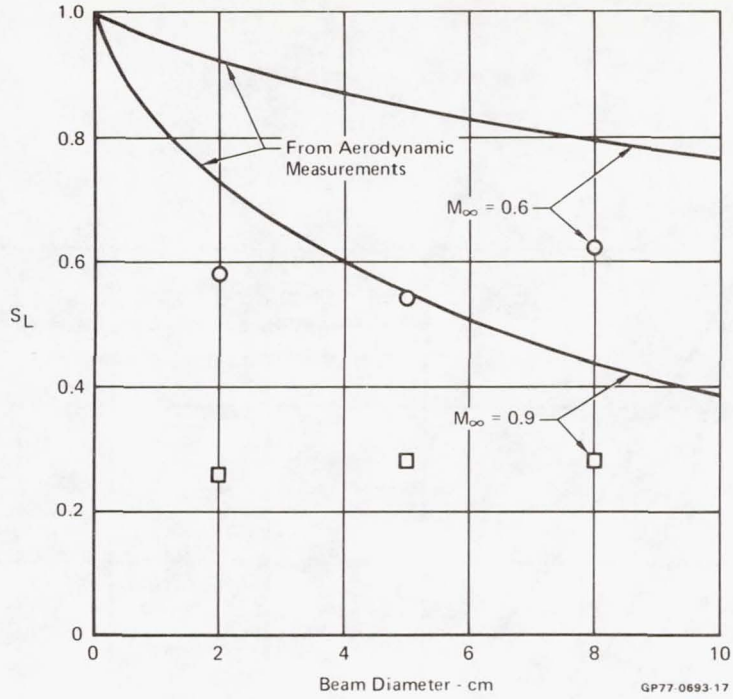

FIGURE 26
LINE SPREAD STREHL RATIO.
Configuration No. 14 - $\dot{m}$ = 0; Re = 9.8 x 10^6/meter

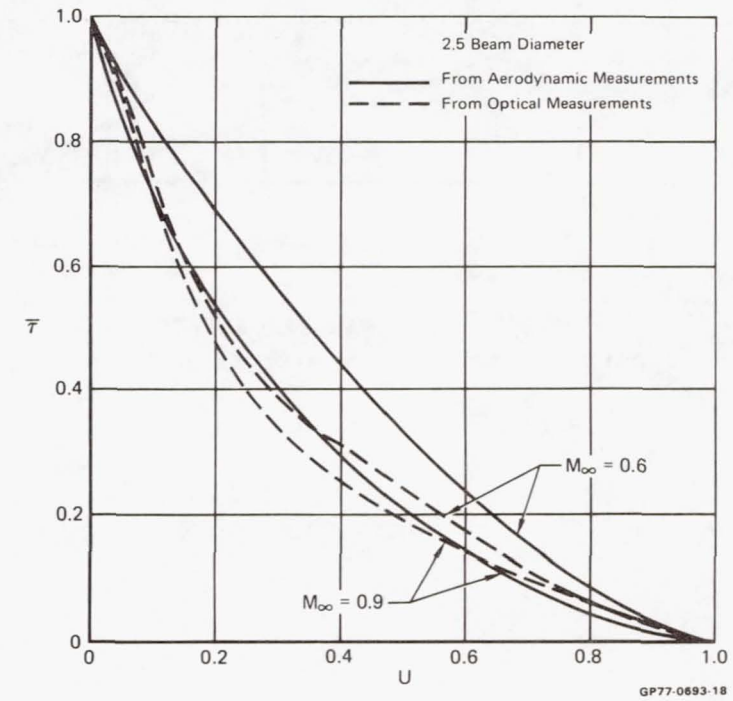

FIGURE 27
MODULATION TRANSFER FUNCTION.
Configuration No. 14 - $\dot{m}$ = 0; Re = 9.8 x 10^6/meter

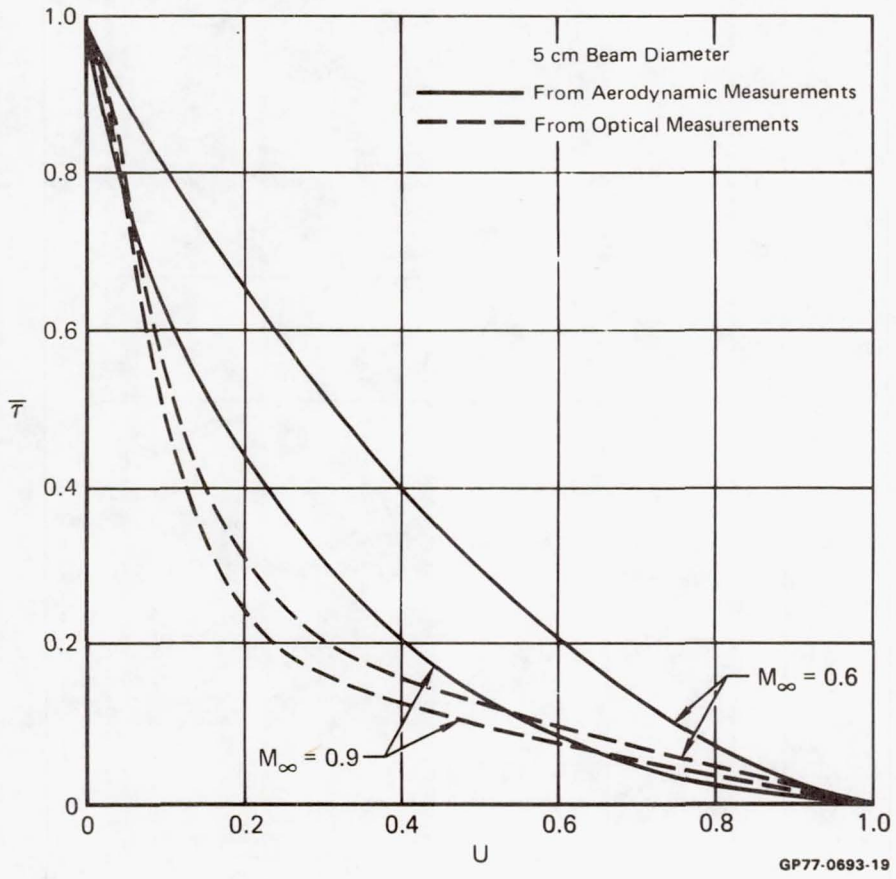

FIGURE 28
MODULATION TRANSFER FUNCTION.
Configuration No. 14 - $\dot{m} = 0$; Re = 9.8 x 10^6/meter

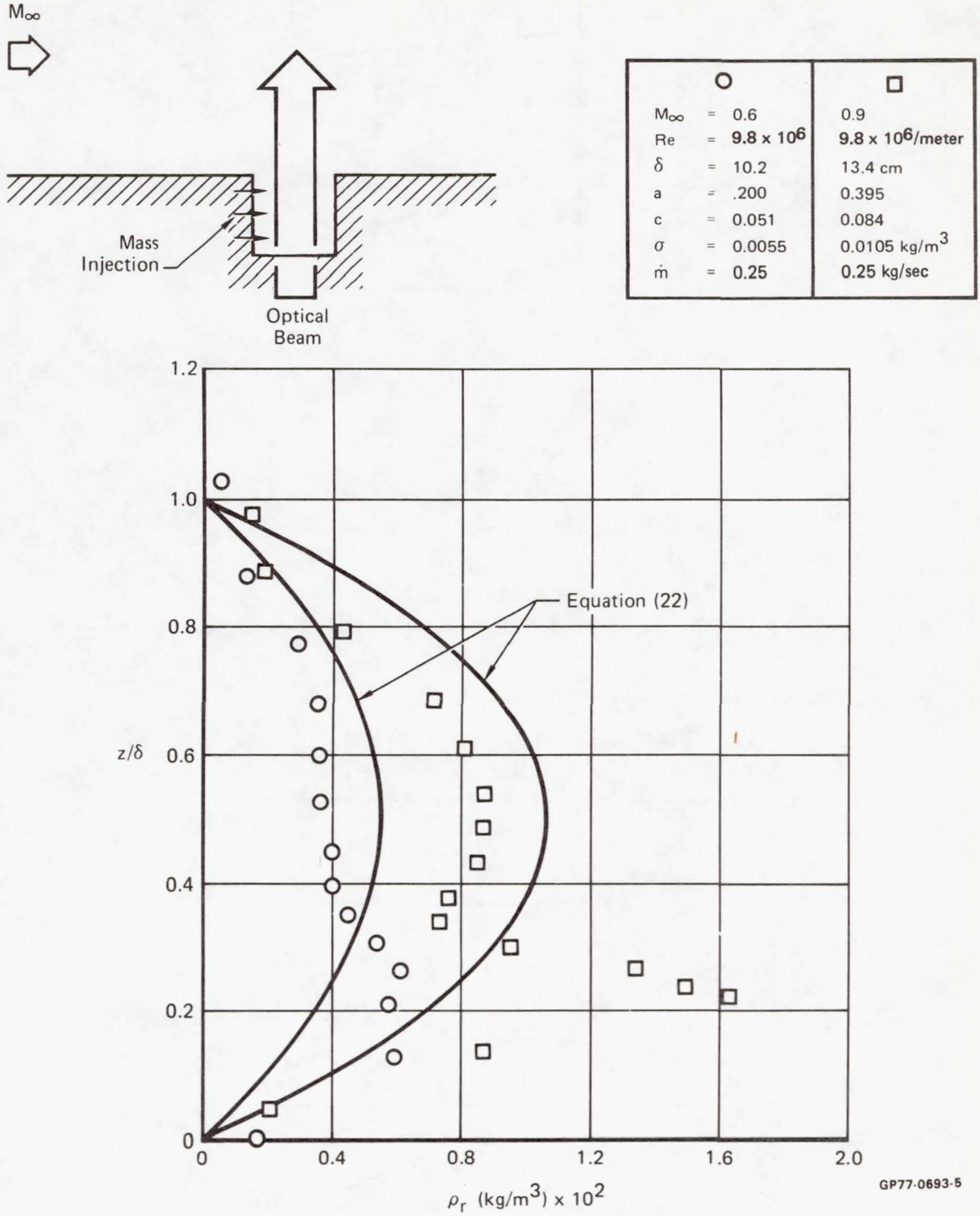

FIGURE 29
SUMMARY OF CONFIGURATION NO. 14 DATA.

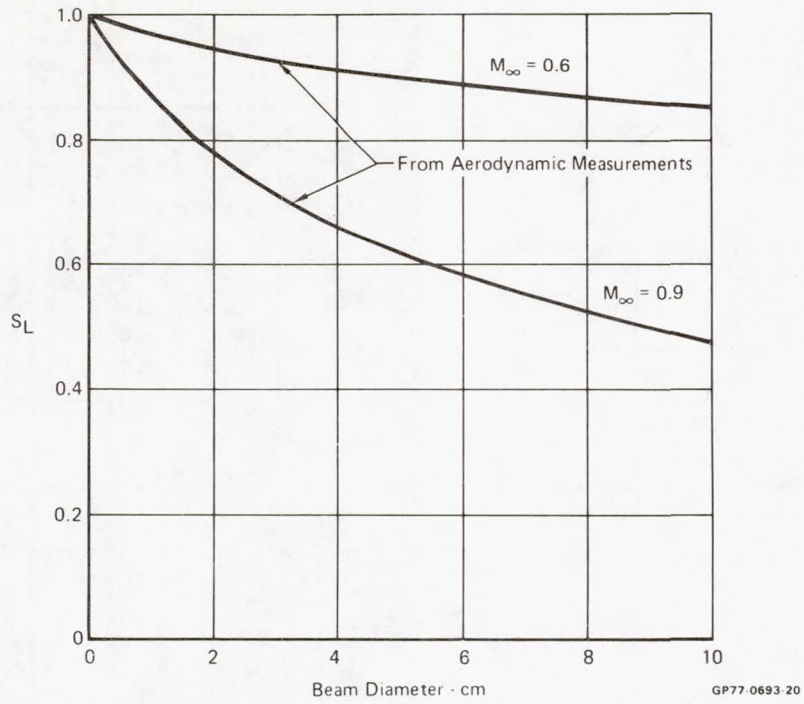

FIGURE 30
LINE SPREAD STREHL RATIO.
Configuration No. 14 - $\dot{m} = 0.25$; Re = 9.8×10^6/meter

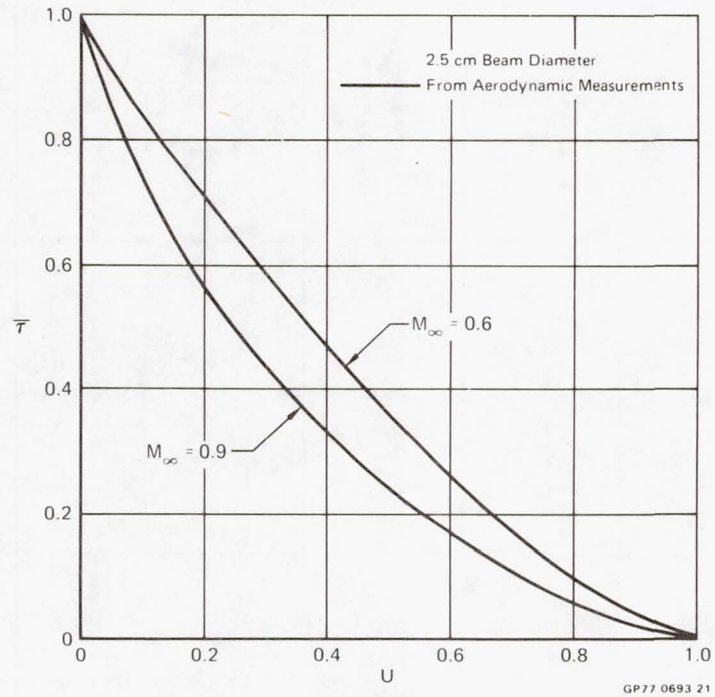

FIGURE 31
MODULATION TRANSFER FUNCTION.
Configuration No. 14 - $\dot{m} = 0.25$; Re = 9.8×10^6/meter

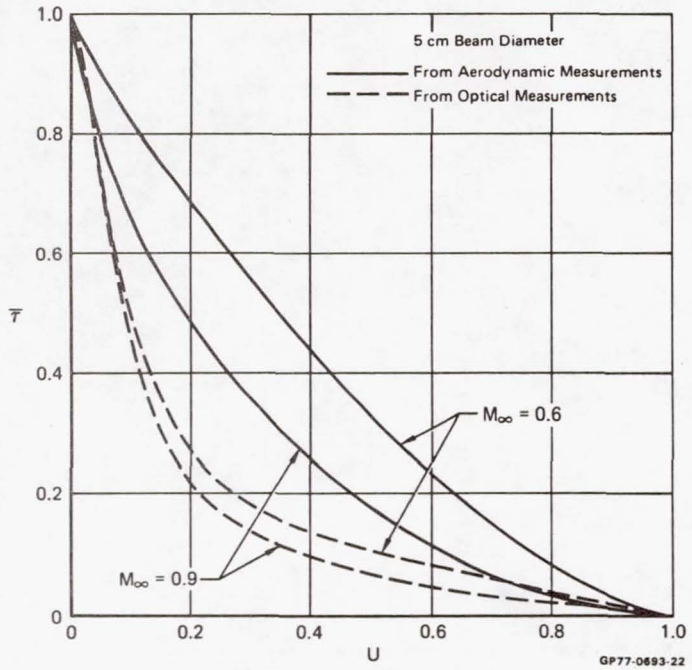

FIGURE 32
MODULATION TRANSFER FUNCTION.
Configuration No. 14 - $\dot{m}$ = 0.25; Re = 9.8 x 10^6/meter

AMP 334

ON OPTICAL IMAGING THROUGH AIRCRAFT TURBULENT BOUNDARY LAYERS*

by

George W. Sutton

Avco Everett Research Laboratory
Everett, Massachusetts

June 1971

*This work was sponsored by the Advanced Research Projects Agency of the Department of Defense under a subcontract of M. I. T. Lincoln Laboratory under Contract No. F19628-70-C-0230, Purchase Order No. B-163.

NOMENCLATURE

c_p = specific heat of air

C = normalization constant for spectrum

D = aperture diameter

$E_{\epsilon\epsilon}(k)$ = spectrum of fluctuations, Eq. (1)

I = light intensity, w/cm^2

k = wavenumber of light, cm^{-1}

ℓ = scale size of turbulence

n = exponent in spectrum

o = initial

r = separation distance

T = temperature

u = velocity in x direction

W = wall

y = distance normal to boundary layer

α = extinction coefficient, cm^{-1}

β = constant Eq. (12)

δ = boundary-layer thickness, cm

Δ = rms value

ϵ = dielectric constant, air

Θ = angle from optical axis

ρ = mass density

ϕ = azimuthal angle

σ = volume scattering

Ω = solid angle

∞ = free stream

ABSTRACT

An analysis is presented of optical resolution quality as affected by aircraft turbulent boundary layers. The wind-tunnel data of Stine and Winovich[1], was analyzed to obtain the variation of boundary layer turbulence scale length and mass density rms fluctuations with Mach number. The data gave good agreement with a mass density fluctuation turbulence spectrum that is either isotropic or orthogonally anisotropic. The data did not match an isotropic turbulence velocity spectrum which causes an anisotropic non-orthogonal mass density fluctuation spectrum. The results indicate that the average mass density rms fluctuation is about 10% of the maximum mass density across the boundary layer and that the transverse turbulence scale size is about 10% of the boundary layer thickness. The results indicate that the effect of the turbulent boundary layer is large angle scattering which decreases contrast but not resolution. Using extinction as a criteria the range of acceptable aircraft operating conditions are given.

INTRODUCTION

The question of the quality of optical imaging through aircraft windows with turbulent boundary layers is important for both reconnaissance and earth resources technology. In general an optical image recorded through such a window may be degraded by both the variation of the mean properties of the boundary layer in the direction parallel to the window and the fluctuations of mass density in the boundary layer on the window, since the index of refraction varies proportionally to the mass density. In this note we consider only the latter, and use the wind tunnel data of Stine and Winovich[1] to determine bounds for the degradation for flight cases. We will compare the differences between this analysis and previous analyses.[2]

The degradation of the image quality depends on two quantities, the extinction number $\alpha\delta$ which represents the scattering of light out of the diffraction pattern, and the ratio of the turbulence scale size to the diameter of the imaging optics.[3] If the turbulent scale size is much smaller than the aperture diameter, the effective resolution is insensitive to $\alpha\,\delta$, but the image intensity at the image plane is decreased[3] by $\exp(-\alpha\delta)$. The light scattered by the turbulent boundary layer raises the apparent background intensity.

Analysis of Wind-Tunnel Data

The differential cross section for scattering from a unit volume of a random medium is given by[1,4]

$$d\sigma/d\Theta = (1/4)\,\pi\,(\Delta\epsilon)^2\,\epsilon^{-2}\,(1+\cos^2\Theta)\,k^4\,E_{\epsilon\epsilon}\left[(2\,k\sin\Theta/2)\right] \qquad (1)$$

where $E_{\epsilon\epsilon}$ is the three dimensional spectrum of fluctuations of the dielectric

constant such that

$$\int_{-\infty}^{\infty} E_{\epsilon\epsilon}(k)\, d\underset{\sim}{k} = 1 \tag{2}$$

The cross section for light intensity scattered out of a cone of half angle Θ is then given by

$$\sigma(\Theta) = 2\pi \int (d\sigma/d\Omega)\, \Theta\, d\Theta \tag{3}$$

and the light energy remaining in the cone is determined from

$$dI(\Theta)/dy = -I(\Theta)\,\sigma(\Theta) \tag{4}$$

Using a general three-dimensional spectrum

$$E_{\epsilon\epsilon} = C\ \ell^3 (1 + k^2\ \ell^2)^{-n} \tag{5}$$

Eq. (3) and (4) may be integrated. Since $k \gg 1$, Θ is always small hence $2 \sin \Theta/2 \cong \Theta$, $\cos \Theta \sim 1$. The result for the light intensity through a small aperture at the focal plane after traversing a boundary layer is:

$$\ell n \left[I(\Theta)/I_o\right] = -\frac{C \pi^2 k^2 \epsilon^{-2}}{2(n-1)} \int_0^{\delta} \frac{\ell (\Delta\epsilon)^2\, dy}{(1 + k^2\ \ell^2\ \Theta^2)^{n-1}} \tag{6}$$

If ℓ and $(\Delta\epsilon)^2$ do not vary greatly through the major portion of the boundary layer, we may take them as constant, equal to their average value. Then Eq. (6) becomes:

$$\ell n \left[I(\Theta)/I_o\right] = -\frac{C \pi^2 k^2 \epsilon^{-2} \ell (\Delta\epsilon)^2 \delta}{2(n-1)} \frac{}{(1 + k^2 \ell^2 \Theta^2)^{n-1}} \tag{7}$$

The intensity "on axis", which corresponds to the image intensity is obtained from Eq. (7) by setting $k\ell\Theta \ll 1$, yielding:

$$\ell n \left[I(0)/I_o \right] = - C \pi^2 k^2 \ell (\Delta\epsilon)^2 \epsilon^{-2} \delta/2(n-1) \equiv -\alpha \delta \qquad (8)$$

which gives the formula for the extinction number. Eq. (7) can then be rewritten as

$$k^2 \ell^2 \Theta^2 = \left\{ \ell n \left[I(0)/I_o \right] / \ell n \left[I(\Theta)/I_o \right] \right\}^{1/(n-1)} - 1 \qquad (9)$$

There exists three unknowns in Eq. (9): ℓ, $I(0)/I_o$, and n, which are found from the experimental data. In the experiment of Ref. 1, collimated light of wavelength 0.52 μm was passed through a wind tunnel with turbulent boundary layers, and refocused. Various aperture stops were used and the total light intensity which passed through the aperture was measured giving $I(\Theta)/I_o$. The radius of the aperture defined Θ.

If the correct value of n is chosen, a plot of $\left\{ \left[\ell n \left(I(\Theta)/I_o \right) \right]^{1/(n-1)} \right\}^{-1}$ vs Θ^2 should be a straight line. For the high Mach number, high density experiments it was found that the best fit of the data to a straight line occurred when n = 2,* (see Fig. 1) which corresponds to an exponential correlation function of the index of refraction fluctuations, with an integral scale equal to ℓ, and $C = \pi^{-2}$. The intersection of the straight line with the abscissa then gives ℓ (since k is known), and the intersection

* The analysis of Ref. 1 assumed that n = 2.

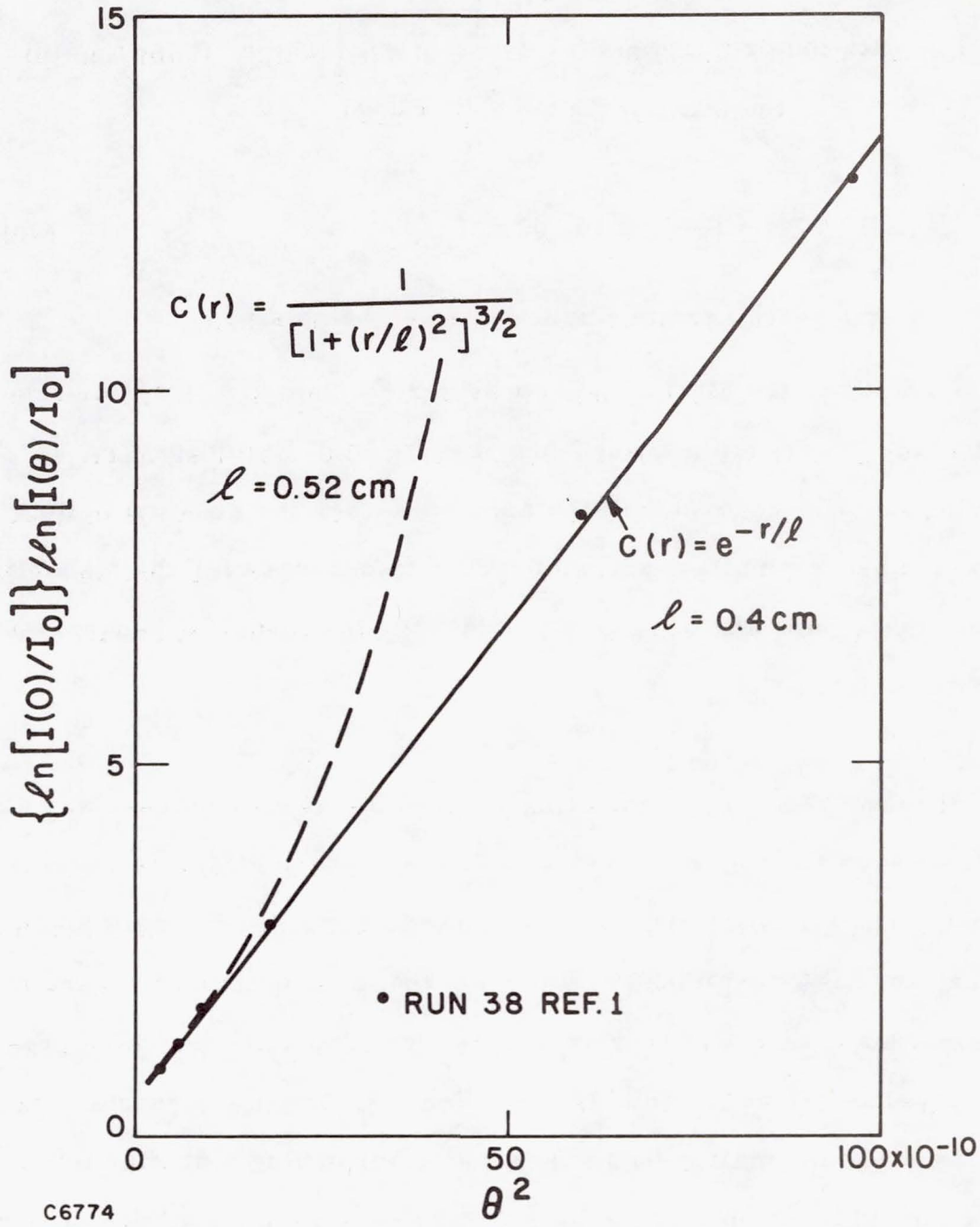

Fig. 1 Theoretical and experimental[1] dependence of light intensity with aperture half angle, for two theoretical correlation functions for dielectric constant fluctuations.

of the line with the ordinate gives $\ell n \left[I(0)/I_o \right]$ which, from Eq. (8) gives $(\Delta\epsilon^2)$. For the wavelength used (0.52μm),

$$(\Delta\epsilon)^2/\epsilon^2 = 4\,(2.76 \times 10^{-4})2(\Delta\rho^2)/\rho_s{}^2 \qquad (10)$$

so that the rms mass density fluctuations can be obtained.

In Ref. 1, the Mach number was varied from 0.4 to 2.5 and the free stream density from about 1 atmosphere to 0.1 atmosphere. In analyzing the data according to the above scheme, the greatest optical effects and hence smallest spread in the data occurred for the higher Mach numbers. We have analyzed only the data for the turbulent boundary layers with natural transition.

RESULTS

Figure 2 shows the resulting ratio of integral turbulence scale to boundary-layer thickness for 38 cases in Ref. 1. Each case is represented by a dot. The triangles represent arithmetic averages for each Mach number range. As explained previously, the largest scatter occurs for the lowest Mach number. However, it is clear for Mach numbers greater than unity that $\ell/\delta \approx 0.1$, and may be somewhat larger for subsonic Mach numbers. These small values are initially surprising since the integral scale ℓ should be about half the longitudinal velocity integral scale (if the turbulence is isotropic). Since it is generally believed that the ratio of the latter to the boundary-layer thickness is about 0.4, we would expect ℓ/δ to be 0.2. However, the scale size of the turbulence is smaller near wall,

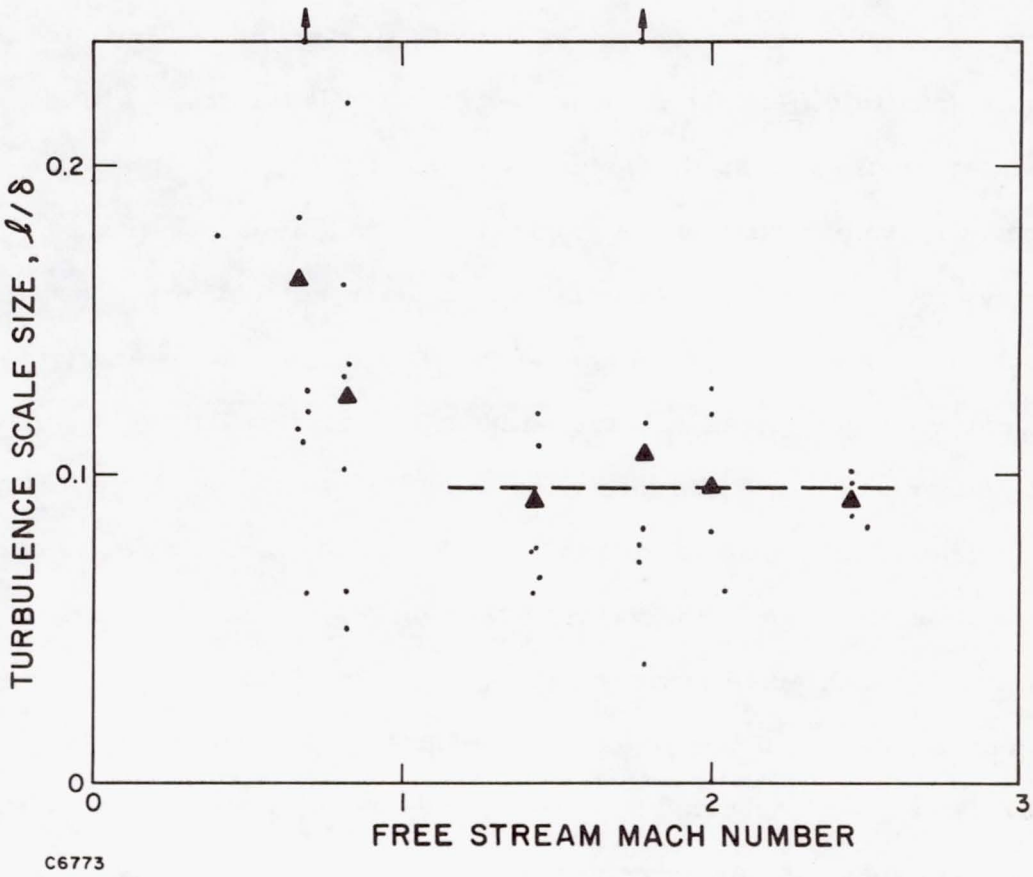

Fig. 2 Ratio of mass density turbulence scale size to boundary-layer thickness, deduced the data of Stine and Winovich.[1]

and the method of interpretation only yields the average value in the boundary layer, weighted by the fluctuations. Thus, the average value of ℓ/δ is not inconsistent with our knowledge of boundary layers.

The deduced mass density fluctuations are shown in Fig. 3, where we have compared the deduced mass density fluctuations to two quantities: the mass density difference across the boundary layer $\rho_w - \rho_\infty$, and the temperature ratio across the boundary layer $T_w/T_\infty - 1$. It was assumed that the wall temperature of the experiment was adiabatic, with a recovery factor of unity. Again there is a large amount of scatter particularly at the lower Mach numbers. The large circles and triangles represent averages for each Mach number range; the former for mass density differences, and the latter for temperature ratio. Except for low Mach numbers, the ratio of ratio of $\Delta\rho$ to $\rho_\infty - \rho_w$ appears to be constant, equal to about 0.1, while the values based on temperature ratio decrease monotonically with Mach number.

The constancy of the mass density fluctuation ratio with Mach number can be demonstrated approximately, as follows: assuming that pressure fluctuations can be neglected, then locally $\Delta\rho/\rho \sim \Delta T/T$. Thus the average value through the boundary layer is

$$\frac{\Delta\rho}{\rho_\infty - \rho_w} = \left(1 - \frac{\rho_w}{\rho_\infty}\right)^{-1} \int_0^1 \frac{\Delta T}{T} \frac{\rho}{\rho_\infty} \, d(y/\delta) \qquad (11)$$

From Ref. 5, $\Delta T/T$ through the boundary layer is approximately constant, given by

$$\frac{\Delta T}{T} \sim \frac{(T_w/T_\infty - 1)}{1/2\,(T_w/T_\infty + 1)} \beta \qquad (12)$$

where β is a constant. We approximate the integral of ρ/ρ_∞ by the arithmetic average at the end points, viz:

$$\int_0^1 \frac{\rho}{\rho_\infty} \, d\,(y/\delta) = 1/2 \left(\frac{\rho_w}{\rho_\infty} + 1 \right) = 1/2 \, \frac{T_\infty}{T_w} \left(1 + \frac{T_w}{T_\infty} \right) \tag{13}$$

Combining Eqs. (11, 12, and 13),

$$\frac{\Delta\rho}{\rho_\infty - \rho_w} = \text{constant} = \beta \tag{14}$$

Thus, the average mass density fluctuation ratios should be insensitive to Mach number. The average value of β from Ref. 5 is about 0.07; from Fig. 3 we deduce that the average value of β is about 0.1. This difference is not significant in view of the approximations made in evaluating Eq. (11); the main point is the constancy of $\Delta\rho/(\rho_\infty - \rho_w)$ with Mach number is consistent with measurements of temperature fluctuations in boundary layers.

To compare with previous results we note that Hufnagel[2] used $\ell/\delta = 0.1$ which is consistent with this analysis, however, his results correspond to a correlation function of the form

$$c\,(r) = (1 + r^2/\ell^2)^{-3/2} \tag{15}$$

Using Eq. (15), with Eqs. (1) and (4), the calculated dependence of $I\,(\Theta)$ diverges greatly from the data, see Fig. 1. In addition, the density fluctuations were taken to vary as

$$\Delta\rho = 0.2\,(T_w - T_\infty)/1/2\,(T_w + T_\infty) \tag{16}$$

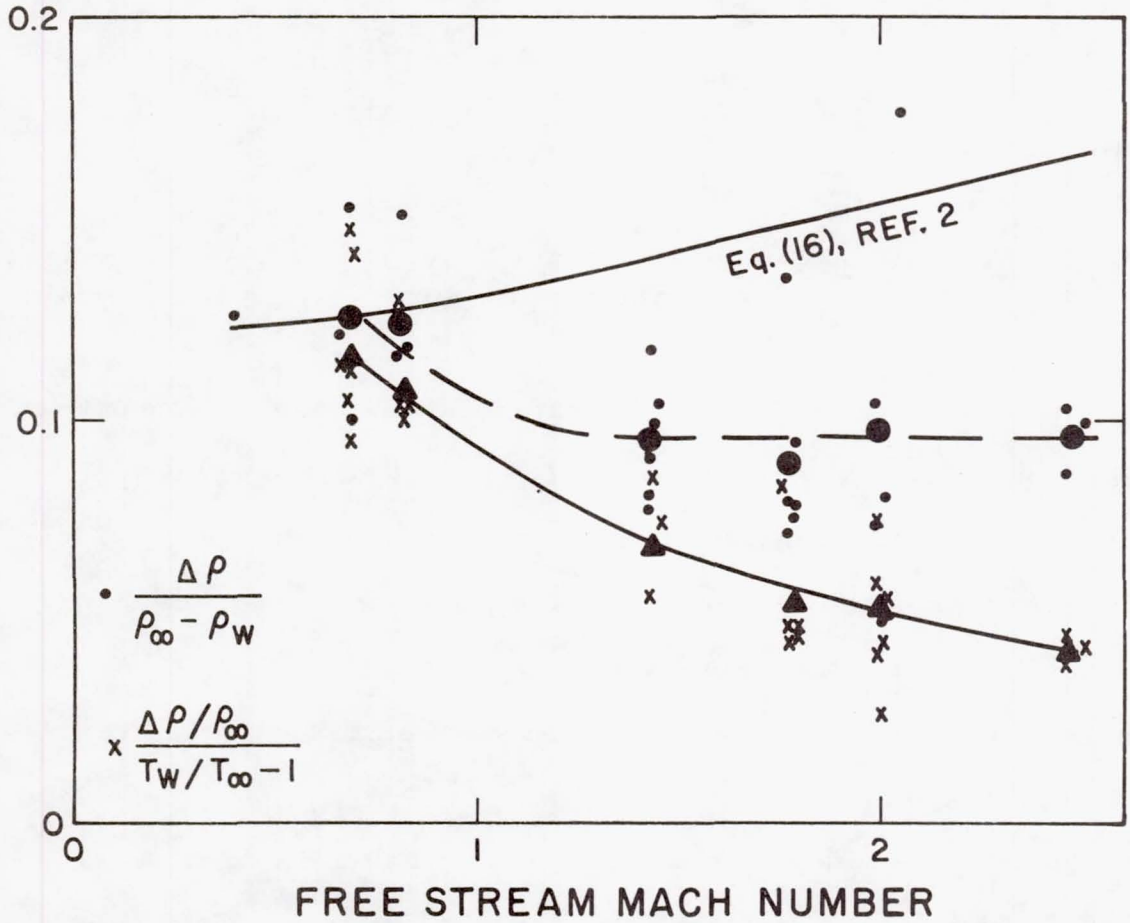

Fig. 3 Mass density fluctuations, deduced from the data of Stine and Winovich. [1]

While this expression passes through the vicinity of the subsonic data points of $\Delta\rho/(\rho_\infty - \rho_w)$, the trend with Mach number disagrees with the values deduced from the experimental data; as we indicated previously $\Delta\rho/(\rho_\infty - \rho_w)$ is approximately constant and does not vary with Mach number.

EFFECT OF ANISOTROPIC TURBULENCE

There is no reason to believe that the spectrum is isotropic, hence we have also investigated several anisotropic spectra; the only assumption being that one principle axis of the spectrum coincides with the direction of propagation. In an actual boundary layer the angle between principle axes of the spectrum and the spatial coordinates is of the order of 20°, hence the latter assumption should be quite good.

For an anisotropic orthogonal density fluctuation spectrum, Eq. (5) becomes:

$$E_{\epsilon\epsilon} = C \ell_1 \ell_2 \ell_3 \left[1 + \sum_i k_i^2 \ell_i^2\right]^{-n} \tag{17}$$

where, for propagation in the y direction,

$$\begin{aligned} k_x &= -k \sin\Theta \cos\phi \approx k\Theta\cos\phi \\ k_y &= k(1 - \cos\Theta) \approx k\Theta^2/2 \\ k_z &= -k \sin\Theta \sin\phi \approx k\Theta \sin\phi \end{aligned} \tag{18}$$

and $d\Omega = d\phi \sin\Theta \, d\Theta$. For $\ell_z = \ell_x \neq \ell_y$, then for $n = 2$, Eq. (7) becomes:

$$\ell n \left[I(\Theta)/I_o \right] = 1/2 \, (\Delta\epsilon)^2 \, \ell_y \, k^2 \, \delta \left[1 + k^2 \, \ell_x^2 \, \Theta^2 \right]^{-1} \qquad (19)$$

Thus the turbulence scattering angle depends on the scale size in the plane normal to the path (ℓ_x) but the extinction depends on the scale size in the direction of propagation (ℓ_y). In this case it is not possible to isolate separately the effects of scale size ℓ_y and density fluctuations since they appear as a product.

Another example of an anisotropic spectrum corresponds to an isoenthalpy flow in the x direction. Then $c_p \, \Delta T = U \Delta u$, and the spectrum for temperature (or density) fluctuations is the same as for Δu, e. g. $E_{\epsilon\epsilon} = E_{11}$. For isotropic velocity fluctuations, we can also use an exponential velocity fluctuation correlation function, for which[6]

$$E_{\epsilon\epsilon} = E_{11} = 2 \, \pi^{-2} \, \ell^5 \, (k^2 - k_1^2) \, (1 + k^2 \, \ell^2)^{-1} \qquad (20)$$

The dependence on aperture angle Θ of light intensity is again obtained by integration of Eq. (1) and (4):

$$\ell n \left[I(\Theta)/I_o \right] = - 1/2 \left(\frac{\Delta\epsilon}{\epsilon} \right)^2 k^2 \, \ell \delta \, (1 + k^2 \, \Theta^2 \, \ell^2)^{-1} \left[1 - (2 + 2 \, k^2 \ell^2 \, \Theta^2) \right]^{-1} \qquad (21)$$

This form is similar to Eq. (1), except that there is some curvature in the plot of $1/\ell n \left[I(\Theta)/I_o \right]$ vs Θ^2 for $k \Theta \ell < 5$. This curvature is not evident in the data; hence the assumption of isoenthalpy and isotropic velocity turbulence which leads to Eq. (21) is rejected.

A third possible anisotropic form for $E_{\epsilon\epsilon}$ corresponds to isoenthalpy flow, but with different scale sizes in the 3 orthogonal directions. A form of the velocity spectrum which satisfies incompressible continuity is:

$$E_{ij} = A\left[\ell_i \ell_j \delta_{ij} \sum_{\ell} k_\ell^2 \ell_\ell^2 - k_i k_j \ell_i^2 \ell_j^2\right] f(k_i \ell_i) \tag{22}$$

For example, if the velocity correlation function is exponential, in the three orthogonal directions, then

$$E_{\epsilon\epsilon} = E_{11} = 2\pi^{-2} \ell_1 \ell_2 \ell_3 \left[(k_2 \ell_2)^2 + (k_3 \ell_3)^2\right]\left[1 + \sum k_\ell^2 \ell_\ell^2\right]^{-3} \tag{23}$$

for which Eqs. (1) and (4) may be approximately integrated to obtain

$$\ell n\left[I(\Theta)/I_o\right] = -1/2\,(\Delta\epsilon^2)\, k^2 \ell_1 \ell_2^3 \ell_3 \delta \ell^{-4}\left[1 + k^2\Theta^2 \ell^2\right]^{-1}\left[1 - (2 + 2k^2\ell^2\Theta^2)\right] \tag{24}$$

where

$$\ell^2 = 3/4\, \ell_2^2 + 1/4\, \ell_1^2 \tag{25}$$

Again, Eq. (24) exhibits curvature near the origin, which is not present in the data. Thus we conclude that either Eq. (7) with n = 2, or its anisotropic form Eq. (19) are most consistent with the data; and that the scattered light is not consistent with isoenthalpy flow with either an isotropic or anisotropic velocity spectrum.

APPLICATIONS TO FLIGHT

For the usual cases that the aperture of the imaging device is much larger than the turbulence scale size, the primary effect on the

diffraction pattern from a distant point source will be attenuation of the light by turbulence scattering, but the resolution will not be changed appreciably[2]. Typical diffraction patterns are shown in Fig. 4. For example the case $\alpha\ \delta = 0.50$ corresponds to a boundary layer 11 cm thick, a Mach number of 0.8, and an altitude of 9 km. While the theoretical resolution is insensitive to the extinction, excessive extinction causes loss of contrast, since the scattered light enters adjacent resolution cells. Thus, we may define some approximate criteria: if $\alpha\delta > 2$, then the ability to image will be poor, but if $\alpha\delta < 0.4$, the ability to image should be quite good. Figure 5 shows these approximate boundaries, for three boundary layer thicknesses, 1, 3, and 10 cm.

From Fig. 5, it can be seen that the seeing effects are very sensitive to Mach number in the vicinity of Mach one, but insensitive to Mach number at high Mach numbers. This latter effect is caused by the fact that $1 - \rho_w/\rho_\infty$ goes asymptotically to unity with increasing Mach number. For all Mach numbers, the "seeing" is sensitive to the boundary-layer thickness, hence there is always a gain in keeping the boundary layer over the window of imaging device as thin as possible. Other techniques may also be useful for improving the imaging, such as cooling the window to reduce the temperature excess, and hence mass density fluctuations. One note of caution: these results are based on a smooth window flush with the aircraft skin. Window moldings, recesses, etc. could degrade the imaging quality by increasing either the optical path through the turbulence layer or the scale size of the turbulence.

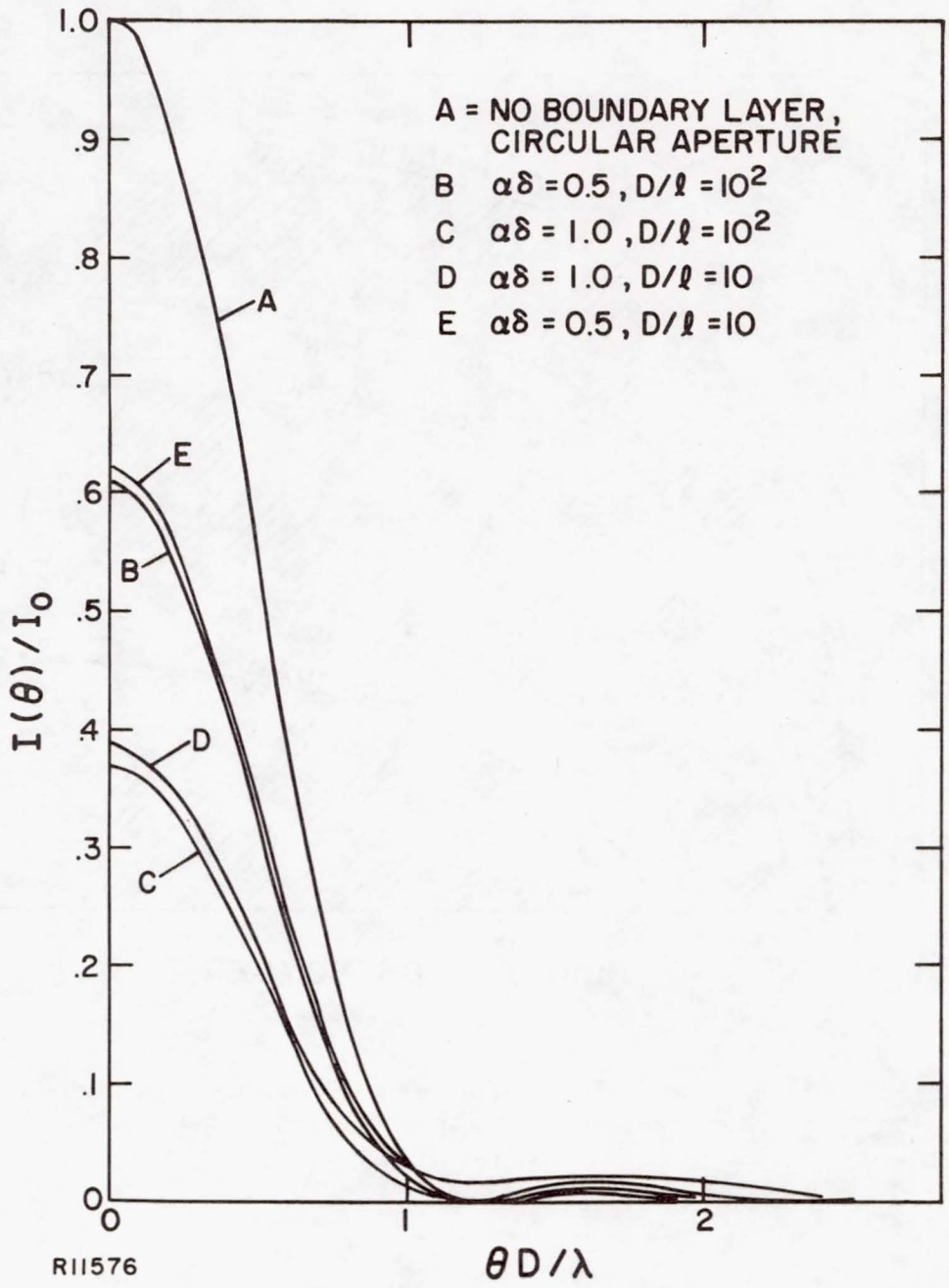

Fig. 4 Diffraction patterns.

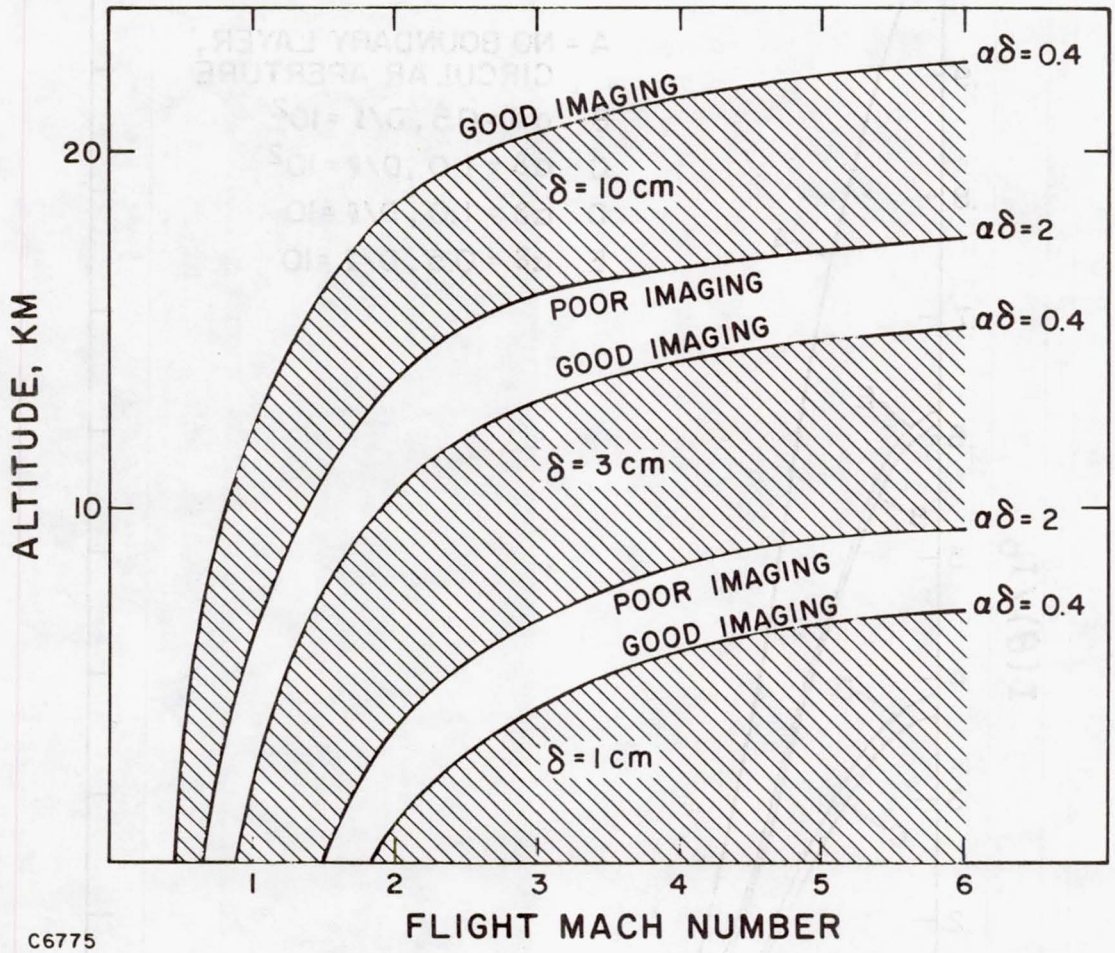

Fig. 5 Imaging quality boundaries for various boundary-layer thicknesses, flight Mach numbers, and altitudes.

ACKNOWLEDGMENTS

The author wishes to thank Mr. D. G. Kocher of Lincoln Laboratory who stimulated the present work and brought the work of Stine and Winowich to the author's attention. The author also wishes to acknowledge the help of Mr. J. Golin, who calculated the diffraction patterns shown in Fig. 4.

REFERENCES

1. Stine, H. A. and Winovich, W., "Light Diffusion Through High-Speed Turbulent Boundary Layers", NACA RM A56B21, May 25, 1956.

2. Hufnagel, R. E., "Random Wavefront Effects", Photographic Science and Engineering, Vol. 9, No. 4, July-August 1965, pp. 244-247.

3. Sutton, G. W., "Effect of Turbulent Fluctuations in an Optically Active Fluid Medium", AIAA Journal, Vol. 7, No. 9., Sept. 1969, pp. 1737-1743.

4. Booker, H. G. and Gordon, W. E., "A Theory of Radio Scattering in the Troposphere", Proc. I.R.E., Vol. 38, No. 4, April 1950, pp. 401-412.

5. Kistler, A. L., "Fluctuation Measurements in a Supersonic Turbulent Boundary Layer", Physics of Fluids, Vol. 2, 1959, pp. 290-296.

6. Hinze, J. O., Turbulence, McGraw Hill Co., New York (1949).

Unclassified

Security Classification

DOCUMENT CONTROL DATA - R&D

(Security classification of title, body of abstract and indexing annotation must be entered when the overall report is classified)

1. ORIGINATING ACTIVITY (Corporate author)	2a. REPORT SECURITY CLASSIFICATION
Avco Everett Research Laboratory 2385 Revere Beach Parkway Everett, Mass.	Unclassified
	2b. GROUP

3. REPORT TITLE

On Optical Imaging through Aircraft Turbulent Boundary Layers

4. DESCRIPTIVE NOTES (Type of report and inclusive dates)

AMP 334

5. AUTHOR(S) (Last name, first name, initial)

Sutton, George W.

6. REPORT DATE	7a. TOTAL NO. OF PAGES	7b. NO. OF REFS
June 1971	17	6

8a. CONTRACT OR GRANT NO.	9a. ORIGINATOR'S REPORT NUMBER(S)
F19628-70-C-0230	AMP 334
b. PROJECT NO.	
c.	9b. OTHER REPORT NO(S) (Any other numbers that may be assigned this report)
d.	

10. AVAILABILITY/LIMITATION NOTICES

11. SUPPLEMENTARY NOTES	12. SPONSORING MILITARY ACTIVITY
	ARPA, Department of Defense, under subcontract of M. I. T. Lincoln Laboratory

13. ABSTRACT

An analysis is presented of optical resolution quality as affected by aircraft turbulent boundary layers. The wind-tunnel data of Stine and Winovich, [1] was analyzed to obtain the variation of boundary-layer turbulence scale length and mass density rms fluctuations with Mach number. The data gave good agreement with a mass density fluctuation turbulence spectrum that is either isotropic or orthogonally anisotropic. The data did not match an isotropic turbulence velocity spectrum which causes an anisotropic non-orthogonal mass density fluctuation spectrum. The results indicate that the average mass density rms fluctuation is about 10% of the maximum mass density across the boundary layer and that the transverse turbulence scale size is about 10% of the boundary-layer thickness. The results indicate that the effect of the turbulent boundary layer is large angle scattering which decreases contrast but not resolution. Using extinction as a criteria the range of acceptable aircraft operating conditions are given.

DD FORM 1 JAN 64 1473

Unclassified

Security Classification

14. KEY WORDS	LINK A		LINK B		LINK C	
	ROLE	WT	ROLE	WT	ROLE	WT
1. Optical Imaging 2. Aircraft 3. Turbulent Boundary Layers 4. Optical Resolution						

INSTRUCTIONS

1. ORIGINATING ACTIVITY: Enter the name and address of the contractor, subcontractor, grantee, Department of Defense activity or other organization *(corporate author)* issuing the report.

2a. REPORT SECURITY CLASSIFICATION: Enter the overall security classification of the report. Indicate whether "Restricted Data" is included. Marking is to be in accordance with appropriate security regulations.

2b. GROUP: Automatic downgrading is specified in DoD Directive 5200.10 and Armed Forces Industrial Manual. Enter the group number. Also, when applicable, show that optional markings have been used for Group 3 and Group 4 as authorized.

3. REPORT TITLE: Enter the complete report title in all capital letters. Titles in all cases should be unclassified. If a meaningful title cannot be selected without classification, show title classification in all capitals in parenthesis immediately following the title.

4. DESCRIPTIVE NOTES: If appropriate, enter the type of report, e.g., interim, progress, summary, annual, or final. Give the inclusive dates when a specific reporting period is covered.

5. AUTHOR(S): Enter the name(s) of author(s) as shown on or in the report. Enter last name, first name, middle initial. If military, show rank and branch of service. The name of the principal author is an absolute minimum requirement.

6. REPORT DATE: Enter the date of the report as day, month, year, or month, year. If more than one date appears on the report, use date of publication.

7a. TOTAL NUMBER OF PAGES: The total page count should follow normal pagination procedures, i.e., enter the number of pages containing information.

7b. NUMBER OF REFERENCES: Enter the total number of references cited in the report.

8a. CONTRACT OR GRANT NUMBER: If appropriate, enter the applicable number of the contract or grant under which the report was written.

8b, 8c, & 8d. PROJECT NUMBER: Enter the appropriate military department identification, such as project number, subproject number, system numbers, task number, etc.

9a. ORIGINATOR'S REPORT NUMBER(S): Enter the official report number by which the document will be identified and controlled by the originating activity. This number must be unique to this report.

9b. OTHER REPORT NUMBER(S): If the report has been assigned any other report numbers *(either by the originator or by the sponsor)*, also enter this number(s).

10. AVAILABILITY/LIMITATION NOTICES: Enter any limitations on further dissemination of the report, other than those imposed by security classification, using standard statements such as:

(1) "Qualified requesters may obtain copies of this report from DDC."

(2) "Foreign announcement and dissemination of this report by DDC is not authorized."

(3) "U. S. Government agencies may obtain copies of this report directly from DDC. Other qualified DDC users shall request through _____."

(4) "U. S. military agencies may obtain copies of this report directly from DDC. Other qualified users shall request through _____."

(5) "All distribution of this report is controlled. Qualified DDC users shall request through _____."

If the report has been furnished to the Office of Technical Services, Department of Commerce, for sale to the public, indicate this fact and enter the price, if known.

11. SUPPLEMENTARY NOTES: Use for additional explanatory notes.

12. SPONSORING MILITARY ACTIVITY: Enter the name of the departmental project office or laboratory sponsoring *(paying for)* the research and development. Include address.

13. ABSTRACT: Enter an abstract giving a brief and factual summary of the document indicative of the report, even though it may also appear elsewhere in the body of the technical report. If additional space is required, a continuation sheet shall be attached.

It is highly desirable that the abstract of classified reports be unclassified. Each paragraph of the abstract shall end with an indication of the military security classification of the information in the paragraph, represented as *(TS), (S), (C), or (U)*.

There is no limitation on the length of the abstract. However, the suggested length is from 150 to 225 words.

14. KEY WORDS: Key words are technically meaningful terms or short phrases that characterize a report and may be used as index entries for cataloging the report. Key words must be selected so that no security classification is required. Identifiers, such as equipment model designation, trade name, military project code name, geographic location, may be used as key words but will be followed by an indication of technical context. The assignment of links, rules, and weights is optional.

GPO 886-551

Second Moments of Optical Degradation Due to a Thin Turbulent Layer

by

W. J. Steinmetz*

*Adelphi University, Garden City, New York 11530.

This work was supported in part by the National Aeronautics and Space Administration under grant NSG-2088.

Abstract

The effect of thin turbulent layers, including boundary layers and shear layers, on light propagation is examined from a theoretical point of view. In particular, a mathematical model is developed to describe the interaction between the aerodynamic or, more precisely, the density fluctuations and the electromagnetic field. It is assumed that the turbulence induces a normally distributed phase aberration which is a homogeneous random function in the plane of the aperture. Hypotheses concerning the density fluctuations in the layer sufficient to guarantee such a phase aberration are exhibited.

The optical degradation is described in terms of the optical transfer function (OTF) and the Strehl ratio (I/I_o) which are random. Expressions for the first and second moments of these two parameters are developed from the definitions. Asymptotic ("large" aperture) approximations to these expressions are derived and discussed. Finally, the exact and approximate results are compared for several "typical" values of the ratios of aperture diameter to scale of density fluctuations and rms phase aberration to wave length respectively.

1. Introduction

The effect of turbulent layers on the propagation of electromagnetic waves has drawn much attention over the past three decades. In 1950, Booker and Gordon [1] developed a theory which explained the scattering of radio waves in the troposphere. In 1956, Stine and Winovich [2] conducted an experimental investigation of light diffusion through turbulent boundary layers which tended to validate the applicability of the Booker-Gordon theory in this new context. Then, in 1971, Sutton [3] analyzed the Stine and Winovich data further and concluded that, for imaging apertures much larger than the turbulence scale size, scattering decreases contrast but not resolution.

While the above investigators were examining the influence of turbulence on resolution by studying the induced scattering, others looked at the influence on the optical (or modulation) transfer function. Hufnagel and Stanley [4] developed an expression for the average or expected value of the MTF. In particular, they showed that the average transfer function can be written as the product of the diffraction limited transfer function and an attenuating factor which incorporates properties of the turbulence. Fried elaborated on this theme in a series of papers [5,6,7,8] in the late 1960's. Much of the recent theoretical development connecting optical and turbulent parameters has been summarized by Wolters [9].

In the present work, we will attempt to present the fundamental theory relating turbulence statistics and mean values of the optical parameters, describing in some detail the relevant statistical assumptions. Also, we will discuss the second moments of the optical parameters when the aperture is much larger than the scale of turbulence.

2. Mathematical Model of Aero-Optic Interaction

The model described below does not originate with the author, but appears, at least implicitly, in much of the current literature on aero-optic interaction. Perhaps the most complete discussion has been given by Wolters [9]. However, because the assumptions and hypotheses aren't always explicit, and because the development is not easily accessible in the literature, it is believed that the somewhat more thorough discussion here is warranted.

We begin by assuming that the turbulent layer of thickness L induces a phase aberration but no amplitude degradation of the optical wave front (monochromatic of wave length λ). Hence the wave field u on the aperture of the receiving optics* can be described as follows (see Figure 1):

$$u(x,y) = \exp\left[ik\Delta(x,y)\right], \tag{2.1}$$

where

$$\begin{aligned}\Delta(x,y) &= \int_0^L n(x,y,z)\,dz \\ &= \int_0^L [1+n_1(x,y,z)]\,dz \\ &= L + \int_0^L n_1(x,y,z)\,dz \\ &= L + \Delta_1(x,y).\end{aligned}$$

In the above, k is the wave number ($2\pi/\lambda$), n is the local refractive index, and n_1 is the deviation of the refractive index from its value

---

*Even though we shall be discussing a passive receiving system, it should be noted that an active or propagating system (e.g., a high energy laser beam) would experience similar degradation.

in a vacuum. The expression (2.1) is the first order geometrical optics approximation, where it has been assumed that $|n_1| << 1$ [10]. The phase shift Δ is sometimes called the optical length of the ray's path through the turbulent layer. (See, for example, [11,p115].)

Without making some assumptions regarding the statistical nature of the random phase Δ_1, further progress would be difficult if not impossible. In particular, we make two assumptions:

(i) The random variable $\Delta_1(x,y)$ is normally distributed for any x and y,

and

(ii) $\Delta_1(x,y)$ is a weakly homogeneous random process; that is,

$$<\Delta_1(x,y)> = \text{constant} \tag{2.2}$$

$$<(\Delta_1(x_1,y_1) - <\Delta_1>)(\Delta_1(x_2,y_2) - <\Delta_1>)> = R(x_2-x_1,y_2-y_1),$$

where < > denotes ensemble average or mathematical expectation.

Assumption (i) can be justified by considering the relationship between the optical parameter Δ_1 and the air density ρ. By the Gladstone-Dale law we have

$$n_1(x,y,z) = G\,\rho(x,y,z), \tag{2.3}$$

where $G = 0.000223\ m^3/kg$ is the so-called Gladstone-Dale constant. Hence, substitution of (2.3) into (2.1) yields:

$$\Delta_1(x,y) = G \int_0^L \rho(x,y,z)\,dz. \tag{2.4}$$

Assume that $L >> \ell_z$, where ℓ_z is the integral scale of the density fluctuations in the direction of wave propagation. It follows that we can partition the random layer into strata of thickness h, with h (and hence N) chosen so that

$$\ell_z < h = L/N << L .$$

We then have that

$$\Delta_1(x,y) = G \sum_{j=1}^{N} \left[\int_{(j-1)h}^{jh} \rho(x,y,z)\,dz \right]. \tag{2.5}$$

But the random variables determined by the integrals in the sum (2.5) are approximately mutually independent (since $h > \ell_z$); then, since $N >> 1$, the Central Limit Theorem [12, p.266] gives the desired result. It should be observed that the assumption $L >> \ell_z$ is often satisfied; indeed, in practice,

$$10 < L/\ell_z < 40.$$

(See, for example, [13 , Tables 1 and 2].)

The first of conditions (2.2) follows from (2.4) if we assume that $< \rho(x,y,z) >$ depends solely on z and not on the aperture coordinates (x,y). The second condition, translation invariance of R, follows from the assumption that the covariance of the density

fluctuations, R_ρ, satisfies

$$R_\rho(x_1,y_1,z_1;x_2,y_2,z_2) = R_\rho(x_2-x_1,y_2-y_1;\ z_1,z_2)\ . \qquad (2.6)$$

Then

$$R(x_2-x_1,\ y_2-y_1) = G^2 \int_0^L \int_0^L R_\rho(x_2-x_1,\ y_2-y_1;\ z_1,z_2)\,dz\ dz_2 . \qquad (2.7)$$

The assumption (2.6) is consistent with experimental evidence which suggests that the rms density and the turbulence scale length in any direction (i.e., ℓ_x, ℓ_y, or ℓ_z) vary with z [13].

In practice, it has been found that R_ρ can, with good accuracy, be represented as follows [14, Figure 20]:

$$R_\rho(x_2-x_1,y_2-y_1;\ z_1,z_2) = R_\rho(x_2-x_1,y_2-y_1;\ u,v) \qquad (2.8)$$

$$= \sigma_\rho^2(u)\exp\left\{-\sqrt{\left(\frac{x_2-x_1}{\ell_x(u)}\right)^2+\left(\frac{y_2-y_1}{\ell_y(u)}\right)^2+\left(\frac{v}{\ell_z(u)}\right)^2}\right\}$$

where

$$u = (z_1+z_2)/2$$
$$\qquad (2.9)$$
$$v = z_2-z_1\ .$$

But, making the change of variables (2.9) in (2.7) we find

$$R(x_2-x_1,y_2-y_1) = G^2\left\{\int_0^{L/2}\int_{-2u}^{2u} R_\rho(x_2-x_1,y_2-y_1;\ u,v)\ dv\ du + \int_{L/2}^{L}\int_{-2(L-u)}^{2(L-u)} R_\rho(x_2-x_1,y_2-y_1;\ u,v)\ dv\ du\right\}. \qquad (2.10)$$

The relations (2.8) and (2.10) allow calculation of R once the z variations of $\sigma_\rho^2, \ell_x, \ell_y$, and ℓ_z have been determined. Finally, from (2.8) and (2.10) it can be shown that

$$\sigma^2 = R(0,0) \sim 2G^2 \int_0^L \sigma_\rho^2(z)\,\ell_z(z)\,dz\ , \qquad (2.11)$$

for $L >> \ell_z$.

3. Second Moments of Optical Parameters

We proceed now to develop expressions for the second order statistics of the optical transfer function τ. We begin with the definition:

$$\tau(x,y) = (4/\pi) \iint_{A_{x,y}} u(\xi + \frac{x}{2}, \eta + \frac{y}{2})\, u^*(\xi - \frac{x}{2}, \eta - \frac{y}{2})\, d\xi d\eta, \qquad (3.1)$$

where $A_{x,y}$ is the area common to two identical apertures (of unit diameter) displaced relative to each other a distance x and y along the ξ and η axes respectively. Note that $\tau(x,y) \equiv 0$ if $x^2+y^2 \geq 1$.* Clearly, since u is random, then τ is itself random. Hence, taking the expectation of (3.1) we obtain:

$$\begin{aligned}
\langle \tau(x,y) \rangle &= (4/\pi) \iint_{A_{x,y}} \langle u(\xi + \tfrac{x}{2}, \eta + \tfrac{y}{2})\, u^*(\xi - \tfrac{x}{2}, \eta - \tfrac{y}{2}) \rangle\, d\xi\, d\eta \\
&= (4/\pi) \iint_{A_{x,y}} \left\langle \exp\left(ik\, [\Delta_1(\xi + \tfrac{x}{2}, \eta + \tfrac{y}{2}) - \Delta_1(\xi - \tfrac{x}{2}, \eta - \tfrac{y}{2})] \right) \right\rangle d\xi\, d\eta \\
&= (4/\pi) \iint_{A_{x,y}} \exp\left(-k^2\, [R(0,0) - R(x,y)] \right) d\xi\, d\eta \\
&= \exp\left(-k^2\sigma^2\, [1 - r(x,y)] \right) \tau_o(x,y), \qquad (3.2)
\end{aligned}$$

where $\sigma^2 = R(0,0)$ is the variance and $r(x,y)$ is the correlation coefficient of the phase aberration Δ_1 and $\tau_o(x,y)$ is the diffraction

---

*The aperture coordinates ξ, η, x, and y have been normalized with respect to the aperture diameter, D. Then (x,y) correspond to spatial frequencies $(f_x, f_y) = (Dx/\lambda R, Dy/\lambda R)$, where R is the focal length of the optical system.

limited optical transfer function associated with the receiving optics. We have invoked both assumptions (i) and (ii) of Section 2 in obtaining (3.2). Hence, the average optical transfer function is just the diffraction limited optical transfer function τ_o attenuated by the factor

$$\tau_{att}(x,y) = \exp\left\{ - (2\pi\sigma/\lambda)^2 [1 - r(x,y)] \right\}. \qquad (3.3)$$

In general, to describe completely the random process $\tau(x,y)$, we must obtain correlations of all orders in addition to the expectation given by (3.2). This has in fact been accomplished by Barakat [15] . We will be concerned here however only with the second order correlation or auto-covariance function. But by following the procedure outlined in the development of (3.2), it is a straightforward task to verify that the auto-covariance function for τ is given by:

$$R_\tau(x,y,x',y') = \tau_{att}(x,y)\,\tau_{att}(x',y')(4/\pi)^2 \iint_{A_{x,y}} \iint_{A_{x',y'}} \left[F(u,v) - 1 \right] d\xi\, d\eta\, d\xi'\, d\eta', \qquad (3.4)$$

where

$$u = \xi' - \xi$$

$$v = \eta' - \eta$$

and

$$F(u,v) = \exp\left\{-(2\pi\sigma/\lambda)^2\left[r\left(u+\frac{x'+x}{2},\ v+\frac{y'+y}{2}\right)\right.\right.$$
$$-r\left(u+\frac{x'-x}{2},\ v+\frac{y'-y}{2}\right) - r\left(u-\frac{x'-x}{2},\ v-\frac{y'-y}{2}\right)$$
$$\left.\left.+r\left(u-\frac{x'+x}{2},\ v-\frac{y'+y}{2}\right)\right]\right\} .$$

It should be observed that since the covariance function R_τ depends explicitly on x,y,x', and y' rather than on the differences x'-x and y'-y, the optical transfer function τ is not a homogenous random process. Indeed, since we are considering only phase aberrations, $|\tau(x,y)| \leq \tau_o(x,y) \leq 1$. Hence τ is clearly not even normally distributed. A fuller discussion of this matter can be found in [15]. Before proceeding, note that the variance of $\tau(x,y)$ is given by

$$\sigma_\tau^2(x,y) = R_\tau(x,y;x,y) . \tag{3.5}$$

We turn now to the so-called Strehl ratio, I/I_o, the ratio of the maximum intensity in the image plane with aberrations, I, to the maximum intensity without aberrations, I_o, both in response to a point source. We will use the following definition (See, for example, [16 , p 88]) :

$$I/I_o = \iint_{-\infty}^{\infty} \tau(x,y)\ dx\ dy \ / \iint_{-\infty}^{\infty} \tau_o\ (x,y)\ dx\ dy . \tag{3.6}$$

Now since $\tau_o(x,y)$ is defined as the normallized convolution of the unaberrated pupil function, it can easily be shown (see, for example, [17 , p 166]) that

$$\int_{-\infty}^{\infty}\int \tau_o(x,y)\ dx\ dy = \pi/4\ .$$

Hence (3.6) can be rewritten as:

$$I/I_o = (4/\pi) \int_{-\infty}^{\infty}\int \tau(x,y)\ dx\ dy\ . \tag{3.7}$$

It follows easily from (3.7) that the first and second moments of the Strehl ratio are given by:

$$< I/I_o > = (4/\pi) \int_{-\infty}^{\infty}\int <\tau(x,y)>\ dx\ dy \tag{3.8}$$

and

$$\sigma^2_{I/I_o} = (4/\pi)^2 \int_{-\infty}^{\infty}\int\int\int R_\tau(x,y,x',y')\ dx\ dy\ dx'\ dy' \tag{3.9}$$

respectively. It is interesting to observe that if the fluctuations in τ at different spatial frequencies (x,y) are perfectly correlated, then $R_\tau(x,y,x',y') = \sigma_\tau(x,y)\sigma_\tau(x',y')$ and hence, from (3.9),

$$\sigma_{I/I_o} = (4/\pi) \int_{-\infty}^{\infty}\int \sigma_\tau(x,y)\ dx\ dy \tag{3.10}$$

In this case, the rms Strehl ratio is determined simply by the volume under the rms optical transfer function. However, in general, the optical transfer function does not fluctuate uniformly over its width and so (3.10) cannot be expected to give accurate results.

The equations for the moments of τ and I/I_o developed above could in principle be used to obtain quantitative results for a given turbulent layer by utilizing a high speed digital computer to carry out the required integrations. This procedure can be quite time consuming however, especially for the four dimensional integrations of (3.4) and (3.9). However, by pursuing an asymptotic ($D \uparrow \infty$) analysis, an approximation to these integrals can be achieved. This approach will be pursued in Section 4 below.

Before proceeding, we should remark that it is of some interest to consider the modulus of the optical transfer function, $|\tau|$, sometimes referred to as the modulation transfer function or MTF. Since τ is in general a complex-valued function, the MTF does not yield information concerning the phase of τ . However, in recent experiments, Kelsall has utilized the fast shearing interferometer [18] which measures the MTF rather than the desired optical transfer function. Although the two parameters are obviously not equivalent, there is a relationship between the two. In particular, it is not difficult to show from their respective definitions that:

$$< \tau > \leq < \text{MTF} > \leq \tau_o \tag{3.11}$$

and

$$\sigma^2_{\text{MTF}} \leq \sigma^2_\tau \leq \tau_o^2 (1 - \tau^2_{\text{att}}) < \tau_o^2 . \tag{3.12}$$

Clearly, from (3.11) and (3.12), the MTF suffers less degradation than does the optical transfer function τ . Note that even though, from (3.2), $< \tau >$ is real, this does not necessarily imply that $< \tau > = < \text{MTF} >$.

4. Asymptotic (Large Aperture) Approximations

The equations developed in Section 3 allow one, in principle, to calculate the first and second moments of the optical transfer function, τ, and the Strehl ratio, I/I_o. Indeed the expression (3.2) for $\langle\tau\rangle$ is explicit and needs no further comment. However, the calculation of σ_τ^2, R_τ, $\langle I/I_o \rangle$, and σ^2_{I/I_o} require multiple numerical integrations which can consume large amounts of computer time. Furthermore, the exact expressions tend to conceal the influence of variables like rms aberration, σ, and aperture size, D, on the parameter in question. Hence, in this section, we will develop approximations for the moment expressions derived in Section 3 for the case $D >> \ell_x$.

Consider first the average Strehl ratio; by (3.2) and (3.8), we have:

$$\langle I/I_o \rangle = (4/\pi) \int_{-\infty}^{\infty}\int \exp\left[-k^2\sigma^2[1-r(x,y)]\right] \tau_o(x,y)\,dxdy$$

$$= (4/\pi)\exp(-k^2\sigma^2) \int_{-\infty}^{\infty}\int \exp\left[k^2\sigma^2 r(x,y)\right] \tau_o(x,y)\,dxdy \quad (4.1)$$

Now expand the exponential part of the integrand in a Taylor series,

$$\exp\left[k^2\sigma^2 r(x,y)\right] = \sum_{p=0}^{\infty} \frac{(k^2\sigma^2)^p}{p!} r^p(x,y) \ .$$

Then, substitution into (4.1) yields:

$$\langle I/I_o \rangle = \exp(-k^2\sigma^2) \left\{ 1 + \frac{4}{\pi} \sum_{p=1}^{\infty} \frac{(k^2\sigma^2)^p}{p!} \iint_{-\infty}^{\infty} r^p(x,y)\,\tau_o(x,y)\,dx\,dy \right\}. \tag{4.2}$$

The expression (4.2) is exact; no approximations have yet been made.

Now let's assume that r is of the form*

$$r(x,y) = \exp\left[- \sqrt{(D/\ell_x)^2 x^2 + (D/\ell_y)^2 y^2} \right]. \tag{4.3}$$

We will consider the limit $D/\ell_x \uparrow \infty$ while ℓ_x/ℓ_y remains constant. Then (4.3) can be rewritten

$$r(x,y) = \exp\left[- (D/\ell_x)\sqrt{x^2 + (\ell_x/\ell_y)^2 y^2} \right]. \tag{4.4}$$

Clearly, as D/ℓ_x grows larger, the graph of r(x,y) becomes narrower. In fact, it is an easy matter to verify (keeping in mind that the volume under the delta function $\delta(x,y)$ is unity) that

$$r^p(x,y) \sim \frac{2\pi}{p^2 (D/\ell_x)(D/\ell_y)}\ \delta(x,y) \tag{4.5}$$

as $D/\ell_x \uparrow \infty$, for any $p > 0$. The details of derivation of (4.5) can be found in the appendix.

Substitution of (4.5) into (4.2) gives

$$\langle I/I_o \rangle \sim \exp(-k^2\sigma^2) \left\{ 1 + \frac{4}{\pi} \sum_{p=1}^{\infty} \frac{(k^2\sigma^2)^p}{p!} \frac{2\pi}{p^2 (D/\ell_x)(D/\ell_y)} \iint_{-\infty}^{\infty} \delta(x,y)\,\tau_o(x,y) \right\}$$

---

*This requires either that the scale lengths ℓ_x and ℓ_y be constant or that $\ell_x(u)$ and $\ell_y(u)$ be replaced by average values in (2.8).

$$= \exp\,(-k^2\sigma^2)\left\{1 + \frac{8}{(D/\ell_x)(D/\ell_y)} \sum_{p=1}^{\infty} \frac{(k^2\sigma^2)^p}{p^2 p!}\right\} \qquad (4.6)$$

as $D/\ell_x \uparrow \infty$. Since the sum occurring in (4.6) will appear again, let us define

$$F(x) = \sum_{p=1}^{\infty} \frac{x^p}{p^2 p!} \quad . \qquad (4.7)$$

(Note that this sum is convergent for all x.) Then, from (4.6), we have

$$\langle I/I_o \rangle \sim \exp\,(-k^2\sigma^2)\left\{1 + \frac{8}{(D/\ell_x)(D/\ell_y)} F(k^2\sigma^2)\right\} \qquad (4.8)$$

as $D/\ell_x \uparrow \infty$. (For reference, the function F has been graphed over an interval of x sufficient for most conceivable aberrations; see Figure 2.) It might be observed that the second term of (4.8) can be viewed as the contribution from what Hogge and his colleagues called the incoherent beam [19]. They concluded that for a phase-aberrated beam, the far-field irradiance distribution can be written as the sum of two beams; one beam is the diffraction limited beam attenuated by the factor $\exp\,(-k^2\sigma^2)$ and the other beam is much wider and contributes an amount, on-axis, proportional to the second term of (4.8).

We turn our attention now to the variance of the optical transfer function. From (3.4) and (3.5), we have

$$\sigma_\tau^2(x,y) = \tau_{att}^2(x,y)(4/\pi)^2 \iint_{A_{x,y}} \iint_{A_{x,y}} \left\{\exp\left[-k^2\sigma^2\, g(\xi,\eta,\xi',\eta')\right] - 1\right\} d\xi\, d\eta\, d\xi'\, d\eta', \qquad (4.9)$$

where

$$g(\xi,\eta,\xi',\eta') = r(u+x,v+y) - 2r(u,v) + r(u-x,v-y)$$

$$u = \xi' - \xi$$

$$v = \eta' - \eta \quad .$$

Following the procedure adopted in the analysis of $\langle I/I_o \rangle$, we expand the exponential in the integrand in a Taylor series and (4.9) becomes:

$$\sigma_\tau^2(x,y) = \tau_{att}^2(x,y)\,(4/\pi)^2 \sum_{p=1}^{\infty} \frac{(-1)^p (k^2\sigma^2)^p}{p!} \iiint_{A_{x,y}} \iint_{A_{x,y}} g^p(\xi,\eta,\xi',\eta')\, d\xi\, d\eta\, d\xi'\, d\eta'. \tag{4.10}$$

The expression (4.10) is exact but not very useful as it stands. It remains to estimate the 4-dimensional integral in the case $D >> \ell_x$.

Again we assume that the correlation function r is of the form (4.3) and note that it approximates a delta function as $D/\ell_x \uparrow \infty$. Specifically, we have the asymptotic approximation given by (4.5). Hence, each of the three terms in g (defined by (4.9) approach a delta function in shape. But, if $(x,y) \neq (0,0)$, each delta function is centered at a different point in the u-v plane. In this case, cross terms in the product g^p can be neglected and we have

$$g^p(\xi,\eta,\xi',\eta') \approx r^p(u+x,\, v+y) + (-1)^p 2^p r^p(u,v) + r^p(u-x,\, v-y)$$

$$\sim \frac{2\pi}{p^2 (D/\ell_x)(D/\ell_y)} \left[\delta(u+x,v+y) + (-1)^p 2^p\, \delta(u,v) + \delta(u-x,v-y) \right], \tag{4.11}$$

as $D/\ell_x \uparrow \infty$. Note that this approximation is least accurate near $(x,y) = (0,0)$. Substitution of (4.11) into (4.10) gives

$$\sigma_\tau^2(x,y) \sim \tau_{att}^2(x,y)\left(\frac{4}{\pi}\right)^2 \frac{2\pi}{(D/\ell_x)(D/\ell_y)} \sum_{p=1}^{\infty}\left\{\frac{(-1)^p(k^2\sigma^2)^p}{p^2 p!}\right. \tag{4.12}$$

$$\left. \iiiint_{A_{x,y}\,A_{x,y}} \left[\delta(u+x,v+y)+(-1)^p 2^p\ \delta(u,v)+\delta(u-x,v-y)\right] d\xi d\eta d\xi' d\eta' \right\} .$$

It remains to evaluate the integral.

We proceed now to analyze the first integral of (4.12). The remaining two will follow directly. We have

$$\iiiint_{A_{x,y}\,A_{x,y}} \delta(u+x,v+y)\ d\xi d\eta d\xi' d\eta'$$

$$= \int_{-\infty}^{\infty}\iiint G_o(\xi+\tfrac{x}{2},\eta+\tfrac{y}{2})G_o(\xi-\tfrac{x}{2},\eta-\tfrac{y}{2})G_o(\xi'+\tfrac{x}{2},\eta'+\tfrac{y}{2})G_o(\xi'-\tfrac{x}{2},\eta'-\tfrac{y}{2})$$
$$\delta(u+x,v+y)\ d\xi d\eta d\xi' d\eta'$$

$$= \int_{-\infty}^{\infty}\iint G_o(\xi+\tfrac{x}{2},\eta+\tfrac{y}{2})G_o(\xi-\tfrac{x}{2},\eta-\tfrac{y}{2})\ G_o(\xi-\tfrac{3x}{2},\eta-\tfrac{3y}{2})\ d\xi d\eta \ , \tag{4.13}$$

where G_o is the unaberrated pupil function; i.e.

$$G_o(x,y) = \begin{cases} 1, & \sqrt{x^2+y^2} \le 1/2 \\ 0, & \sqrt{x^2+y^2} > 1/2 \end{cases} .$$

From Figure 3, it can be seen that (4.13) is just the area of intersection of three circles of unit diameter. In fact, the middle circle contributes nothing, and we can rewrite (4.13) as follows:

$$\iint_{A_{x,y}} \iint_{A_{x,y}} \delta(u+x,\ v+y)\, d\xi d\eta d\xi' d\eta' = \iint_{-\infty}^{\infty} G_o(\xi+\tfrac{x}{2}, \eta+\tfrac{y}{2})\, G_o(\xi-\tfrac{3x}{2}, \eta-\tfrac{3y}{2})\ d\xi d\eta$$

$$= \tfrac{\pi}{4}\, \tau_o(2x,2y)\ . \qquad (4.14)$$

The remaining integrals in (4.12) can be evaluated similarly and we find:

$$\sigma_\tau^2(x,y) \sim \frac{8}{(D/\ell_x)\ (D/\ell_y)}\, \tau_{att}^2(x,y) \left[F(2k^2\sigma^2)\, \tau_o(x,y) + 2F(-k^2\sigma^2)\, \tau_o(2x,2y) \right], \qquad (4.15)$$

as $D/\ell_x \uparrow \infty$, where F is given by (4.7).

One could conceivably carry out analogous arguments to estimate R_τ and hence σ^2_{I/I_o} . However this was not attempted.

5. Conclusions

In order to judge the accuracy of the asymptotic approximations derived in Section 4, those expressions and the corresponding exact results from Section 3 have been calculated for several values of phase aberration σ/λ and aperture size D/ℓ_x. These calculations were carried out on a Burroughs 6800 digital computer.

Figure 4 illustrates the variation of average Strehl ratio with D/ℓ_x for three phase aberrations. The exact Strehl ratio was calculated from (3.8) and (3.2) using, successively, Simpson's rule and the four-point Gaussian quadrature formula to evaluate the double integral. Note that if $D \ll \ell_x$, the optics are essentially insensitive to the turbulent layer. Then, as D/ℓ_x grows larger, the average Strehl ratio decreases to an asymptote determined by the aberration σ/λ. It is clear from Figure 4 and (4.8) that the so-called "infinite aperture" (or zeroth order) approximation

$$< I/I_o > \sim \exp(-k^2\sigma^2)$$

is reasonably accurate for $D > 6\ell_x$. The first order correction (given by the second term of (4.8)) varies from about 3% for $\sigma/\lambda = 0.08$ to 22% for $\sigma/\lambda = 0.2$ when $D = 6\ell_x$.

It is appropriate here to relate the expression for $< I/I_o >$ given by (4.8) to the work of Hogge, Butts, and Burlakoff [19]. In obtaining (4.8) from (4.1), the exponential term $\exp[k^2\sigma^2\, r(x,y)]$ was expanded in a power series. In [19], only the first two terms of this series were retained, thus limiting the validity of those results

to σ/λ no larger than about 0.1. No such limitation applies to the results derived here. On the other hand, Hogge, et al, reached important conclusions regarding the shape of the focal plane irradiance distribution (discussed in Section 4), whereas the spatial distribution of irradiance has not been considered here.

Figures 5, 6, and 7 illustrate the correspondence between the exact (Equation (3.5)) and the approximate (Equation (4.15)) values of σ_τ for successively larger D/ℓ_x (3,6, and 10) with $\sigma/\lambda = 0.2$. The exact expression (3.5) was evaluated using a Monte Carlo technique to approximate the four-dimensional integration. As expected, agreement is best for $D/\ell_x = 10$. In fact, for this case, the accuracy of the Monte Carlo method employed to evaluate (3.5) is questionable and, hence, given the inherent computational errors, the exact and approximate values of σ_τ can be said to agree. It is clear, especially from Figure 5, that

$$\sigma_\tau \text{ (approx.)} \uparrow \infty \text{ as } x/D \downarrow 0.$$

This anomaly is the result of the assumption that (x,y) is not near (0,0) which leads to (4.11).

The work described here suggests further research toward understanding the second-order statistics of the optical parameters I/I_o and τ, namely:

1. It is desirable to obtain approximations for R_τ and σ_{I/I_o}. Since the exact expression for these parameters involve complicated four-dimensional integrations, an approximate (closed form) expression would be especially useful. An

analysis similar to that described in this paper might prove fruitful.

2. Perhaps by obtaining higher order asymptotic ($D/\ell_x \uparrow \infty$) approximations to $< I/I_o >$ and σ_τ, better accuracy can be achieved for smaller values of D/ℓ_x. This would require a more accurate description of the aberration correlation $r(x,y)$ than the δ-function analysis provides.

3. Finally, the experimental data tends to substantiate the mathematical model employed here. For example, see Reference 13 for a discussion of the aperture scaling inferred by Figure 4. Also, a comparison can be made between the data and the expression for $< \tau >$ given by (3.2). However, there has been very limited effort expended to compute σ_{I/I_o} from measured data and virtually no attempt to compute σ_τ. Since these calculations can be accomplished routinely by modifying existing data reduction codes, it is strongly urged that this information be provided in future reports of experimental data.

APPENDIX

The defining properties of the two-dimensional delta function, $\delta(x-x_o, y-y_o)$, are as follows:

$$\int_{-\infty}^{\infty}\int_{-\infty}^{\infty} f(x,y)\ \delta(x-x_o, y-y_o)\ dx\ dy = f(x_o,y_o)$$

$$\delta(x-x_o, y-y_o) = 0, \quad (x,y) \neq (x_o,y_o).$$

Although no ordinary function can satisfy these requirements, it is possible to construct sequences of functions, $S_k(x-x_o, y-y_o)$, which approach the symbolic "function" $\delta(x-x_o, y-y_o)$ as $k \uparrow \infty$.
In particular, if

$$\int_{-\infty}^{\infty}\int_{-\infty}^{\infty} S_k(x-x_o, y-y_o)\ dx\ dy = 1,$$

for every k, and

$$\lim_{k\uparrow\infty} S_k(x-x_o, y-y_o) = 0, \quad (x,y) \neq (x_o,y_o),$$

then we say that

$$\lim_{k\uparrow\infty} S_k(x-x_o, y-y_o) = \delta(x-x_o, y-y_o).$$

Now, consider the function

$$r^p(x,y) = \exp\left(- p\sqrt{(D/\ell_x)^2x^2 + (D/\ell_y)^2y^2} \right).$$

Then, after transforming from rectangular coordinates (x,y) to elliptic coordinates (r,θ), where

$$r^2 = (D/\ell_x)^2 x^2 + (D/\ell_y)^2 y^2,$$

we have

$$\iint_{-\infty}^{\infty} r^p(x,y)\, dx\, dy = \int_0^{2\pi} \frac{d\theta}{(D/\ell_x)^2 \cos^2\theta + (D/\ell_y)^2 \sin^2\theta} \int_0^{\infty} e^{-pr}\, r\, dr$$

$$= \frac{2\pi}{p^2 (D/\ell_x)(D/\ell_y)} .$$

Then, it follows that

$$\lim_{(D/\ell_x)\uparrow\infty} \frac{p^2 (D/\ell_x)(D/\ell_y)}{2\pi}\, r^p(x,y) = \delta(x,y) .$$

REFERENCES

[1] H.G. BOOKER and W.E. GORDON, A Theory of Radio Scattering in the Troposphere, Proc. I.R.E., 38(1950), pp. 401-412.

[2] H.A. STINE and W. WINOVICH, Light diffusion through high-speed turbulent boundary layers, NACA RM A56B21, 1956.

[3] G.W. SUTTON, On optical imaging through aircraft turbulent boundary layers, AMP 334, Avco Everett Research Laboratory, 1971.

[4] R.E. HUFNAGEL AND N.R. STANLEY, Modulation transfer function associated with image transmission through turbulent media, J. Opt. Soc. Am., 54(1964), pp. 52-61.

[5] D.L. FRIED, Optical resolution through a randomly inhomogeneous medium for very long and very short exposures, J. Opt. Soc. Am., 56(1966), pp. 1372-1379.

[6] _____ , Limiting resolution looking down through the atmosphere, J. Opt. Soc. Am., 56(1966), pp. 1380-1384.

[7] _____ and J.D. CLOUD, Propagation of an infinite plane wave in a randomly inhomogeneous medium, J. Opt. Soc. Am., 56(1966), pp. 1667-1676.

[8] _____ , Propagation of a spherical wave in a turbulent medium, J. Opt. Soc. Am., 57(1967), pp. 175-180.

[9] D.J. WOLTERS, Aerodynamic effects on airborne optical systems, MDC A2582, McDonnell Douglas Corporation, 1973.

[10] P. CHOW, Perturbation methods in stochastic wave propagation, SIAM Review, 17(1975), pp. 57-81.

[11] M. BORN and E. WOLF, Principles of Optics, 5th edition, Pergamon Press, 1975.

[12] A. PAPOULIS, Probability, Random Variables, and Stochastic Processes, McGraw-Hill, 1965.

[13] K. GILBERT, Aircraft aero-optical turbulent boundary-layer/shear-layer measurements, Laser Digest, AFWL-TR-78-15(1978), pp. 154-176.

[14] W.C. ROSE, Measurements of aerodynamic parameters affecting optical performance, AFWL-TR-78-191, 1979.

[15] R. BARAKAT, The influence of random wavefront errors on the imaging characteristics of an optical system, Optica Acta, 18(1971), pp. 683-694.

[16] E.L. O'NEILL, Introduction to Statistical Optics, Addison-Wesley, 1963.

[17] J.D. GASKILL, Linear Systems, Fourier Transforms, and Optics, Wiley, 1978.

[18] D. KELSALL, Interferometric evaluation of the imaging characteristics of laser beams propagated through the turbulent atmosphere, Photogr. Sci. Eng., 21(1977), pp. 123-129.

[19] C.B. HOGGE, R.R. BUTTS, and M. BURLAKOFF, Characteristics of phase-aberrated nondiffraction-limited laser beams, Applied Optics, 13(1974), pp. 1065-1070.

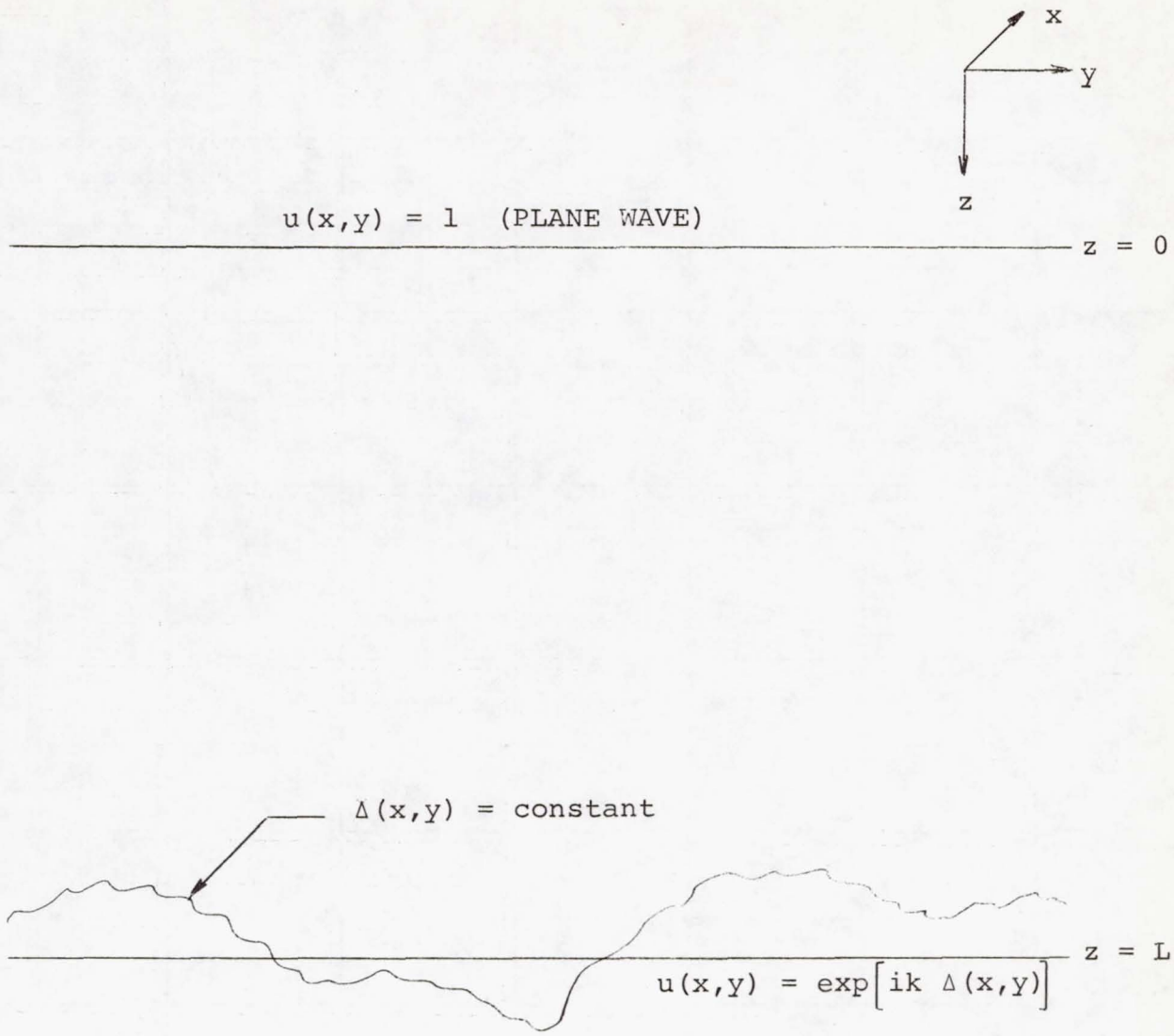

Figure 1. Phase-aberrated plane wave.

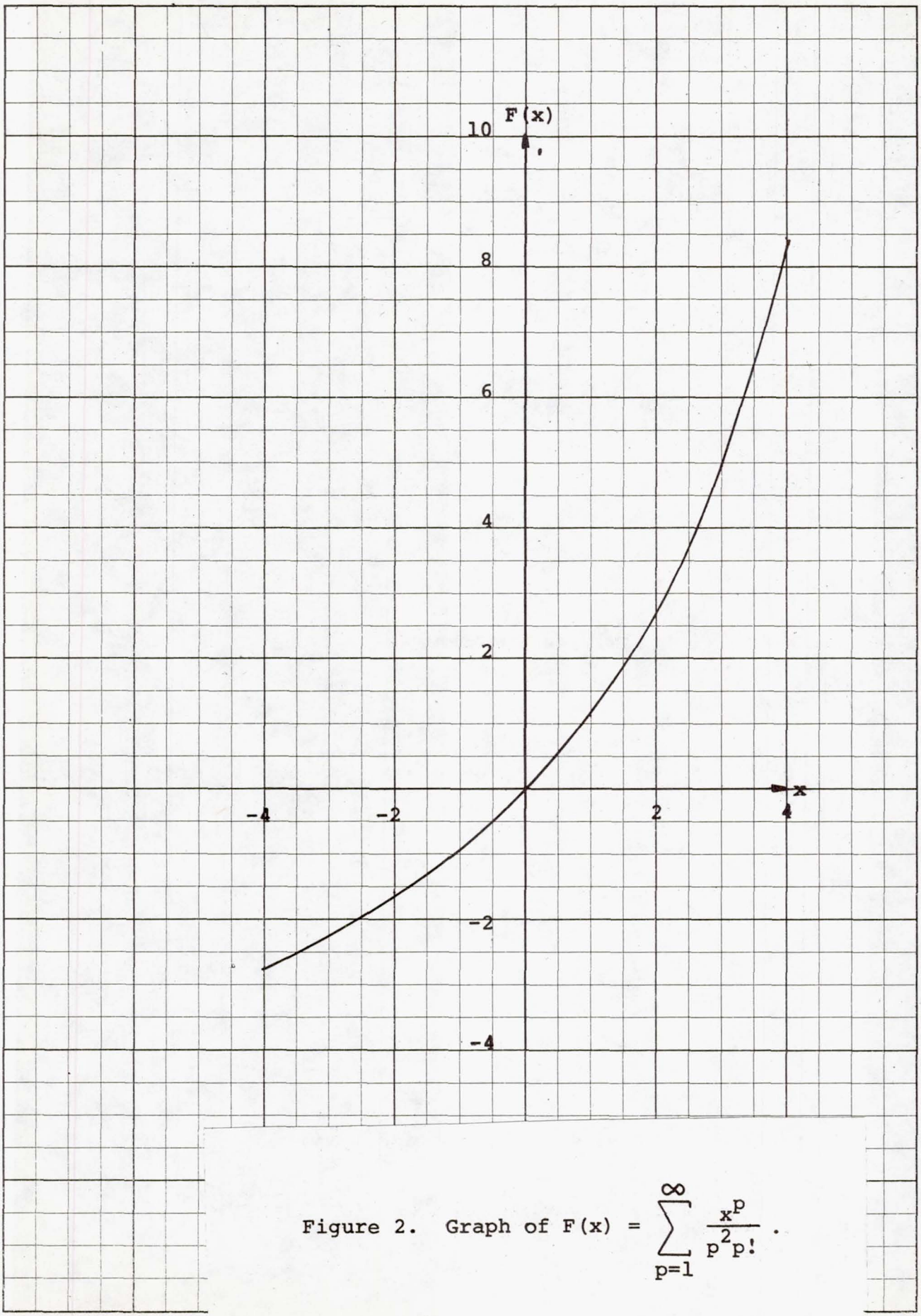

Figure 2. Graph of $F(x) = \sum_{p=1}^{\infty} \frac{x^p}{p^2 p!}$.

4 Squares
to the Inch

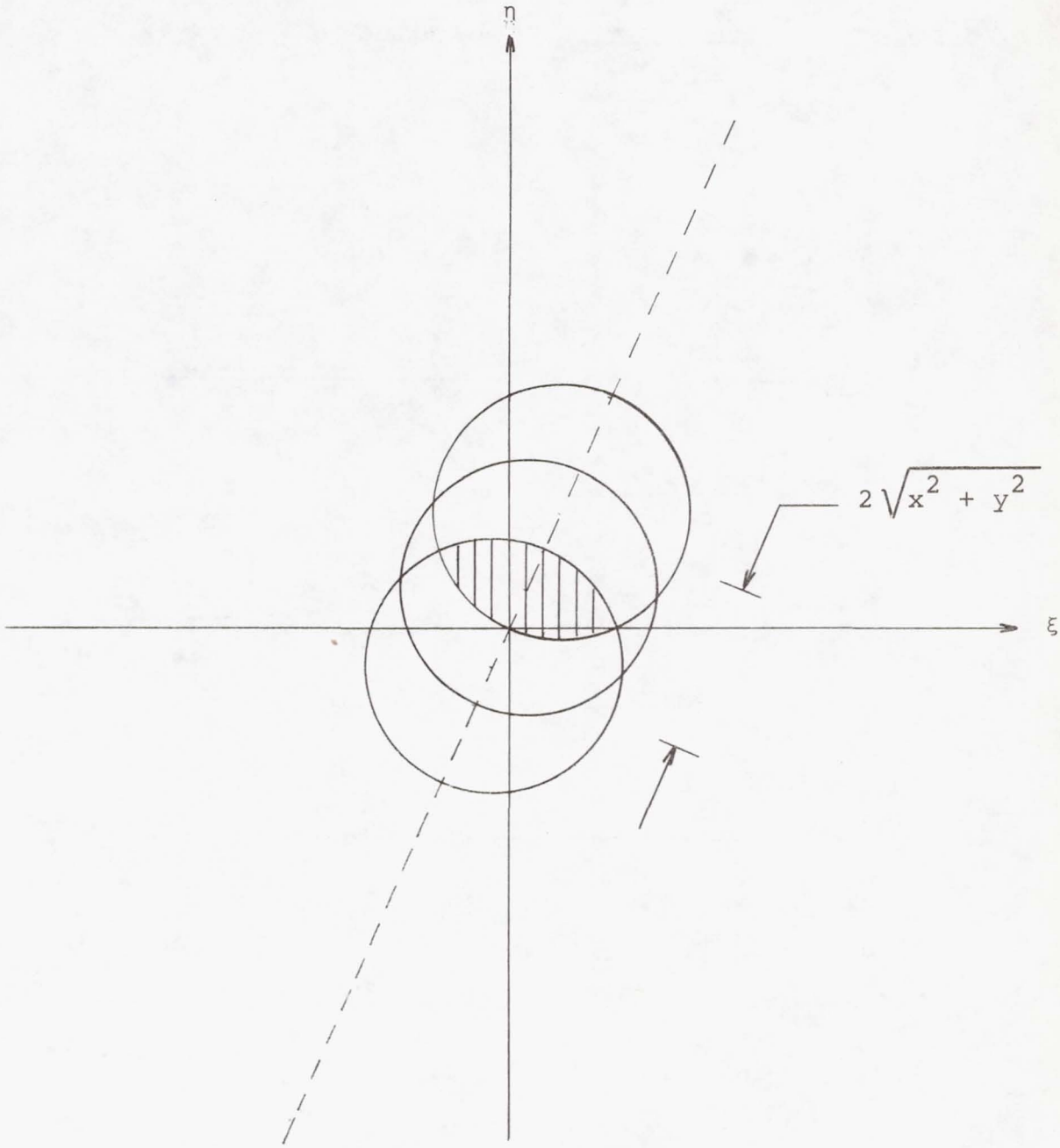

Figure 3. $\iint_{-\infty}^{\infty} G_0(\xi+\frac{x}{2},\eta+\frac{y}{2})\ G_0(\xi-\frac{x}{2},\eta-\frac{y}{2})\ G_0(\xi-\frac{3x}{2},\eta-\frac{3y}{2})\ d\xi\ d\eta$.

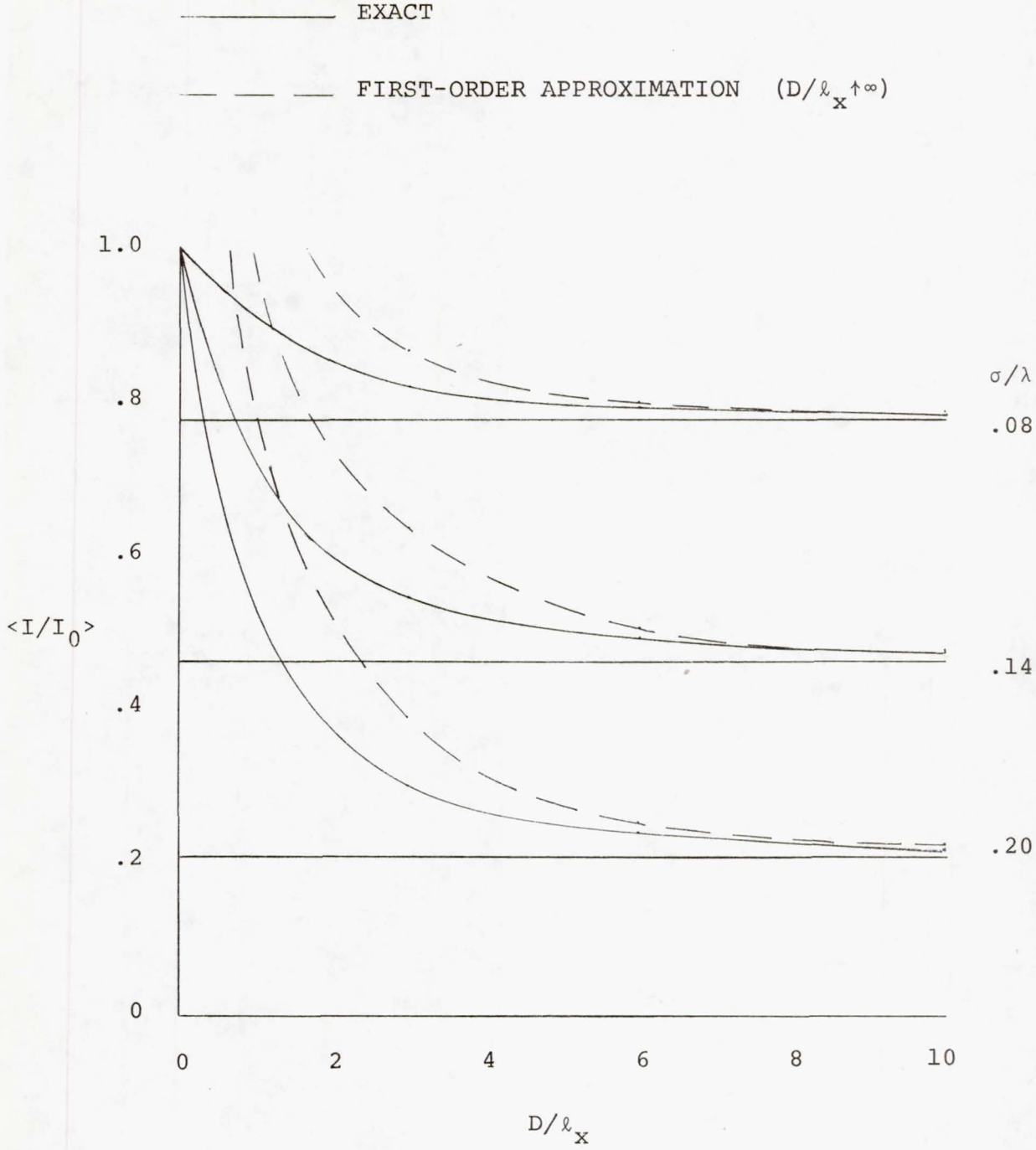

Figure 4. Variation of average Strehl ratio with aperture size ($\ell_x/\ell_y = 2$).

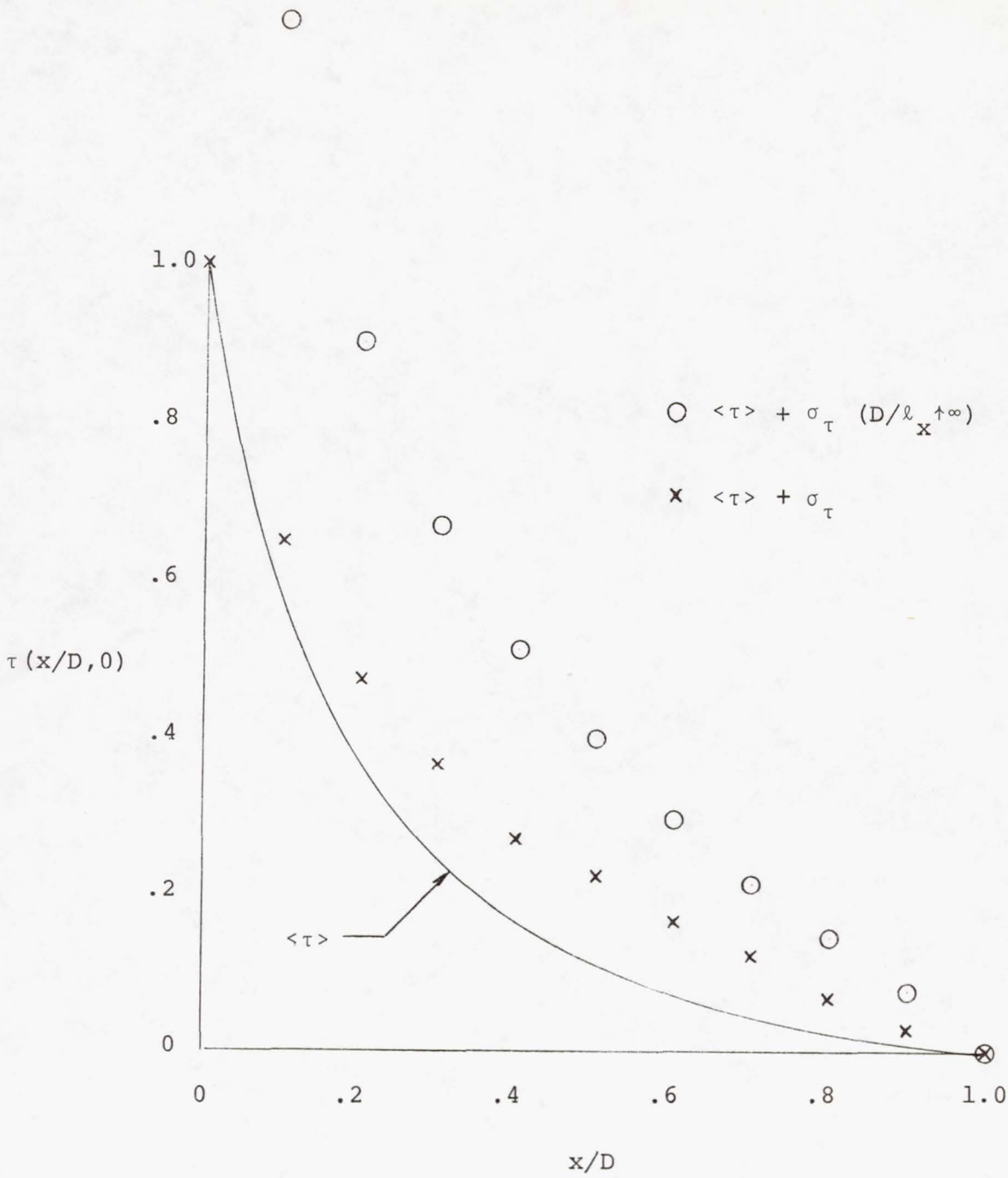

Figure 5. Second-order statistics of the optical transfer function for $D/\ell_x=3$ ($\ell_x/\ell_y=2$, $\sigma/\lambda=.2$).

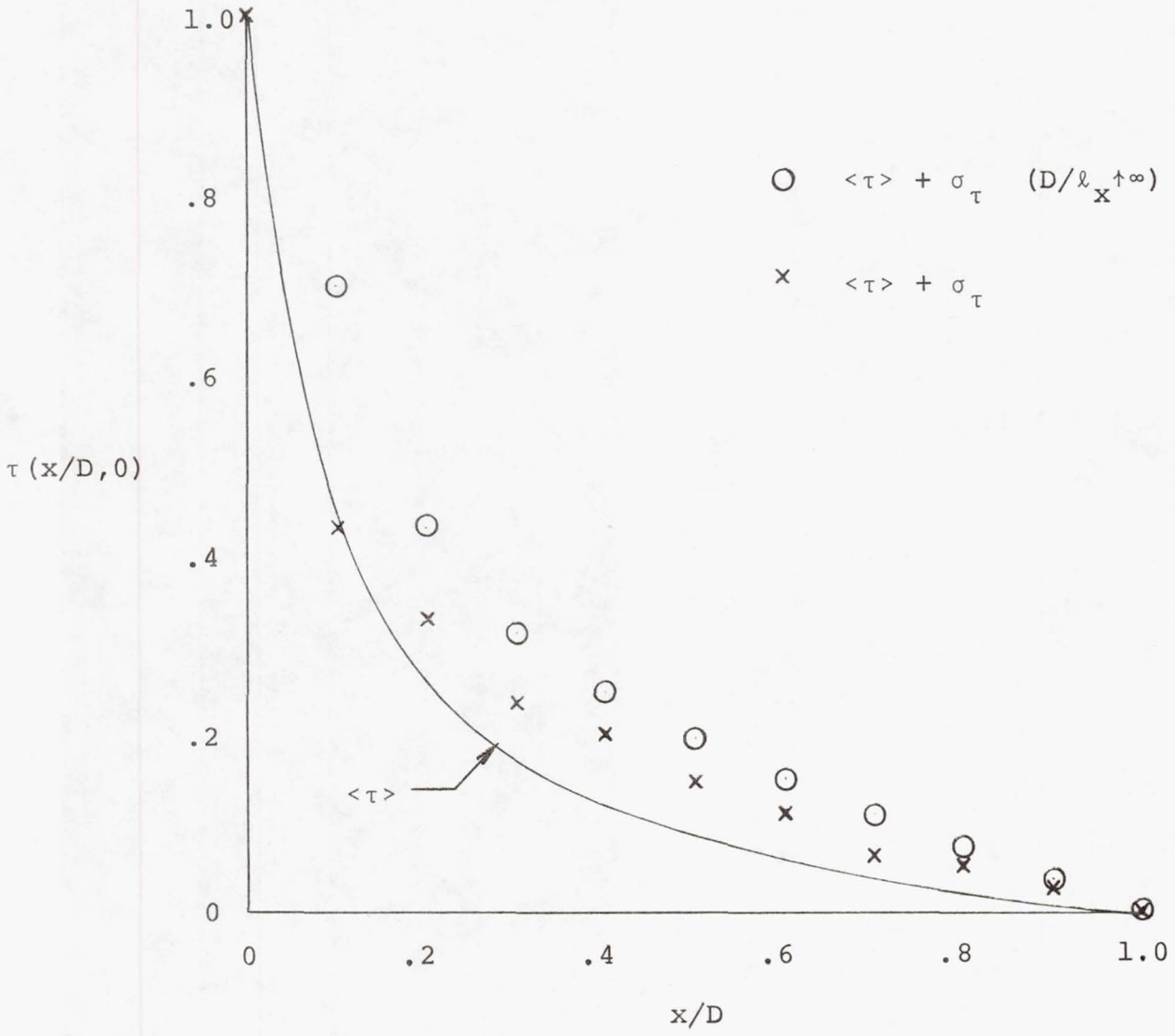

Figure 6. Second-order statistics of the optical transfer function for $D/\ell_x=6$ ($\ell_x/\ell_y=2$, $\sigma/\lambda=.2$).

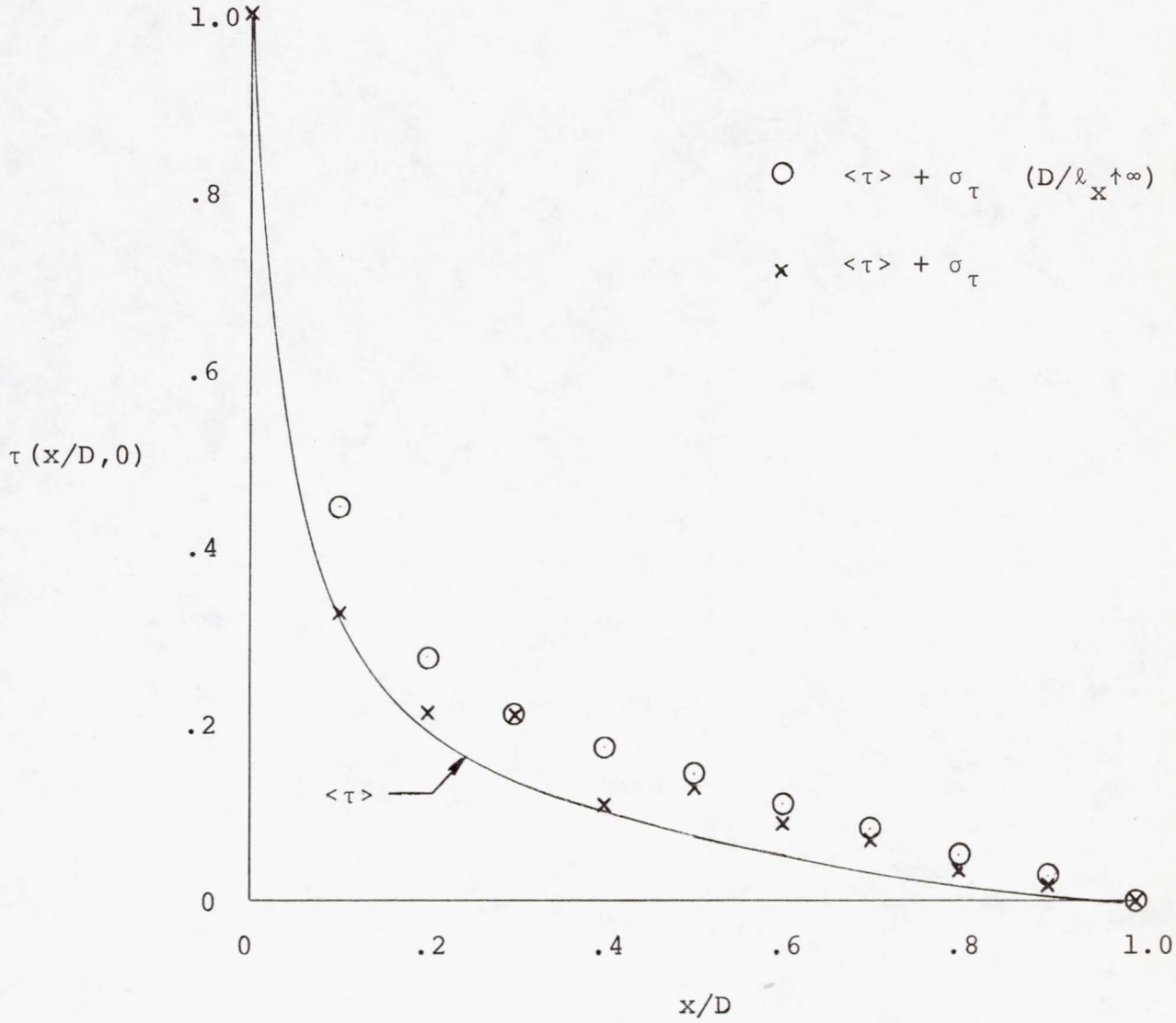

Figure 7. Second-order statistics of the optical transfer function for $D/\ell_x=10$ ($\ell_x/\ell_y=2$, $\sigma/\lambda=.2$).

OPTICAL PHASE DISTORTION DUE TO COMPRESSIBLE FLOW OVER LASER TURRETS

by

Allen E. Fuhs
Distinguished Professor
Naval Postgraduate School
Monterey, California, 93940

and

Susan E. Fuhs
Student, Chemical Engineering
California Institute of Technology
Pasadena, California, 91125

ABSTRACT

Compressible flow over a laser turret causes variation in density and the index of refraction. As a result, a laser beam develops a phase distortion. Phase distortion has been calculated for both blunt and small perturbation turrets. For the blunt turret, the Janzen-Rayleigh technique was used to determine the flow field. Phase distortions of 2.2 wavelengths at 3.8 microns were calculated for the blunt turret. For small perturbation turrets a versatile analytical model was developed for a turret on a fuselage with circular cross section. With a two-dimensional Fourier series representation of the turret, any shape can be considered. Both subsonic and supersonic flows can be calculated. Phase distortions of 1.2 wavelengths at 3.8 microns were calculated for one turret at high subsonic Mach number. In addition to being of value for laser turrets, the methods are applicable to reconnaissance aircraft using photographic equipment and cruise missiles using celestial navigation.

INTRODUCTION

Large scale laser telescopes are being installed aboard aircraft [1, 2]. Airflow over the laser turret causes density variations. Since the index of refraction depends on density, a phase distortion is generated as the beam

ACKNOWLEDGMENT. The work reported in this paper was funded by the Air Force Weapons Laboratory, Kirtland Air Force Base, NM. The effort was monitored by LtCol Keith Gilbert, Dr. Barry Hogge, and Captain Richard Cook.

propagates outward from the laser telescope. A phase distortion may tilt, defocus, or focus the beam. Higher-order aberrations, such as astigmatism and coma, may also occur.

Denote the characteristic geometric scale of the laser turret by ℓ. The diameter of the telescope aperture is D. The ratio D/ℓ tends to be much greater for laser installations than for other optical devices commonly installed on board aircraft. As an example, consider the pilot's eye. For this case, ℓ is the size of the canopy, and D is several millimeters. The pilot does not experience optical distortion due to the small value of D/ℓ.

Laser turrets tend to differ from camera installations aboard reconnaissance aircraft [3]. Due to the large size of D and the desire to have wide angular coverage, laser turrets protrude into the airstream. Camera installations usually have flat windows which are flush mounted in the fuselage. Furthermore, camera apertures may be considerably less than laser apertures. As a result of these two facts, degradation of photographic image quality usually is not a serious problem. However, in the event of image degradation, the methods of this paper could be applied to remove distortions.

Cruise missiles with intercontinental ranges may use celestial navigation which requires precise measurement of angular location of stars. A distorted lens created by the ambient flow field causes an error in measurement. Knowledge of the external aerodynamics is important [3].

Optical distortion due to the external flow field can be divided into two categories [4]. Viscous flow phenomena fall into one category and include shear layers, laminar and turbulent boundary layers, and the shedding of discrete vortices. The other category involves the external inviscid flow field. Based on the preceding discussion, the reader recognizes that this paper treats the latter category.

Laser turrets can be classified as either blunt or small perturbation turrets. If a turret has a surface with a normal vector, $\vec{n}$, aligned parallel or nearly so, to the freestream velocity vector, $\vec{V}_\infty$, the turret is "blunt." If the angle between the normal vectors of the turret surface and the freestream velocity is everywhere large, e.g., 60^o to 90^o, then the turret is "small-perturbation." Both types of laser turrets are discussed in this paper.

BACKGROUND INFORMATION

Critical Mach Number

A useful concept is the critical Mach number, M^*_∞. At the critical Mach number, somewhere on the body a local Mach number is sonic. When $M_\infty > M^*_\infty$, the flow becomes inherently nonlinear and shock waves appear. The transonic flow equations must be solved when $M_\infty \cong M^*_\infty$. The occurrence of shock waves usually implies severe degradation of the laser beam quality.

The critical Mach numbers for several body geometries are listed in Table I. One advantage of the solution developed later in this paper is the fact that the critical Mach number can be calculated. Results are shown in Table I for a cosine shaped turret which will be discussed in more detail in the section Turret on a Circular Fuselage: Subsonic Flow.

Laser Turret Map

Different analytical models must be developed for different laser turret geometries. A map can be drawn showing the various flow regions for the different turret geometries. Figure 1 is a laser turret map. The abscissa is the freestream Mach number, M_∞. The ordinate is the maximum slope of the turret. Various regions are defined by capital letters.

The flow within region ABCD can be described with sufficient accuracy using the linearized small perturbation equations. The line CD represents the

Table I. Critical Mach Numbers for Several Geometric Shapes

Body Shape	Ratio ε/R_0	Critical Mach Number
Circular cylinder with axis normal to flow [5]	-	0.3985
Sphere [5]	-	0.5868
Hemisphere-cylinder with cylinder axis parallel to flow [6,7]	-	< 0.7
Cosine shaped turret on circular fuselage [3]	0.05	0.88
	0.10	0.82
	0.15	0.76
	0.20	0.72
	0.25	0.68
	0.30	0.65

ε = amplitude or maximum height of turret

R_0 = radius of circular fuselage

turret length/fuselage radius ratio = 1.005

critical Mach number. The line BC is shown at a slope of 30^{o}. The assumptions involved in the linearization of the potential flow equation become less and less valid as the maximum slope increases. The region CDJ, which resembles an inverted triangle, requires solution of the nonlinear, small perturbation, transonic, potential flow equation.

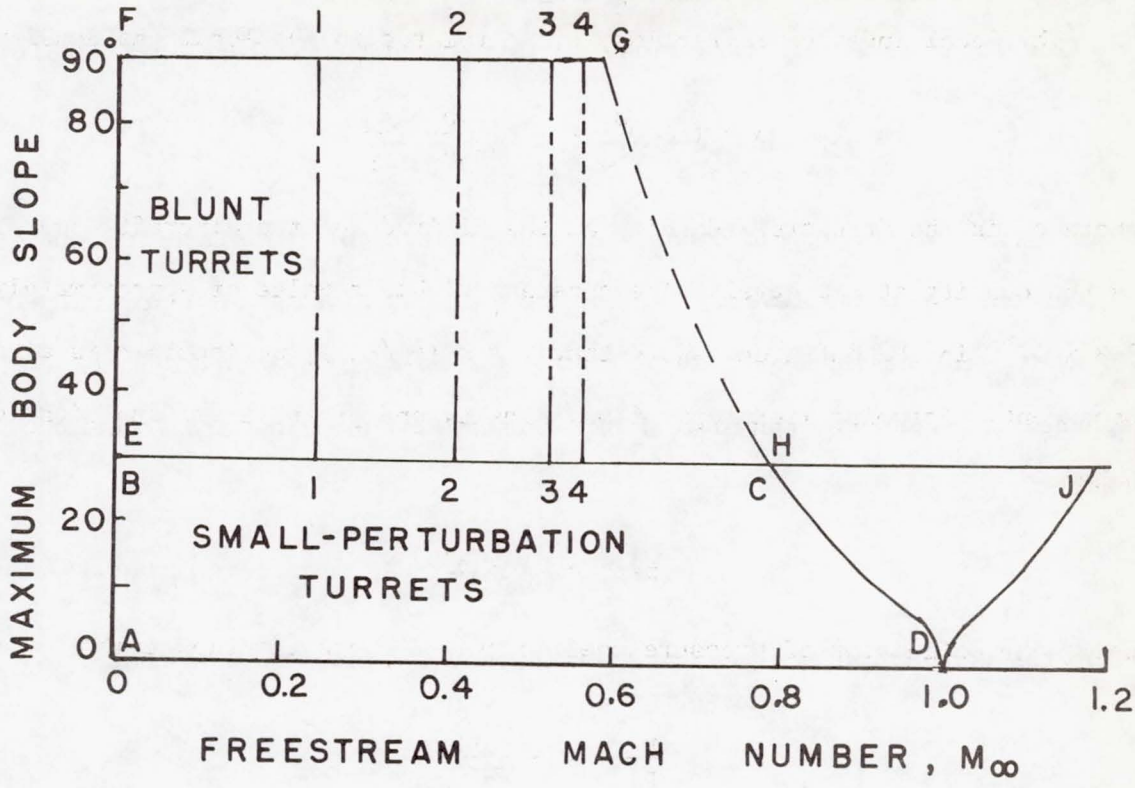

Figure 1. Freestream Mach Number Regions for Application of Various Analytical Models.

EFGH defines the region where the solution to the blunt-body nonlinear flow equations is necessary. The line GH, which defines the critical Mach number, is shown dashed; the critical Mach number is a function of turret shape. Hence GH is intended to suggest qualitatively the upper bound for Mach number for blunt turrets. Within region EFGH the Janzen-Rayleigh [5,8,9,10] technique is most useful.

Vertical lines 1, 2, 3, and 4 occur within region EFGH. These lines represent the upper bound of applicability of the first, second, third, and fourth-order solutions when the Janzen-Rayleigh technique is used. The first-order solution may be applied with region F11E; the second-order solution, within F22E; etc. The hemispherical turret considered in the following section is an example of a turret falling along line FG.

Phase Distortion, Index of Refraction and Pressure Coefficient

The local index of refraction, n, is related to the local gas density, ρ, by

$$n = 1 + \kappa\frac{\rho}{\rho_\infty} = 1 + \kappa'\frac{\rho}{\rho_\infty}\frac{\rho_\infty}{\rho_{SL}} \tag{1}$$

where ρ_∞ is the freestream density at the altitude of the aircraft, and ρ_{SL} is the density at sea level. The constant κ' has a value of approximately 2.3×10^{-4} in the infrared. Note that $\kappa = \kappa'(\rho_\infty \not{\rho} \rho_{SL})$; obviously κ is altitude dependent. Assuming isentropic flow, density and pressure are functions of each other

$$p/p_\infty = (\rho/\rho_\infty)^\gamma \tag{2}$$

Using the definition of pressure coefficient, C_p, one can show that

$$\frac{p}{p_\infty} = 1 + \frac{\gamma M_\infty^2 C_p}{2} \tag{3}$$

In equations (2) and (3) γ is the ratio of heat capacities, and M_∞ is the freestream Mach number. Combining equations (1) to (3) yields

$$n = 1 + \kappa'\frac{\rho_\infty}{\rho_{SL}}\left(1 + \frac{\gamma M_\infty^2 C_p}{2}\right)^{1/\gamma} \tag{4}$$

Since C_p may be positive or negative, n may be increased or decreased by the flow.

Optical path length, L, is defined as

$$L_i = \int_a^b n(s)\,ds \tag{5}$$

where s is the distance along a ray, and points a and b are positioned on the ray. The index of refraction n is a function of s. The subscript i identifies a particular ray within the laser beam. The difference in optical path length between two rays i and j is

$$\Delta L = L_j - L_i = \int_a^b [n(s_j) - n(s_i)]ds \tag{6}$$

The optical path length has the dimensions of length, e.g., meter; to make L nondimensional, the wavelength of radiation, λ, can be used as a reference. The ratio $\Delta L/\lambda$ is known as the phase distortion P. Combining equations (4) and (6) gives a formula for P,

$$P = \frac{K'}{\lambda} \frac{\rho_\infty}{\rho_{SL}} R_0 \int_0^\infty \left(1 + \frac{\gamma M_\infty^2 C_p}{2}\right)_j^{\frac{1}{\gamma}} - \left(1 + \frac{\gamma M_\infty^2 C_p}{2}\right)_i^{\frac{1}{\gamma}} d\left(\frac{s}{R_0}\right) \tag{7}$$

Equation (7) shows the dependence on altitude. The solutions for the various flow fields give values of C_p.

Zernike Polynomials

A wavefront shape or the same thing, the phase distortion, can be expressed in terms of Zernike polynomials [11]. Equations (8) through (17) can be found in the paper by Hogge and Butts [12].

$$F_1(r) = \left(\frac{1}{\pi R^2}\right)^{1/2}, \quad \text{(uniform phase shift)} \tag{8}$$

$$\left.\begin{aligned} F_2(r) &= \left(\frac{4}{\pi R^4}\right)^{1/2} x, \\ F_3(r) &= \left(\frac{4}{\pi R^4}\right)^{1/2} y, \end{aligned}\right\} \quad \text{(tilt)} \tag{9, 10}$$

$$F_4(r) = \left(\frac{12}{\pi R^6}\right)^{1/2} \left(x^2 + y^2 - \frac{R^2}{2}\right), \quad \text{(refocus)} \tag{11}$$

$$\left.\begin{aligned} F_5(r) &= \left(\frac{6}{\pi R^6}\right)^{1/2} (x^2 - y^2), \\ F_6(r) &= \left(\frac{24}{\pi R^6}\right)^{1/2} (xy), \end{aligned}\right\} \quad \text{(astigmatism)} \tag{12, 13}$$

$$F_7(r) = \left(\frac{8}{\pi R^8}\right)^{1/2} (x^3 - 3xy^2), \tag{14}$$

$$F_8(r) = \left(\frac{8}{\pi R^8}\right)^{1/2} (y^3 - 3yx^2), \tag{15}$$

$$F_9(r) = \left(\frac{8}{\pi R^8}\right)^{1/2} (3x^2 + 3y^2 - 2R^2)x, \tag{16}$$

$$F_{10}(r) = \left(\frac{8}{\pi R^8}\right)^{1/2} (3x^2 + 3y^2 - 2R^2)y. \tag{17}$$

(coma)

The Zernike polynomials are an orthonormal set of functions over an aperture of radius R. The phase distortion can be represented as

$$P = \sum_{j=1}^{10} A_j F_j(r) \tag{18}$$

where A_j is a constant which characterizes the phase distortion P. A_j is given by

$$A_j = \int_0^{2\pi} \int_0^R P(r,\theta) F(r,\theta) r dr d\theta \tag{19}$$

In equation (19) one could have used x and y as variables; however, use of θ and r is more appropriate for a circular aperture.

Since the Zernike polynomials are related to the various aberrations, knowledge of the coefficients A_j indicates the magnitude of each aberration [12]. Further, the values of A_j are helpful for designing adaptive optics systems to overcome partially the aberrations.

BLUNT LASER TURRET

As an example of phase distortion due to compressible flow over a blunt turret, a hemispherical turret was selected [13,14]. Another shape amenable to analytical solution would be an ellipsoidal turret.

Janzen-Rayleigh Solution

The geometry is shown in Figure 2. A beam of radius R_b' is propagated from a turret of radius R. The elevation of the beam above the y-z plane is θ'. Distance along the beam is s. Points within a plane normal to the beam are located by coordinates R' and α. The windward and leeward sides of the laser beam can be determined from the flow arrow.

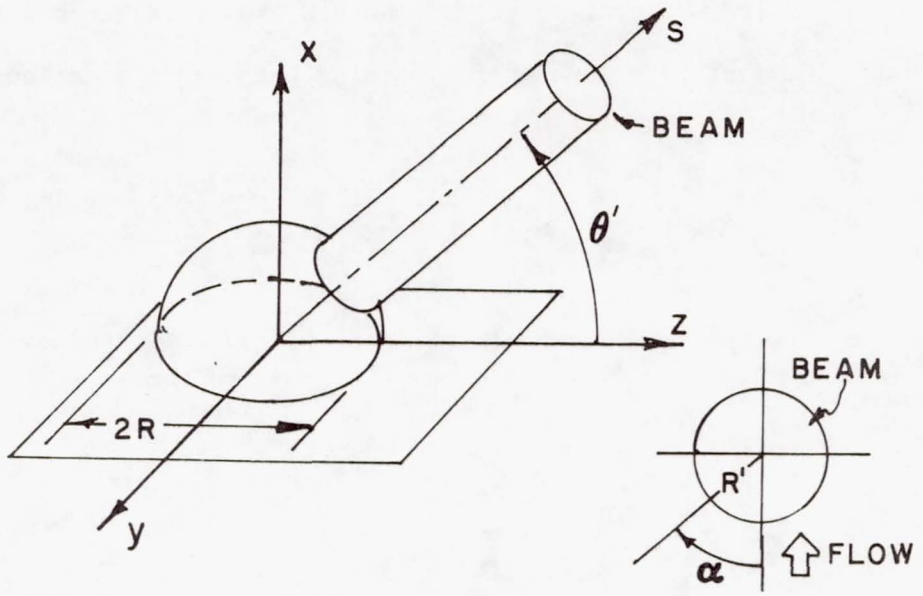

Figure 2. Geometry of Hemispherical Laser Turret Used for Phase Distortion Calculation.

In spherical coordinates, the equations of motion are as follows:

$$u \frac{\partial u}{\partial r} + \frac{v}{r} \frac{\partial u}{\partial \theta} - \frac{v^2}{r} = - \frac{1}{\rho} \frac{\partial p}{\partial r} = - \frac{a^2}{\rho} \frac{\partial \rho}{\partial r} \tag{20}$$

$$u \frac{\partial v}{\partial r} + \frac{v}{r} \frac{\partial v}{\partial \theta} + \frac{uv}{r} = - \frac{1}{\rho r} \frac{\partial p}{\partial \theta} = - \frac{a^2}{\rho r} \frac{\partial \rho}{\partial \theta} \tag{21}$$

$$\frac{1}{\rho}\left(u \frac{\partial \rho}{\partial r} + \frac{v}{r} \frac{\partial \rho}{\partial \theta}\right) + \frac{1}{r^2} \frac{\partial}{\partial r}(r^2 u) + \frac{1}{r \sin \theta} \frac{\partial}{\partial \theta}(v \sin \theta) = 0 \tag{22}$$

Equations (20) and (21) are Euler's equations; equation (22) is the continuity equation. For flow over a sphere, the azimuth angle is not a dependent variable. Multiplying equation (20) by + u/a^2 and equation (21) by - v/a^2, adding, and combining with equation (22) yields

$$\frac{1}{r^2}\frac{\partial}{\partial r}(r^2u) + \frac{1}{r \sin\theta}\frac{\partial}{\partial \theta}(v \sin\theta) = \frac{1}{a^2}\left(u^2\frac{\partial u}{\partial r} + \frac{uv}{r}\frac{\partial v}{\partial \theta} + uv\frac{\partial v}{\partial r} + \frac{v^2}{r}\frac{\partial v}{\partial \theta}\right) \quad (23)$$

The speed of sound, a, is the local value and changes from point to point in the flow. Variations in a must be accounted for. Using the energy equation along a streamtube, one can show that

$$\frac{a^2}{a_\infty^2} = 1 + \frac{\gamma - 1}{2}M_\infty^2\left(1 - \frac{u^2 + v^2}{U^2}\right) \quad (24)$$

Inviscid flow is considered. A potential function, ϕ, can be introduced for the velocity components

$$u = U\frac{\partial \phi}{\partial r} \quad (25)$$

and

$$v = \frac{U}{r}\frac{\partial \phi}{\partial \theta} \quad (26)$$

Combining equations (23) to (26) yields an equation in which the only dependent variable is ϕ.

The Rayleigh-Janzen expansion considers the potential function to be given as

$$\phi = \phi_0 + M_\infty^2\phi_1 + M_\infty^4\phi_2 + \ldots \quad (27)$$

The solution ϕ_0 is considered to be the first-order solution; the solution involving both ϕ_0 and ϕ_1 is termed the second-order solution. In this paper only the first and second-order solutions are discussed. For ease of writing, the following definition is introduced:

$$\psi = M_\infty^2\phi_1 \quad (28)$$

Substitution of ψ into the potential equation gives

$$\nabla^2\phi_0 + \nabla^2\psi = M_\infty^2\left(\phi_r\phi_{rr} + \frac{2}{r^2}\,\phi_r\phi_\theta\phi_{\theta r} - \frac{1}{r^3}\,\phi_\theta^2\phi_r + \frac{1}{r^4}\,\phi_\theta^2\phi_{\theta\theta}\right) \tag{29}$$

where <u>all</u> terms on the right-hand side are determined from the first-order potential function, ϕ_0. The result of equating coefficients of like powers in M_∞^2 yields two equations

$$\nabla^2\phi_0 = 0 \tag{30}$$

and

$$\nabla^2\psi = M_\infty^2\nabla^2\phi_1 = M_\infty^2\left(\phi_r^2\phi_{rr} + \frac{2}{r^2}\,\phi_r\phi_\theta\phi_{r\theta} - \frac{1}{r^3}\,\phi_\theta^2\phi_r + \frac{1}{r^4}\,\phi_\theta^2\phi_{\theta\theta}\right) \tag{31}$$

Equation (31) is Poisson's equation.

The first-order solution can be obtained from Milne-Thompson [15], Lamb [16], or Karamcheti [17]. It is

$$\phi_0 = U\left(r\cos\theta + \frac{R^3\cos\theta}{2r^2}\right) \tag{32}$$

Equation (32) can be used to evaluate the right-hand side of equation (29).

In July, 1916, Lord Rayleigh [10] reported the solution for the second-order function. The Legendre functions

$$P_1 = \cos\theta \tag{33}$$

and

$$P_3 = \frac{5}{3}\cos^3\theta - \frac{3}{2}\cos\theta \tag{34}$$

are introduced into equation (31). The result is

$$\nabla^2\phi_1 = \frac{U}{2}\left[\left(-\frac{36}{5}\,\frac{R^6}{r^7} + \frac{9}{2}\,\frac{R^9}{r^{10}}\right)P_1 + \left(6\,\frac{R^3}{r^4} - \frac{24}{5}\,\frac{R^6}{r^7} + \frac{3}{2}\,\frac{R^9}{r^{10}}\right)P_3\right] \tag{35}$$

Using the defining equation for the Legendre function, equation (35) can be solved to yield

$$\phi = \phi_0 + M_\infty^2 \phi_1 = \left[U\left(r + \frac{R^3}{2r^2}\right)P_1\right] + UM_\infty^2\left[\left(\frac{R^3}{3r^2} - \frac{R^6}{5r^5} + \frac{R^9}{24r^8}\right)P_1 + \left(-\frac{3R^3}{10r^2} + \frac{27R^5}{55r^4} - \frac{3R^6}{10r^5} + \frac{3R^9}{176r^8}\right)P_3\right] \tag{36}$$

Equation (36) can be inserted into equations (25) and (26) to find u and v. Knowing u and v, equation (24) can be evaluated. To evaluate equation (1) for n, one needs ρ/ρ_∞. Since the flow is isentropic

$$\frac{\rho}{\rho_\infty} = \left(\frac{1 + \frac{\gamma - 1}{2}M_\infty^2}{1 + \frac{\gamma - 1}{2}M^2}\right)^{\frac{1}{\gamma-1}} \tag{37}$$

The local Mach number is given by

$$M^2 = \frac{1}{a^2}\left[\left(\frac{\partial\phi}{\partial r}\right)^2 + \left(\frac{1}{r}\frac{\partial\phi}{\partial\theta}\right)^2\right] \tag{38}$$

Combining equations (1) and (36) through (38) with equation (5) allows calculation of the optical path length.

Geometry for Calculating Phase Distortion

Refer once again to Figure 2. The flow properties, e.g., density and Mach number, are functions of r and θ. These are polar coordinates. Consequently it is necessary to express r and θ in terms of θ', s, α, and R'. The equations are

$$r^2 = [(R + s)\sin\theta' - R'\cos\alpha\cos\theta']^2 + R'^2\sin^2\alpha + [(R + s)\cos\theta' + R'\cos\alpha\sin\theta']^2 \tag{39}$$

and

$$\theta = \tan^{-1}\frac{\sqrt{[(R + s)^2\sin\theta' - R'\cos\alpha\cos\theta']^2 + R'^2\sin^2\alpha}}{[(R + s)\cos\theta' + R'\cos\alpha\sin\theta']} \tag{40}$$

Equations (39) and (40) allow calculation of independent variables for the flow in terms of a location in the laser beam as specified by s, R', α, and θ'.

Figure 3 illustrates the distance along the beam, s, and the gap which exists between the surface of the turret and the s = 0 plane. The phase distortion is given by

$$P = \frac{\kappa'}{\lambda}\frac{\rho_\infty}{\rho_{SL}} R \int_0^s \frac{\rho - \rho_0}{\rho_\infty}\frac{ds}{R} + \frac{\kappa'\rho_\infty}{\lambda\rho_{SL}} R \int_{-s'}^0 \frac{\rho - \rho_r}{\rho_\infty}\frac{ds}{R} \qquad (41)$$

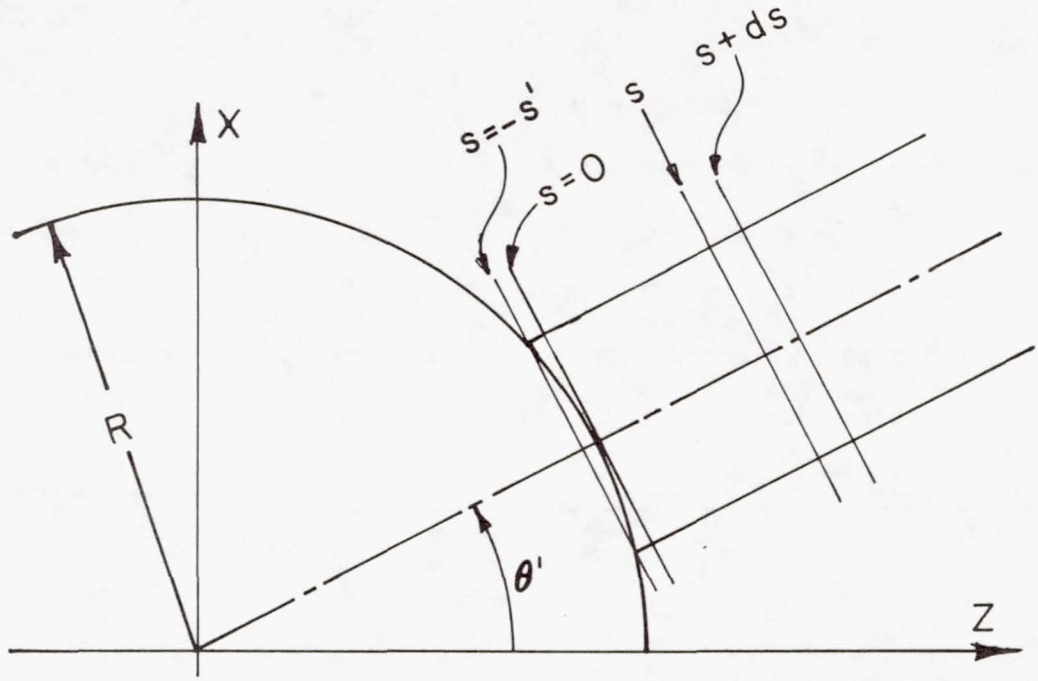

Figure 3. Cross Section of Turret and Beam in x-z Plane.

where ρ_0 is the density along the axis of the beam and ρ_r is a reference density. The second integral in equation (41) has been termed the "gap integral."

Graphical Presentation of Results

A computer program has been developed for the HP9830 which calculates the phase distortion, P, as a function of sphere radius, R; elevation angle, θ'; radius within the beam, R'; angle within the beam, α; freestream Mach number, M_∞; wavelength, λ; index of refraction constant, κ'; ratio of heat capacities, γ; freestream speed of sound, a_∞; and density ratio, ρ_∞/ρ_{SL}. Values used in the

calculations are as follows:

$$\text{beam diameter} = R/2 = 0.4572 \text{ meter}$$

$$R = 0.9144 \text{ meter}$$

$$\lambda = 3.8 \times 10^{-6} \text{ meter}$$

$$\kappa' = 2 \times 10^{-4}$$

$$a = 342 \text{ meters/sec}$$

$$\gamma = 1.4$$

$$\rho_\infty/\rho_{SL} = 1.0$$

M_∞, R', α, and θ' have been varied. Calculations have been performed to the extent necessary to plot phase distortion maps.

Plots of isocontours of phase shift were made for steps of 18^o starting with $\theta' = 0$ and $\theta' = 90^o$. The calculations ignore the gap integral; evaluation of gap integral is somewhat arbitrary. However, to provide insight to the magnitude of the gap integral, the quantity was evaluated with $\rho_r = \rho_\infty$ in equation (41). Results are shown in Table II.

Table II. Maximum Value of Gap Integral

Beam Elevation Angle θ'	Maximum Value of Gap Integral and Location Within Beam	
0	0.368	*
18	0.654	0^o
36	0.678	0^o
54	-0.836	180^o
72	-0.863	120^o
90	-0.866	90^o

*Does not depend on α.

The quantity, maximum value of gap integral, is the maximum phase distortion, P, caused by the gap between the plane s = 0 and the surface of the turret. From Table II, the large value of the gap integral indicates that the gap cannot be ignored.

The plots of isocontours of phase shift are shown in Figures 4 to 9. To avoid awkward decimal values, the phase distortion has been multiplied by 100. Hence 250 from the graphs is 2.5 wavelengths phase distortion; a value of 25 from the curves would be a quarter wavelength. Recall the beam axis is used as the reference for the phase shift, P. Reference to equation (41) shows that P is positive when ρ along the ray in question exceeds ρ_∞. A positive value of P means the wavefront lags behind the front at the beam axis.

The critical Mach number 0.587 was chosen for the calculations. The outer edge of each plot is, of course, the outer edge of the beam. The ratio of turret diameter to beam diameter is 4.0. The significance of the maps will be discussed in the following subsection.

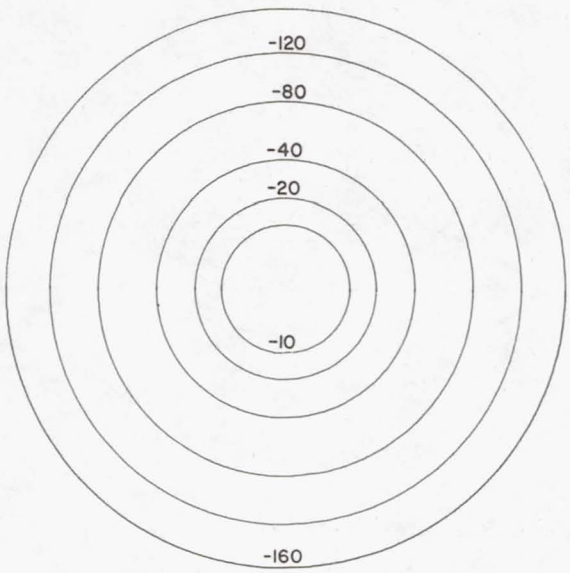

Figure 4. Contours of Constant Phase Shift for $\theta' = 0^\circ$.

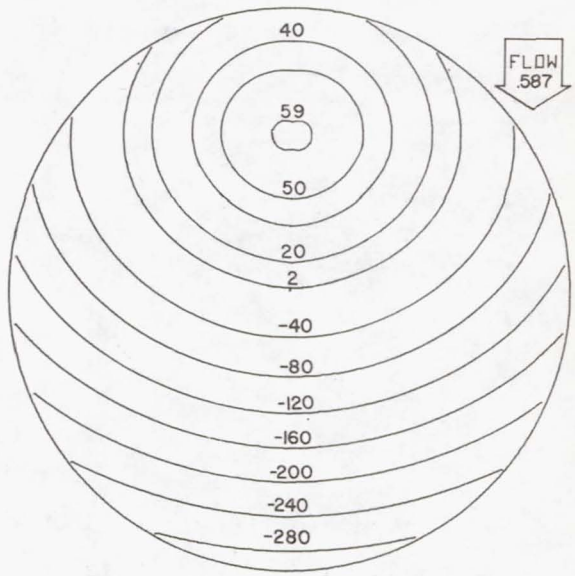

Figure 5. Contours of Constant Phase Shift for $\theta' = 18^\circ$.

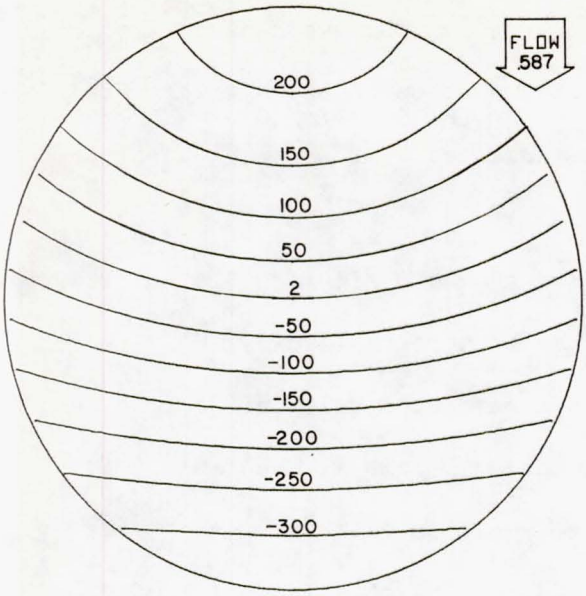

Figure 6. Contours of Constant Phase Shift for $\theta' = 36^{o}$.

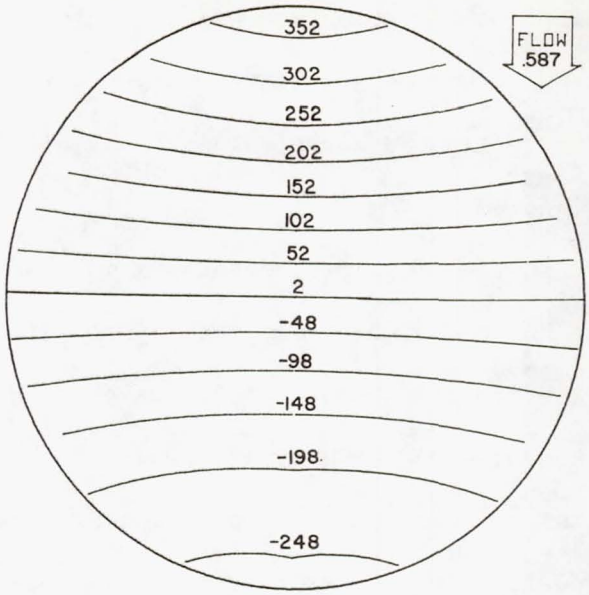

Figure 7. Contours of Constant Phase Shift for $\theta' = 54^{o}$.

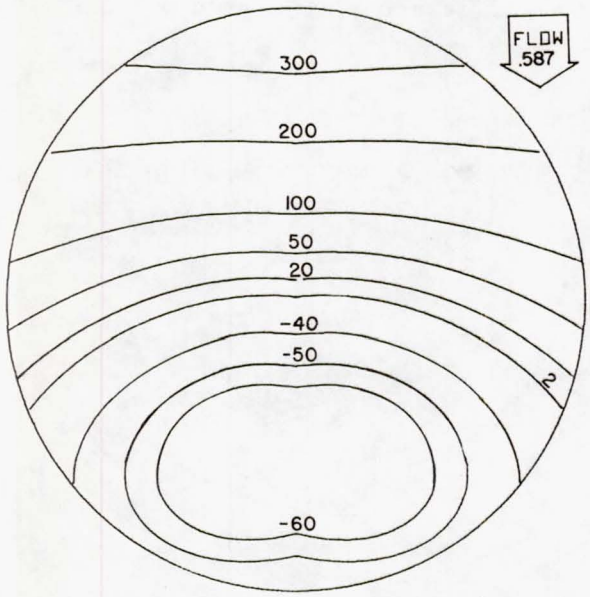

Figure 8. Contours of Constant Phase Shift for $\theta' = 72^{o}$.

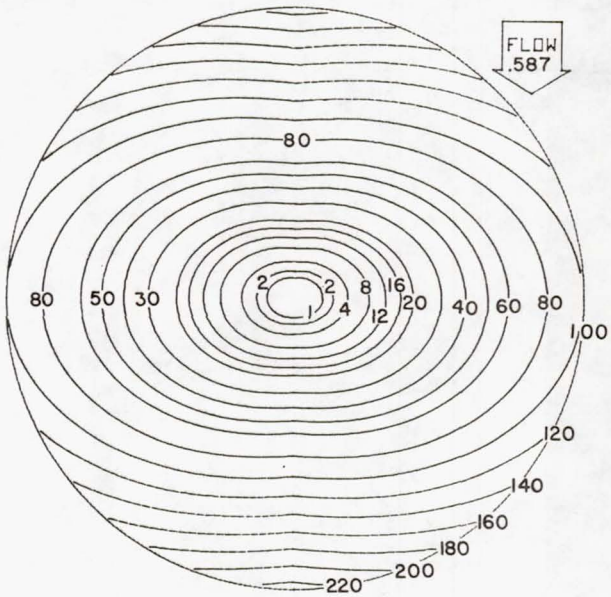

Figure 9. Contours of Constant Phase Shift for $\theta' = 90^{o}$.

An important question is the rate of decay of the integrand in equation (41). Calculations were made of

$$\frac{\partial P}{\partial (s/R)}$$

which is the phase distortion per unit distance along the beam. Results of the calculation are shown in Figure 10. The phase distortion, P, is the area enclosed by one of the curves. Most of the phase distortion occurs within a distance of one turret radius.

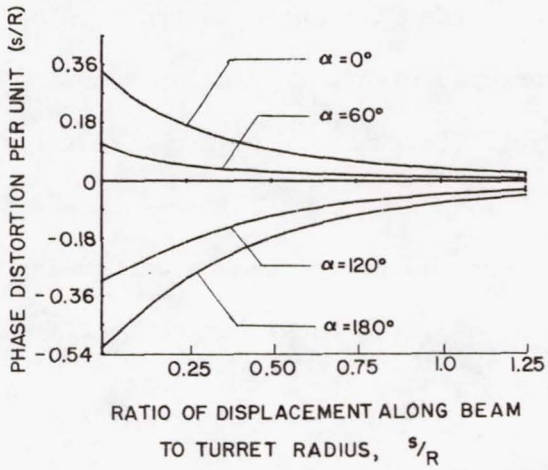

Figure 10. Phase Distortion per Unit (s/R) as a Function of (s/R) for Rays at $\alpha = 0^{o}$, 60^{o}, 120^{o}, and 180^{o} Within the Beam. Elevation angle was $\theta' = 18^{o}$.

The windward side of the beam is at $\theta = 0^{o}$. When $\theta' = 18$ and $\theta = 0$, the air is compressed and P is positive. When $\theta = 180^{o}$, i.e., on the leeward side of the beam, the air is expanded and P is negative.

Interpretation of Results

The contours in Figure 4 are a series of concentric circles with a negative value of phase shift. Hence, the beam is being focused. The focal length, F, can be estimated from

$$F = \frac{R_b'^2}{\lambda P} \qquad (42)$$

Using $R_b' = R/4 = 0.2286$ meter, $\lambda = 3.8$ micron, and $P = 1.6$, the value of F is 8.6 km.

For $\theta' = 54^o$ in Figure 7, the contours are almost straight lines. The algebraic signs of phase shift indicate the beam is being tilted in a direction opposite to the relative wind, i.e., the beam is leaning into the wind. The tilt angle is given by

$$(\text{tilt angle}) = \lambda \frac{\partial P}{\partial R'} \tag{43}$$

Inserting values from Figure 7, the tilt angle is found to be 26.5 microradians. This tilt angle should be compared with the pointing accuracy of the pointer-tracker which forms the turret. Fortunately tilt can be corrected easily by adaptive optics.

For $\theta' = 90^o$, the flow over the turret causes defocusing of the beam; see Figure 9. Using equation (42), the focal length is $F = -6.3$ km. The flow gives effectively a negative lens.

Scaling of Phase Distortion

Using equation (41) one can demonstrate the scaling relationships for altitude (density), turret size, and laser wavelength. The equation is

$$\frac{P_2}{P_1} = \frac{\lambda_1}{\lambda_2} \frac{\rho_2}{\rho_1} \frac{R_2}{R_1} \frac{\kappa_2'}{\kappa_1'} \tag{44}$$

where subscripts 1 and 2 refer to two different hemispherical turrets at the same M_∞. The phase distortion becomes more severe as wavelength decreases. Throughout the infrared region, the value of κ' is nearly constant; however, as one approaches the visible, κ' tends to increase with decreasing wavelength. Of course, for constant diffraction, the ratio R/λ will tend to be constant. Since ρ follows an exponential decay with altitude, the phase distortion falls rapidly with increasing altitude.

TURRET ON A CIRCULAR CROSS SECTION FUSELAGE: SUBSONIC FLOW

Using the solution for the wavy wall on a cylinder [18] and Fourier analysis, a turret of any shape can be described mathematically, and the flow field can be obtained. A question about this model concerns the effect of fuselage ends.

Fuselage End Effects

For the analytical model to apply, the fuselage shown in Figure 11 must extend to infinity in both directions. Obviously real aircraft have finite length. What is the influence of aircraft fuselage ends?

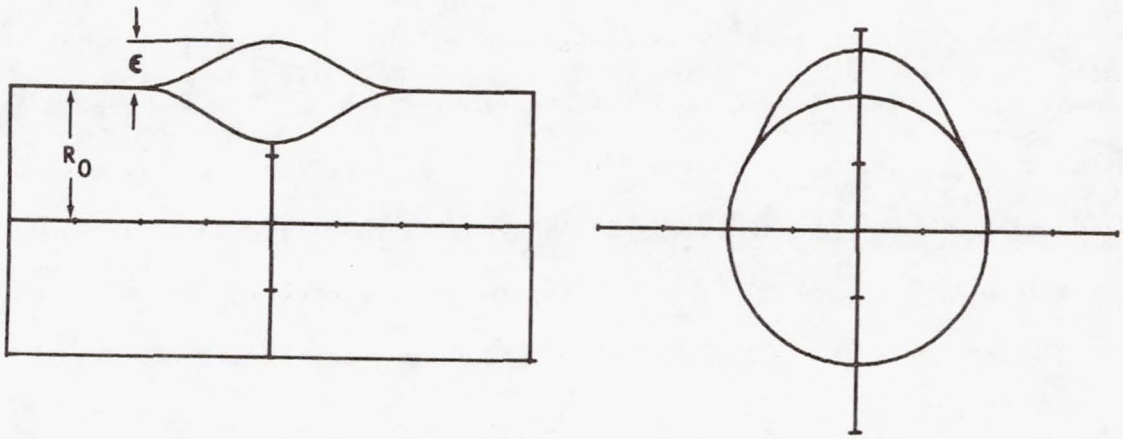

Figure 11. A Small Perturbation Turret on a Circular Cross Section Fuselage.

To gain insight to this question, the pressure distribution on the surface of several axisymmetric bodies has been calculated assuming potential flow. The fineness ratio of the fuselage, i.e., the ratio of length to diameter, was varied.

The potential equation for axisymmetric flow is

$$\frac{\partial^2 \phi'}{\partial z'^2} + \frac{1}{r'} \frac{\partial}{\partial r'}\left(r' \frac{\partial \phi'}{\partial r'}\right) = 0 \qquad (45)$$

where z' is distance in the flow direction and r' is radial distance using cylindrical coordinates. Equation (45) assumes incompressible flow although the calculated flow may be accurate to $M_\infty = 0.3$, depending on body bluntness.

A body surface is generated by a source-sink combination separated by a distance ℓ. Lengths are made nondimensional using ℓ. The potential function is nondimensionalized by the following

$$\phi = \phi'/U_\infty \ell \tag{46}$$

where U_∞ is the freestream velocity.

There are two other lengths in the problem in addition to ℓ. First, there is the body diameter. Second, there is the distance from the source to the upstream stagnation point which is designated as z*. Once again z* is a nondimensional length using ℓ as a reference. Incidentally, the upstream and downstream stagnation points are saddle point singularities; this is a fact to be remembered when the equations are integrated to obtain the body surface.

The velocity components are $u = u'/U_\infty$ in the z-direction, and $v = v'/U_\infty$ in the r-direction. The equations for u and v are as follows:

$$u = 1 + \frac{z^{*2}(z^* - 1)^2 z}{(1 - 2z^*)(z^2 + r^2)^{3/2}} - \frac{z^{*2}(z^* - 1)^2 (z - 1)}{(1 - 2z^*)[(z - 1)^2 + r^2]^{3/2}} \tag{47}$$

and

$$v = \frac{z^{*2}(z^* - 1)^2 r}{(1 - 2z^*)(z^2 + r^2)^{3/2}} - \frac{z^{*2}(z^* - 1) r}{(1 - 2z^*)[(z - 1)^2 + r^2]^{3/2}} \tag{48}$$

The flow is in the direction of the positive z axis with the source at z = 0 and the sink at z = 1. Consequently, the upstream stagnation point occurs at a location where z* is a negative number. When z* approaches negative infinity, the body approaches a sphere. When z* approaches zero, the length of the fuselage, which is $L = \ell(1 + 2z^*)$, approaches infinity. Any value of z*

satisfies equation (47) when u = 0 (a stagnation point), z = z*, and r = 0. However different values of z* change the length to diameter ratio of the body.

To find the body surface, the differential equation relating velocity components and the slope of the body surface is solved numerically; the equation to be solved is

$$\frac{dr}{dz} = \frac{u}{v} \tag{49}$$

Integration starts at z = - |z*| and r = 0. Since the rear stagnation point is a saddle point singularity, one cannot integrate to z = + |z*| and r = 0. The flow is known to be symmetric relative to z = 0.5; this fact was used to obtain the body for z > 0.5.

The pressure coefficient in terms of nondimensional velocities is

$$C_p = \frac{p - p_\infty}{\rho U_\infty^2/2} = 1 - u^2 - v^2 \tag{50}$$

At the front and rear stagnation points, C_p has a value of unity. When C_p is zero, the local static pressure exactly equals the static pressure at infinity, and the local flow velocity is U_∞. When C_p is negative, the local flow velocity exceeds U_∞.

Results of sample calculations are shown graphically in Figures 12 to 17. In Figure 12 the length to diameter ratio, L/D, is 1.004, which is nearly a sphere. The curves from A to B and from E to F are the pressure coefficient along the stagnation streamlines. The curve BCDE is C_p on the surface of the body. For a sphere, the pressure coefficient is

$$C_p = 1 - \frac{9}{4} \sin^2\theta \tag{51}$$

When $\theta = 90^\circ$, $C_p = -5/4$. When $\theta = 41.8^\circ$, $C_p = 0$, which corresponds to point C in Figure 12.

For all figures, the sharp positive peaks are at $C_p = +1.0$. Note that for L/D = 1.004, the C_p curve for the body surface is concave. For L/D = 2, the C_p

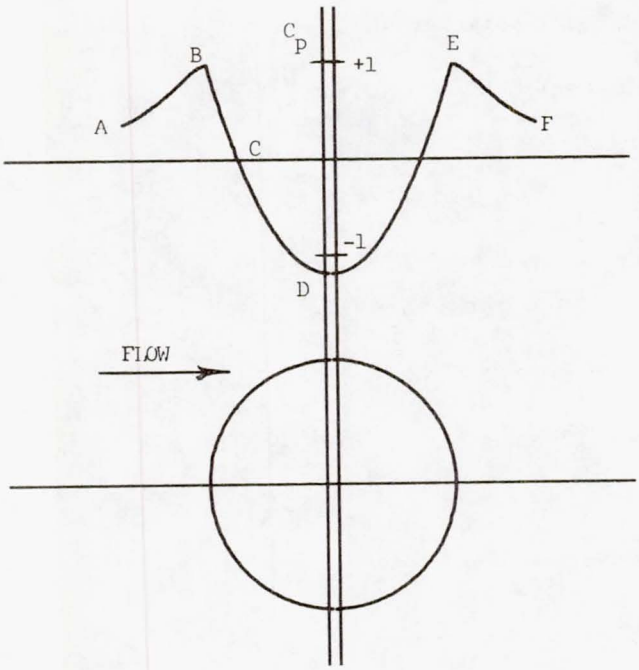

Figure 12. Pressure Coefficient on Stagnation Streamline and Body Surface. L/D = 1.004

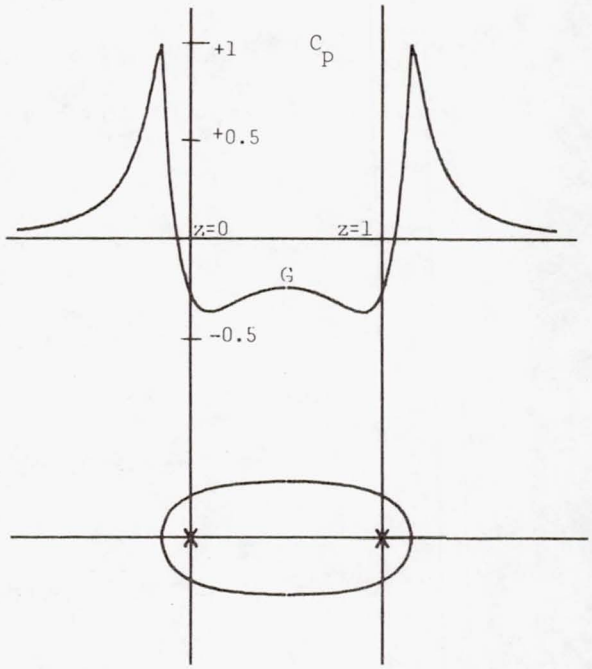

Figure 13. C_p for L/D = 2. (The x's are the source and sink.)

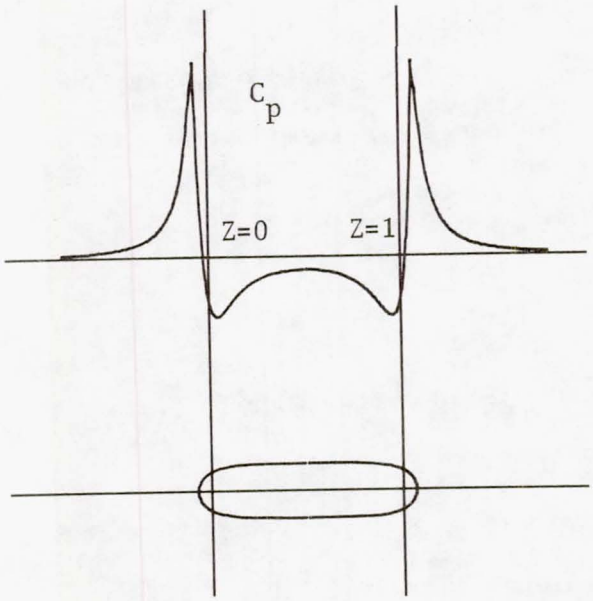

Figure 14. C_p for L/D = 4.

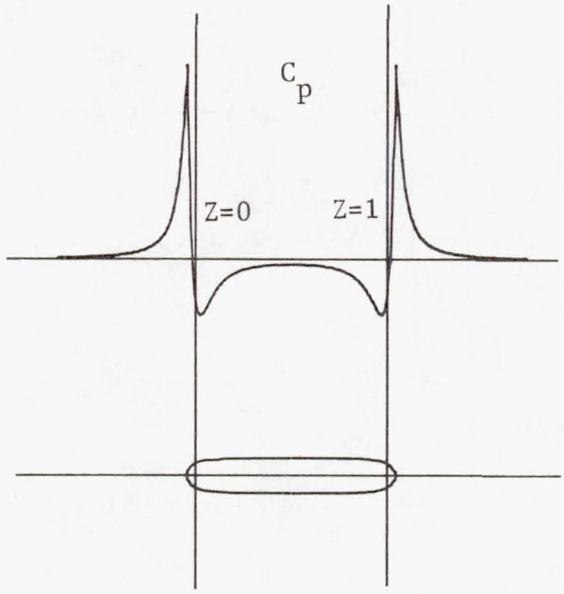

Figure 15. C_p for L/D = 6.

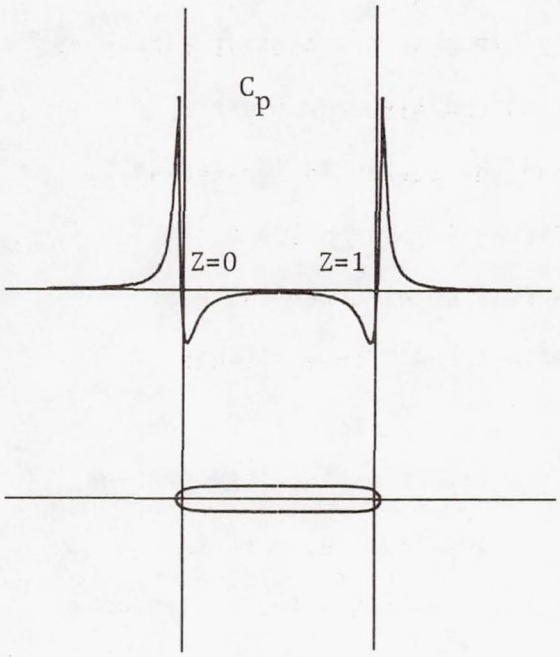

Figure 16. C_p for L/D = 8.

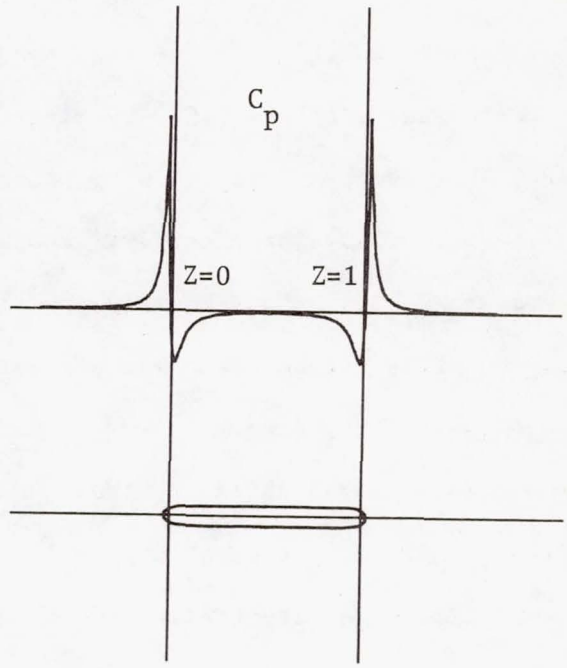

Figure 17. C_p for L/D = 10.

curve is convex at z = 0.5; this is point G in Figure 13. Although not shown, for L/D = 1.58, the C_p curve dips negative but remains flat for $0.1 < z < 0.9$. In Figure 13, the x's are the source and sink. In each figure there are two vertical lines passing through the source and sink; the vertical lines are located at z = 0 and z = 1.

As L/D increases, it is apparent from the figure sequence that C_p at z = 0.5 becomes less negative and approaches zero. At L/D equal to 6, C_p is less than 3 per cent of the positive peak for the stagnation point. A laser turret installed at z = 0 on a fuselage with L/D = 6 would experience freestream velocity within 1.5 per cent. Using equation (50) and the binomial expansion, one can show that

$$u = 1 - \frac{C_p}{2} \tag{52}$$

Application of equation (52) to the case of L/D = 6 gives u = 1.015.

The Boeing 707-320 has a fineness ratio of 10; and the French Caravelle, 10.4. The stretch DC-8 has L/D considerably more than 10. The Boeing 747SP, which is a standard 747 with a section of fuselage removed, has L/D near 6. Another wide body jet, the DC-10, has L/D near 8.6. The laser turret on the Airborne Laser Laboratory, ALL, is on a fuselage with L/D of 10, and the turret is located at nondimensional z = 0.3 approximately. Looking at Figure 17, one notes C_p is nearly zero at z - 0.3. Consequently, the turret should be experiencing near freestream velocity. (The preceding statement ignores interference effects of other components, e.g., wing.)

A potential flow solution provides insight to the effect of fuselage ends on the airflow likely to be present near a laser turret. For L/D = 6, a turret near z = 0.5 will have essentially freestream velocity. For L/D = 10, freestream conditions prevail in the interval $0.3 < z < 0.7$.

Formulation of Subsonic Flow over a Laser Turret

For small perturbation flow, the potential equation as derived in Liepmann and Roshko [18] is

$$\pm \beta^2 \phi_{xx} + \phi_{rr} + \frac{1}{r} \phi_r + \frac{1}{r^2} \phi_{\theta\theta} = 0 \tag{53}$$

The (+) sign applies to subsonic flow; and the (-) sign, to supersonic flow. the definition of β is

$$\beta^2 = |1 - M_\infty^2| \tag{54}$$

The function ϕ is the perturbation potential yielding only the changes from the freestream velocity. Equation (53) is given in cylindrical coordinates which are appropriate for the cylindrical fuselage. A solution to equation (53) can be obtained using the separation of variables. For the flow field external to the fuselage

$$\phi(r,\theta,x) = A \cos n\theta \sin qx \, K_n(\beta qr) \tag{55}$$

where A is a constant, n is an integer, and q is to be determined. See Fuhs and Fuhs [2] for development of the solution in detail.

The turret shape is defined by

$$R(x,\theta) = R_0 + \varepsilon X(x)T(\theta) \tag{56}$$

where $X(x)$ and $T(\theta)$ are functions. The height of the turret is ε as shown in Figure 11. As an example, a cosine shaped turret will be used. For a cosine shaped turret

$$X(x) = \frac{1}{2}(1 + \cos \frac{\pi x}{\ell}) \tag{57}$$

and

$$T(\theta) = \frac{1}{2}(1 + \cos f\theta) \tag{58}$$

Equations (58) and (59) apply for $|x| \leq \ell$ and $|\theta| \leq 2\pi/f$. Outside this region $R = R_0$. The quantity $1/f$ is the fraction of the 2π-circumference occupied by the turret, and ℓ is the length of the turret. For a cosine shaped turret, the appropriate Fourier series are

$$X(x) = \frac{\varepsilon\ell}{2L} + \frac{\varepsilon\ell}{L} \sum_{m=1}^{\infty} \frac{\sin m\pi\ell/L}{m\pi\ell/L} \frac{1}{1 - (m\ell/L)^2} \cos \frac{m\pi x}{L} \tag{59}$$

and

$$T(\theta) = \frac{1}{2f} + \frac{1}{f} \sum_{n=1}^{\infty} \frac{\sin n\pi/f}{n\pi/f} \frac{1}{1 - (n/f)^2} \cos n\theta \tag{60}$$

In equation (59) the spacing between periodic turrets on an infinitely long fuselage is L. The turret generated by equations (56), (59), and (60) is shown in Figure 11.

At the body surface for inviscid flow, there can be no flow through the wall. Mathematically this is expressed by

$$\vec{n} \cdot \vec{V} = 0 \tag{61}$$

where $\vec{n}$ is a unit vector normal to an element of the surface and $\vec{V}$ is the vector representing the local fluid velocity. If one can express the shape of a body by an equation of the form $f(r,\theta,x) = 0$, then

$$\vec{n} = \vec{\nabla} f / |\vec{\nabla} f| \tag{62}$$

Using the potential function for determining $\vec{V}$, the boundary condition at the body surface is

$$\vec{\nabla}\Phi \cdot \vec{\nabla} f = 0 \tag{63}$$

where Φ is the full potential related to the perturbation potential by

$$\Phi = \phi + xU_\infty \tag{64}$$

For small perturbation, equation (63) reduces to

$$\frac{\partial f}{\partial x} + \frac{\partial \Phi}{\partial r} = 0 \tag{65}$$

Equation (65) is derived in Appendix A of reference [3].

Solutions for Subsonic Flow

In view of equations (56), (59), and (60), the potential function is assumed to have the form

$$\phi(r,\theta,x) = \sum_n \sum_m \phi_{nm}(r,\theta,x) \tag{66}$$

Using appropriate nondimensional variables, ϕ_{nm} is found to be

$$\phi_{nm}(r,\theta,x) = -\frac{2A_{nm} \cos n\theta \sin \frac{m\pi x}{L} K_n(\beta m\pi r/L)}{\beta[K_{n+1}(\beta m\pi/L) + K_{n-1}(\beta m\pi/L)]} \tag{67}$$

K_n is a Bessel function discussed in the book by Hildebrand [19]. The constant A_{nm} is given by

$$A_{nm} = -\frac{\varepsilon \ell}{fL}\left[\frac{1}{1-(\ell m/L)^2}\,\frac{\sin(m\pi\ell/L)}{(m\pi\ell/L)}\right]\left[\frac{1}{1-(n/f)^2}\,\frac{\sin(n\pi/f)}{(n\pi/f)}\right] \tag{68}$$

Combining equations (66) to (68), one has the complete perturbation potential equation. The perturbation velocities are calculated using $\vec{\nabla}\phi$; these velocities are shown explicitly in reference [3]. With velocities in nondimensional form, the pressure coefficient for axisymmetric flow is

$$C_p = -2u - v^2 \tag{69}$$

Equation (69) can be evaluated, and the results inserted in equation (7) to calculate the phase distortion P.

Before discussing typical results for phase distortion, calculation of critical Mach will be presented. Equation (3) relates p/p_∞ to the pressure coefficient, C_p. Assume the flow is isentropic; this assumption permits use of the following relation between static pressure where the local Mach number is unity, p*, and the static pressure at infinite distance from the turret, p_∞:

$$\frac{p^*}{p_\infty} = \left[\frac{2}{\gamma+1}\left(1 + \frac{\gamma-1}{2}M_\infty^2\right)\right]^{\frac{\gamma}{\gamma-1}} \tag{70}$$

Combining equations (3) and (70) establishes an equation for the critical pressure coefficient

$$C_p^* = \frac{2}{\gamma M_\infty^2}\left\{\left[\frac{2}{\gamma+1}\left(1 + \frac{\gamma-1}{2}M_\infty^2\right)\right]^{\frac{\gamma}{\gamma-1}} - 1\right\} \tag{71}$$

When C_p given by equation (69) equals C_p^*, the local velocity is sonic. Equations (69) and (71) were used to calculate the critical Mach numbers given in Table I.

Typical Results

As an example, the phase distortion was calculated for a laser beam leaving the turret of Figure 11. The beam was pointed at an angle 90^o to the axis of the fuselage and was symmetrically located relative to the turret. The beam radius was

$\ell/2$. The pressure coefficient and optical path length were calculated for a ray starting at $x = -\ell/2$ and for the reference ray at $x = 0$. The pressure coefficient along the two rays is shown in Figure 18. The values used in the calculation were as follows:

$M_\infty = 0.62$	$R_0 = 1$ meter	$L = 5$
$\varepsilon = 0.35$	$\lambda = 3.8$ microns	$\theta = 0$
$\rho_\infty/\rho_{SL} = 1.0$	$\ell = 1.005$	$\kappa' = 0.00023$

The quantity $\partial P/\partial(s'/R_0)$ was evaluated for the two rays specified above. The results are shown in Figure 19, which is a graph of increment of phase distortion as a function of radial distance s'. About one-half of the phase distortion occurs within a distance along the beam of approximately 0.35 R_0. Expressed in terms of turret height, ε, one-half of the phase distortion is generated within approximately one turret height.

The integrated phase distortion, which is the area under the curve, is 1.17. In terms of wavelengths, the integrated distortion is 1.17λ.

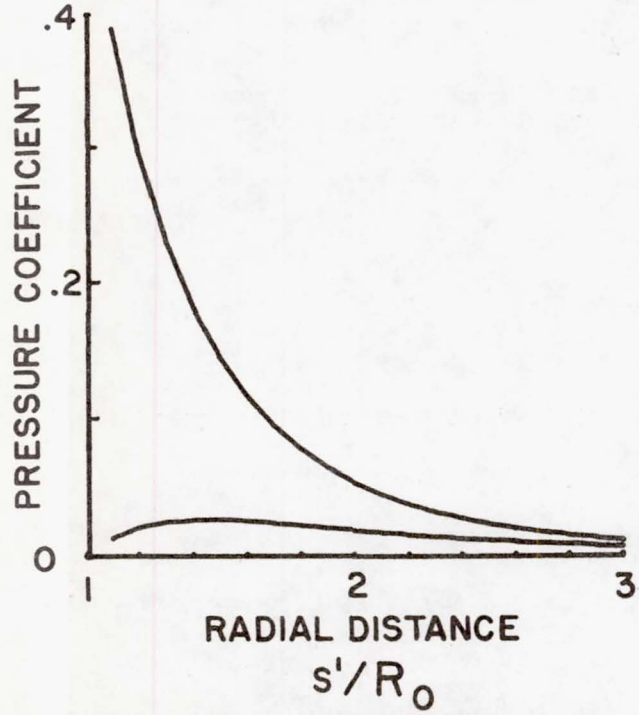

Figure 18. Pressure Coefficient along Two Rays Selected for Phase Distortion Calculation.

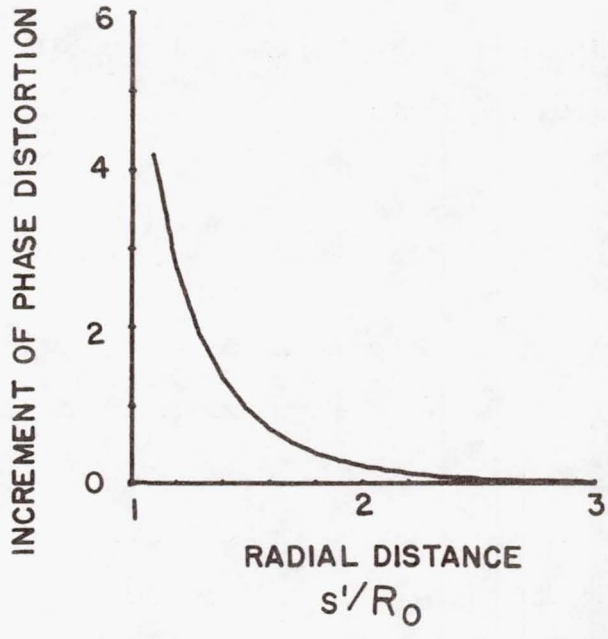

Figure 19. Increment of Phase Distortion along Beam.

TURRET ON A CIRCULAR CROSS SECTION FUSELAGE: SUPERSONIC FLOW

The potential flow equation for supersonic flow is equation (53) with use of the (-) sign. Once again the turret shape is illustrated by Figure 11. A more general formulation for turret geometry is developed in this section.

Turret Geometry

The function X(x) of equation (56) is a polynomial

$$X(x) = 1 + \sum_{k=1}^{K} \tilde{a}_k x^k \tag{72}$$

Likewise the function T(θ) of equation (56) is another polynomial

$$T(\theta) = 1 + \sum_{j=2,4,}^{p} \tilde{b}_j \theta^j \tag{73}$$

Note that only even powers of θ are used since the turret is symmetric in the θ-direction. As before, ε is the height of the turret at x = θ = 0. Each term in the polynomial is expanded separately as a Fourier series [20].

$$x^k = \sum_{m=0}^{\infty} a_{mk} \cos \frac{m\pi x}{L} + b_{mk} \sin \frac{m\pi x}{L} \tag{74}$$

Hence

$$X(x) = \sum_{k=1}^{K} a_k \left(\sum_{m=0}^{\infty} \tilde{a}_{mk} \cos \frac{m\pi x}{L} + b_{mk} \sin \frac{m\pi x}{L} \right) \tag{75}$$

In a similar manner

$$\theta^j = \sum_{n=0}^{\infty} a_{nj} \cos n\theta \tag{76}$$

Consequently

$$T(\theta) = \sum_{j=2,4,}^{p} \tilde{b}_j \left(\sum_{n=0}^{\infty} a_{nj} \cos n\theta \right) \tag{77}$$

The Fourier coefficients are as follows:

$$a_{mk} = \frac{\ell^k}{m\pi} [(-1)^k + 1] \sin \frac{m\pi\ell}{L} - \frac{kL}{m\pi} b_{m,k-1} \tag{78}$$

$$b_{mk} = -\frac{\ell^k}{m\pi} [(-1)^{k+1} + 1] \cos \frac{m\pi\ell}{L} + \frac{kL}{m\pi} a_{m,k-1} \tag{79}$$

Equations (78) and (79) are recursion relations. To start the sequence one needs a_{0k} and b_{0k} which are

$$a_{0k} = \frac{[(-1)^k + 1]\ell^{k+1}}{2L(k+1)} \tag{80}$$

and

$$b_{0k} = 0 \tag{81}$$

Also both $a_{m,-1}$ and $b_{m,-1}$ are zero. Beginning with k = 0, the Fourier coefficients for any order polynomial can be obtained using equations (78) to (81). If k is an even number, then b_{mk} is zero. If k is an odd number, then a_{mk} is zero.

Equations (72) through (81) define a turret of length 2ℓ which is periodic every x = 2L. In the circumferential direction, the turret is positioned between $-\theta_t \leq \theta \leq \theta_t$, where θ_t defines the boundary of the turret. To evaluate equation (77), one needs a_{nj}. Equations (78) to (81) can be used to determine a_{nj} by making the following substitutions:

$$m \to n \qquad L \to \pi$$

$$k \to j \qquad \ell \to \theta_t$$

Note that j has only even values.

The coefficients $\tilde{a}_k$ and $\tilde{b}_j$ will be varied; however, because of the geometry not all coefficients may be independent. Due to equations (56), (72), and (73), the turret height at $x = \theta = 0$ is always ε. To have a continuous surface for the fuselage, $X(x) = 0$ for $|x| = \ell$; also, $T(\theta) = 0$ for $|\theta| = \theta_t$. In addition, conditions may be imposed such that $dX/dx = 0$ at $|x| = \ell$, etc.

For each boundary condition imposed, one coefficient of the polynomial is eliminated as an independent variable. The coefficients which are not used to satisfy boundary conditions can be used as design variables. In a companion paper [21], the design variables are selected so as to optimize phase distortion.

Solution to Potential Equation for Supersonic Flow

Once again separation of variables is used to solve equation (53). The solution has the form

$$\phi(r,\theta,x) = R(r)\Theta(\theta)X(x) \tag{82}$$

where

$$R(r) = AJ_n(\beta qr) + BY_n(\beta qr) \tag{83}$$

$$\Theta(\theta) = C \sin n\theta + D \cos n\theta \tag{84}$$

$$X(x) = E \sin qx + F \cos qx \tag{85}$$

Both J_n and Y_n are Bessel functions discussed by Hildebrand [19]. For symmetry with respect to $\theta = 0$, C is zero. Since both J_n and Y_n are finite for large r, neither A nor B can be set equal to zero. In contrast to the subsonic flow solution, the supersonic flow solution has one additional constant to be determined. Matching waves in the far field permits evaluation of the additional constant [22]. For a simple cosine wavy wall on a cylinder, the potential equation has the form as derived by Fuhs [23]

$$\phi(r,x) = A[(\sin \alpha x - \cos \alpha x)Y_0(\alpha\beta r) + (\sin \alpha x + \cos \alpha x)J_0(\alpha\beta r)] \tag{86}$$

The constant A is related to the amplitude of the cosine wavy wall. Equation (86) implies an eigenvalue given by

$$Y_1(\alpha\beta R_0) = - J_1(\alpha\beta R_0) \tag{87}$$

The wavenumber of the wavy wall is α.

The requirement for no flow through the turret boundary is given by equation (65). For the turret of Figure 11, the boundary condition becomes

$$\frac{v}{U} = \frac{\partial R}{\partial x}\Big)_{r=R_0} = \frac{1}{U}\frac{\partial \phi}{\partial r}\Big)_{r=R_0} \tag{88}$$

The surface of the turret is given by

$$R(\theta,x) = R_0 + \sum_n \sum_m \left[A_{nm} \cos \frac{m\pi x}{L} + B_{nm} \sin \frac{m\pi x}{L}\right] \cos n\theta \tag{89}$$

Based on equation (86), the potential function is assumed to have the form

$$\phi(r,\theta,x) = U_\infty x + \sum_n \sum_m \phi_{nm} \tag{90}$$

where

$$\begin{aligned}\phi_{nm}(r,\theta,x) = \lambda_{nm} \cos n\theta \Bigg[&\left(\sin \frac{m\pi x'}{L} - \cos \frac{m\pi x'}{L}\right) Y_n\left(\frac{\beta m\pi}{L} r\right) \\ &+ \left(\sin \frac{m\pi x'}{L} + \cos \frac{m\pi x'}{L}\right) J_n\left(\frac{\beta m\pi}{L} r\right)\Bigg]\end{aligned} \tag{91}$$

Equation (87) establishes an eigenvalue, which is the root of equation (87). For a Fourier series, the wavenumber α is determined by the series. The flight Mach number determines β. Hence R_0 is not arbitrary. As a result one must introduce an eigenvalue cylinder which has the same wavenumber as the cylinder required by the Fourier series; however, the eigenvalue cylinder has a different radius.

Further, the eigenvalue cylinder is shifted in phase. The equation for a cosine shaped eigenvalue cylinder is

$$R_{nm}(\theta,x) = R_{mn} + \varepsilon_{mn} \cos n\theta \cos \frac{m\pi x'}{L} \tag{92}$$

The boundary condition for the eigenvalue cylinder is

$$\left.\frac{\partial \phi_{nm}}{\partial r}\right)_{r=R_{nm}} = \frac{\partial R_{nm}}{\partial \chi} \tag{93}$$

The phase shift, x_{nm}, is given by

$$x' = x + x_{nm} \tag{94}$$

Carefully note that $R_{nm}(\theta,x)$ and ϕ_{nm} are formulated with x' whereas $R(\theta,x)$ is in terms of x.

Consider first the cosine wavy wall defined by equation (92). Use of the boundary condition of equation (93) gives the eigenvalue equation

$$\frac{\beta m\pi R_{nm}}{L}\left[Y_{n+1}(C_m) - J_{n+1}(C_m)\right] - n\left[Y_n(C_m) - J_n(C_m)\right] = 0 \tag{95}$$

where

$$C_m = \frac{\beta\pi m R_{nm}}{L} \tag{96}$$

There is only one value of R_{nm} which satisfies equation (95); hence equation (95) provides a method to calculate R_{nm} in equation (92).

From the boundary condition of equation (93), one finds

$$\varepsilon_{nm} = \frac{\lambda_{nm}\left\{ C_m\left[Y_{n+1}(C_m) + J_{n+1}(C_m)\right] - n\left[Y_n(C_m) + J_n(C_m)\right]\right\}}{\frac{m\pi R_{nm}}{L}} \tag{97}$$

Using the boundary condition for the turret as given by equation (88), the phase shift, x_{nm}, can be determined

$$\tan \frac{m\pi x_{nm}}{L} = \frac{D_{nm} - E_{nm}}{D_{nm} + E_{nm}} \tag{98}$$

where D_{nm} and E_{nm} are defined as

$$D_{nm} = -\frac{\beta m\pi}{L} Y_{n+1}\left(\frac{\beta\pi m R_0}{L}\right) + \frac{n}{R_0} Y_n\left(\frac{\beta\pi m R_0}{L}\right) \tag{99}$$

and

$$E_{nm} = -\frac{\beta m\pi}{L} J_{n+1}\left(\frac{\beta m\pi R_0}{L}\right) + \frac{n}{R_0} J_n\left(\frac{\beta\pi m R_0}{L}\right) \tag{100}$$

Continuing with the boundary condition for the turret, define

$$a_{nm} = D_{nm} + E_{nm} \tag{101}$$

and

$$b_{nm} = D_{nm} - E_{nm} \tag{102}$$

The amplitude of ϕ_{nm} term, which is λ_{nm}, is related to A_{nm} of equation (89) by

$$\lambda_{nm} = -\frac{m\pi A_{nm}}{L[a_{nm}^2 + b_{nm}^2]^{1/2}} \tag{103}$$

The value of A_{nm} is determined by turret shape. Combining equations (91), (94), (98), and (99) through (103), one obtains

$$\phi_{nm}^c(r,\theta,x) = -\frac{(m\pi/L)A_{nm} \cos n\theta}{a_{nm}^2 + b_{nm}^2}\Bigg\{ (a_{nm} + b_{nm}) \sin \frac{m\pi x}{L} Y_n\left(\frac{\beta m\pi r}{L}\right)$$

$$- (a_{nm} - b_{nm}) \cos \frac{m\pi x}{L} Y_n\left(\frac{\beta m\pi r}{L}\right)$$

$$+ \left[(a_{nm} - b_{nm}) \sin \frac{m\pi x}{L} + (a_{nm} + b_{nm}) \cos \frac{m\pi x}{L}\right] J_n\left(\frac{\beta\pi m r}{L}\right)\Bigg\} \tag{104}$$

Following a similar procedure for the sine shaped wavy wall, one finds

$$\phi^{s}_{nm}(r,\theta,x) = -\frac{(m\pi/L)B_{nm}\cos n\theta}{a^2_{nm} + b^2_{nm}} \Bigg\{ - (a_{nm} + b_{nm}) \cos \frac{m\pi x}{L} Y_n(\frac{\beta m\pi r}{L})$$

$$+ (a_{nm} - b_{nm}) \sin \frac{m\pi x}{L} Y_n(\frac{\beta m\pi r}{L})$$

$$- [(a_{nm} - b_{nm}) \cos \frac{m\pi x}{L} - (a_{nm} + b_{nm}) \sin \frac{m\pi x}{L}] J_n(\frac{\beta m\pi r}{L}) \Bigg\} \qquad (105)$$

The combined potential equation is

$$\phi(r,\theta,x) = U_\infty x + \sum_n \sum_m (\phi^{c}_{nm} + \phi^{s}_{nm}) \qquad (106)$$

Equation (106) can be used to determine the velocity components. With the velocity components, equation (69) can be evaluated for the pressure coefficient, C_p. In turn, the pressure coefficient can be inserted into equation (7) to determine the phase distortion, P.

Results of a Sample Calculation

The flow over a cosine shaped turret was determined. The turret was defined by equations which approximate a cosine

$$X(x) = 1.0 - 0.5(x/\ell)^2 + 0.0625(x/\ell)^4 \qquad (107)$$

and

$$T(\theta) = 1.0 - 1.82(\theta/\theta_t)^2 + 0.0832(\theta/\theta_t)^4 \qquad (108)$$

The Mach number was $M_\infty = 2.0$, $\varepsilon = 0.2$, $\ell = 2R_0$, and $\theta_t = 60^o$.

Figure 20 shows the phase distortion map for the case being considered here. The distortion is almost pure tilt.

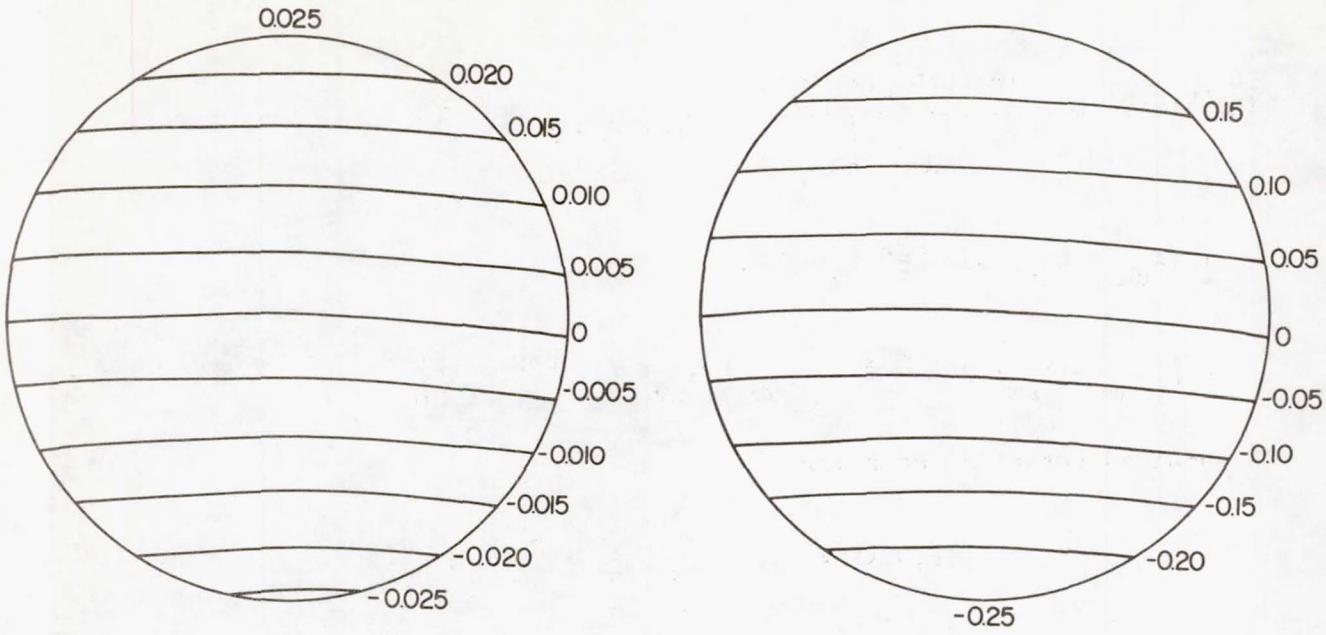

(a) $M_\infty = 0.5$ (b) $M_\infty = 2.0$

Figure 20. Map of Phase Distortion. Azimuth 0^o; Elevation 45^o; Mirror Radius = $R_0/20$.

CONCLUSIONS

Laser turrets may be classified as blunt or small perturbation depending on maximum slope of the turret surface. Analytical models were developed for both categories of turrets.

As an example of a blunt laser turret, the flow over a hemispherical turret was solved using Janzen-Rayleigh expansion technique. Terms to the second order were obtained and were used to calculate the phase distortion. At the critical Mach number for a hemispherical turret, the phase distortion was several wavelengths. The phase distortion varied from a positive focus for 0^o elevation to combined focus and tilt at intermediate elevations and to negative focus for 90^o elevation. The distortion can be expressed in terms of Zernike polynomials.

A versatile analytical model was developed for a laser turret on an infinitely long circular cylinder. The laser turret is described by a two-dimensional Fourier series using the solution for the flow over a wavy wall on a cylinder. The turret can have any shape subject to the constraint that the turret is a small perturbation in the flow. Both subsonic and supersonic solutions were obtained.

End effects were examined. For a fuselage with length to diameter ratio of 6.0, the laser turret mounted at the midpoint of the fuselage would experience freestream velocity with 1.5 per cent. For an aircraft with L/D of 10, such as ALL, any location between $z/D = 0.3$ to $2/D = 0.7$ would have freestream conditions.

The analytical model permits calculation of critical Mach number for the turret. The critical Mach number is important because of the change from linearized subsonic flow solution to nonlinear transonic flow.

For the subsonic case, the maximum observed distortion was a fraction of wavelength. Similar results were found at Mach 2.

The supersonic flow solution has eigenvalues which require introduction of an eigenvalue cylinder. A cylinder of arbitrary radius cannot yield a satisfactory solution. A cylinder slightly smaller can satisfy the boundary conditions and becomes the eigenvalue cylinder. For large radial distances from the cylinder, the solution approaches that of a planar wavy wall.

In addition to useful calculations for laser turrets, the analytical models are useful for reconnaissance aircraft using cameras and cruise missiles using celestial navigation.

REFERENCES

1. P. J. Klass, "Special Report: Laser Weapons. Advanced Weaponry Research Intensifies," Aviation Week and Space Technology, Vol. 103, No. 7, August 18, 1975.

2. Anonymous, "High Energy Laser Development," International Defense Review, Vol. 12, No. 3, p. 316, 1979.

3. A. E. Fuhs and S. E. Fuhs, "Phase Distortion at High Subsonic Mach Numbers for a Small Perturbation Laser Turret," Proceedings of Electro-optical Systems Design Conference - 1976, New York, pp. 9-19, published by Industrial and Scientific Conference Management, Inc., 222 W. Adams St., Chicago, IL, 60606.

4. A. E. Fuhs, "Potential Flow: Nonlinear Compressible Flow," Lecture 3B, Short Course on Laser Aerodynamics, presented April 11-22, 1977, at AF Weapons Laboratory, Kirtland, AFB, NM.

5. M. Van Dyke, Perturbation Methods in Fluid Mechanics, Academic Press, New York, 1964.

6. T. Hsieh, "Hemisphere-Cylinder in Transonic Flow, $M_\infty = 0.7 - 1.0$," AIAA Journal, 13, pp. 1411-1413, 1975.

7. T. Hsieh, "Hemisphere-Cylinder in Low Supersonic Flow," AIAA Journal, 13, pp. 1551-1552, 1975.

8. H. W. Liepmann and A. E. Puckett, Introduction to Aerodynamics of a Compressible Fluid, John Wiley and Sons, New York, 1947. See Chapter 10.

9. K. Oswatitsch, Gas Dynamics, Academic Press, New York, 1956. See pages 328-334.

10. Lord Rayleigh, "On the Flow of Compressible Fluid Past an Obstacle," The London, Edinburgh, and Dublin Philosophical Magazine and Journal, Sixth Series, Vol. 32, No. 187, July, 1916.

11. M. Born and E. Wolf, Principles of Optics, Pergamon Press, New York, 1964.

12. C. B. Hogge and R. R. Butts, "Frequency Spectra for the Geometric Representation of Wavefront Distortions Due to Atmospheric Turbulence," IEEE Transactions on Antennas and Propagation, Vol. AP-24, pp. 144-154, 1976.

13. A. E. Fuhs and S. E. Fuhs, "Phase Distortion due to Airflow over a Hemispherical Laser Turret," Naval Postgraduate School Report NPS-69FU76101, September, 1976.

14. A. E. Fuhs, "Distortion of Laser Turret Optics Due to Aircraft Mainstream Flow," Journal of the Optical Society of America, 66, p. 1137, 1976.

15. L. M. Milne-Thompson, Theoretical Hydrodynamics, Macmillan Co., New York, Fourth Edition, 1960.

16. H. Lamb, Hydrodynamics, Dover Publications, New York, Sixth Edition, 1945.

17. K. Karamcheti, Principles of Ideal-Fluid Aerodynamics, John Wiley and Sons, New York, 1966.

18. H. W. Liepmann and A. Roshko, Elements of Gasdynamics, John Wiley and Sons, New York, 1957.

19. F. B. Hildebrand, Advanced Calculus for Engineers, Prentice-Hall, Inc., New York, 1949.

20. A. E. Fuhs and G. N. Vanderplaats, "Aero-optics: Polynomial Representation of Laser Turret in Subsonic Flow and Completion of Formulation of Supersonic Flow," Progress Report 77-1 to AFWL, 10 November 1976.

21. G. N. Vanderplaats, A. E. Fuhs, and G. A. Blaisdell, "Optimized Laser Turret for Minimum Phase Distortion," Paper, This Conference.

22. A. E. Fuhs, "Aero-optics," Progress Report No. 2 to AFWL, 20 November 1975.

23. A. E. Fuhs, "Aero-optics," Progress Report No. 1, to AFWL, 6 September 1975.

INVISCID FLOW FIELD EFFECTS: EXPERIMENTAL RESULTS

L. J. Otten and K. Gilbert

Introduction

Inviscid effects due to aircraft laser turrets generally manifest themselves as aerodynamic lenses. The resulting optical errors are mainly tilt and focus. Because these effects are approximately steady for a given look angle and Mach number, they would be relatively simple to rectify with adaptive optics systems. It is the purpose of this paper to present the measured tilt and focus for a representative configuration.

Data Base

The data to be presented include two sources--one theoretical and one empirical. Main flow effects for a sphere were calculated by Wolters (ref. 1) and are presented because a sphere represents a very fundamental laser turret geometry. These estimates are valid for forward-look angles and for Mach numbers less than 0.66. An actual aircraft turret might be a section of a sphere and so would not have as severe a main flow-induced optical effect as a complete sphere. The fact that the sphere will be seen to produce a large effect, however, indicates that inviscid effects must be considered as a credible source of optical degradation.

The experimental data base is derived from the Air Force Weapons Laboratory (AFWL) wind-tunnel tests accomplished on the 0.3 scale Airborne

Laser Laboratory (ALL) Cycle III/IV turret assembly. These experiments were performed in the NASA Ames 14 by 14 foot subsonic tunnel during July/August 1976. The model setup is shown in figure 1. Tunnel Mach numbers ranged from 0.6 to 0.75. The aerodynamic instrumentation that was used to infer steady density consisted of the three linear arrays shown in figure 2. These hemispherical angle of attack pressure probes actually measure local velocity, v. Local density (ρ) then follows from the relationship (ref. 2)

$$\frac{\rho}{\rho_\infty} = \left[1 - \left(\frac{\gamma - 1}{2}\right)\left(\frac{v^2 - v^{2\infty}}{a^2}\right)\right]^{\left(1/(\gamma-1)\right)} \qquad (1)$$

where ρ_∞ = free-stream density

v_∞ = free-stream velocity

a = speed of sound in gas

γ = ration of specific heats

A more complete description of these probes is found in reference 3.

Maximum inviscid effects were observed for M = 0.75. Data for M = 0.75, M = 0.60 and M = 0.50 are shown in figure 3 for three rake locations. The ordinate axis is in units of free-stream density, ρ_∞. Next, the techniques employed to reduce these data to salient optical parameters are described.

In general, the index of refaction n and density ρ are related via the Gladstone-Dale constant K

$$n = 1 + K\rho$$

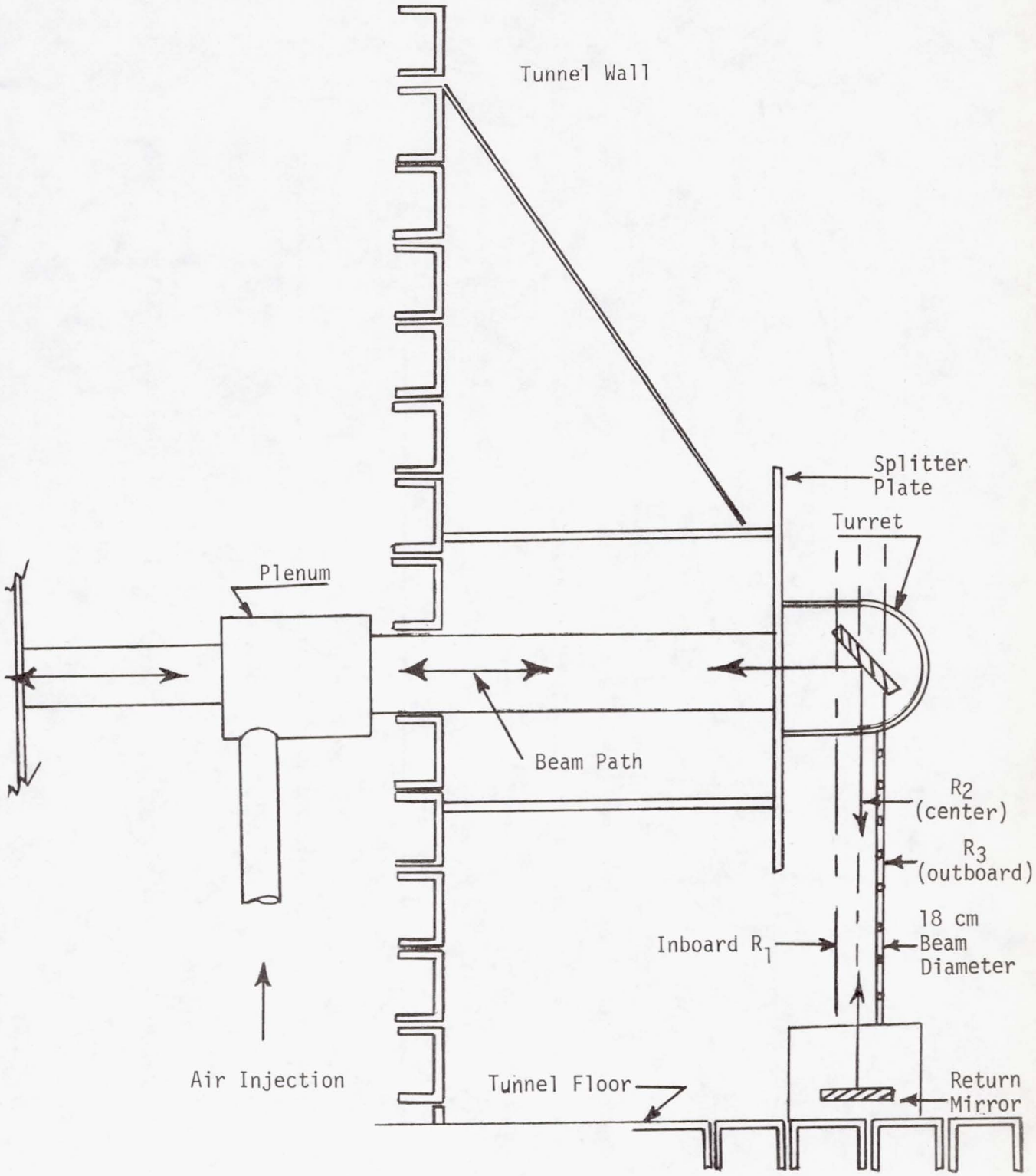

Figure 1. 0.3 Scale All Cycle III/IV APT Cross Section Flow Direction is into Paper (R_1, R_2, and R_3 are steady pressure rakes separated by 9 cm).

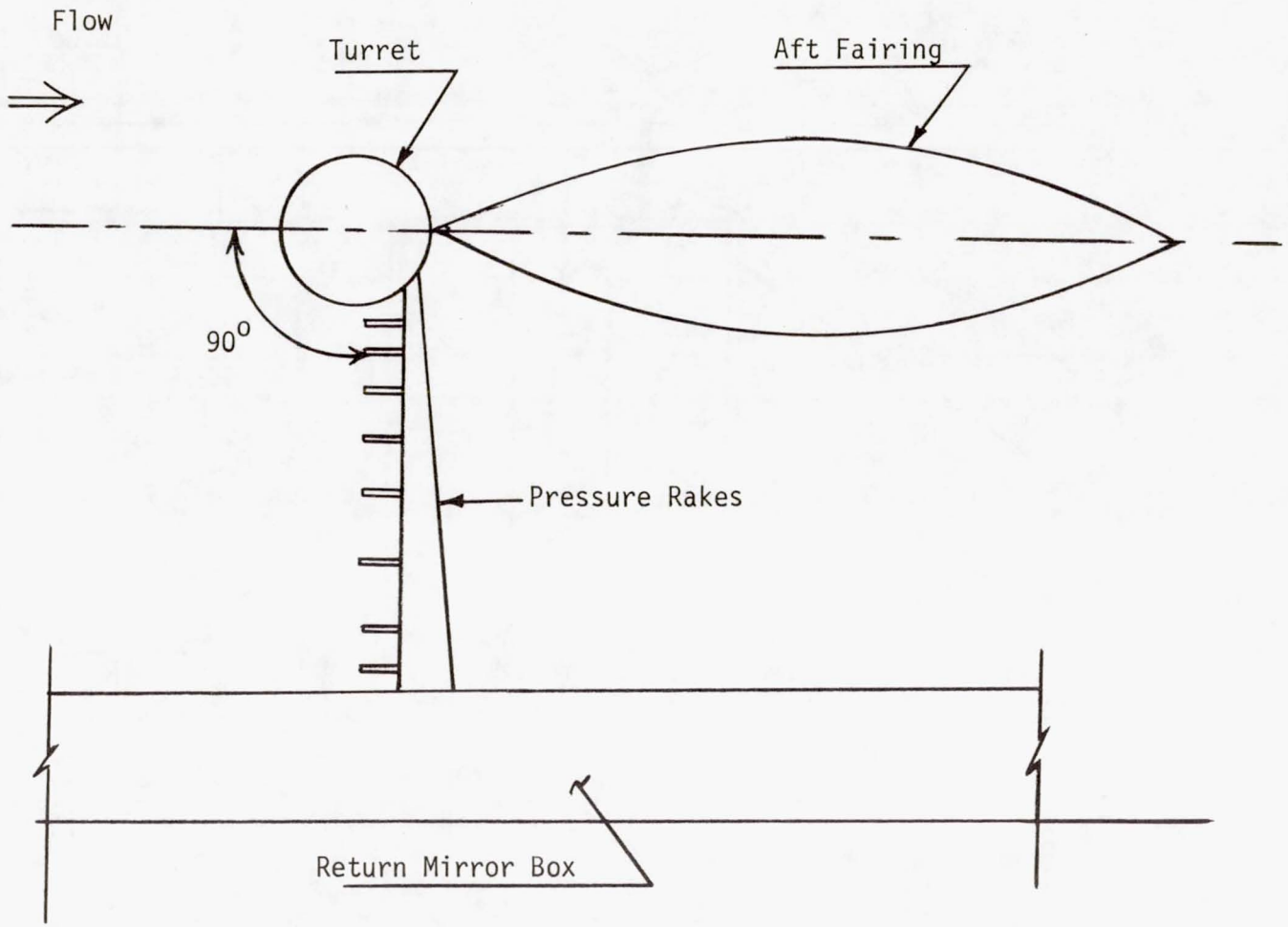

Figure 2. Side View of 0.3 Scale Cycle III/IV APT (Aximuthal angle of rakes is 90°. Elevation angle is 0°, i.e., in plane of flow.)

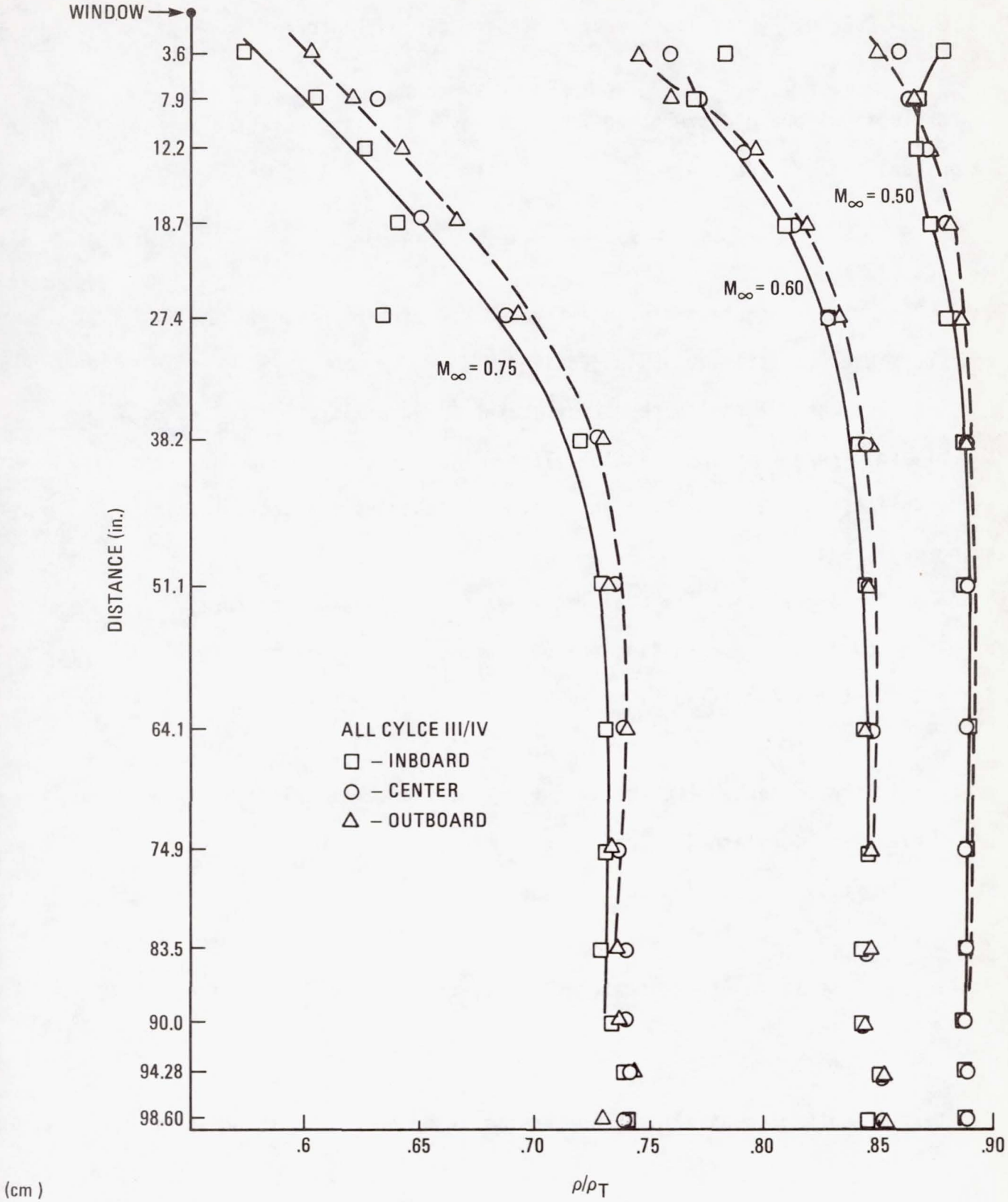

Figure 3. Spatial variation of density.

where $K = 0.22\ cm^3/g$ for laser wavelengths of current interest.

Now the optical phase disturbance $\Delta\phi$ caused by a density variation across an optical axis is (ref. 4)

$$\Delta\phi = K\int_0^L (\Delta\rho)\, dz \qquad (3)$$

where L is the propagation distance through the disturbance. Next, the procedure used to estimate $\Delta\phi$ is detailed:

(a) For each of the three optical paths (figure 1), $\phi = K\int_0^L \Delta\phi\, dz$ is calculated, where L is approximately 75 cm. In addition, a boundary condition is stipulated, $\Delta\phi\ (0) = 0$ where the origin is taken as the center of the outgoing wavefront.

(b) The three values of ϕ are then fit with polynomial of form $\phi = Ax^2 + Bx + C$. The resulting phase in microns (μ) across the aperture, for a free-stream density of $1.09 \times 10^{-3}\ g/cm^3$, is

$$\phi = -3.85x^2 - 2.11x \qquad (4)$$

where x is the distance from the center of the window in units of dimensionless diameter. This function is graphed in figure 4 for M = 0.75.

(c) Finally, these wind-tunnel measurements included a free-stream density (ρ_∞) of $1.09 \times 10^{-3}\ cm^3/g$ and an aperture radius (R) of 9 cm. Scaling of results to other altitudes and aperture sizes follows from

$$\phi^1 = \phi\, \frac{\rho'_\infty}{\rho_\infty}\, \frac{R^1}{R}$$

Similarly, scaling to other Mach numbers is in accordance with equation (1).

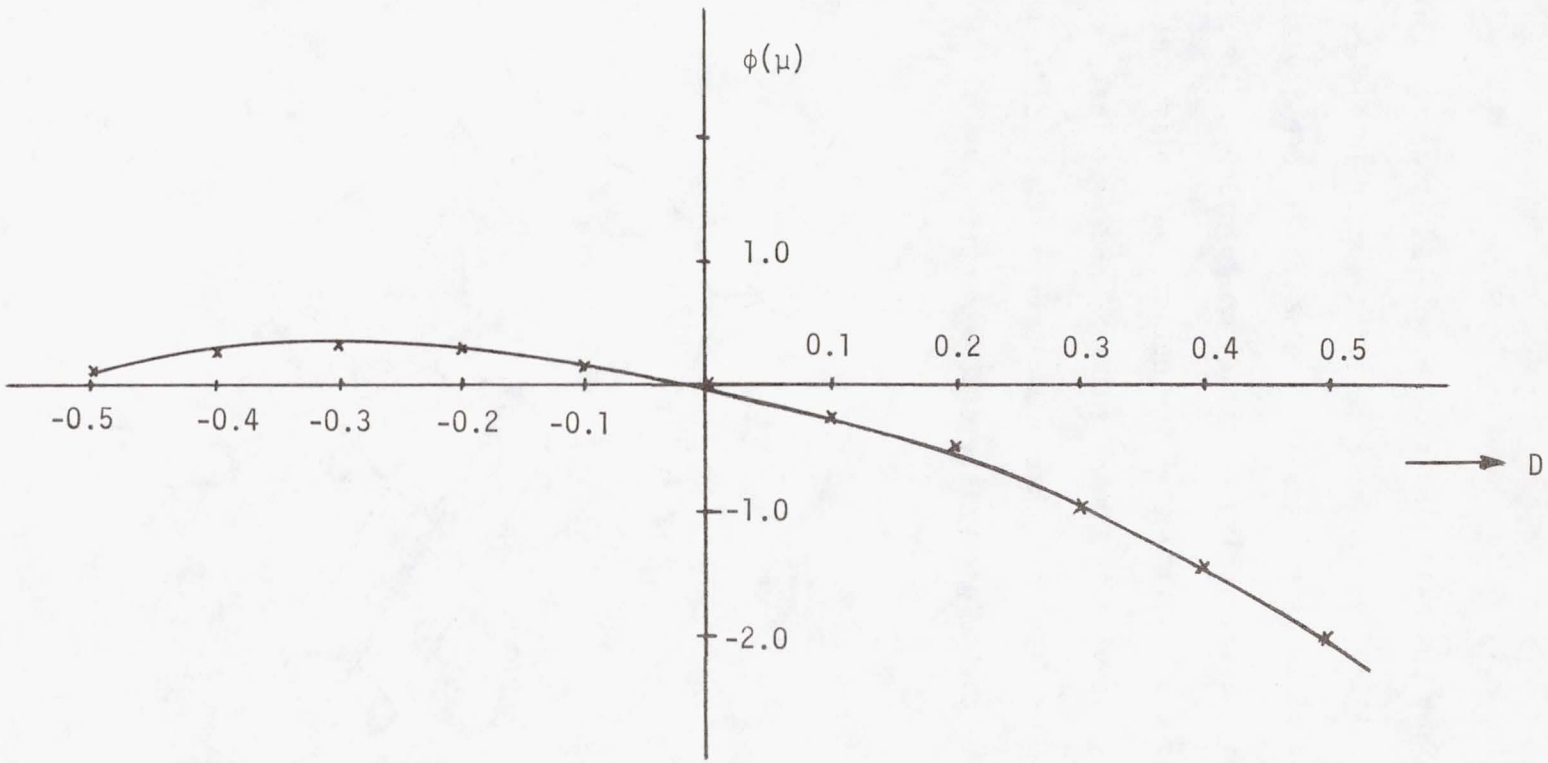

Figure 4. Measured Phase Across Aperture for 0.3 Scale ALL APT Cycle III/IV Turret (The aperture diameter is 18 cm, and the thermal free-stream density is $\rho_\infty = 1.19^{-3}$ g/cm^3.)

Implications of Data

The geometry for the main flow sphere problem is depicted in figure 5, while the results of Wolter's calculation appear in figure 6. A laser turret radius of 25 cm and sea-level atmospheric density are assumed. The wind-tunnel data, scaled to the 25 cm aperture radius, are also shown in figure 6. Notice that the optical path differences calculated from the wind-tunnel data are of the same order as those predicted for the sphere. The fact that these represent markedly different geometries lends credence to the generality of the results.

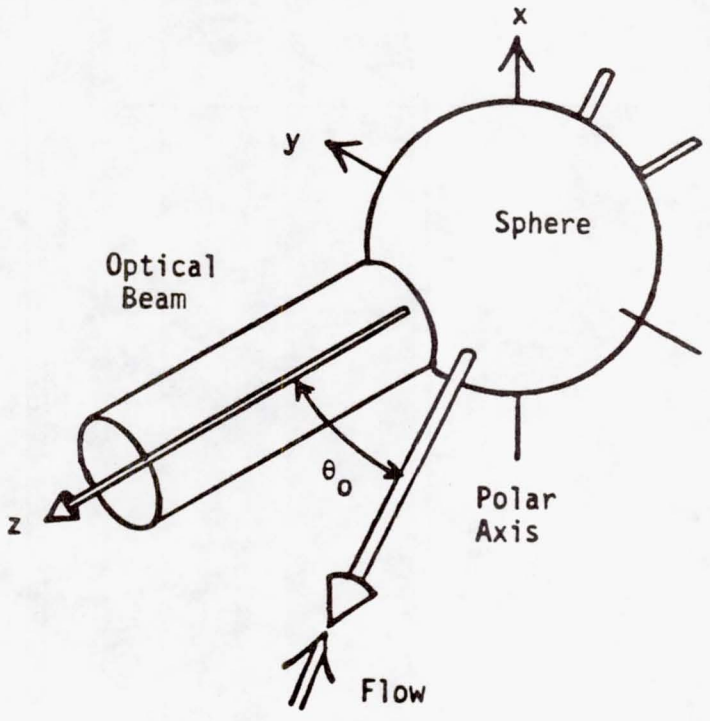

Figure 5. Coordinate System for Main-Flow Sphere Problem.

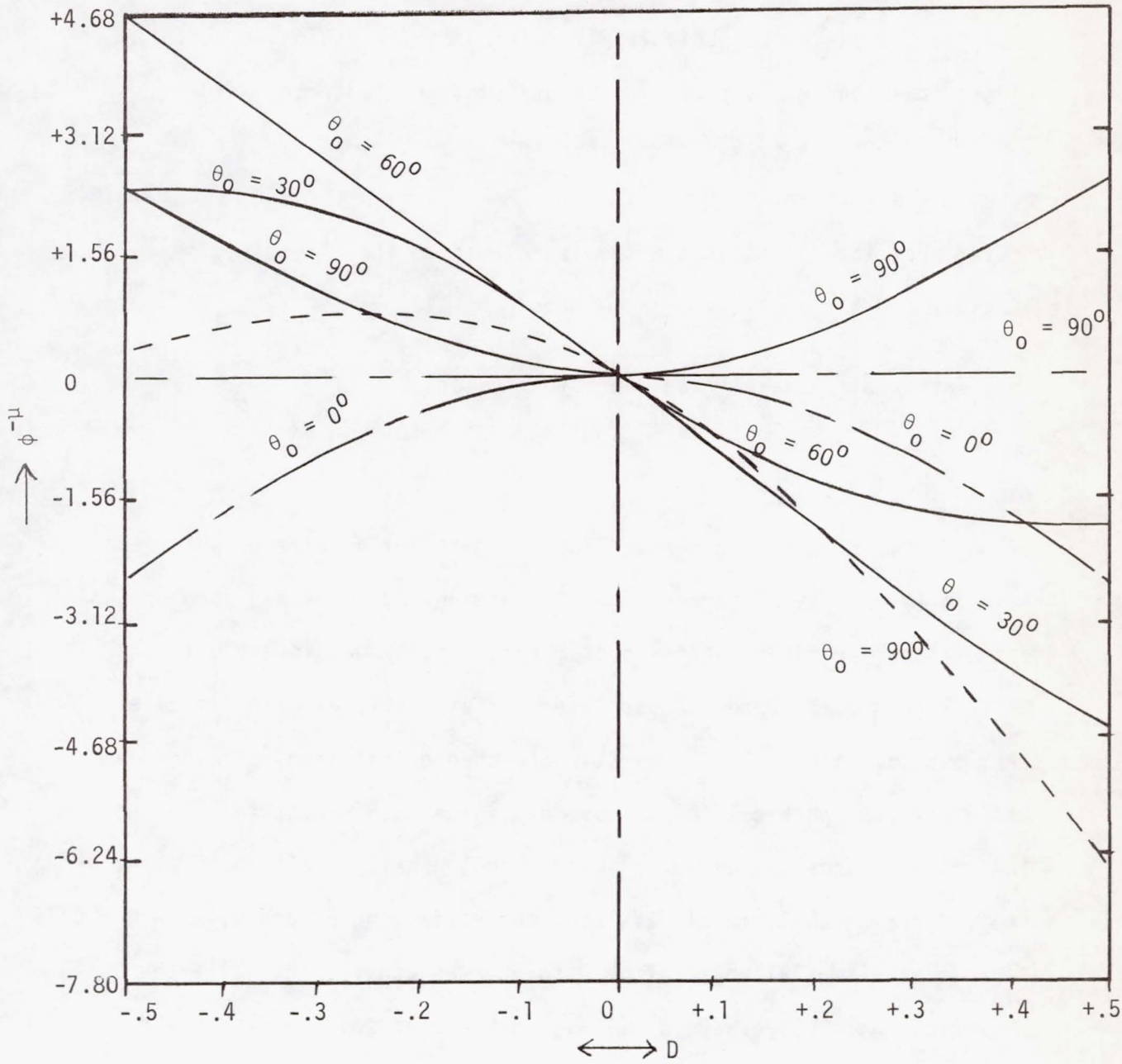

The solid lines (——) reflect main flow calculations for a sphere at M = 0.6, while the dashed line (---) represents 0.3 scale ALL turret (M = 0.75). θ_o is the look angle, while $\rho_\infty = 1.25^{-3} g/cm^3$.

Figure 6. Variation of Optical Path Across 50 cm Diameter Aperture.

The effective focal length of the aero-optical aberration estimated from the 0.3 scale ALL Cycle III/IV fairing can be estimated as follows. First, equation (4) is rewritten in units of centimeters

$$\phi = -4.93^{-7} x - 1.34^{-5} x \qquad (5)$$

with $0 \leq x \leq 25$ cm

Noting that the coefficient of x^2 is related to the effective focal length F by $\frac{1}{2F} = -4.93^{-7}$ cm $^{-1}$ then F = -11.1 km

This represents a fairly weak aerodynamic lens.

Conclusions

Airborne Laser turrets generally induce invisid flow effects which can lead to laser optical degradations. The magnitude of these aero-optical distortions for future optics system requirements was investigated. Optical path differences across laser turret apertures were estimated from two data sources. The first was a theoretical study of main flow effects for a spherical turret assembly for a Mach number (M) of 0.6. The second source was an actual wind-tunnel density field measurement on the 0.3 scale ALL Cycle III/IV laser turret/fairing assembly, with M = 0.75. A range of azimuthal angles from 0 to 90^{o} was considered, while the elevation angle was always 0^{o} (i.e., in the plane of the flow). The calculated optical path differences for these two markedly different geometries were of the same order. Scaling of results to sea level conditions and an aperture diameter of 50 cm indicated up to 7×10^{-4} cm of phase variation across the aperture for certain forward look angles and a focal length of F = -11.1 km. These values are second order for a 10.6μ system.

REFERENCES

1. Aerodynamic Effects on Airborne Optical Systems, D. J. Wolters, McDonnell Douglas Report MDC A2582, 1973.

2. Aerodynamics for Engineering Students, Houghton & Brock, Arnold Ltd, 1970.

3. The Dynamics and Thermodynamics of Compressible Fluid Flow, A. H. Shapiro, The Ronald Press Co., New York, 1953.

4. "Flight Calibration Tests of a Nose-Boom-Mounted Fixed Hemispherical Flow-Direction Sensor," NASA TN-D-7461, 1973.

OPTIMIZED LASER TURRETS FOR MINIMUM PHASE DISTORTION

by

Dr. G. N. Vanderplaats
NASA Ames Research Center
Moffett Field, CA, 94035

Dr. Allen E. Fuhs
Naval Postgraduate School
Monterey, CA, 93940

and

Mr. Gregory A. Blaisdell
Student, Applied Mathematics
California Institute of Technology
Pasadena, CA, 91125

ABSTRACT

Phase distortion due to compressible, inviscid flow over small perturbation laser turrets in subsonic or supersonic flow was calculated. The turret shape was determined by a two-dimensional Fourier series; in a similar manner, the flow properties are given by a Fourier series.

Phase distortion was calculated for propagation at several combinations of elevation and azimuth angles. A sum was formed from the set of values, and this sum became the objective function for an optimization computer program. The shape of the turret was varied to provide minimum phase distortion.

INTRODUCTION

For many applications of a high energy laser on board an aircraft, the beam must be propagated with minimum phase distortion. The well known Strehle

---

ACKNOWLEDGMENT. The work reported in this paper was supported by the Air Force Weapons Laboratory, Kirtland Air Force Base, NM, and was monitored by LtCol Keith Gilbert, Dr. Barry Hogge, and Captain Richard Cook.

relation [1] gives the decrease in far field intensity as a consequence of the rms phase distortion. As a result of the dependence of index of refraction on mass density, compressible flow over laser turrets causes phase distortion. The variable density and variable index of refraction surrounding an aircraft laser turret may be the result of viscous flow phenomena or inviscid flow. This paper focuses on the inviscid flow problem.

In regard to the solution of the phase distortion problem due to inviscid compressible flow, several options exist. Location of the turret on the aircraft is an important consideration. Adaptive optics may be used. Correct shape of the turret can reduce significantly phase distortion. The approach taken in this paper is to minimize phase distortion through turret shape.

An alternate approach would be to consider combined adaptive optics and turret shape. Higher order distortions, e.g., astigmatism and coma, are more difficult to remove by adaptive optics than lower order distortions. Using this approach to design, the turret shape should be modified so as to minimize higher order distortions.

In passing, a comment should be made about adaptive optics. Adaptive optics for compensation of atmospheric turbulence and thermal blooming requires mirror displacements of a fraction of wavelength at frequencies of 25 kHz or so. In contrast, the adaptive optics for compensation of laser turret phase distortion requires mirror displacements of a few wavelengths at frequencies of a few Hertz.

An analytical model for describing laser turret geometry and the associated compressible flow field has been described in the papers by Fuhs [2] and Fuhs and Fuhs [3,4]. A companion paper in this conference proceedings [5] discusses the analytical model. The turret shape is described by a two-dimensional Fourier series.

Using the flow over a wavy wall on a circular cylinder as the basic solution, a Fourier series can be found for the potential function. In contrast to a direct numerical integration of the equations of motion of gas dynamics, an explicit analytical solution is obtained. As a result, computer time is significantly less.

At a plane normal to the beam sufficiently far from the aircraft, the phase distortion is calculated. One method to represent the phase distortion is to use a series with Zernike polynomials [6]. The advantage of using a Zernike series is that the coefficients in the series are related directly to the magnitude of the various types of distortion, i.e., tilt, focus, defocus, astigmatism, etc.

A computer program [7,8] has been developed which can find the values of design variables yielding a minimum value of an objective function subject to constraints. The program has been applied to a variety of problems [9,10]. For the case at hand, the design variables are the coefficients describing the turret geometry. Also gas density inside the turret and the location of the laser turret primary mirror were treated as design variables; X_M and ε_M in Figure 1 define location of the mirror. The objective function was the weighted sum of phase distortion for several sets of elevation and azimuth angles. Constraints included the maximum slope of the laser turret as well as maximum turret height.

PHASE DISTORTION

Optical path length, L_i, is defined as

$$L_i = \int_a^b n(s)\,ds \qquad (1)$$

where n is the index of refraction and s is distance along a particular ray. Points a and b are on the ray. The subscript i identifies the ray. The difference in

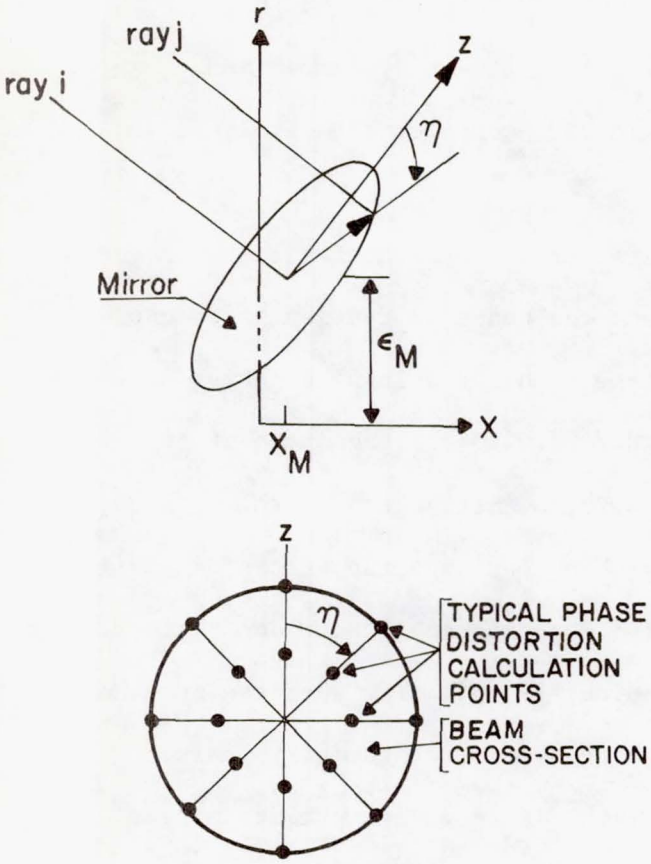

Figure 1. Geometry for Calculation of Phase Distortion.

optical path length for two adjacent rays i and j can be calculated; see Figure 1. The phase distortion, P, is the difference in optical path length divided by the wavelength.

$$P = \frac{L_i - L_j}{\lambda} \qquad (2)$$

The index of refraction is related to mass density, ρ, by

$$n = 1 + \kappa' \frac{\rho_\infty}{\rho_{SL}} \frac{\rho}{\rho_\infty} \qquad (3)$$

where κ' is a weak function of wavelength in the infrared, ρ_∞ is the freestream density, and ρ_{SL} is the sea level density. The form of equation (3) was used to highlight the dependence of n on altitude. The ratio ρ_∞/ρ_{SL} is a function of flight altitude.

The inviscid flow over the laser turret is assumed to be isentropic; thus the usual isentropic relation between pressure, p, and density, ρ, can be used. Further, the pressure coefficient, C_p, can be introduced with the result

$$\frac{\rho}{\rho_\infty} = \left[1 + \frac{\gamma M_\infty^2 C_p}{2}\right]^{1/\gamma} \qquad (4)$$

The pressure coefficient for small perturbation axisymmetric flow is given by Liepmann and Roshko [11] as

$$C_p = - 2u - v^2 \qquad (5)$$

where u is the perturbation velocity in the freestream direction and v is the radial velocity which is normal to the fuselage axis. Equations (1) to (5) can be combined to give an integral for the phase distortion in terms of pressure coefficient; see equation (7) of Reference [5]. When the potential function for the flow is known, both u and v can be calculated.

METHODS TO COMPENSATE FOR PHASE DISTORTION

The options available for compensating for phase distortion due to inviscid compressible flow over the laser turret were mentioned in the Introduction. Adaptive optics is one technique. Wolters and Laffay [12] demonstrate the effectiveness of adaptive optics.

Another method to compensate for phase distortion is to use a laser turret of proper shape. This is the approach of this paper. Turret geometry constitutes a passive technique. Turret geometry as a means to lessen phase distortion is discussed in the following sections.

A method to represent phase distortion is to use Zernike polynomials [1,6]. The polynomials, which are given in the paper by Hogge and Butts [6], are an orthonormal set of functions. The phase distortion is

$$P = \sum_{j=1}^{n} A_j F_j \qquad (6)$$

where A_j is a coefficient and F_j is the jth Zernike polynomial. The summation extends from 1 to n, where F_n is the highest order polynomial considered. Typically n = 10 is adequate. The coefficient A_q is obtained by multiplying both sides of equation (6) by F_q and integrating over the aperture or beam cross section. All

terms in the summation vanish except for the term j = q. Equation (19) of Reference [5] gives the results and a formula for A_j.

An alternate method to compensate for phase distortion is to combine adaptive optics and turret geometry. Higher order phase distortions are more difficult to compensate by adaptive optics. Form an objective function which is

$$B = \sum W_i A_i \tag{7}$$

where W_i is a weighting factor for the ith coefficient in Zernike series for phase distortion. The larger i, the larger is the value of W_i. As the turret shape is varied, the value for B changes. Using COPES/CONMIN computer program [7], the value of B can be minimized through variations of turret geometry. The consequence is that the effectiveness of adaptive optics is enhanced since higher order distortions are minimized.

The technique of adaptive optics employs segmented or deformable mirrors. Phase is controlled by mirror displacement. Further, the frequency of the mirror motion is determined by the frequency of the adverse phenomenon being overcome through use of adaptive optics. Hence, different types of adaptive optics can be thought of as occupying different locations in the mirror amplitude/frequency plane. Compensation for atmospheric turbulence occurs in the low amplitude, high frequency region of the adaptive optics map. Compensation for the adverse influence of flow over the turret occurs in the high amplitude, low frequency region of the adaptive optics map. The frequency response is dictated by turret slew rates or aircraft maneuver rates.

ANALYTICAL MODEL

The linearized potential equation for axisymmetric flow is

$$\pm \beta \phi_{xx} + \phi_{rr} + \frac{1}{r} \phi_r + \frac{1}{r^2} \phi_{\theta\theta} = 0 \tag{8}$$

The (+) sign is for subsonic flow, and the (-) sign is for supersonic flow. The quantity β is

$$\beta^2 = |1 - M_\infty^2| \tag{9}$$

where M_∞ is the freestream Mach number. The potential ϕ is the perturbation potential and yields the perturbation velocities

$$u = \frac{\partial \phi}{\partial x} \quad ; \quad v = \frac{\partial \phi}{\partial r} \quad ; \quad w = \frac{1}{r} \frac{\partial \phi}{\partial \theta} \tag{10}$$

The velocities appearing in equation (5) can be obtained from equation (10). The boundary conditions for equation (8) and a wavy wall on a circular cylinder are discussed in Reference [4]. A solution is obtained for one spatial frequency for the wavy wall. The solution is the basic function from which a Fourier series for the flow is constructed. The turret is represented by two polynomials

$$f(x) = 1 + \sum_{k=1}^{K} \tilde{a}_k x^k \tag{11}$$

and

$$f(\theta) = 1 + \sum_{j}^{p} \tilde{b}_j \theta^j \tag{12}$$

To obtain a symmetric turret in the θ-direction, only even values of j are used in equation (12). In terms of $f(x)$ and $f(\theta)$, the turret geometry is

$$R(x,\theta) = R_0 + \varepsilon f(x) f(\theta) \tag{13}$$

where R is the radial distance to the surface of the turret or fuselage. Equation (13) is represented by a Fourier series which leads to the coefficients in the Fourier series for the potential flow.

Figure 2 shows the geometry. The maximum turret height is ε, and the length of the turret is 2ℓ. The meaning of θ_{max} is that $f(\theta)$ is zero for $|\theta| > \theta_{max}$. Figure 3 is an artist's concept of the laser turret. Two comments are applicable to

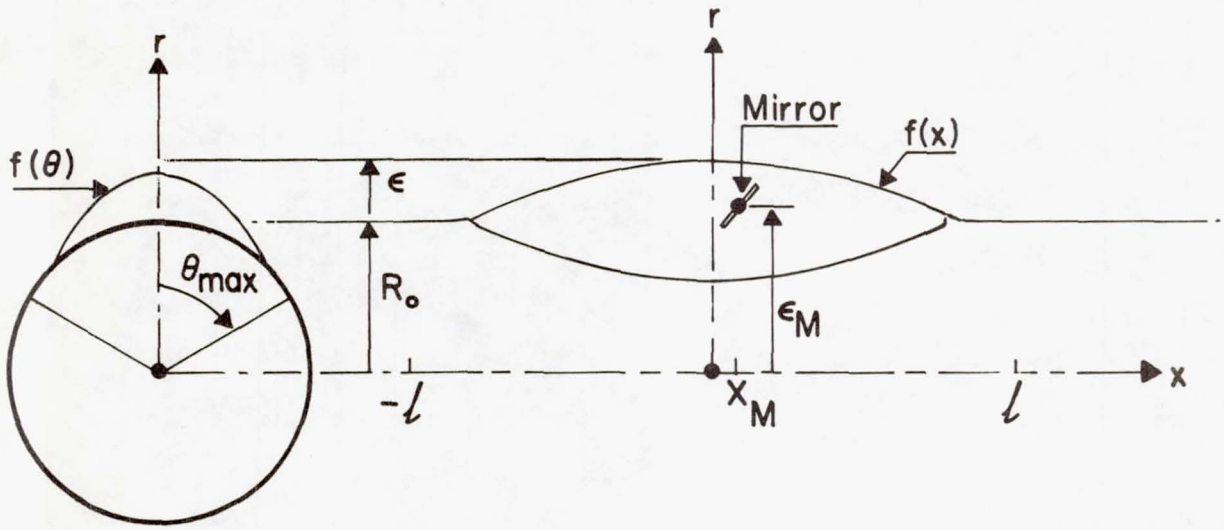

Figure 2. Geometry of a Small Perturbation Laser Turret on a Circular Fuselage.

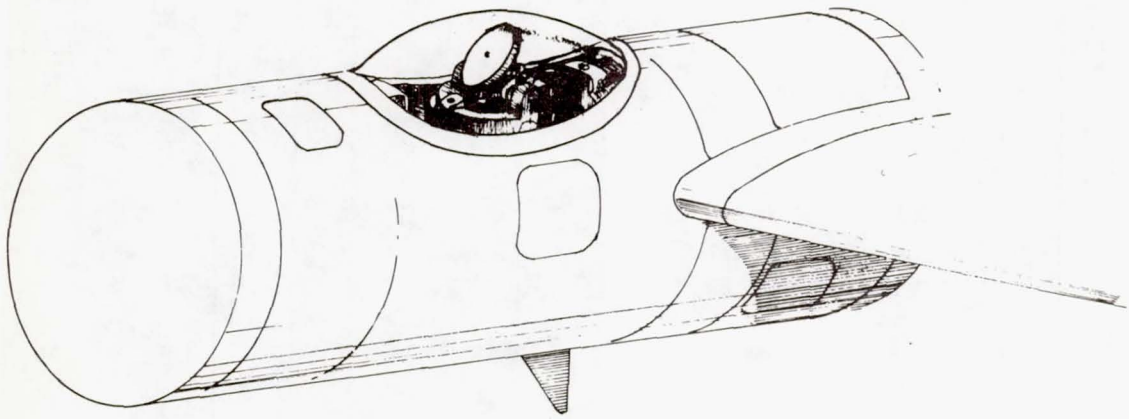

Figure 3. Artist's Concept of Laser Turret.

Figure 3. First, the turret will become operational at some future date when laser canopies can be manufactured! Second, the model does not include perturbation effects of wings, blade antennas, and similar items.

Figure 4 illustrates the coordinate system used to describe the direction of the beam relative to the aircraft. A Cartesian coordinate system X, Y, Z is oriented as shown. The Z-axis forms the polar axis for a spherical coordinate system. The beam is at azimuth angle ϕ and elevation γ.

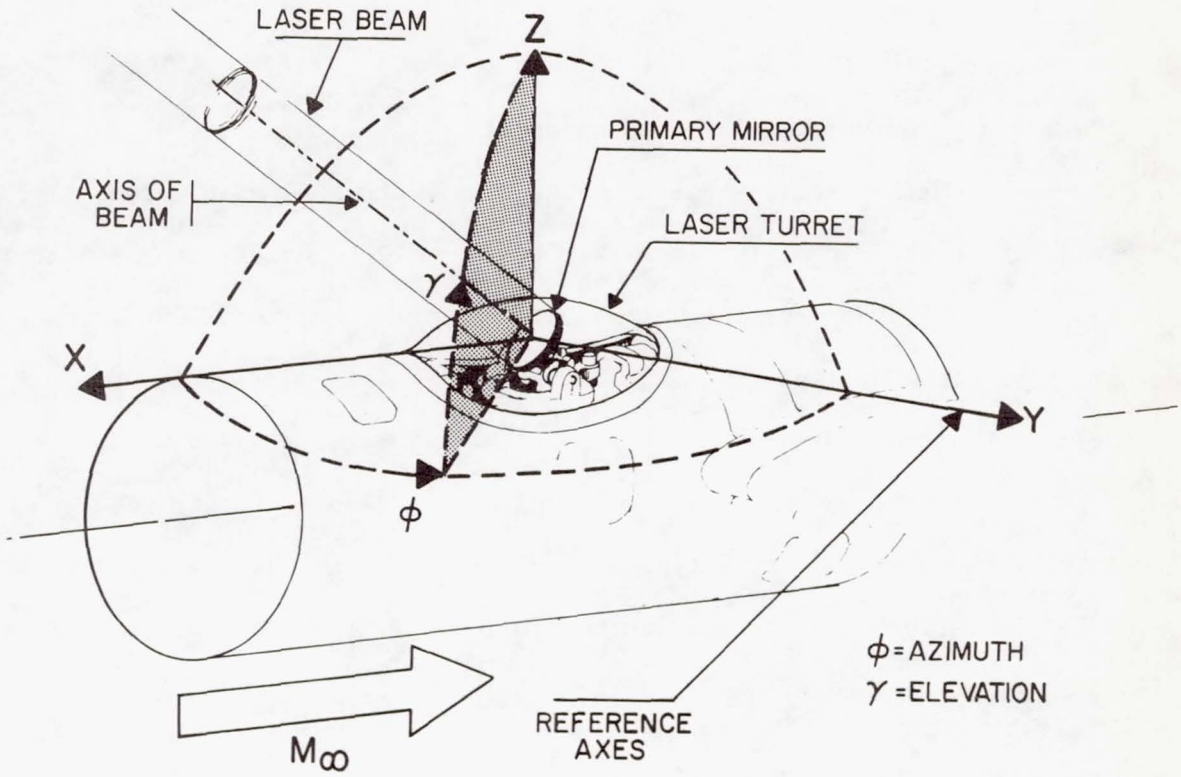

Figure 4. Coordinate System for Direction of Laser Beam Propagation.

The design variables become $\tilde{a}_k$ and $\tilde{b}_j$. Conditions at $|\theta| = \Theta_{max}$ and $|x| = \ell$ reduce the number of independent design variables. Typical conditions are

$$R(\theta_{max}, x) = R(\theta, \ell) = R_0 \tag{14}$$

and

$$\left(\frac{\partial R}{\partial x}\right)_{x=\pm\ell} = 0 \quad ; \quad \left(\frac{\partial R}{\partial \theta}\right)_{\vartheta=\theta_{max}} = 0 \tag{15}$$

The intercept between a ray and the turret surface is a particularly difficult problem in analytical geometry. An iteration scheme was used to find the intercept as follows:

a. At a given point $s = s'$ on the ray, calculate x, θ, R.

b. For these values of x and θ, calculate the radial component of the turret surface R_T.

c. Iterate to find a value of s' such that $R = R_T$.

The iteration procedure is described in detail by Vanderplaats [13].

In equation (1), the integration starts at a and ends at b. The start of integration, a, is at the primary mirror surface. The end of integration, b, is at a point sufficiently far from the laser turret so that additional integration by an amount δs yields a negligible change in the value of the integral. Since integration starts at the mirror surface, a portion of the ray between a and b is within the laser turret. Hence the density within the turret is a factor in the phase distortion. Even if the air external to the turret were uniform, a phase distortion could be generated by the air within the turret. In this study, the turret window is assumed to be of zero thickness so as to be distortionless.

OPTIMIZATION OF LASER TURRET SHAPE

For any given azimuth, ϕ, and elevation angle, γ, the phase distortion of any ray in the beam can be calculated using the center ray of the beam as a reference. At a specified beam orientation, the phase distortion typically will be calculated using equation (7) of Reference [5] at two radial locations for each of eight angular locations, i.e., η of Figure 1 occurs every 45°. Furthermore, to provide optimum overall system performance, several beam orientations are considered. By squaring the values of phase distortion and summing over all rays and orientations, a measure of total performance, S, is obtained as

$$S = \sum_{\phi} \sum_{\gamma} W_{\phi\gamma} \sum_{z} \sum_{\eta} P^2 \qquad (16)$$

The variable z is defined in Figure 1; z gives the radial location within the beam. $W_{\phi\gamma}$ is a weighting function. Values of $W_{\phi\gamma}$ are determined from mission studies. For a particular mission, the laser beam may be pointed most of the time at a particular direction, i.e., particular values of ϕ and γ. For that direction, $W_{\phi\gamma}$ is larger. For more extensive mission studies, sufficient information can be obtained so that a meaningful function can be defined for $W_{\phi\gamma}$; the function is a two-dimensional probability density function giving the probability the beam points in the direction specified by ϕ and γ.

The objective of the optimization was to minimize S by determining the proper combination of design variables. The design variables have been mentioned earlier. To summarize, the design variables are as follows:

independent variables from	$\tilde{a}_k$
independent variables from	$\tilde{b}_j$
mirror location	ε_M, X_M
density within turret	ρ_t

The analysis capability presented in this paper and Reference [5] has been coded in FORTRAN to produce maps of phase distortion for given azimuth and elevation angles. Figures 5 to 7 are phase distortion maps. For all three maps the windward side of the beam is at the top of the map. This fact can be determined from the equation for phase distortion

$$P = \frac{K'}{\lambda} \frac{R_0}{\rho_{SL}} \left\{ (s_j - s_i)\rho_t + \rho_\infty \int_{s_j}^{\infty} \left[1 + \frac{\gamma M_\infty^2 C_p}{2}\right]_j^{\frac{1}{\gamma}} \frac{ds}{R_0} - \rho_\infty \int_{s_i}^{\infty} \left[1 + \frac{\gamma M_\infty^2 C_p}{2}\right]_i^{\frac{1}{\gamma}} \frac{ds}{R_0} \right\} \qquad (17)$$

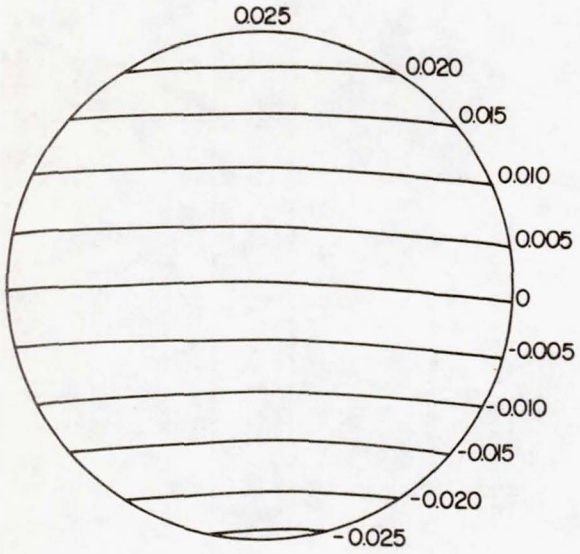

Figure 5. Phase Distortion Map. Azimuth, $\phi = 0^{o}$; Elevation, $\gamma = 45^{o}$. $M_{\infty} = 0.5$. $\rho_t/\rho_{\infty} = 1.0$. Cosine Turret.

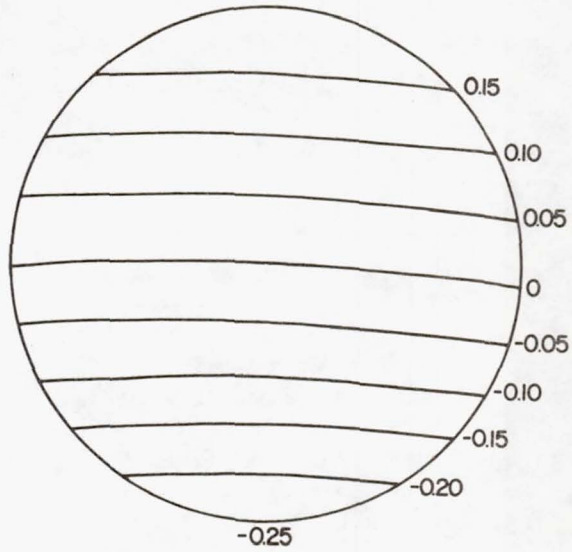

Figure 6. Phase Distortion Map. Azimuth, $\phi = 0^{o}$; Elevation, $\gamma = 45^{o}$. $M_{\infty} = 2.0$. $\rho_t/\rho_{\infty} = 1.0$. Cosine Turret.

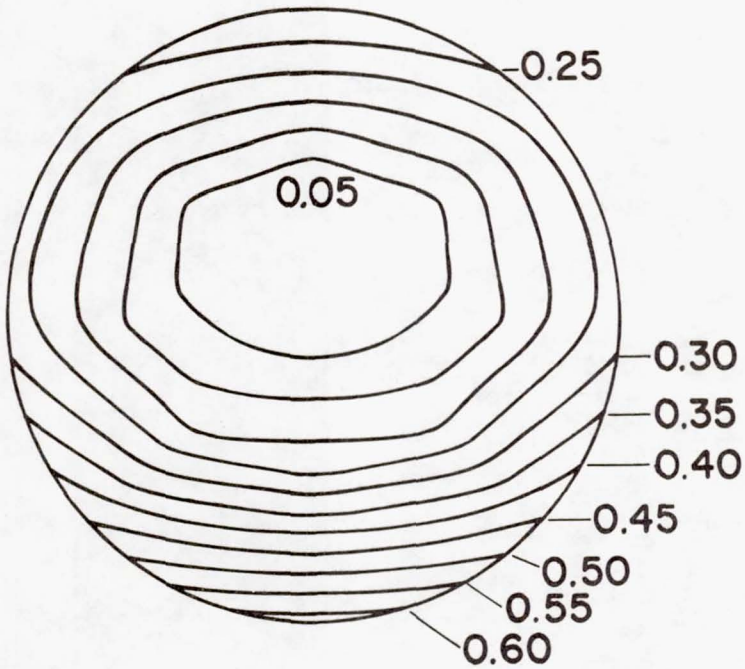

Figure 7. Phase Distortion Map. Azimuth, $\phi = 0^{o}$; Elevation, $\gamma = 90^{o}$. $M_{\infty} = 2.0$. $\rho_t/\rho_{\infty} = 0.309$. Optimized Turret.

In equation (17), s_j is the distance from the surface of the primary mirror to the intercept of ray j with the laser turret surface. The laser radiation has wavelength, λ. When the pressure coefficient C_p along ray j exceeds that along ray i, a positive contribution to the value of phase distortion occurs. Refer to Figure 2 or Figure 4. For an elevation angle of $\gamma = 45^o$ and the laser beam in the plane of symmetry of the fuselage, $s_j > s_i$. Consequently, the term $(s_j - s_i)\rho_t$ in equation (17) is also positive on the windward side. A positive phase distortion, P, means a lag of wavefront for ray j compared to wavefront of ray i.

The laser turret geometry and the associated flow were coded in subroutine form compatible with the general purpose optimization program.

COPES/CONMIN [7]

The COPES/CONMIN program solves the design problem of the following form:

$$\text{Minimize} \quad F(\vec{x}) \tag{18}$$

subject to the constraints

$$G_j(\vec{x}) \leq 0 \quad , \quad j = 1 \ldots m \tag{19}$$

where $F(\vec{x})$ is called the objective function and is defined by equation (16). The vector of design variables, $\vec{x}$, contains the design variables summarized above. $G_j(\vec{x})$ are the constraints. The constraints that were considered at one time or another during the study were the maximum slope of the turret in the streamwise direction, no discontinuity at turret fuselage boundary, and the conditions of equation (15). The slope was restricted, at the most, to a value of 0.3 since the linearized flow equations become inaccurate for larger values. The choice of objective and constraint functions is somewhat arbitrary; the only restriction is that both functions must be continuous functions of the design variables, $\vec{x}$, with continuous first derivatives. In general, $F(\vec{x})$ and $G_j(\vec{x})$ may be any linear or non-linear functions of $\vec{x}$.

TWO EXAMPLES OF LASER TURRET DESIGN

Two design examples are presented here, the first being for subsonic flow and the second being for supersonic flow. The design conditions are listed in Table I. Calculations were conducted for six beam orientations and sixteen rays within the beam.

Table I. Design Conditions

AERO-OPTICS		
Mach number	Case 1	$M_\infty = 0.5$
	Case 2	$M_\infty = 2.0$
Ratio of heat capacities		$\gamma = 1.4$
Wavelength of laser radiation		$\lambda = 3.8$ microns
Density ratio		$\rho_\infty/\rho_{SL} = 0.3$
Constant for index of refraction		$\kappa' = 0.00023$

GEOMETRY	
Fuselage radius	$R_0 = 1.0$
Spacing of turrets	$L = 5.0$
Mirror location	$\varepsilon_M = 1.125$
	$X_M = 0$
Turret length	$\ell = 2.0$
Turret height	$\varepsilon = 0.2$
Mirror radius	$R_m = 0.05$
Maximum angle extent of turret	$\theta_{max} = 60^o$

GEOMETRIC BOUNDARY CONDITIONS

x/ℓ	$f(x)$	$df(x)/dx$	θ/θ_{max}	$f(\theta)$	$df(\theta)/d\theta$
- 1.0	0	0	$\pm$ 1.0	0	varies
0	1.0	varies	0	1.0	0
1.0	0	0			

Table I Continued. Design Conditions

BEAM ORIENTATIONS

Beam Number	Azimuth, ϕ, degrees	Elevation, γ, degrees
1	0	45
2	0	90
3	0	120
4	45	45
5	90	30
6	90	60

PHASE DISTORTION CALCULATION POINTS

Rays defined by all combinations of:

radius within beam $z/R_0 = 0.025, 0.050$

angle within beam $\eta = 0, 45, 90, \ldots 315$

Note: All rays are shown in Figure 1.

CONSTRAINT IN SLOPE

$$-0.3 \leq \frac{df(x)}{dx} \leq 0.30$$

for $\theta = 0$

As a reference, flow over a cosine-shaped turret was calculated. The equations for turret geometry were

$$f(x) = 1.0 - 0.50\left(\frac{x}{\ell}\right)^2 + 0.0625\left(\frac{x}{\ell}\right)^4 \tag{20}$$

and

$$f(\theta) = 1.0 - 1.824\left(\frac{\theta}{\theta_{max}}\right)^2 + 0.832\left(\frac{\theta}{\theta_{max}}\right)^4 \tag{21}$$

Phase distortion maps are shown in Figures 5 and 6 for the turret specified by equations (20) and (21). The perturbation velocities, u and v, were calculated in the plane of symmetry of the fuselage and are shown in Figures 8 and 9. Figure 8 is for the subsonic flow example, and Figure 9 is for the supersonic flow example. The radial perturbation velocity, v, is dictated by the boundary condition at the turret surface. Hence v is identical in both Figures 8 and 9. The axial perturbation velocity, u, is different for subsonic flow as compared to supersonic

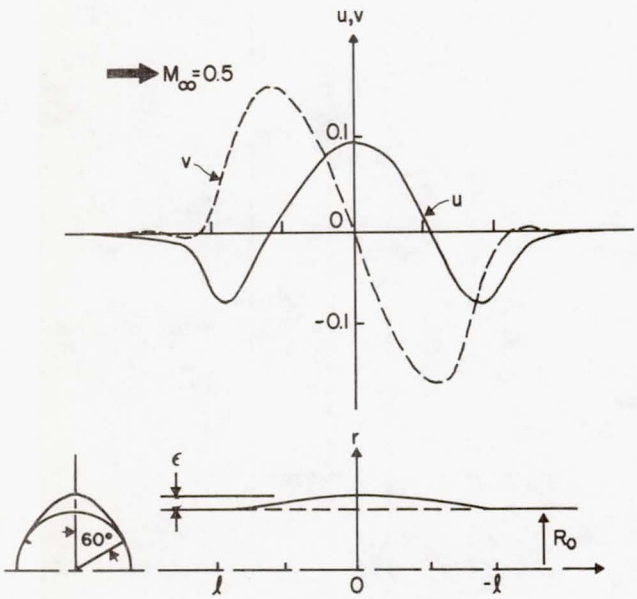

Figure 8. Perturbation Velocities for a Cosine Turret in Subsonic Flow.

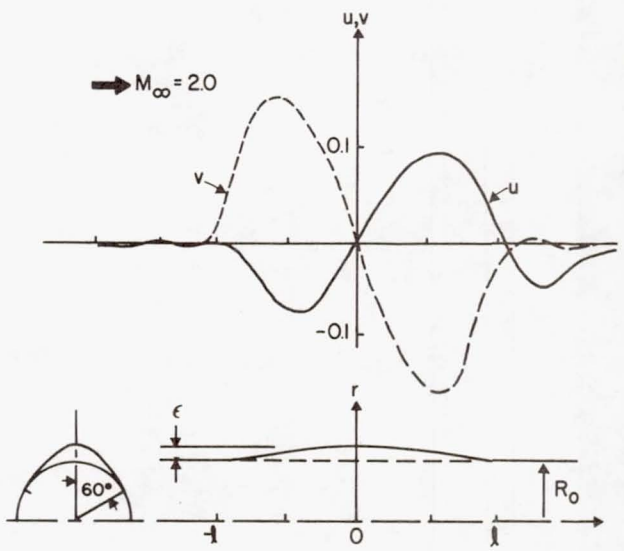

Figure 9. Perturbation Velocity for a Cosine Turret in Supersonic Flow.

flow. In subsonic flow, the maximum value of u occurs at x = 0, while in supersonic flow, at x = 0, the value of u is zero. In supersonic flow, the flow is compressed ($u < 0$) on the forward or windward side of the turret; on the leeward side of the turret, the flow is expanded ($u > 0$).

Results for the two examples are summarized in Table II. In Table II the values of the coefficients $\tilde{a}$ and $\tilde{b}$ are listed for both the initial and optimized laser turrets. Using these values of $\tilde{a}$ and $\tilde{b}$, the laser turrets have been drawn and appear in Figures 10 to 12. Figure 10 is the cosine-shaped turret used as reference.

Table II. Summary of Laser Turret Design Results

TURRET GEOMETRY

Polynomial Exponent	Initial Turret		Optimized Turrets Case 1 (Subsonic)		Case 2 (Supersonic)	
	$\tilde{a}$	$\tilde{b}$	$\tilde{a}$	$\tilde{b}$	$\tilde{a}$	$\tilde{b}$
0	1.0	1.0	1.0	1.0	1.0	1.0
1	0	0	0	0	0.2651	0
2	-0.5	-1.824	-1.5596	-1.83	-0.6077	-1.858
3	0	0	-0.0006	0	-0.1326	0
4	0.0625	0.8315	0.5923	0.8426	0.1163	0.8933
5	0	0	0.00015*	0	0.0166*	0
6	0	0	-0.0662*	-0.005*	-0.0067*	-0.0282*

*Design Variable

VALUE OF OBJECTIVE FUNCTION, S, AND DENSITY RATIO

Quantity	Initial Turret		Optimized Turrets	
	Subsonic	Supersonic	Case 1 (Subsonic)	Case 2 (Supersonic)
S	36.02	2.69	31.22	1.55
ρ_t/ρ_∞	0.7	0.3	0.7	0.3094

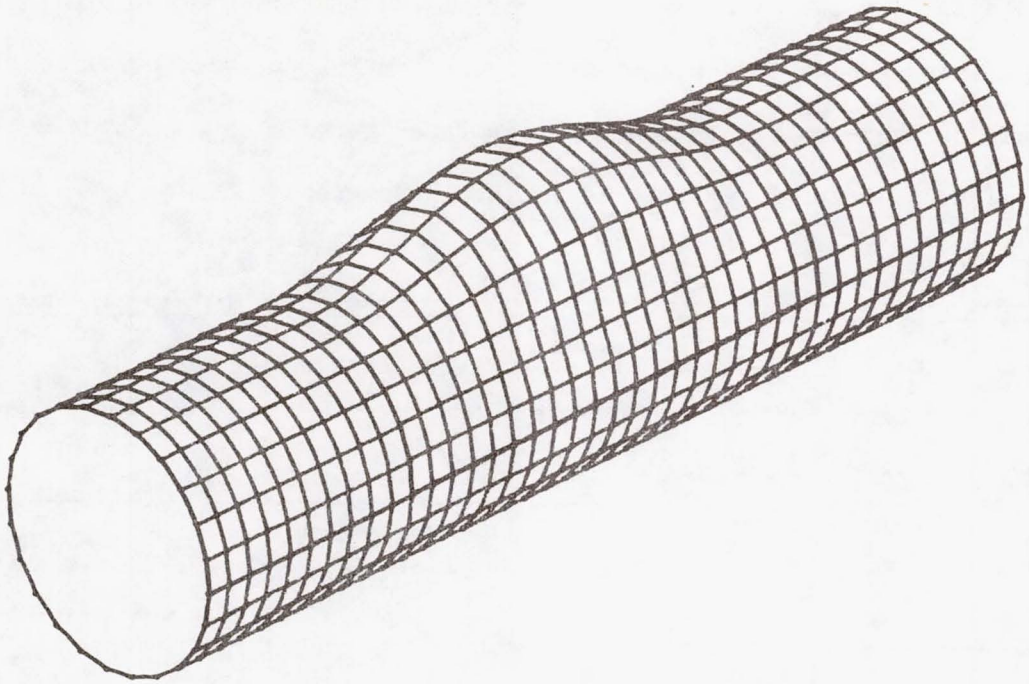

Figure 10. Cosine Shaped Laser Turret Used as Reference.

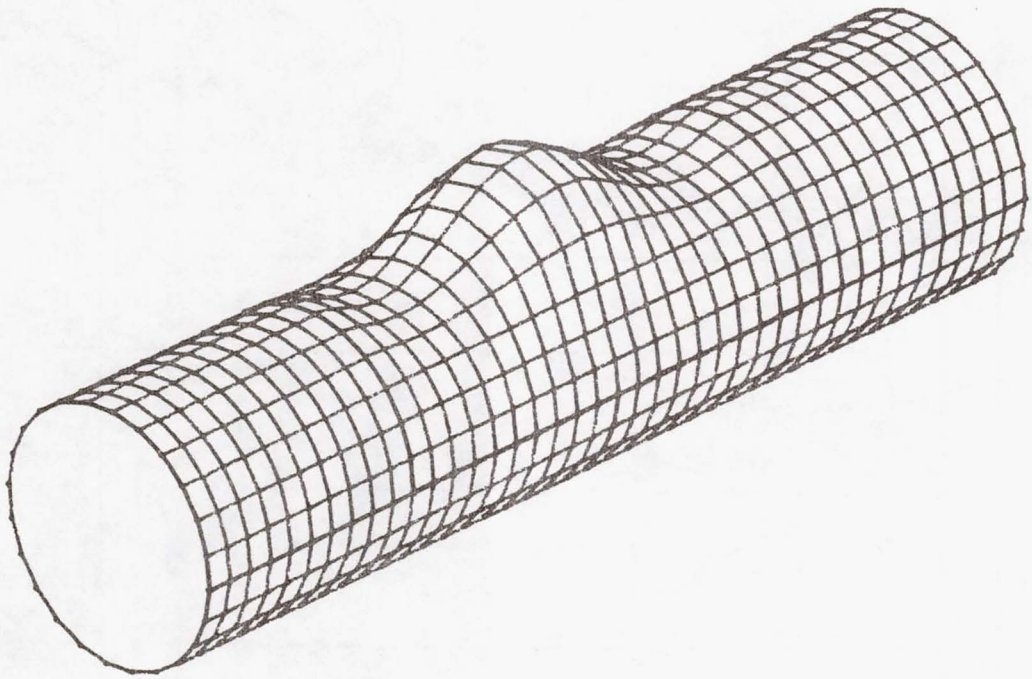

Figure 11. Optimized Laser Turret for Subsonic Flow. $M_\infty = 0.5$.

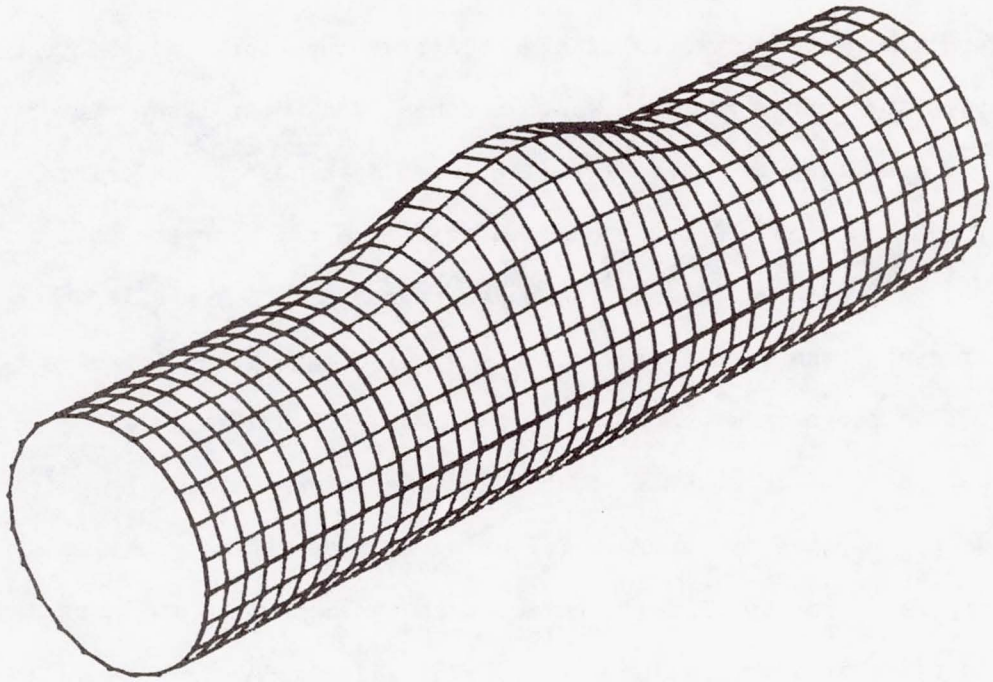

Figure 12. Optimized Laser Turret for Supersonic Flow. $M_\infty = 2.0$.

Figure 11 is the optimized laser turret for subsonic flow. Figure 12 is the optimized laser turret for supersonic flow. Comparing Figures 10 and 12, very little difference between the cosine-shaped and the optimized turret for supersonic flow can be seen. However, reference to Table II shows the optimized turret has odd powers for f(x); note that $a_1 = 0.2651$, $a_3 = -0.1326$, and $a_5 = 0.0166$.

For the calculations summarized in Table II, all the weighting values $W_{\phi\gamma}$ were unity. Using the COPES/CONMIN optimization computer program, the objective function, S, defined by equation (16), was reduced from 36.02 to 31.22 for the laser turret optimized for subsonic flow. The reduction is 13 per cent. The objective function, S, for the laser turret designed for supersonic flow was reduced from 2.69 to 1.55. The reduction is 42 per cent. Also note that a density within the turret, ρ_t, less than ambient helps to reduce the phase distortion; see Table II.

EXAMPLE OF LASER TURRET GIVING LEAST AND WORST PHASE DISTORTION

To illustrate the range of values of the objective functions, S, that can be obtained by varying the turret geometry, both the best and worst laser turret were designed. Details are given in Table III. The cross sections of the initial turret, the best turret, and the worst turret are shown in Figure 13. For the case at hand, the initial turret yielded S = 0.0115. The worst turret gave S = 0.0918 which is a change of 690 per cent. The best turret has S = 0.0012 which is an improvement in S of 890 per cent. The range from the worst to the best is 0.0918/0.0012 = 78.5.

Table III has the coefficients A_j for the Zernike polynomials. The phase distortion can be represented by equation (6) using A_j from Table III. The reader should compare A_j for the initial turret with the other two turrets. The best turret has a slightly larger value for A_4. The value of A_9 is reduced greatly.

For the laser turret giving the worst distortion, all coefficients are increased except for A_4. The focus coefficient is slightly smaller. The average value A_1 has little significance.

Compared to the two examples of the previous section, the turrets in this section were optimized for only one beam direction. The beam direction was at an azimuth, $\phi = 45^{\circ}$ and an elevation, $\gamma = 45^{\circ}$.

COMPUTER CODE FOR LASER TURRET OPTIMIZATION

An extensive and versatile computer code has been written by Vanderplaats and Fuhs [14]. The computer code is based on References [2,3,5,7,8,13]. The program calculates the optical path length and phase distortion arising from the density field surrounding a laser turret in compressible flow. Further, the program finds the optimum turret shape yielding minimum phase distortion. The optimization and control codes are thoroughly discussed in Reference [14]. Sample data input and

Table III. Summary of Results for Phase Distortion

Zernike Coefficient	Physical Significance	Initial Turret	Laser Turret Shape Least Distortion	Laser Turret Shape Worst Distortion
A_1	average value	-3.331E-04	3.967E-04	-4.193E-03
A_2	x-tilt	0.02129	4.391E-03	0.05995
A_3	y-tilt	-7.643E-03	5.422E-03	-0.03595
A_4	focus	-3.947E-04	4.759E-04	-3.650E-03
A_5	astigmatism	6.576E-05	3.320E-05	3.748E-04
A_6	astigmatism	9.183E-04	3.973E-05	9.944E-04
A_7	coma	-1.638E-05	-7.172E-06	-5.610E-04
A_8	coma	-5.123E-06	3.136E-05	-8.846E-04
A_9	coma	0.01656	3.428E-03	0.04549
A_{10}	coma	-5.951E-03	4.285E-03	-0.02840

Mach number = .500

Flight altitude = sea level

Turret height/fuselage radius = .200

Beam radius/fuselage radius = .05

Elevation angle = 45^{o}

Azimuth angle = 45^{o}

sample output are given. The material is presented in sufficient detail so that Reference [14] constitutes a user's manual for LASTOP.

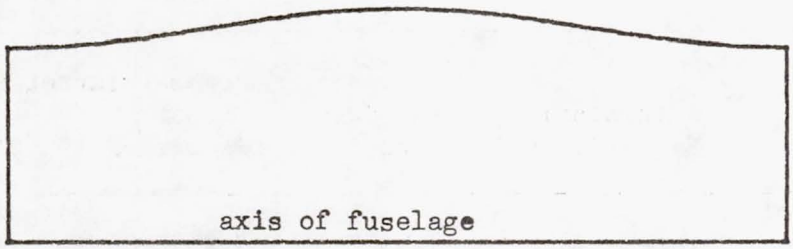

(a) Nominal turret. Objective function has value of 0.0115.

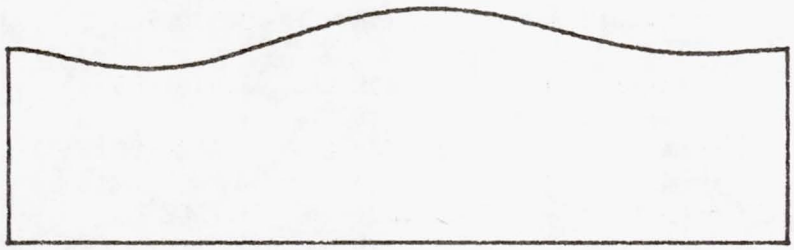

(b) Turret yielding greatest distortion. Objective function has value of 0.0918.

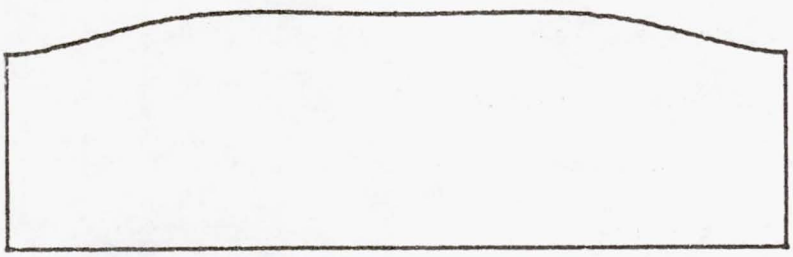

(c) Turret yielding least distortion. Objective function has value of 0.0012.

Figure 13. Cross Section Shape of Turrets in the Plane of Symmetry.

COMMENTS AND CONCLUSIONS

A versatile analysis and computer program has been developed which optimizes laser turret geometry to obtain minimum phase distortion. The turrets are located on a fuselage of circular cross section. Turret slope is limited so as not to exceed the perturbation allowed by the linearized equations for the flow. The computer code is described in Reference [14].

Examples have been given which show the decrease in objective function, S in equation (16), that can be achieved.

REFERENCES

1. M. Born and E. Wolf, Principles of Optics, Pergamon Press, New York, 1964.

2. A. E. Fuhs, "Distortion of Laser Turret Optics Due to Aircraft Mainstream Flow," Journal of Optical Society of America, 66, p. 1137, 1976.

3. A. E. Fuhs and S. E. Fuhs, "Phase Distortion Due to Airflow over a Hemispherical Laser Turret," Naval Postgraduate School Report NPS-69FU76101, September, 1976.

4. A. E. Fuhs and S. E. Fuhs, "Phase Distortion at High Subsonic Mach Numbers for a Small Perturbation Laser Turret," Proceedings of Electro-Optical Systems Design Conference--1976, New York, pp. 9-19, published by Industrial and Scientific Conference Management, Inc., 222 W. Adams St., Chicago, IL, 60606.

5. Allen E. Fuhs and Susan E. Fuhs, "Optical Phase Distortion Due to Compressible Flow over Laser Turrets," Paper This Conference.

6. C. B. Hogge and R. R. Butts, "Frequency Spectra for the Geometric Representation of Wavefront Distortions Due to Atmospheric Turbulence," IEEE Transactions on Antennas and Propagation, Vol. AP-24, pp. 144-154, 1976.

7. Garret N. Vanderplaats, "CONMIN--A FORTRAN Program for Constrained Function Minimization," NASA TM X-62282, August, 1973.

8. Garret N. Vanderplaats, "The Computer for Design and Optimization," Computing in Applied Mechanics, AMD Vol. 18, ASME, Dec., 1976.

9. Garret Vanderplaats and Allen E. Fuhs, "Aerodynamic Design of a Conventional Windmill Using Numerical Optimization," Journal of Energy, 1, pp. 132-134, 1977.

10. S. E. Fuhs, G. N. Vanderplaats, and A. E. Fuhs, "Land Contouring to Optimize Wind Power," AIAA 16th Aerospace Sciences Meeting, 1978, Paper 78-279.

11. H. W. Leipmann and A. E. Puckett, Introduction to Aerodynamics of a Compressible Fluid, John Wiley and Sons, New York, 1947. See Chapter 10.

12. D. J. Wolters and P. J. Laffay, "Mainstream Flow Effects on F-15 Turret Optics," McDonnell Aircraft Company Report MDC A3179, January 3, 1975.

13. G. N. Vanderplaats, "Inviscid Flow over Turrets; Optimum Turret Shape," Lecture 5A, Laser Aerodynamics, a Short Course at the Air Force Weapons Laboratory, Kirtland Air Force Base, NM, April 11-22, 1977.

14. G. N. Vanderplaats and A. E. Fuhs, "LASTOP - A Computer Code for Laser Turret Optimization of Small Perturbation Turrets in Subsonic or Supersonic Flow," Naval Postgraduate School, Technical Report NPS 69-77-004, December, 1977.

OVERVIEW OF RECENT AERO-OPTICS FLIGHT TESTS

L. J. Otten III
Major, USAF

The final expression of any flight related investigation is actual flight data. Historically, this only occurs after exhaustive ground testing. Aero-optics did not follow this trend. Indeed it was early flight testing (circa late 1950s-early 1960s) that indicated the presence of a near-field aero-optics problem. Aero-optics flight testing had the advantage of advancing with the state of the art in aero-optics ground testing--this by virtue of "non-interference" testing during the ALL Cycle II Program. The flight testing portion of the aero-optics culminated in a series of dedicated tests commonly called Cycle II.5. This paper will trace these flight tests in a summary manner while highlighting the objectives and conclusions from the tests.

Figure 1 shows a chronological listing of the relevant aero-optics flight testing along with the objectives of each flight. Flights before project PRESS have not been included. We will now summarize each of these test series.

The first credible flight aero-optics data were collected during the Lincoln Laboratory project "PRESS" flights. "PRESS" flights were reentry observation missions using optical trackers looking through slightly recessed optical quality windows on an Air Force NC-135A. While tracking fixed sources, i.e., stars, an unusual amount of blurring was observed during flight as compared to ground tracking. The obvious losses in

seeing were attributed to the aircraft boundary layer, the small shear layer over the recessed viewing ports, and heat transfer through the aircraft skin. Optical losses were estimated at 5 to 20 μrad using a shearing interferometer.[1] The boundary layer thickness at the point of measurement was approximately 30 cm, with a small (1.5 cm) shear layer next to the fuselage. In addition to documenting the observed optical losses of the PRESS flights, the effects of turbulent supression techniques were investigated.[2] These attempts were in general unsuccessful.[1,2] The PRESS flights represented the first documented aero-optics flight data. These data were limited in scope and tended to serve the PRESS mission. The data did give rise to a variety of explanations of the source of degradation and provided the stimulator for further study.

The next significant aero-optics flights were a dedicated series performed on NASA AMES' Lear 23 in January 1975. The Lear tests were designed to unravel some of the mysteries surrounding the existing flight and wind tunnel data. Specifically, the applicable aerodynamic scaling laws were sought as was the characteristic scale size of the near field turbulence. Toward these objectives additional data were provided, but firm conclusion were not to be found due to limited diagnostics. Ten dedicated missions were flown over a Mach range of 0.3 to 0.8 and from $1.5X10^3$m to $12.2X10^3$m altitude. Constant dynamic pressure and constant Mach profiles were flown. Optical instrumentation consisted of Kelsall's fast shearing interferometer[3] and an AFWL line spread function measurement (LSF).[4,5] The experimental set up is shown in Figure 2 and Figure 3.

Both turbulent boundary layers and fence generated shear flows were observed using integrated path optical techniques (Figure 4). These flight tests showed the expected aperture scaling (Figure 5a) and indicated that shear flows were optically less desirable (Figure 5b).[4] Unfortunately, the flights did not show the expected dependence on free-stream density and Mach number and the expected correlation between the MTF and LSF was not always present.[4] Scaling of the observed HeNe wavelength data to 10.6μ did provide a timely indication that near field distortions were not an issue for long wavelengths. Most important, these tests represented the first dedicated aero-optics flight tests and underscored the need for a more thorough investigation. The flights also provided an airborne checkout of equipment designated for the ALL Cycle II tests.

Chronologically, the next flight aero-optics data were obtained as part of the ALL Cycle II tests. The ALL Cycle II program was a linear propagation and tracking demonstration of the ALL flight hardware. The flights afforded the opportunity to look at both the mechanical and optical properties of the ALL tracker which had recently been investigated in a series of wind-tunnel tests (Ref 6, 7, 8, 9, 10). One of the Cycle II objectives was "to isolate and measure beam degradation due to near field aircraft induced effects and natural turbulence effects."[11,12] Two classes of measurements were used in these optical tests - an overall ALL optical train degradation examination using a 10.6μ Fast Shearing Interferometer (FSI) with an angle of arrival (AOA) detector and a boundary-layer/free-stream turbulence examination from a pointer in-

dependent platform using a visible FSI (the same one used in the Lear Jet work) and a scintillometer (Figures 6 and 7). Alignment between the two aircraft was obtained through two ALPE computer driver trackers using HeNe sources (Figure 8). The ALL tracker provided its own track capability. Additionally, atmospheric turbulence data were obtained using a fine hot wire mounted on a T-39 which measured C_T^2 from which C_N^2 was inferred (Figure 9). Twenty-one flights over an eight-month period were used to collect the Cycle II propagation data. The T-39 data were generated over a two-year span.

As apparent in Figures 6, 7, and 8, the Cycle II tests were fairly complex, involving multiple simultaneous measurement and several aircraft. The FSI proved to be a significant improvement over the slow shearing predecessor. Its high speed (an MTF every 3 msec) froze the atmospheric turbulence and allowed statistically meaningful samples to be processed. Even more so than the slow shearing interferometer, the FSI was vibrationally insensitive (vibration data being collected with the AOA). Additional data included pointer system performance obtained from the tracker error signals and a large number of accelerometers and pressure transducer to document the aero-dynamic parameters.

Some interesting conclusions were drawn from the Cycle II aero-optics flights. Both the FSI and AOA data indicated that, for 10.6μ, atmospheric turbulence and near field turbulence are not major factors in total system performance, a result forecasted from the Lear Jet tests. Platform jitter was the largest contributor to system degradation. As in

previous aero-optics flight tests, correlation to aircraft flight parameters were not readily obvious (Figure 10). AOA and MTF data were sensitive to flight configuration with the non-full forward fairing having the highest jitter and largest distortion (Figure 11). Turret/fairing aerodynamic performing was gratifying in that it matched predictions (Figures 12 and 13).

Observed natural turbulence data (C_N^2) obtained from the T-39 was roughly in keeping with other observations but with a significant discrepancy being observed in the measured frequency spectra data versus theoretical spectra (Figures 14 and 15a, b). These data were collected under a variety of conditions (0.5 to 12.5 km) with data being analyzable from 1 Hz to 200 Hz. An operational consideration was the problems encountered with the survivability of the probe with frequent probe breakage occurring. In these measurements, C_T^2 was measured using temperature fluctuations only, with Mach number and velocity (i.e. compressibility) not being accounted for, an assumption which later tests showed to be generally reasonable.

In general, the Cycle II flight data contributed significantly to the aero-optic program by delegating 10.6μ atmospheric and near field turbulence to second order effects while highlighting the importance of airframe aerodynamic buffet. The flights did not, however, quantify the entire airborne aero-optics problem and continued undersettled the aero-

dynamic scaling laws and correlation between optical data inferred by using aerodynamic measurements.

Cycle II.5 was a dedicated aero-optics program conducted in the Summer of 1977 using an NKC-135A. This aircraft was modified to incorporate an aft aero-optics data station. Diagnostics, finally, included a serious aerodynamic effort using the advances in aero-optical tunnel testing techniques (ref.13, 14, 15). Multiple hot wires (constant current and constant temperature) mounted to two independently movable probes (a total of 4 wires), an LDV using an argon laser, and a visible FSI were installed. The starboard side of the aircraft was smoothed forward of the measurement station and incorporated a noninterference FSI return mirror and LDV directing assembly (Figure 16a, b). An optical quality ($< \lambda/10$) window was flush-mounted at the measurement station to transmit the HeNe FSI signal. Provisions were made to mount a series of porous fences at various positions upstream of the measurement station to allow investigation of shear flows as well as boundary layers. The extended displacement of the measurement station from the nose of the aircraft produced actual Reynolds Number $> 10^7/m$, values impossible to achieve for transonic speeds by wind-tunnel simulation.

The prime objective of the Cycle II.5 flights was to demonstrate the scalability of aero-optics data. In essence, the NASA Ames 6 x 6 aero-optics wind-tunnel experiments were repeated at flight Reynolds numbers allowing a direct scaling comparison. Additionally, the contribution of

heat transfer through the the aircraft skin on the optical quality of the near field flow was quantified as was the feasibility of using aero measurements to infer optical phenomena. The flight tests encompassed about 50 hours of flight test time and covered the entire aircraft flight envelope ($0.20 \leq M_\infty < 0.88$, $0.1\text{km} \leq \text{altitude} \leq 15.24$ km)

Conclusions from the Cycle II.5 tests were encouraging. Scaling of wind tunnel data was demonstrated and non-dimensional quantities were verified.[16,17,18] Correlation between direct FSI measurements of near field optical losses to inferred losses using aerodynamic parameters (i.e. density magnitude and scale sizes) was very high--a much sought after result since aero-inferred measurements, which are integrated point data, are generally easier to quantify and obtain. Aircraft thermal gradients were shown to have insignificant effects on near field optical seeing[19] for the observed flight conditions ($0.2 < M < 0.9$). The comparison of shear layer data to boundary layer data showed all the optical losses occurring in the small shear layer region with losses being not too different from turbulent boundary of corresponding intensity (an observation leading to a "conservation of fluctuating index of refraction theory"). As an unforecasted bonus, the anemometers, which accounted for Mach effects, were shown to have promise in measuring a broad spectrum of free-stream turbulence. Resolution of turbulence scales from several mm to several km was shown to be feasible at least to heights of 4.7 km. This last observation encouraged the development of an atmospheric turbulence probe for use during the ALL Cycle III tests.

Cycle II.5 was the last aero-optics flight test. Because of the Cycle II.5 results, ground testing of near-field losses was shown to be clearly feasible for any specific flight configuration--with subscale results being accurately scalable. Current aero-optics flight investigations are limited to an atmospheric turbulence probe installed on the nose of the ALL diagnostic aircraft. The probes (Figure 17) carries constant current and constant temperature fine wires and are free from engine induced broad band noise (they do, however, see turbine compressor noise). Recent work with this probe have shown it capable of resolving atmospheric turbulence up to 17 km altitude over scale sizes of 5mm to 0.5km.[20] The probe is presently being used to quantify atmospheric turbulent sources (thunderstorms, topographic, etc) and to contribute to the atmospheric turbulence data base.

It is apparent that aero-optics flight testing has reached its apex and further extensive flight measurements are not required. Such is the hallmark of a developed discipline. The papers to follow will cover in detail the more relevant of the forementioned tests.

REFERENCES

1. Bryant, B. W., "Airborne Image Studies," Lincoln Laboratory, Optics Research, No 1, 1971.

2. Project PRESS - Performance Analysis of Airborne Telescopes for Reentry Observations, Cornell Aeronautical Lab Final Report No. BE-1475-H-1, 15 October 1961.

3. Kelsall, D., "Rapid Interferometric Technique for MTF Measurements in the Visible or Infrared Region," Appl. Opt. 12, 1398, 1973.

4. Gilbert, K.G., Terwilliger, D. F., Cook, R. J., "Laser Propagation Through an Aircraft Turbulent Boundary Layer: Lear Jet Experiments," Laser Digest, AFWL-TR-75-229, October 1975.

5. Bailey, Wade H., "Line Spread Instrumentation for Propagation Measurements, Optical Engineering, Vol. 17, No. 4, 1978.

6. Visinsky, W. L., "Propagation Through Aerodynamic Boundary Layers," Laser Division Digest, AFWL-LRD-72-1, June 1972.

7. Pape, L.E. and Visinsky, W. L., "Preliminary Results from Wind Tunnel Experimentation," Laser Digest, AFWL TR-R-73-131, June 1973.

8. Van Kuren, James T. and Connors, William R., Laser Beam Propagation in Transonic Flow, AFFDL-TM-107-FX, July 1973.

9. Otten, L. J. III and Davis, J. A., 0.3 Scale Open Port ALL Turret Tunnel Test Results, AFWL-TR-73-17, 1973.

10. Steerken, W. G., et al, Wind Tunnel Investigation of 0.3 Scale APT Closed-Port Turret and Fairing Model: Vol I Test Results and Analysis," General Dynamics, Report FZA-458, 1972.

11. Sher, L. and Gilbert, K. G., The Airborne Laser Laboratory Cycle II: Low Power Experiments, AFWL-TR-271, May 1977.

12. Otten, L. J., Measurements and Analysis of the External Unsteady Pressures on the Airborne Laser Laboratory, AFWL-TR-73-141, Aug 1973.

13. Otten, L. J., and Van Kuren, J. T., "Artificial Thickening of Transonic Boundary Layers," AIAA Paper 76-51, Jan 1976.

14. Rose, W. C. and McDavid, E. P., "Turbulence Measurements in Transonic Flow," 9th AIAA Aerodynamics Testing Conference, June 1976.

15. Johnson, D. A. and Rose, W. C., "Turbulence Measurements in Transonic Boundary Layers and Free-Shear Flows Using Laser Velocimeter and Hot-Wire Anemometer Techniques, AIAA Paper 76-399, June 1976.

16. Gilbert, K.G., "Aircraft Aero-Optical Turbulent Boundary Layer/ Shear Layer Measurements," Laser Digest - Fall 1977, AFWL-TR-78-15, April 1978.

17. Rose, W. C., Johnson, D. A., and Otten, L. J., "Application of Hot Wire Anemometry and Laser Velocimetry to In-Flight Measurements of Turbulent Flow Properties," AIAA Paper 78-285, April 1978.

18. Rose, W. C., "Measurement of Aerodynamic Parameters Affecting Optical Performance," AFWL-TR-78-191, May 1979.

19. Gilbert, K.G., "Thermo-Optical Turbulent Boundary Layer Measurements," Laser Digest - Fall 1977, AFWL-TR-78-15, April 1978.

20. Rose, W.C., and Otten, L.J., "Airborne Measurement of Atmospheric Turbulence," USAF/NASA Aero-Optics Symposium, Aug 1979.

SYMBOLS

I/I_o	Strehl ratio
I_F/I_{NF}	Ratio of peak intensities for a fence to a non-fence
δ_b	Boundary-layer thickness
δ_F	Fence height
λ	Probe laser wavelength
M_∞	Free-stream Mach number
MTF	Modulated transfer function
L_o	Characteristic turbulence scale size
ℓ_o	Characteristic turbulence scale size
$\Phi(K)$	Power spectral density function of the fluctuating temperature
K	Frequency
C_N^2	Index of refraction coefficient
C_T^2	Temperature coefficient
Φ	Characteristic value of $\Phi(K)$
CP_{rms}	Root mean square of the fluctuating static pressure
f	Frequency
$\overline{\Phi}$	Normalized power spectral density function of the fluctuating static pressure
U_∞	Free-stream velocity
q_∞	Free-stream dynamic pressure
D	Characteristic length (turret diameter)

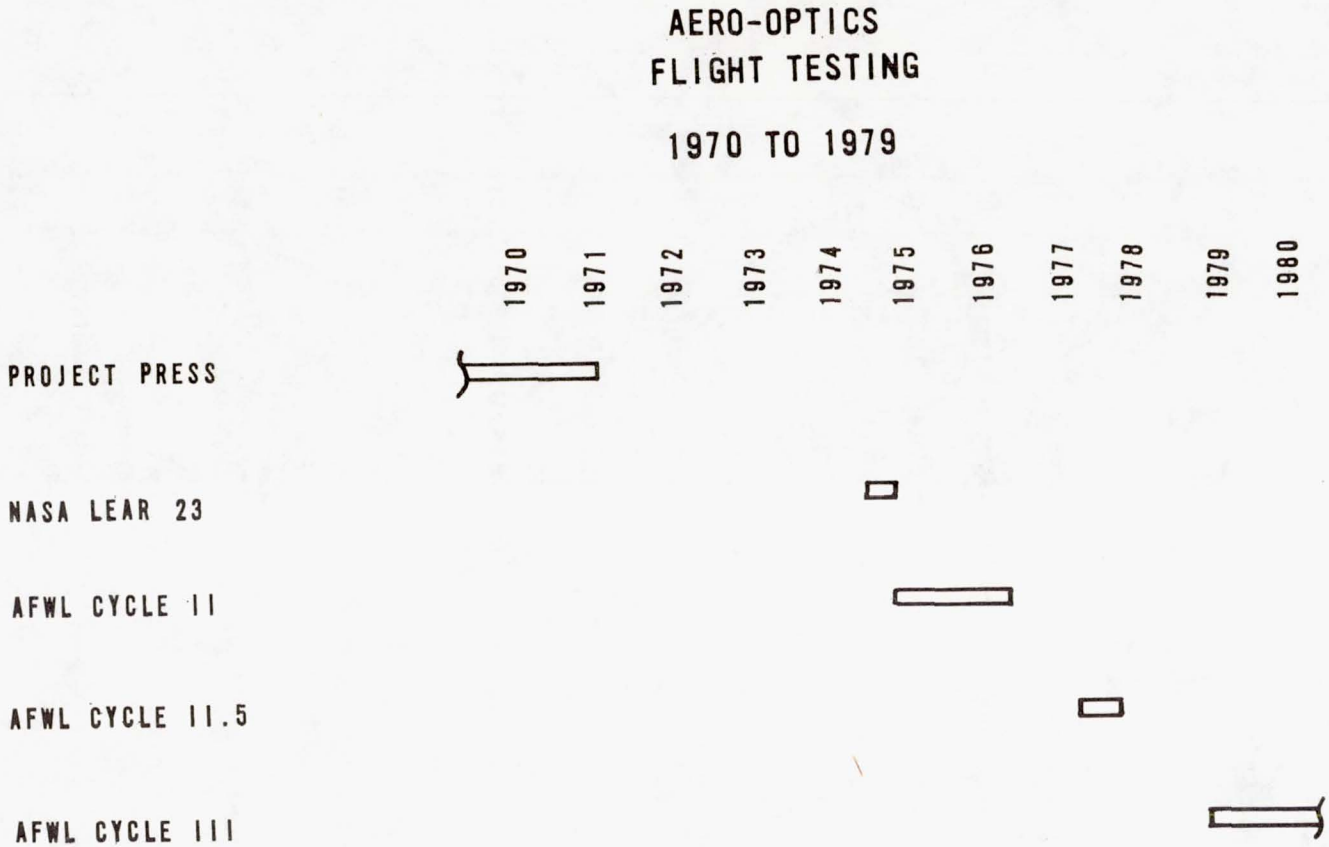

Figure 1. Chronological listing of aero-optics flight tests 1970-1979.

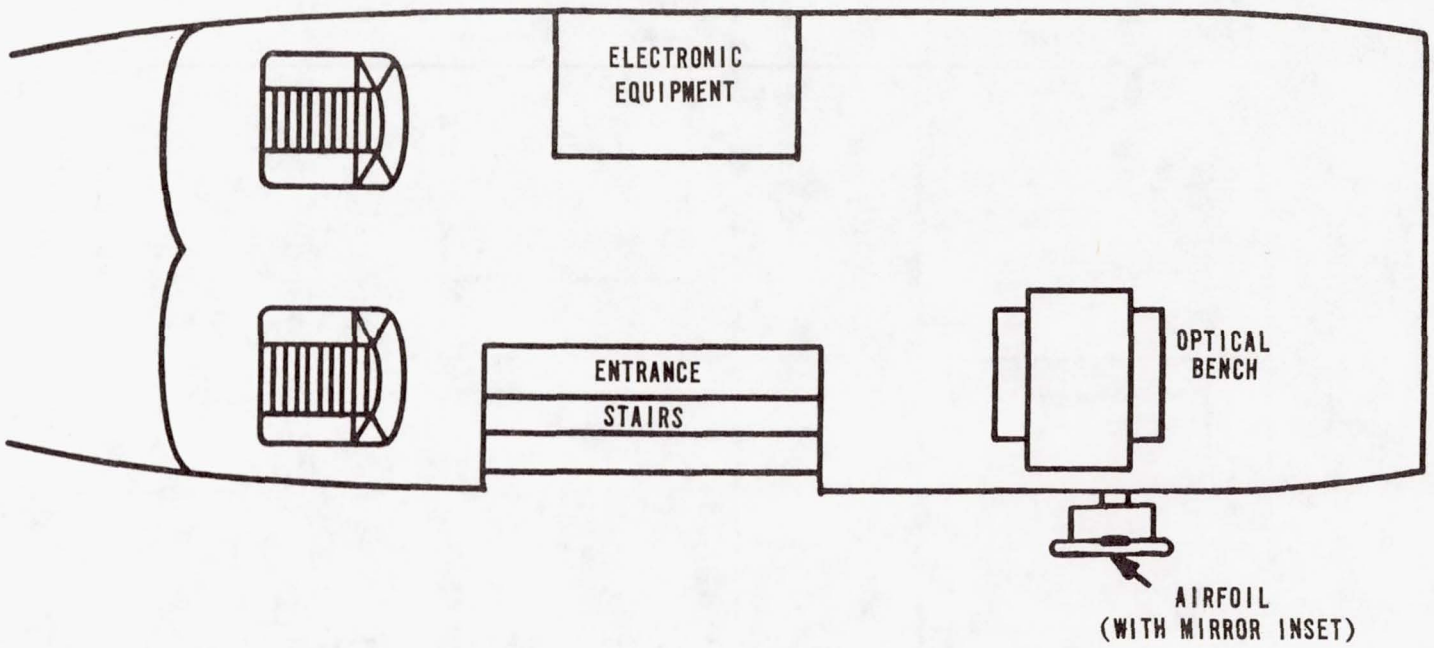

Figure 2. Lear Jet experimental layout: top view.

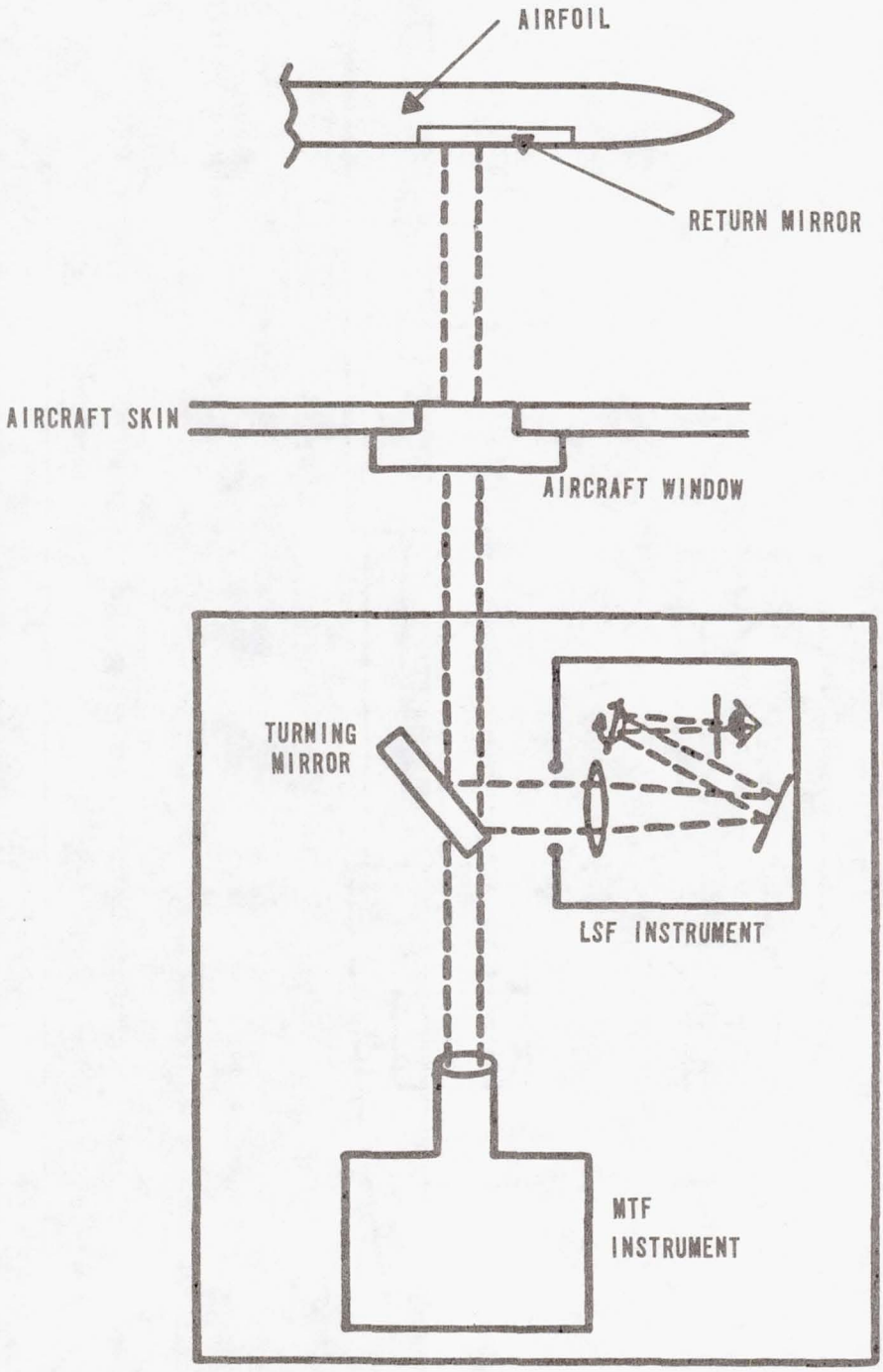

Figure 3. Lear Jet optical bench.

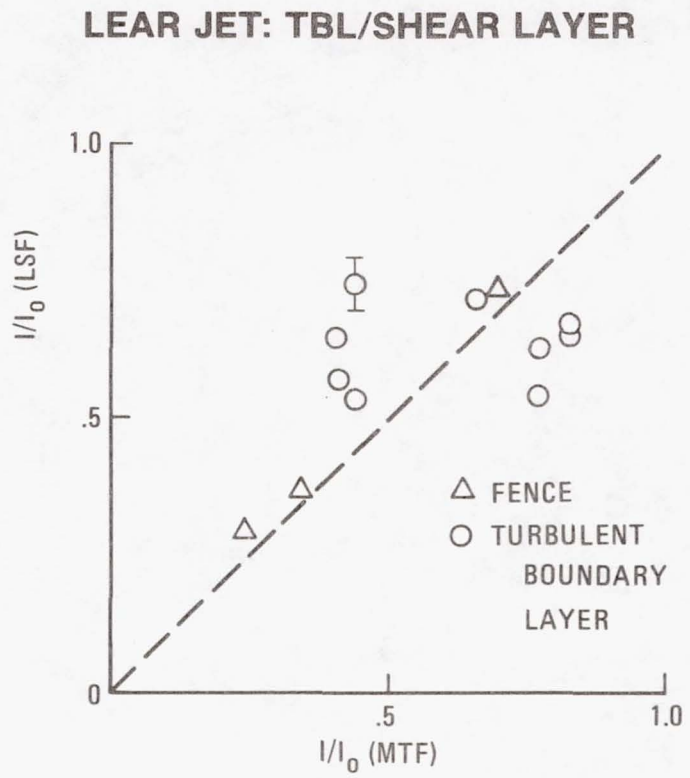

Figure 4. Comparison of LSF and MTF data for fence and turbulent boundary layers.

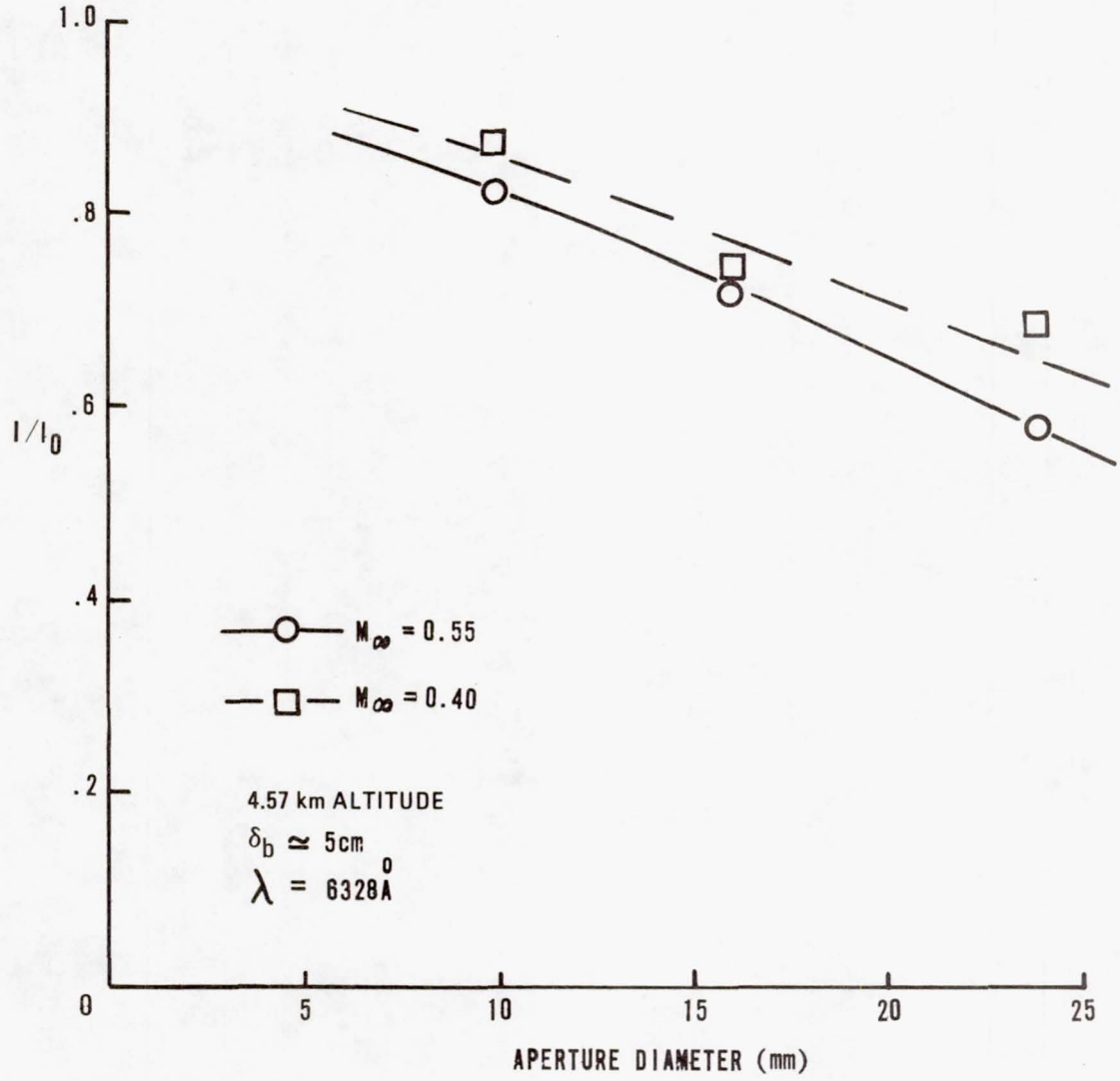

Figure 5a. Effect of aperture diameter on I/I_o for a turbulent boundary layer.

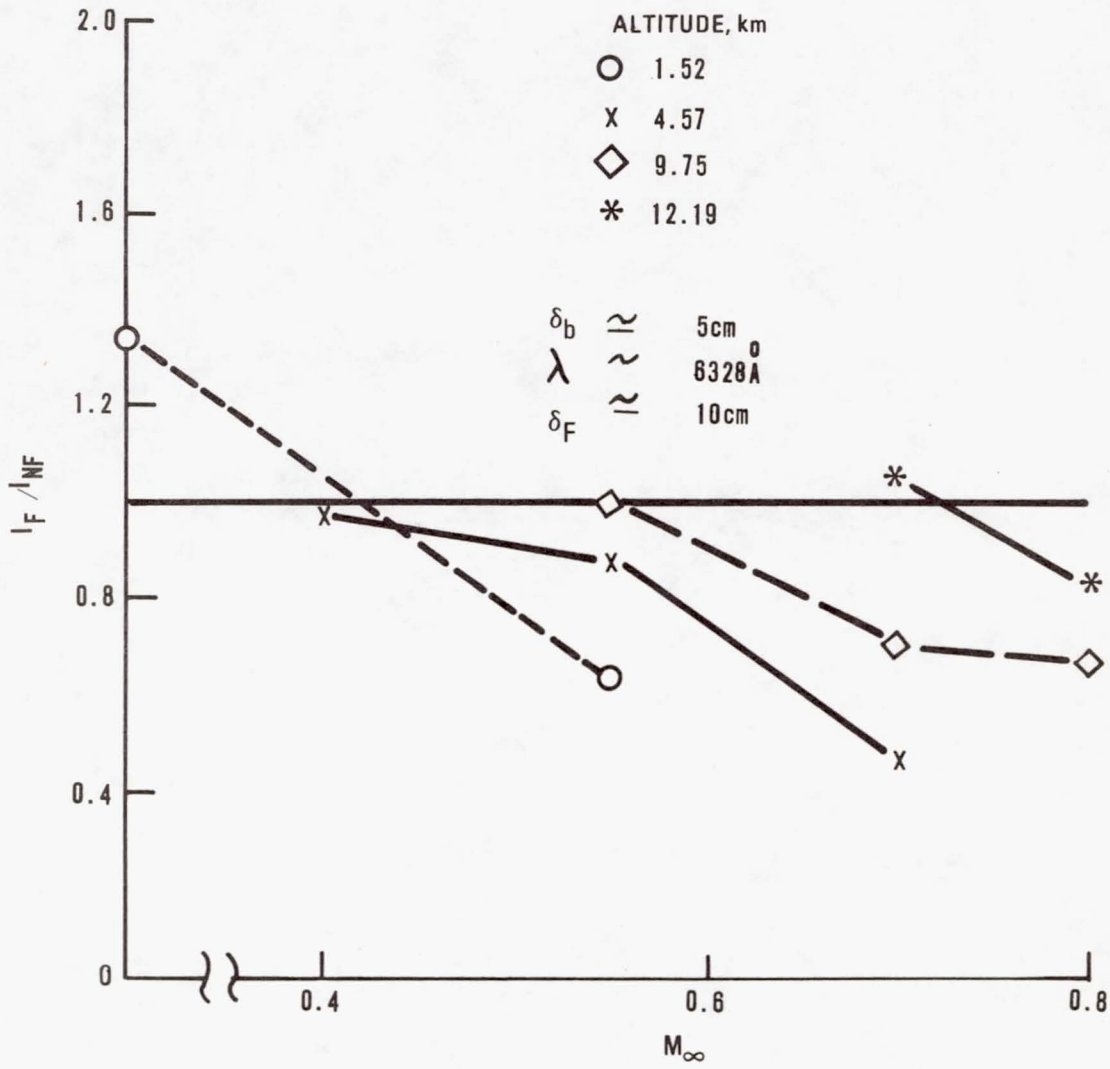

Figure 5b. Relative effect of fences as a function of Mach number for a 24mm aperture.

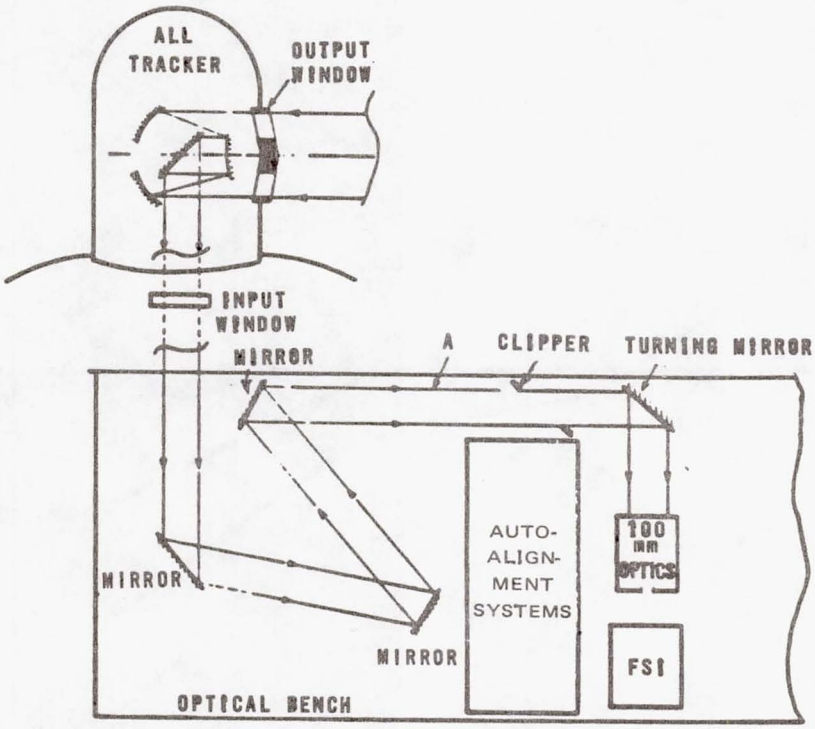

Figure 6. Cycle II optical diagnostic layout.

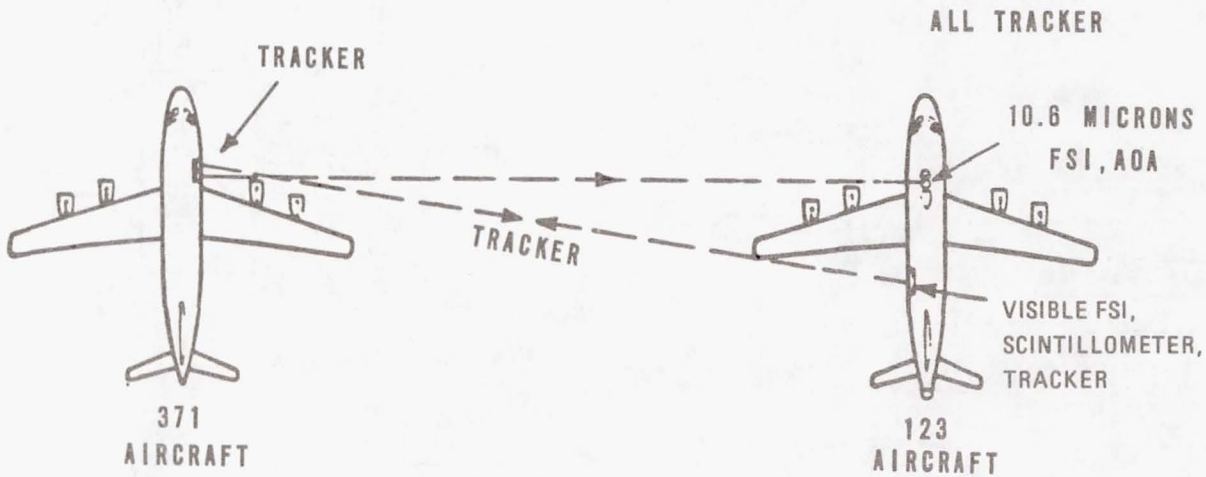

Figure 7. Cycle II experimental setup.

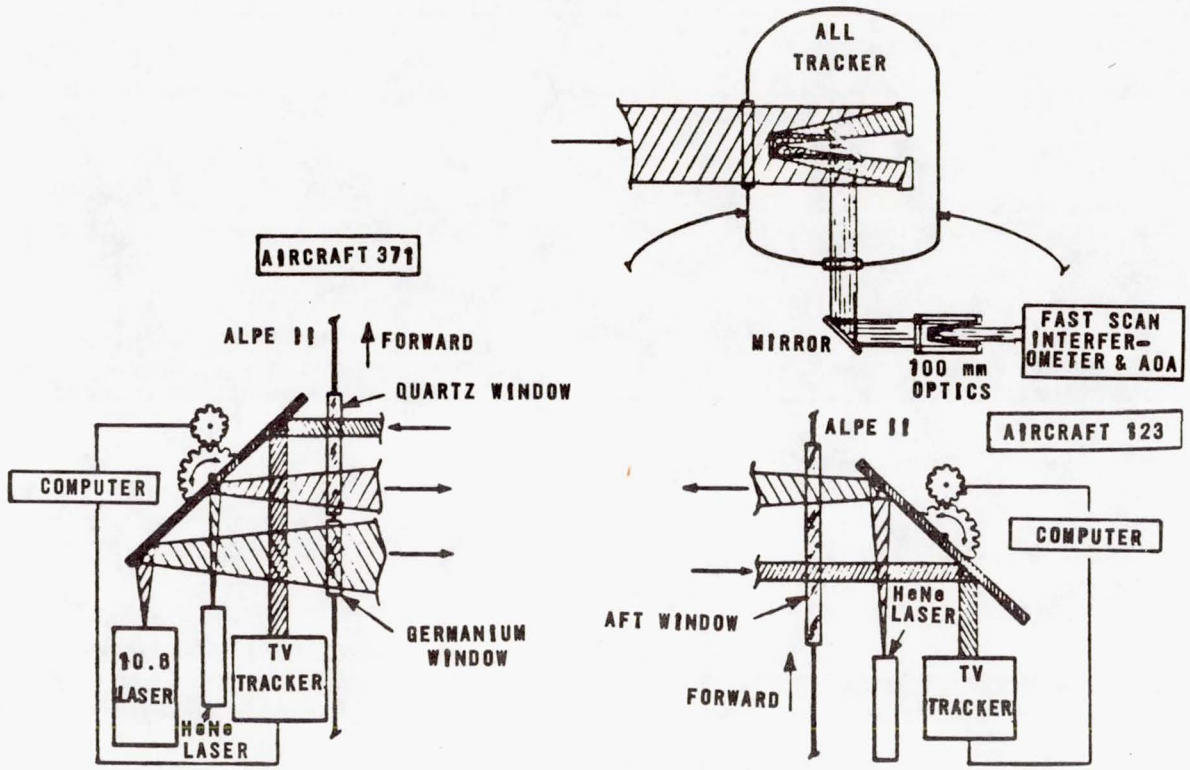

Figure 8. Cycle II tracker system for propagation measurement.

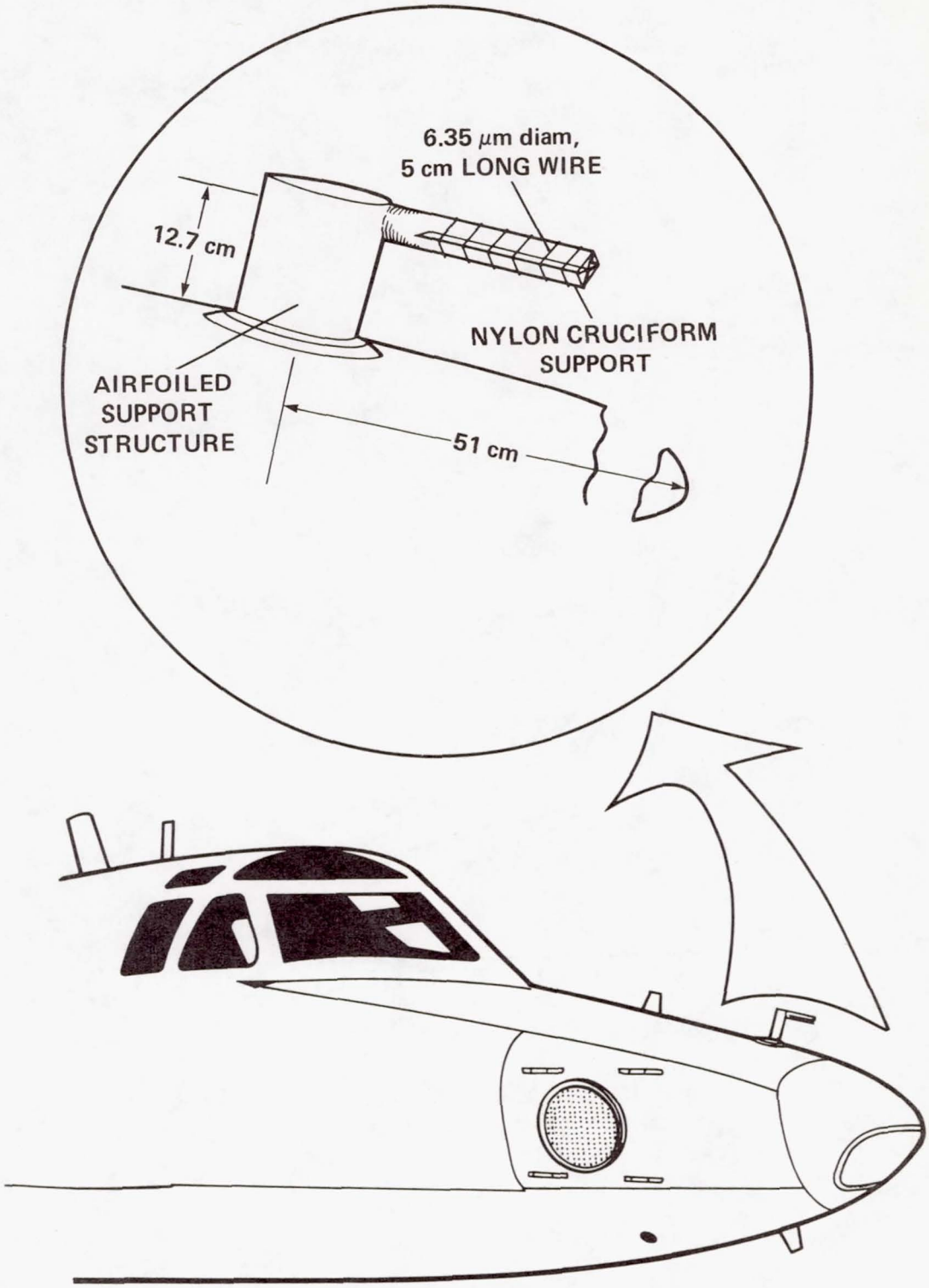

Figure 9. Fine wire mounted on a T-39.

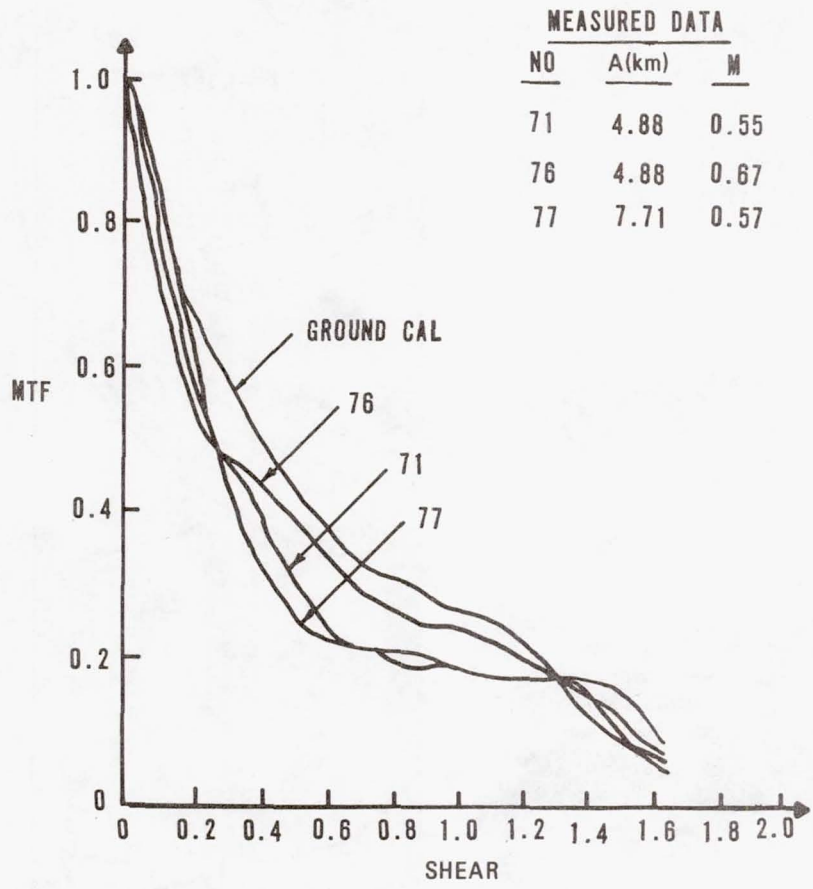

Figure 10. Sample Cycle II data showing the effect of altitude and Mach number on optical degradation.

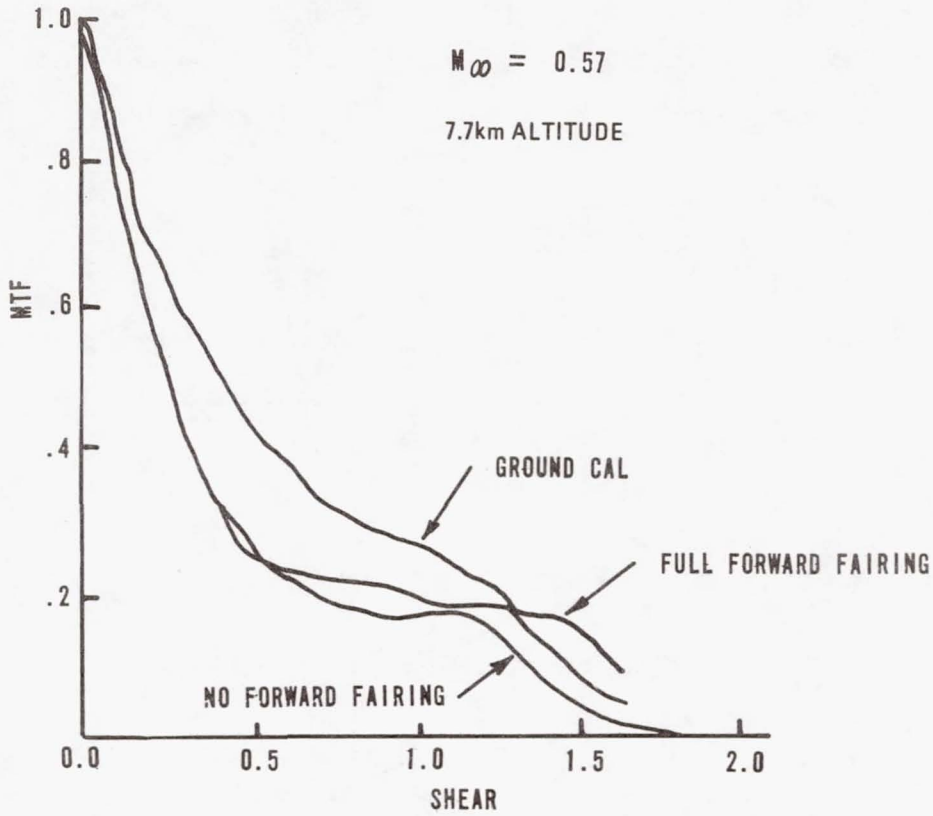

Figure 11. Effect of aircraft configuration on optical degradation.

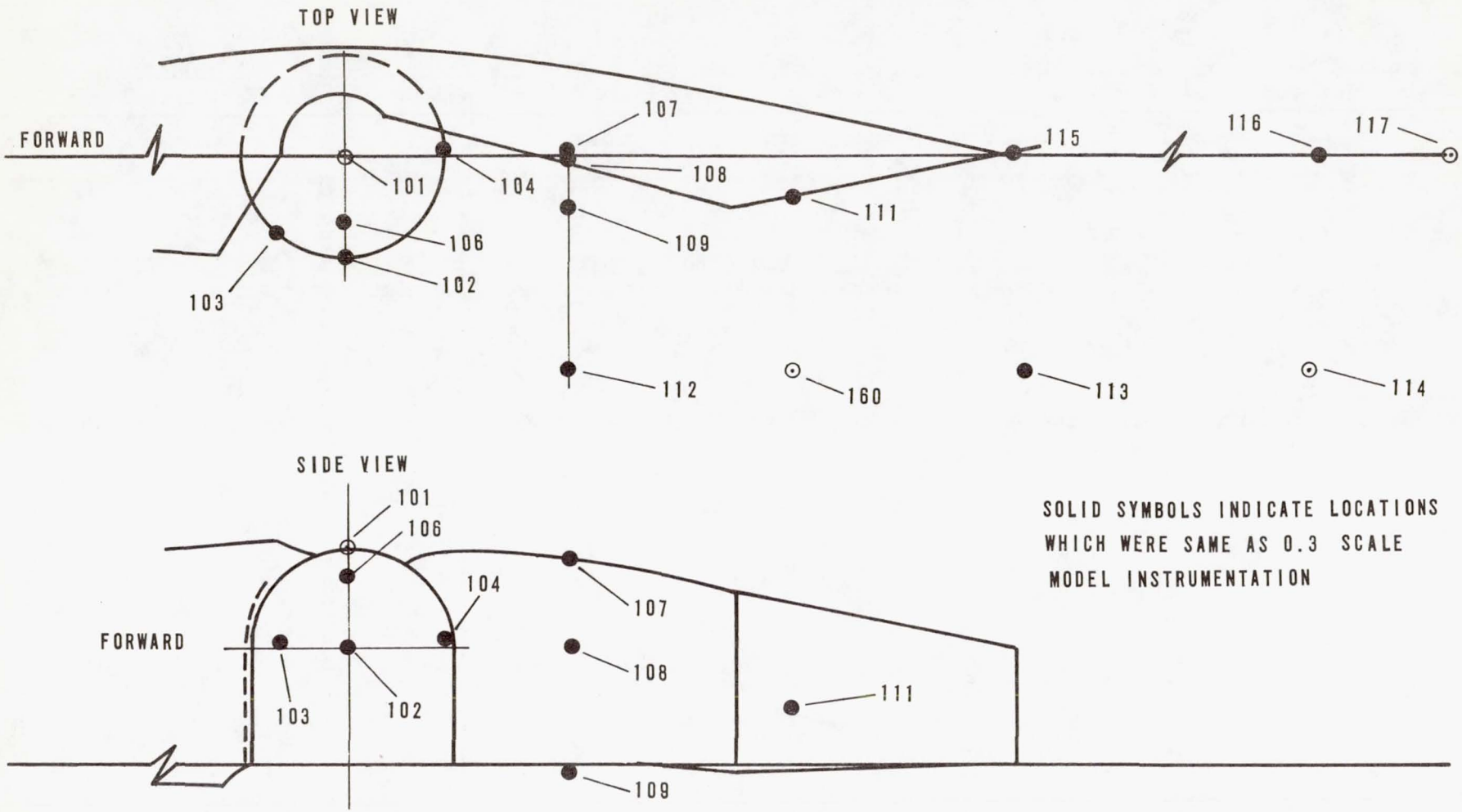

Figure 12a. Location of transducers used in flight to ground simulation comparison.

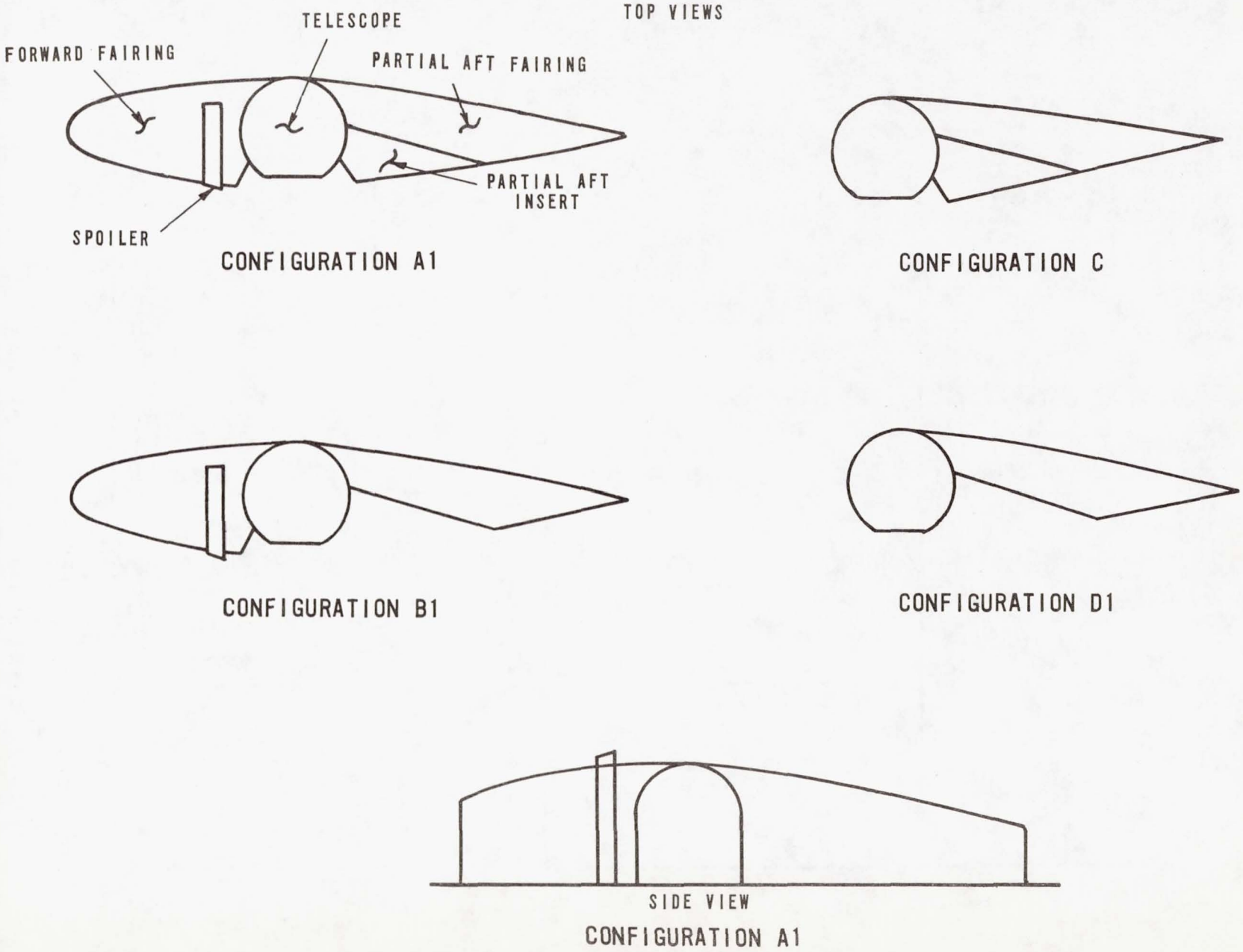

Figure 12b. Fairing configurations.

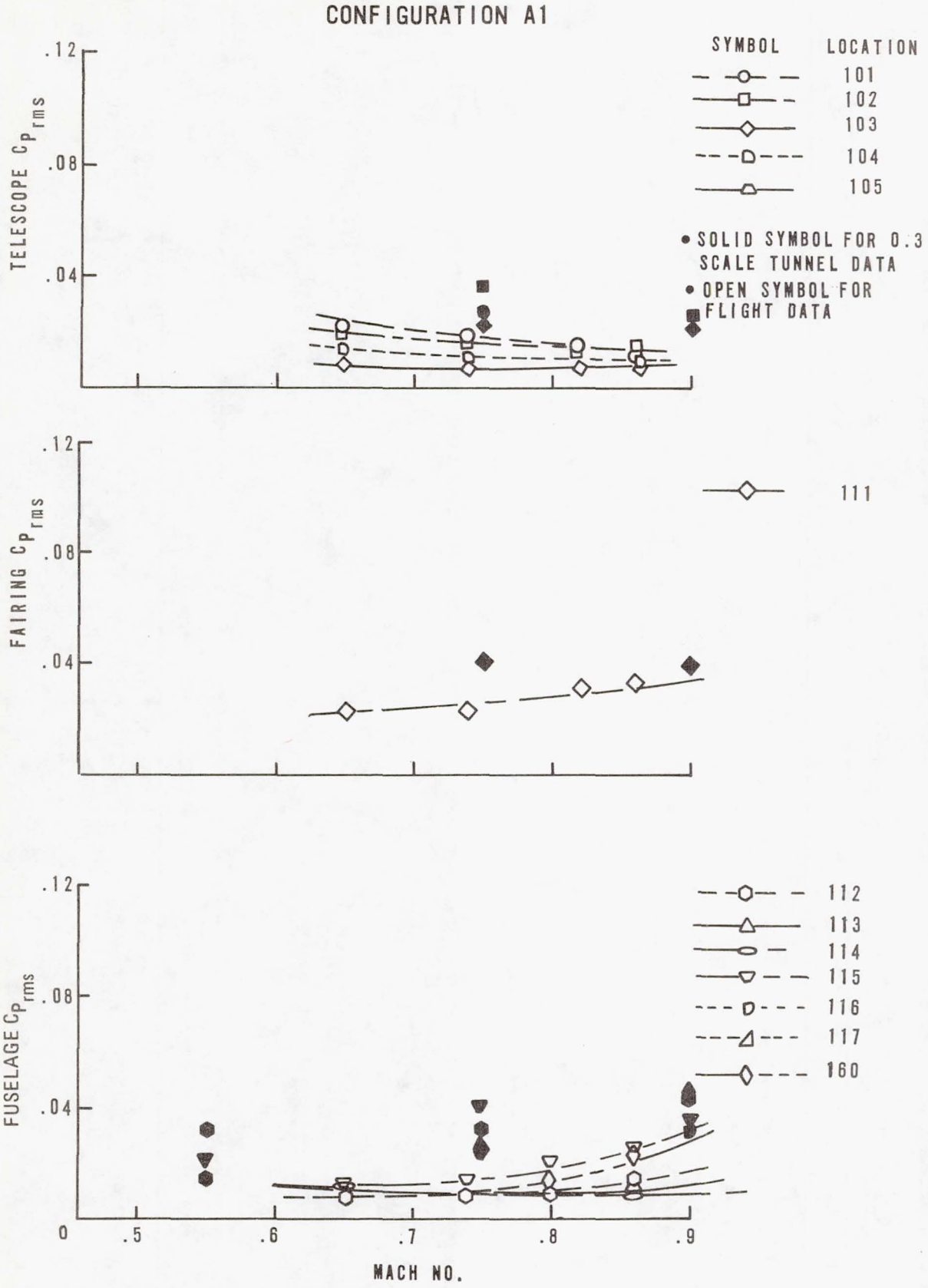

Figure 13a. Sample of flight and ground pressure spectral data.

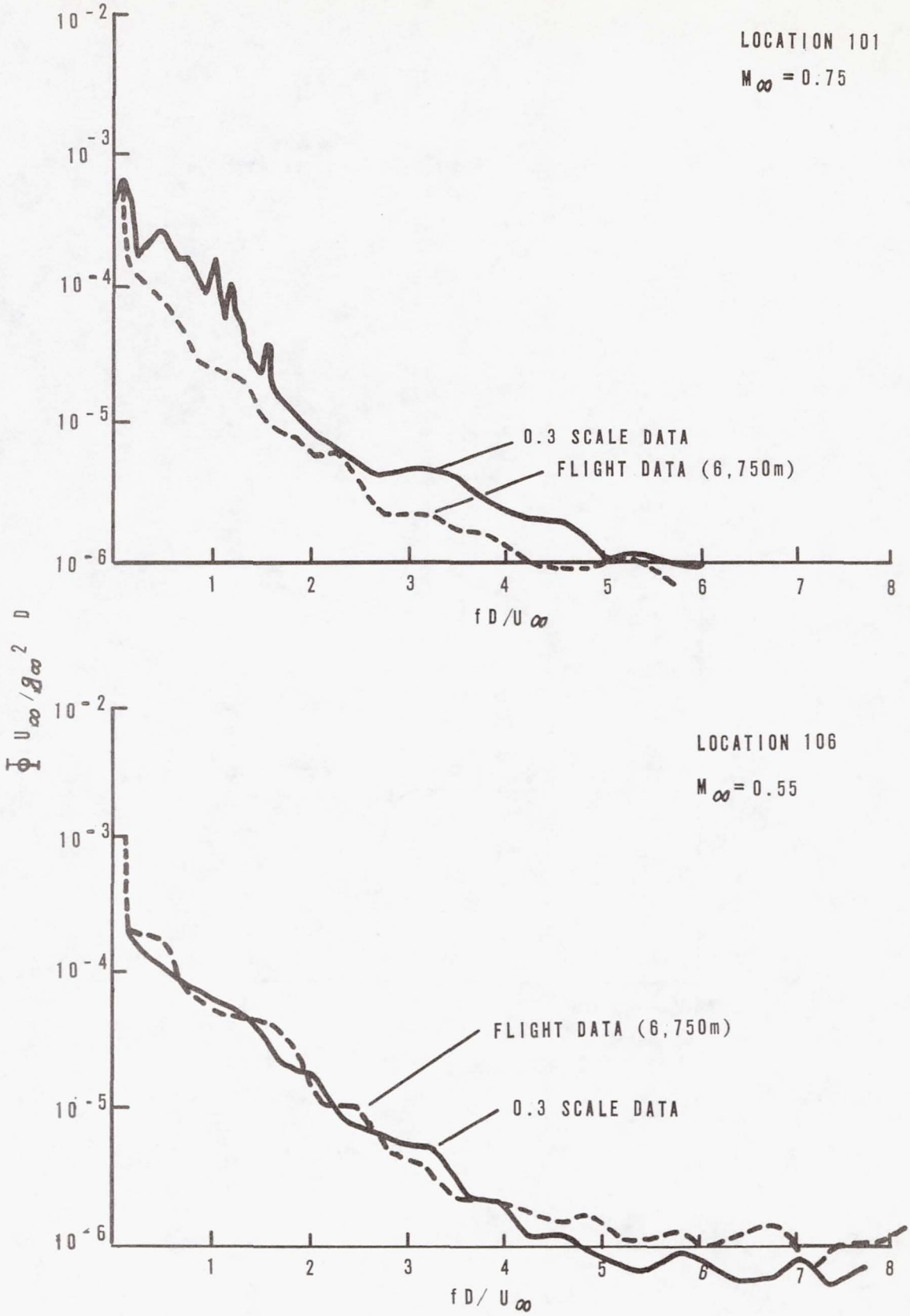

Figure 13b. Sample of flight and ground pressure spectral data.

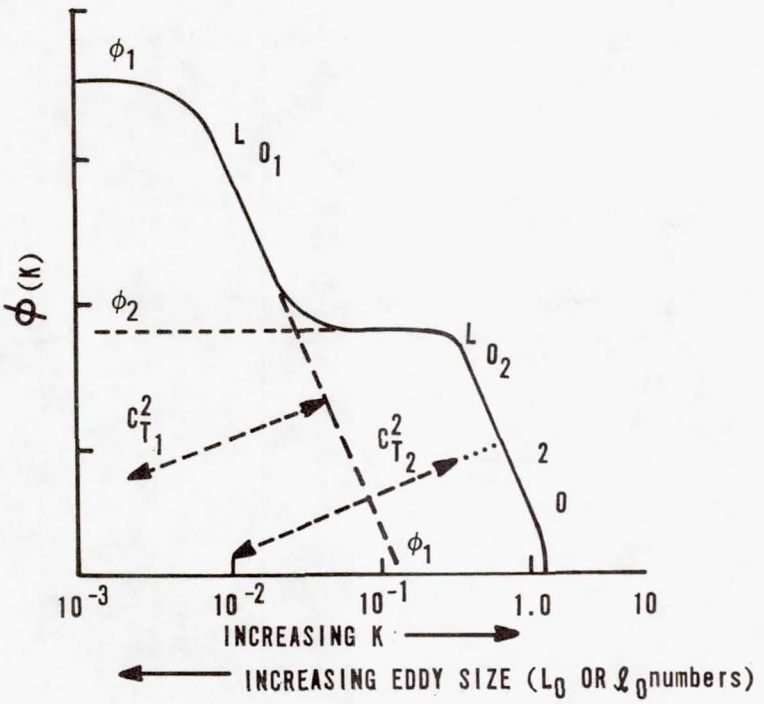

Figure 14. Typical Cycle II hot wire spectrum from the T-39.

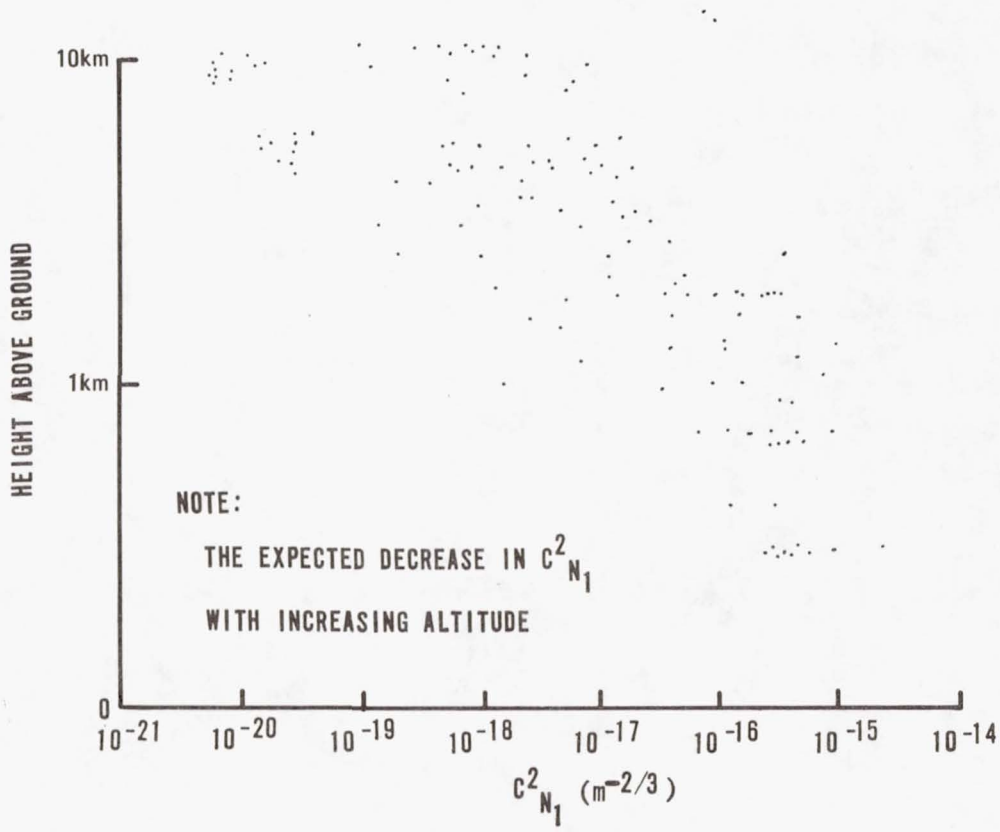

Figure 15a. Correlations of C_N^2 with altitude. From Cycle II T-39 data.

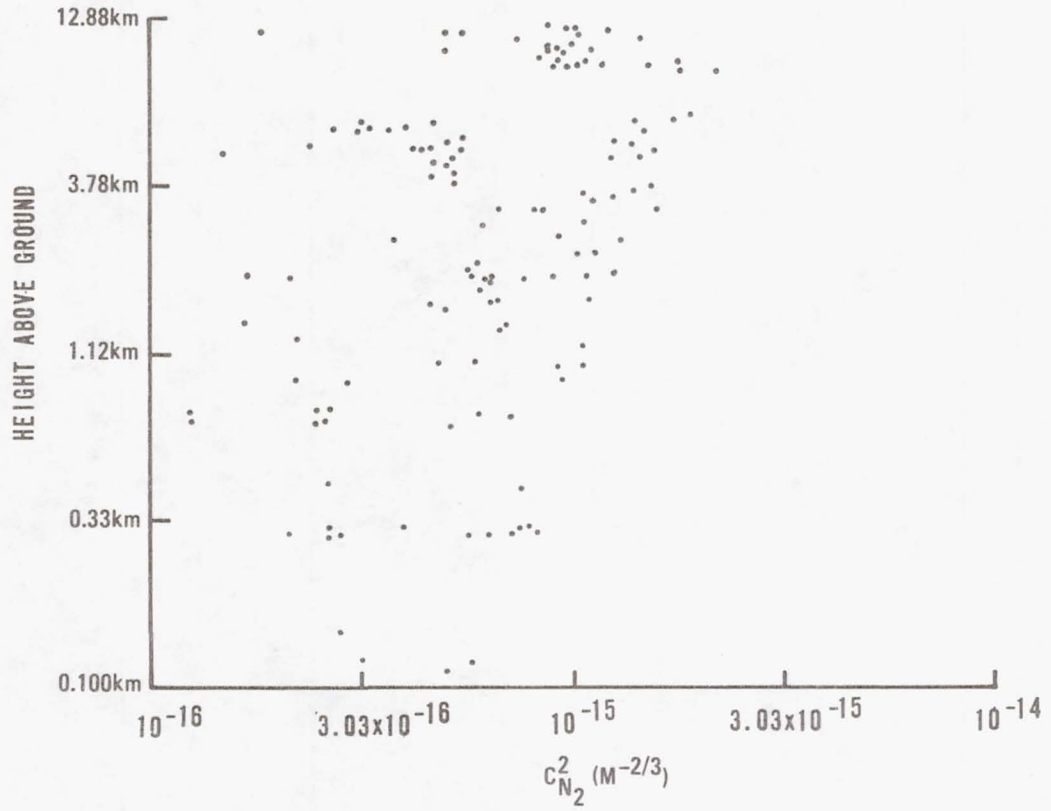

Figure 15b. Correlation of C_N^2 with altitude. From Cycle II T-39 data.

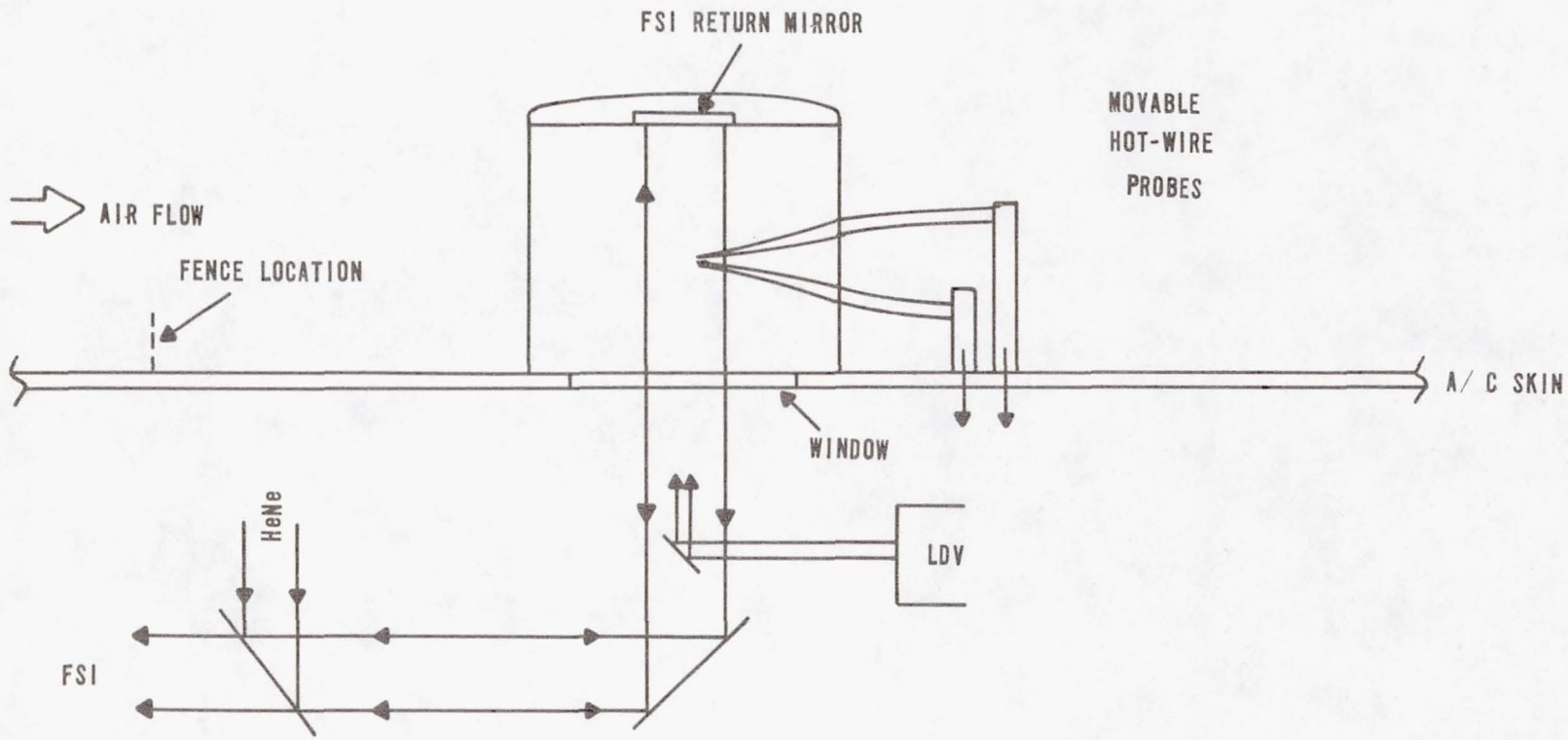

Figure 16a. Cycle II.5 experimental setup.

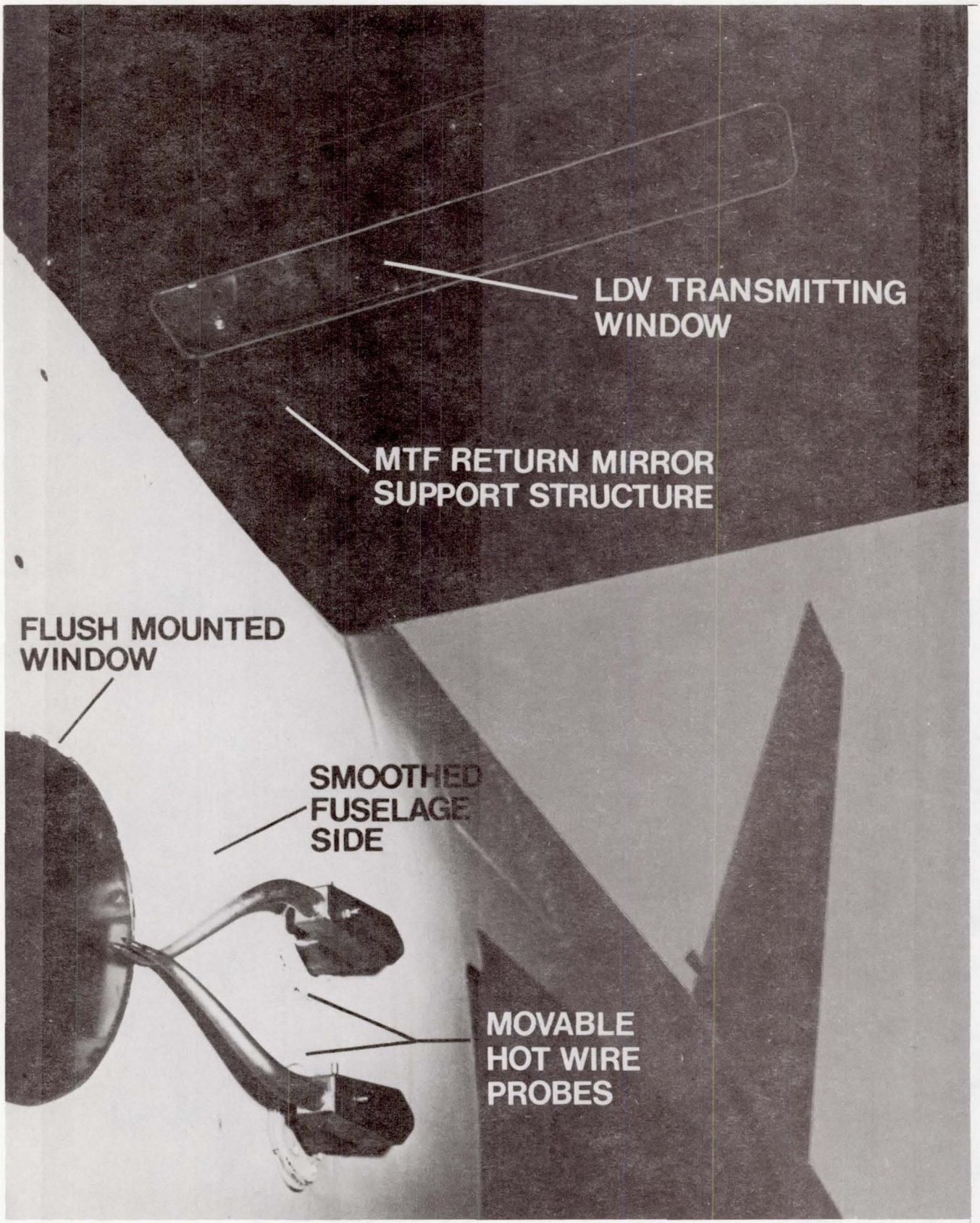

Figure 16b. Cycle II.5 experiment station.

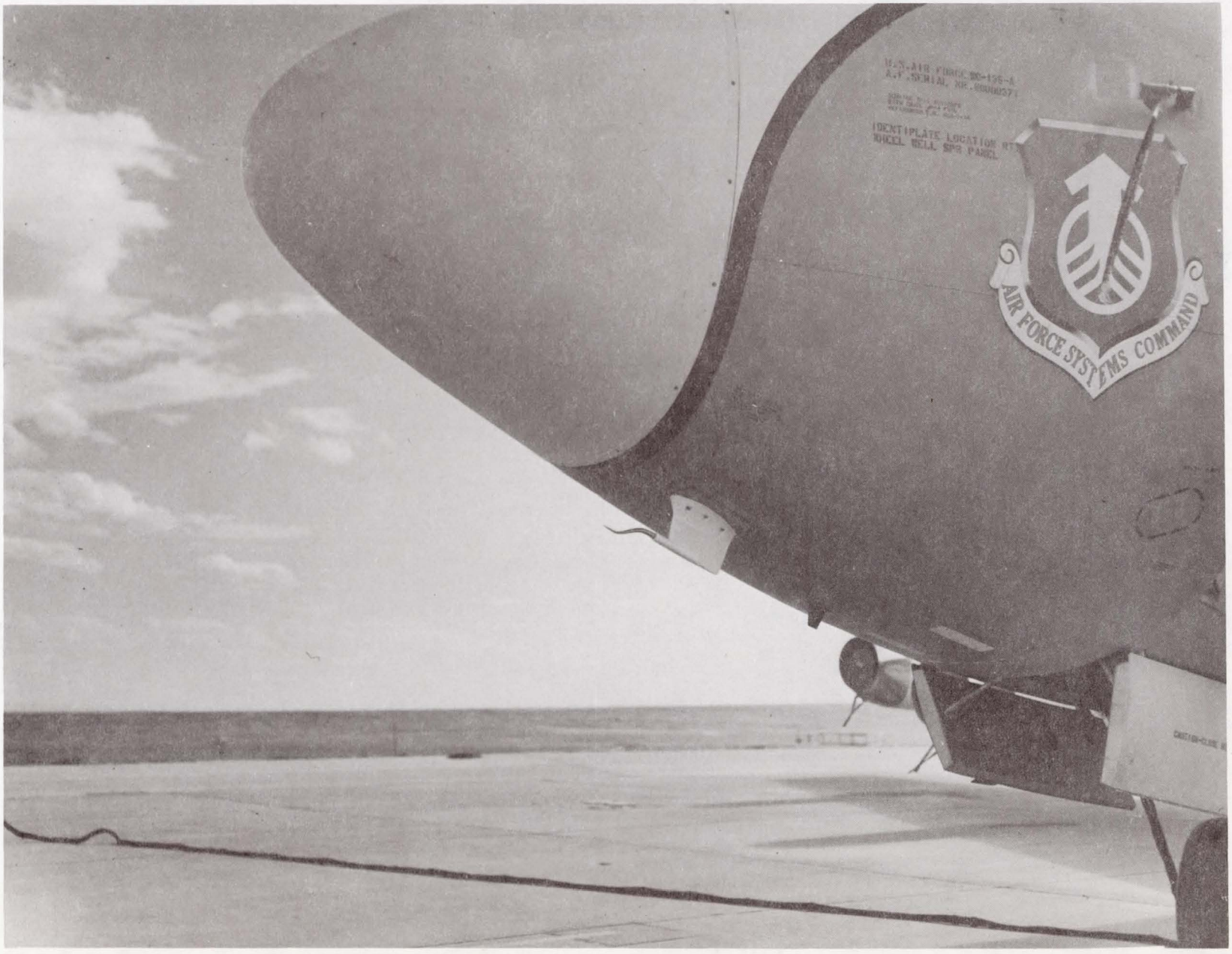

Figure 17. Atmospheric turbulence probe mounted to the nose of an Air Force NC135A.

LEAR JET BOUNDARY LAYER/SHEAR LAYER LASER PROPAGATION EXPERIMENTS

ABSTRACT

In early 1975 the Air Force Weapons Laboratory, in concert with NASA Ames and Lincoln Laboratory, conducted aircraft turbulent boundary layer and shear layer experiments using a Lear jet. Test objectives included these:

1. Compare optical degradations of aircraft turbulent boundary layers with shear layers generated by aerodynamic fences for a range of altitudes and Mach numbers;

2. Compare Modulation Transfer Function (MTF) and Line Spread Function (LSF) measurements for the same flight conditions.

A collimated 2.5 cm diameter helium-neon laser (0.63μ) traversed the approximate 5 cm thick natural aircraft boundary layer in double pass via a reflective airfoil located 25 cm from the fuselage. In addition, several flights examined shear layer-induced optical degradations produced by an aerodynamic fence located 20 cm upstream of the optical axis. Flight altitudes ranged from 1.5 to 12 km, while Mach numbers were varied from 0.3 to 0.8. Average Line Spread Function (LSF) and Modulation Transfer Function (MTF) data were obtained by averaging a large number of tilt-removed curves. Fourier transforming the resulting average MTF yields an LSF, thus affording a direct comparison of the two optical measurements. Agreement was good for the aerodynamic fence arrangement, but only fair in the case of a turbulent

boundary layer. Values of phase variance inferred from the LSF instrument for a single pass through the random flow and corrected for a large aperture ranged from 0.08 to 0.11 waves (λ = .63μ) for the boundary layer. Corresponding values for the fence vary from 0.08 to 0.16 waves. Extrapolation of these values to 10.6μ suggests negligible degradation for a CO_2 laser transmitted through a 5 cm thick, subsonic turbulent boundary layer.

LEAR JET BOUNDARY LAYER/SHEAR LAYER EXPERIMENTS

K. Gilbert

Introduction

The AFWL, together with NASA Ames and Lincoln Laboratory, have conducted aircraft boundary layer and shear layer laser measurements using a NASA Lear jet. These experiments were designed to:

1. Compare optical degradations of aircraft turbulent boundary layers with shear layers generated by aerodynamic fences;

2. Compare Modulation Transfer Function (MTF) and Line Spread Function (LSF) measurements for the same flight conditions. These are Fourier Transform pairs.

Experiments were conducted at Moffett Field, California, during January 1975. A collimated helium-neon laser (6328Å) was the source. The aperture diameter was 25 millimeters. A 7 cm fused quartz window and a reflective airfoil located 25 cm from the fuselage permitted a double pass of the laser beam through the approximate 5 cm thick aircraft boundary layer. The equipment was arrayed on an optical bench in the Lear jet. A beam splitter permitted simultaneous MTF and LSF measurements. However, because of limited space for experimenters, each flight was dedicated to one of the two measurements.

Aircraft missions were flown at altitudes ranging from 1.6 to 12 kilometers. Mach numbers were varied from 0.3 to 0.8. Typical flight durations

were 2.5 hours. A total of seven data missions were flown in this series. Three flights studied the effects of an aerodynamic fence located just upstream of the optical axis. The remaining four missions examined fundamental aircraft boundary layers (i.e., fence removed).

All data were recorded on magnetic tape. A storage oscilloscope and camera provided inflight "quick look" capability. Oscillograms were generated between flights for additional experimental guidance.

Description of Experiment

Figure 1 shows an experimental overview. The airfoil is 25 cm from the aircraft fuselage skin. A 4.3 cm diameter mirror was flush mounted on the airfoil, and served to direct the laser beam back into the aircraft. An internal mirror was used to provide an inflight reference beam. In addition, both pre-and post-flight calibrations were performed.

Figure 2 depicts the aerodynamic fence arrangement. The fence is 7.5 cm high and 45 cm long. Hole diameters are 6 mm, while the overall porosity of this fence is about 50 percent. The distance from the fence to the center of the laser optical axis is 20 cm.

Figure 3 shows the internal optical table, on which are mounted the MTF and LSF instruments.

Line Spread Function Measurements

The LSF instrumentation consists of a 30 centimeter focal length lens; a variable iris of 24 mm, 16 mm, and 10 mm; a silicon photodetector; and a dual-slit aperture. An additional reference detector and a divider circuit were included in order to remove any fluctuations introduced by variations in the laser output intensity. The lens was used to focus the laser beam

onto the dual-slit aperture located in front of the detector. The parallel slits are 2 microns wide and separated by 100 microns, thus, providing a reference on the oscilloscope display for accurately measuring the width of each LSF curve. The scanning mirror was driven by a 60 Hz triangular waveform to dither the focused spot back and forth across the slits. Total excursion at the detector was about 2 mm. As the focused spot traverses each slit, the detector response traces out a waveform on the oscilloscope that corresponds to the LSF. The experimental procedure will be discussed next.

LSF Data Processing

The LSF data was recorded on a Sangamo Sabre III analog tape recorder. Some photos were taken while the data were being recorded, but it proved to be much simpler to take postflight photos from the tape recorder playback. At AFWL, preliminary estimates were extracted from visicorder records of the taped data. These estimates were later compared with computer results and found to be in good agreement.

This program locates the peak of each LSF curve, centers each curve about its peak value, then overlays about 1000 randomly selected curves in order to obtain the average LSF for any particular experimental condition. Figures 4 and 5 are examples of average LSF curves obtained for a calibration and an in-flight condition, respectively.

Modulation Transfer Function Device

The Modulation Transfer Function (MTF) of these random flows was measured via a fast shearing interferometer. The MTF is the modulus of the Optical Transfer Function (OTF) which is in turn defined as the Fourier transform of the point spread function of the optical system. The OTF is also the autocorrelation of the system's pupil function. The pupil function

describes not only the shape of the system's limiting aperture, but also the phase of the optical wave across it. Phase perturbations induced on a beam by the turbulent boundary layer are included in the system pupil function, and therefore in the OTF. It can be argued that for a random phenomenon such as turbulence, the phase of the OTF averages to zero, and so OTF and the MTF of the turbulent layer are identical.

The measurement of the boundary layer MTF was done with a fast scanning, shearing interferometer (FSI) designed by Kelsall. A thorough description of the principle and operation of the FSI can be found in references 1 and 2 and we mention only the pertinent points here.

This common path interferometer contains a beam splitter, mirrors, a rotating glass plate called the shear plate, light collecting optics, and a detector. The incoming beam is split into two beams, which pass through the shear plate and are eventually recombined and pass to the detector. The rotating shear plate displaces one beam laterally with respect to the other and introduces a time varying path difference between the beams. After recombination, the beams constructively and destructively interfere, depending on the phase distribution across the beam and the path difference. The resulting signal at the detector is, neglecting terms of no importance in this experiment,

$$F(S) = 1 + |\tau(S)| \cos k\delta(t) \qquad (1)$$

where $\delta(t)$ is a linear function of time describing the path difference between the beams, and S is a normalized displacement, called shear value, and is directly related to the spatial frequency, k. Thus, the output of the interferometer is (apart from a d-c term) a sinusoidal whose envelope is the system MTF, $\tau(S)$. The shear plate rotates at 3600 rpm, resulting in the

measurement of an MTF in about 1.5 milliseconds, with successive MTF's measured every 8 milliseconds.

Finally, note that the output of the FSI is

$$\tau_{FSI}(S) = \tau_o(S)\ \tau_{BL}(S) \qquad (2)$$

That is, the measured MTF is the product of the optical system MTF without turbulence and the MTF of the turbulent boundary layer. The unperturbed system MTF is measured before flight and thus can be removed from the flight measurements. MTF-interred intensity degradation I/I_o was obtained by first averaging 53 randomly selected curves for a particular flight event. The Fourier transform of this average was then taken. Finally, dividing this transform by the calibration transform yields the predicted line spread functions. Because LSF and MTF are a transform pair, this affords a direct comparison of I/I_o via independent measuring techniques.

Figure 6 shows a correlation plot of the average I/I_o value directly measured by the LSF with the corresponding MTF-inferred value of I/I_o. Agreement is only fair for the boundary layer measurements, yet quite good in the case of the aerodynamic fence.

Table 1 is an expanded view of the data base. Column 1 contains the altitude, Mach number and experimental configuration - "TBL" denotes turbulent boundary layer, and "F" aerodynamic fence. The double pass line spread functions shown in Figure 6 appear in columns 2 and 3. Column 4 contains the predicted Strehl ratio for a <u>single</u> pass of the 2.4 cm diameter beam through the random flow. In Appendix A this is shown to be the square root of the LSF in double pass. Column 5 shows the estimated Strehl value for an infinite aperture, that is, one large compared with correlation lengths within the random flow. The final column depicts phase variances associated with the large aperture Strehl values in units of helium-neon

laser wavelength (λ = 0.69μ).

Table 1

COMPARISON OF (I/Io)MTF AND (I/Io)LSF

Altitude	Mach No.	Configuration	I/I_oMTF	I/I_oLSF	I/I_oPS	$I/I_{o\,\infty}$	σ
40K	0.8	TBL	0.77	0.63	.79	.70	.10
32K	0.8	TBL	0.41	0.65	.81	.73	.09
32K	0.8	TBL	0.82	0.65	.81	.73	.09
32K	0.7	TBL	0.44	0.74	.86	.80	.08
32K	0.55	TBL	0.44	0.54	.73	.62	.11
15K	0.7	TBL	0.82	0.67	.82	.73	.09
15K	0.55	TBL	0.41	0.57	.75	.63	.11
5K	0.4	TBL	0.77	0.54	.73	.62	.11
15K	0.7	F	0.24	0.30	.55	.39	.16
5K	0.55	F	0.34	0.37	.61	.46	.14
5K	0.4	F	0.69	0.73	.85	.80	.08

Experimental Error

Pre-and Post-flight Line Spread Function (LSF) calibrations were performed for each aircraft mission. In all cases these two calibration peak intensity values agreed to within 5%. An average of these two numbers was then used as the reference intensity, I_o, for that flight.

The use of operational amplifiers, precision resistors and components, and mercury batteries insured short-term stability within 5%. The reference detector and divider circuit, designed to null out laser source amplitude fluctuations, contributed less than 1% error. Likewise, digitization of the magnetic tape data with subsequent analysis resulted in a comparably negligible error.

The primary source of error lay in the non-uniform response of the LSF detector for laser spots small compared with the sensing surface - this was indeed the case for the nominal 30 micron diameter spots scanning across the two micron slits. During system checkout, it was found that vertical beam motion of 1 millimeter up and down a slit resulted in detector response vari-

ations of ±5%. This would correspond to a beam angle of arrival fluctuation of ±1.5 milliradians. Observed in flight angle-of-arrival fluctuations were small compared with this value. Therefore, total experimental error for the LSF measurement is within ±10%.

Conclusions

Laser propagation experiments through the boundary layer of a Lear jet have been accomplished. Measurement techniques consisted of a Modulation Transfer Function (MTF) device and a Line Spread Function (LSF) instrument. Both techniques measure the decrease in focal plane beam intensity after a collimated laser beam has made a double pass through the aircraft disturbance. Aperture diameter for the helium-neon laser (6328Å) was 2.5 cm. Aircraft altitudes ranged from 1.6 to 12 km, with Mach numbers covering the 0.3 to 0.8 domain. Major conclusions from this series are as follows:

(1) Aerodynamic fences are optically noisier than free turbulent boundary layers. Ironically, fences are generally placed in the vicinity of an open port to aerodynamically quiesce flows in that cavity;

(2) MTF and LSF measurements correlated very well for the fence (F); less well for no fence (NF). These two measurements are Fourier Transform pairs;

(3) Values of phase variance inferred from the LSF instrument and corrected for a single pass through the random disturbance and an infinite aperture (i.e., beam diameter much larger than flow correlation lengths) range from 0.08 to 0.11 waves ($\lambda = 0.63\mu$) and 0.08 to 0.16 waves for the boundary layers and shear layers, respectively.

REFERENCES

1. Kelsall, D. "Rapid Interferometric Technique for MTF Measurements in the Visible or Infrared Region", Appl. Opt. 12, 1398, (1973).

2. Kelsall, D., "Optical 'Seeing' Through the Atmosphere by an Interferometric Technique", J. Opt. Soc. Amer. 63, 1472, (1973).

APPENDIX A

THEORY OF LINE SCAN DEVICE

In the line scan device the point spread function associated with a certain aperture and phase aberration is scanned across a thin slit, and the power passing through the slit is recorded as a function of time. If $i(x,y)$ is the point spread function then time dependent irradiance in the focal plane for a point spread function moving with velocity V along the x axis is $J(x,y,t) = i(x + Vt, y)$ and the power passing through a slit of width ε parallel to the y axis is

$$I(t) = \int_{-\infty}^{\infty} \int_{-\varepsilon/2}^{\varepsilon/2} J(x,y,t)\,dx\,dy \tag{A1}$$

If the slit is narrow compared with the diameter of the point spread function and if the slit is centered about x = 0 equation A1 becomes

$$\begin{aligned} I(t) &= \sum_{-\infty}^{\infty} \int J(o,y,t)\,dy \\ &= \sum_{-\infty}^{\infty} \int i(Vt,y)\,dy \end{aligned} \tag{A2}$$

the quantity I(t) is the quantity directly measured in the experiment.

The degradation produced by a random phase aberration is usually expressed in terms of the Strehl ratio

$$S = \frac{i(o)}{i_o(o)} \tag{A3}$$

This is the ratio of the peak value $i(o)$ of the point spread function with aberration to the peak value $i_o(o)$ of the point spread function without aberration. For small rms phase aberration or when the scale size of the

phase aberration is much smaller than the aperture size of the instrument, the Strehl ratio is given by the expression

$$\frac{i}{i_o} = \exp\{-k^2\sigma^2\} \qquad \text{(A4)}$$

where $k = 2\pi/\lambda$ is the wave number and σ^2 is the variance of the aberration function (i.e., it is the variance of the optical path length through the aberrating medium, where the average is taken over the aperture of the instrument).

To obtain the point spread function i(x,y) from the line scan function I(t) one must in general solve the integral in equation A2. However, if the degradation of the point spread function is represented by a simple spreading then it can be shown that the relation between the Strehl ratio and the ratio of the peak values of the line scan function, with and without phase aberration is given by

$$\left(\frac{I}{I_o}\right)^2 = \frac{i}{i_o} = \exp\{-k^2\sigma^2\} \qquad \text{(A5)}$$

For this preliminary analysis we shall use this simple relation to estimate the Strehl ratio.

Now in the experiment the beam passes through the aircraft boundary layer twice. In applications, on the other hand, one is interested in the decrease of peak irradiance for one pass through a boundary layer. If σ_1^2 is the variance of the optical path length for one pass through the boundary layer the Strehl ratio for one pass would be

$$\left(\frac{i}{i_o}\right)_1 = \exp(-k^2\sigma_1^2) \qquad \text{(A6)}$$

For two passes through the boundary layer the variance is $\sigma^2 = 4\sigma_1^2$.

It follows that if in the experiment one observes a line scan peak ratio I/I_o then for a beam making one pass through the boundary layer the estimated Strehl ratio is just

$$\frac{i}{i_o} = \sqrt{\frac{I}{I_o}} \qquad \text{(A7)}$$

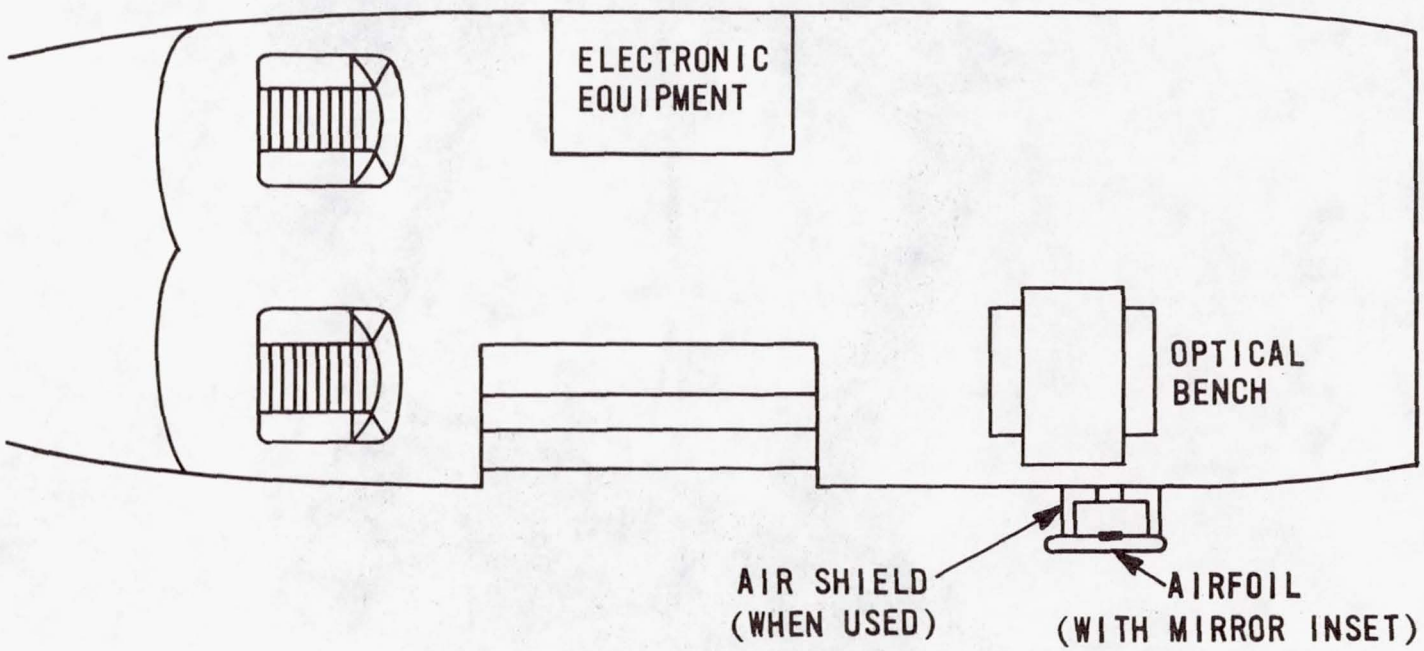

Figure 1.- Lear Jet experimental overview.

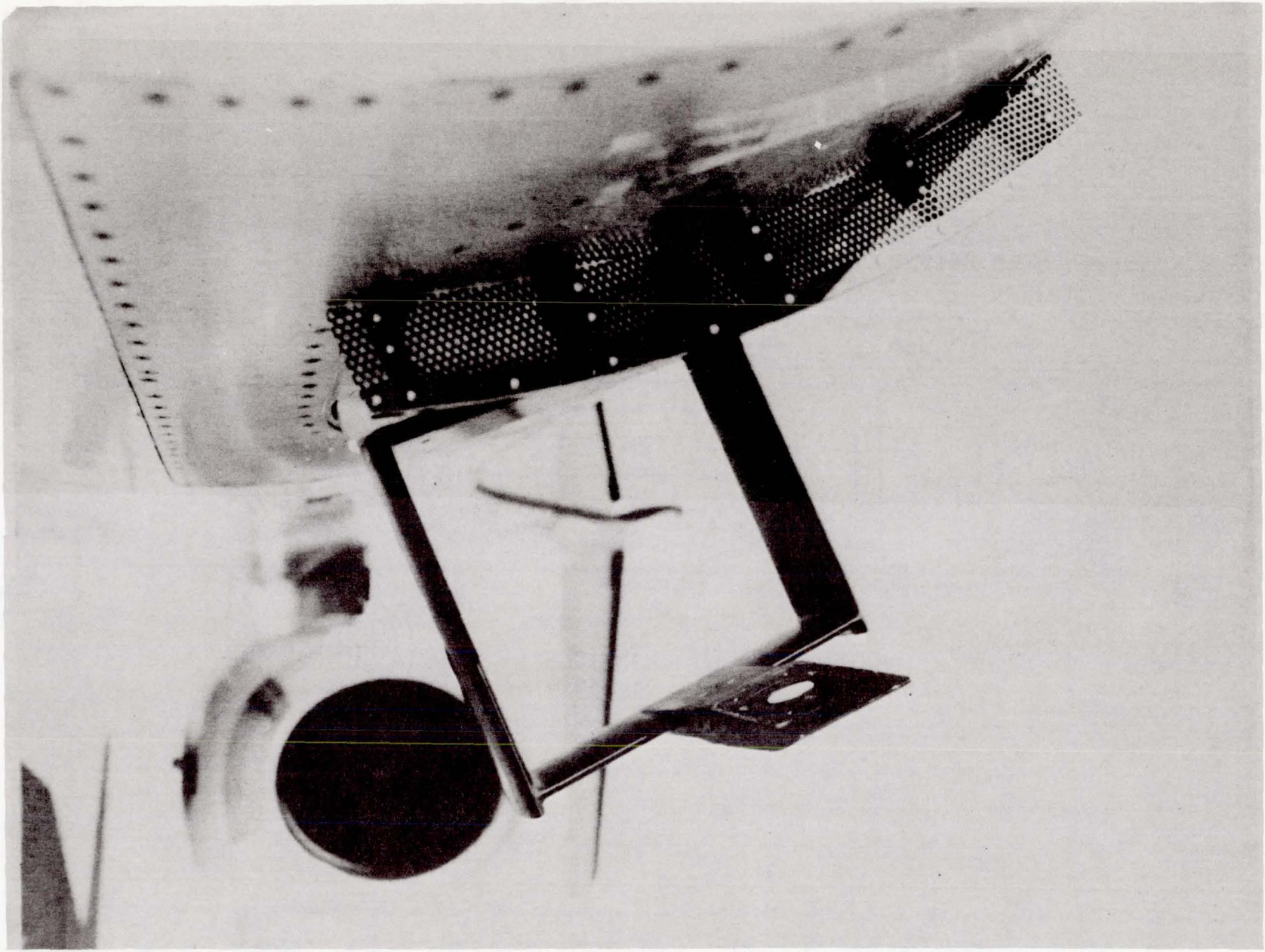

Figure 2 - Aerodynamic fence arrangement.

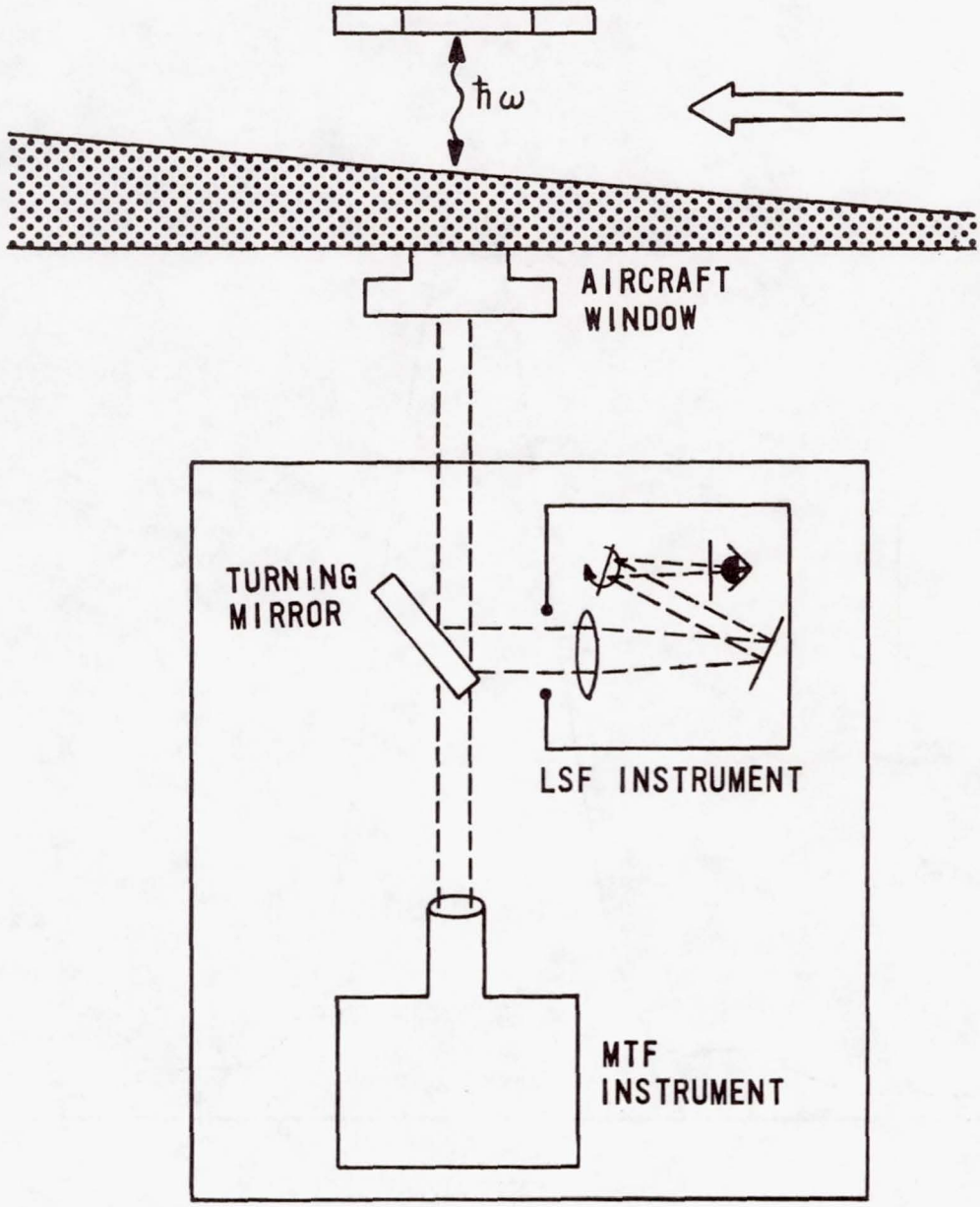

Figure 3.- Instrumentation setup.

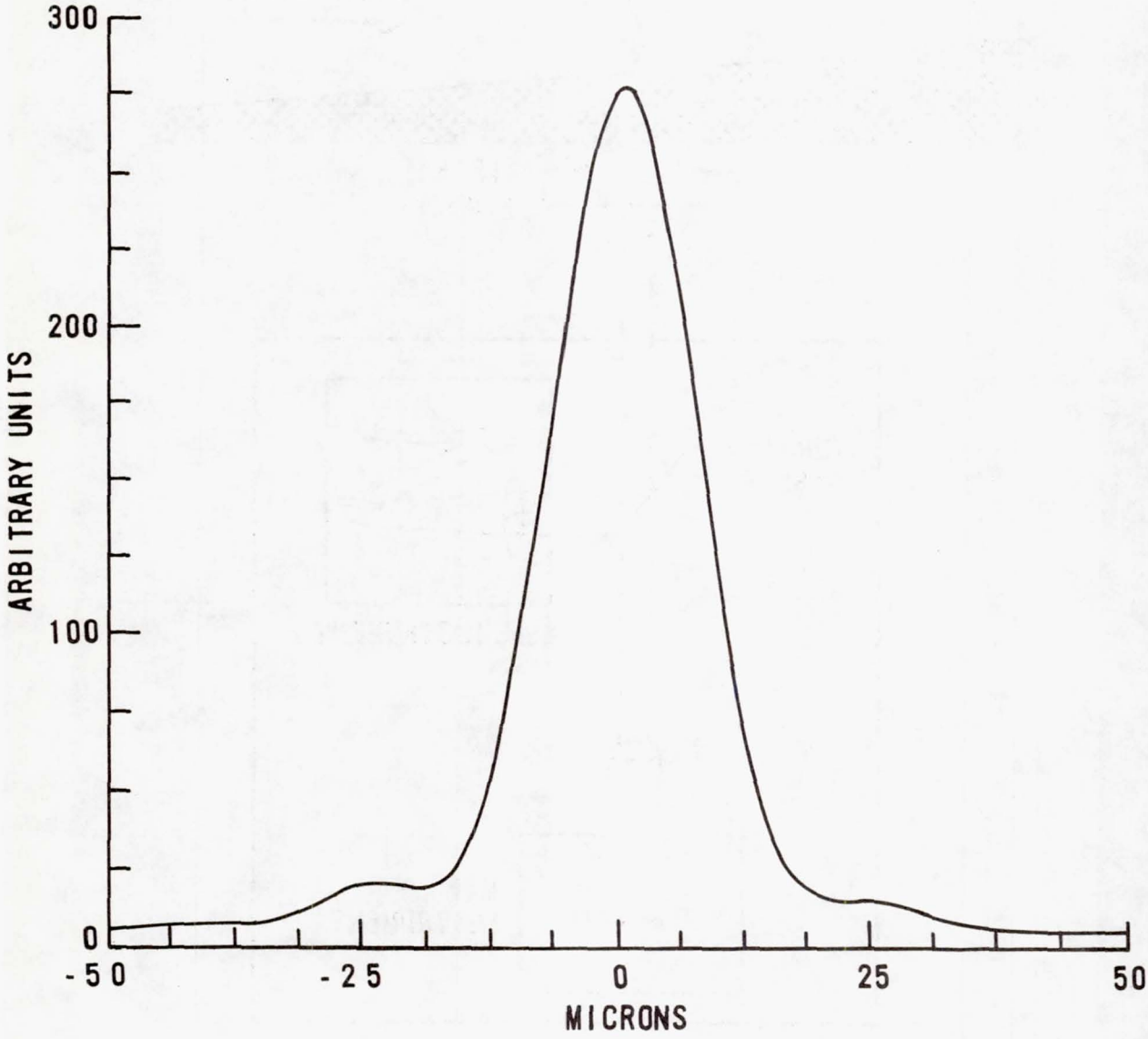

Figure 4.- Typical LSF calibration curve.

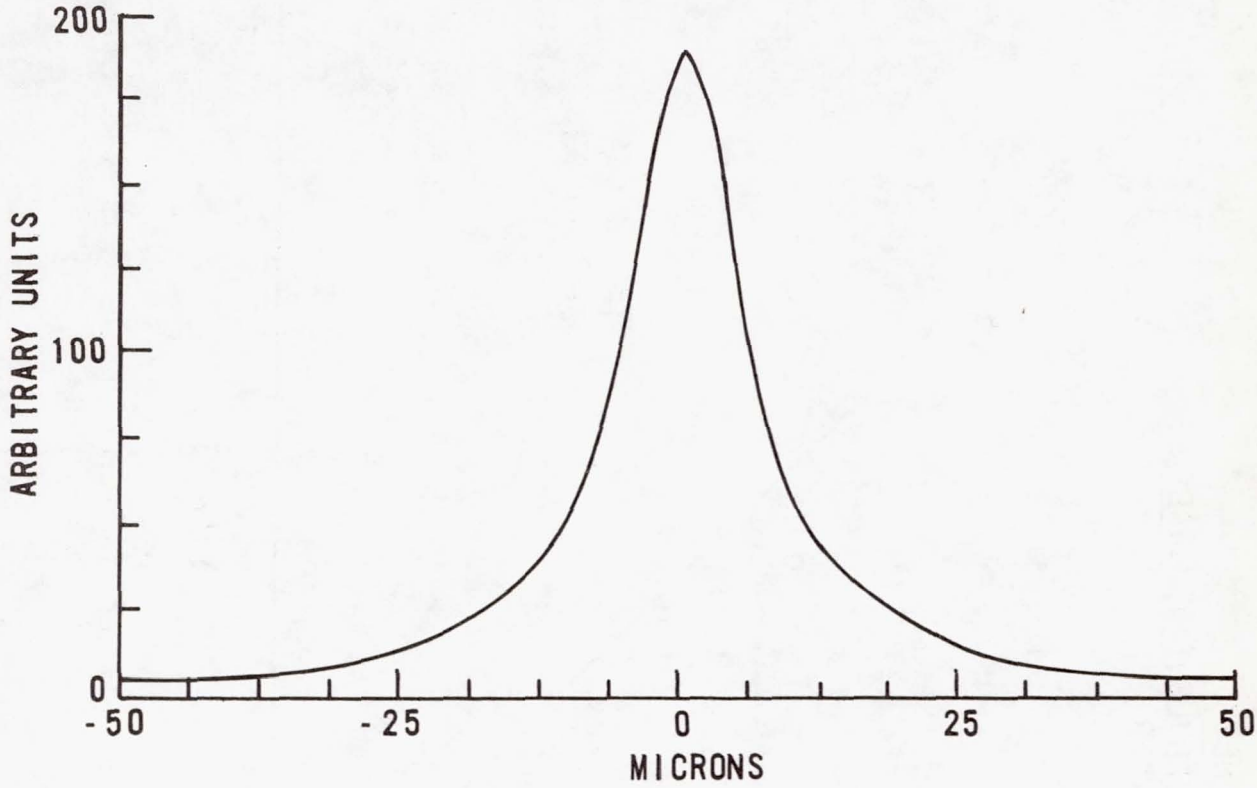

Figure 5.- Typical LSF in flight data curve.

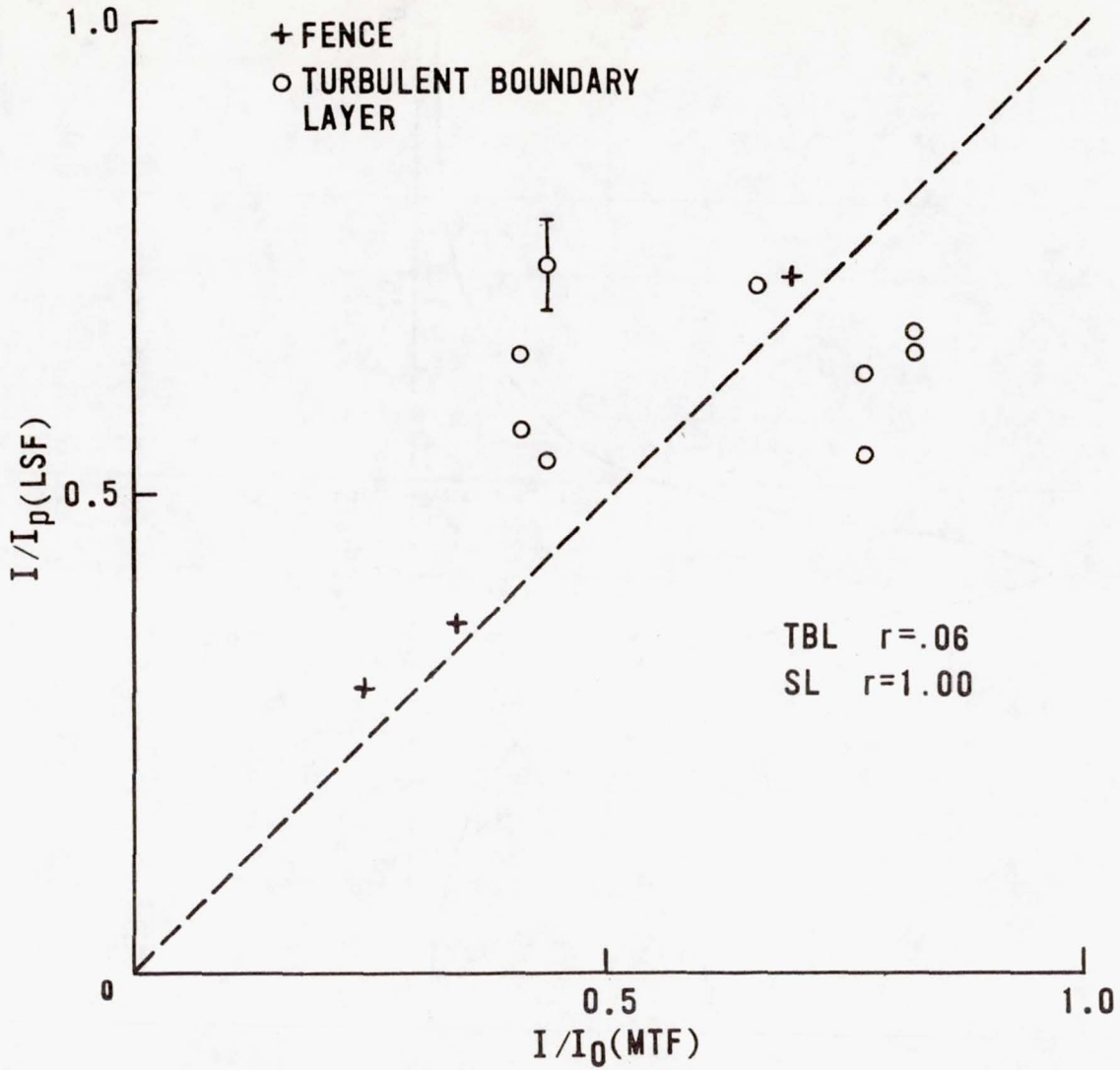

Figure 6.- Correlation plot of line spread functions inferred from LSF and MTF measurements.

OPTICAL MEASUREMENTS OF DEGRADATION IN AIRCRAFT BOUNDARY LAYERS*

Dennis Kelsall

Massachusetts Institute of Technology
Lincoln Laboratory
Lexington, Massachusetts 02173

ABSTRACT

A review is given of visible wavelength measurements of the degradation of optical beams when transmitted through the thin aerodynamic boundary layers around an aircraft.

*This work was sponsored by the Department of the Air Force.

OPTICAL MEASUREMENTS OF DEGRADATION IN AIRCRAFT BOUNDARY LAYERS*

SUMMARY

The optical degradation produced at the turbulent boundary layer near the skin of a high altitude jet aircraft has been studied in detail over the past several years by M.I.T. Lincoln Laboratory. Some early investigations into the imaging of stars by a telescope located on a KC-135 jet aircraft indicated that the optical degradation of these images might be attributed to an in-flight aircraft boundary layer.

Interferometric techniques to measure these degradations in terms of an optical modulation transfer function (MTF) were developed and a wide range of both wind-tunnel and aircraft field measurements were subsequently conducted by M.I.T. Lincoln Laboratory. The measured MTF data could be curve fitted to an expression for the time averaged MTF of the following form

$$< D\ (s, \Psi)\ > = D_0(s)\ \exp -k^2\sigma^2 \left\{ 1 - \exp -\left(\frac{sD}{2\ell}\right)^2 \right\}$$

where $D_0(s)$ is the optical telescope diffraction limited MTF, with a diameter D and focal length f, k is the wavelength constant, s is the reduced spatial frequency parameter given by $s = 2\lambda R\ f/D$. Here λ is the wavelength in millimeters, and R the spatial frequency in cycles per millimeter in the image plane.

Therefore, from these measurements, the rms wavefront distortion (σ) and the correlation length (ℓ) due to the boundary-layer degradation for the transmitted light beam could be determined. These values were characteristics of the aperture diameter D, but could be extrapolated to equivalent infinite aperture values σ_0 and ℓ_0 by means of aperture scaling relationships.

Analytical evaluation of the expected σ and ℓ values from aerodynamic theory has been carried out by D'Amato, and some of these theoretically derived values are compared with the experimentally obtained data discussed here.

A summary of the measurements and data obtained in experiments on a Lear Jet Aircraft and on KC-135 airplanes is described here.

*This work was sponsored by the Department of the Air Force.

1. INTRODUCTION

A turbulent aerodynamic boundary layer near the skin of a high-altitude jet aircraft can degrade the optical quality of a light beam propagated from an aircraft platform. Stine and Winovich[1] first reported an experiment in which the scattering of a light beam due to a turbulent boundary layer, generated inside a wind tunnel, was measured. From these measurements, both the average integral scale and the intensity of the density fluctuations could be estimated. The results of the Stine and Winovich experiment have subsequently been analyzed by Hufnagel,[2] Sutton,[3] Veed and Tuttle[4] amongst others, in order to estimate the probable optical degradation that can be expected by propagating an optical beam through an aerodynamic boundary layer.

Measurements made from a high-altitude jet aircraft (a KC-135), obtaining Modulation Transfer Function data by photographing star images and analyzing these in the laboratory to evaluate the overall atmospheric degradation (over a long path), have been reported by Luke.[5] More recently, a series of experiments to identify and measure the various sources of airborne image degradation was carried out by M.I.T. Lincoln Laboratory. The results of photographic experiments were discussed by Bryant,[6] while the results of interferometric electro-optical experiments were reported by Kelsall.[7] An analysis of the aerodynamic effects on airborne optical systems was carried out and outlined by Wolters.[8] Nevertheless, at this stage in the study of aerodynamic boundary layers, there was a complete lack of any detailed set of experimental data for airplanes over any known and controlled range of flight conditions. It was difficult, if not almost impossible, to predict with any certainty the optical degradation of a light beam propagated out from an aircraft in flight. This was because of the many variables that one must take into account in an aerodynamic environment, as was pointed out by Visinski.[9] A simple theoretical approach to the problem was found to be inadequate when preliminary attempts to compare this simple theory with experiment were made.[10,11,12]

There was no readily available instrumentation or method in existence for carrying out these detailed investigations, and for obtaining a large amount of reliable data. It was necessary to explore and develop new optical techniques for carrying out these experiments satisfactorily,[13,14] and it was necessary to define and perfect corresponding data reduction techniques in order to handle and reduce the large amounts of data by computer methods. Finally, these data must be analyzed, first optically, and then correlation of the results made with the physical and aerodynamical properties of the air turbulence regions through which optical beams were propagated.

2. OPTICAL THEORY

A simplified outline of the optical theory will be given in order that the physical-optical processes can be understood and that the approach adopted to carry out the optical analysis of the data can be explained. No account of the aerodynamic analysis will be given here since this is reported by D'Amato.[12]

If a light beam is propagated through a region in which refractive index fluctuations caused by density fluctuations in the turbulent media are present, the resultant beam is optically degraded. If $f(x,y)$ is the complex amplitude of the degraded beam (in the pupil plane), then the complex amplitude in the image plane will be $A(u,v)$ where these two functions are Fourier transform pairs

$$f(x,y) \rightleftarrows A(u,v)$$

$$I(u,v) \rightleftarrows |A(u,v)|^2$$

and where (x,y) represent coordinates in the pupil plane, (u,v) represent coordinates in the image plane, and $I(u,v)$ is the image intensity distribution (Fig. 1).

The optical transfer function (OTF), $D(s,\psi)$ can be written as follows:

$$D(s,\psi) = M(s,\psi)\, e^{i\theta(s,\psi)} \tag{1}$$

and

$$D(s,\psi) = \int_{-\infty}^{\infty}\int I(u,v)\, \exp[-i(u\cos\psi + v\sin\psi)\, s]\, du\, dy \tag{2}$$

where $D(s,\psi)$ is the one-dimensional OTF, $M(s,\psi)$ is the one-dimensional MTF, and $\theta(s,\psi)$ is the one-dimensional phase transfer function (PTF). The OTF, $D(s,\psi)$, is measured along an optical diameter along a direction which makes an angle ψ with the x-axis. The parameter s is a reduced spatial frequency which can be written as

$$s = \frac{\lambda R}{\sin\alpha} = 2\lambda\,\frac{Rf}{D}$$

where α is the angular aperture size, R is the spatial frequency in the image plane of the optics of diameter D and focal length f, and λ is the wavelength of light.

In practice, the OTF can be measured by means of a shearing interferometer designed to take the autocorrelation of the pupil function[15,16] $f(x,y)$:

$$D(s,\psi) = \int_A\int f(x,y)\, f^*(x - s,y)\, dx\, dy \tag{3}$$

where A is the area of the interferogram. Details of the optical Fourier theory which describes these techniques are in Reference 17.

The complex pupil function, $f(x,y)$ describes the amplitude $A(x,y)$ and phase $\phi(x,y)$ conditions over the wave front and is given by

$$f(x,y) = A(x,y)\ e^{-i\phi(x,y)} \tag{4}$$

In those cases where there is uniform irradiation over the cross-sectional area of the beam, $A(x,y)$ does not normally vary significantly and has little effect on the transfer function, even for large variation of $\phi(x,y)$, and for practical purposes we write $A(x,y) = 1$.

The phase component, $\phi(x,y)$, is measured from a fixed reference sphere (see Fig. 1), and with respect to this reference sphere can be either positive or negative. If we consider the wave front at one instant of time, the "best fit" to the wave front can be represented by $\overline{\phi(x,y)}$ as shown in Fig. 1. If we write the optical wave front distortion at each x,y point as $\Delta\phi(x,y)$, then

$$\Delta\phi(x,y) = \overline{\phi(x,y)} - \phi(x,y) \tag{5}$$

In principle, the fast shearing interferometer (FSI) measures the optical transfer function which depends only on the $\Delta\phi(x,y)$ distribution over the wave front. The mean phase term, $\overline{\phi(x,y)}$, does not influence the measurement made by the FSI. This $\overline{\phi(x,y)}$ term will include a tilt component (which again does not influence the interferometer measurement of the OTF). In the case of thin turbulent air regions, such as aircraft boundary layers, the tilt term is expected to be relatively small although it cannot be ignored. In the case of propagation through the random refractive index medium of the atmosphere, it will be more appropriate to take the averaged value of the OTF. It has been shown by O'Neill[18] and Barakat[19] that the averaged value of the optical transfer function can be written in the form†

$$\langle D(s,\Psi)\rangle = D_o(s)\ \exp -k^2\sigma^2 \left\{1 - \exp -\left(\frac{sD}{2\ell}\right)^2\right\} \tag{6}$$

where $D_o(s)$ is the deterministic transfer function of the optics (usually this is diffraction limited) whose receiving diameter is D. Here k is the wave number, σ

† Here Barakat tentatively assumed a Gaussian correlation function. In D'Amato's aerodynamic analytical treatment, he found it more appropriate to use an exponential correlation function. This will only introduce a small difference in the resulting correlation length evaluation, of the order of 10 percent difference, and for all practical purposes here need not be of any concern. The Gaussian correlation function yields a correlation length ℓ which is smaller by the factor $\sqrt{\pi}/2$ or 0.89 times the length derived using an exponential correlation length.

is the optical rms wave-front distortion, and s is the reduced spatial frequency (or shear value). The length ℓ is a correlation length related to the correlation between the density fluctuations in the medium of the atmosphere. Here σ^2 is the averaged optical mean-square wave-front distortion given by

$$\sigma^2 = \overline{<\Delta\phi^2(x,y)>} \tag{7}$$

where the over bar denotes spatial averaging over the pupil of diameter D, and the brackets <> denote an ensemble average which must be taken because the parameters are varying with time. The main features in the steps to calculate the optical rms phase distortion will be outlined here in order to more clearly describe the treatment of the experimental data obtained, and to clarify the relationships between the optical theory and the aerodynamic analysis of D'Amato.[12] Hogge[20] discussed a similar approach to the analysis of the Strehl Ratio. From Eqs. (5) and (7)

$$\sigma^2 = <\overline{[\phi(x,y) - \phi(x,y)]^2}>$$

$$= <\overline{\phi^2(x,y)}> - <\overline{\phi(x,y)}^2> \tag{8}$$

$$= \sigma_o^2 - (\bar{\sigma}^2 + \overline{k^2}) \tag{9}$$

the spatial averaging (overlap) being done over the area of the pupil (diameter D) where

$$\sigma_o^2 = <\overline{\phi^2(x,y)}>$$

$$\bar{\sigma}^2 = <\bar{\phi}^2> \quad \text{(independent of x,y)}$$

$$\overline{k^2} = <k^2(x^2 + y^2)> \quad \text{(the tilt term)}$$

$$\overline{\phi(x,y)} = \bar{\phi} + k\,(x \cos\phi + y \sin\phi)$$

and k is the amount of tilt measured along an axis making an angle ϕ to the x-axis. Equation (8) can also be written in the general form

$$\sigma^2 = \sigma_o^2 - \pi \int_o^D C_\phi(sD)\ D_o(s)s\ ds \tag{10}$$

where $C_\phi(sD) = \langle \overline{\phi(x_1,y_1)} \quad \phi(x_2,y_2) \rangle$ for $x,y \leq D$ is the covariance function (which here includes the mean fluctuation and any components due to tilt of the wave front), both of which can be evaluated from the aerodynamics. $D_o(s)$ is the diffraction-limited optical transfer function (of the receiving optics). In this way, the σ value measured optically can be compared with the predictions from theory, computing the corresponding values from aerodynamics. A correlation length ℓ can also be computed from the aerodynamics as described by D'Amato[12] and compared with the optically measured values. It should be noted that the optical value of σ obtained depends on the diameter of the optics used to make the measurement determined by the second factor in Eq. (8). As $D \to \infty$, then $C_\phi(sD) = 0$ and $\sigma \to \sigma_o$. It is assumed that over the observation times in question that $\langle \phi(x,y) \rangle = 0$ and $\langle \overline{\phi(x,y)} \rangle = 0$.

In summary, in order to evaluate the optical degradation σ^2 in an optical beam, the different degradation components which make up Eq. (9) must be taken into account and where necessary, scaled with aperture diameter. The result will depend on whether a short averaging time (tilt independent) or a long averaging time (tilt dependent) is considered. In order to calculate the MTF (from which the image intensity pattern can be calculated by a Hankel Transform) or the Strehl Ratio, the optical degradation σ_s^2 or σ_L^2 is first found as follows:

(1) Tilt-independent (short time average) degradation:

$$\sigma_s^2 = \sigma^2 = \sigma_o^2 - \bar{\sigma}^2 - \overline{k^2}$$

(2) Tilt-dependent (long time average) degradation:

$$\sigma_L^2 = \sigma^2 + \overline{k^2} = \sigma_o^2 - \bar{\sigma}^2$$

The bar refers to spatial averaging over the optics diameter D where σ is the optical degradation, $\overline{k^2}$ is the tilt component degradation, $\bar{\sigma}^2$ is the total mean variance, and σ_o^2 the total fluctuation variance of the wave-front distortion. For large (infinite) apertures, $\sigma_s = \sigma_L = \sigma_o$ depends on the density fluctuations in the boundary layer and can be calculated as described by D'Amato from the aerodynamics, while $\bar{\sigma}^2$ and $\overline{k^2}$ approach zero in this case. From the calculations of D'Amato, the form of σ_s^2 and σ_L^2 vs (ℓ_o/D) is shown in Fig. 2. For small optical

diameters, the effective optical degradation decreases very significantly, while the effect of the tilt term (shown by the difference between σ_L^2 and σ_S^2) is relatively small and becomes negligible for large diameters. The largest tilt component for any aperture here will only produce roughly an additional 0.10 amplitude drop in either the MTF degradation or in the Strehl Ratio, and for most practical purposes here can be neglected. This aperture scaling behavior describes the measured variation of σ with aperture in the experiments with optics diameters of 25, 50, and 89 mm, respectively, and also accounts for the observed differences between the 89- and 178-mm optics. The Lear Jet data were taken with a 25-mm optics diameter, and the boundary-layer thickness and the correlation lengths are much less than in the later KC-135 airplane experiments, and these factors are reflected in the data in question.

The scaling relationship for the correlation lengths derived by D'Amato are shown in Fig. 3 where (ℓ/D) is shown plotted vs (ℓ_o/D). From this plot for a measured ℓ (with the FSI), for a given beam diameter D, the infinite aperture correlation length (ℓ_o) can be determined, and then scaling to any other beam diameter can be obtained. The corresponding ℓ_o determined in this manner can then be used by reference to Fig. 2 to scale the measured σ for a given diameter to any other beam diameter. The corresponding beam degradation for σ, ℓ, and D can then be computed by means of Eq. (6) to evaluate the MTF.

There remains one further possible limitation that arises with regard to measuring the time-averaged MTF and using Barakat's Eq. (6), which refers to the averaged OTF, and carrying out the curve-fitting operation to evaluate σ and ℓ. In the experiments described here, the data from the FSI can yield both the MTF (proportional to signal amplitude), and the phase transfer function PTF (determined from the carrier frequency or the signal phase measurement). The platform on which the FSI was located however, was subjected to severe vibrations and was not spatially stable. These instabilities give rise to angle-of-arrival fluctuations in the optical beam measured by the FSI, producing additional fluctuations in the carrier signal frequencies. They do not however, affect the amplitude of the signal. While accurate MTF data can be obtained in these field environments, it is not possible to process the data and extract the phase transfer function because of the larger, noisier, angle-of-arrival fluctuations. It requires a very stable environment to obtain accurate phase transfer function data, even in the laboratory. Therefore, it is important to consider the question

of whether the average MTF data measured here are equal to the averaged OTF, and whether one can curve fit our experimentally measured data to an expression of the form given by Barakat. It has been shown by both Cook[21] and Weaver[22] that a simple analysis of the problem leads to a relationship of the following form

$$\langle D(s,\psi)\rangle = \langle M(s,\psi)\rangle e^{\frac{-i\Delta^2}{2}}$$

where Δ^2 is the variance of the phase transfer function. In principle, the variance Δ^2 is a measure of the amount of nonsymmetry in the fluctuations in the transfer function. It might be expected that in an approximately isotropically random fluctuating medium that Δ^2 might be small, and particularly in the case of a thin turbulent boundary layer, it is provisionally assumed that $\Delta^2 \ll \sigma^2$ where σ^2 is the variance of the wave-front distortions. If this is true, then as a first approximation

$$\exp - \frac{i\Delta^2}{2} \to 1 \quad \text{and} \quad \langle D(s\psi)\rangle \to \langle M(s\psi)\rangle$$

In order to test this hypotheses, the measured data were test fitted to the Barakat expression Eq. (6). Good curve fits to the measured data were obtained and it was concluded that the average MTF data measured could be used to evaluate the optical wave-front variance σ^2 as explained earlier. An outline of the theory of operation of the fast scanning interferometer used to measure the MTF is given in Reference 13, and this technique will not be described here.

3. STAR SOURCE DEGRADATION MEASUREMENTS

In some early measurements of the imaging of stars taken from a KC-135 aircraft in flight, a degradation of the images was observed, which was attributed to the flight environment. Using a corner cube shearing interferometer and an 89 mm diameter receiving telescope, MTF measurements were obtained from star source observations with the airplane flying between 7 km and 12 km altitude. These data were well below the diffraction limited capability of the telescope employed, and some representative data are shown in Fig. 4, for four different star sources viewed (these are averages of several points). In these experiments each MTF point was recorded on tape, but took up to a minute for a single point, and only a limited amount of data could be obtained. Nevertheless, a boundary-layer degradation was observed, and several series of different experimental configurations were employed to obtain confirmation of the results, as was described in Reference 7.

4. LASER SOURCE FAST SHEARING INTERFEROMETER MEASUREMENTS

A much more detailed and comprehensive set of boundary-layer measurements has subsequently been carried out. For this program a fast shearing and very stable triangular configuration interferometer was designed and built. A more extended series of experiments on airplanes, in which the flight conditions were carefully controlled, has been carried out and will be outlined here.

A. LEAR JET EXPERIMENTS

In this experiment, the FSI was mounted on a bench in the Lear Jet aircraft and an airfoil mounted outside a window in the airstream to hold a small mirror about 25 cm away from the skin of the aircraft. An optical schematic shown in Fig. 5 illustrates how the optical degradation in the boundary-layer airstream between this mirror and the aircraft window was examined to obtain MTF data. A 5-mW HeNe CW laser was mounted underneath the FSI. A high-quality 50-mm-aperture laser beam expanding telescope was used to provide a collimated and coherent laser beam. A mirror and a beam splitter were arranged to direct the 50-mm collimated laser beam through a 75-mm-diameter window in the side of the aircraft. The beam then propagated through the airstream (the boundary layer) to a 30-mm-diameter gold-coated mirror supported by the airfoil outside the aircraft.

It was reflected back from this mirror again through the boundary layer and then back through the window to the inside of the airplane. Experiments were also performed with an aerodynamically designed tube (an airflow shield) fitted prior to a flight between the gold-coated mirror and the 75-mm optical window to enclose completely and shield the 25-cm light path outside the aircraft from the flight boundary layer.

The returned laser beam finally passed through the beam splitter to a 24-mm-aperture telescope which reduced the laser beam in diameter to about 8 mm. This then entered the interferometer. The auxiliary optical components arranged in this experimental setup were of very high optical quality to ensure that the wave-front entering the interferometer in the absence of the boundary layer was plane to within one-tenth wave. A photograph of the Lear Jet airplane is shown in Fig. 6. The airfoil mounted outside the window forward of the wing and near the entry door at point A can just be seen, the optical axis being located 4.9 m from the airplane nose. The mounting of the FSI, the optics for the autocollimation system, and the laser source located inside the aircraft, are shown in Fig. 7. The electronics are mounted in the rack on the left. The flight conditions could

be varied over a wide range. At each condition, the effect on the MTF could be observed in real time, focus adjustments (on the receiving-beam reducing optics on the front of the FSI) could be quickly and accurately made, and the alignment of the system could be checked and corrected (since in flight due to aerodynamic loads, the airfoil changed slightly and consequently caused some changing of the optical alignment).

B. KC-135 OPTICAL PROPAGATION EXPERIMENTS

The optical propagation experiments were directed towards evaluating and characterizing the optical degradation measurements from an aircraft platform. Propagation measurements were made through the local aircraft boundary layers as well as over longer paths (free-stream atmospheric regions). Two similar KC-135 airplanes were instrumented for these experiments. Optical propagation measurements were conducted from each of these two aircrafts. Visible beam propagation measurements (at one wavelength λ = 632.8 nm) were made through the window just behind the wing in the aft airplane section in the side of the #1 airplane (located 24.8 m from the nose of the airplane).

Similar visible beam propagation measurements were made through the forward section window (located 10.4 m from the nose of the airplane) on aircraft #2. In practice, the two airplanes were arranged to fly together in formation at a suitable distance apart which varied from about 0.30 to 3 km. In this measurements program it was difficult to always have control of the measurement conditions. Weather conditions intervened, flights sometimes had to be aborted or limited. It was not possible to always optimally perform these field measurements.

A schematic is shown in Fig. 8 to illustrate the series of visible-wavelength measurements through the two airplane windows, one forward on aircraft #2, the second aft on aircraft #1. A visible-wavelength laser beam was propagated from one airplane to the other (this could be done in either direction). A second configuration allowed the visible laser beam from the aft window on aircraft #1 to be directed at a retroreflector located on its wingtip. On reflection, the beam retracted its path and passed through the same window for making measurements. A photograph showing the position of the retroreflector on the wingtip of aircraft #1 seen from the aft window is shown in Fig. 9 which also shows aircraft #2 flying in the distance.

The distance from the retroreflector to the optics inside the aircraft was 18.3 m. Note that in this case the outgoing beam passing through the boundary layer was quite small although it irradiated the whole retroreflector (with enough

overlap to keep it irradiated uniformly as the wing moved up and down during flight). A spherical reflected beam, whose origin was close to the retroreflector on the wingtip, was then propagated back to the aircraft and received by the 89-mm optics. The MTF degradation measurement was therefore representative of one single pass, as the beam made the return trip from the retroreflector through the boundary layer, the beam diameter being determined by the receiving optics aperture.

In the flight experiment using the two aircraft, the optical degradation produced in the boundary layer outside each window was measured using the FSI instrument which could be located on an optical bench on either aircraft just inside the window. It was necessary to use an optical beam reducing system just in front of the FSI, since the maximum input diameter beam that could be handled by the FSI was about 10 mm. Two alternative ruggedized and temperature-stabilized Invar Questar telescopes, each combined with an 85-mm focal length collimating lens, were used for this purpose. Diameters of 178 and 89 mm were employed for these two telescopes and they were each coupled to an 85-mm fl collimator lens to produce (the same for each) an output beam diameter of 6.8 mm. A photograph of the FSI together with the 178-mm Questar telescope is shown in Fig. 10 located on the optical bench in aircraft #2. The exit window is on the right and the light path from the Questar to the window area was shielded by a tube (to exclude internal air turbulence), as shown in this photograph.

The laser source located on one aircraft was diverged (roughly to 15 to 30 mrad) and propagated through the window of this airplane to irradiate the window of the second airplane, and be subsequently collected by the Questar telescope. On transmission through the source aircraft window, the beam diameter was very small and was not influenced by the boundary layer at this window. On reaching the receiving airplane, however, the beam was large (roughly 15 to 30 m in diameter) and the receiving optics collect a beam equal in diameter to either the 89- or 178-mm aperture, according to whichever Questar optics was used.

The boundary-layer turbulence at this receiving optics window degraded the beam. Therefore the boundary-layer MTF measurement made refers to that aircraft on which the measuring (FSI) system was located, and the effective beam diameter was determined by the receiving optics diameter.

C. KC-135 AIRFOIL EXPERIMENTS

This third and last set of measurements was developed as a culmination of the earlier flight experiments. A more comprehensive series of flight optical boundary-layer degradation measurements very similar in principle to those carried out earlier on the Lear Jet was planned. The optical configuration was similar in concept to that carried out on the Lear Jet, except that an optical beam of 89-mm diameter was employed.

A schematic of the optical experiment is shown in Fig. 11. A photo of the FSI instrument, the 100-mm optical beam expander (stopped down to 89 mm for the measurements), and the HeNe laser source, together with the auxiliary optics (beam splitter, mirrors, and laser beam expander) is shown in Fig. 12. This equipment was mounted on an optical bench along the aircraft fuselage (near the window which was located at point A, 22.9 m from the nose of the airplane). A photo of the airplane showing the location of the airfoil is shown in Fig. 13.

Thirty seconds of MTF data were recorded on FM magnetic tape. Data were taken at each flight condition for which shear directions were either along ($\psi = 0°$) or perpendicular to ($\psi = 90°$) the airflow direction (using the "K" mirror wave-front rotator). The flight profiles were planned so that data could be taken either along a constant Reynolds number line, or alternatively along a constant Mach number line, as aircraft altitude was changed.

In making measurements during these flights, real-time focusing was done as each flight condition was changed. A Nicolet Model 1070 signal-averaging system installed in the airplane was used to look at the real-time-averaged MTF signals. The Tropel 100-mm beam expander was focused for the best (highest) MTF while looking at the average of up to 1000 MTF curves. In the earlier experiments this had not been possible, and focusing by viewing an ever-changing MTF curve observed on an oscilloscope had been rather difficult and tedious. A wave-front rotator on the front of the FSI permitted the MTF measurement to be made along any direction between $\psi = 0°$ (along the air flow in the boundary layer) and $\psi = 90°$ (perpendicular to the airflow in the boundary layer).

Focusing was initially optimized for the $\psi = 0°$ direction and checked for the $\psi = 90°$ measurement. It was noticed that after focusing on the $\psi = 0°$ position, then going to the $\psi = 90°$ position (also some intermediate settings for $\psi = 45°$ were done), a refocusing of the optics was sometimes necessary to optimize

the MTF. Apparently a small amount of residual astigmatism arose and one reason for this could be attributed to a small distortion in any one of the mirrors - the airfoil mirror or the turning mirror in the airplane on the optical bench. It was therefore necessary to ensure that temperature effects or flight-induced stresses from the mounting of these mirrors did not introduce distortions during flights.

In all these experiments, the test window consisted of a double (thermopane) window (Fig. 11), (while only a single window had been used in the earlier experiments), to minimize the temperature gradient effects in the window. The outer window was flush with the skin of the airplane. The airfoil mirror was flush with the airfoil surface within 1 mm and was located 60 cm from the skin of the airplane so that it essentially was outside the effective boundary layer. The optical path inside the airplane had also been carefully shielded from internal thermal air currents by a plastic sheet on all flights. An additional test carried out was to make measurements for a range of different aperture sizes, from 25 to 89 mm for two constant altitudes and one constant Mach number.

A great deal of effort was spent on testing all the optical components, mirrors, and windows, since these were more critical than in any of the earlier experiments due to the larger aperture beam making a double pass through all the components. Calibration measurements were made on the ground (to the airfoil) and in flight (with an internal aircraft mirror) as well as in the laboratory. This was needed to both check out the optics and to accurately determine the shear scale. In the experiments with the 89-mm aperture, the beam size entering the interferometer was over 9 mm (which is somewhat larger for visible wavelength than was the case in all the earlier experiments). At the higher shear values for the visible FSI, the shear scale is nonlinear by up to 7 or 8 percent. Therefore, this nonlinearity was corrected during the data reduction and computer processing. Note that this correction depends on the properties of the shear plate, its refractive index and thickness, and in none of the earlier experiments was it necessary to make this correction.

5. FLIGHT DATA RESULTS

All the data were computer processed to yield averaged MTF data, and standard deviations of MTF, the processed averaged MTF data obtained for all these experiments were next fitted to the theoretical "Barakat" expression and the equivalent optical rms wavefront deviation (σ) in wavelengths (for λ = 632.8 nm) and correlation length (ℓ mm) factors calculated for the series of data reported here. The values of σ and ℓ for the different experiments were then plotted as a function of altitude.

In the case of the Lear Jet and the airfoil experiments, the σ evaluated from the MTF data corresponds to double passes through the boundary layer. In order to compute the equivalent single pass, it is necessary to know how σ varies with path length. If the refractive index fluctuations for a double pass through the boundary layer can be assumed on the second pass (assuming the time of propagation is very much smaller than the fluctuation time of the refractive-index variations) to be correlated, then it will be assumed that the single-pass σ value is just half the double-pass σ value. This point has been recently discussed by Hogge and Gilbert.[23] D'Amato described the development of an aerodynamic model[12] and gave a theoretical analysis of the characteristics of the boundary layer to show how calculations of the density fluctuations could be made from the boundary-layer parameters. It was necessary to make a number of assumptions in applying his aerodynamic model, taking as a starting point a standard atmosphere and extrapolating from the known properties of the flow over a simple flat plate.

The experimental results encompass a wide range of test conditions in which the aerodynamic parameters of the boundary layers can be expected to vary by substantial amounts. A comparison of the experimental data with the predictions from D'Amato is shown in Figs. 14 and 15 (a) and (b). The points (shown by open symbols as indicated on the figure) computed by D'Amato[12] are plotted for many of the corresponding experimental points. For the KC-135 airfoil test data, points derived from some NASA aerodynamics measurements (see K. Gilbert, Reference 24, on page 163) are shown compared to the optical measurements in Fig. 14(c). For the propagation experiments, the measured data showed little or no variation with airplane speed, and only the averaged data point over all Mach numbers is shown. The amplitude of typical error

bars which denote the standard deviation of the mean value taking the average of 40 separate MTF measurements is shown on the figures, using that data computed from the standard deviation of a single reading for the MTF.

The Lear Jet and propagation experimental data are significantly more degraded than D'Amato's values. The airfoil data σ value points show a reasonably good agreement with the points derived from the aerodynamic measurements. The Lear Jet and propagation experiments were flown in late January and between the winter months of September and March, during which ambient temperatures were appreciably colder at most altitudes. The airfoil experiments were carried out in June and July, and were the only case where detailed aerodynamic data were taken (by NASA Ames). Actual measurement data were not available for these factors to be taken explicitly into account in the D'Amato computations. However, some estimates of the sensitivity to temperature changes (which will produce corresponding changes in the boundary-layer turbulence) have been discussed by D'Amato and indicate that ambient temperature may play a critical part in these computations. It should be pointed out that in the earlier cube corner interferometer experiments a marked increase in degradation was observed as the airplane flew at constant altitude and speed into a cold front.[7] At this point, while the D'Amato theory appears to be able to make predictions of the degradation, only by making the aerodynamic measurements can it be expected that good agreement of calculated with measured optical data will be obtained.

There are several details in the comparison shown in Figs. 14 and 15 that should be enlarged upon for clarity. The Lear Jet data shown in Fig. 14(a) relate to a 25-mm optical diameter and for this reason, as well as the boundary layer itself being much smaller, these data are less degraded than the propagation and airfoil data in Figs. 14 (b) and (c). These later experiments were taken mostly with an 89-mm-diameter beam (except where indicated differently) on a KC-135 airplane with a thicker boundary layer than on the Lear Jet. In the final analysis, it is the absolute values of σ_o and ℓ_o of the boundary layer that must be determined, and these are readily scaled for a given diameter optical beam to the corresponding σ and ℓ values in order to compute the optical degradation with any given optical aperture.

The Lear Jet data showed only small variation with Mach number, except at 1.5 km altitude where a large difference for 0.4 and 0.55 Mach number was observed. The theoretical calculations at all altitudes showed little change with Mach number so that at 1.5 km altitude, there is an additional difference between theory and experiment in the magnitude of the dependence on aircraft speed.

For the propagation data, two theoretical points are shown at each altitude (for two different Mach numbers) representing the slowest and fastest speed flown at that altitude. In these cases the theoretical computations refer to the case of the boundary layer at the aft location on the KC-135 aircraft. In Fig. 14(b), the theoretical points indicated at each altitude are different for the two limiting aircraft speeds (minimum and maximum for the experimental data taken). In the experimental data, these differences are hidden in and less than the spread of the data points experimentally observed. However, in taking data at different Mach numbers at a constant altitude, the environmental changes in the aerodynamical conditions were not as large as when changing altitude, and the spread of data was generally less. Both variations in the boundary-layer characteristics due to the changing flight environment as well as experimental variation in the data may therefore account for these differences. These disparities are not a serious discrepancy, but provide some indication of the complexity of the interaction of the aerodynamic parameters in the turbulent boundary-layer problem.

Comparison of the correlation lengths shown in Fig. 15 from theory and experiment, shows good agreement for the Lear Jet, but less so for the propagation data. The two low-altitude measured data with long correlation lengths (greater than 30 mm) are exceptions and may indicate that the measured degradation here was not solely due to the boundary layer. For the KC-135 airfoil experiment, D'Amato's calculations predicted correlation lengths of the order of 20 mm, and similar correlation lengths were also obtained from the aerodynamic data (selected data from Ref. 24 are shown in Fig. 15(c). All the other data for the KC-135 airplanes yield experimentally measured correlation lengths slightly shorter than predicted by theory. The disparities are most likely mainly due to the uncertainty in the aerodynamic environmental conditions and parameters.

In Figs. 16 and 17 the aperture scaling measurements from the airfoil data are compared with the theoretical predictions for optical beam diameters of 89, 50, and 25 mm, taken at constant Mach number (0.57) and for two constant altitudes. All the data at each altitude were gathered within an approximately 30-min time interval, and environmental conditions were expected to be relatively constant. The lower altitude was flown first, and in this case good agreement between the measured and predicted data points can be observed. At the higher altitude, the measured data were more degraded than expected (when compared with data for the 89-mm aperture taken on earlier flights), and for all aperture sizes the σ values measured were larger than predicted by theory.

The spread in the measured data over the 25- to 89-mm aperture diameters in question, is much smaller at both altitudes than the predictions from theory, and the uncertainties in the aerodynamic quantities are suspected of being the source of the error in this case. There is no doubt that the variations in environmental conditions produce large spreads in the data.

6. CONCLUSIONS

When this work was started, there were no detailed experimental or theoretical results that could provide realistic estimates of the amount of degradation to be expected from an in-flight aircraft boundary layer. The initial emphasis was placed on obtaining experimental measurements of the flight boundary-layer degradation together with doing a preliminary optical analysis. This has subsequently been followed by a more detailed aerodynamical analysis (by D'Amato) making use of these measured data.[12]

A description of these experiments together with an outline of the optical analysis has been discussed here, and the measured data compared with some of the theoretical predictions in the case of the boundary-layer degradation. There are many factors that enter into each one of these series of tests. Intermittent fluctuations in the environmental conditions caused changes in the experimentally measured data for a given flight condition. Each series of tests used different geometric configurations, and effects due to the airfoil structures, and due to airplane geometry itself, may give rise to environmental changes and effects. The theoretical calculations of D'Amato were based upon estimated "steady state" conditions since no experimentally measured aerodynamic data were available.

The boundary-layer degradation measured in these experiments varied with altitude, airplane speed, and Reynolds number, in a complex way, and also depended on the ambient temperature. Data obtained from experiments conducted over the winter months were more degraded than expected. The Lear Jet data, where the boundary layer was significantly thinner than in the later tests (and also were taken using smaller diameter optics), were less degraded than the later tests. (The boundary-layer thickness in the KC-135 was from 3 to 5 times thicker than the Lear Jet.) There were also different boundary layers for the two window locations on the two different aircraft (aft and forward positions). However, there were only small differences between the results for these two cases, the forward position (thinner boundary layer) giving rise to more degradation than the aft position.

To summarize, the measured results indicated degradation levels for the KC-135 airplanes between $\sigma = 0.10\lambda$ to 0.13λ increasing to 0.18λ. When scaled to infinite aperture, these correspond to degradation levels of $\sigma_o = 0.2\lambda$ to 0.26λ and increase to 0.36λ. For the Lear Jet, degradation with a 25-mm diameter optics was roughly $\sigma = 0.07\lambda$ and on scaling to infinite aperture, corresponds to a degradation level of $\sigma_o = 0.14\lambda$ which is less than that observed on the KC-135 as was expected. The corresponding measured correlation lengths of roughly 12 mm for the KC-135 aircraft and 6 mm for the Lear Jet scale to roughly 20 and 25 mm, respectively, for infinite apertures. These boundary-layer correlation lengths do not appear to reflect the different boundary-layer thicknesses on the two different aircraft. To interpret the data and to extrapolate and predict the final imaging characteristics, the appropriate aperture scaling must be taken into account. There is clearly no simple rule-of-thumb answer to estimating the degradation in a light beam propagated through the aerodynamic boundary layer of an aircraft. However, in those cases when aerodynamic measurements are made, these show good agreement with optical measurements.

REFERENCES

1. H.A. Stine and W. Winovich, "Light Diffusion Through High Speed Turbulent Boundary Layers," NACA-RMA 56 B21 (May 1956).

2a. R.E. Hufnagel, "A Theory for the Image Degrading Effects of Turbulent Aerodynamic Boundary Layers," Engineering Report 7677, Perkin-Elmer Corp. (6 May 1964).

2b. R.E. Hufnagel and R.V. Shack, "The Effective Transfer Function of a Turbulent Boundary Layer," Engineering Report 7673, Perkin-Elmer Corp. (1964).

3a. G.W. Sutton, "On Optical Imaging Through Aircraft Turbulent Boundary Layers," Avco-Everett Report AMP334 (June 1971).

3b. G.W. Sutton, AIAA J. 7, 1737 (1969).

4. A.M. Veed and J.W. Tuttle, "Derivation of an Optical Modulation Transfer Function for Turbulent Boundary Layers," General Dynamic Report ERR-RW-347 (29 September 1964).

5. C.A. Luke, "Atmospheric Turbulence MTF Measurements for Airborne Surveillance Techniques," Technical Report AFAL TR-68-253, Part II, Air Force Avionics Laboratory (May 1969).

6. B.W. Bryant, "Experiments on Airborne Seeing from a High Altitude Jet Aircraft," Project Report AOR-29, Lincoln Laboratory, M.I.T. (18 September 1973), DDC AD-896818-L.

7. D. Kelsall, JOSA 63, 1472 (1973).

8. D.J. Wolters, "Aerodynamic Effects on Airborne Optical Systems," Report MDCA2582, McDonnell Aircraft Co., St. Louis (14 December 1973).

9. W.L. Visinsky, "Boundary Layer Turbulence," Air Force Weapons Laboratory, Laser Division Digest LRD-72-1, (June 1972). p. 109.

10. AFWL/Optics Semiannual Technical Summary, Lincoln Laboratory, M.I.T. (15 March 1973), P. 13, DDC AD-526201-L.

11. K. Gilbert, D.F. Terwilliger, R.J. Cook, "Laser Propagation Through an Aircraft Turbulent Boundary Layer: Lear Jet Experiments," Air Force Weapons Laboratory, Laser Digest TR-75-229 (October 1975), p.143.

12. R. D'Amato, AFWL/Optics Final Report, "Optical Degradation by Aerodynamic Boundary Layers-Part II," Lincoln Laboratory, M.I.T. (30 September 1977).

13. D. Kelsall, Appl. Opt. 12, 1398 (1973).

14. D. Kelsall, (a) Proc. SPIE 46, 124 (1974), (b) Phot. Sci. Eng. 21, 123 (1977).

15. H.H. Hopkins, Opt. Acta, 2, 23 (1955).

16. H.H. Hopkins, Proc. R. Soc. 231, 91 (1955).

17. M. Born and E. Wolf, Principles of Optics (Pergamon Press, New York, 1964).

18. E.L. O'Neill, Introduction to Statistical Optics (Addison-Wesley, Reading, Mass., 1963).

19. R. Barakat, Opt. Acta, 18, 683 (1971).

20. C.B. Hogge, AFWL internal communication, "Random Phase Variations Effect on the Strehl Ratio" (23 September 1977).

21. R.J. Cook, AFWL internal communication, "Comment on MTF Data Analysis" (1976).

22. L.D. Weaver, Lincoln Laboratory, M.I.T. internal communication, "Calculation of the Average OTF in the Presence of Random Fluctuations" (31 March 1976).

23. K. Gilbert, "Thermo-optical Turbulent Boundary Layer Measurements," Air Force Weapons Laboratory, Laser Digest, AFWL TR-78-15 (April 1978), p. 140.

24. K. Gilbert, "Aircraft Aero-Optical Turbulent Boundary-Layer/Shear-Layer Measurements," Air Force Weapons Laboratory, Laser Digest, AFWL TR-78-15 (April 1978), p.154.

ACKNOWLEDGMENTS

The work described in this report was carried out by a team of M.I.T. Lincoln Laboratory personnel at the Albuquerque Airborne Optics Site (AAOS) operated by Lincoln Laboratory at Kirtland Air Force Base, New Mexico, together with a wide range of support from many different participants who have contributed in one way or another to this program. In particular, I am grateful to E. J. Casazza and J. R. Theriault for their help during the earlier laboratory and field testing experiments. R. A. Bollman, R. G. Garnes, L. W. Chaulk, D. M. Corbosiero, D. A. Page, J. Swedberg, and Dr. L. D. Weaver at AAOS played the major part in planning, designing, building, and testing of the experimental setups, and in the overall flight measurements program. The development of the data handling, data reduction, and the implementation of the computer analytical procedures was carried out with the assistance initially of the Lexington Lincoln Laboratory Data Analysis Group, and later at AAOS by R. A. Bollman, G. Prade, and J. W. Tolleson (Lincoln Laboratory personnel) working with the Kirtland Air Force Computation Center during the flight experimental measurements phase of the program.

The help of General Dynamics (an Air Force contractor at AFWL) during the construction and assembly of the Cycle II$\frac{1}{2}$ equipment, and for the use of several optical facilities, the assistance of the Air Force Optical Testing Facilities (run by International Lasers Systems, Inc.) is also much appreciated. The continuous support and help provided by the Air Force Weapons Laboratory Project Officers, Lt. Col. K. Gilbert, Captains G. Bock, J. Otten, and L. Pape, with whom the AAOS worked closely during the course of these experiments is gratefully acknowledged. In addition, mention must also be made of the help provided by NASA-Ames in the case of the Lear Jet experiments conducted from Moffet Field in California, and by the Air Force flight crews and support personnel who made the flight experiments both possible and very successful.

Finally I am indebted to E. S. Cotton for both his support and for discussions with him, since the inception of this work, to R. D'Amato for his inputs and discussions on the aerodynamics, and to Dr. R. H. Rediker for his comments.

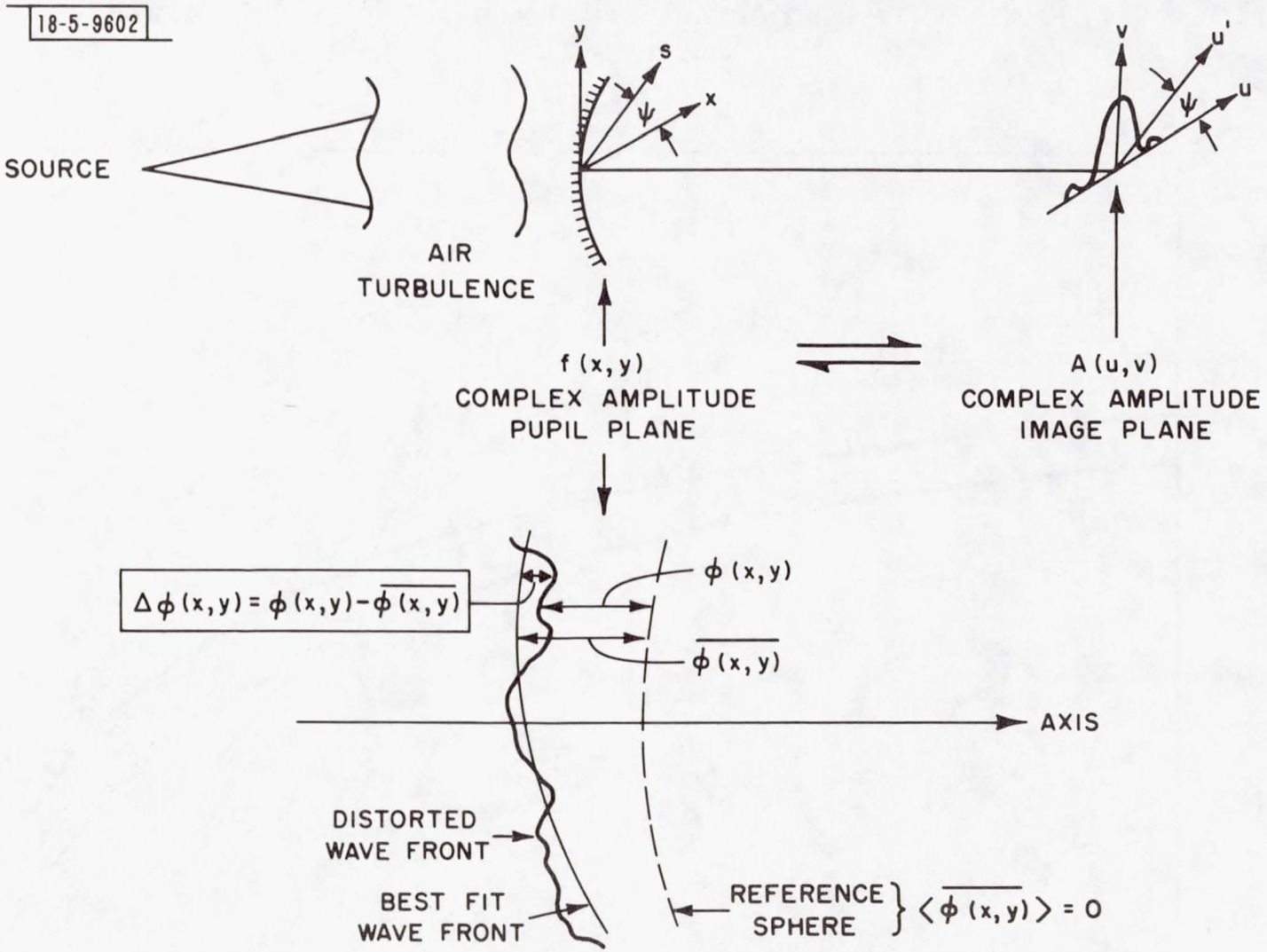

FIG. 1. OPTICAL RELATIONSHIPS.

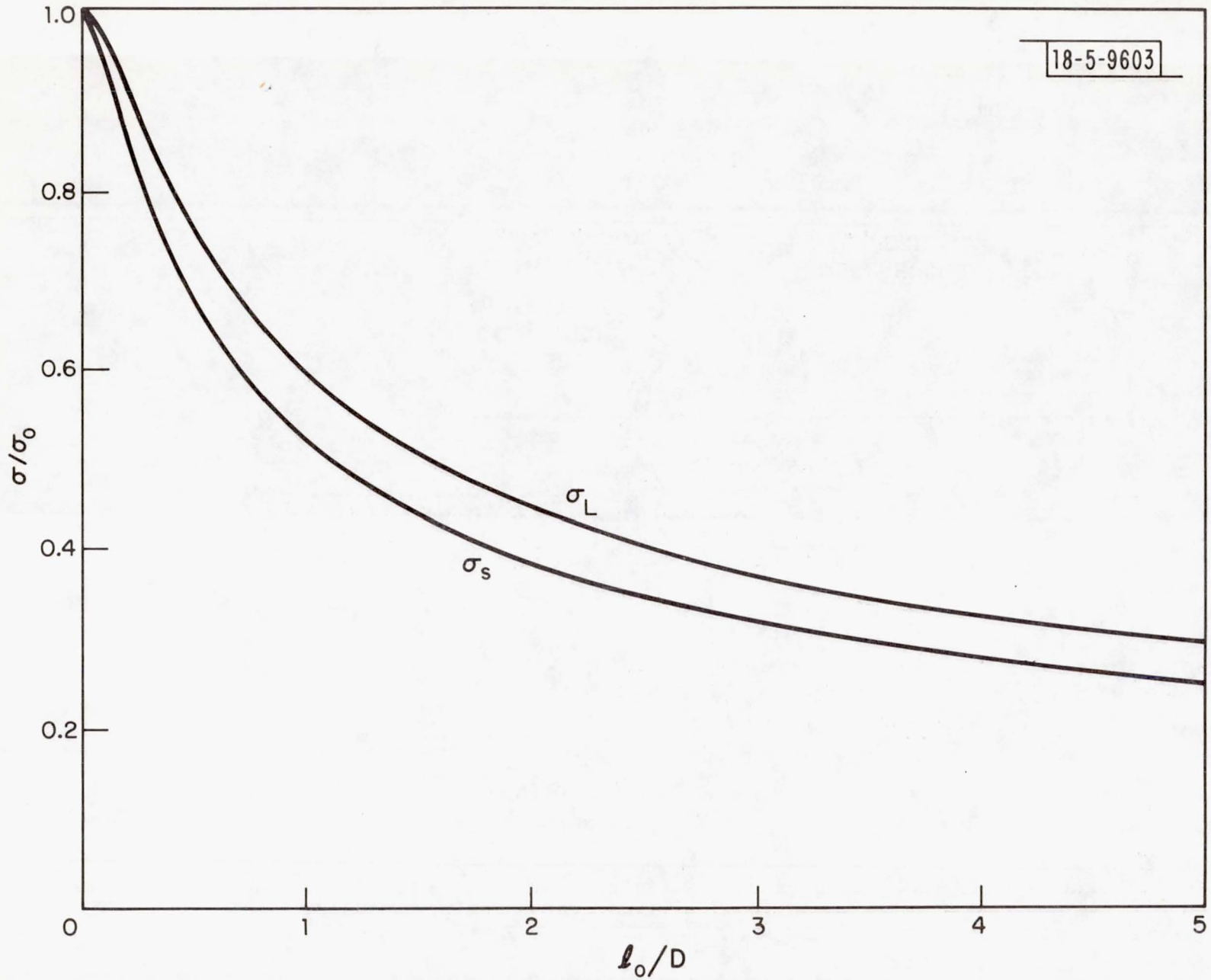

FIG. 2. SCALING OF OPTICAL σ WITH APERTURE (D) AND CORRELATION LENGTH (ℓ_o).

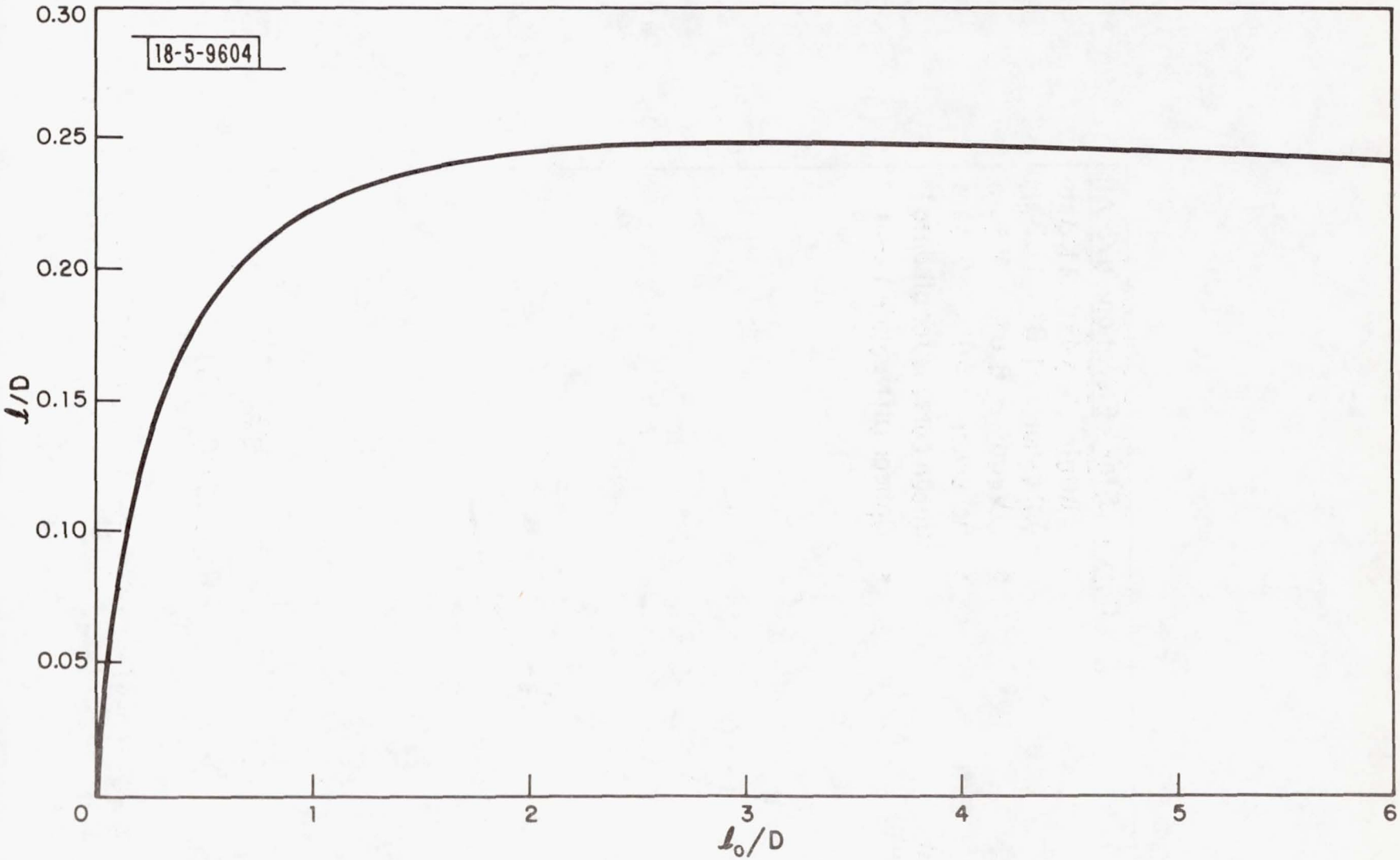

FIG. 3. SCALING OF OPTICAL ℓ WITH APERTURE (D) AND CORRELATION LENGTH (ℓ_o).

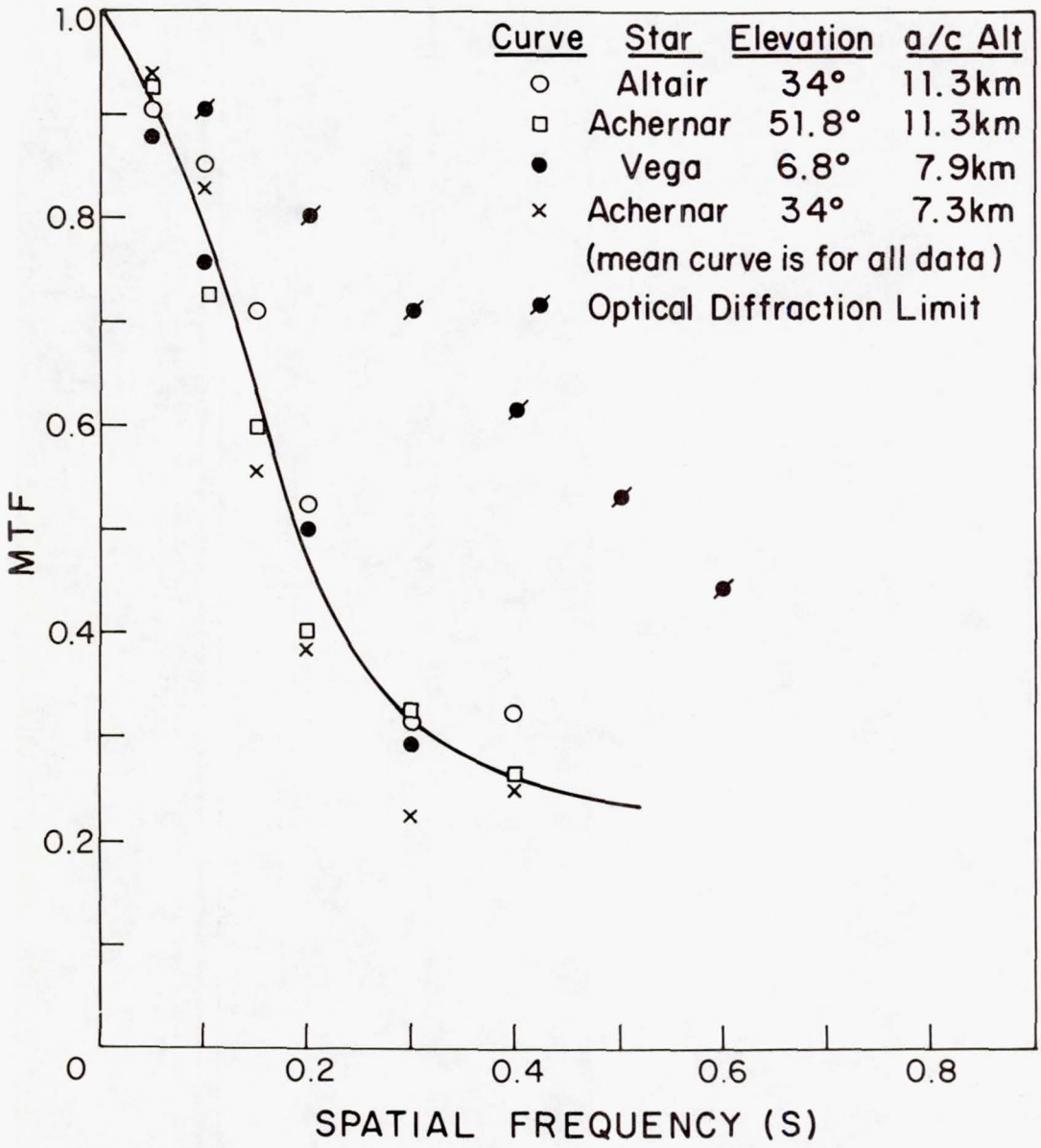

FIG. 4. MTF MEASUREMENTS FROM A KC-135 AIRCRAFT VIEWING STAR SOURCES.

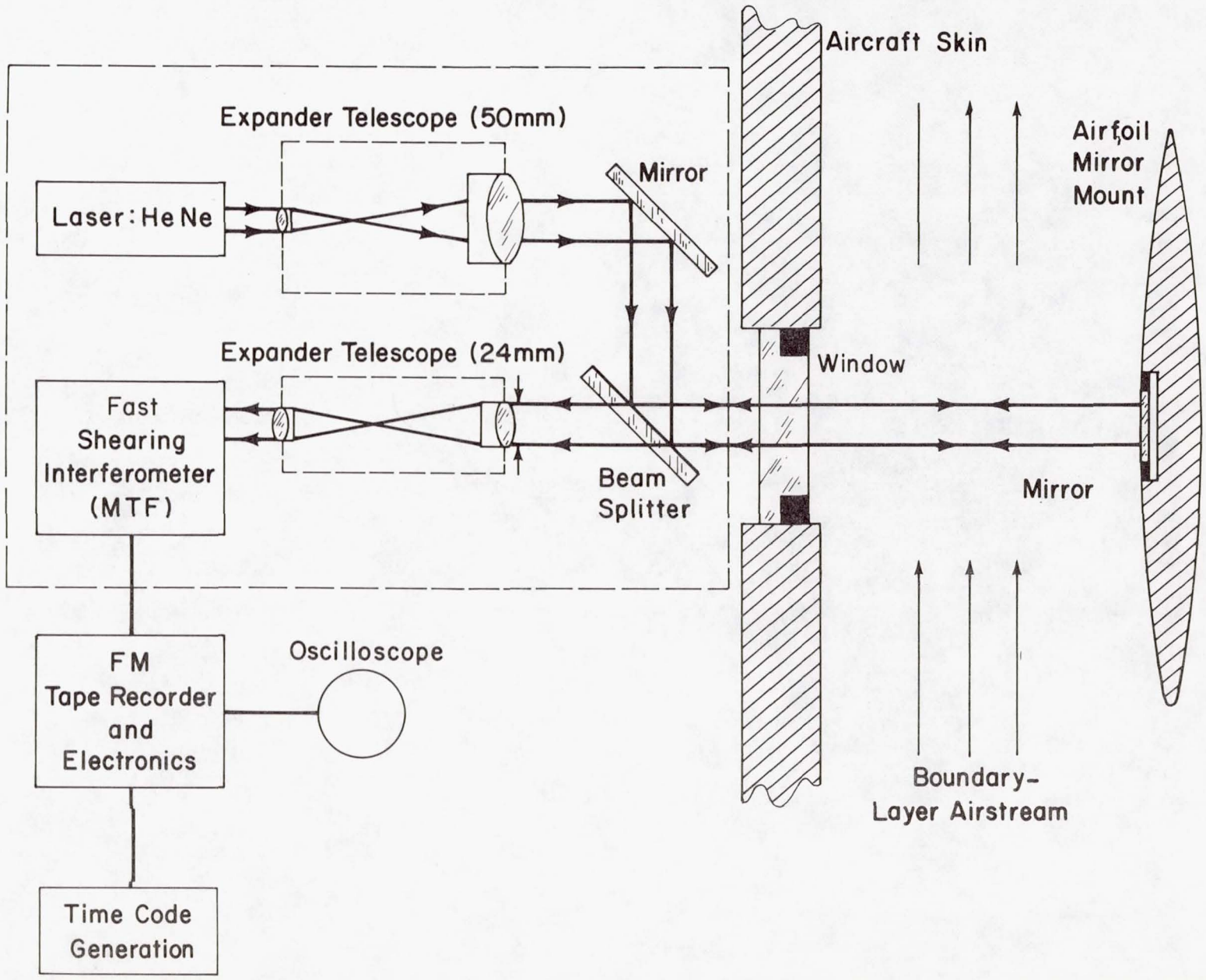

FIG. 5 OPTICAL SCHEMATIC LEAR JET EXPERIMENT.

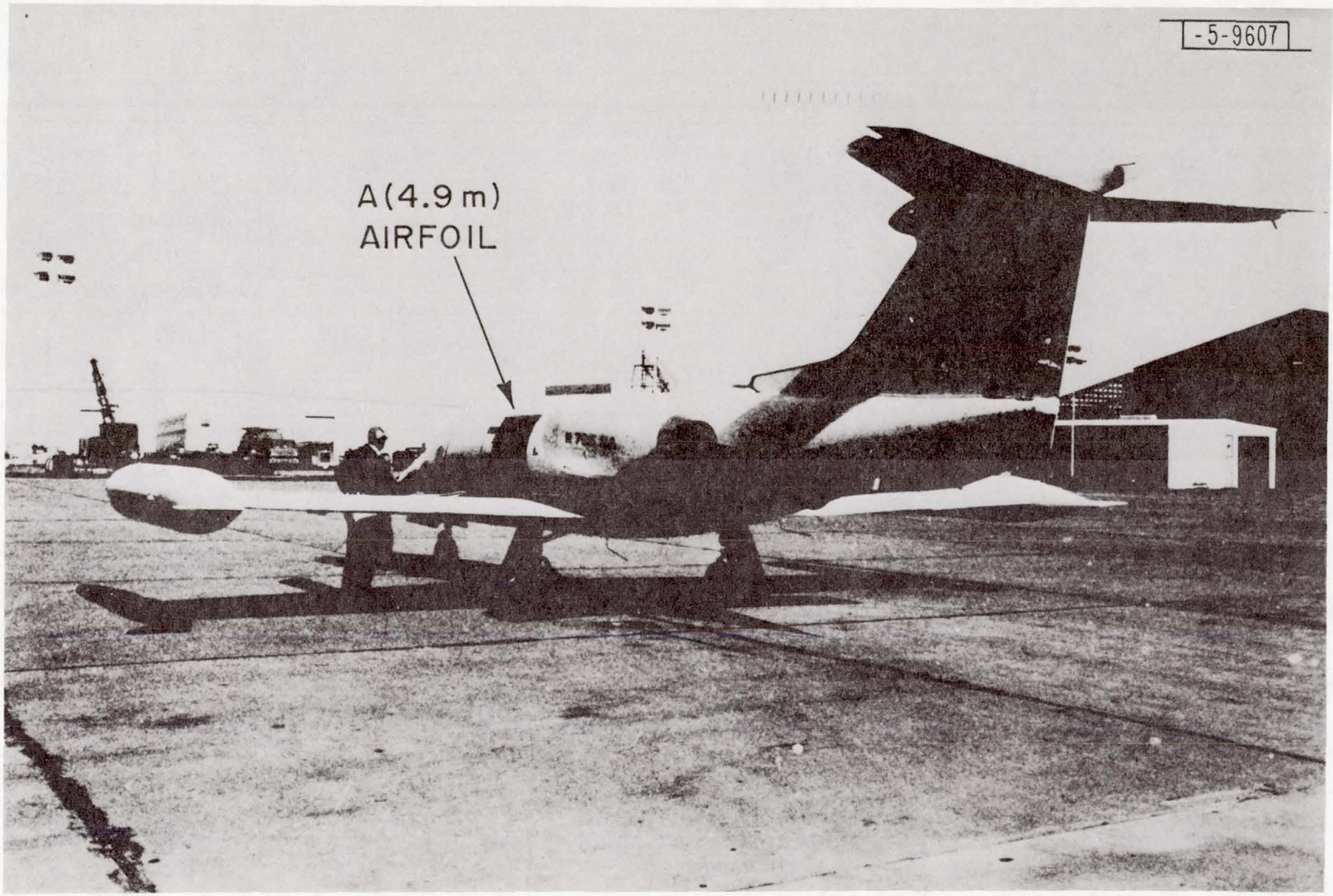

FIG. 6. LEAR JET WITH AIRFOIL ON SIDE.

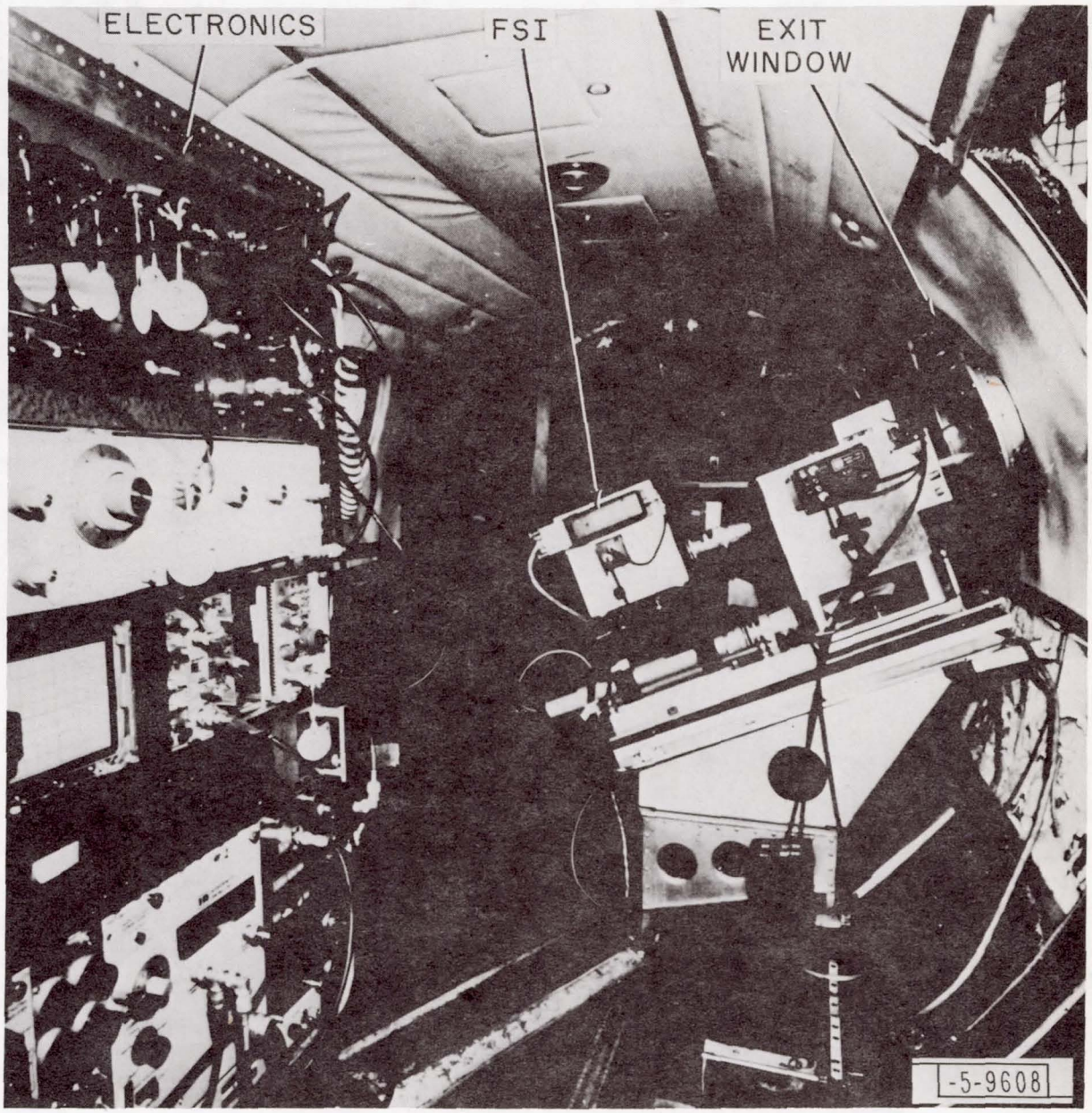

FIG. 7. FSI INSIDE LEAR JET.

18-5-9611-1

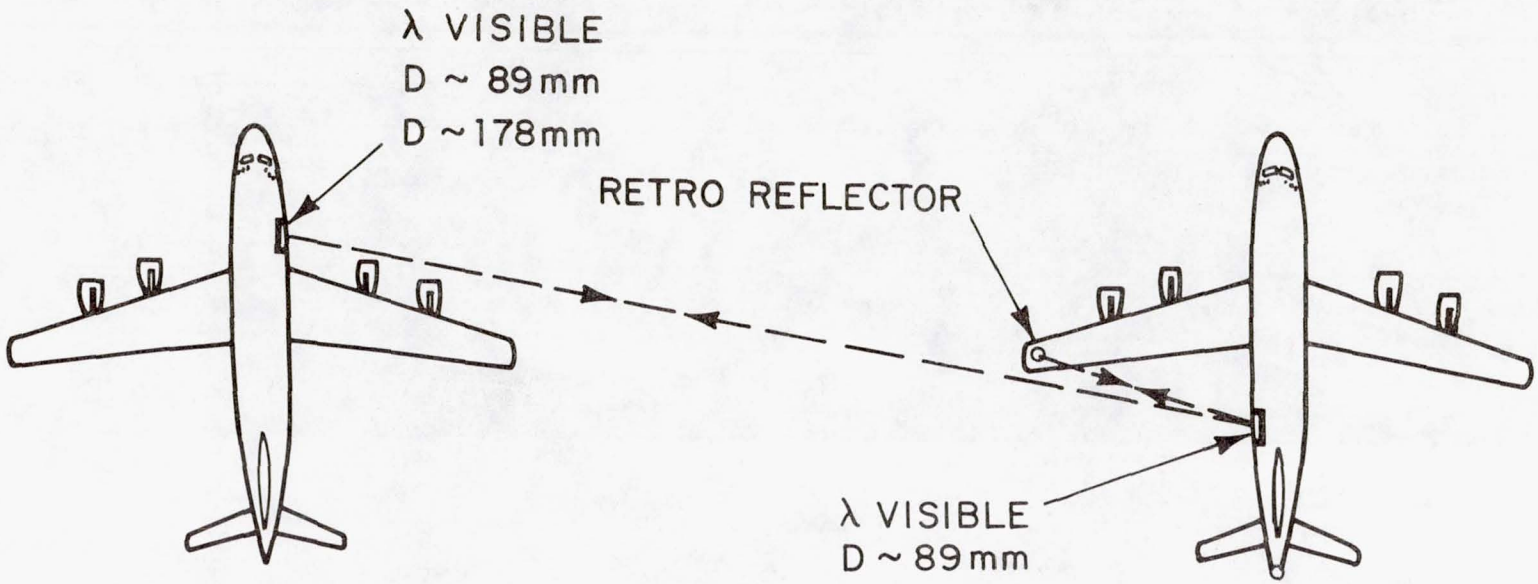

FIG. 8 AIRCRAFT PROPAGATION SCHEMATIC FOR PROPAGATION EXPERIMENT (KC-135 airplanes).

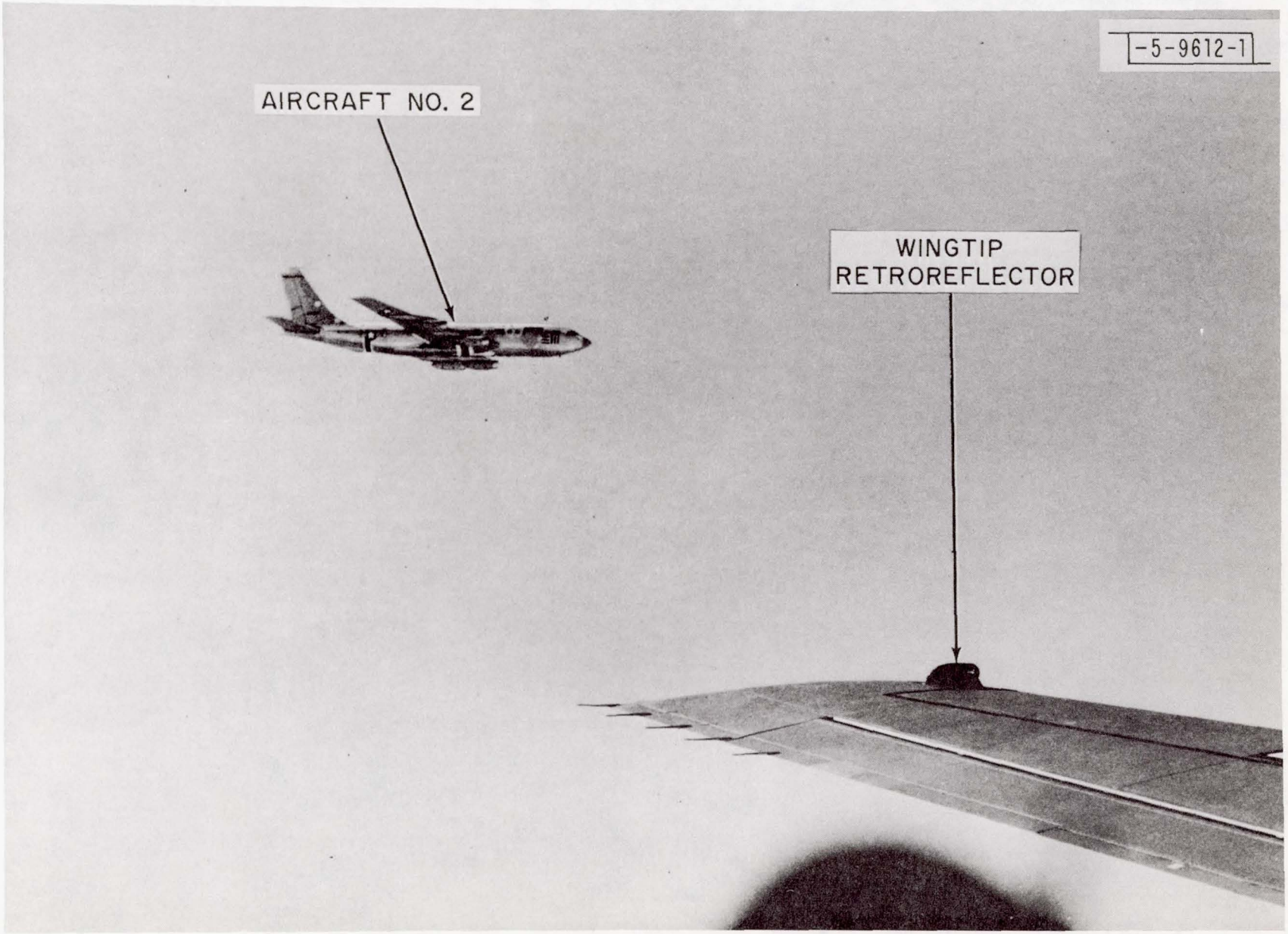

FIG. 9. WINGTIP RETROREFLECTOR ON A/C #1 (WITH A/C #2 IN BACKGROUND).

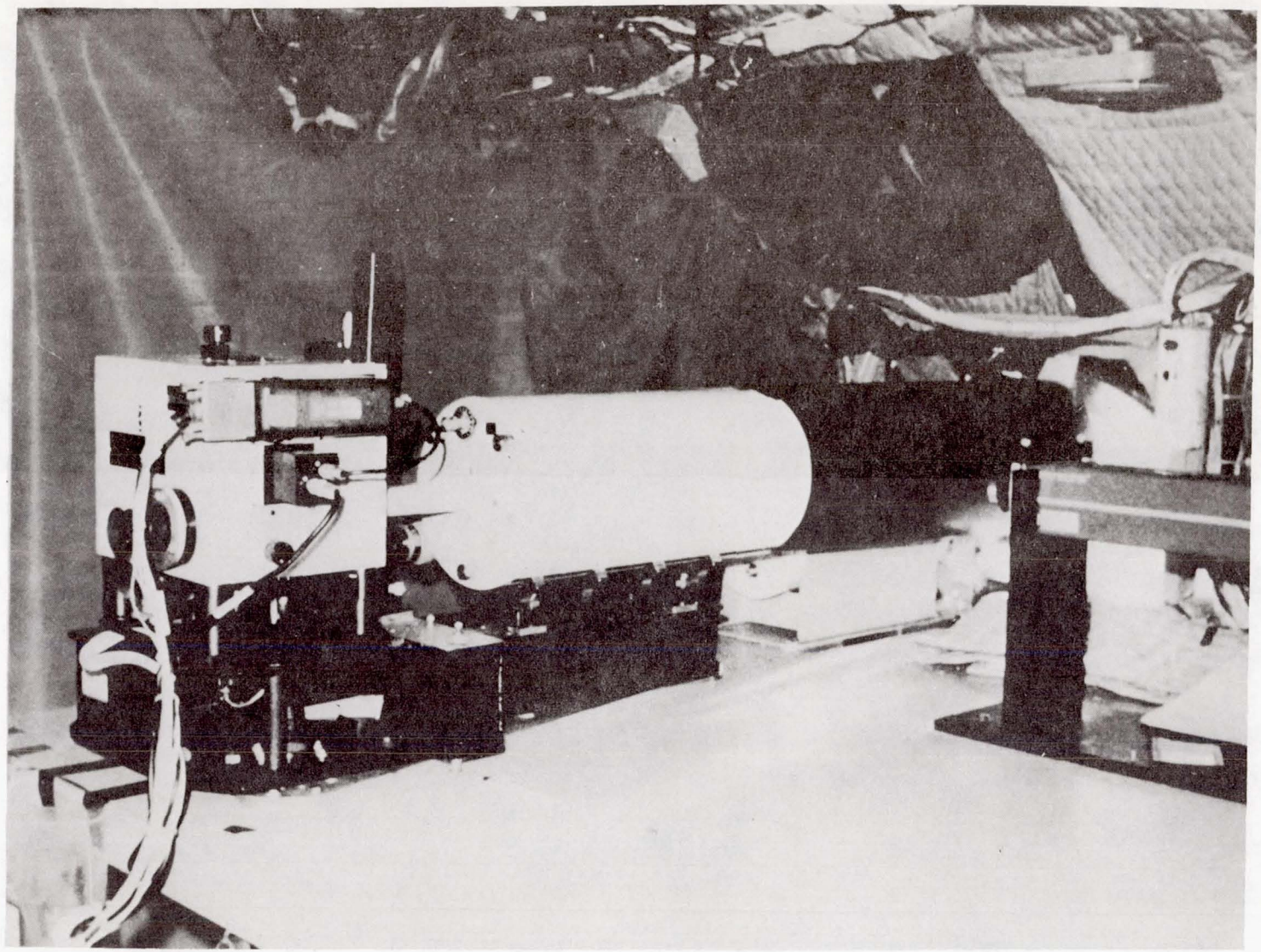

FIG. 10 FSI AND 178mm OPTICS ON A/C NO. 2 (propagation experiment).

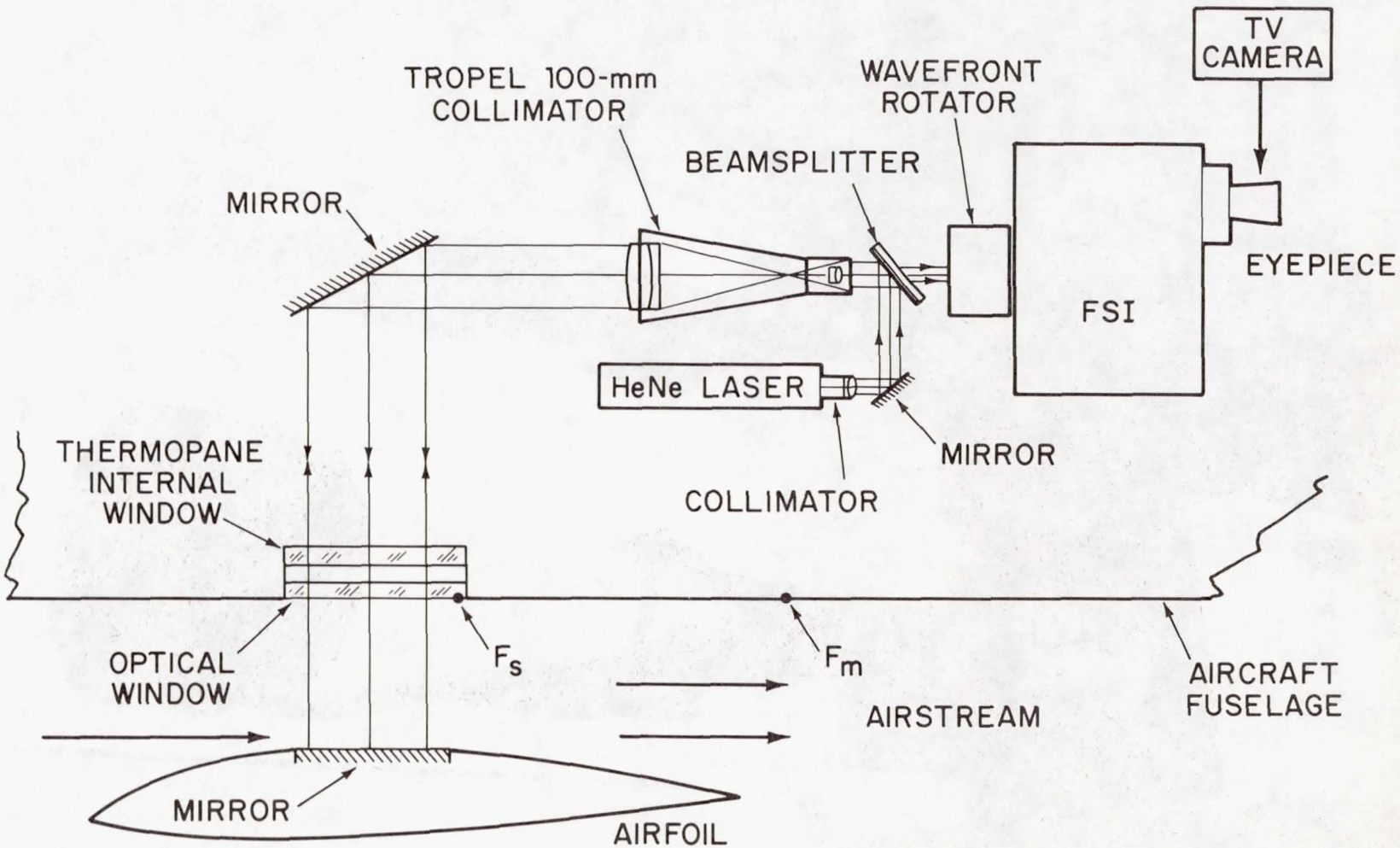

FIG. 11 OPTICAL SCHEMATIC KC-135 AIRFOIL EXPERIMENT.

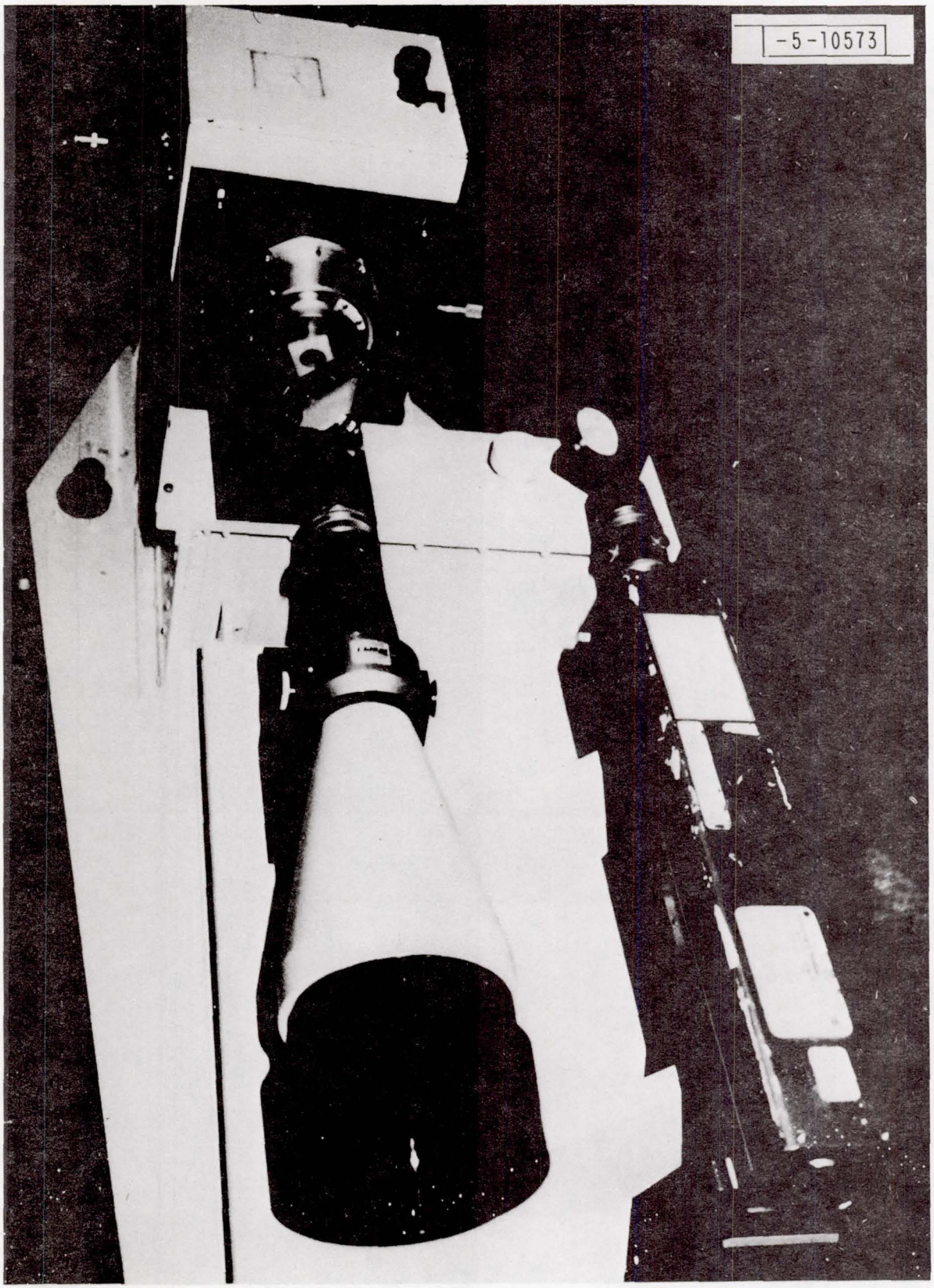

FIG. 12. FSI, 100-MM OPTICS, AND LASER SOURCE FOR KC-135 AIRFOIL EXPERIMENT.

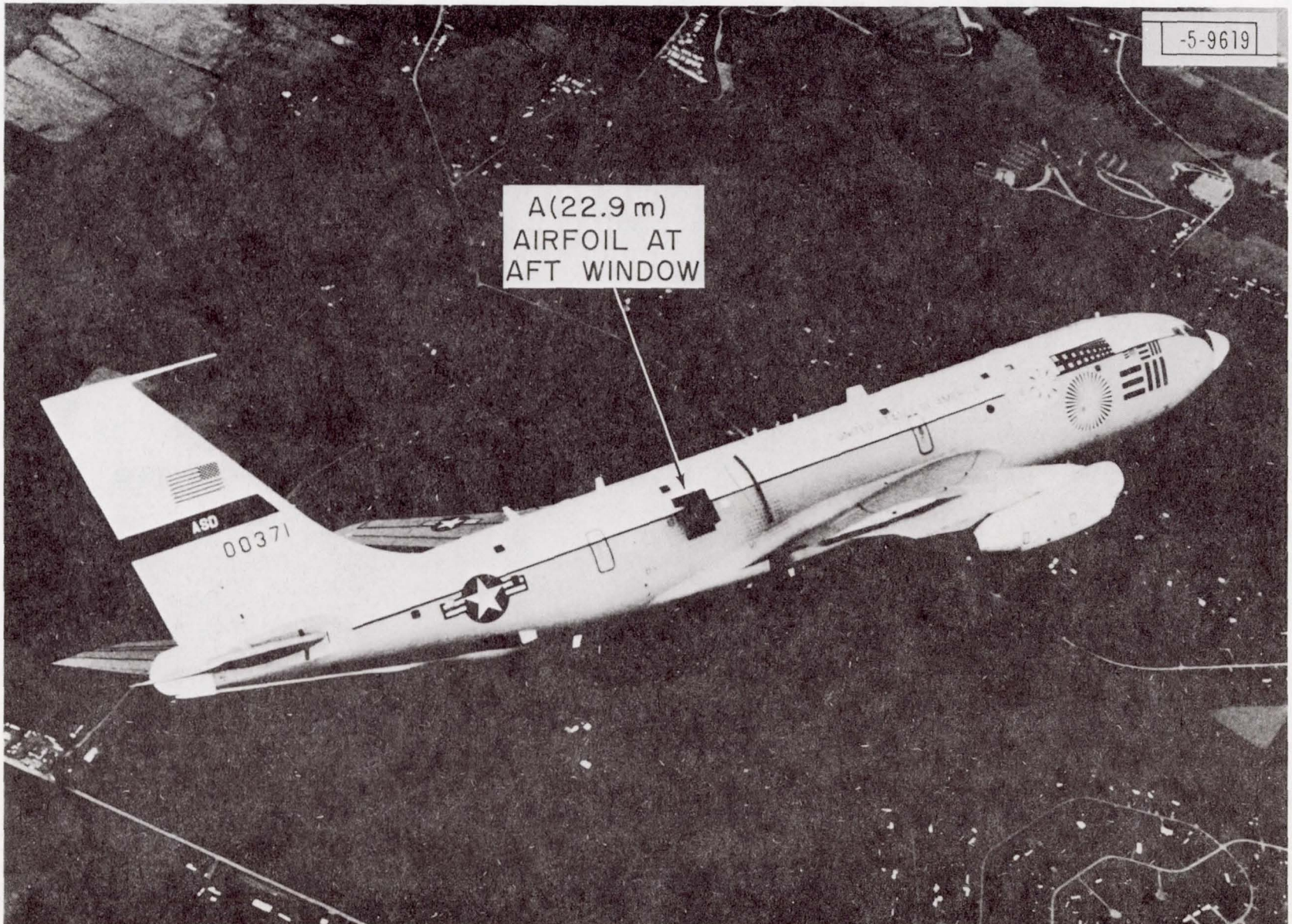

FIG. 13. AIRFOIL ON A/C #2 FOR KC-135 AIRFOIL EXPERIMENT.

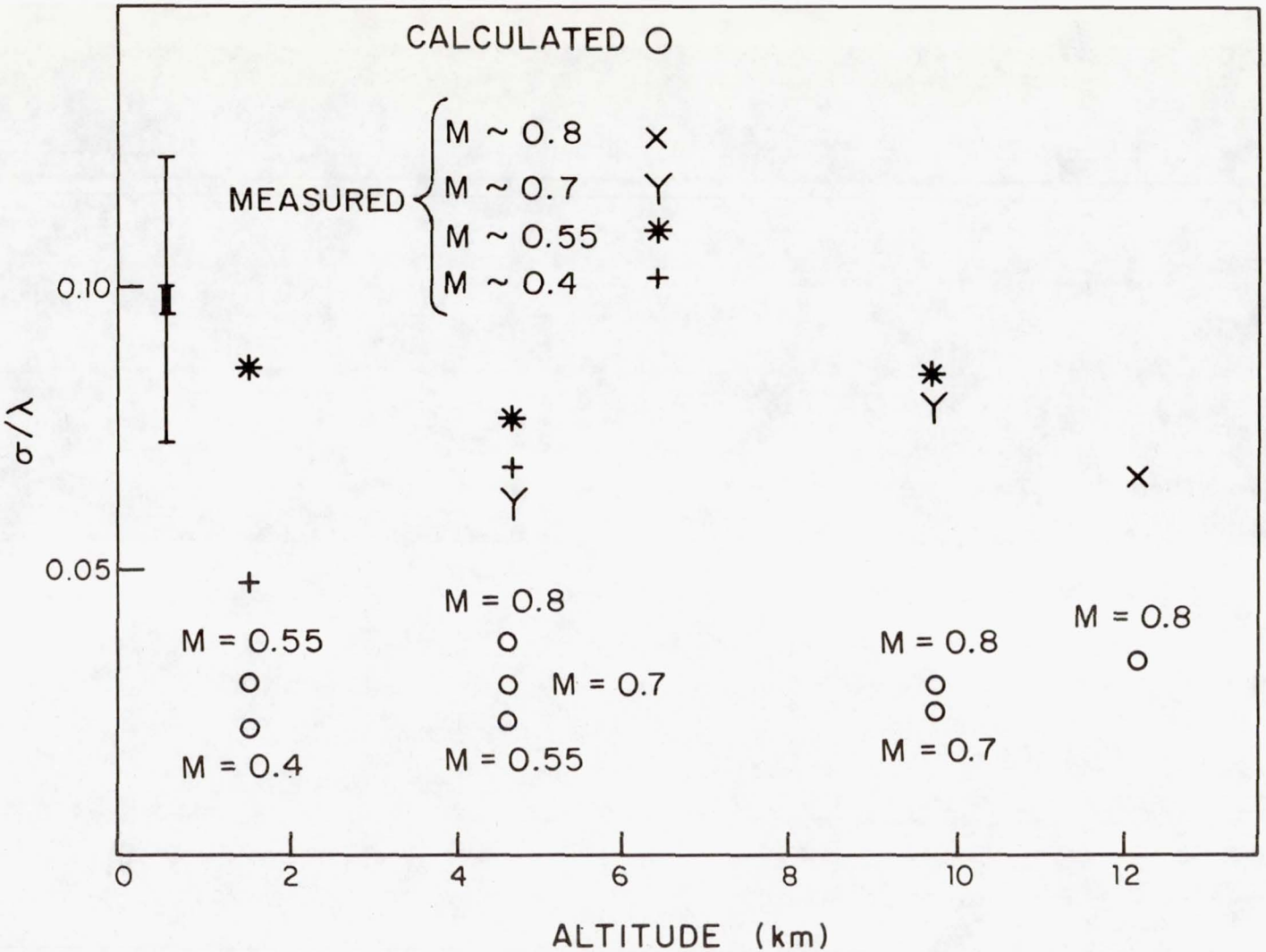

(a) LEAR JET.

FIG. 14 FLIGHT BOUNDARY LAYER σ DATA.

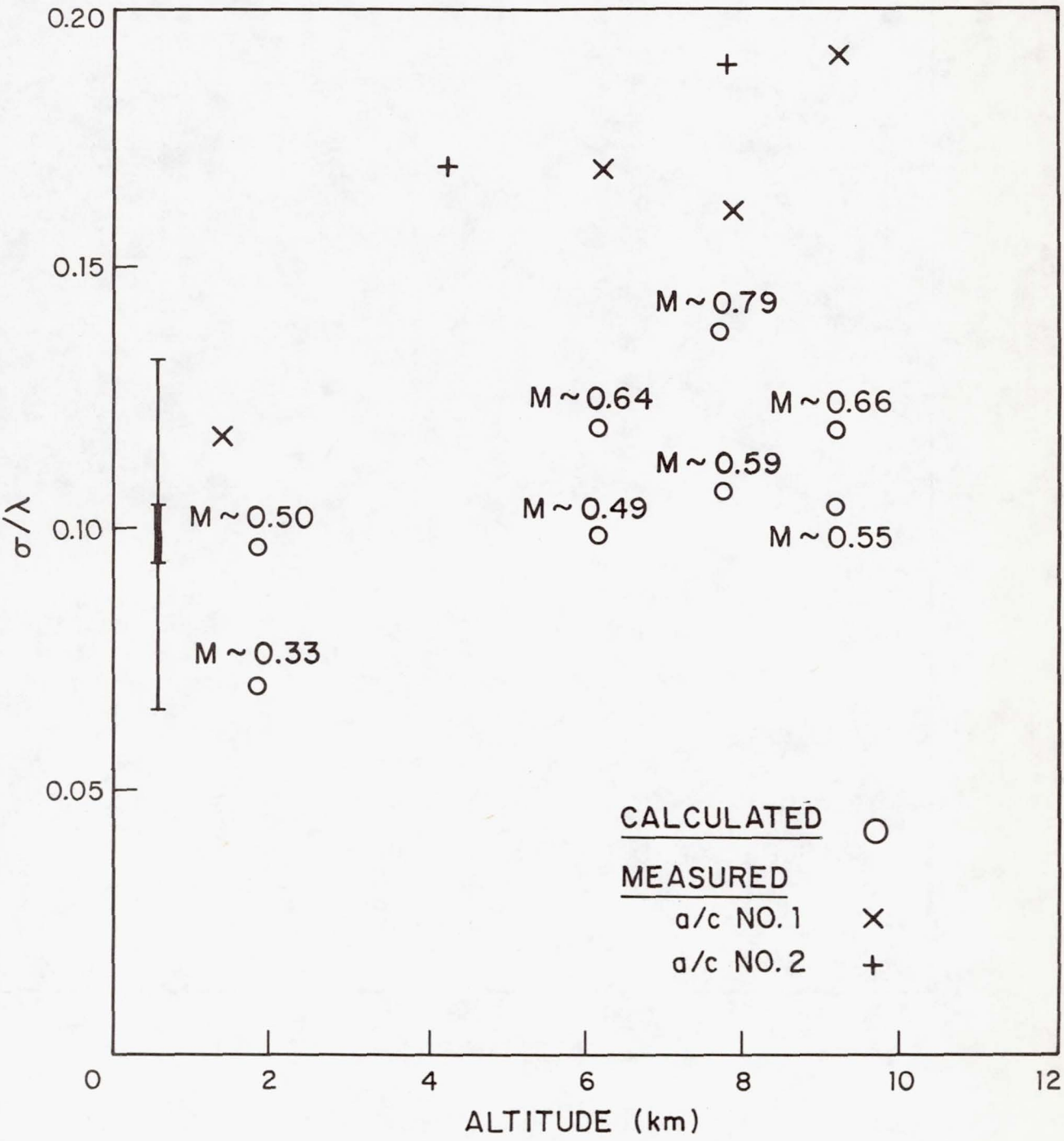

(b) KC-135 PROPAGATION EXPERIMENTS.

FIG. 14 FLIGHT BOUNDARY LAYER σ DATA.

18-5-9640-1A

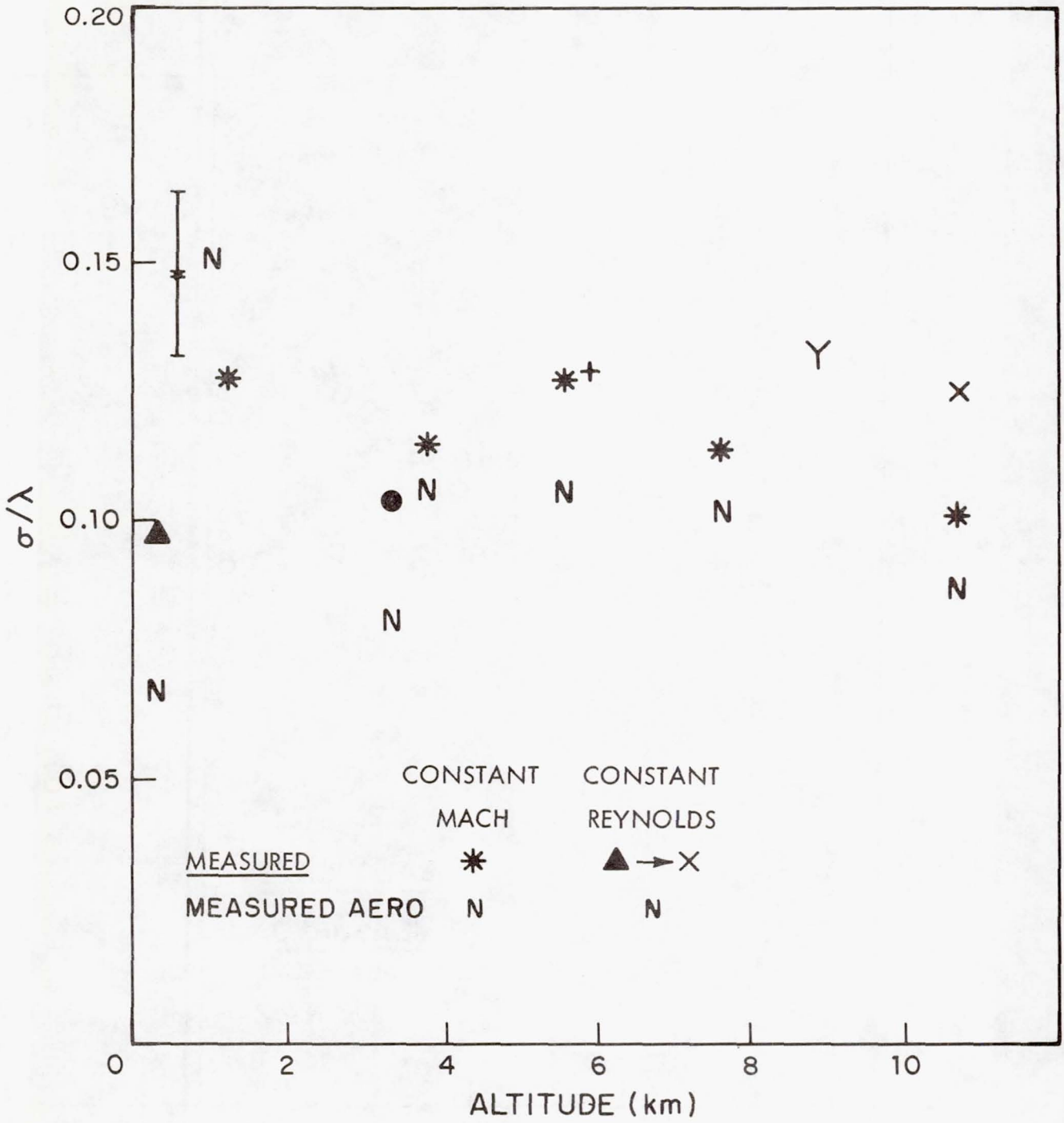

(c) KC-135 AIRFOIL EXPERIMENTS.

FIG. 14 FLIGHT BOUNDARY LAYER σ DATA.

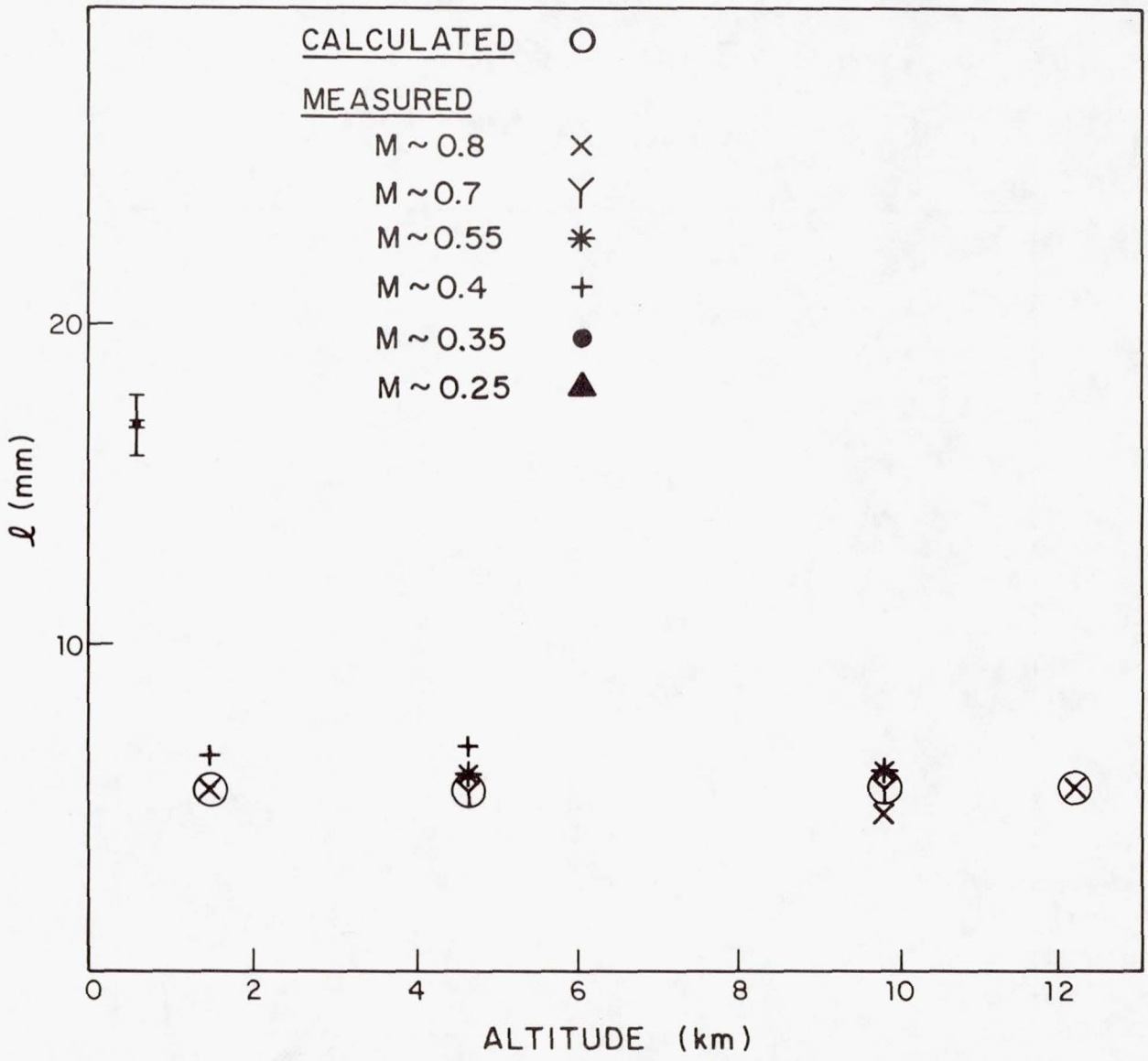

(a) LEAR JET.

FIG. 15. FLIGHT BOUNDARY LAYER & DATA.

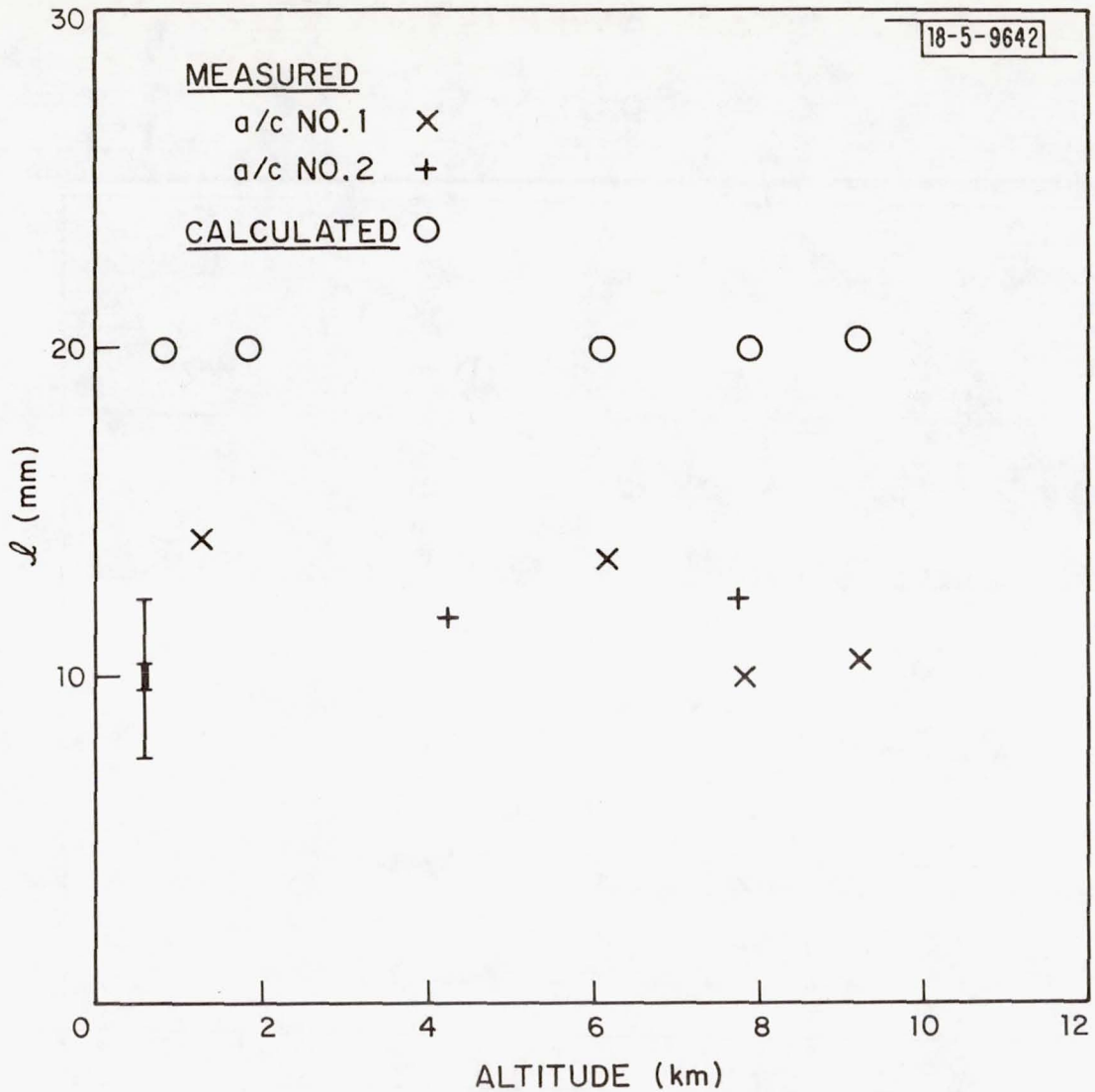

(b) KC-135 PROPAGATION EXPERIMENTS.

FIG. 15 FLIGHT BOUNDARY LAYER & DATA.

18-5-9643-1A

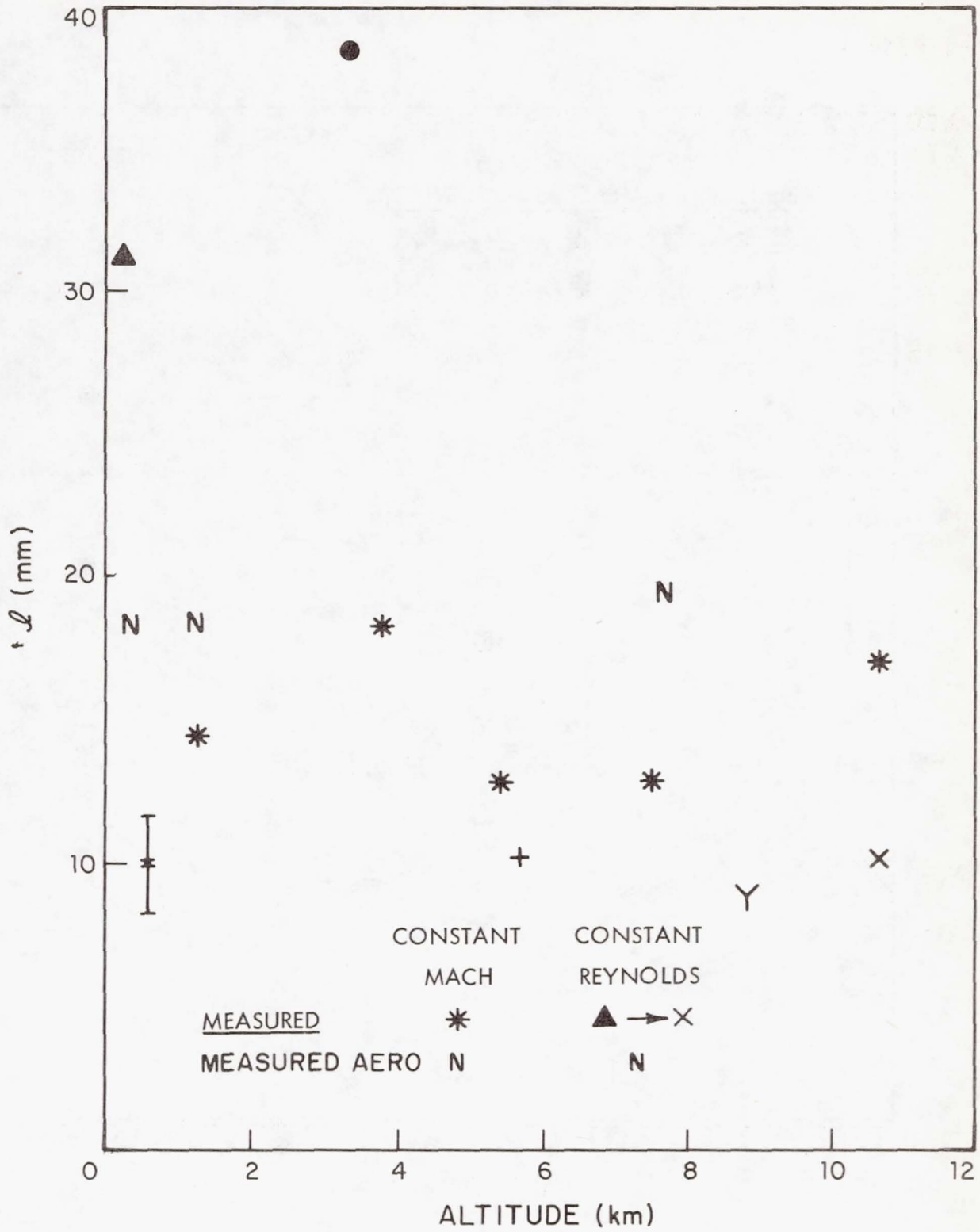

(c) KC-135 AIRFOIL EXPERIMENTS.

FIG. 15 FLIGHT BOUNDARY LAYER & DATA.

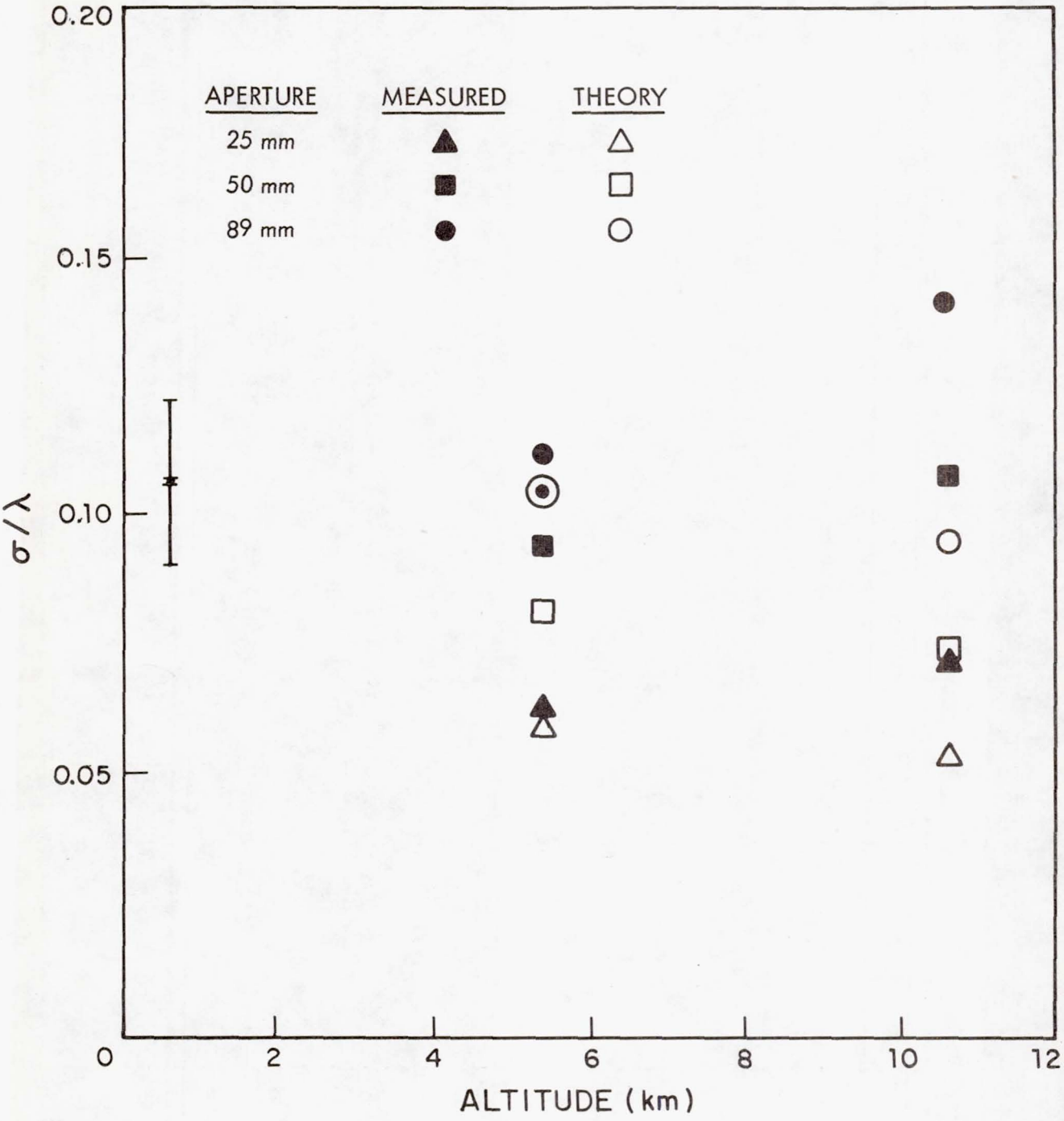

FIG. 16 σ APERTURE SCALING.

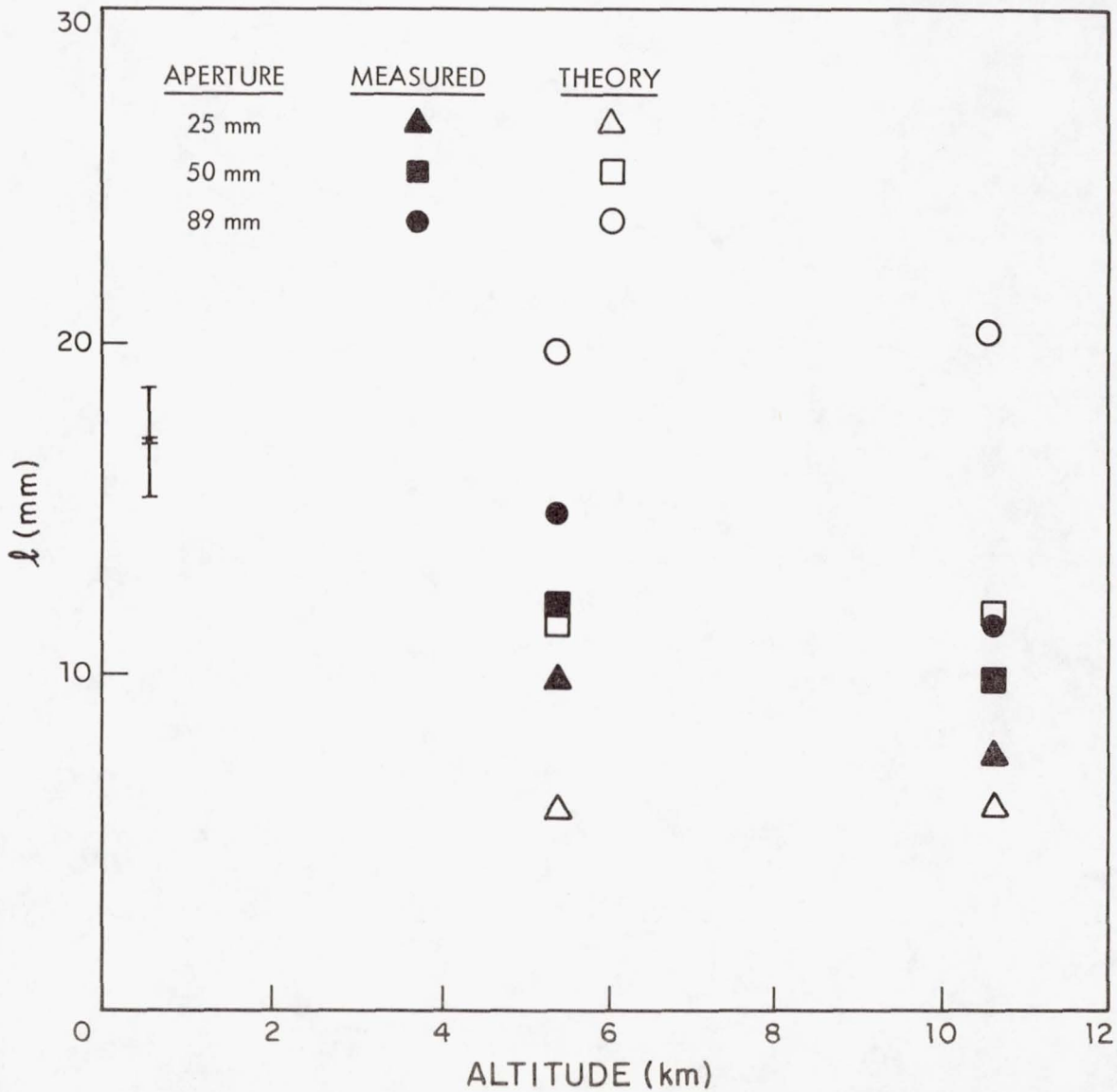

FIG. 17 APERTURE SCALING.

SUMMARY OF ALL CYCLE II.5 SHEAR AND BOUNDARY LAYER MEASUREMENTS - AERODYNAMICS

W.C. ROSE

Rose Engineering and Research, Inc.

Incline Village, NV 89450

D.A. JOHNSON

NASA - Ames Research Center

Moffett Field CA 94035

and

L. J. OTTEN, III, MAJOR, USAF

AFWL/LR-2

Kirtland AFB, NM 87117

SUMMARY OF ALL CYCLE II.5 SHEAR AND BOUNDARY LAYER MEASUREMENTS - AERODYNAMICS

W.C. Rose
Rose Engineering & Research, Inc.
Incline Village, NV 89450

D.A. Johnson
NASA-Ames Research Center
Moffett Field, CA 94035

and

L.J. Otten, III, Major USAF
AFWL/LR-2
Kirtland AFB, NM 87117

Abstract

The two measurement systems were used to measure mean velocity and velocity, mass flux and total temperature fluctuations in the turbulent boundary on the fuselage of a KC 135 aircraft. The boundary layer thickness ranged between about 20 and 30 cm for the range of flight Mach numbers from about 0.25 to 0.85 and Reynolds numbers between 3 and 6 $\times 10^6$/m. The adaptation of each system for use in airborne applications is discussed. The data obtained from each system are given and compared with each other and they indicate that the two systems represent viable ones for use in future airborne turbulence experiments.

Introduction

Ground testing and aerodynamic simulation techniques can reproduce flight conditions in only a few applications. The primary parameter that cannot be accurately simulated is Reynolds number. Therefore, the accurate determination of quantities that are known to be sensitive to the Reynolds number may require the instrumentation of the component or the entire aircraft for in-flight experimentation. Several difficulties arise in regard to flight testing, one being the measurement of turbulent flow-field quantities at high speeds. These turbulence quantities (such as streamwise and cross-stream fluctuation intensities, Reynolds shear stress, and spectra) are sensitive to the Reynolds number and are critical to the success of present computational-fluid-dynamics codes that use subgrid closure schemes. Thus, there is a clear need to measure turbulence at realistic Reynolds numbers.

In the last few years, technical advances in hot-wire anemometry and the development of the laser velocimeter have made the measurement of turbulence properties in compressible flows realizable (e.g., Johnson and Rose[1,2]). Wind tunnel experience has proven that hot-wire probes can be constructed to withstand a wind tunnel environment almost indefinitely. Also, the wire response for transonic flows is now sufficiently understood that quantitative measurements of turbulent flow properties can be made for this flow regime.[3] Both the laser velocimeter and hot-wire anemometer are proven techniques for use in high-speed wind tunnels; their potential contribution to flight testing should not be overlooked.[4]

Recently, these two techniques were used in a flight experiment to probe the viscous flow on an aircraft fuselage. This application to in-flight flow-field measurements is the subject of the present paper. The approaches taken to adapt the two techniques for flight measurements are discussed and the performance is evaluated. Problems unique to flight applications are also addressed. Examples of data taken are presented to indicate the overall success of the flight program. The following section briefly describes the experimental setup.

Experimental Apparatus

The flight experiment evolved from a joint program between Air Force Weapons Laboratory, Kirtland AFB, and NASA-Ames Research Center on the propagation of light through the turbulent boundary layers of aircraft. The desire to measure both local turbulence properties and optical distortion effects of the flow field dictated the design of the experiment.

To measure the light propagation properties of the boundary layer, a mirror was mounted away from the fuselage to return the transmitted beam to the airplane. Figure 1 shows the return mirror support system mounted aft and above the wing of an Air Force KC-135. The window for the light propagation studies and the two holders for the hot-wire probes are apparent. The airfoil-shaped upper and lower support struts for the return mirror housed part of the laser velocimeter optics. Windows for the laser velocimeter (not visible in the photograph) were located midchord of the two struts. The return mirror was approximately 1 m from the fuselage; the side support struts were separated from each other by about this same distance.

Two 5-μm tungsten wires (one to measure mass-flux fluctuations and the other to measure total-temperature fluctuations) were mounted on each of the two probe supports in Fig. 1. Mass-flux fluctuations were measured using DISA model 55M01 constant-temperature anemometer systems with high overheat ratio settings. Constant-current anemometer systems operating at very low overheats were used to measure the total temperature. To reduce the possibility of wire breakage during takeoff and landing the probes were turned backward to the flow during these periods.

The 5-μm sensors were spot-welded to nickel electrodes that had been epoxied into a ceramic body. The probe was about 2 cm in length and about 5 mm in diameter. These probe bodies held four electrodes, making two sensors with a length-to-diameter ratio of about 100. All sensors were

calibrated before the flights in the Ames 2- by 2-Foot Transonic Wind Tunnel. Although the wind tunnel cannot duplicate flight-length Reynolds numbers, it can duplicate the range of wire Reynolds numbers encountered in flight. Thus, the required individual calibration of wire sensors over the range of flow variables encountered in flight could be realized. The constant-current sensor and anemometer were calibrated by a no-flow oven test, followed by a wind-tunnel test to establish the variation of wire recovery factor with Mach number. The constant-temperature sensor and anemometer were calibrated in the wind-tunnel flow using a ratio of heated-temperature to recovery-temperature of 2.0. The remainder of the calibration procedure, described in detail by Rose and McDaid[4] has been used extensively in previous wind-tunnel tests.[2] The hot-wire anemometer data reduction procedures used were the same as those described by Johnson and Rose.[2] Finally, the two pair of wires could be positioned continuously at any distance from the fuselage surface up to about 35 cm by use of two independent lead screws and crank mechanisms. This allowed the determination of correlation length scales in the transverse direction by fixing the location of one probe and cross-correlating the outputs as the separation between the probes increased.

A laser velocimeter system for determining both the mean and unsteady streamwise velocity component was installed in the aircraft such that flow-field measurements could be made at essentially the same locations as the hot-wire probes. Figure 2 shows a schematic of the velocimeter setup. Because of the expected highly turbulent and/or separated flow produced by the test geometry (discussed below), a Bragg cell was used to ensure an adequate number of fringe crossings for all possible particle trajectories. The beam divider cube was cut so that two parallel beams (one shifted in frequency by 40 MHz) were transmitted to the lower airfoil strut. There, a lens and mirror focused and crossed the beams at the sensing volume in the center of the two airfoil struts. A leadscrew and crank system allowed a continuous positioning of the crossover at any distance from the fuselage up to about 35 cm. The off-axis optics used to collect the forward light scatter signals were housed in the upper airfoil strut. The mirror and lens of the collection optics could also be traversed by a leadscrew and crank system. The photodetector was mounted inside the aircraft cabin. The single particle signals were collected by a zero-crossing-counter-type signal processor. A multichannel analyzer was used to generate histograms of the incoming data, which were then processed by a Hewlett Packard 9830 calculator to produce mean and rms streamwise velocity values. Of course, the laser velocimeter is an absolute system in the sense that no calibrations in a known flow are required once the fringe spacing has been chosen. Details of the data-reduction procedures used in the present study are essentially the same as those described by Johnson and Rose.[2]

As mentioned above, test geometries that produced separated, highly turbulent flows were investigated in flight. Again, the test geometries were dictated by the desire to measure optical distortion effects due to various flow fields. The three distinct flows studied are shown schematically in Fig. 3. The first flow was the fuselage turbulent boundary layer as it arrived at the measurement station approximately 30 m aft of the aircraft nose. Note that for any given aircraft weight, flight Mach, and Reynolds numbers, the boundary layer that was surveyed has an unknown trajectory over the aircraft, and, thus, has an unknown pressure gradient history. The history of the pressure gradient has a significant effect on both the turbulence properties and mean-flow properties of a turbulent boundary layer, no matter what the local pressure gradient is at the measuring station. Therefore, the results, shown later, should be taken as unique measurements rather than measurements characteristic of a flat plate flow (zero pressure gradient). Furthermore, changes in aircraft weight and flight conditions may change the pressure gradient history, making universal correlation of the data with Mach and Reynolds numbers difficult if not impossible.

The second and third test geometries, also shown in Fig. 3, involve porous "fences" or vertical obstructions that are 14.5 cm high and have a 48% porosity. The height of the fences is about one-half the height of the undisturbed boundary layer. They are typical of those used to eliminate resonance conditions over open ports although no open port was used in the present study. The measuring station remained fixed and the fences were attached at two positions. One, denoted the near fence, was about 8 cm upstream of the measuring station, while the midfence was located about 80 cm upstream of the measuring station.

Results and Discussion

A total of 12 flights, each about 5 hr in duration, were made aboard the instrumented KC-135. In the last stage of the test, six additional flights were made with the mirror support system removed to check that it had not affected previous flow measurements. Indeed, sufficient flight time was available to appraise the suitability of the measurement techniques for flight applications. The test envelope covered Mach numbers from 0.25 to 0.85 and altitudes from 0.3 to 10.7 km. The low-altitude tests were conducted over the Gulf of Mexico.

The primary concern in using hot-wire anemometry in flight was wire breakage. However, in more than 100 hr of flight time, wire breakage occurred only once, when ice crystals were encountered below a cirrus layer. Although the ice crystals were not visually apparent, particle arrival rates registered by the laser velocimeter reached 50,000 sec^{-1} before the wires broke. In subsequent flights, flying immediately below cirrus clouds was avoided. Unavoidably, many low-lying clouds were encountered but fortunately did not cause wire breakage. Apparently, the wires were strong enough to shear the water droplets.

The two main concerns of the laser velocimeter were the availability of atmospheric particles for light scattering and the ability to maintain optical alignment. For the test envelope, particle arrival rates ranged from several thousand per second for low altitudes of 0.3 to 1.2 km (1000 to 4000 ft) over the Gulf of Mexico to as low as 5 sec^{-1} for some of the high-altitude flights. However, the rates were sufficiently high under all conditions to obtain mean velocities and turbulence intensities. Regions of high-particle density were not sought out; in fact, they were

avoided because of the hot-wire probes. Optical misalignment in flight did not occur. This was especially fortunate, since realignment of the system would have been impossible during flight.

The laser velocimeter was used to obtain mean velocity and turbulence intensity profiles. The hot-wire instrumentation provided mass-flux and total-temperature fluctuation profiles as well as streamwise and cross-stream length scales across the boundary layer. Samples of the data are presented in Figs. 4, 5, 6, and 7. Figure 4 shows the mean and unsteady profiles for each of the three test geometries. The hot-wire data were reduced to values of u' from mass-flux fluctuations using the techniques outlined by Horstman and Rose.[3] The velocimeter values of u are consistent with the expected flows. No reverse mean velocities were observed in the flows downstream of the fences. While the boundary-layer profile (Fig. 4a) is very full, recall that this flow came from an unknown pressure gradient history, including the acceleration over the wing root section. Also evident in Fig. 4a are the relatively low values of $\langle u' \rangle / \bar{u}$ (even considering the high Reynolds number $Re_x \approx 2 \times 10^8$). It is not possible to determine if these lower values are the result of the very low free-stream turbulence characteristic of the atmosphere or are simply a pressure gradient history effect. The general agreement between the laser velocimeter and hot-wire anemometer results for the rms of $u'(\langle u' \rangle)$ are consistent with comparisons made between the two systems in wind tunnel applications.[3] The comparisons for the fence configurations (Figs. 4b, 4c) are nominally acceptable, considering that the near fence has fluctuations of $\langle u' \rangle / \bar{u}$ in excess of 40% where the hot-wire anemometer cannot yield any more than a qualitative indication of turbulence. However, for the mid-fence, values of $\langle u' \rangle / \bar{u}$ of up to 20% appear to be accurately determined by the hot-wire.

Although the nonintrusive feature of the laser velocimeter appears ideally suited to airborne measurements, the present limitations on signal processing and valid signal occurrence rates make some fluid mechanical functions difficult to obtain. Two such functions are the correlation lengths and spectra, both of which were required in the present study. The continuous analog signals from the hot-wire anemometer, analog correlators, and spectrum analyzers make the determination of these functions straightforward. Figure 5 presents the correlation function $\overline{u_1' u_2'} / \overline{u_1'^2}$ as a function of probe separation in the transverse direction. An exponential curve appeared to best fit all the data. The curve fits can be integrated easily to yield the integral scale in the cross-stream direction L_z. A value of L_z may be determined at each point in the boundary layer to produce a plot such as shown in Fig. 6, which shows L_z variations throughout the layer. The streamwise integral scales L_x shown in Fig. 6 were determined from time autocorrelations and an assumed convection velocity, $u_c \approx 0.8\bar{u}$. Values of L_z/δ and L_x/δ are about 0.1 and 0.3, respectively, consistent with wind-tunnel boundary layers.

Finally, a spectrum obtained in the boundary layer is shown in Fig. 7. Most of the turbulence energy is below 3 kHz and indicates a near Kolmogorov energy decay as would be expected.

Concluding Remarks

The overall in-flight performance of the laser velocimeter and hot-wire anemometer was remarkably good. After wire breakage and other assorted equipment failures on the first flight, the remaining flights were relatively uneventful. Although the rate of valid data signals at high altitudes was low, enough particles were present to make meaningful velocimeter measurements in the aircraft boundary layer. The hot-wire anemometer also appears usable for in-flight aerodynamic research.

References

[1]Johnson, D. A. and Rose, W. C., "Laser Velocimeter and Hot-Wire Anemometer Comparison in a Supersonic Boundary Layer," *AIAA Journal*, Vol. 13, April 1975, pp. 512-515.

[2]Johnson, D. A. and Rose, W. C., "Turbulence Measurements in a Transonic Boundary Layer and Free-Shear Flow Using Laser Velocimetry and Hot-Wire Anemometry Techniques," AIAA Paper 76-399, San Diego, Calif., July 1976.

[3]Horstman, C. C. and Rose, W. C., "Hot-Wire Anemometry in Transonic Flow," *AIAA Journal*, Vol. 15, March 1977, pp. 395-401.

[4]Rose, W. C. and McDaid, E., "Turbulence Measurement in Transonic Flow," *AIAA Journal*, Vol. 15, Sept. 1977, pp. 1368-1370.

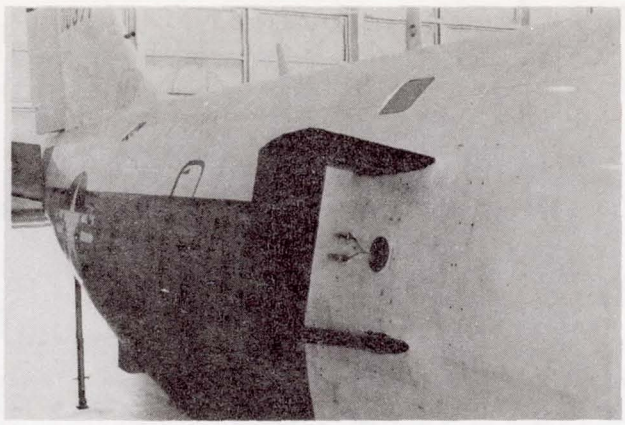

Fig. 1 Photograph of aero-optics experimental installation on aircraft.

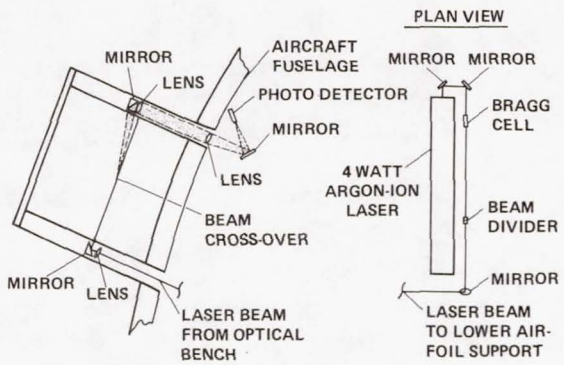

Fig. 2 Schematic of laser velocimeter.

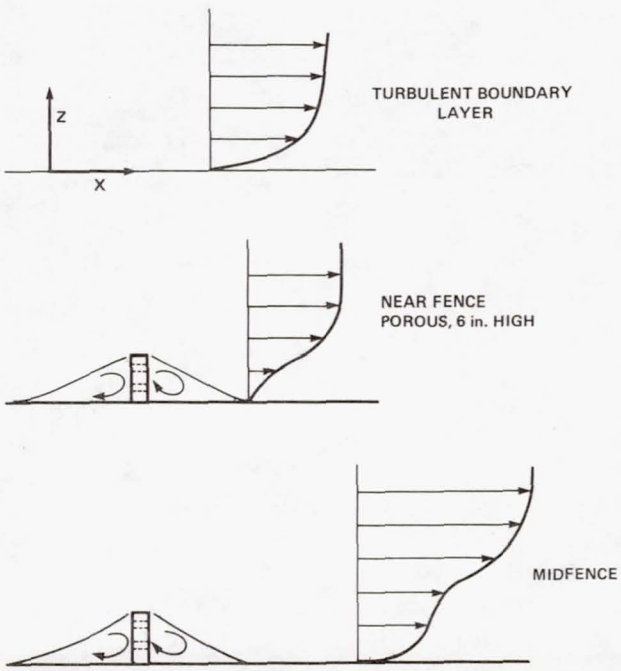

Fig. 3 Sketch of flow conditions studied.

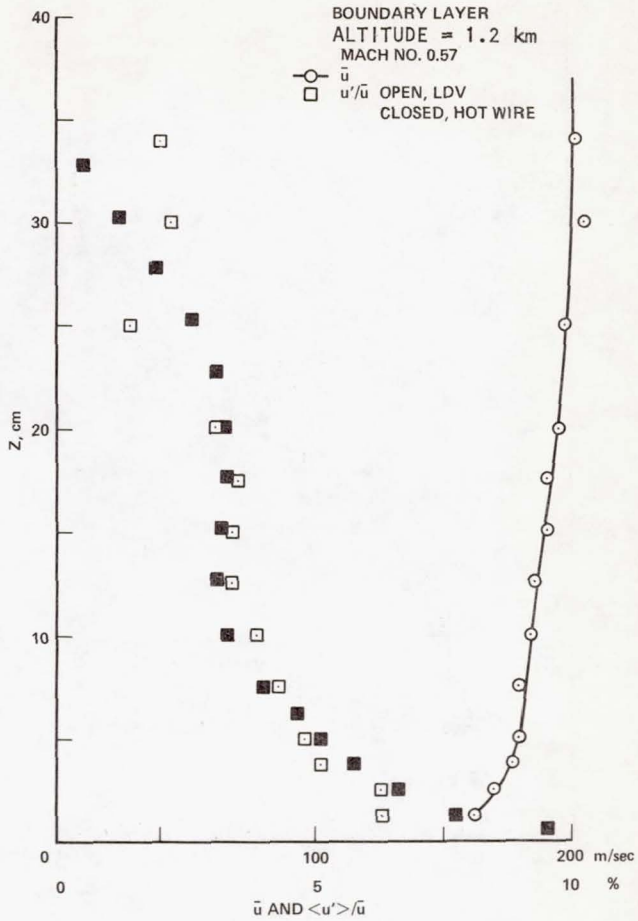

a) Boundary layer.

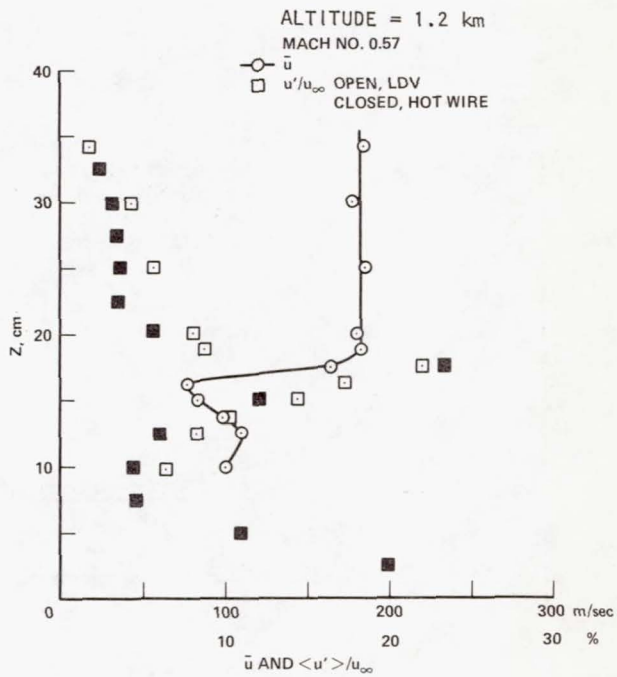

b) Near fence.

Fig. 4 Measured mean and fluctuating properties typical of those obtained.

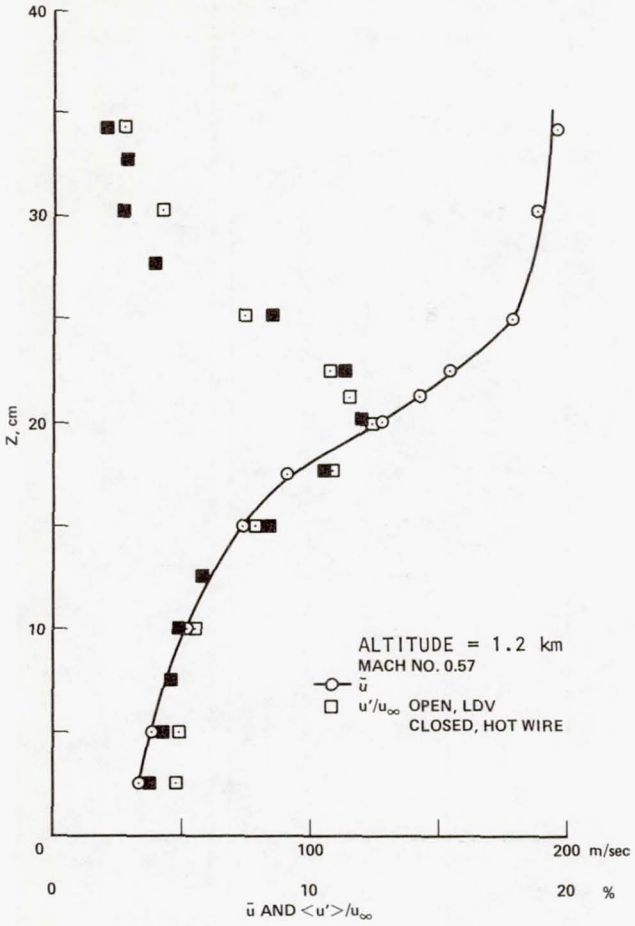

c) Midfence.

Fig. 4 Concluded.

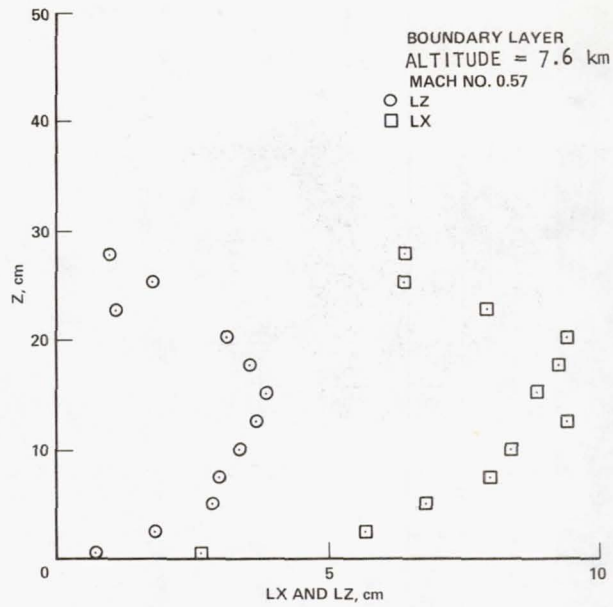

Fig. 6 Typical integral correlation lengths.

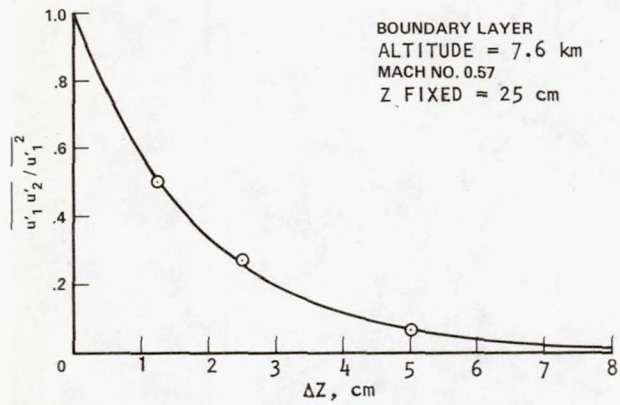

Fig. 5 Typical correlation data and exponential curve fit.

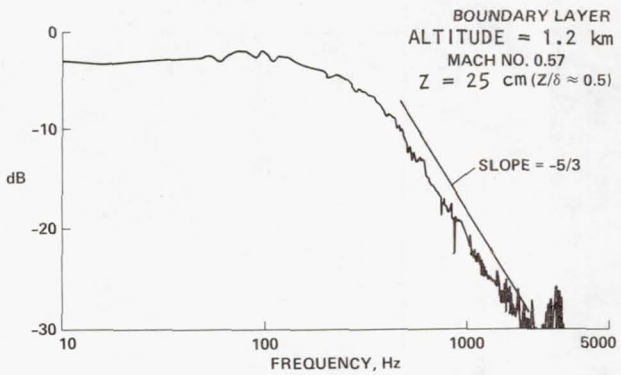

Fig. 7 Typical turbulence spectrum.

KC-135 AERO-OPTICAL TURBULENT BOUNDARY LAYER/SHEAR LAYER MEASUREMENTS

ABSTRACT

Recent Air Force Weapons Laboratory (AFWL) airborne laser propagation experiments have examined aero-optical effects associated with propagating a laser beam through aircraft turbulent boundary layers and shear layers. This series sought to compare observed laser optical performance levels with those inferred from aerodynamic measurements of unsteady densities and correlation lengths within these random flows. Optical instrumentation included a fast shearing interferometer (FSI). A 9cm diameter collimated helium neon laser beam made a double pass through the aircraft random flow via an airfoil mirror located one meter from the fuselage. Typical aircraft turbulent boundary layer thicknesses measured 0.3 meters. Averaging many FSI generated Modulation Transfer Functions (MTFs) and Fourier transforming this average yields the expected far-field intensity degradation associated with an aircraft-mounted laser system. Aerodynamic instrumentation included fine wire probes to measure unsteady temperature and mass flux. A laser doppler velocimeter measured unsteady velocity within the flows. An analysis of these data yielded point measurements of unsteady density and correlation length. Integration of these aerodynamic parameters through the random flow region in turn yields predictions of optical performance via the Gladstone-Dale law. Thirteen flights were flown at altitudes ranging from 0.3 to 11.3 kilometers while Mach numbers varied from 0.25 to 0.85. In addition to fundamental boundary layers, two identical fence configurations were examined located 8 cm and 80 cm upstream of the optical axis. An array of

thermocouples was attached to the inside skin of the aircraft to examine heat transport to the boundary layer. Correlations between the turbulent boundary layer (TBL) aerodynamically-inferred Strehl ratio I/I_0 and its MTF optical counterpart (correlated to large aperture) were very good. Single pass phase variances varied from 0.08 to 0.18 waves (λ= 0.63μ) for aircraft dynamic pressures ranging from 0.04 to 0.19 standard atmospheres. Measured TBL correlation lengths varied from 1.0 to 3.5cm for the 30cm thick disturbances. The correlation functions themselves appear to have an exponential character. Corresponding unsteady densities ranged up to 0.5 percent. The aircraft skin acts like an adiabatic wall. A strong shear layer forms at the top edge of aerodynamic fences. Measured correlation lengths are generally smaller (1.0 to 1.5cm) than for TBLs though the strength of the disturbance is significantly greater (0.5 to 3 percent). The majority of the optical path degradation is produced within this thin shear layer. Measured phase variances for the fences varied from 0.08 to 0.26 waves (λ = 0.63μ). Degradation is generally independent of fence location over the range of experimental parameters. The existing data base allows scaling these data with wavelength and aperture as well as aircraft parameters such as boundary layer thickness and dynamic pressure. These results suggest that as shorter wavelength laser weapon systems evolve ($\lambda \lesssim 2\mu$), aircraft random flow fields will contribute significantly to the system error budget. Near term adaptive optics is unable to cope with these flows due to their small spatial and large bandwidth requirements. Several passive aerodynamic techniques include using windows with laser turrets to preclude shear layer formation and moving the turret as far forward as possible to minimize boundary layer thickness. Active aerodynamic techniques cry out for creativity, and include suctioning or diverting TBLs and shear layers.

CYCLE II.5

AIRCRAFT AERO-OPTICAL TURBULENT BOUNDARY-LAYER/SHEAR-LAYER MEASUREMENTS

K. Gilbert

Introduction

The Air Force Weapons Laboratory (AFWL) has completed a series of airborne laser propagation through aircraft turbulent boundary layers and shear layers. These airborne tests, in a sense, are the culmination of a 3-year program at AFWL to investigate aircraft viscous airflow effects. The primary objective was to make two independent assessments of optical performance through these random flows. The first is an integrated path optical measurement using a Fast Shearing Interferometer (FSI). The second technique involves inferring point measurements of unsteady densities and correlation lengths within the flows. This in turn leads to optical degradation predictions via the Gladstone-Dale law. By integrating along these points, one then obtains an independent prediction of net optical degradation. The purpose of this paper is to summarize these data vis-a-vis future airborne laser weapon systems.

Optical instrumentation included a Fast Shearing Interferometer (FSI) developed by Lincoln Laboratory, together with a helium-neon laser source. The 9-cm collimated laser beam made a double pass through the aircraft boundary layer via reflection from an airfoil mirror located about 1 meter from the fuselage. Averaging a large number of Modulation Transfer Functions (MTFs) for a particular aircraft condition and Fourier transforming this average yields the expected far-field intensity degradation for an aircraft-mounted laser system.

Aerodynamic measurements within the boundary layer included fine wire probes to measure temperature and mass flux fluctuations. A laser Doppler velocimeter employed a 5-watt argon-ion laser to measure unsteady velocity. This, in turn, leads to optical degradation predictions via the Gladstone-Dale law. The aerodynamic equipment was developed largely by NASA Ames. In addition, an array of thermocouples was attached to the skin of the aircraft to measure heat transfer between the cabin and the external flow. This is a parameter critical to the understanding of the source of density fluctuations within the aircraft boundary layer.

The 13-flight measurement program examined fundamental aero-optical properties of fuselage turbulent boundary layers and shear layers (the latter formed via a fence sans cavity arrangement.) The experimental setup and instrumentation employed were analogous to previous wind tunnel tests and are shown in Figure 1. Altitudes ranged from 0.3 km to 11.3 km while Mach numbers varied from 0.25 to 0.85. Two fences, located in two positions relative to the optical axis, were examined.

The hot-wire anemometer and laser Doppler velocimeter probes could be moved continuously through the aircraft random flow regions and into the free stream. By making certain assumptions, including the neglect of total temperature and pressure fluctuations in the flow, the fluid unsteady density (ρ') and its correlation length in the propagation direction (ℓ_z) could be inferred at a series of points from the fuselage skin out into the free stream. Integrating along this path, one can obtain an estimate of the Strehl ratio I/I_o from the relation (ref. 1)

$$\frac{I}{I_o} = e^{-\sigma^2 K^2} \tag{1}$$

where

$$K = \frac{2\pi}{\lambda} \tag{2}$$

$$\sigma^2 = \sqrt{\pi}\ \beta^2 \int_0^L \langle \rho' \rangle^2\ \ell_z\ dz \tag{3}$$

β = Gladstone-Dale constant

L = Thickness of random flow region

Note the expression for the $_{rms}$ phase variance in equation 1 assumes a Gaussian correlation function. However, the data were found to be more closely fit by an exponential correlation function. In this case, a multiplicative factor of two replaces π in the above expression for σ. The assumption of an exponential correlation function will be assumed herein. A large aperture is an implicit assumption in equation 1 ($D >> \ell_z$). Details of these aero measurements appear elsewhere (ref. 2).

A direct and independent estimate of this Strehl ratio I/I_o is afforded by the integrated path double pass MTF measurement. By averaging approximately 250 of this tilt-insensitive MTFs and then Fourier transforming this average, a prediction of far-field degradation is obtained. However, to provide a direct comparison with the aero prediction (equation 1), a correction for the experimental noninfinite aperture MTF (i.e., $D \not\gg \ell_z$) must be applied. This follows by taking the general expression for tilt-insensitive MTF (ref. 3).

$$\tau\left(s, \frac{D}{\ell_z}\right) = M_a\ e^{-\sigma^2}\left[1 - e^{-\left(Ds/2\ell_z\right)^2}\right] \tag{4}$$

where

M_a = MTF of optics

σ^2 = rms phase variance

D = telescope aperture diameter

s - shear frequency, $0 \leq s \leq 2$

and integrating under τ for several values of σ and D/ℓ_z. A Strehl family of curves (Figure 2) is obtained. From the measured value of ℓ_z, one can then obtain an infinite aperture Strehl value. Then the average value of ℓ_z from the aerodynamic measurements, together with the empirical value of I/I_0, yields an estimate of the infinite aperture Strehl value. We now turn to a discussion of the aero-optical data.

Turbulent Boundary Layer Data

Figure 3 shows a sampling of unsteady density profiles following from hot-wire anemometer and laser Doppler velocimeter turbulent boundary layer measurements. Figure 4 shows the corresponding correlation lengths measured in the direction of propagation.

A summary of this turbulent boundary layer data appears in Table 1. Columns 1 through 3 show the aircraft parameters of altitude, Mach number, and dynamic pressure, respectively. Column 4 lists the average correlation lengths in the propagation direction, while column 5 depicts the approximate boundary layer thicknesses. The maximum unsteady density is shown in column 6, with ρ_∞ being the free stream value of density. The measured (MTF) integrated path Strehl ratio appears in column 7, here corrected to represent a single pass through the boundary layer. Column 8 lists the extrapolated optical Strehl for an infinite aperture ($D >> \ell_z$), using Figure 2. The adjacent column 9 shows the corresponding Strehl number predicted from the unsteady density and correlation length profiles, using equation 1. In columns 7 and 9 the errors shown are rms values associated with the several

aerodynamic or optical measurements at that test point. The final column represents the rms phase variance in units of HeNe (λ 0.63 μm) wavelength following from the aerodynamic Strehl prediction, $(I/I_o)_A$. A correlation plot of the aerodynamically and optically inferred values of I/I_o appears in Figure 5.

Table 1
BOUNDARY LAYER DATA

A(km)	M	q	$\overline{\ell}_z$(cm)	L(cm)	$\frac{\rho' \text{ max}}{\rho_\infty}$	$(I/I_o)_{OPT}$	$(I/I_o)_{\infty \text{ OPT}}$	$(I/I_o)_A$	$\sigma(\lambda)$
0.3	0.25	0.04	1.1	25	0.13	0.80±0.11	0.73	0.77	0.081
3.3	0.35	0.06	1.8	29	0.22	0.85±0.04	0.78	0.69	0.097
10.7	0.57	0.07	3.3	32	0.47	0.75±0.06	0.50	0.64±0.01	0.106
7.6	0.57	0.10	2.6	30	0.42	0.65±0.10	0.44	0.61±0.02	0.112
5.5	0.57	0.12	2.6	32	0.46	0.57±0.09	0.32	0.54±0.10	0.125
3.8	0.57	0.15	1.9	34	0.41	0.63±0.10	0.46	0.54±0.01	0.125
1.2	0.57	0.19	3.4	33	0.49	0.62±0.10	0.30	0.27	0.182

Shear Layer Data

Two fences, each mounted flush with the aircraft fuselage, were examined in this test series. Both were 14.5 cm in height and 48 percent porosity. The near fence (F_s) was mounted 8 cm upstream of the optical axis, while its counterpart (F_m) was located 80 cm upstream. The fences had hole diameters of 0.7 mm. Each fence had a smooth top edge.

Figure 6 shows unsteady density profiles for two cases representative of the near fence (F_s) and middle fence (F_m) data base. Again the z = 0 intercept corresponds with the aircraft fuselage. Notice the shear layer

thickness for the near fence (F_s) is of the order of a few centimeters, while that for (F_m) is approximately 25 cm. Average density correlation lengths in the z-direction ($\overline{\ell}_z$) lengths range from a sizable fraction of the F_s shear thickness to about 1/20th of the F_m shear layer breadth. These are shown in Figure 7. In general, the average correlation lengths are considerably smaller than those for corresponding boundary layer conditions, while the unsteady density strength is somewhat greater.

Table 2 is a synopsis of the fence data. The columns here are defined as in Table 1. Again, the optical MTF infinite aperture Strehl number (column 9) is obtained using Figure 2 and the measured value of $\overline{\ell}_z$. Errors

Table 2
SUMMARY OF FENCE DATA

A(km)	q	M	L(cm)	$\overline{\ell}_z$	$\frac{\rho'max}{\rho_\infty}$	$(I/I_o)_{OPT}$	$(I/I_o)_{\infty OPT}$	$(I/I_o)_A$	$\sigma(\lambda)$
Configuration F_s									
0.30	0.04	0.25	30	1.1	0.4	0.77	0.69	0.73	0.089
11.3	0.06	0.57	34	2.1	1.2	0.71	0.55	0.70	0.095
7.6	0.10	0.57	32	1.3	1.3	0.64	0.50	0.49	0.134
5.5	0.12	0.57	34	1.4	1.0	0.57	0.42	0.41	0.148
1.2	0.19	0.57	33	0.9	2.6	0.48	0.33	0.07	0.260
Configuration F_m									
0.30	0.04	0.25	35	0.9	0.2	0.84	0.80	0.76	0.083
10.7	0.06	0.57	35	1.3	0.8	0.72	0.59	0.70	0.095
7.6	0.10	0.57	35	1.2	0.8	0.66	0.54	0.61	0.112
5.5	0.12	0.57	35	1.2	0.9	0.64	0.51	0.46	0.140
1.2	0.19	0.57	35	0.9	1.0	0.59	0.36	0.26	0.185

are not specified in this table. However, both the aero and optical data were more consistent than the turbulent boundary layer results. In no case did the variation among multiple measurements for a given test point exceed 5 percent. Again, a correlation plot of the aerodynamic and optical Strehl values appears in Figure 8.

Discussion

Correlations between the integrated path MTF optical measurement ($D >> \bar{\ell}_z$) and the aerodynamically inferred Strehl value (assuming an exponential density correlation function) are, in general, very good. The rms phase variances, calculated from the aerodynamic Strehl ratios, ranged from 0.08 to 0.18 HeNe (λ = 0.63 μm) waves over an aircraft dynamic pressure variation of 0.04 to 0.19 (standard) atmospheres.

The fence shear layer data were very self-consistent. The free shear formed at the top edge of the fences contained the expected smaller correlation lengths than corresponding fuselage boundary layers. However, the strength of the fluctuating density component was greater. Since the rms phase variance scales approximately as $\ell_z \overline{<\rho'>^2}$, the result was a greater observed optical degradation in shear layers. In general, the rms phase variance ranged from 0.09 to 0.26, and 0.08 to 0.19 for the near fence (F_s) and middle fence (F_m), respectively (same q variation as boundary layer). Another interesting facet of the fences was the nearly equal levels of optical degradation observed for F_s and F_m under the same flight conditions. To first approximation, it appears that optical seeing behind a fence is independent of the downstream location of the optical axis.

The results of the fuselage heat flux measurements were detailed in an earlier article (ref. 4). It was found that varying cabin temperatures from 9° to 40°C had negligible effect on either the aerodynamically inferred

unsteady density profiles on the optical MTF (I/I_0) measurements. The aircraft skin appears to act as an adiabatic wall vis-a-vis turbulent boundary layers and shear layers.

Because tomorrow's airborne laser systems may operate across a broad spectrum of wavelengths, telescope diameters, and aircraft conditions, it is essential to detail scaling laws for the data.

Wavelength Scaling

A previous article (ref. 5) has discussed implications of the present data base for short wavelength lasers. Again, in the infinite aperture limit ($D >> \bar{\ell}_z$), wavelength (λ) scaling is in accordance with equation 1, which we rewrite here as

$$I/I_0 = e^{-(2\pi\sigma/\lambda)^2} \qquad (5)$$

Figure 9 shows the dependence of Strehl ratio on λ, using the largest q values from Tables 1 and 2 (i.e., altitude 1.2 km, Mach #0.57). Shown in each case are both the infinite aperture optical MTF result and the aerodynamic prediction of I/I_0. The thick boundary layer (33 cm) in this case renders these results rather conservative; nevertheless, it is seen that the fuselage viscous flow field will probably be an important source of laser optical degradation for $\lambda \lesssim 2$ μm. Moreover, fence effects associated with windowless turret operation are essentially independent of boundary layer thickness (ref. 6) and hence location on the aircraft. Shear layer-induced far-field degradation is likely to be the dominant error source for short wavelength ($\lambda \lesssim 2$ μm) airborne laser systems.

Aperture Scaling

Experiments (ref. 1) have shown that for a constant average density correlation length $\bar{\ell}_z$, the variation of far-field intensity (Strehl ratio) with aperture size closely follows the family of curves depicted in Figure 2, both for

shear layers and for natural aircraft boundary layers. Thus, from MTF measurements for several aperture diameters, one can infer the Strehl ratio I/I_o, and hence estimate the rms phase variance σ. In the infinite aperture limit, equation 1 applies.

Turbulent Boundary Layer Thickness Scaling

Scaling with boundary thickness L has been found to go approximately as (ref. 2)

$$\frac{I}{I_o} = e^{-c\ (KL^{2/3})^3} \qquad (6)$$

where

$K = 2\pi/\lambda$

c is a constant

Figure 10 shows the dependence of far-field intensity degradation on L, again using the boundary layer high q value of $(I/I_o)_A$ as a baseline, and assuming $\lambda = 0.63\ \mu m$. Clearly, to minimize boundary layer optical degradation, the airborne laser telescope should be placed as far forward as possible on the aircraft.

Scaling with Aircraft q

Tables 1 and 2 show that, in general, optical degradation increases as the aircraft dynamic pressure increases. Figure 11 shows this dependence for both boundary layer and fence data. Here, dimensionless rms phase variance ($\overset{*}{\sigma}^2$) plots against aircraft dynamic pressure q indicate a reasonably good correlation between these two parameters.

Conclusions

Aero-optical properties of aircraft turbulent boundary layers and fence-induced shear layers have been examined for altitudes up to 12 kilometers and Mach numbers extending into the high transonic region. Aerodynamic instrumentation included movable hot-wire anemometer probes and a laser Doppler velocimeter, enabling point measurements of fluctuating density strengths and correlation lengths within the random flow region. Integration across the layer then leads to an estimate of the rms optical phase variance and, hence, the Strehl ratio (I/I_o) for a laser beam traversing the region.

An independent optical MTF measurement was performed in autocollimation using a 9-cm diameter helium-neon laser and a reflective airfoil located in the free stream. By averaging a large number of MTFs, Fourier transforming, and correcting for a single pass through the boundary layer, an optical assessment of I/I_o was obtained. An array of thermocouples was also attached to the inside skin of the aircraft to examine the prevalent adiabatic wall assumptions vis-a-vis boundary layers. The principal conclusions from these aircraft tests include the following.

1. Correlations between the turbulent boundary layer (TBL) aerodynamically inferred Strehl ratio $(I/I_o)_A$ and its MTF optical counterpart $(I/I_o)_{OPT}$ (the latter corrected for large aperture) were good. The RMS phase variance was observed to increase from 0.08 to 0.18 wave (λ = 0.63 μm) for aircraft dynamic pressures q ranging from 0.04 to 0.19 standard atmosphere.

2. Measured TBL density correlation lengths varied from about 1.0 to 3.5 cm, representing 5 to 10 percent of the total boundary layer thickness. The correlation functions themselves appear to be exponential.

3. Maximum TBL unsteady density strength $(\rho'/\rho_\infty)_{max}$ was of order 0.5 percent over the experimental range of aircraft dynamic pressures.

4. The aircraft skin appears to act as an adiabatic wall. Neither the aerodynamic probes nor the integrated path MTF measurements showed appreciable evidence of heat transport between the fuselage and the TBL.

5. A strong shear layer (SL) is formed at the top edge of an aerodynamic fence. Measured correlation lengths are generally smaller (1 to 1.5 cm) than for TBLs, though the strength of the turbulence is significantly greater (0.5 to 3 percent). Most of the total path optical degradation is produced within the SL itself.

6. Identical fences (no cavity) were examined for two locations--8 and 80 cm upstream of the optical axis; to first order, the observed optical degradations were the same for the two locations for equal values. This indicates that optical degradation is essentially independent of fence location within this experimental domain.

7. For both the near fence (F_s) and the middle fence (F_m), sound correlations were observed between the aero Strehl prediction $(I/I_o)_A$ and the optical measurement. An exception is for the highest q values. The reason for this discrepancy is not understood. Inferred $_{rms}$ phase variances for F_s and F_m were 0.09 to 0.26 and 0.08 to 0.19 wave (λ = 0.63 μm), respectively.

8. The experiments involved a single wavelength (λ=0.63 μm), one MTF aperture diameter (9 cm), and a single location on the aircraft fuselage (station 25 meters). Clearly it is crucial to understand the scaling of this data base for other airborne laser conditions. Previous AFWL wind tunnel and aircraft experiments have established these relationships. We now detail these.

a. Aperture Scaling. Operational airborne laser weapon systems will probably have telescope diameters which are large compared with fuselage random flow-field density correlation lengths (i.e., $D >> \ell_z$). This condition did not prevail. Thus, a correction was applied to the optical data, using an expansion for the tilt-removed MTF, which has been verified in wind tunnel experiments. The magnitude of the correction for the data varied from about 5 to 50 percent.

b. Wavelength Scaling. For a large aperture system, wavelength scaling follows from the established relationship

$$\frac{I}{I_o} = e^{-K^2\sigma^2} \tag{7}$$

with

$K = 2\pi/\lambda$ (wave vector)

σ = RMS phase variance

Notice the strong sensitivity of Strehl ratio with wavelength; indications are that airborne systems employing lasers with wavelengths less than 2 μm can expect moderate-to-strong optical degradation due to turbulent boundary layers and severe effects from SLs.

c. Scaling with Boundary Layer Thickness. Fence-induced optical effects are essentially independent of turbulent boundary layer thickness. Rather, the strong shear layer formed at the top edge of the fence dominates. In the case of a pure boundary layer, however, as might exist for a flush-mounted turret with an exit material window, the $_{rms}$ phase variance has been found to scale roughly as

$$\sigma^2 \propto L^{4/3} \tag{8}$$

where L is the thickness of the random domain. It clearly behooves one to install this turret as far forward on the aircraft as possible.

d. Scaling with Aircraft Dynamic Pressure q. For both the fence (shear layer) results and the natural aircraft boundary layer, the phase variance is roughly proportional to q.

9. The results established the relevancy of previous wind tunnel experiments. Fluctuating density strengths and correlation lengths are in general agreement, both for the artificially thickened wind tunnel boundary layers and shear layers. These latter were examined both in a cavity-fence and a cavity-mass injection configuration. Though anomalies exist, the general conclusion is that the random flow fields created in wind tunnels have the same general characteristics as those observed in the airborne experiments.

10. Near-term adaptive optics systems will be unable to cope with boundary layers and shear layers due to their small spatial and large bandwidth requirements.

11. Aircraft random flow fuselage effects in the transonic region are not an important source of laser optical degradation for wavelengths in the middle IR region ($\lambda \gtrsim 2$ μm). However, as the evolution of shorter wavelength systems continues, the importance of these aircraft effects will assume major dimensions. This present data base suggests the following guidelines for developing short wavelength airborne laser systems.

a. Operate the laser turret closed port (i.e., window) if possible; flush mount to preclude formation of shear layers.

b. Place the turret as far forward as possible to minimize boundary layer thickness.

If windowless turret operation is required, or look angle requirements lead to propagation through a shear layer, the resultant degradation could be stifling. Support research aimed at diverting, suctioning, or otherwise ameliorating the effects of random flow fields on short wavelength systems, in the long run may be a key to the successful evolution of these future airborne weapon systems.

REFERENCES

1. Gilbert, K. G., et al., Laser Propagation Through Turbulent Boundary Layers, Shear Layers and Cavity Flows: Wind Tunnel Experiments, Laser Digest, AFWL-TR-78-15, 1978.

2. Rose, W., Aerodynamic Measurements of KC-135 Turbulent Boundary Layers, NASA CP-2121, 1980.

3. Barakat, R., OPT. ACTA, 18, 683 (1971).

4. Gilbert, L., Cycle II.5 Thermo-Optical Turbulent Boundary Layer Measurements, Laser Digest, AFWL-TR-78-15, 1978.

5. Gilbert, K., Implications of Recent Aircraft Random Flow Field Experiments for Short Wavelength Laser Systems, Laser Digest, AFWL-TR-78-15, 1978.

6. Gilbert, K., Open Port Laser Turret Optical Performance: Recent Experiments, Laser Digest, AFWL TR-78-15, 1978.

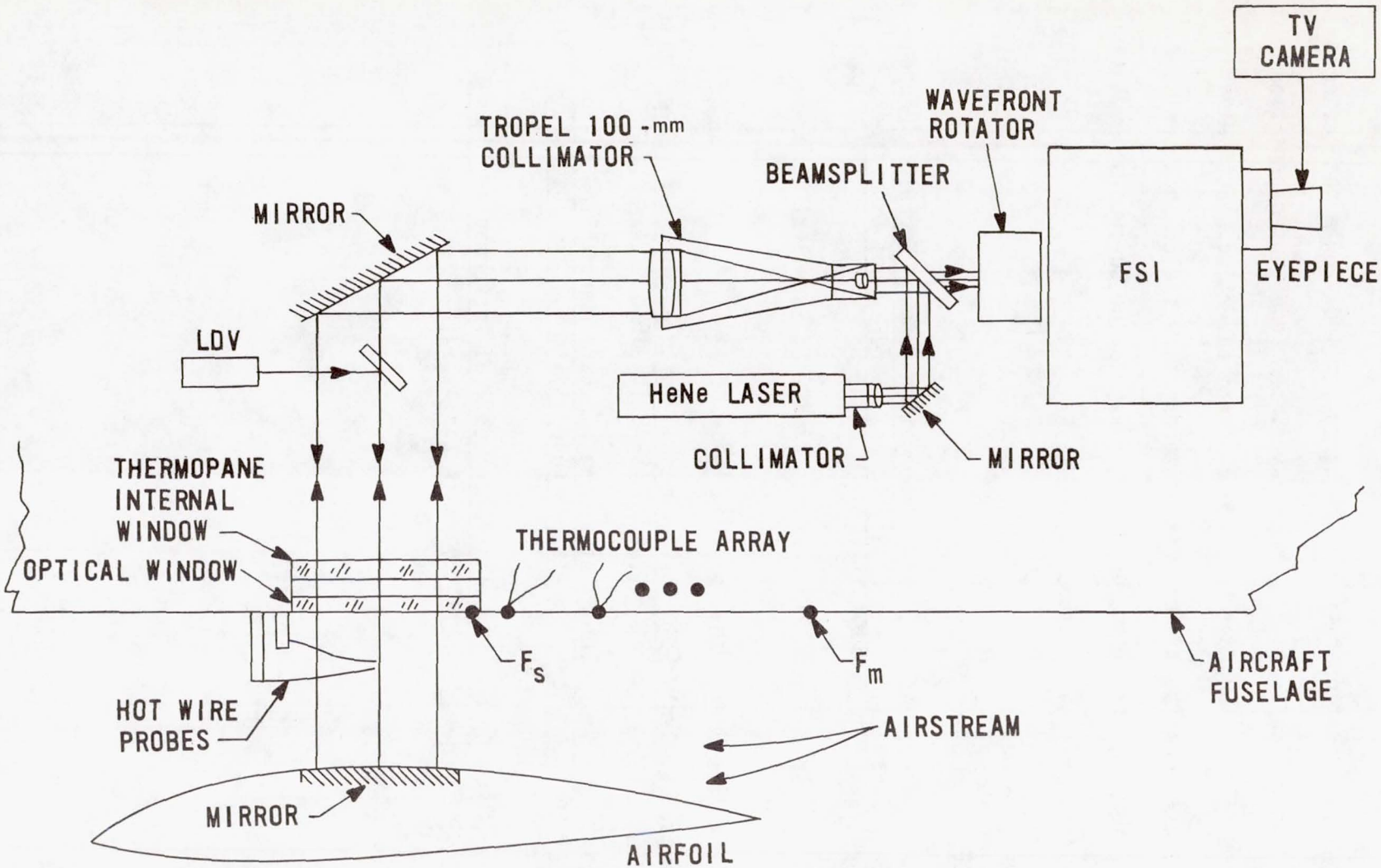

Fig. 1a Schematic for KC-135 Aero-Optical Experimental Setup.

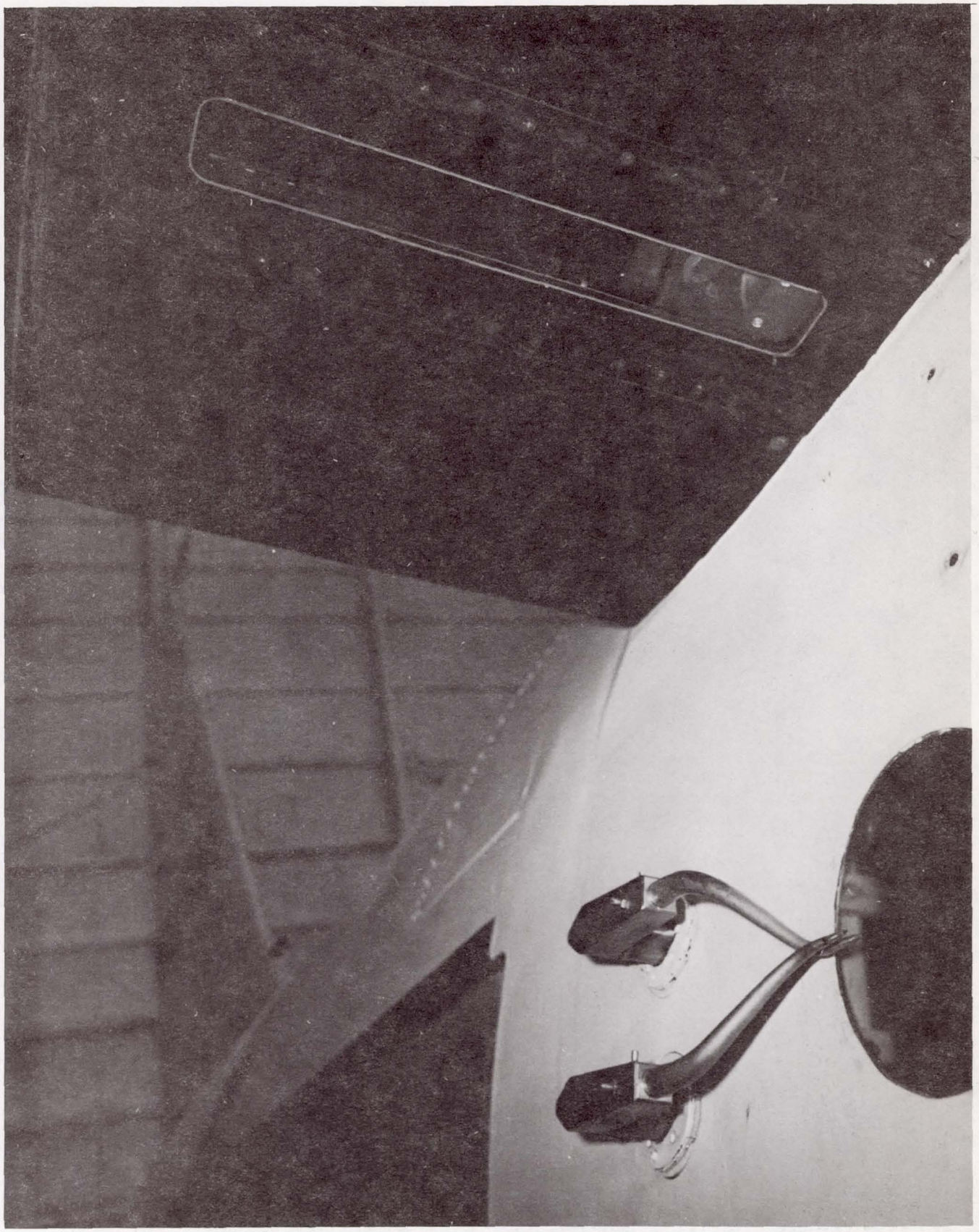

Fig. 1b Hardware for KC-135 Aero-Optical Experimental Setup.

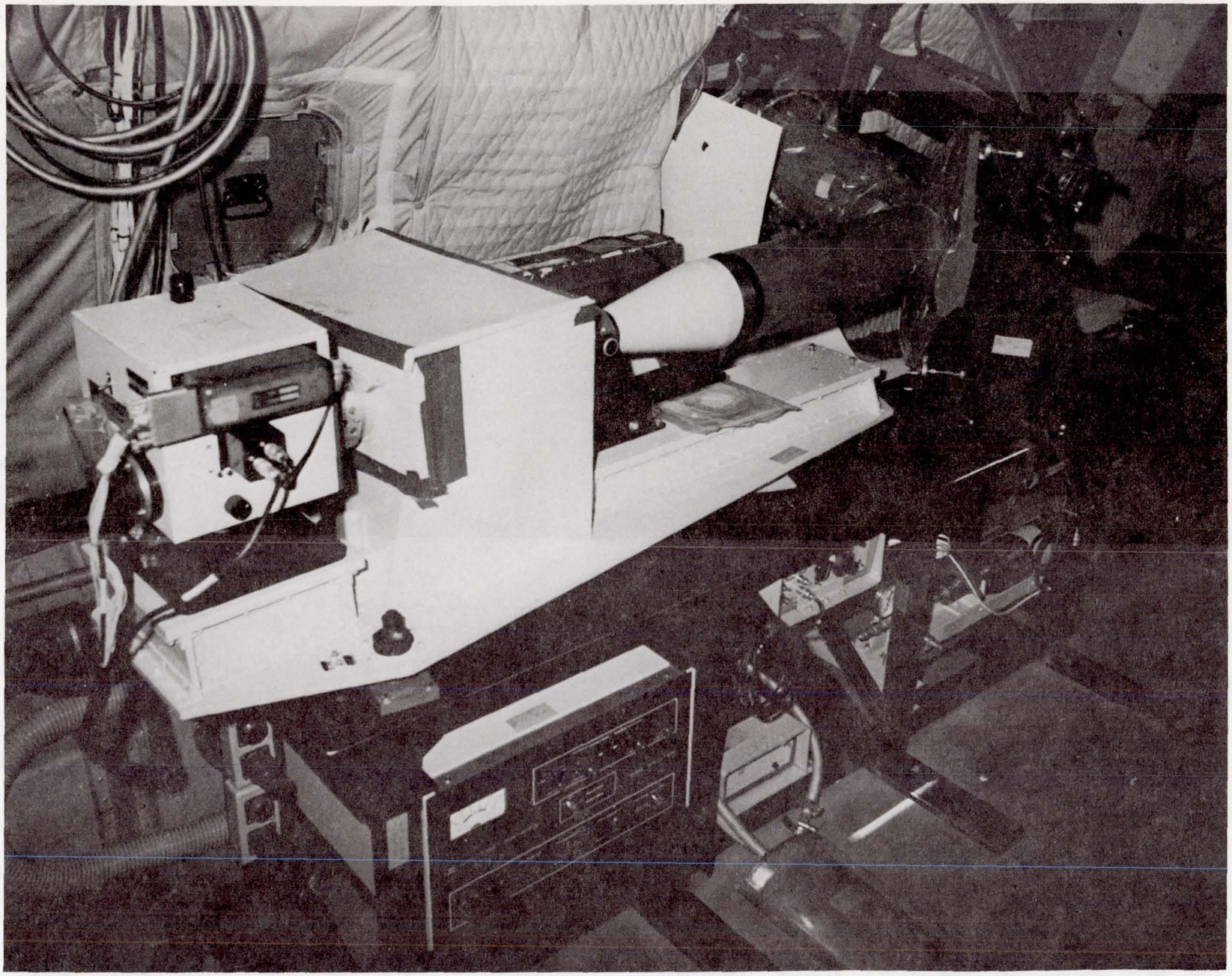

Fig. 1c Test bench for KC-135 Aero-Optical Experimental Setup.

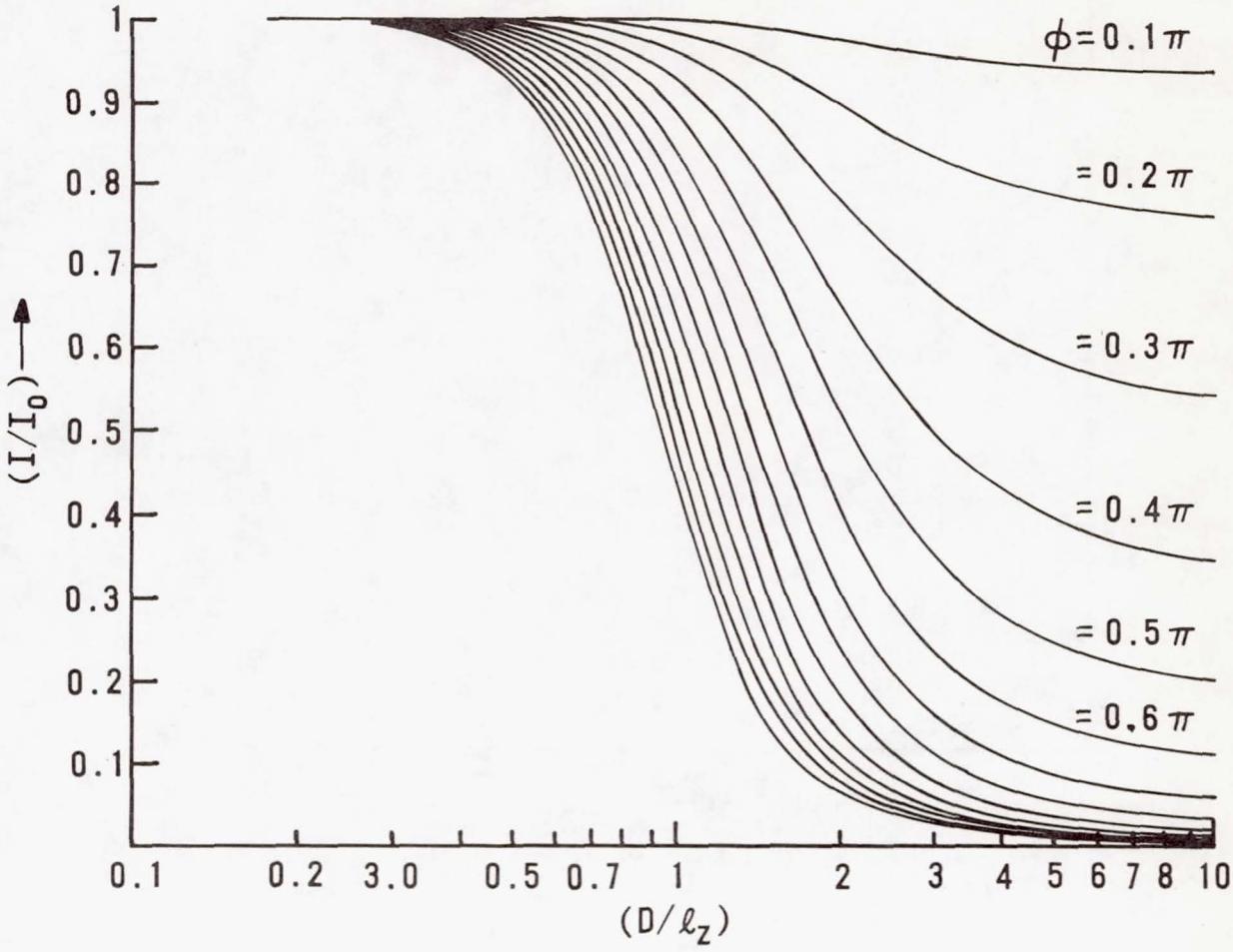

Fig. 2 Strehl family of I/I_0 Curves.

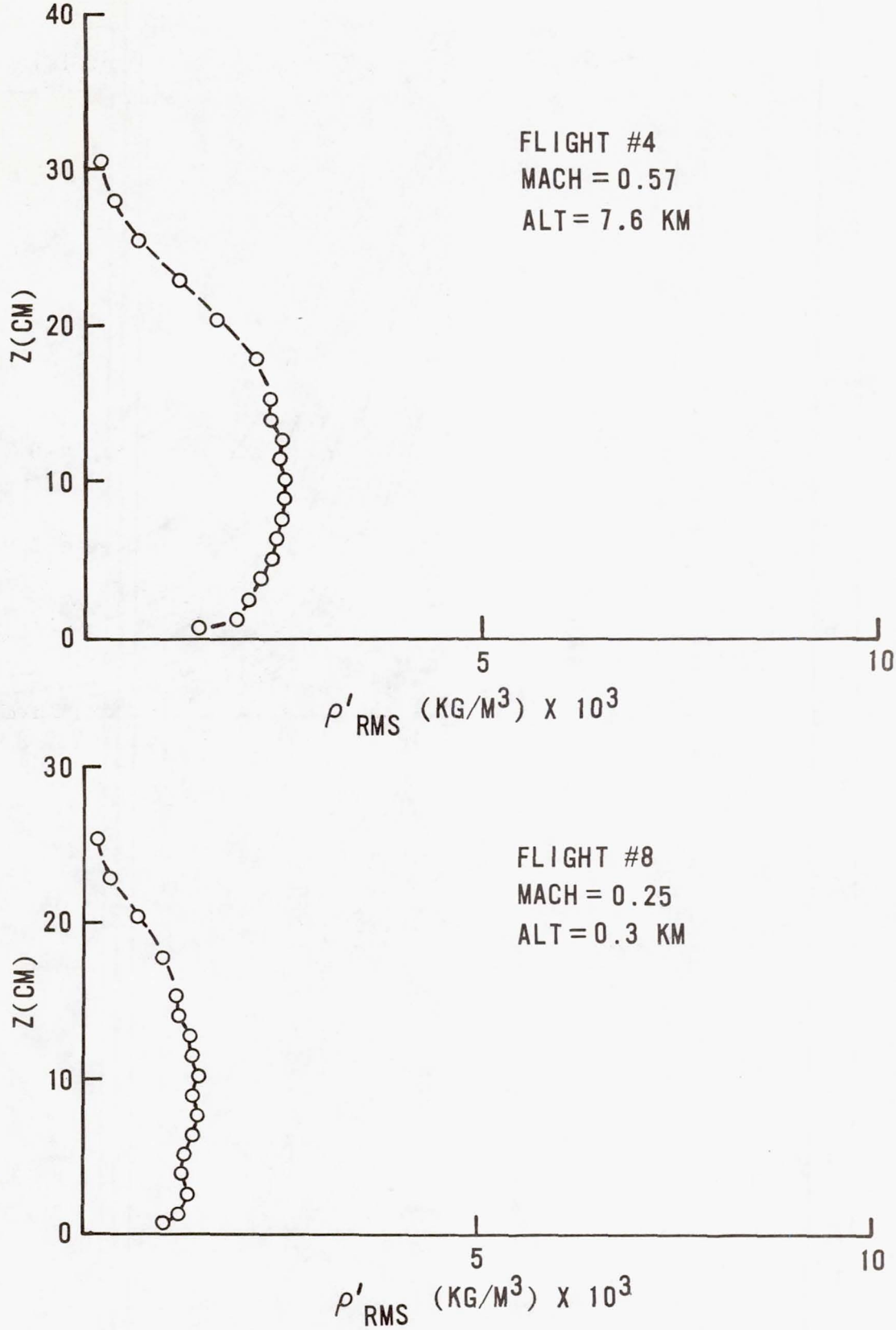

Fig. 3 Turbulent Boundary Layer Unsteady Density Profiles.

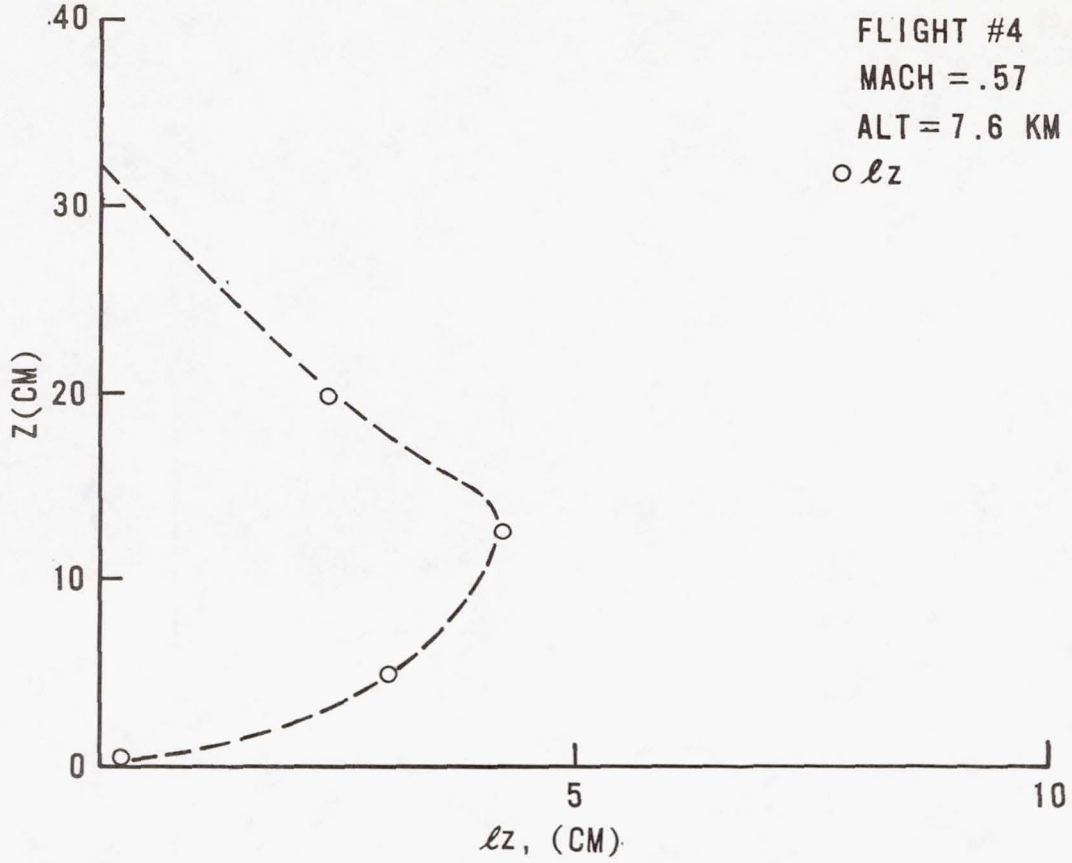

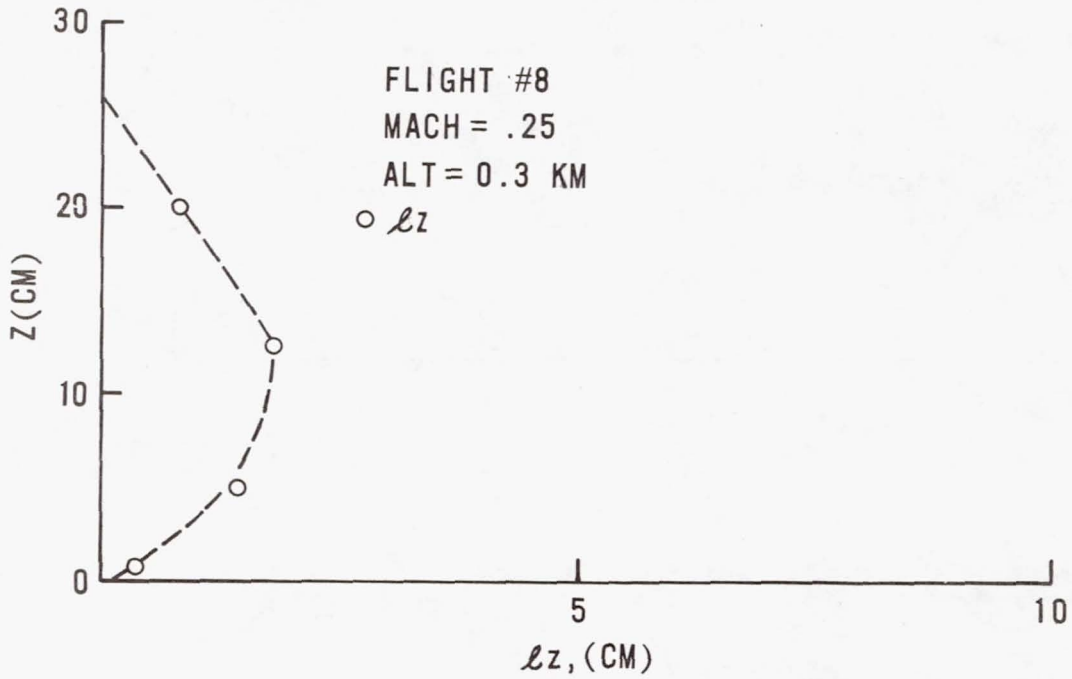

Fig. 4 Turbulent Boundary Layer Correlation Length Profiles.

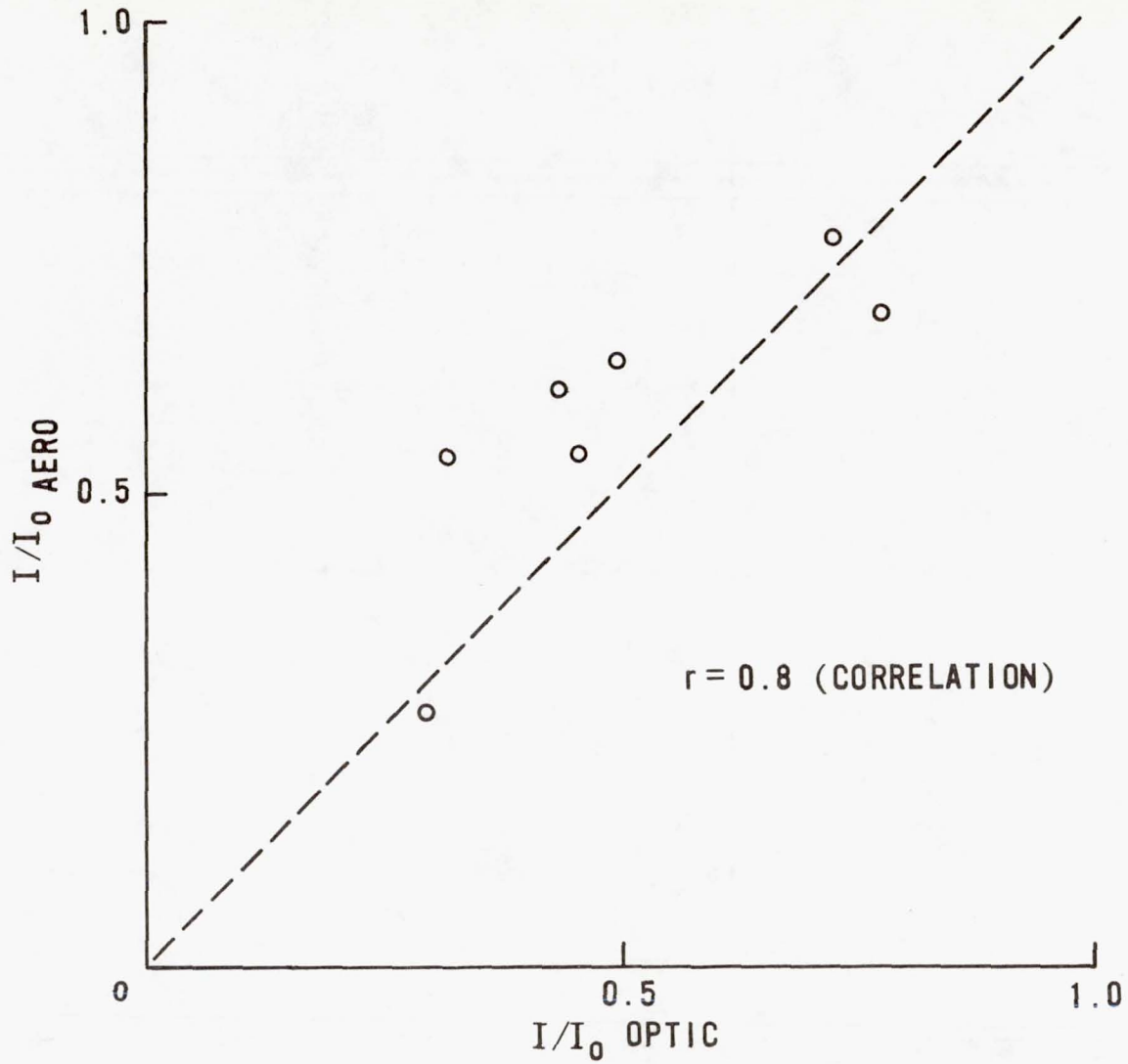

Fig. 5 Turbulent Boundary Layer Correlation Plot: Aerodynamic versus Optical Strehl Ratios.

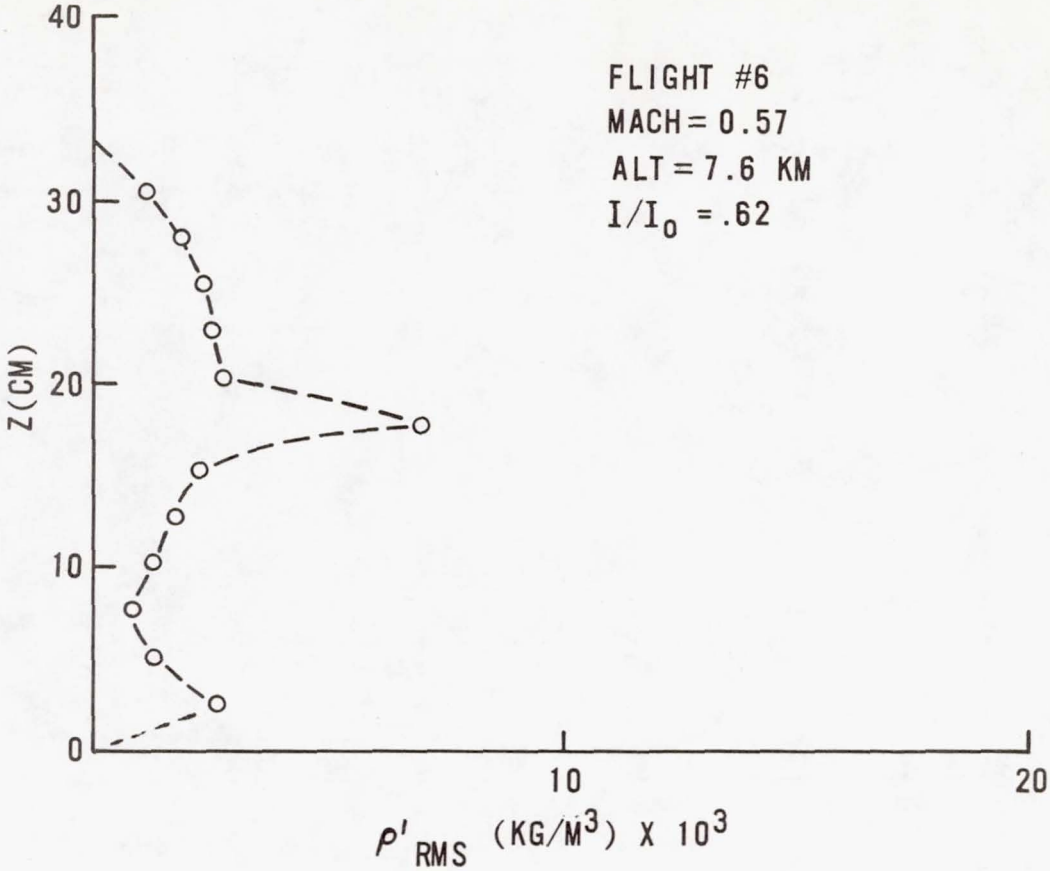

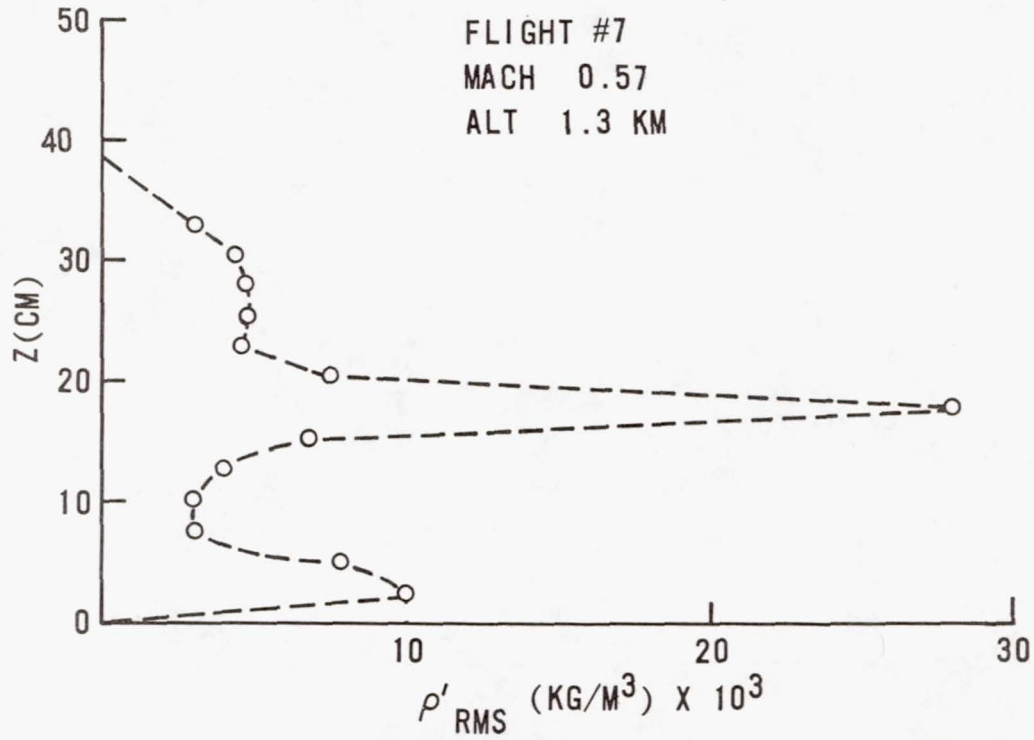

Fig. 6 Shear Layer Unsteady Density Profile.

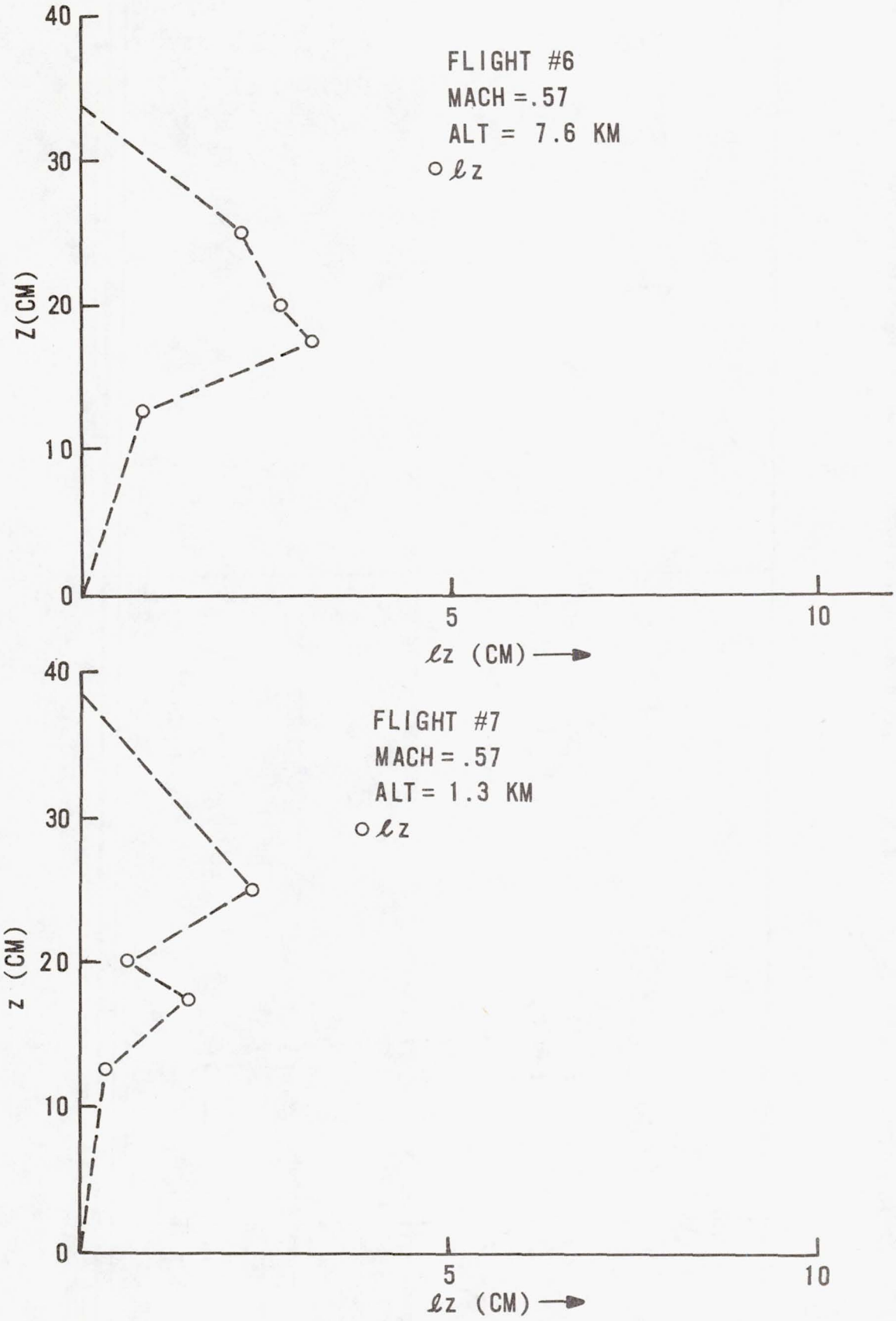

Fig. 7 Shear Layer Correlation Length Profiles.

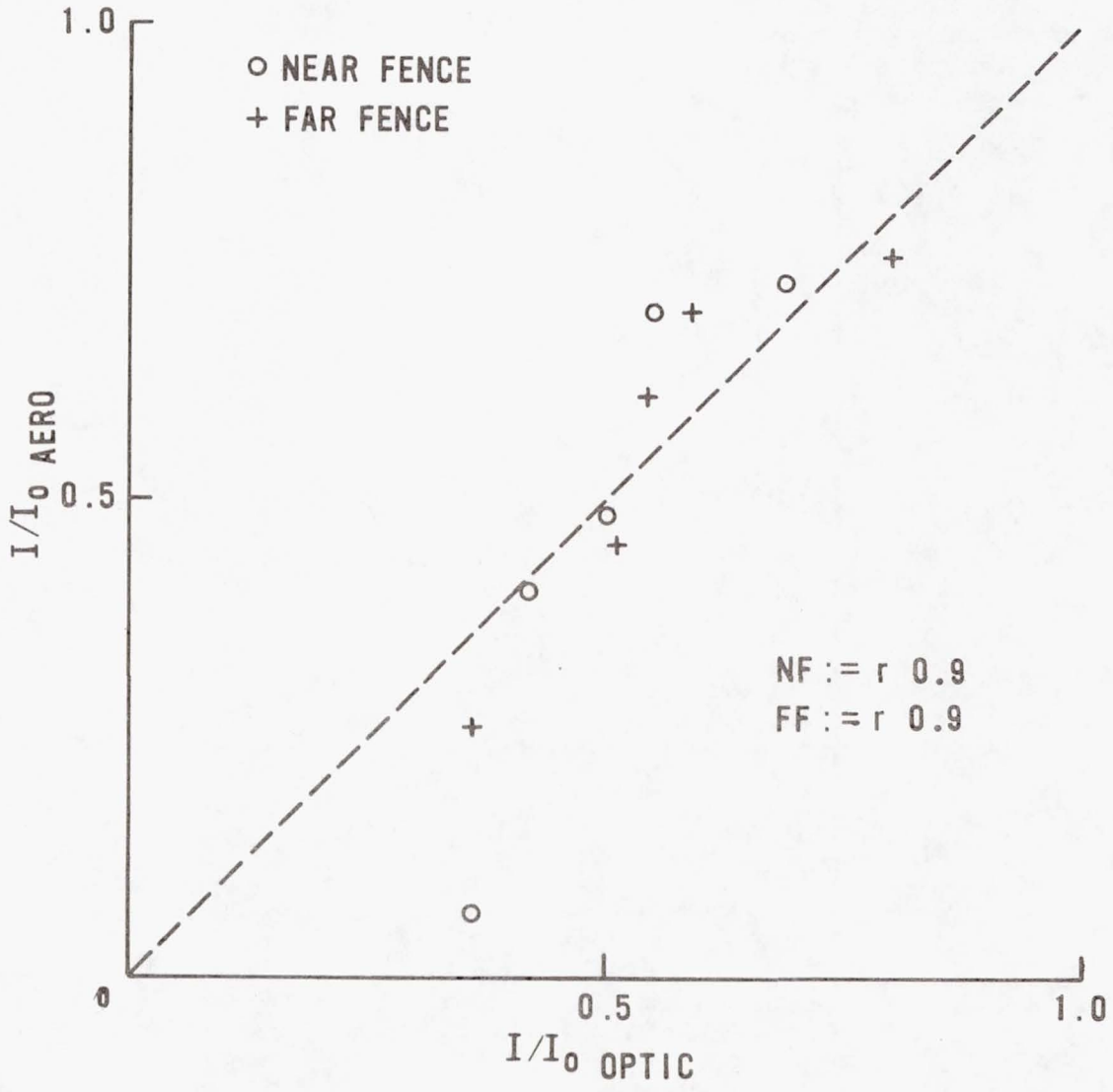

Fig. 8 Shear Layer Correlation Plot: Aerodynamic versus Optical Strehl Ratios.

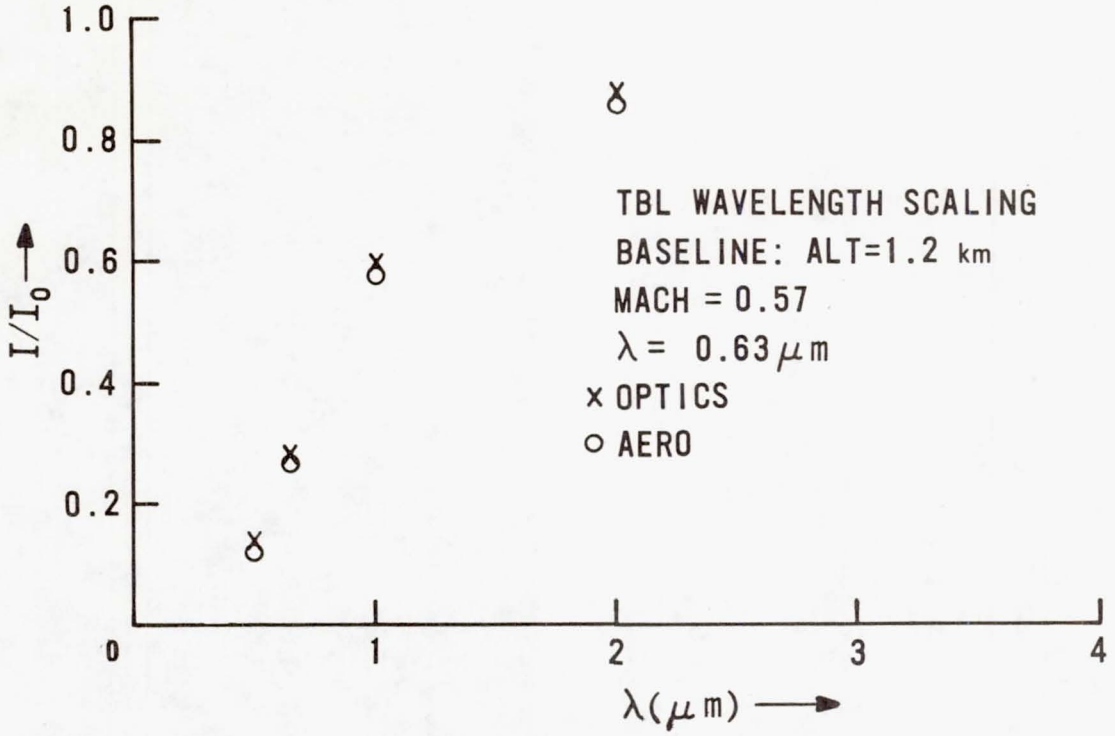

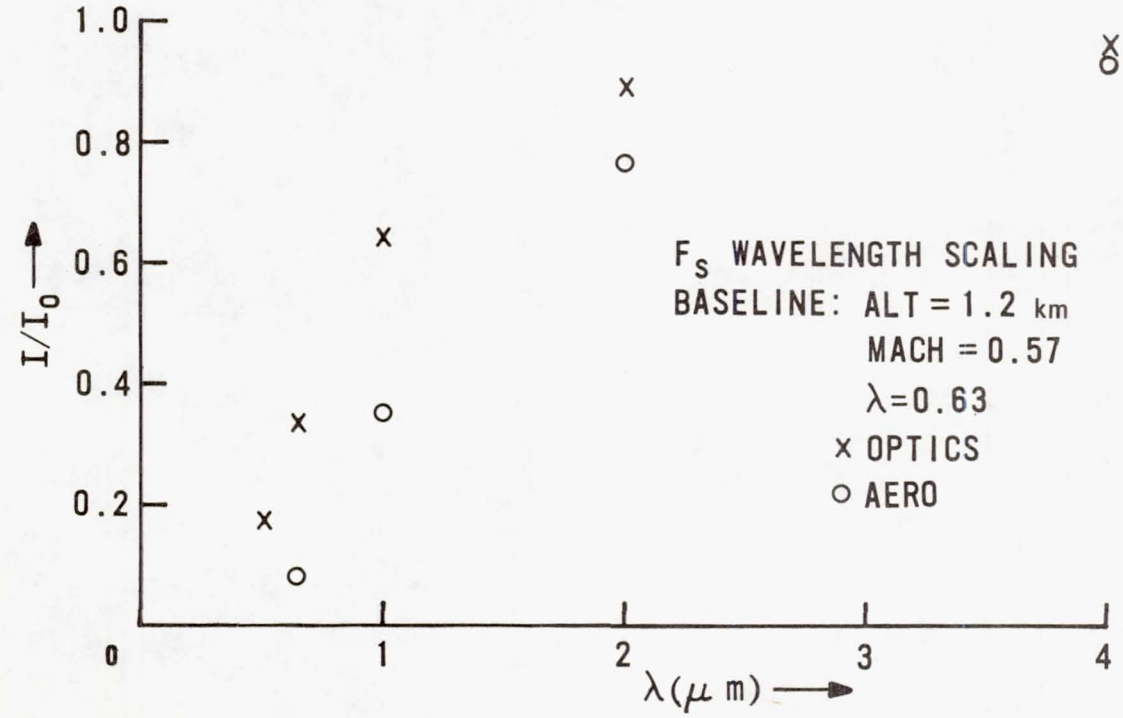

Fig. 9 Wavelength Scaling of Strehl Ratio I/I_o.

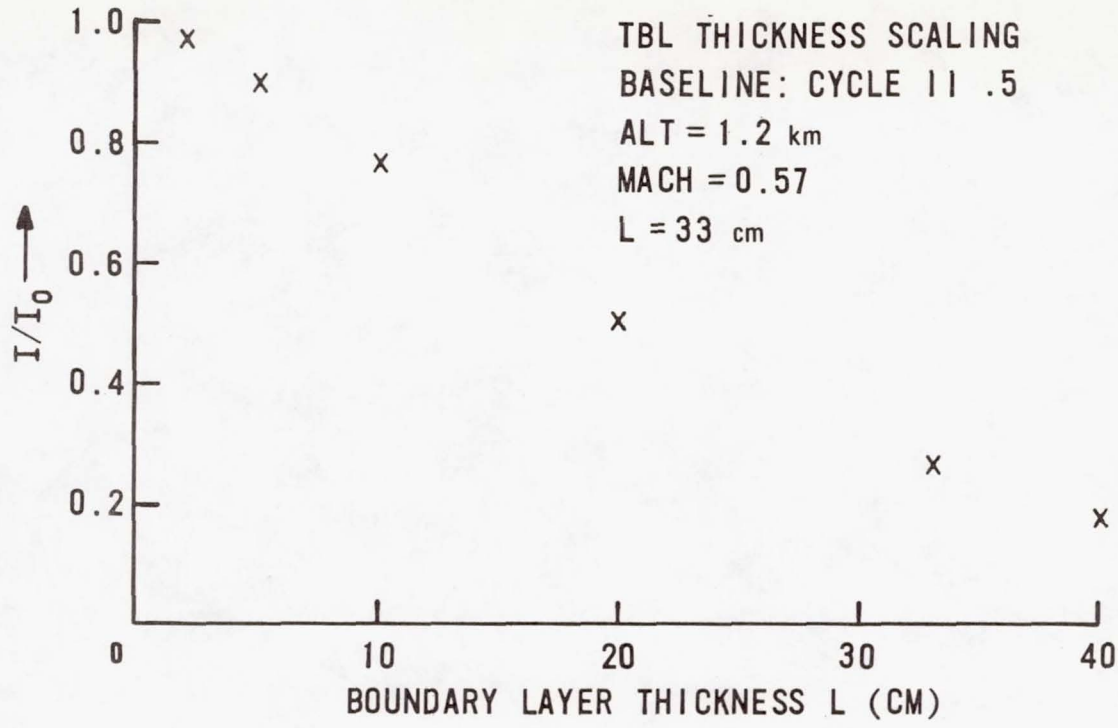

Fig. 10 Turbulent Boundary Layer Thickness Scaling of Strehl Ratio I/I_o.

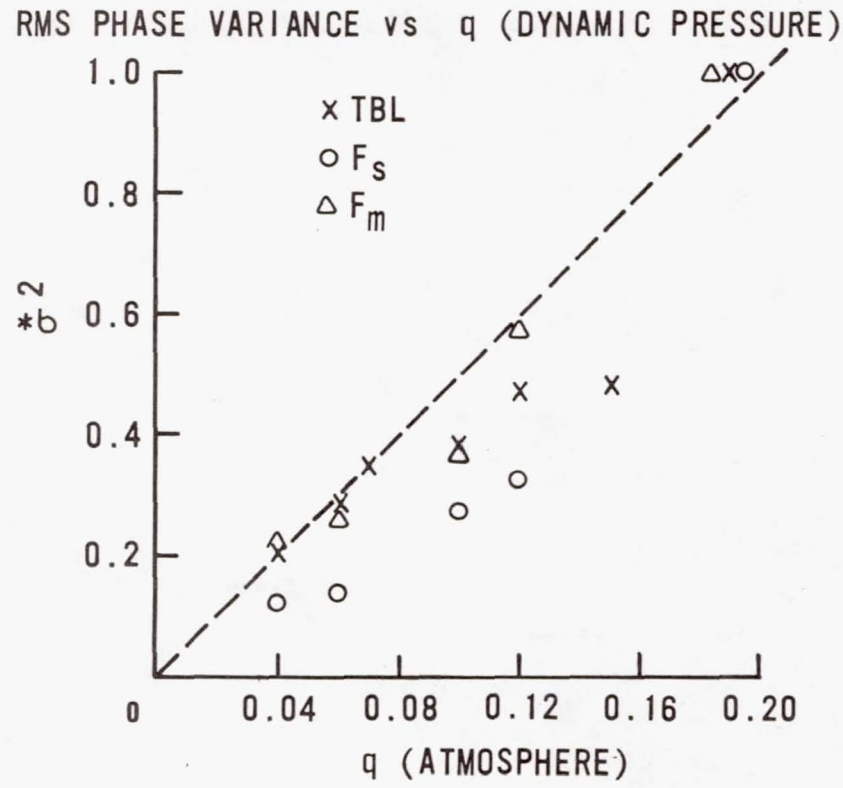

Fig. 11 Optical Phase Variance Scaling with Aircraft Dynamic Pressure (q).

AIRBORNE MEASUREMENT OF ATMOSPHERIC TURBULENCE

by

William C. Rose

Rose Engineering and Research, Inc.

Incline Village, Nevada 89450

and

Leonard J. Otten, III, Major USAF

AFWL/LR-2

Kirtland AFB, NM 87117

Paper presented at

USAF / NASA Aero-Optics Symposium

14-15 August 1979

NASA Ames Research Center

Moffett Field, California 94035

Abstract

A system is described that is capable of making measurements of fluctuating atmospheric density and spatial scales required in assessing the quality of coherent radiation propogation. The airborne platform for the system is an NC-135 Air Force research aircraft. This system is completely operational and has flown successfully for approximately 60 hours to date. Scales from hundreds of meters to millimeters have been measured from near ground level to 12 km. A heated and unheated fine wire sensor are used to produce signals from the atmospheric turbulence as the aircraft flies through the turbulence. These signals are analyzed using techniques developed for use in high-speed wind tunnels. With these data interpretation techniques available, the aircraft Mach number may be arbitrarily high -- even supersonic flight presents no problem. With such high velocities possible, extensive regions of the atmosphere may be traversed in a relatively short time. This report will describe the special sensors, aircraft installation, data reduction procedures, and other special requirements necessary to obtain meaningful atmospheric turbulence data. Preliminary results that indicate density fluctuation levels and their spectral distribution will be presented.

SECTION I

Background

Interest in atmospheric turbulence dates to the first astronomical observations, which may be hampered by the random variations in index of retraction due to the turbulent changes in air density. More recently, flight through the atmosphere has generated significant interest in clear air turbulence as well as turbulence associated with meteorological phenomena and terrain variations. Desire to fly aircraft with laminar flow surfaces without atmospheric-turbulence-induced transition to turbulent flow has heightened this interest. The transport and dispersal of pollutants in the atmosphere are largely governed by near-surface turbulence. The production, convection and diffusion by viscous forces of atmospheric turbulence has long been of interest to basic researchers studying the atmosphere. With the advent of sophisticated detection and surveillance systems involving all wave lengths of radiation, the effect of atmospheric turbulence on the output of such systems has become important. The propogation of coherent radiation through the atmosphere can be seriously affected by the random phase shifts induced by atmospheric turbulence. Both the levels of the fluctuations and their size (or scale) are important in the effect that atmospheric turbulence will have on any of the above areas of interest.

Investigations too numerous to cite have been conducted in the general study of atmospheric turbulence. Meteorological balloons are the classical system used for study. Variations in temperature,

for example, are recorded with increasing altitude to yield the values of the fluctuating field. The scales of the fluctuations are determined typically by having two temperature sensors whose signals can be correlated which are separated by a known distance. Balloons give useful results and are usually quite reliable; however, they give information about the atmosphere over a very small volume. In addition, the scales that can be detected are limited to those larger than the separation distance between the sensors.

In other studies, fixed-wing aircraft have been used to increase the data base for atmospheric turbulence. A major program known as ALLCAT (all altitude critical air turbulence), supported by the Air Force, and other government agencies interested in atmospheric turbulence was undertaken around 1965. Data on gust loads sensed by gust probes, accelerometers, pressure transducers and other onboard instrumentation were taken. Aircraft ranging from the U-2 to F-106 to a C-131B were used to investigate turbulence in various flight altitude bands. The LOCAT program investigated low altitudes -- HICAT investigated high altitudes, etc. Results from these studies are presented in reports too numerous to give here, however, the interested reader is referred to Reference 1 and the bibliography given there. Because of the size of the aircraft used and relatively slow response instrumentation, only large scale motions could be accurately detected. Here large scale implies integral scale lengths greater than 10 to 20 meters. For interest in the statistics of atmospheric turbulence in the large scale region the results of the ALLCAT

program represent an enormous data base obtained at a cost of millions of dollars. As extensive as these data may be, they do not contain useful information in the small turbulence scales, say from the order of 1 meter down to the dissipation scales of the order of millimeters.

To make accurate measurements of small-scale atmospheric motions from aircraft, high response instrumentation such as the hot-wire anemometer can be used. Previous experiments have been performed (see References 2, 3 and 4 for example) using hot-wire anemometry, however, the interpretation of the data resulting from these experiments is not clear because of the data reduction techniques employed. This is particularly true when attempting to measure the variations in atmospheric density and their scales for determining optical transmissibility. Since data for optical use is desired over extensive regions of the atmosphere at all flight altitudes, aircraft with large operating envelopes and high speeds must be used.

This report describes a system developed for atmospheric turbulence research by the USAF Weapons Laboratory at Kirtland AFB, New Mexico. The airborne platform for the system is an NC-135 aircraft used in various Air Force research projects. A pair of fine wire sensors are located near the nose of the aircraft (see Figures 1 and 2) and are driven with high response anemometer systems. Through the use of this aircraft, two independent sensors and data

reduction procedures developed for high speed wind tunnel testing, both large and small scale turbulence (down to 5 mm) can be measured at high speeds from near ground level to 12 km.

SECTION II

Discussion

In order to accurately measure atmospheric turbulence down to scale sizes of the order of 10 mm in high speed flight, one requires instrumentation with a very high frequency response. For example, at a flight velocity of 200 m/s a 10 kHz response is needed to measure a turbulent burst 10 mm long. By comparison, if the aircraft slowed to 100 m/s, this same instrumentation could detect a 5 mm scale. Laboratory or wind tunnel instrumentation can easily operate today at up to 20 to 40 kHz. A system having this high response that can be used in making velocity and/or density turbulence measurements is the hot-wire anemometer. This system consists of a fine (typically less than 25 μm diameter) wire, either heated or unheated, and the appropriate electronics (referred to as anemometers) to produce electrical signals that can be interpreted as fluctuations in the physical variables. A drawback of the hot-wire anemometer is the fragile nature of the sensors. Researchers have been reluctant to attempt using fine wires on aircraft because of this; however, techniques for producing durable sensors have been developed in high speed wind tunnel testing. Recently, a system using 5 μm sensors and high response laboratory anemometers

was used to survey the fuselage boundary layer of a large transport aircraft (Ref. 5). This system was used successfully in over 80 hours of flight time. Wire breakage occurred only once when ice crystals were encountered. With this encouraging record, it was decided to move the sensor location to the nose of the aircraft and attempt to make atmospheric turbulence measurements.

In making measurements at low speeds (i.e., $M < \cong 0.3$) the signals produced by anemometer/sensor combinations are easily related to the fluid flow variables. For a constant density flow, the velocity fluctuations are sensed by a heated wire driven by either a constant temperature or constant current anemometer. Constant temperature systems are usually used at present because of their higher frequency response, although compensating amplifiers are available for use with the constant current systems. Fluid temperature (i.e., the aerodynamic static temperature) fluctuations are sensed by an unheated wire driven by a constant current anemometer, compensated to increase its frequency response.

As flight speeds increase above the $M \cong 0.3$ value, or the flow is no longer one of constant density, fluid compressibility effects become important and the values sensed by wires placed in the stream no longer respond to the simple velocity and fluid temperature. For example, consider the unheated or temperature sensing wire. Since the flow over the wire is essentially brought to rest at the wire surface, it will respond to the temperature known as the recovery

temperature. This, in turn, can be related to the aerodynamic total temperature, which is related to the fluid static temperature through the energy relationship

$$T_t = T_t + u^2/2c_p \qquad (1)$$

or

$$T_t = T\ (1 + \frac{\gamma-1}{2} M^2) \qquad (2)$$

Now it is evident that, for increasing Mach numbers, the difference between the total temperature (actually sensed by the wire) and the desired fluid temperature will increase. For a flight Mach number of 0.8, there is about a 13% error in the mean value. Since, in atmospheric turbulence studies, we are interested in not the mean values but their indicated fluctuations, we must examine a differential form of equation (2).

$$(1 + \frac{\gamma-1}{2} M^2)\ \frac{T'}{\bar{T}} = \frac{T'_t}{\bar{T}_t} + (\gamma-1)\ M^2\ \frac{u'}{\bar{u}} \qquad (3)$$

Equation 3 relates the instantaneous fluctuations away from the mean values (primed variables) than can exist at a point in the fluid. Again, for low Mach numbers we have

$$\frac{T'_t}{\bar{T}_t} = \frac{T'}{\bar{T}}$$

so that an unheated wire will sense the desired fluctuations in static temperature. For increasing Mach numbers, the values of the velocity fluctuations present in the atmosphere will contribute to the measured

T_t' values. Keep in mind that the behavior described above comes about only through the aircraft's flight Mach number and has nothing to do with the motions and variations present in the atmosphere. If one were to use only a single, unheated wire, it would be impossible to measure the value of fluid temperature fluctuations from a high speed aircraft. Even to measure the spectrum of the fluctuations requires the assumption that the velocity and temperature spectra are identical.

To surmount this apparent impasse, another wire, heated to at least twice the stream temperature, is required. This wire, when cooled by the air flow, becomes sensitive only to the mass flow past it. The mass flow is the product of fluid static density, ρ, and the velocity, u, past the wire. The term actually measured by the heated wire is $(\rho u)'/\bar{\rho}\bar{u}$. For the small fluctuation levels usually encountered in turbulent flows, this term may be written as

$$\frac{(\rho u)'}{\bar{\rho}\bar{u}} = \frac{\rho'}{\bar{\rho}} + \frac{u'}{\bar{u}} \qquad (4)$$

Notice that the heated wire produces a signal proportional to the sum of two desired turbulence quantities ρ' and u'. Once again, if one were to operate only a single, heated wire it would, in general, be impossible to determine the magnitude of the velocity fluctuations, since the density fluctuations from, say, temperature variations, would also produce a contribution to the signal. This is true independent of the aircraft's flight Mach number. Spectra can be obtained, however, under the assumption that the spectra of ρ' and u' are identical.

At this point we have the unique situation that at high speeds we have two systems capable of measuring two fluid parameters, neither of which is desired to deduce information about the atmosphere, in general. In high speed wind tunnel testing, it has been known that combining the two measurements can yield the desired information about the fluctuating velocity and temperature or density. To do this we examine a form of Equation 3 that has used a differential form of the equation of state

$$\frac{p'}{\bar{p}} = \frac{\rho'}{\bar{\rho}} + \frac{T'}{\bar{T}}$$

to give

$$(1 + \frac{\gamma-1}{2} M^2) \frac{T_t'}{\bar{T}_t} = \frac{p'}{\bar{p}} - \frac{\rho'}{\bar{\rho}} + (\gamma-1) M^2 \frac{u'}{\bar{u}} \qquad (5)$$

Adding and subtracting $(\gamma-1) M^2 \frac{\rho'}{\bar{\rho}}$ on the right-hand side of Equation (5) gives

$$(1 + \frac{\gamma-1}{2} M^2) \frac{T_t'}{\bar{T}_t} = \frac{p'}{\bar{p}} - (1 + (\gamma-1) M^2) \frac{\rho'}{\bar{\rho}} + (\gamma-1) M^2 \frac{(\rho u)'}{\bar{\rho}\bar{u}} \qquad (6)$$

For small scale motions, the atmosphere is incapable of supporting pressure fluctuations (other than weak sound waves) so that the $p'/\bar{p}$ term may be neglected in Equation 6. This leaves a relationship involving three fluctuation terms, two of which are measured:

$$(1 + \frac{\gamma-1}{2} M^2) \frac{T_t'}{\bar{T}_t} = - (1 + (\gamma-1) M^2) \frac{\rho'}{\bar{\rho}} + (\gamma-1) M^2 \frac{(\rho u)'}{\bar{\rho}\bar{u}} \qquad (7)$$

so that the density fluctuation can be deduced. Phase lags between the two systems prevent the use of Equation 7 directly so that a time-averaged equation must be used. We first write Equation 7 as

$$A \frac{\rho'}{\bar{\rho}} = B \frac{(\rho u)'}{\bar{\rho}\bar{u}} - C \frac{T_t'}{\bar{T}_t}$$

and then square and time average to get

$$A^2 \frac{\overline{\rho'^2}}{\bar{\rho}^2} = B^2 \frac{\overline{(\rho u)'^2}}{(\bar{\rho}\bar{u})^2} - 2BCR_{\rho u T_t} \frac{\langle (\rho u)' \rangle \langle T_t' \rangle}{\bar{\rho}\bar{u}\bar{T}_t} + C^2 \frac{\overline{T_t'^2}}{\bar{T}_t^2} \qquad (8)$$

Here $R_{\rho u T_t}$ is the zero-phase lag cross-correlation coefficient between $(\rho u)'$ and T_t', which is obtained from the recorded data. Thus $\overline{\rho'^2} / \bar{\rho}^2$ can be determined.

Static temperature fluctuations instead of density fluctuations can be determined by using

$$\frac{\overline{T'^2}}{\bar{T}^2} = \frac{\overline{\rho'^2}}{\bar{\rho}^2}$$

Velocity fluctuations are obtained by using Equation 5 and adding and subtracting $u'/\bar{u}$ from the right-hand side to give

$$(1 + \frac{\gamma-1}{2} M^2) \frac{T_t'}{\bar{T}_t} = \frac{p'}{\bar{p}} - \frac{(\rho u)'}{\bar{\rho}\bar{u}} + (1 + (\gamma-1) M^2) \frac{u'}{\bar{u}} \quad (9)$$

Again for small $p'/\bar{p}$, we have

$$A \frac{u'}{\bar{u}} = \frac{(\rho u)'}{\bar{\rho}\bar{u}} + C \frac{T_t'}{\bar{T}_t}$$

or

$$A^2 \frac{\overline{u'^2}}{\bar{u}^2} = \frac{\overline{(\rho u)'^2}}{(\bar{\rho}\bar{u})^2} + 2CR_{\rho u T_t} \frac{\langle(\rho u)'\rangle\langle T_t'\rangle}{\bar{\rho}\bar{u}\bar{T}_t} + C^2 \frac{\overline{T_t'^2}}{\bar{T}_t^2} \quad (10)$$

Note that Equation (10) must be used to determine the magnitude of the velocity fluctuations even for very low-speed flight. These relationships were used in the present study to produce the results discussed next.

SECTION III

Results

Representative results from flights at various Mach numbers and altitudes are presented here and discussed in light of their implications for optical transmission through the measured atmospheric volumes. The data presented here were obtained on two flights made on 23 and 26 Feb, 1979. Conditions for the flights are given in Table 1. Data points are referenced throughout by file number.

File No.	Alt, km	$\bar{u}$, m/s	M	Date
1	3.66	234	0.57	2/23/79
2	3.66	153	0.48	2/23/79
3	3.66	124	0.37	2/23/79
4	3.66	93	0.28	2/23/79
5	8.84	271	0.83	2/26/79
6	11.89	237	0.80	2/26/79

Table I. Flight Conditions.

Expected optical degradation is desired from the present measurements of atmospheric turbulence. The random phase variations can be calcuated from the measured density fluctuations and integral length scale through a total distance by

$$\sigma^2 = 2\ \beta^2\ \overline{\rho'^2}\ l\ L \qquad (11)$$

so that both the fluctuation levels and their scales must be known. The following discussion presents the method for determining them from the measured data.

A typical spectrum of the mass flux and total temperature (from File 1) in the frequency domain is shown in Figure 3. A -5/3

slope is evident as low as 10 Hz and continues into the noise level at about 5 kHz. Since both the total temperature and mass flux fluctuations follow the Kolmogoroff energy cascade, then, through Equations 8 and 10, so will both the velocity and density fluctuations. For the flight speeds shown in Table 1, these frequencies correspond to scales from 10 m to 10 mm. In optical applications, the integral scale of the density fluctuations are of interest and can be obtained easily by integrating the time auto-correlation function of either the mass flux or the total temperature to obtain the integral time scale and then using the mean velocity through the turbulence to calculate the integral spacial scale.

Spacial scales found for the present data are given below. The variation indicated for the 3.66 km data (Files 1-4) results from different values calculated as the flight speed changed by nearly a factor of 2.5. The relatively small variation gives one confidence that accurate scale size measurements can be obtained independent of flight speed. Presently used and conceived optical systems have apertures in the range of 0.5 to 2 meters, so that the relatively large turbulence scale to aperture ratio will produce low frequency rather than high frequency phase aberrations that may be compensated for by use of adaptive optical systems.

Alt, km	l, integral scale, meters
3.66	6.0 ± 5%
8.84	7.1
11.89	10.9

To determine the density fluctuation level, Equation 8 is used with measurements of mass flux and total temperature fluctuations along with their measured cross-correlation coefficient. For the data examined here, indicate that the cross-correlation between mass flux and total temperature fluctuations is essentially zero, so that the complexity of Equation 8 is reduced and the density fluctuations can be calculated:

$$[1+(\gamma-1)M^2]^2 \frac{\overline{\rho'^2}}{\bar{\rho}^2} = [(\gamma-1)M^2]^2 \frac{\overline{(\rho u)'^2}}{\bar{\rho}^2\bar{u}^2} + [(1+\frac{\gamma-1}{2}M^2]^2 \frac{\overline{T_t'^2}}{\bar{T}_t^2} \qquad (12)$$

Fluctuations in mass flux and total temperature were determined from the recorded data filtered at 5 kHz to eliminate noise present in the signals beyond that limit. For the data analyzed here, the primary contribution to density fluctuations is from total temperature fluctuations. Even for the data, for which the Mach number was 0.83, the error in neglecting the mass flux term was only 10%. These findings are similar to those discussed by Levis (Ref. 6), although they may not hold universally. RMS data obtained in the present study are given below:

File No.	$\frac{\langle(\rho u)'\rangle}{\bar{\rho}\bar{u}}$, %	$\frac{\langle T_t'\rangle}{\bar{T}_t}$, %	$\frac{\langle\rho'\rangle}{\bar{\rho}}$, %
1	0.028	0.014	0.014
2	0.026	0.011	0.011
3	0.023	0.0067	0.0067
4	0.025	0.0064	0.0064
5	0.026	0.021	0.019
6	0.021	0.0062	0.0070

With these data one can calculate the expected phase aberrations with Equation 11. The number of waves of distortion per kilometer are given in Table 2 for two wave lengths of interest.

Altitude, km	Waves of Distortion	
	λ = 0.63 μm	λ = 10.6 μm
3.66	2.1 - 4.7	0.12 - 0.28
8.84	3.9	0.23
11.89	1.2	0.07

Table 2. Expected optical distortion over 1 km.

The variation in atmospheric properties with altitude, location and time are evident in the wide range of values shown. Because of the large-scale of the turbulence, on target intensities for 10.6 μm should be near diffraction limited even though λ/4 aberrations are present.

In calculating the velocity fluctuations from Equation 10 and the RMS values given above, it can be seen that up to a 100% error in $\langle u' \rangle / \bar{u}$ could result by neglecting the total temperature term in Equation 10.

SECTION IV

Conclusions

Atmospheric turbulence of scales down to 10 mm have been measured with an airborne system capable of making measurements up to altitudes of 12 km. It is shown that both a heated and unheated wire are required in general to accurately determine either the velocity or density fluctuations. Further, for high speed flight, compressible effects on the instrumentation output must be considered to accurately deduce informaton about the atmosphere. Integral scales of the atmospheric turbulence can be accurately determined independent of flight speed. Typical data obtained to date show a -5/3 spectral decay to scales of 10 to 20 mm.

References

1. Loving, N.V., "Technical and Meteorological Planning to Meet the ALLCAT Program Objectives," in Clear Air Turbulence and Its Detection, edited by Y-H. Pao and A. Goldburg, Plenum Press, NY 1969, pp. 127, 143.

2. MacCready, P.B., Jr., "Turbulence Measurements by Sailplane," J. Geophysical Research, Vol 67, No. 3, March 1962.

3. Thompson, D.W., Coulter, R.L., and Warhaft, Z., "Simultaneous Measurements of Turbulence in the Lower Atmosphere Using Sodar and Aircraft," J. Applied Meteorology, Vol 17, June 1978, pp. 723, 734.

4. Lenschow, D.H., Friehe, C.A., and LaRue, J.C., "The Development of an Airborne Hot-Wire Anemometer System," Fourth Symposium on Meteorological Observations and Instrumentation, April 10-14, 1978, Denver, CO, published by the American Meteorological Society, Boston, MA, pp. 463-466.

5. Rose, W.C., Johnson, D.A. and Otten, L.J., III, "Application of Hot-Wire Anemometry and Laser Velocimetry to In-Flight Measurements of Turbulent Flow Properties," AIAA paper 78-825, 10th Aerodynmaic Testing Conference, San Diego, CA, April 19-21, 1978.

6. Levis, C.A. and Serafin, J.P., Analysis of Aero-Optical Turbulence Measurements, Final report for Contract F29601-78-C-0024, September 1978.

ABBREVIATIONS AND SYMBOLS

L	path length through turbulence
l	correlation length
M	Mach number
p	pressure
T	fluid temperature
u	velocity
β	Gladstone-Dale constant
γ	ratio of specific heats
λ	wave length of radiation
ρ	fluid density
σ	optical phase variance

Superscripts

$( )'$	fluctuation in a quantity
$(\overline{\ })$	time average of a quantity
$\langle\{ \ \} \rangle$	rms of a quantity

Subscripts

t	total or stagnation conditions

Figure 1. USAF Research Aircraft.

Figure 2. Closeup Showing Probe Installation and Sensor.

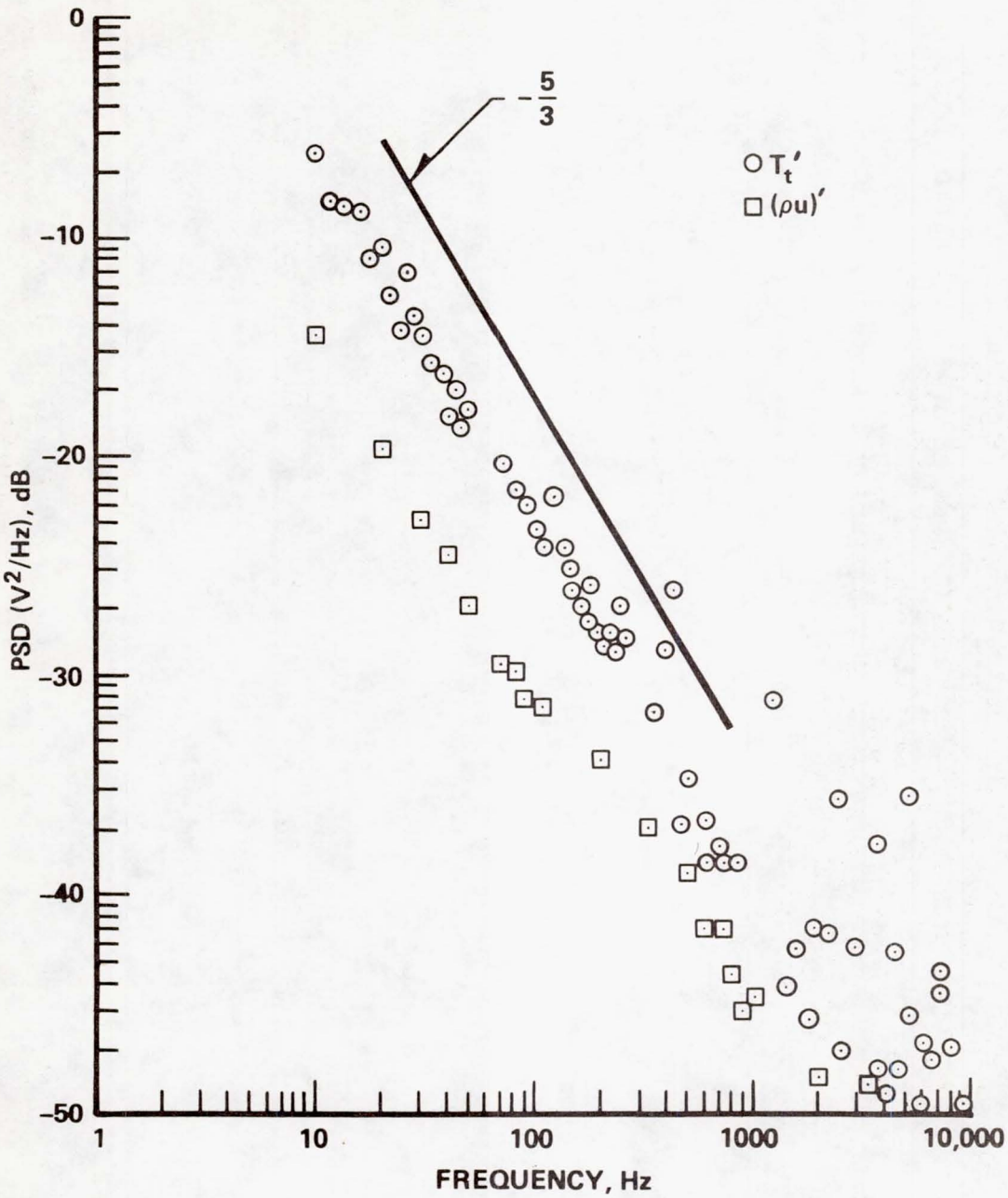

Figure 3. Spectra of Mass Flux and Total Temperature Fluctuations, 3.6 km, M = 0.57, 23 February 1979.

SUMMARY OF AERODYNAMIC VIBRATION EFFECTS ON A.L.L. TURRET

P. MERRITT

L. SHER

Air Force Weapons Laboratory, Kirtland AFB NM

The use of a laser system in an aircraft requires an understanding of the effects of the airborne environment on the laser system. The time averaged intensity of the laser at the target will be reduced if the optical elements of the system are caused to be jittered. The airborne environment provides sources of angular and linear vibrations that cause laser beam jitter. These vibrations can come fom the vehicle itself or, if the optical elements are exposed or vented to the airstream, this can provide a direct torque disturbance on the optical elements. Figure 1 schematically depicts these two main sources of jitter. In the upper figure, the optical element is shown on bearings which give it two degrees of freedom. The mirror would actually be surrounded by a telescope housing which would be rotated to point the beam. When the use of a window is precluded, such as for very high power, the external airstream provides a direct torque excitation to the mirror. In general, for a arbitrary pressure distribution, the torques on the mirror would be

$$M_x(t) = -\iint_A y \; p(x,y,t)dxdy$$

$$M_y(t) = \iint_A x \; p(x,y,t)dxdy$$

If the pressures were constant in space over halves of the mirror, e.g.,

$$p(x,y,t) = p_1(t) \qquad y>0$$

$$p(x,y,t) = p_2(t) \qquad y<0$$

then

$$M_x(t) = 0.08\ D^3\ [p_2(t) - p_1(t)]$$

$$M_y(t) = 0$$

where D is the mirror diameter. The torque is seen to scale with diameter cubed. Given the power and cross spectra of the pressures then the power spectrum of the torque would be

$$\Phi_{Mx}(f) = (.08D^3)^2\ [\Phi_{p_1} + \Phi_{p_2} - 2Re\psi_{p_1p_2}]$$

where Φ denotes a power spectrum and ψ denotes a cross spectrum. For p_1 and p_2 equal but uncorrelated, or perhaps correlated 180° out of phase, one sees that a torque will still result.

The optical system is pointed at the target by using some type of optical tracking system. However the primary mirror, the one disturbed by the pressure fluctuations, is inertially stabilized by using gyroscopes attached to the back of the mirror. A simplified schematic of such a system is shown in Figure 2. If the transfer function from torque, T_q to mirror motion, ε, is calculated it is found to be;

$$(\varepsilon/T_q) = (1/J_m)/(s^2 + K_T/J_m)$$

This transfer function is a constant, $1/K_T$, for low frequencies, and reduces at 40 dB per decade above the corner frequency K_T/J_m. This indicates that the system only rejects low frequencies by the strength of its torquer.

Higher frequency torques are rejected by the inertia of the primary mirror and its structure. The closed loop bandwidth, K_T/J, is typically 100 Hz, therefore the response of the telescope mirror to direct torques may be considered as two frequency regions, from d.c. to K_T/J, and from K_T/J to infinity. The following equations permit us to consider the previous developed PSD expressions based on pressure, to evaluate the mean square error,

$$\bar{\varepsilon}^2 = \int_0^{K_T/J} (\Phi_M K_T^2)\,d\omega \quad \text{for } 2\pi f < K_T/J$$

$$\bar{\varepsilon}^2 = \int_{K_T/J}^{\infty} (\Phi_M/J^2\omega^4)\,d\omega \quad \text{for } 2\pi f > K_T/J$$

The other effect of the flow is the motions of the turret induced by the steady and fluctuating pressure. The motion of the turret can be coupled to the optical elements by several mechanisms which are shown in Figure 3. The motion of the turret in response to the aerodynamically generated torques, T_t, are determined by the inertia of the turret, J_t, and its mounting compliance, K. A mechanical transfer function from torque to angular motion, θ, results in a transfer function of the same form as developed for the mirror motion. Therefore, at low frequencies the motion of the turret is $(\theta/T_t) = (1/K)$

At high frequencies

$$(\theta/T_t) = (1/J\omega^2)$$

The first flights of the Airborne Laser Laboratory (ALL) in the Cycle I test program gave an indication that the optical jitter, ε, varied with the flight dynamic pressure, q_∞, see e.g. Figure 4. Since the net pressure difference either across the mirror or across the turret is the quantity of interest it makes sense that the torque, and thus the jitter will scale with q_∞. Theoretically it, probably makes more sense to use the difference between stagnation pressure P° and static pressure P_∞ as the dependent variable, i.e.,

$$p^\circ - p_\infty = [(p^\circ/p_\infty)-1]\ p_\infty$$

The function p°/p_∞ is a complicated function of Mach number and specific heat. For $M<0.6$, one can approximate the above to within 10% by

$$p^\circ - p_\infty = q_\infty = \tfrac{1}{2}\ \rho_\infty\ V_\infty^2$$

Early tests of a dummy turret with a cavity on a KC-135 in which fluctuating pressures were measured, Reference 1, indicated numerous acoustic resonances and torque levels approaching 2000 inch lbs on the exposed mirror. A comprehensive test series in wind tunnels, reference 2, led to dramatic reductions in the levels of fluctuating torques on the mirror to the order of 50 in lbs by the addition of external fences on the Advanced Pointing and Tracking. In addition, the acoustic resonances were reduced in intensity. In the next flight program of the Airborne Laser Laboratory, Cycle II, the actual pointing and tracking telescope was instrumented with pressure transducers, see Figure 5, which were differenced and suitably scaled for telescope area and moment arm to indicate torque. The results are shown in Figure 6, where the torque spectrum for wind tunnel results and for the airborne measurements are shown. The torque spectra have been normalized by

$$L^6 M^4 P^2 / S$$

Where L - Aperture diameter

M - Mach Number

P - free stream pressure

and

$S = V/L$

Where V - free stream velocity.

The wind tunnel data shown in Figure 6 was obtained using the on gimbal telescope model used for the Large Pointing System test series. An attempt was also made to use the 0.3 scale APT model test results, however poor correlation was obtained. It was discovered that the APT model was not vented internally and thus did not match the actual airborne telescope which is vented to the turret.

The magnitude of the torque measured for the modified flight turret was insignificant in terms of the jitter generated. An attempt to correlate a pressure measurement in the cavity with the jitter of the telescope is shown in Figure 7. Just observing the pressure spectrum and the jitter spectrum, one might be tempted to infer that the pressure spectrum is driving the jitter. However, the coherence spectrum shown at the center shows correlation only at several high frequency spikes. The coherent power between pressure and jitter indicated only about 3 percent of the jitter was correlated with pressure fluctuations. Follow-on tests with a window installed over the cavity yielded essentially the same telescope jitter as the open cavity again verifying the direct aerodynamics torques on the mirror were insignificant.

The Cycle II test series conducted numerous tests to explore the potential variables that influence system jitter. Based on the measurements of fluctuating pressures in the cavity, it was concluded that the vibration of the turret was the main source of jitter excitation. Attempts to correlate jitter with dynamic pressure are shown in Figure 8, which shows a large spread in the data. However by restricting several variables, the correlation of jitter with dynamic pressure, in particular the circled data points, was much more obvious. However a lack of angular instrumentation made it impossible to acquire data during Cycle II to accurately correlate turret vibration with flight parameters such as dynamic pressure and Mach number.

Prior to Cycle III flight testing the Air Force acquired some precision angular displacement transducers to install on the turret. These transducers along with several pressure transducers were installed on a dummy turret in the initial flight tests of the ALL for Cycle III. Further, it was possible to define a series of tests where one flight parameter was varied while holding others fixed. In particular, a series of tests were run where q_∞ was held constant and Mach number changed, and a similar series where the Mach number was held constant and the q_∞ was changed.

The flight tests have yielded some interesting and unexpected results. Figure 9, shows the effect on roll angular vibration when changing q_∞ with Mach held constant. The data indicates that the vibration does change linearly with q_∞ but it also shows a distinct dependency on Mach number. The higher Mach number shows considerably less vibration. The effect is further amplified by referring to Figure 10 which shows the effect of

changing Mach number while holding a constant dynamic pressure. The data shows a nonlinear decrease in vibration with increasing Mach number. The spike in Figure 10 labeled "Shudder experiment" is another interesting aspect of the vibration. The ALL crew had described a strong vibration effect at .51 Mach number. In the data of Figure 10 labeled Mission 5 the pilot attempted to "feel out" the high vibration point and hold it for several seconds. The plotted spike in the data confirms the aircraft "Shudder Area".

It was also possible to analyze the flight test data for frequency content. This data is shown in Figures 11 and 12. The effect of changing q_∞ while holding Mach number constant appears to change the entire level of the PSD with little effect on the frequency content. This is shown as Figure 11. However, when the Mach number was lowered, a distinct increase in low frequency vibration, below 20 Hz was obvious, see Figure 12. The low Mach numbers must change the flow pattern over the turret in such a way that the airflow imparts a much stronger driving torque to the APT turret.

Pressure measurements on the external pressures at 4 points on the dummy turret were taken concurrent with the vibration data. Figure 13 is included to show the pressure from a transducer labeled R103 which was at the vertical center of the turret and 50 degrees CCW from the leading edge and transducer R104 which was at vertical center and aft. It is interesting to see that the pressure measurements follow the same trend as the vibration measurements. Notice that the 50° transducer shows more variation the PSD at various Mach numbers, but the aft transducer contains considerable more energy in the PSD. The RMS level plots of the transducers were

similar in shape to the angular vibration shown in Figure 10.

The data now available well documents the base motion response of the turret to air loads during flight. This data can be used to select flight conditions for this aircraft that will yield low base motion. However the data does not provide an understanding of the physics of the aerodynamic phenomena. If the vibration is to be reduced by using different fairings or if this data is to be used to design a future turret, the physical basis of the airflow needs to be understood. Since this paper has pointed out that turret base motion is the major driving source for jitter, it would be most beneficial to pursue this analytical area. Probably wind tunnel tests are not the correct approach since the problem requires convolving structural design of the turret with aerodynamic loading. However, a large amount of flight data is available, including pressures, angular, and linear vibration data.

In conclusion, this paper has summarized the effects of the airborne environment on a pointing and tracking system using a turret external to an aircraft. The data has covered a series of flight tests and a span of seven years. The two major airborne effects were shown to be direct pressure loading of optical elements and vibrations of the entire turret. The direct optical loading problem has been minimized by clever fence designs for the turret, however the turret vibration problem is a poorly understood area. A large amount of data has recently been obtained to document the turret vibration but a physical understanding of the problem is yet to be attempted.

REFERENCES

1. "Estimation of Steady and Unsteady Torques Acting on a Large Cavity Fairing into the Airstream," GD Convair Div, Fort Worth, TX, Report No. F2A-453, September 1971.

2. Van Kuren, James T., et al, "Acoustic Phenomena of Open Cavity Airborne Cassegrainian Telescopes", AIAA paper No. 74-196, AIAA 12th Aerospace Science Meeting, Jan 30, 1974.

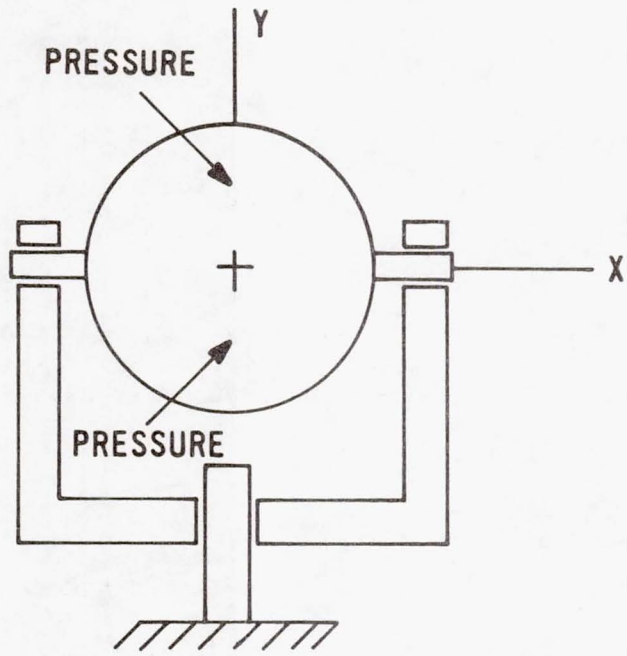

DIRECT LOADING OF OPTICAL ELEMENT

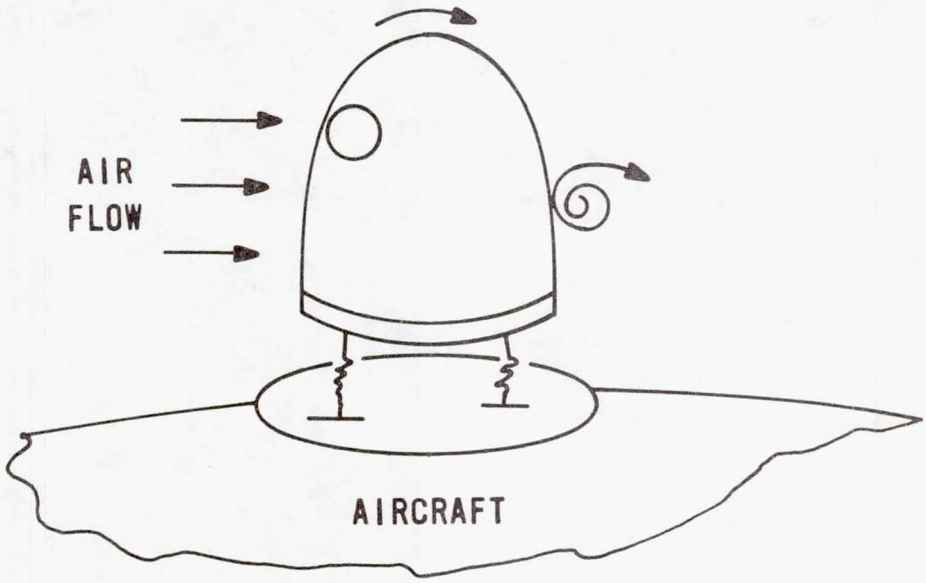

FLOW INDUCED TURRET VIBRATION

Figure 1. Sources of Aerodynamic Jitter.

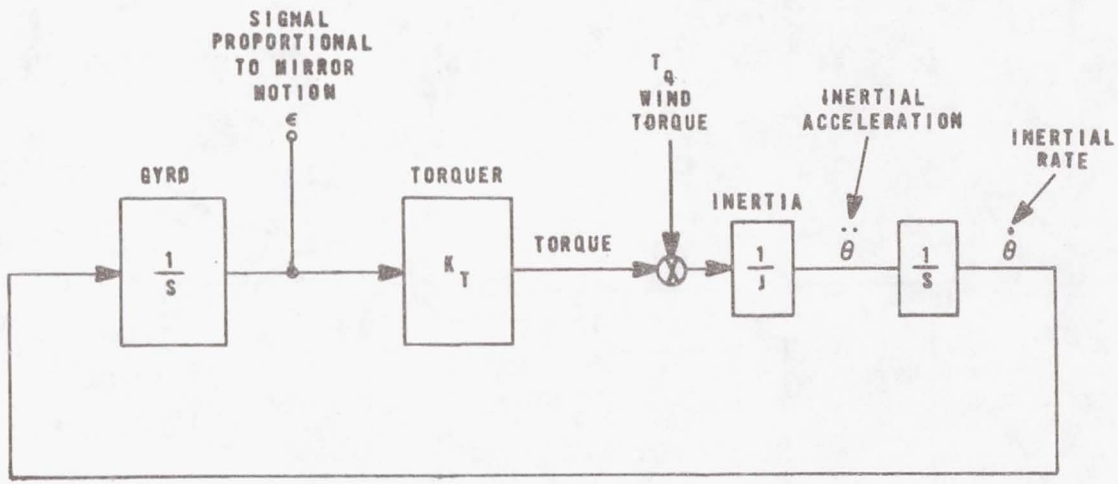

Figure 2. Servosystem Diagram for Gyro Stabilized Pointing Mirror.

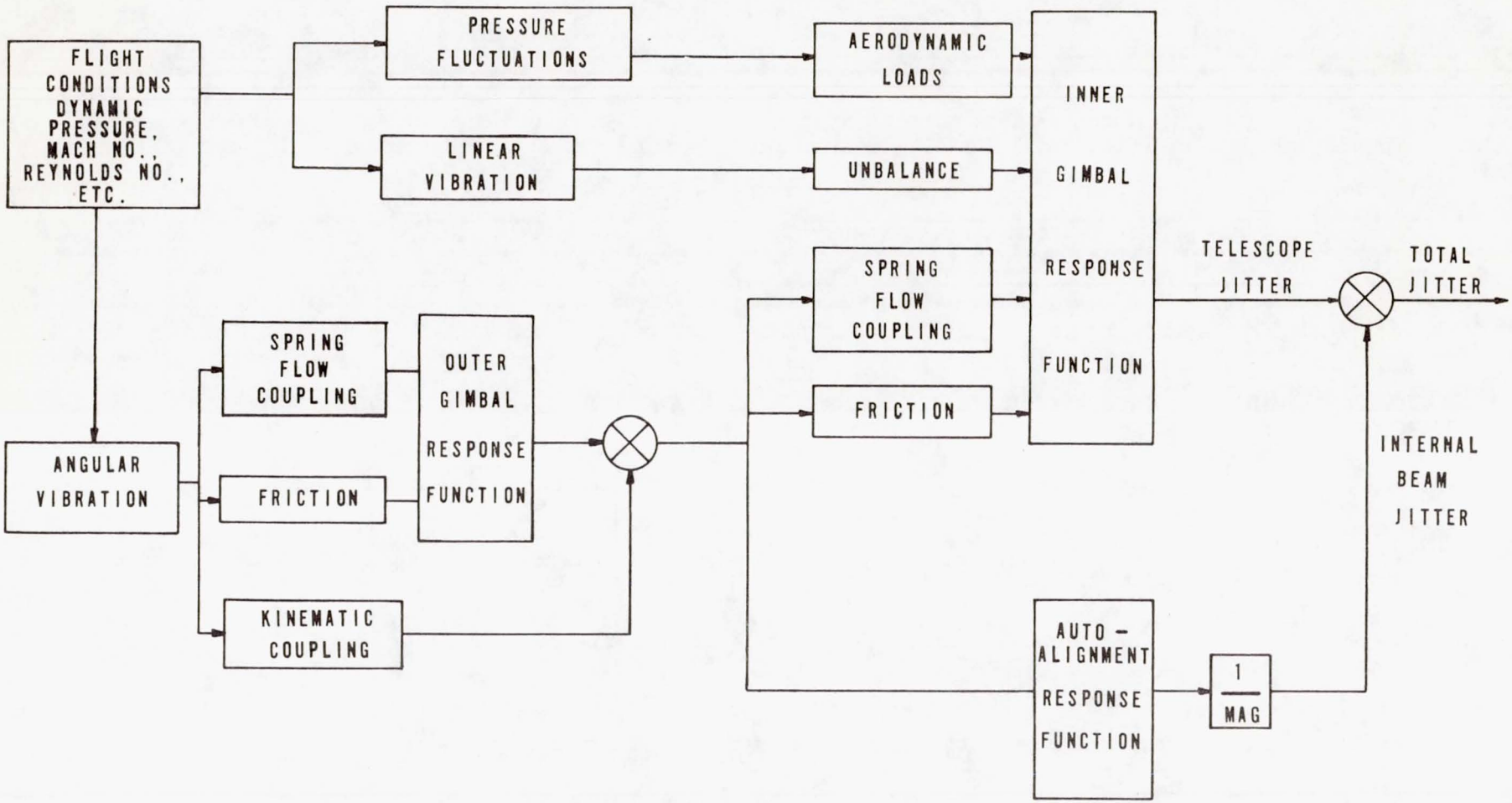

Figure 3. Coupling Paths Between Vibration and Beam Jitter.

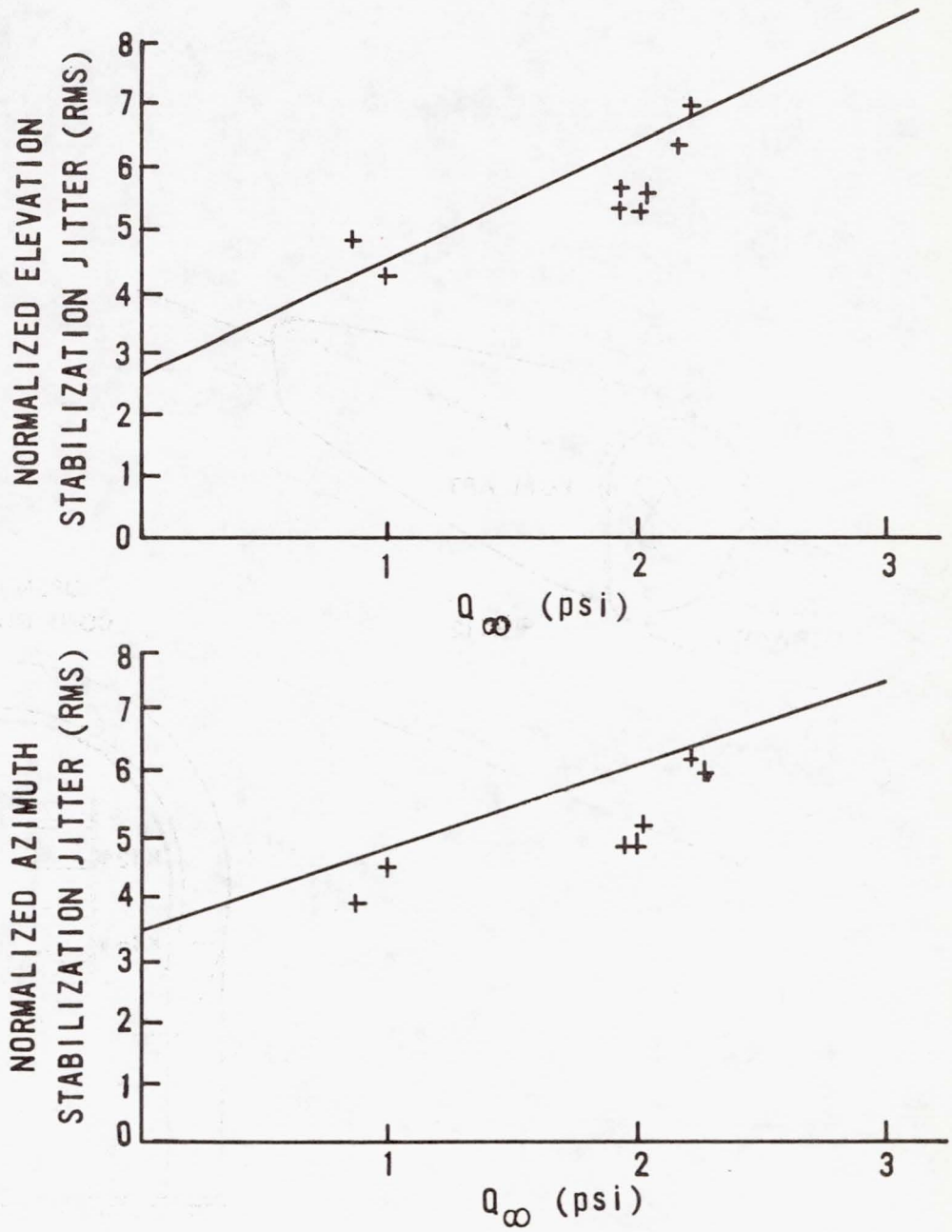

Figure 4. Stabilization Jitter from Cycle I Versus Dynamic Pressure.

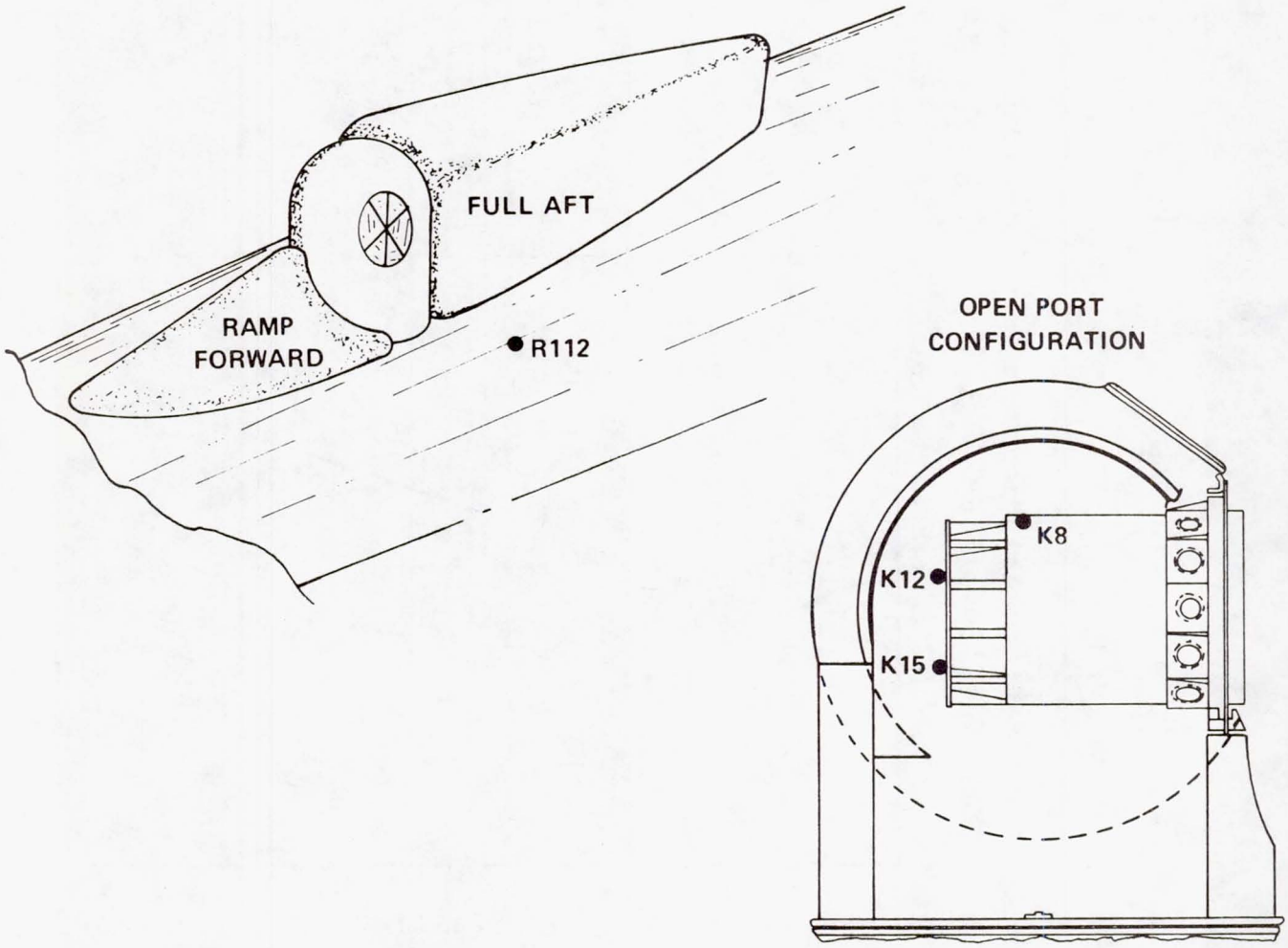

Figure 5. Location of Pressure Transducers for Cycle II Flight Tests.

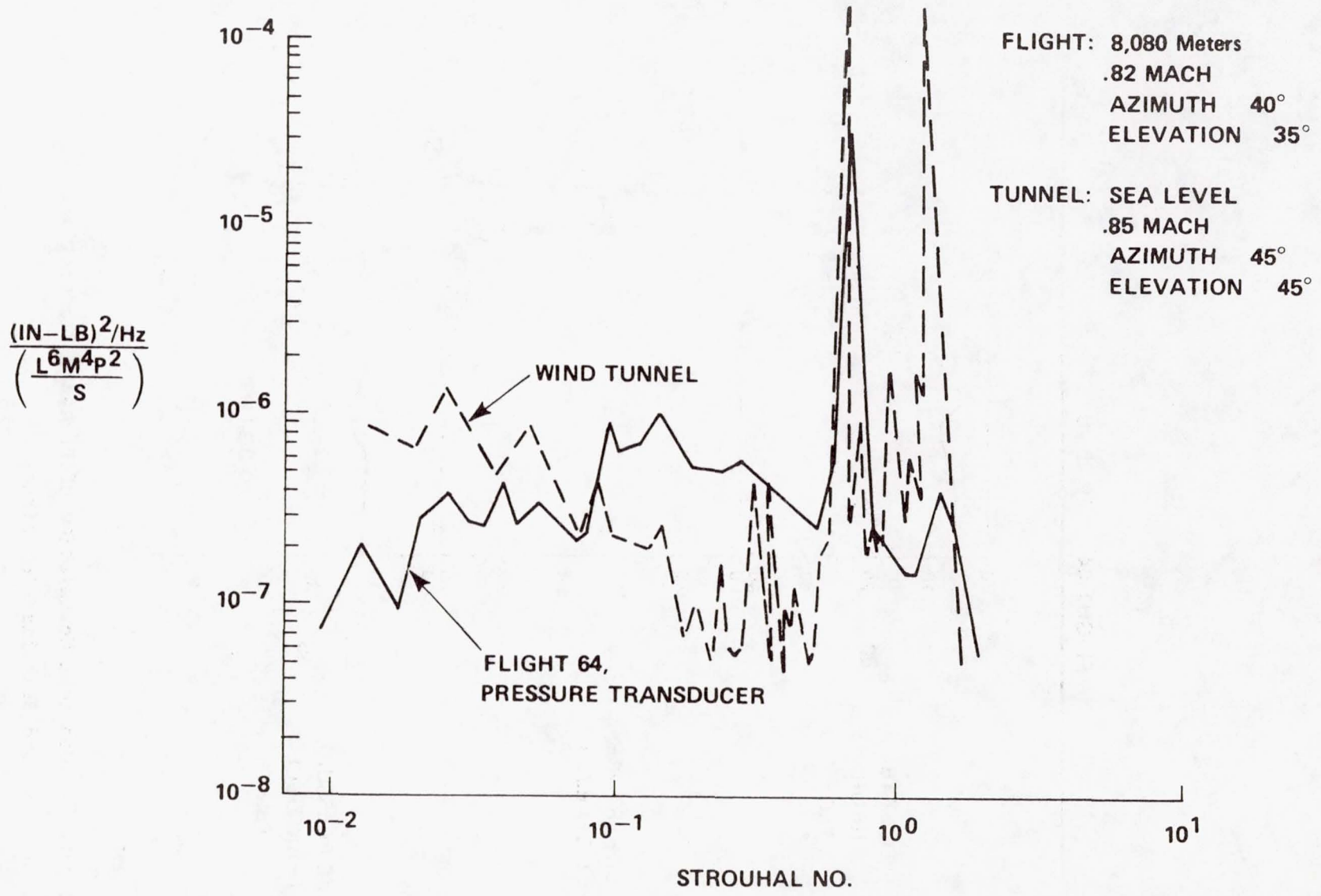

Figure 6. Correlation of Wind Tunnel and Flight Test Torques.

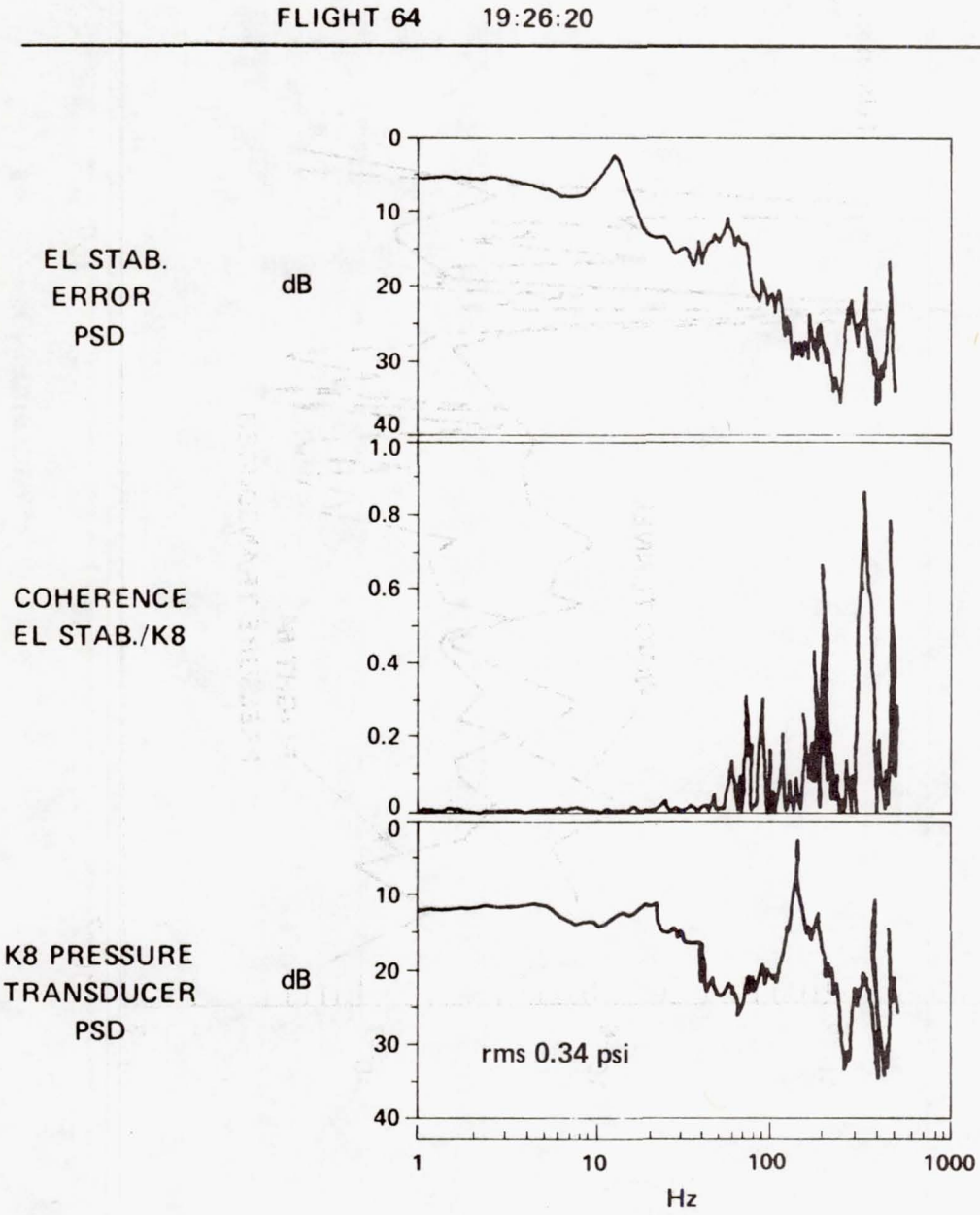

Figure 7. Coherent Correlation of Pressure Fluctuations and Stabilization Jitter.

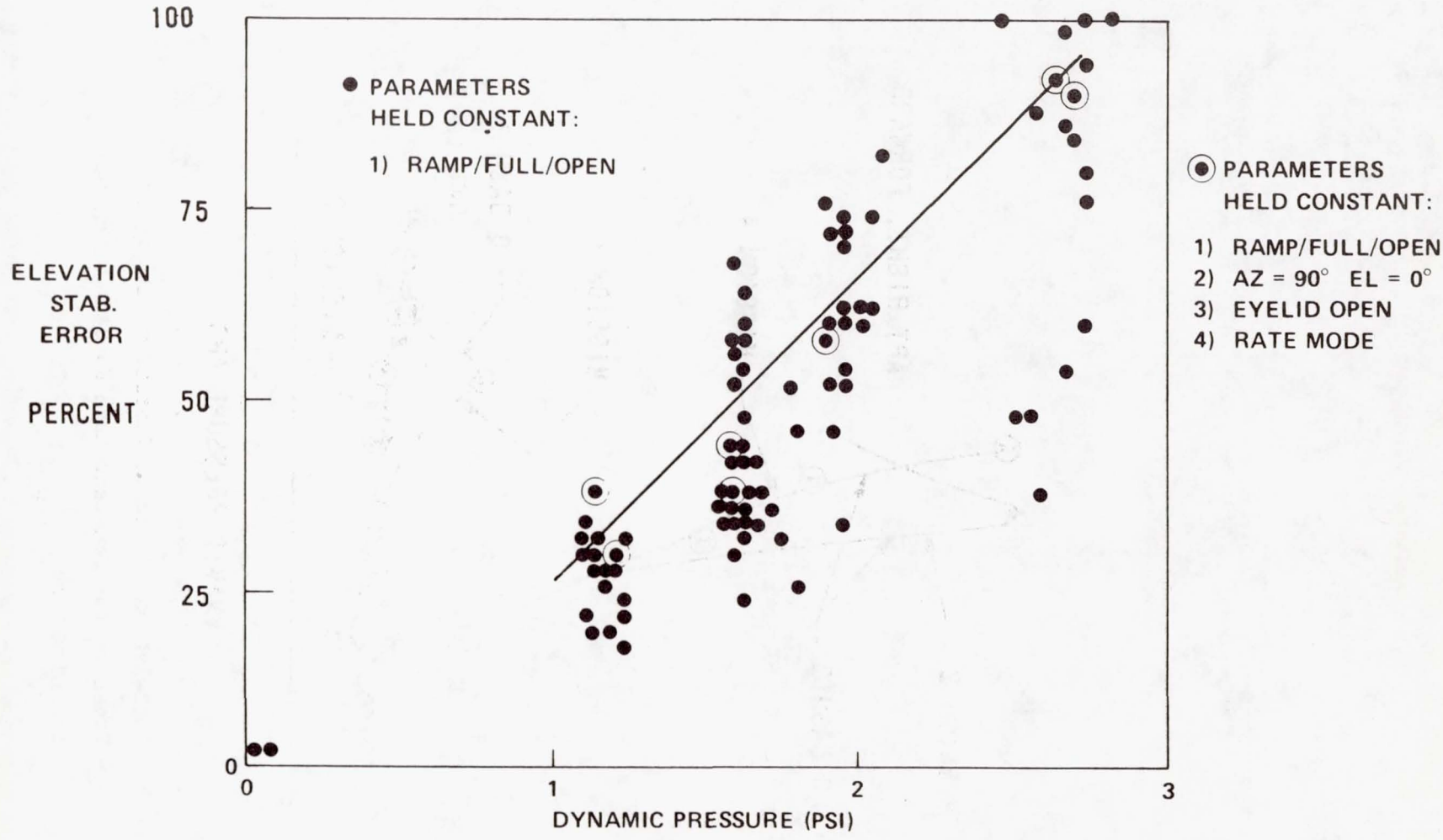

Figure 8. Correlation of Cycle II Stabilization Jitter With Dynamic Pressure.

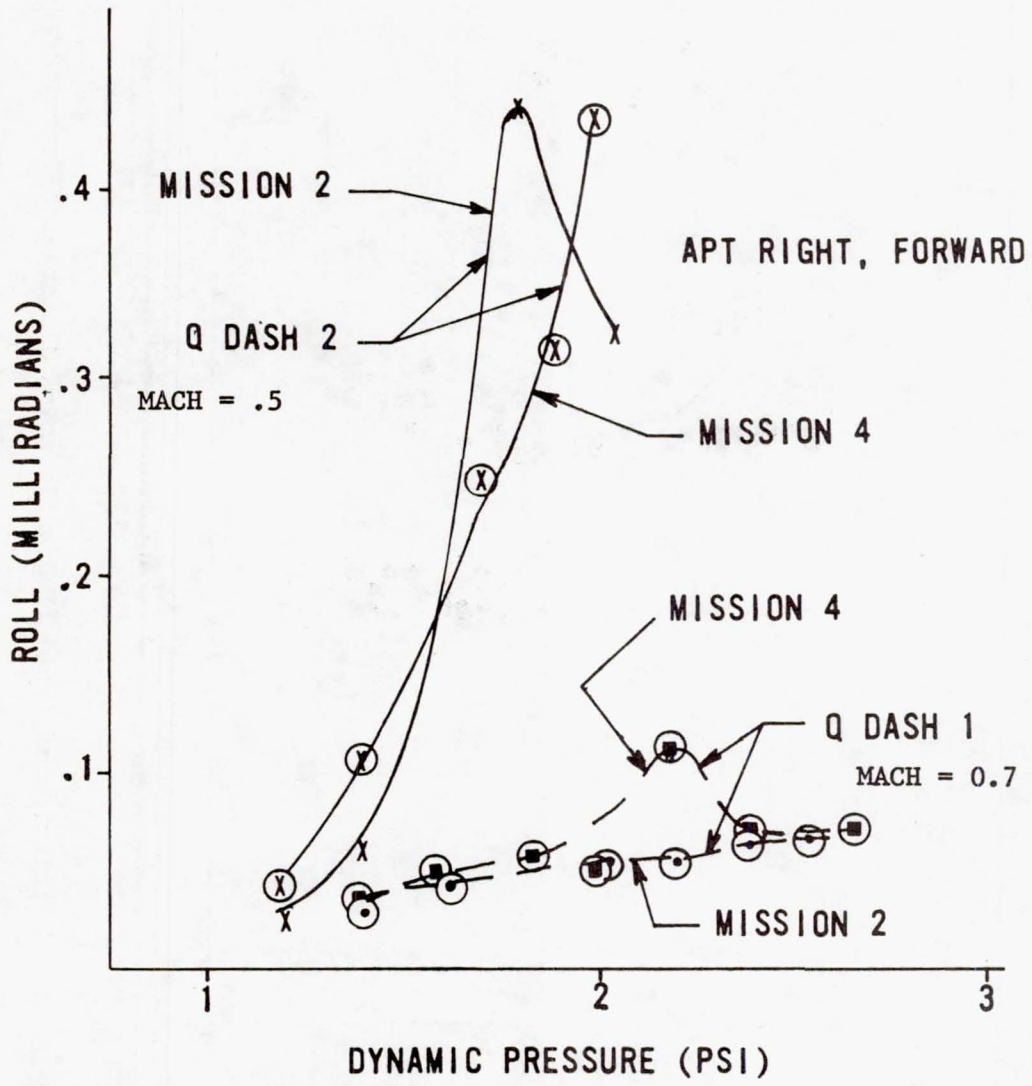

Figure 9. Correlation of Turret Vibration With Dynamic Pressure for Constant Mach Number (Vibration levels are rms).

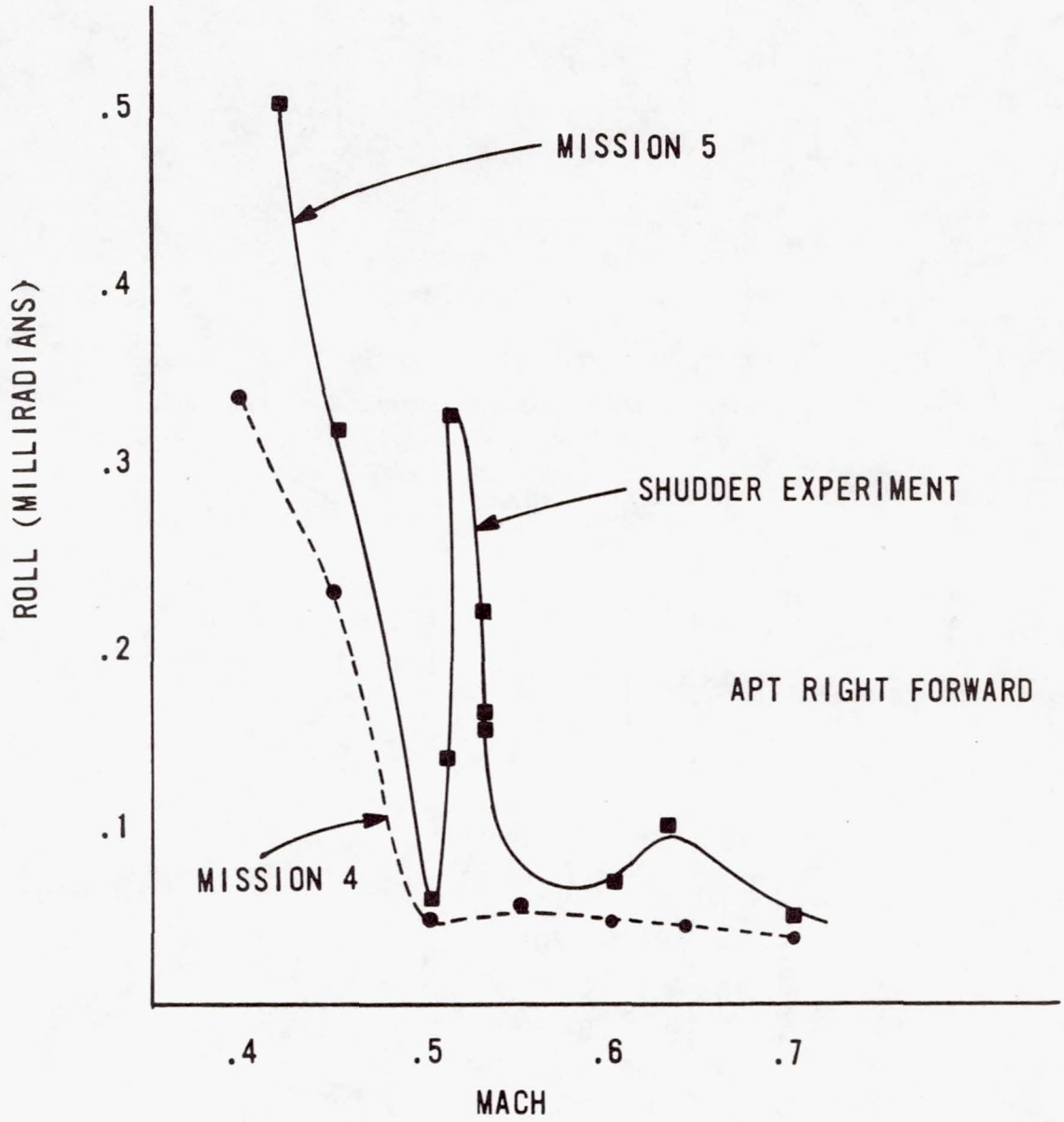

Figure 10. **Correlation of Turret Vibration With Mach Number, Dynamic Pressure Constant at 1.25 psi** (Vibration levels are rms).

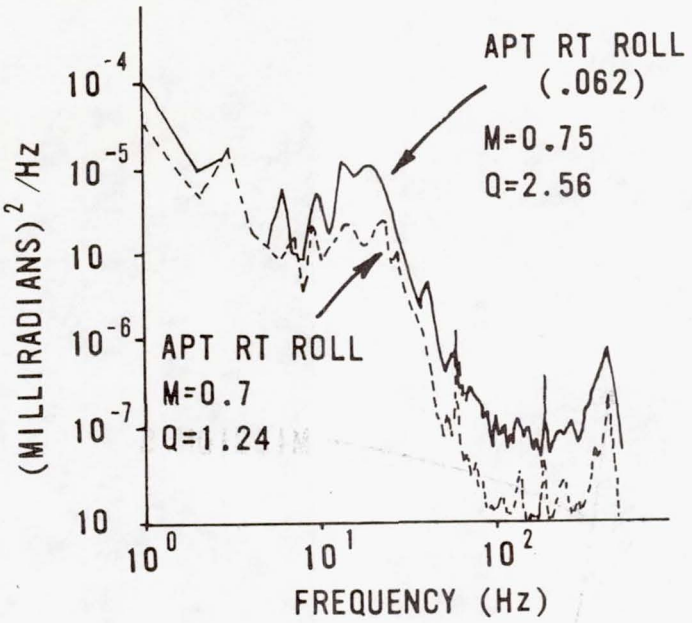

Figure 11. PSD's of Turret Vibration for Two Different Dynamic Pressures, Constant Mach.

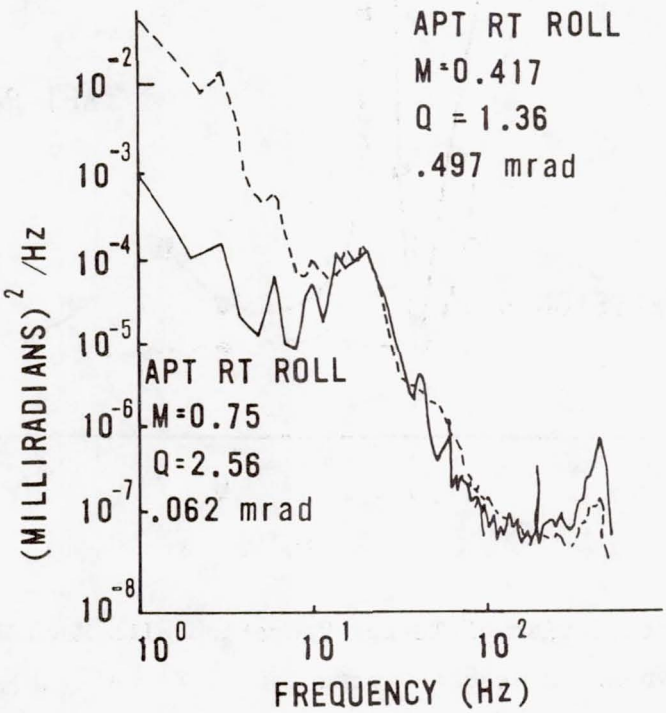

Figure 12. PSD's of Turret Vibration for Changes in Mach Number and Dynamic Pressure.

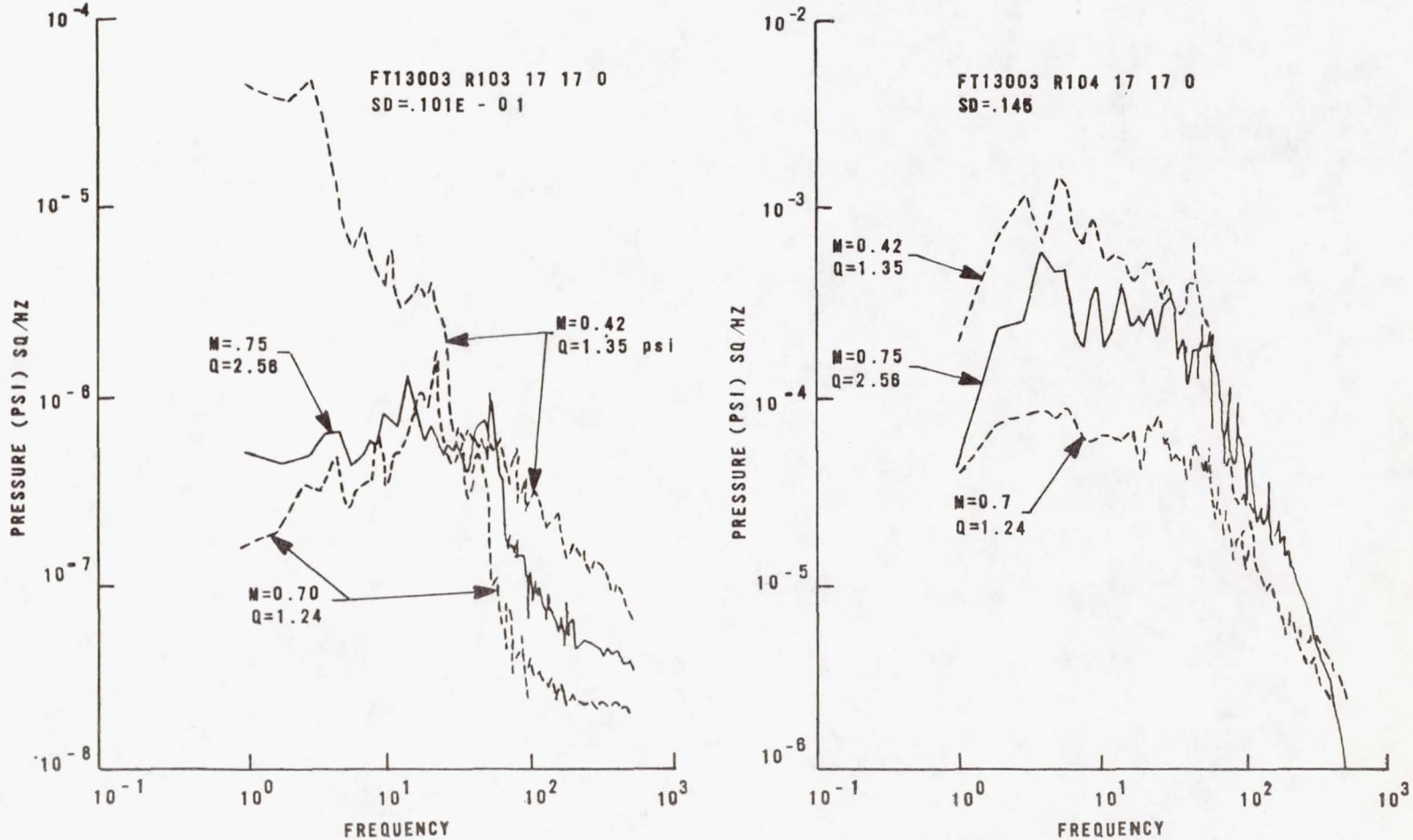

Figure 13. PSD Analyses of Pressure Transducers on Exterior Surface of Dummy Turret.

FLOW VISUALIZATION TECHNIQUES

IN THE AIRBORNE LASER LABORATORY PROGRAM

by

R. E. WALTERICK
J. T. VAN KUREN

I INTRODUCTION

The design and testing of a three-dimensional structure, such as a turret/fairing assembly for laser applications, is a complex empirical problem. The attendant flow field is characterized by large scale turbulent structures, which are difficult to map without some form of flow visualization.

Toward this end, wind tunnel testing has been done in the Airborne Laser Laboratory (A.L.L.) program, using flow visualization techniques. The techniques used have included the methods of tufting, encapsulated liquid crystals, oil flow, sublimation and schlieren and shadowgraph photography.

The results have been directly applied to the design of fairing shapes for minimum drag and reduced turret buffet. In addition, the results are of primary importance to the study of light propagation paths in the near flow field of the turret cavity. Depending on the cavity azimuth and elevation angles this can involve a propagation path through shock patterns, separated flow regions, shear layers, or a combination of all three.

Therefore, the flow in the vicinity of the turret is an important factor for consideration in the design of suitable turret/fairing or aero-optic assemblies.

This presentation is in chronological order of wind tunnel tests. The different methods of flow visualization for each test are listed and discussed based on accompanying photographic figures.

SECTION II

RESULTS AND DISCUSSION

a. The first wind tunnel test covered in this presentation was termed the "Transonic Ten Pin Phase I Test" conducted in the Air Force Flight Dynamics Laboratory/Trisonic Gasdynamics Facility (hereafter referred to as AFFDL/TGF) from September to December, 1971.[1]

The flow visualization techniques used consisted of tufting and the use of encapsulated liquid crystal. Tuft results (Fig. 1) for Mach numbers (M_∞) of 0.55 and 0.60 indicate a large turbulent wake behind the on-gimbal turret, extending downstream beyond the right hand edge of the photographs. The tufts on the nose of the model are lying flat and unperturbed indicating a region of steady attached flow. Those farther downstream and not within the wake region are in unsteady motion indicative of a turbulent boundary layer.

The use of encapsulated liquid crystals (temperature sensitive material) to detect boundary layer transition and regions of high heat transfer (turbulent flows) is shown in figure 2. Warmer temperatures are revealed by blue-green color variations and cooler temperatures by red shades. A grit strip was applied to the nose of this particular model and existence of the resultant turbulent boundary layer is shown by the blue-green shades of the strips.

b. The next test covered was referred to as the "AMES I Test" conducted in the NASA Ames Research Center 14 ft wind tunnel during January and February, 1972.[2]

A shadowgraph is shown in Figure 3. The view is looking down on the turret with the turret cavity oriented 120 degrees downstream from the wind axis. A multiple shock system is apparent on the turret at an azimuth

angle of 80 degrees. The formation of this shock system is dependent on the cavity azimuth angle (Fig. 4).

c. Now we turn to a different test and a lesser practiced form of flow visualization. The test was called "Transonic Ten Pin Phase II" and was run in the AFFDL/TGF during May through August, 1972.[3] The flow visualization method used was sublimation of freon crystals. A timed sequence of photographs (Fig. 5) taken of an on-gimbal turret on a flat plate shows the areas where higher heat transfer rates occur. By definition these areas include the characteristic vortices on the turret and those shed from the turret/flat plate intersection.

Included in the flow visualization techniques for this test were oil flow and schlieren photography. Figure 6 is a schlieren photograph of an on-gimbal turret on simulated aircraft fuselage at $M_\infty = 0.90$. Due to the large model frontal area to test section area the flow is choked as evidenced by the strong shocks on the model nose and on the aft section of the model. Also evident in this schlieren are the turret turbulent wake and the buildup of the fuselage boundary layer.

The same configuration at the lower Mach number of 0.75 is shown in Figure 7 along with an oil flow at the same conditions. The flow features discussed in the last figure are still there only the shocks are weaker. The turret shock and resultant separation is confirmed by the oil flow which abruptly ends at mid turret. Several vortices on the turret appear as well as the large vortex behind the turret. This large vortex is just one of a pair of counter-rotating vortices that exist behind the turret. As will be seen later this vortex pair rapidly gives way to fully turbulent flow within three turret diameters downstream of the turret.

d. The technique of spraying oil on a model, as opposed to painting, was used at the Air Force Academy's Transonic Wind Tunnel during September, 1972.[4] The objective of this test was to develop minimum drag fairings. Oil flow visualization was used to map separated flow regions which contribute to the overall drag of the configuration. The fairing designated VK-6 (Fig. 8) shows some separation at the rear of the fairing as with all aft fairing designs. The aft portion of the turret is also in separated flow as is again the case with most turret/fairing assemblies.

e. Another entry into the Ames 14 ft wind tunnel with the same turret was termed the "Ames II Test" conducted from October to November, 1972. In this test the visualization technique of oil flow was applied. Figure 9 shows a turret/fairing combination designed by General Dynamics referred to as the full forward and partial aft fairing. The fence apparatus on the full forward portion of the fairing was designed to produce fully turbulent flow over the turret and eliminate adverse acoustic phenomena within the turret cavity. The oil was applied by a spray technique which resulted in a uniform "speckling" of the model surface. Hence, any separated flow regions would remain speckled and those of attached flow would streak. As can be seen the entire cutout region is in separated flow except for a small portion of the turret crown. Otherwise flow on the fairing is attached.

An AFFDL design (Fig. 10) named the FDL T-2 fairing consisting of a turret with rear fairing only was also tested. Again the cutout region (this time symmetrical) is in separated flow. Flow on the turret itself separates at mid turret. As seen in the previous shadowgraph a shock is located in this region. Therefore we can attribute flow separation to a shock-boundary layer interaction.

f. The Air Force Academy was used in January, 1976 for testing of a different fairing concept now being flown on the A.L.L. KC-135 aircraft (Fig. 11). This involved a fairing designed with simple geometric shapes that was both higher and wider than the turret irself. The objective behind this was to obtain a more definite flow reattachment after separation from the turret. The reattachment point now occurs within the cutout region between the turret and fairing. It is interesting to note the effect that turret cavity orientation has on the reattachment point. On the cavity side reattachment is delayed, while on the non-cavity side reattachment is early. Also evident from this figure are the characteristic separation at the fairing rear as well as the diverging wake of the turret/fairing assembly.

g. Returning to the NASA Ames 14 ft wind tunnel for further A.L.L. Cycle III/IV tests during October, 1976 we see the use of tufts on a 3/10ths scale model mounted to a flat plate (Fig. 12).[5] The unsteady flow in the cutout region is evident from the blurred images of the tufts, indicating several oscillations of the tufts within the camera exposure time setting. The flow is attached and smooth further back on the fairing. A composite sketch (Fig. 13) of two photographs reveals the attached flow on the rear of the fairing and on the forward portion of the turret.

h. In December of 1977 the full scale on-gimbal turret plus Cycle III/IV fairing was flight tested at Edwards Flight Test Center in California. Flow visualization consisted of tufting the turret, fairing and a large portion of the fuselage.[6] Photographs (Fig. 14) were then taken from a chase plane. These reveal a significant region of unsteady flow in the turret/fairing cutout. The tufts in this region have either been removed or frayed due to the violent unsteady flow.

In 1978 during a flight from Kirtland AFB, New Mexico to Wright-Patterson AFB, Ohio some oil flow studies were performed on the turret/fairing assembly (Fig. 15). The flow patterns correspond well with small scale oil flows. However, flow details are not apparent due to the higher viscosity oil used and its sparse application. A closeup of the cutout region (Fig. 16) shows attachment only one turret diameter downstream from the fairing leading edge.

i. The A.L.L. Cycle III/IV fairing was used in conjunction with a similar on-gimbal turret in a test in support of the B-52 Short Range Applied Technology (SRAT) program. The test was conducted during August-September, 1978 in the AFFDL/TGF.[7] Oil flow studies were made with the turret/fairing assembly mounted just upstream of the large vertical stabilizer (Fig. 17). Flow patterns on the turret and fairing are similar to previous ones. The only observable differences are a spreading of the turret/fairing wake and larger flow separation at the rear of the fairing/fuselage juncture.

j. Finally a test was run from April to May, 1979 in the AFFDL/TGF in support of the Advanced Airborne Demonstrator (AAD) program.[8] Flow visualization was by oil and detailed photographs were obtained. An interesting look at the flow about an on-gimbal turret mounted to fuselage (Fig. 18a) shows the double vortex pattern behind the turret. The turret cavity is at 60 degrees azimuth to the wind axis, hence the downstream location of the lower vortex member. Separation on the turret is distinct as well as the wake formation and spreading. The coelostat turret (Fig. 18b) exhibits the same flow patterns except for the location of the vortex pair on the turret itself and a less divergent wake.

The coelostat turret plus an aft fairing (Fig. 19a) with cutout region and small radius leading edges show the retention of the vortex pair. In

addition flow separation off of the leading edges and at the rear of the fairing exists. Partially filling the cutout region (Fig. 19b) and increasing the radii of the leading edges eliminates flow separation. However, there still is separation at the fairing trailing edge.

III CONCLUSION

Although all six methods of flow visualization have been used in the A.L.L. wind tunnel testing program it is perhaps easy to state that the most useful, in terms of the amount of information gained as well as the minute flow details revealed, have been the oil flow and schlieren photography. Tuft studies are helpful but too coarse to reveal the small detail of any large scale structures. Their use should be restricted to determining separated flow regions and unsteady flow regions.

Encapsulated liquid crystal use should probably be restricted to determination of transition location and shock location.

Sublimation techniques, again being of a coarse nature, are best used to reveal the location of regions of high heat transfer as in vortices.

Shadowgraph photography produces results identical to schlieren photography but its application is more restricted than that of schlieren.

Finally oil flow and schlieren photography are easy methods to apply. Large quantities of data can be collected by these methods and the flow details are exceptionally clear.

REFERENCES

1. Van Kuren, J.T. and Golden, W.J. "Transonic Ten Pin Test Phase I - Basic Flow Studies and Preliminary Propagation Results, "AFFDL-TM-75-87-FX, December, 1972 revised June, 1975.

2. Van Kuren, J.T. and Otten, L.J., "Acoustic Phenomena of Open Cavity Airborne Cassegrainian Telescopes, "AFFDL-TM-73-54-FX, May, 1973.

3. Van Kuren, J.T. and Conner, W.R., "Transonic Ten-Pin Test Phase II-Configuration Studies and Open Port Pressure Fluctuations, "AFFDL-TM-73-159-FXM, September, 1972.

4. Van Kuren, J.T. and Conner, W.R.,"Fairing Design for Fuselage Mounted Turret in Transonic Flow, "AFFDL-TM-73-115-FXM, September, 1973.

5. Van Kuren, J.T., Unpublished Data.

6. Otten, L.J., Unpublished Data.

7. Thomas, J.P., "Test of Turret/Fairing Configurations for the B-52 SRAT Program", AFFDL-TM-FXM-79-21, February, 1979.

8. Walterick, R.E., Unpublished Data.

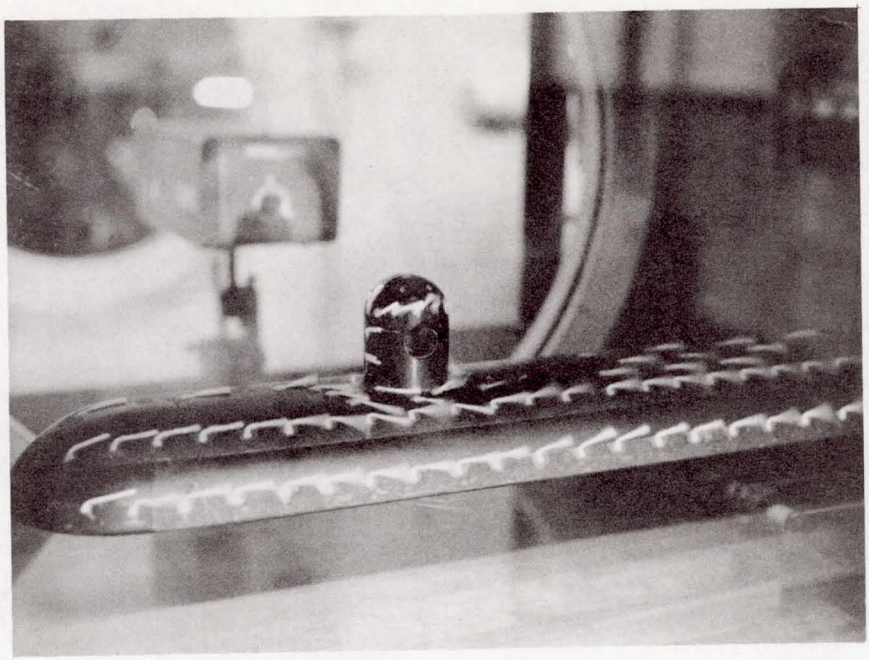

$M_\infty = 0.55$

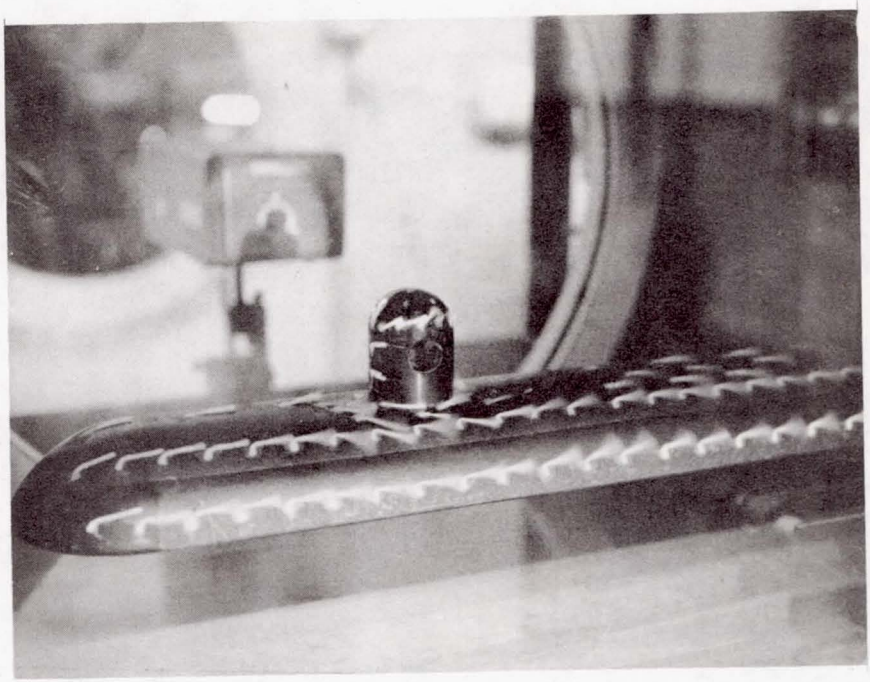

$M_\infty = 0.60$

FIGURE 1
ON-GIMBAL TURRET TUFT FLOW

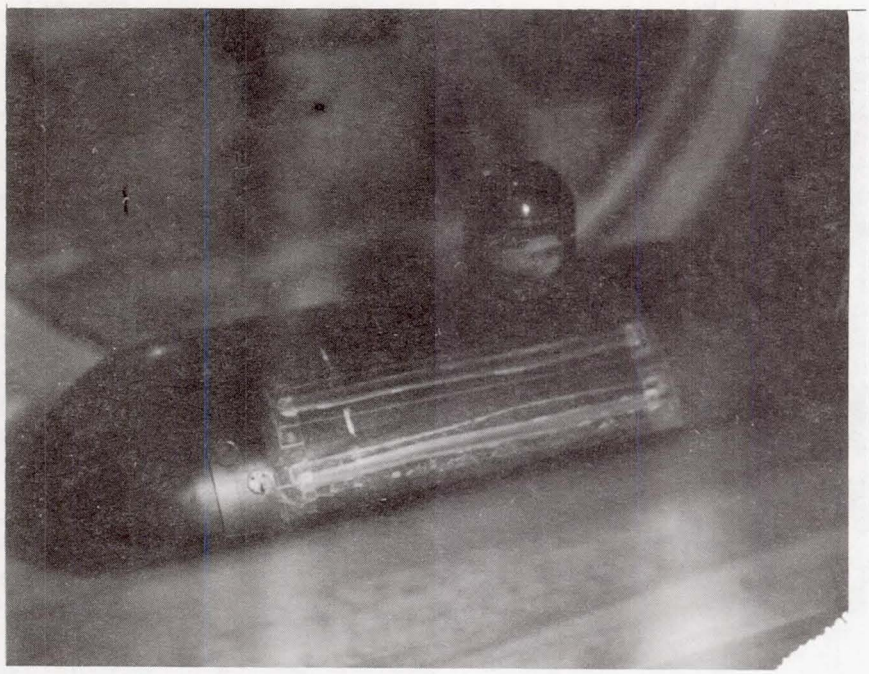

$M_\infty = 0.55$

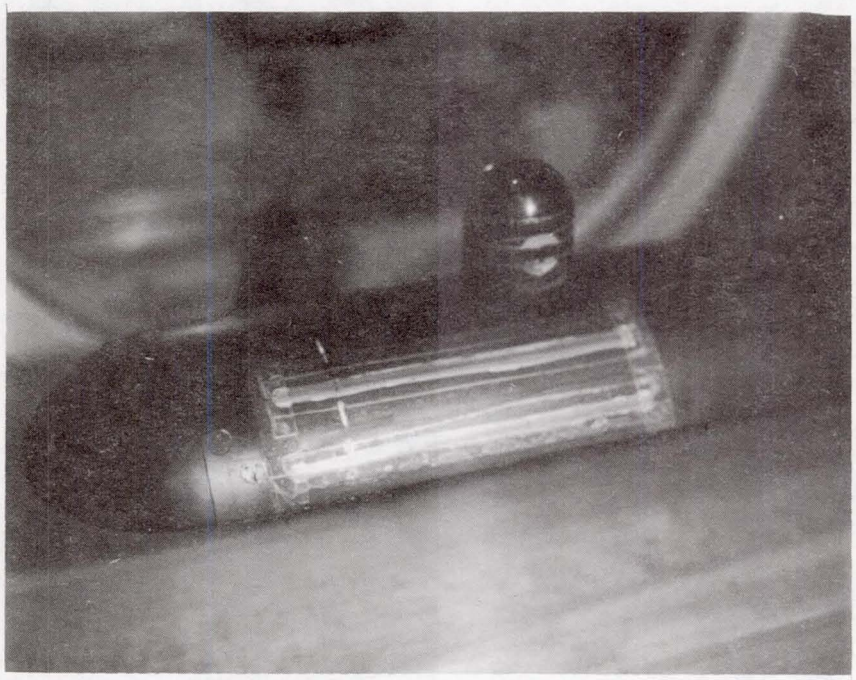

$M_\infty = 0.65$

FIGURE 2
ON-GIMBAL TURRET LIQUID CRYSTAL RESULTS

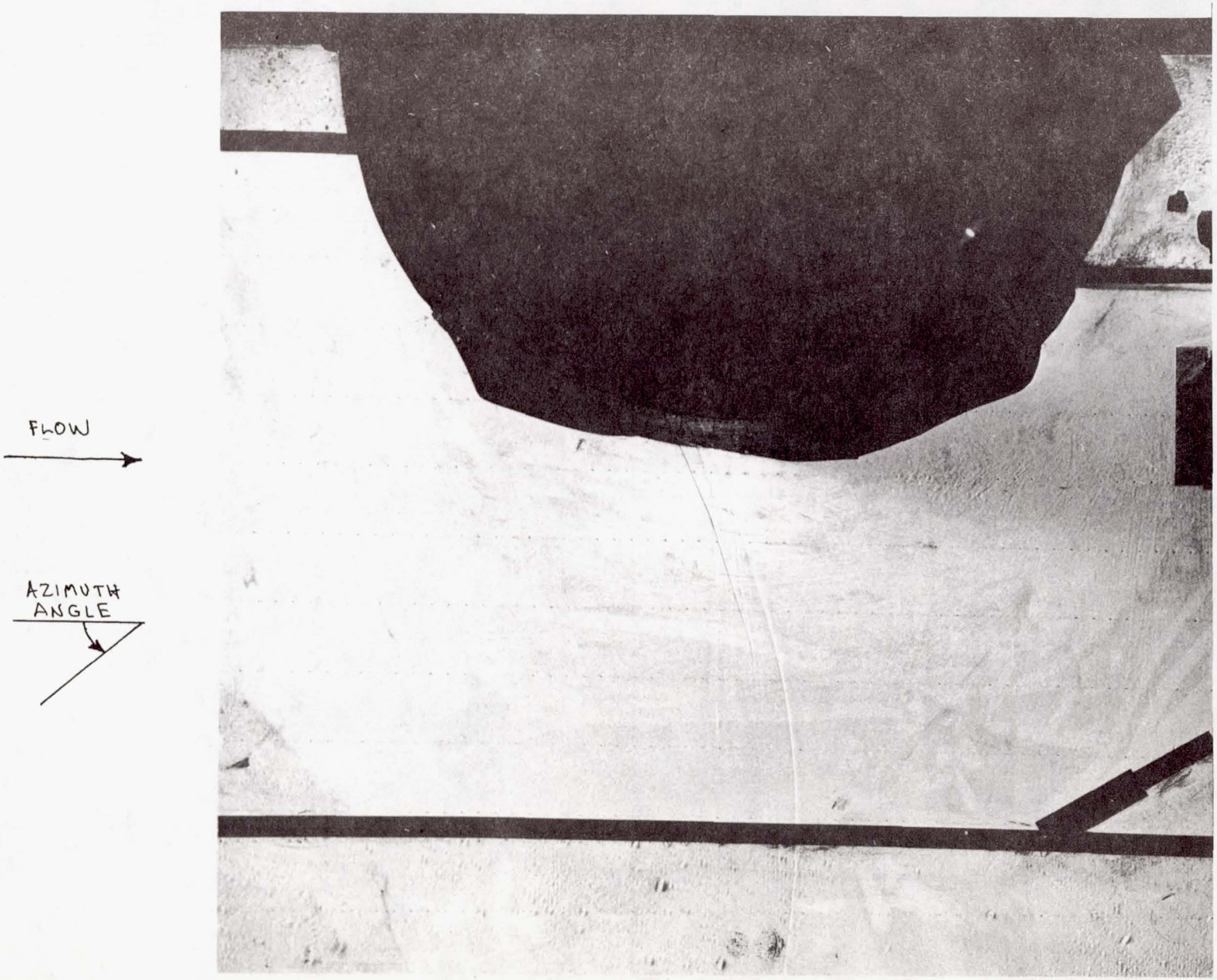

FIGURE 3
ON-GIMBAL TURRET SHOCK PATTERN, $M_\infty = 0.75$

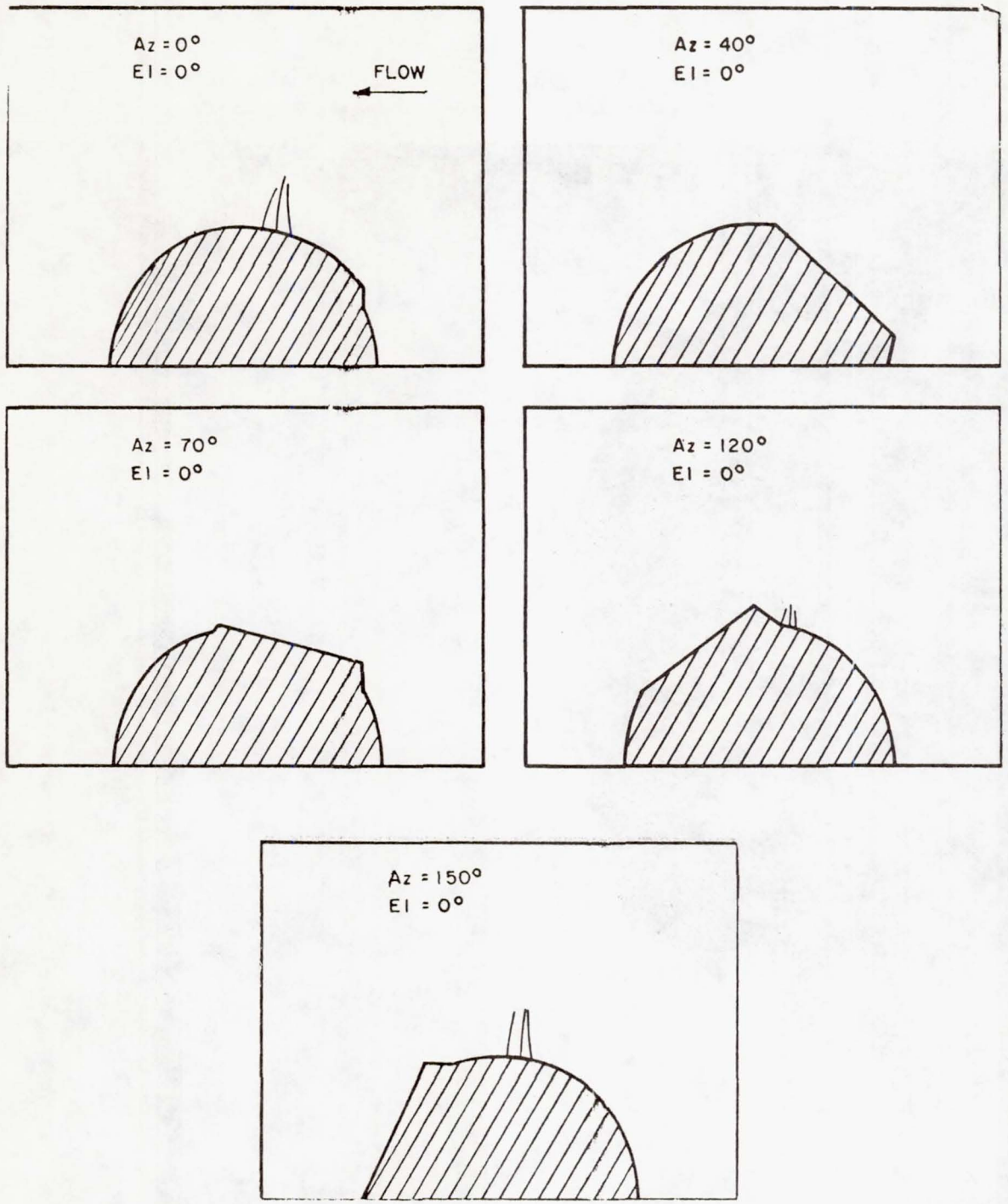

FIGURE 4

ON-GIMBAL TURRET SHOCK PATTERN
VARIATION WITH AZIMUTH ANGLE, $M_\infty = 0.75$

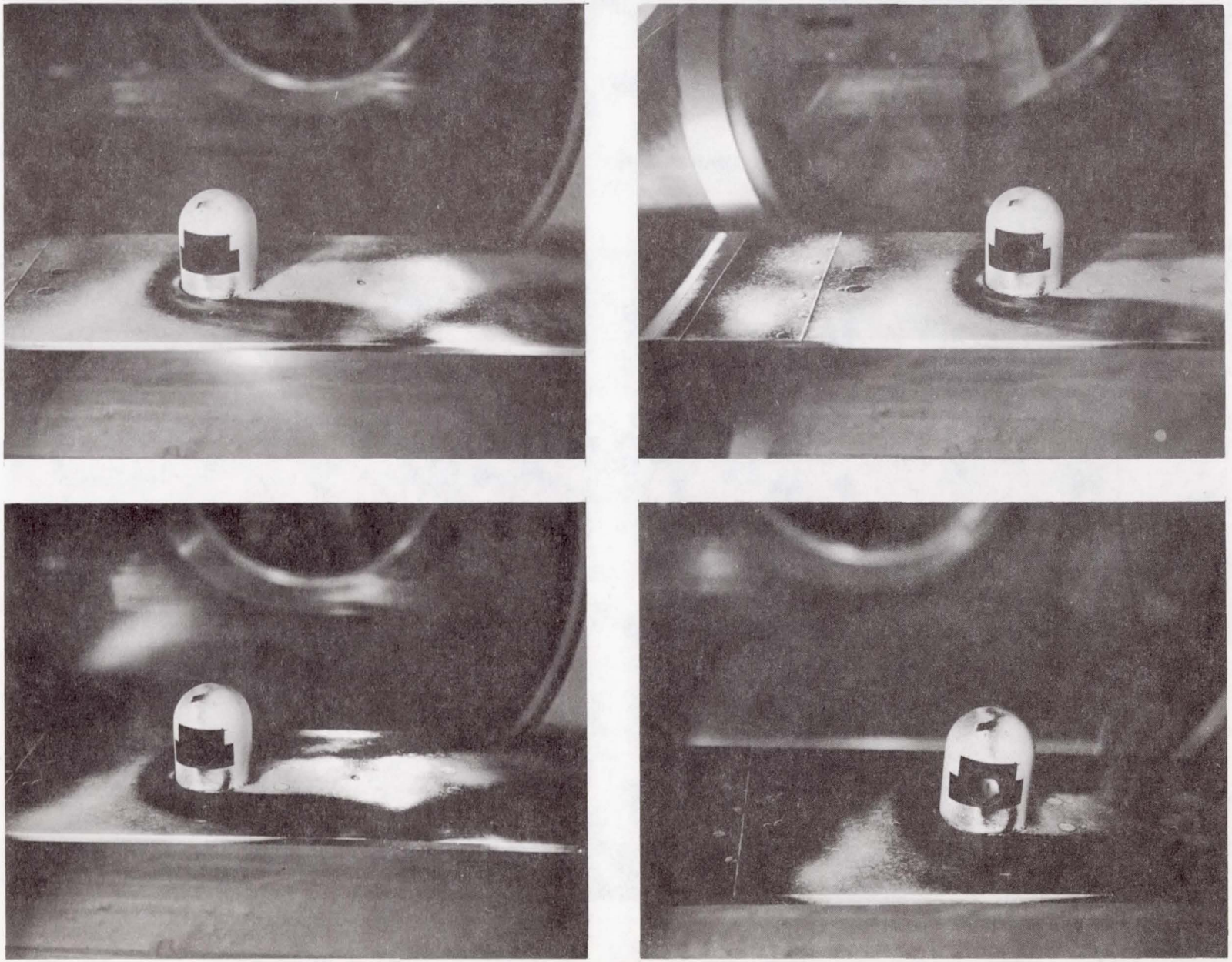

FIGURE 5

ON-GIMBAL TURRET SUBLIMATION, $M_\infty = 0.75$

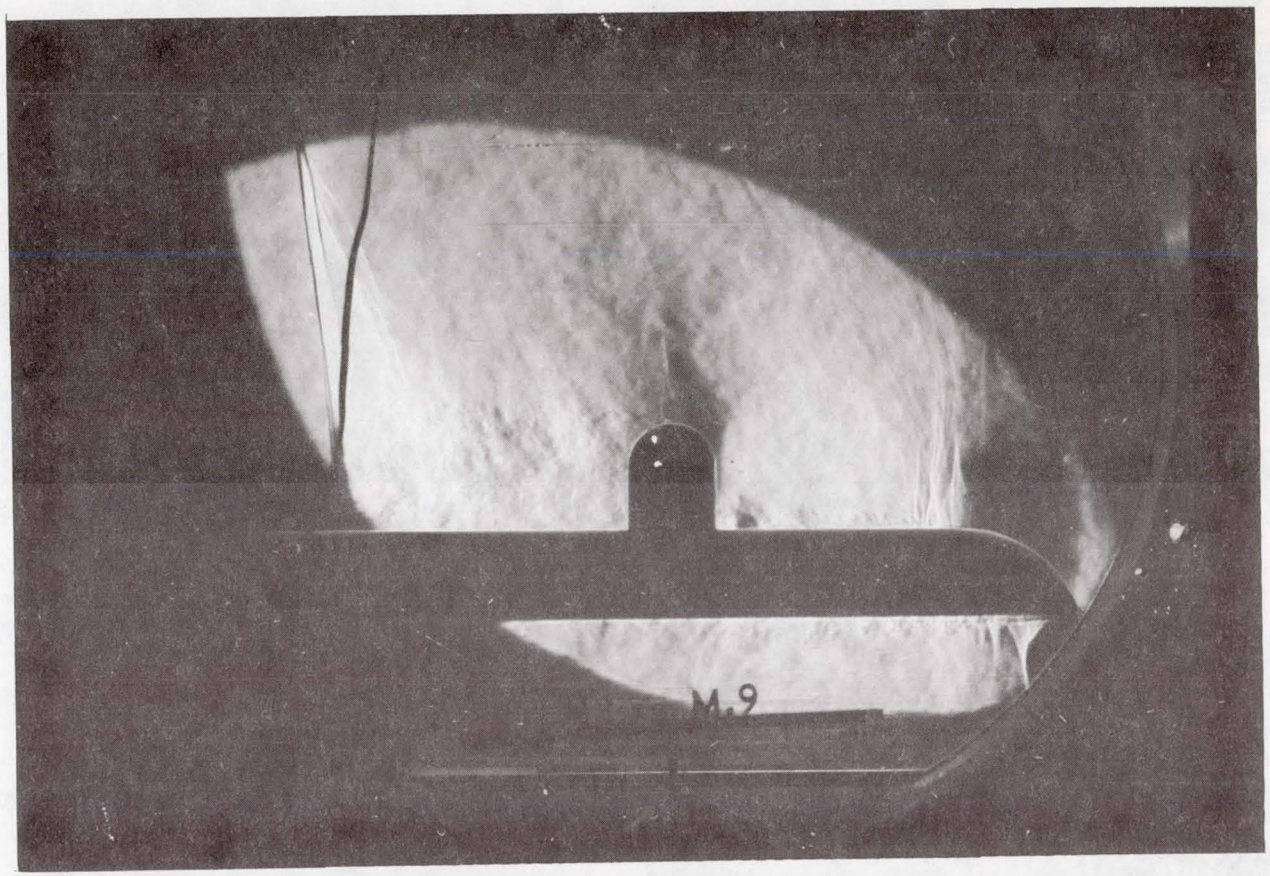

FIGURE 6
ON-GIMBAL TURRET SCHLIEREN PHOTOGRAPH, $M_\infty = 0.90$

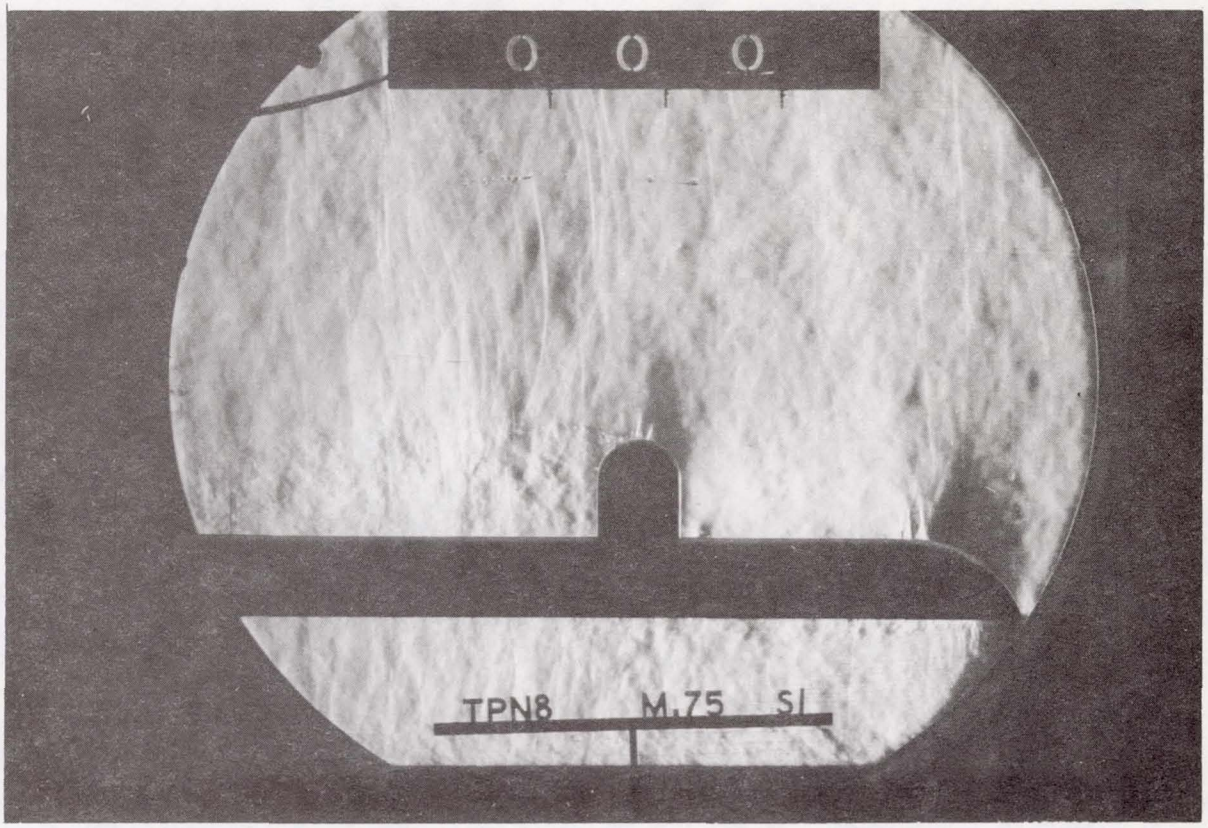

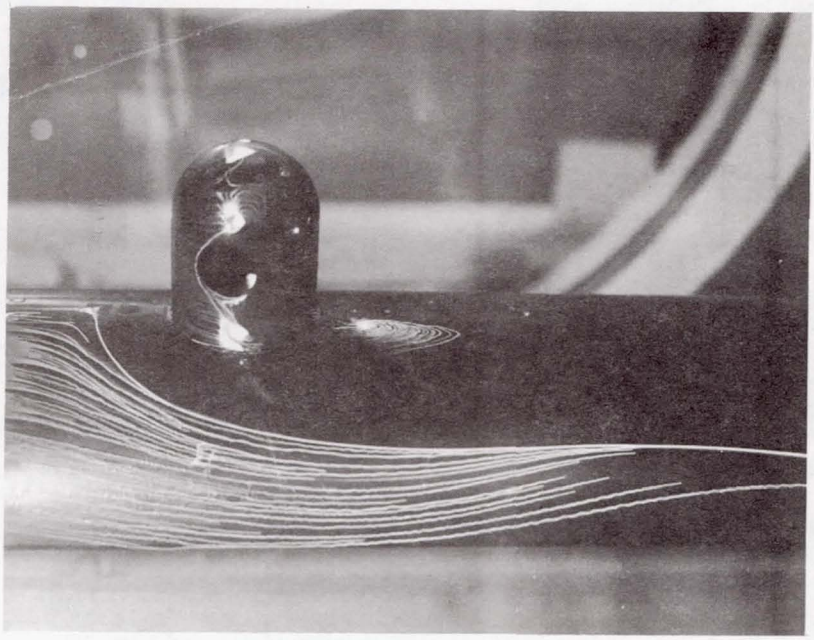

FIGURE 7

ON-GIMBAL TURRET SCHLIEREN AND

OIL FLOW PHOTOGRAPHS, $M_\infty = 0.75$

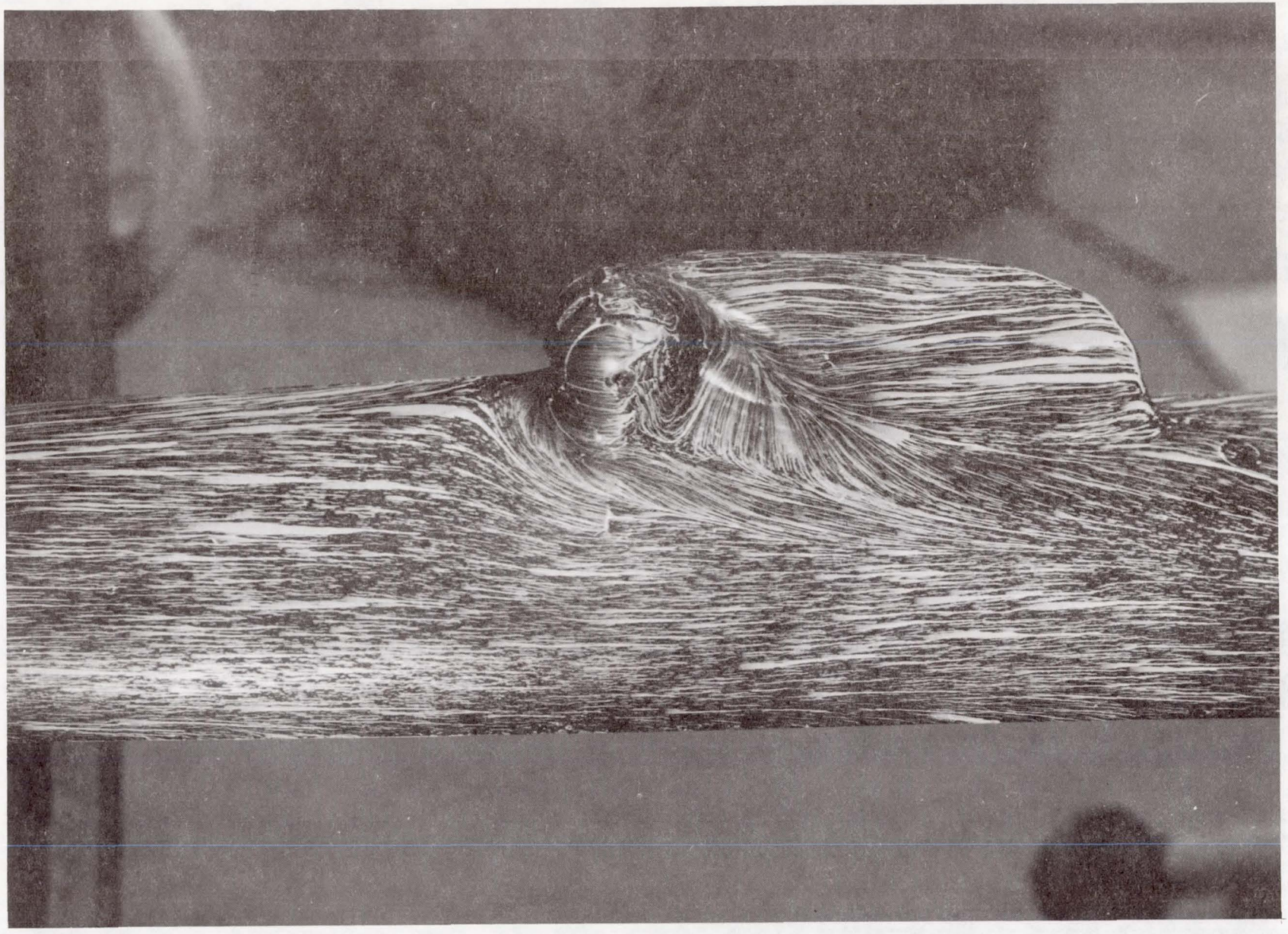

FIGURE 8

OIL FLOW VK-6 FAIRING, $M_\infty = 0.66$

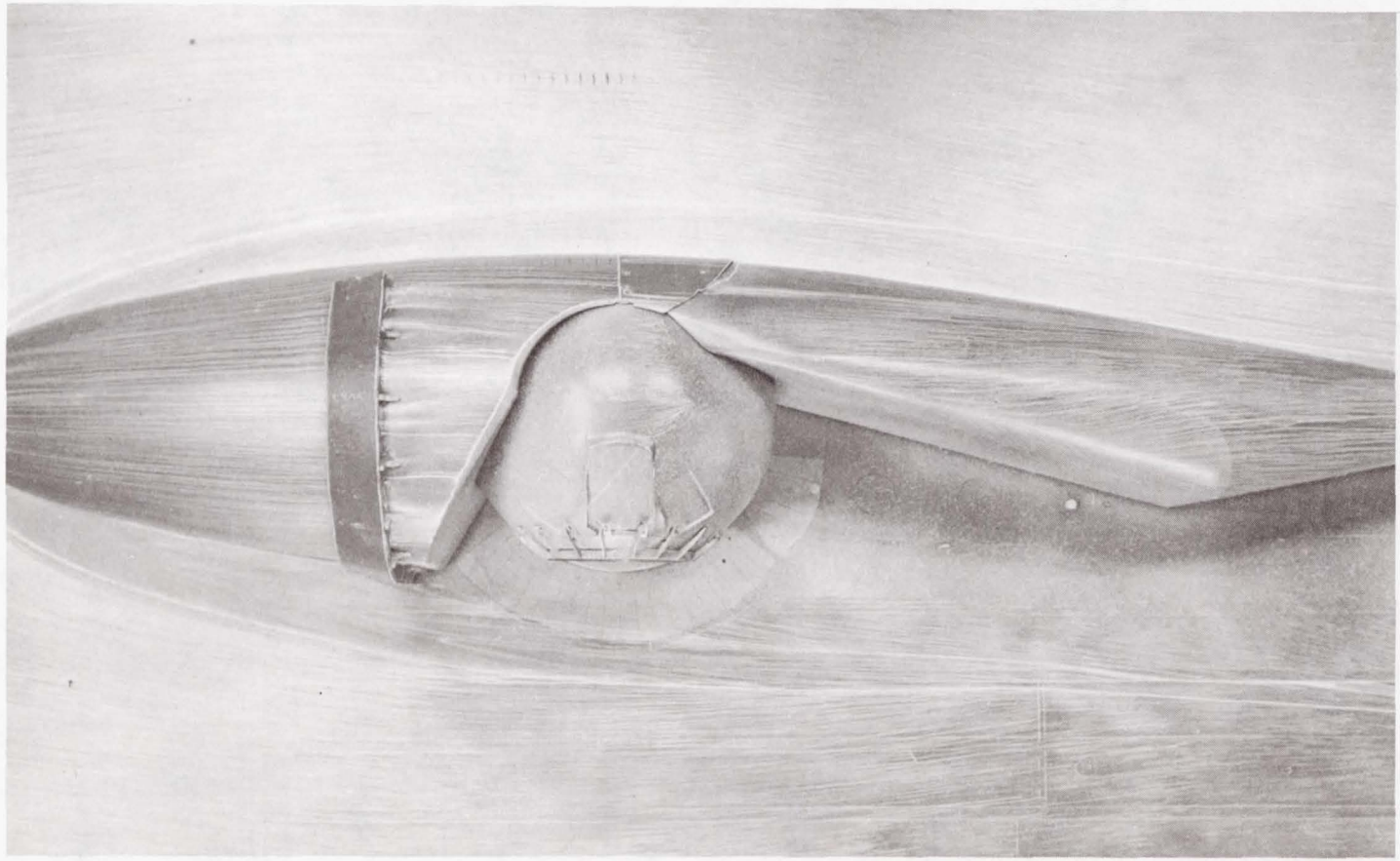

FIGURE 9
GENERAL DYNAMICS CYCLE II TURRET/FAIRING OIL FLOW

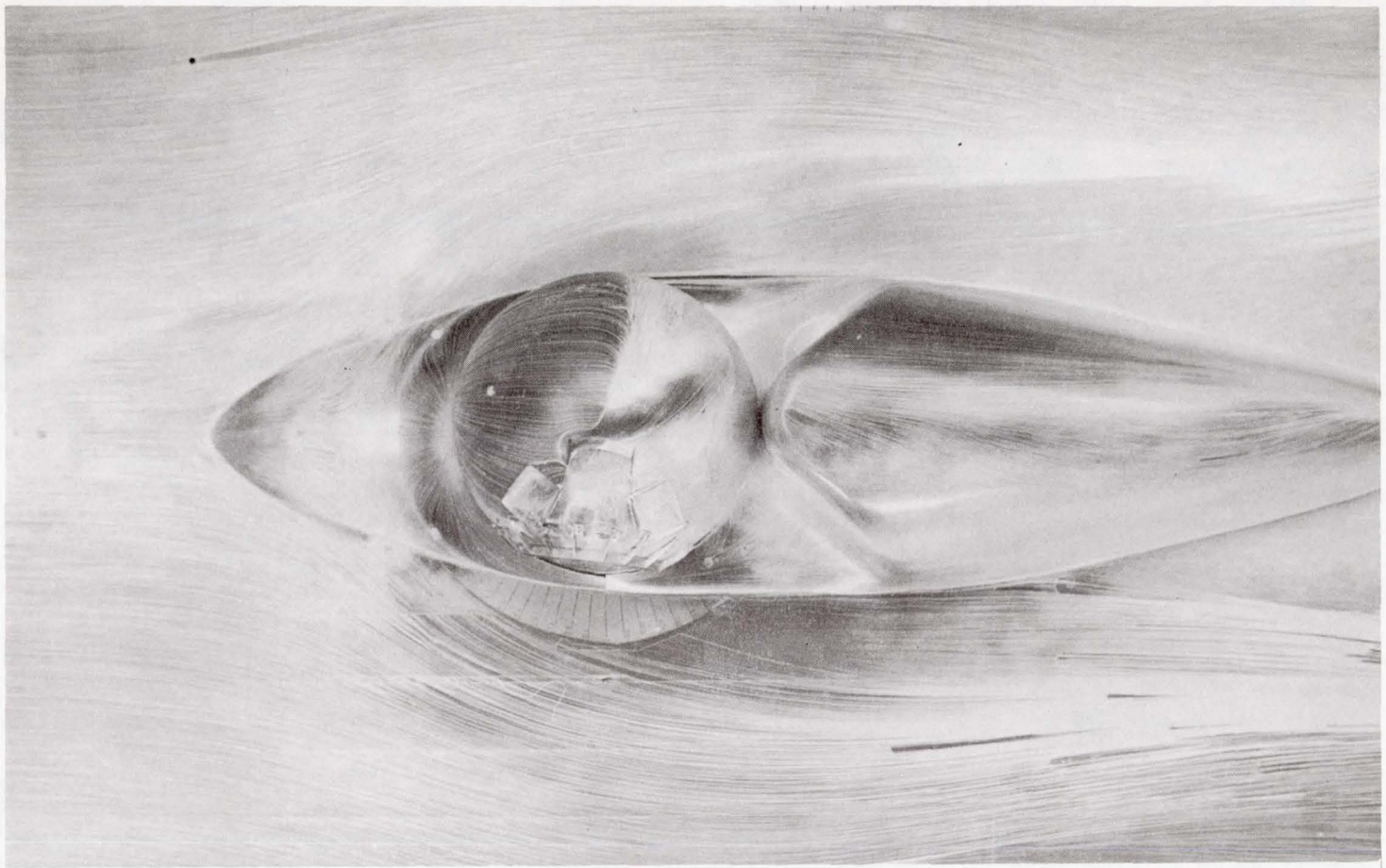

FIGURE 10
AFFDL T-2 FAIRING OIL FLOW

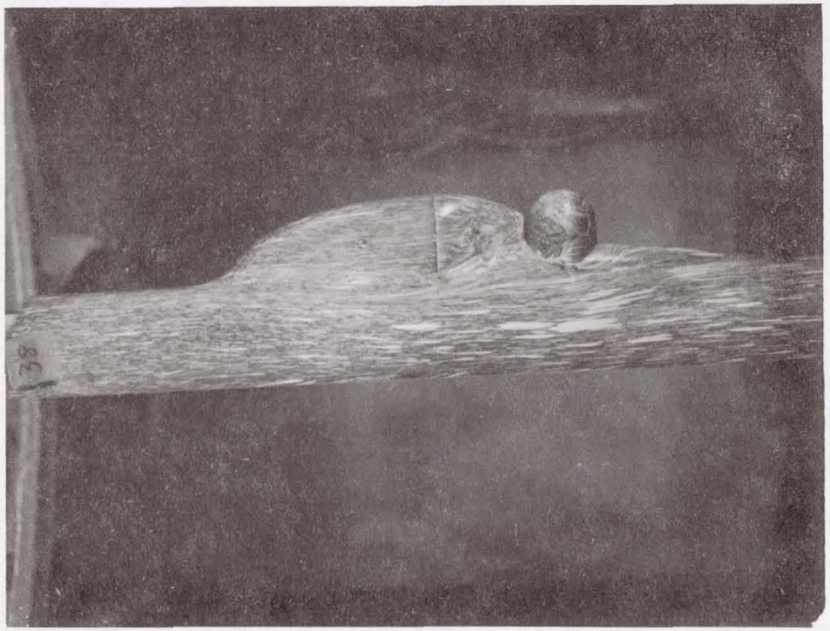

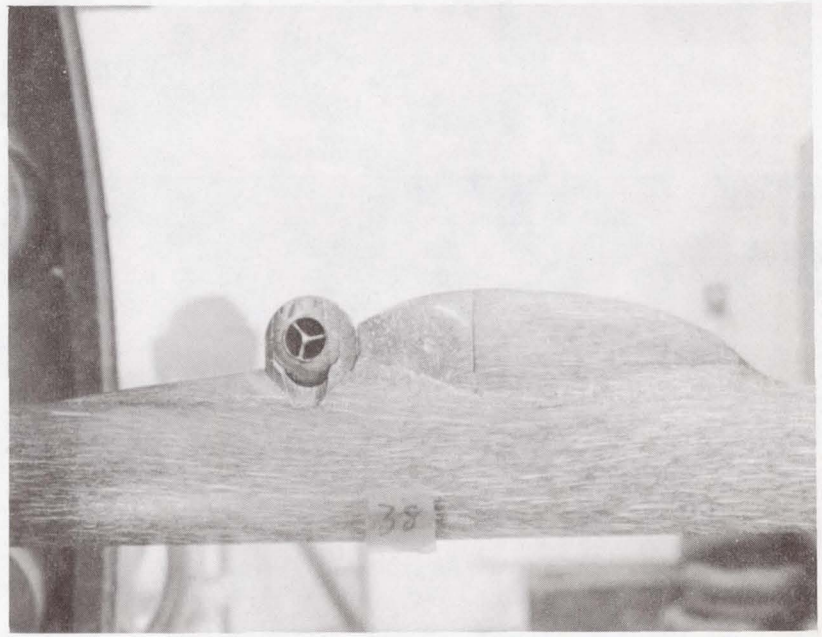

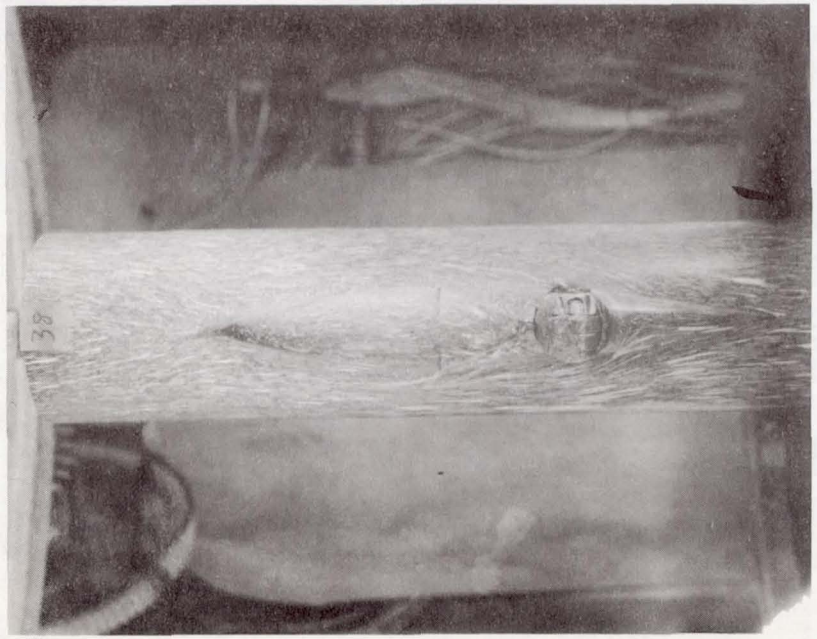

FIGURE 11
OIL FLOW CYCLE III/IV FAIRING, $M_\infty = 0.77$

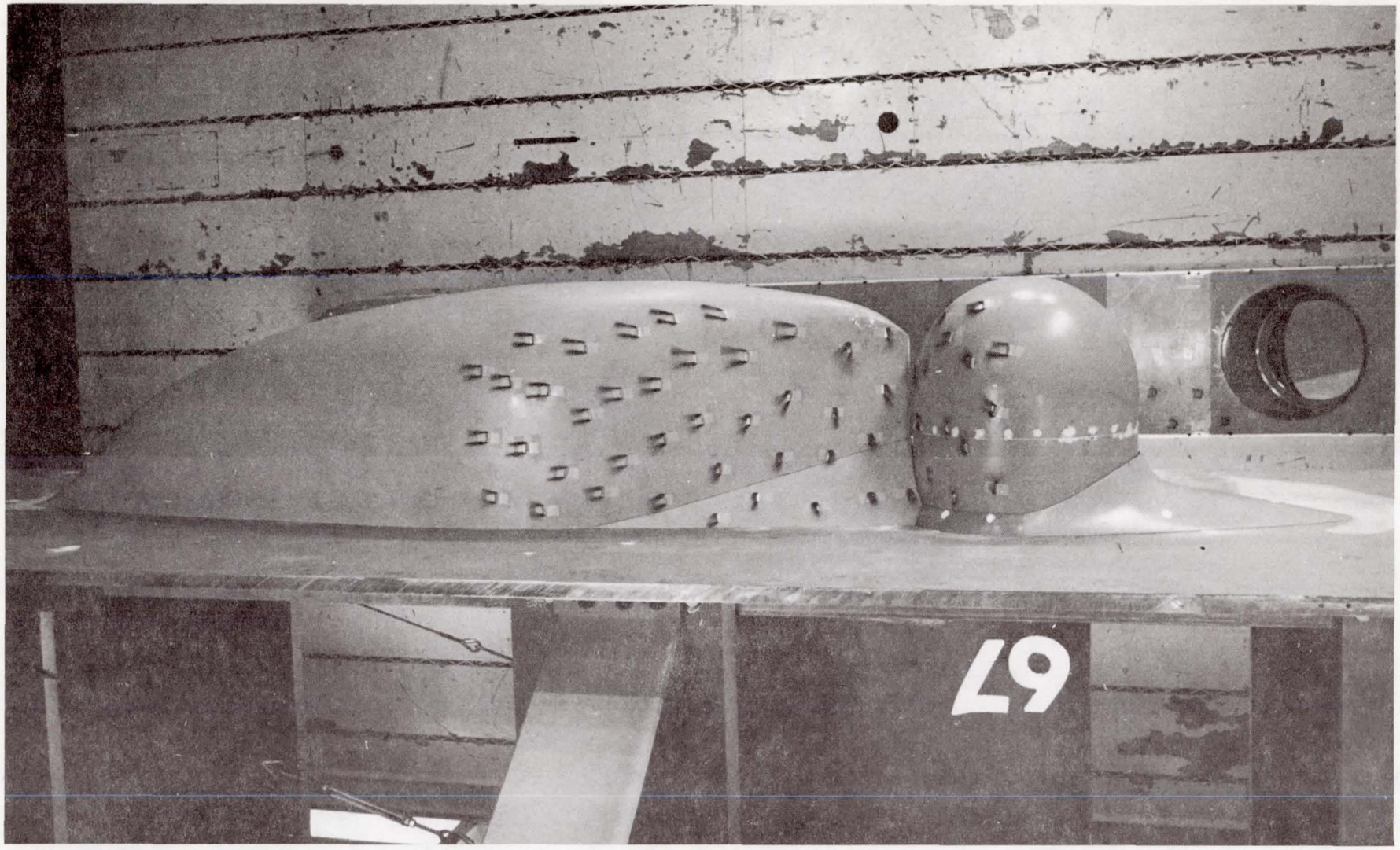

FIGURE 12
TUFT FLOW CYCLE III/IV FAIRING, M_∞ = 0.50

$M_\infty = 0.5$

$Re/L = 2.35 \times 10^6 \quad FT^{-1}$

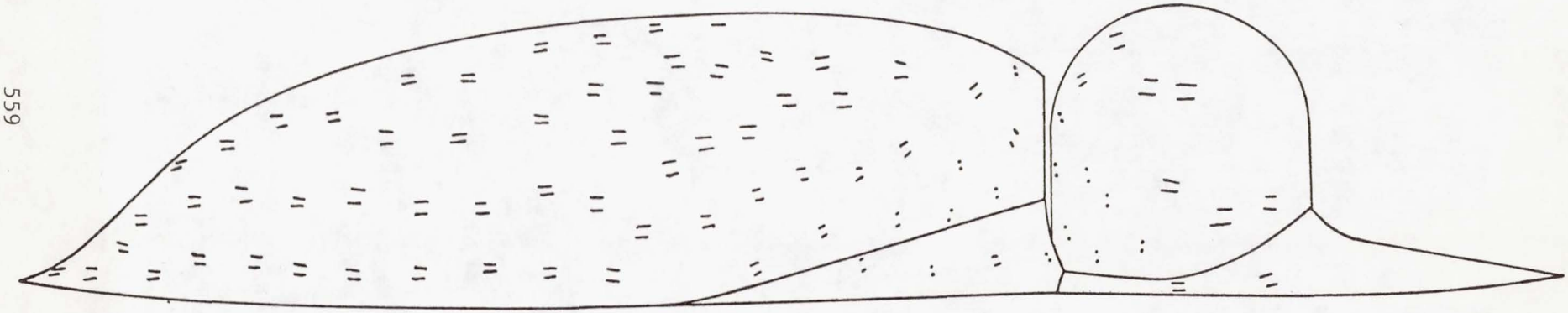

FIGURE 13

A.L.L. 3/10ths SCALE MODEL TUFT DIAGRAM

FIGURE 14
FULL SCALE FLIGHT TUFT FLOW

FIGURE 15
FULL SCALE FLIGHT OIL FLOW

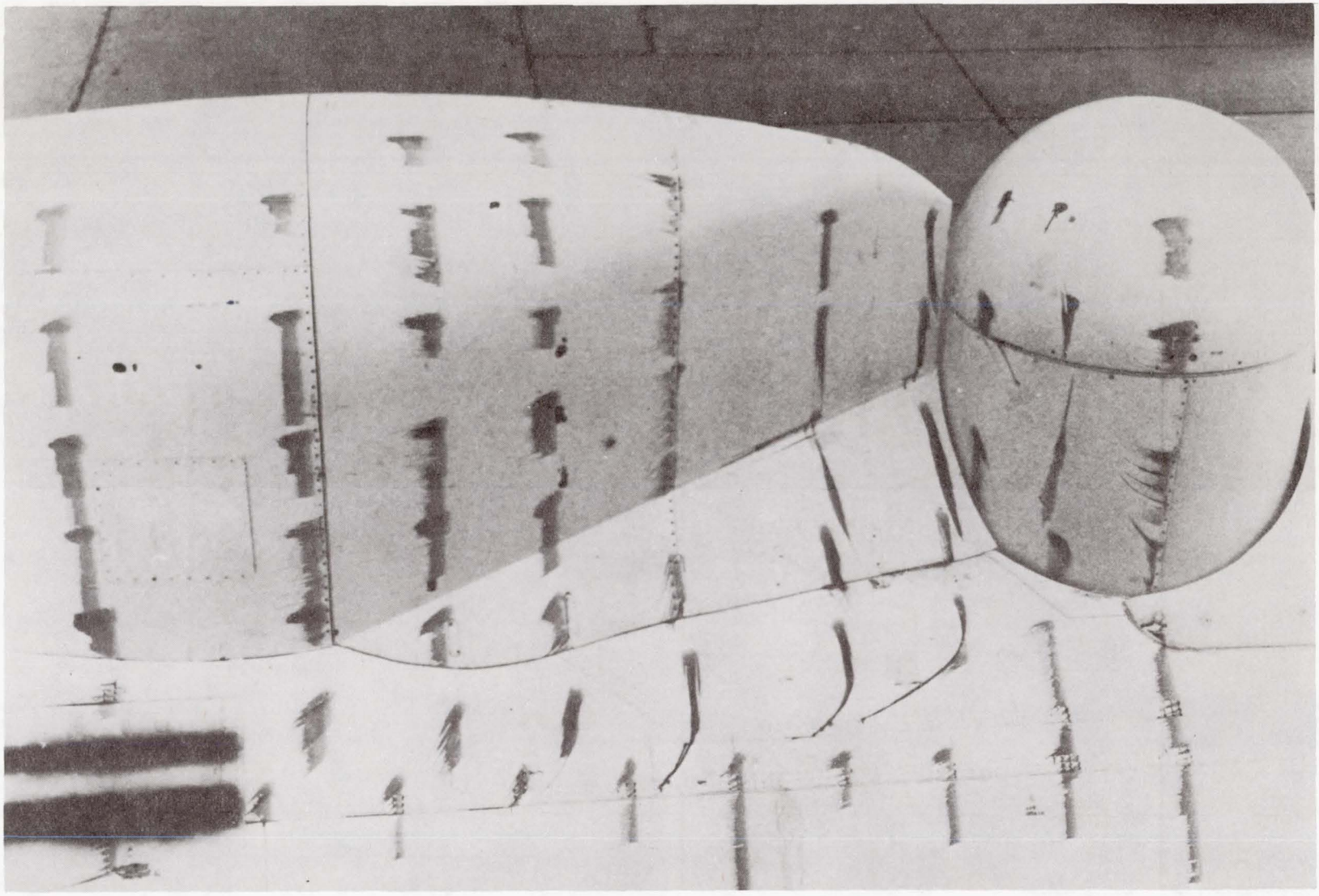

FIGURE 16
FULL SCALE FLIGHT OIL FLOW, CLOSEUP CUTOUT REGION

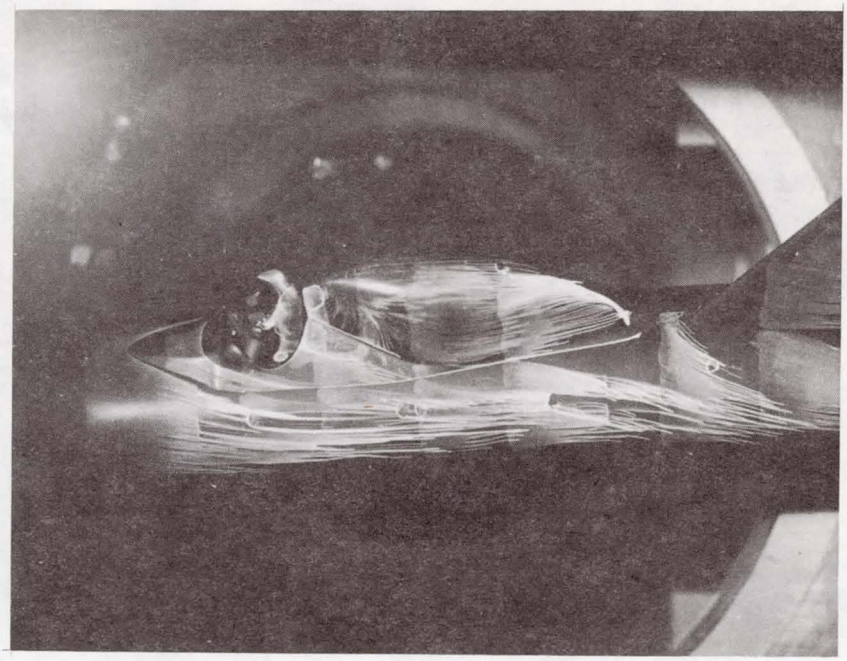

$M_\infty = 0.55$

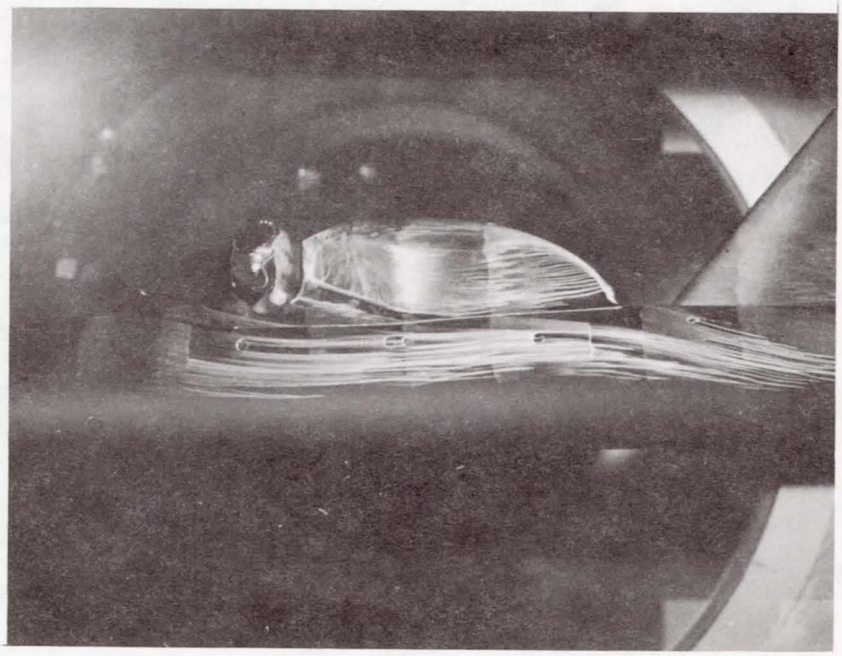

$M_\infty = 0.70$

FIGURE 17

B-52 SRAT/CYCLE III/IV FAIRING OIL FLOW

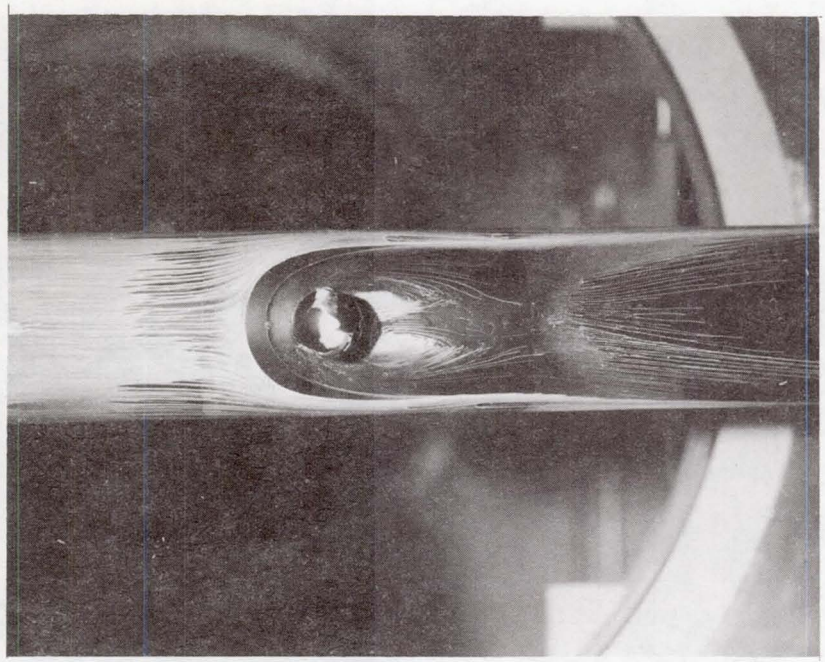

a.
ON-GIMBAL TURRET

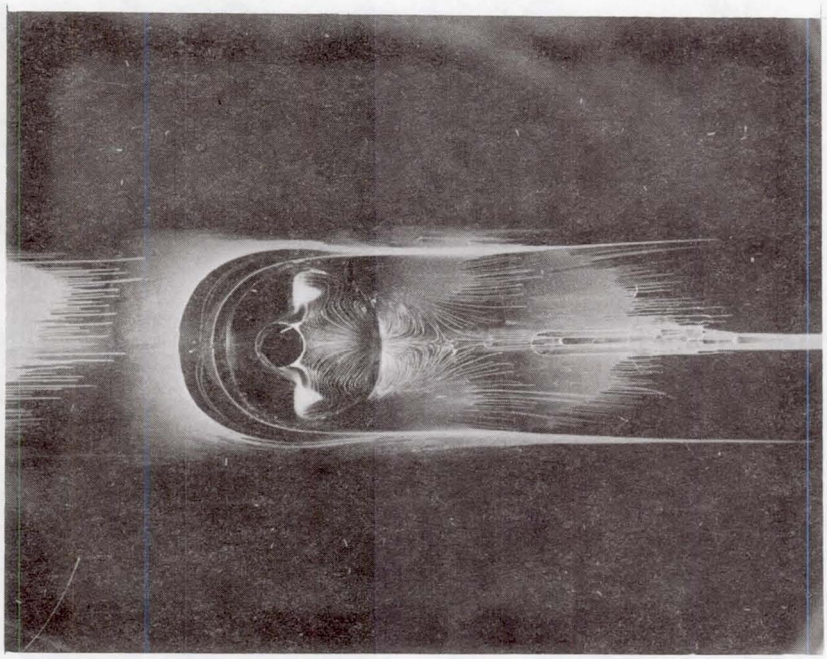

b.
COELOSTAT TURRET

FIGURE 18
TURRET OIL FLOWS, M_∞ = 0.75

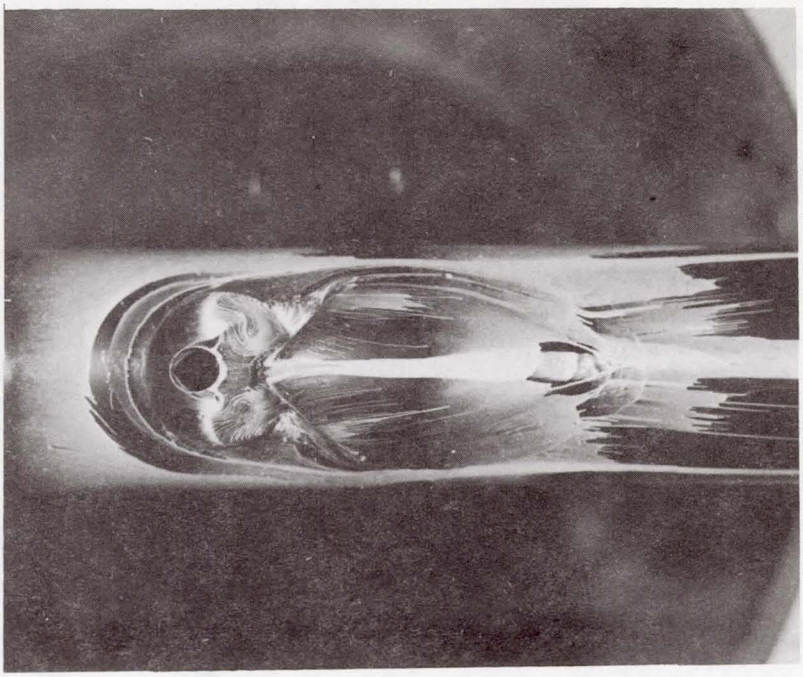

a.
FULL CUTOUT

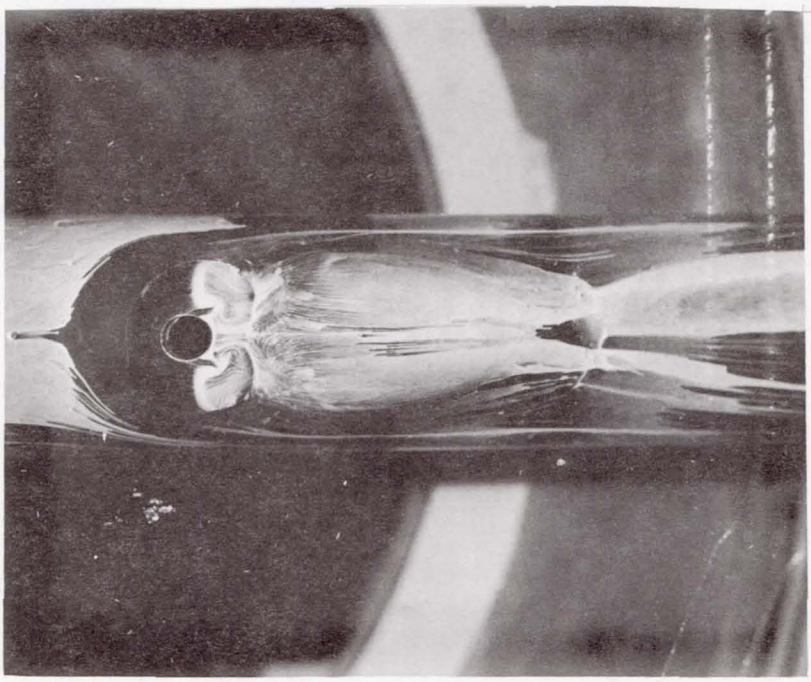

b.
CUTOUT PARTIALLY FILLED

FIGURE 19
COELOSTAT TURRET/FAIRING OIL FLOW, $M_\infty = 0.75$

REDUCTION OF UNSTEADY WIND TORQUES

ON AN OPEN PORT AIRBORNE OPTICAL TURRET

by

John P. Thomas, Jr., Lt, USAF

and

James T. Van Kuren, PhD

I. INTRODUCTION

The use of an aero/optics system on an aircraft during flight requires the development of a pointing and tracking assembly for the telescope. This optical system is normally contained within a turret assembly, of which two major types are pre-eminent. Figures 1 and 2 contain diagrams of these two designs, which are called the "on-gimbal" and "Coelostat" turrets, respectively. A major feature of these turrets is the open port optical cavity. At the present time most aero/optics applications require the use of a cavity open to the free stream of the airflow about the turret in flight.

The turrets are designed to allow rotation of the entire system about the central axis, plus rotation of an inner gimbal containing the cavity and telescope about an axis perpendicular to the central axis of symmetry. These two types of rotation, called rotations in azimuth and elevation, respectively, are depicted in Figure 3. The drive mechanisms which induce these rotations must overcome the steady and unsteady wind torques caused by the airflow about the turret. The "on-gimbal" turret shown in Figure 1 utilizes "inner" and "outer" drive mechanisms. The outer drives are powerful devices intended for large angular rotations of the entire turret, whereas the inner drives control only the inner gimbal of the turret and provide the fine adjustment to the telescope system. The torque capacities of the inner drives are much lower than those of the outer mechanisms. In particular, the unsteady wind torques, acting on the inner gimbal portion of the turret must be minimized if this drive system is to perform as desired.

The objective of this paper is to present techniques for reducing the unsteady torques acting on the inner gimbal of a turret of the types shown in Figures 1 and 2. The reductions in the unsteady torques are obtained by using "fixes" that alter undesirable flow characteristics or change the acoustic properties of the turret cavity. These "fixes" are designed to be used in the subsonic and transonic flow regimes. The flow field about the turret is generally three-dimensional and turbulent, and shock waves can form because of the rapid acceleration of the compressible gas about the blunt turret. The situation is further complicated by the presence of the cavity flow, and the fact that the mouth of the cavity must sweep through a wide angular variation relative to the direction of the freestream. The extreme complexity of this flow situation has precluded an analytical approach to the problem. Instead, several experimental investigations have been conducted by the Air Force and NASA to obtain aerodynamic torque data and to attempt various methods for reducing torgue unsteadiness on turrets of the types described earlier. A 3/10 scale open port turret test was conducted in the NASA Ames 14 T Wind Tunnel facility in January - February 1972. Although the primary emphasis of this test was to consider various shapes fore and aft of the turret to minimize drag and buffet, some progress was made towards turret inner gimbal unsteady torque reduction. It was determined that significant reductions of the unsteady pressures measured in the turret cavity could be obtained by the use of porous wind screens around the aperature of the cavity mouth. The use of these wind screens was motivated in part by some previous results presented in Reference 1. A subsequent test at Ames from September-November 1972 considered the problem of unsteady torque reduction in much greater detail, with a

variety of methods considered. Much of the results obtained in this test are described in an unpublished Air Force Weapons Laboratory document (Reference 2). A synopsis of the test results were presented in an AIAA paper (Reference 3), but a detailed description of these methods of torque reduction has not appeared in the open literature. The intention of the present work is to present in a fairly detailed manner the effectiveness of the various approaches to torque reduction, with particular emphasis on the comprehensive results of the second Ames test noted above.

II. MECHANISMS OF FLOW INDUCED UNSTEADY TORQUE GENERATION

It is essential that an understanding of the primary mechanisms of flow induced unsteady torque generation be achieved before a rational approach can be made to the methods of reduction of this torque. As a consequence, this section will include a brief account of the primary features of the flow about the turret and cavity which are thought to contribute significantly to the magnitude of the unsteady wind torque.

The most basic aspect of the flow that suggests a source of unsteady torques is the well known phenomenon of the excitation of cavity resonance by airflow. Analytical work in this area began with the classical efforts of Helmholtz and Rayleigh (Reference 4). More recently, notable experimental efforts to study cavity flow have been conducted by Roshko (Reference 5), Dunham (Reference 6), and others. A simplified model of the flow situation is obtained if one considers the shear layer across the mouth of the cavity as a region of instability resulting from the presence of inflection points in the velocity profile. Dunham (Reference 6) references some unpublished smoke tunnel work by Brown and Quinn that includes photographs and high speed motion pictures. This and other work indicates that the inflection points and pressure gradient in the flow across the mouth of the cavity results in vortices which eventually strike the downstream lip of the cavity. (See Figure 4) When these vortices satisfy the condition

$$f_i = \frac{nUe}{L_s} \qquad (2.1)$$

where n is an integer number of vortices in the shear layer, Ue is the velocity of the vortices along the shear layer, L_s is the length of the shear layer over the cavity, and f_i is the frequency of the ith resonant mode of the cavity, then the cavity is said to be in resonance. The coupling of the cavity oscillations with the flow induced forcing functions tends to further contribute to the magnitude of the oscillations. The existence of a resonance condition in the cavity is a major contributor to unsteady, periodic torques on the inner gimbal of the turret.

It is evident from this brief discussion of flow induced cavity resonance that two separate approaches may be taken to diminish the effects of this problem. Either the shear layer over the mouth of the cavity must be modified so that the layer is stabilized or moved out of the cavity, or the cavity itself must be altered so that it dampens the propagation of the acoustic disturbances. The various methods employed at the NASA Ames tests mentioned earlier and elsewhere have included the use of porous wind screens around the cavity opening, variation of the radius of the lip of the cavity, the injection of air into the cavity through a porous cylindrical insert, the injection of air through slots around the cavity lip, inserts of various porosity used

as the cylindrical walls of the cavity, and the insertion of dense foam liners of several compressibilities and thicknesses along the cavity walls. It is evident from the extent of the effort in this area that the problem of cavity resonance is considered to be the major contributor to the torque unsteadiness that can be alleviated by relatively simple methods.

It should be recognized that cavity resonance is not the only cause of unsteady torques on the inner gimbal of the turret. It has already been mentioned that shock waves can form on the turret, even at relatively low Mach numbers ($M_\infty > 0.55$). These shock waves can interact with the turret boundary layer in an unstable and often periodic manner. Pressure fluctuations can propagate through the subsonic boundary layer and provide a further input to the cavity pressure fluctuations. The turret is also subject to the shedding of vortices in the wake, which provides a periodic side force to the turret. A description of this type of vortex shedding may be found in Reference 7. A large variety of fairings of various designs have been used to alleviate both the problem of vortex shedding and to lower the drag levels on the turret. The size of the fairings is limited due to the desirability of a large field of view for the turret. Tests such as the ones previously mentioned at NASA Ames have indicated that the fairings have little effect on the unsteady pressures inside of the cavity at transonic speeds. However, results given in Reference 8 indicate that at subsonic Mach numbers less than about $M_\infty = 0.55$ the presence of the fairing can have a dramatic effect on the cavity unsteady pressures. These effects seem to be negligible at all Mach numbers higher than $M_\infty = 0.55$. Since most applications of these optical turrets involve Mach numbers in the transonic range, the low Mach number pressure effects of the fairings will not be of concern here. Results presented in this work will therefore be for a single turret/fairing combination.

III. INSTRUMENTATION, MODEL AND TEST DETAILS

It has been previously mentioned that the bulk of the Air Force/NASA effort in unsteady torque reduction took place during the wind tunnel test at the Ames 14T facility in the autumn of 1972. In this section further details of the experimental set-up and instrumentation used in this test are presented.

The NASA Ames 14 Foot Wind Tunnel facility is a closed-circuit, atmospheric facility. The basic turret and fairing model used in the test was mounted on a splitter plate that was 3.74 meters long by 1.37 meters wide. This splitter plate was mounted to a side wall of the tunnel on six 1.14 meter legs (See Figure 5). The Advanced Pointer Tracker (APT) turret was remotely driven in azimuth and elevation. Although this turret was tested with a variety of fairings, the only combination considered in the present work is that shown in Figure 6.

The measurement of the unsteady inner gimbal torques was accomplished using appropriately located high response pressure transducers. Twenty-eight locations were chosen to provide the contributions to the unsteady torques about the inner gimbal axes of the APT turret. Each instrumentation location was considered to be the the centroid of a representative area. The resulting nondimensionalized torque

coefficients were obtained using the following equation:

$$C_T = \frac{\sum_{i=1}^{28} p_i A_i r_i}{q_\infty D^3} \qquad (3.1)$$

where q_∞ was the freestream dynamic pressure. D was the turret diameter, p_i was the ith unsteady pressure. A_i was the ith area associated with a pressure, and r_i was the moment arm of the ith pressure location about the appropriate axis. As noted earlier, the use of Equation (3.1) to obtain the nondimensionalized torques neglects the effects of skin friction. The unsteady pressure signals were summed on a real-time basis to determine the unsteady torque signal. Figure 7 indicates the locations of unsteady pressure transducers inside the cavity of the turret.

The first of the various types of "fixes" used were the external wind screens (EWS). The typical geometry of these screens is represented in Figure 8. These screens were all constructed from sheet metal perforated with circular holes of uniform distribution which provided a range of porosity from 10% to 37%. The heights of these screens varied from 0.63 cm to 2.53 cm above the surface of the turret. The screens were cylindrical in shape, with the central axis coincident with the telescope axis. Two varieties of screens were tested - the other EWS had a diameter of 25.7 cm, which corresponded to a ratio of screen to aperature diameter of 1.275, whereas the inner EWS diameter equaled the aperature diameter of 20.1 cm. For some tests, spacers were placed under the EWS's to provide a gap between the surface of the turret and the screen.

Various types of inserts were used to provide acoustic treatment of the internal walls of the cavity. These "internal wind screens" (IWS) (Figure 9) corresponded to an aperature diameter of 20.1 cm. In some cases, simple sheet metal with circular holes to provide 10% to 30% porosity were tried. During other test runs porous plastic foam of various thicknesses was placed over the IWS's. Foam with acoustic impedances of 20 to 60 rayls/cm were experimented.

The configuration of the tip of the cavity was expected to influence cavity resonance. Three lip radii were tried to determine separation and re-attachment interactions with the cavity. The three radii were 0 (sharp lip), 0.76 cm and 1.71 cm.

Another approach to resonance suppression was the injection of air through the 37% porous IWS or through slots along the cavity lip (Figure 10). For the latter, the lip was split into two 180° segments connected to separately controlled air lines.

IV. EXPERIMENTAL RESULTS

The various configurations were compared under similar test conditions. Elimination of resonance and a reduction of rms pressures, forces and torques were used to determine the effectiveness of the various antiresonant devices.

Effect of Fairings. Vortex shedding from the blunt turret seemed to be a source of noise for the cavity. Practically any kind of aft fairing or splitter and a low forward fairing reduced the opportunity for cross communication of pressure waves and therefore reduced the rms pressures in the cavity at subsonic speeds below Mach number 0.55. At higher Mach numbers the low interference fairing (Figure 6) had only slightly reduced pressure fluctuations. These results were encouraging enough that development of fairings continued to the point of the present Airborne Laser Laboratory Cycle III fairings.

Effects of Porous Fences. The lip fences (external wind screens) had two effects on the open cavity and shell; one was favorable. Figure 11 shows that considerable reduction in rms pressure could be achieved by increasing the height of a 50% porous fence. The improvement occurred regardless of transducer position and was attributed to increased shear layer thickness over the opening. The unfavorable effect was that the fences had relatively high aerodynamic drag which was transmitted to the shell as external torque (Figure 12). Solid and 30% porous fences were also tested. Evaluation of all of the data, including that not shown in this paper, lead to the conclusion that a 30% porous fence with height (h) approximately 1/16 of the cavity diameter (D) was a satisfactory compromise (Figure 12).

Effect of Lip Radius. Three lip radii were tried during the tests. The lowest RMS torques and pressures were obtained with a sharp lip (Figure 13). The output was very sensitive to transducer position but unsatisfactorily high in all cases. As shown on the figure, the addition of the lip fence reduced the rms pressures considerably.

Effect of Cavity Inserts. A solid cavity side wall (cylindrical), one with 10% porosity (equally spaced circular holes), and a 37% porous wall were investigated. Plastic foam liners were subsequently added to the solid wall as another approach at pressure reduction. Increased porosity reduced rms pressure (Figure 14) at all transducer locations. The foam proved to be even more beneficial. Figure 15 is plotted in terms of rms torques and shows the large reductions to be obtained with low density foam.

Discussion. Considering the open cavity in an unprotected shell with minimal fairings as a base line, the best combination tested with mechanical fixes was a shell with a low interference fairing, a 1/16 h/D 30% porous lip fence around a sharp lip, and low density sidewall insert. The effect of this configuration on dynamic pressure and internal torque was significant (Figure 16). RMS pressures were reduced by the best configuration to about 1% of the dynamic pressure, values normally sensed for boundary layer turbulence. The steady azimuth and elevation torques were also reduced to negligible values for "side look" arrangements. However, for determining the size of the positioning servo motors for telescope gimbals, it is necessary to know what the maximum unsteady loads would be. At any given Mach number, the maximum load occurs at some different combination of azimuth and elevation angles. These maxima increase in value with Mach number, so the attempts to reduce loads should be concentrated at the highest Mach number of the application. Though not shown on the figures, a torque reduction of approximately 50% at M = 0.9 between protected and unprotected cavities was realized in this study.

Effect of Mass Injection. Gaseous mass injection was found to be a significant new method of reducing resonance in open port cavities. Resonance occurred at certain azimuth angles resulting in large values of rms torque (Figure 16). Injection of gas through the pores in the 37% internal insert resulted in reductions in unsteady pressure and torque below the best mechanical configuration. The flow rate of gas required is related to the size of the opening and the mass flux (kg/m^2 sec) of the free stream air. For flight applications it is necessary to minimize the gas flow. Injection of the air through a narrow slit on the upstream edge of the opening produced a reduction in the required mass flow rate by approximately 50%.

V. CONCLUSIONS AND RECOMMENDATIONS

The occurrence of acoustic resonance and internal torque in open cavities on blunt protuberances is dependent on Mach number, Reynolds number and the angle of the plane of the opening relative to the free stream direction.

Several techniques were investigated for reducing the unsteady pressures and torques.

Fairings are necessary to protect the external shell from excessive loads, and have a beneficial effect on internal pressures.

A lip fence with 30% porosity and height equal to 1/16 the cavity diameter reduced rms pressures by an order of magnitude and reduced torques by 50%.

Porous cavity walls of 37% reduced the overall unsteady pressure levels by 30% to 60% depending on the location of the transducer. Low density foam likewise reduced unsteady internal torques by an order of magnitude.

Injection of air over the opening was more efficiently done with a thin slot on the upstream lip. Maximum torques were reduced 75% by this technique.

In summary, it is recommended that a combination of configurations be used for protecting an open port optical system from steady and unsteady aerodynamic loads in an airborne environment. Dynamic surface pressures can be maintained at levels similar to those experienced from boundary layer turbulence.

REFERENCES

1. Buell, D. A., "An Experimental Investigation of the Airflow over a Cavity with Anti-Resonance Devices," NASA TN D6205 (1971).

2. Davis, J. A., "Investigation of the 0.3-Scale Open Port APT Turret at NASA Ames 14T: Phase II," unpublished AFWL TR (1974).

3. Van Kuren, J. T., "Acoustic Phenomena of Open Cavity Airborne Cassegranian Telescopes," AIAA Paper No. 74-195 (1974).

4. Rayleigh, J. W. S., "The Theory of Sound," Mac Millan Co., Ltd., Vol. 2, pp. 412-414, 170-235 (1896).

5. Roshko, A., "Some Measurements of Flow in a Rectangular Cutout," NACA TM 3488 (1955).

6. Dunham, W. H., "Flow-Induced Cavity Resonance in Viscous Compressible and Incompressible Fluids," Office of Naval Research, ACR-92 (1962).

7. Roshko, A., "Structure of Turbulent Shear Flows: A New Look," AIAA Journal, Volume 14, pp. 1349-57 (1976).

8. Thomas, J. P. Jr., "Test of Turret/Fairing Configurations for the B-52 SRAT Program," AFFDL-TM-FXM-79-21 (1979).

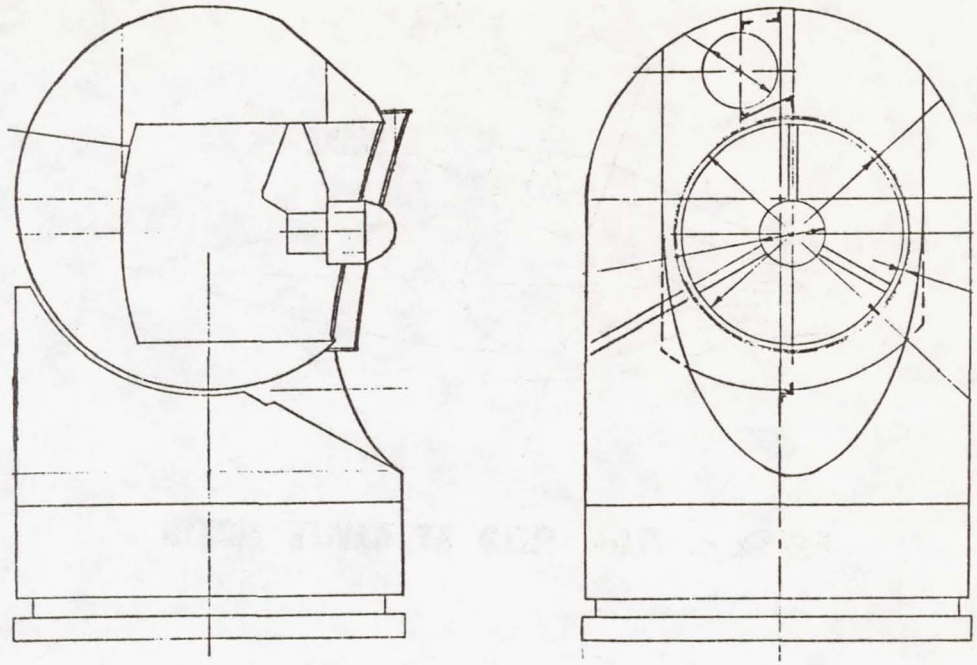

FIGURE 1. ON-GIMBAL TURRET.

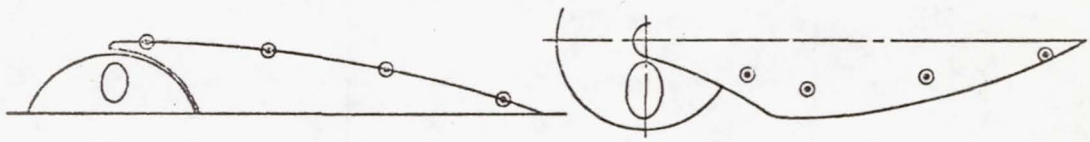

FIGURE 2. COELOSTAT TURRET.

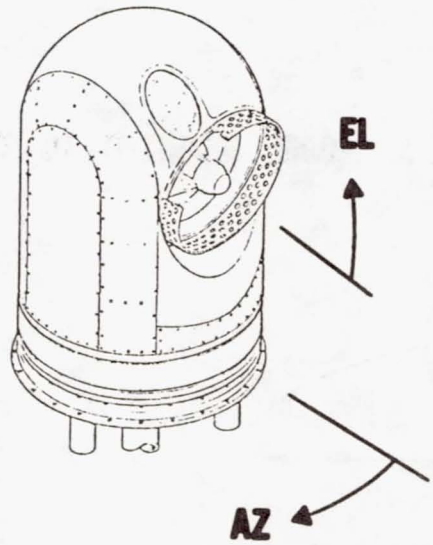

FIGURE 3. AZ AND EL ANGLES.

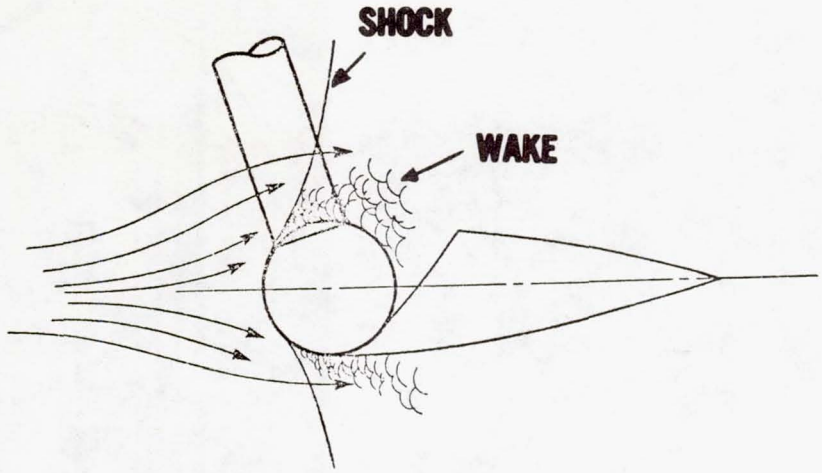

FIGURE 4. FLOW FIELD AT CAVITY MOUTH.

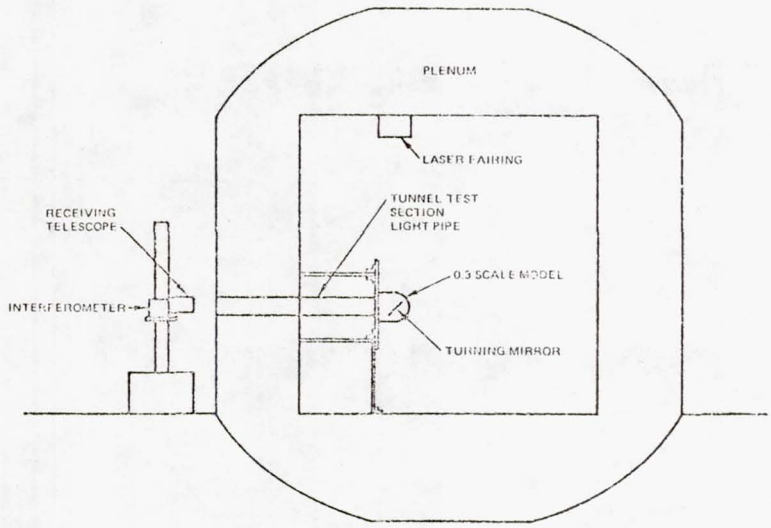

FIGURE 5. MODEL MOUNTED TO TUNNEL WALL.

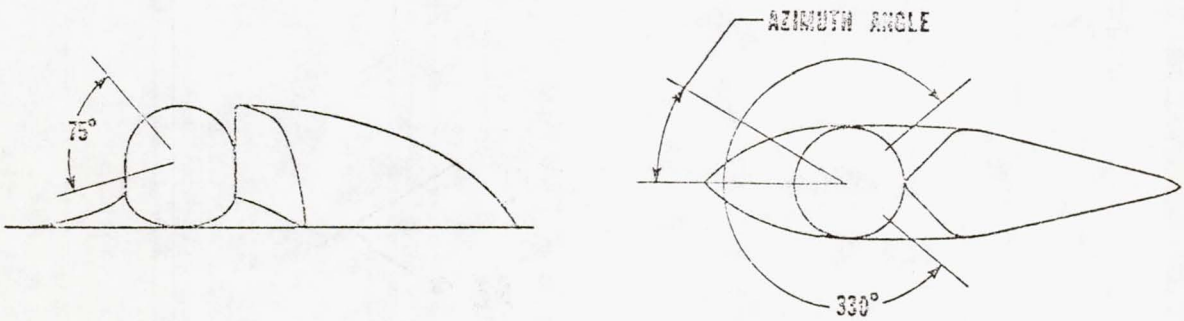

FIGURE 6. NON-INTERFERENCE FAIRING.

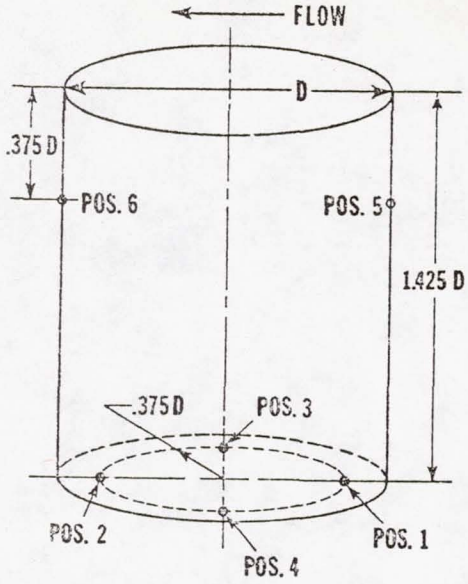

TRANSDUCER NOTATION

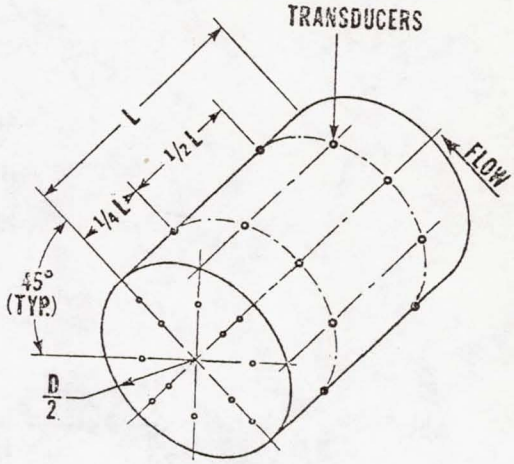

CAVITY INSTRUMENTATION
(FOR OBTAINING TORQUES)

FIGURE 7. TRANSDUCER LOCATIONS.

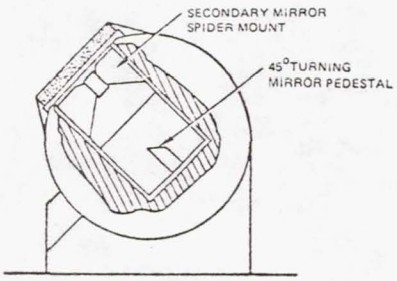

EXTERNAL WIND SCREENS
(SOLID, 30% POROSITY,
50% POROSITY)

FIGURE 8. EXTERNAL WIND SCREEN.

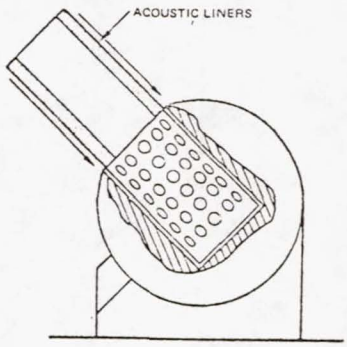

FULL INSERTS
(SOLID, 10% POROSITY,
AND 37% POROSITY)

FIGURE 9. INTERNAL WIND SCREEN.

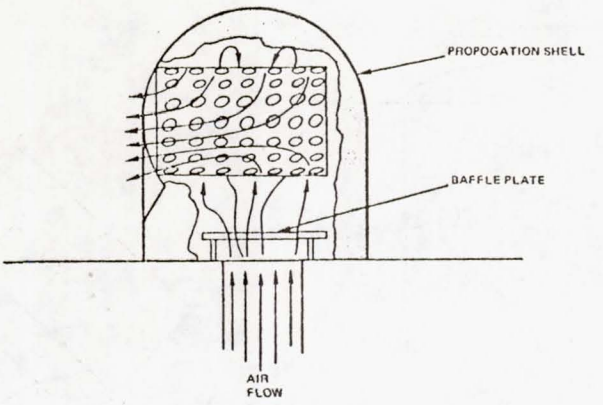

BASE INJECTION

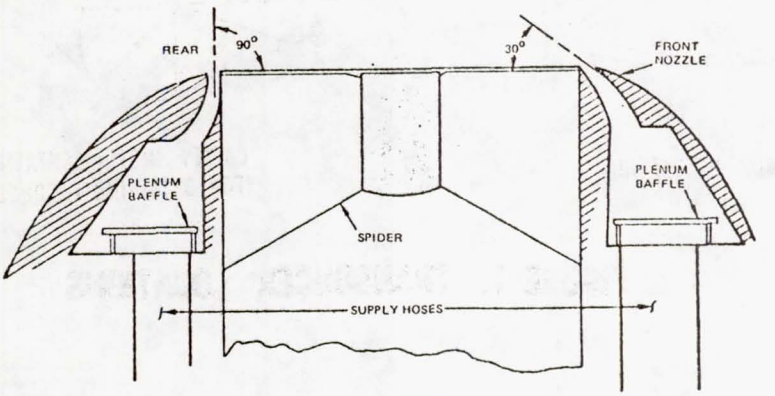

LIP BLOWING

FIGURE 10. TECHNIQUES FOR AIR INJECTION.

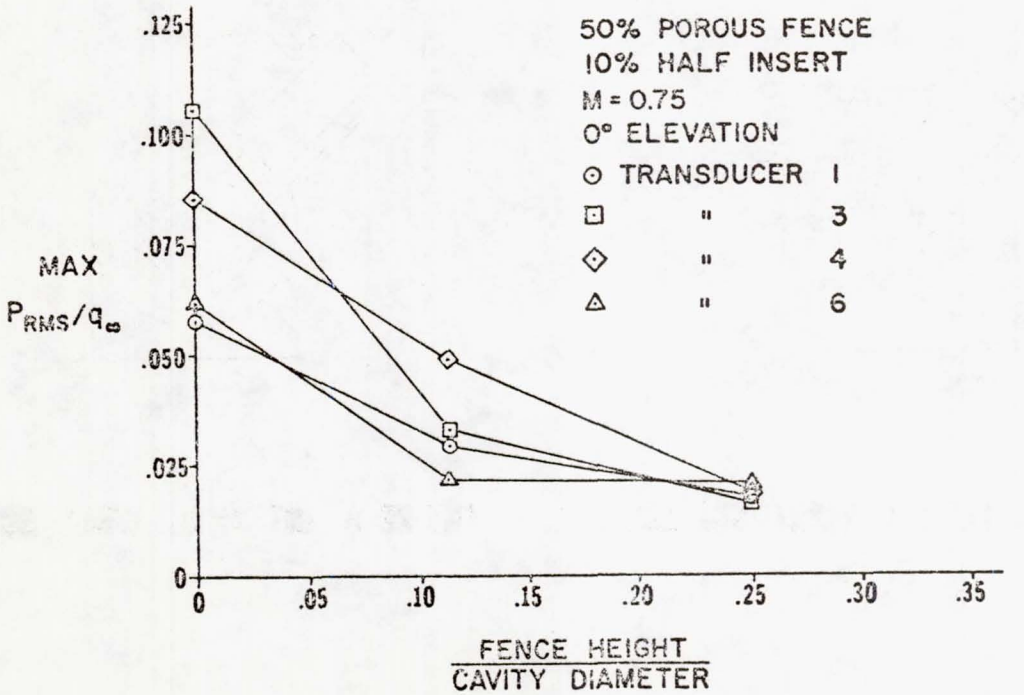

FIGURE 11. LIP FENCE HEIGHT VS CAVITY UNSTEADY PRESSURES.

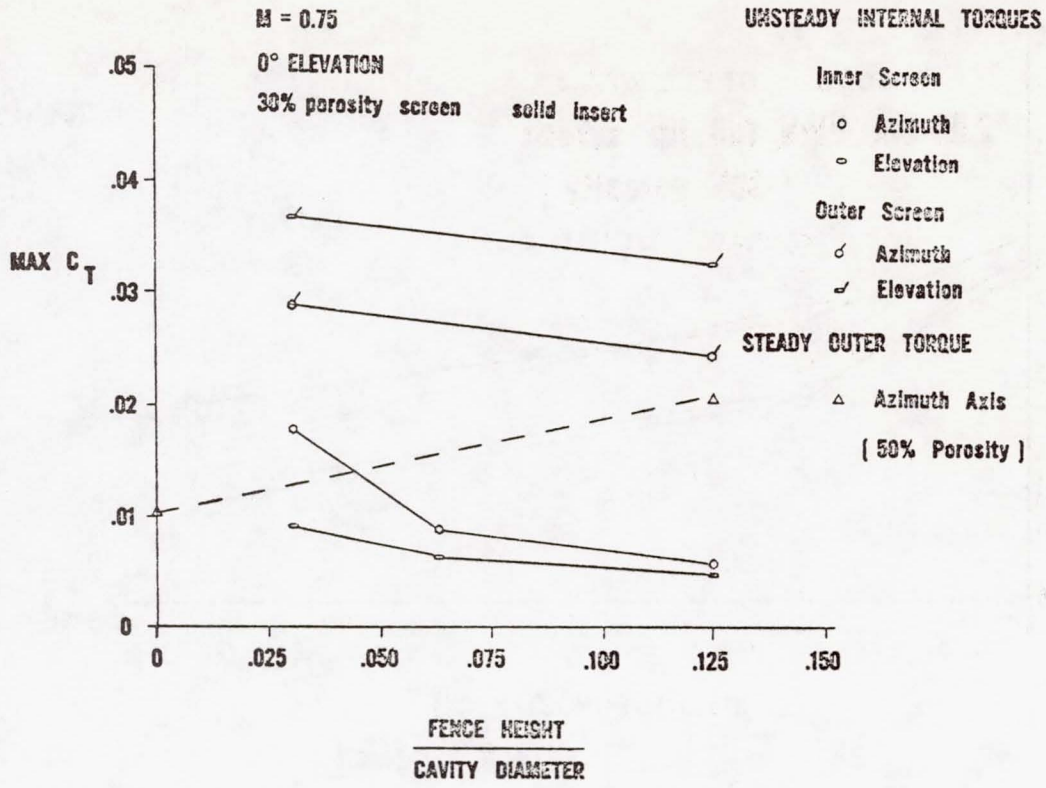

FIGURE 12. LIP FENCE HEIGHT VS UNSTEADY AZIMUTH TORQUES.

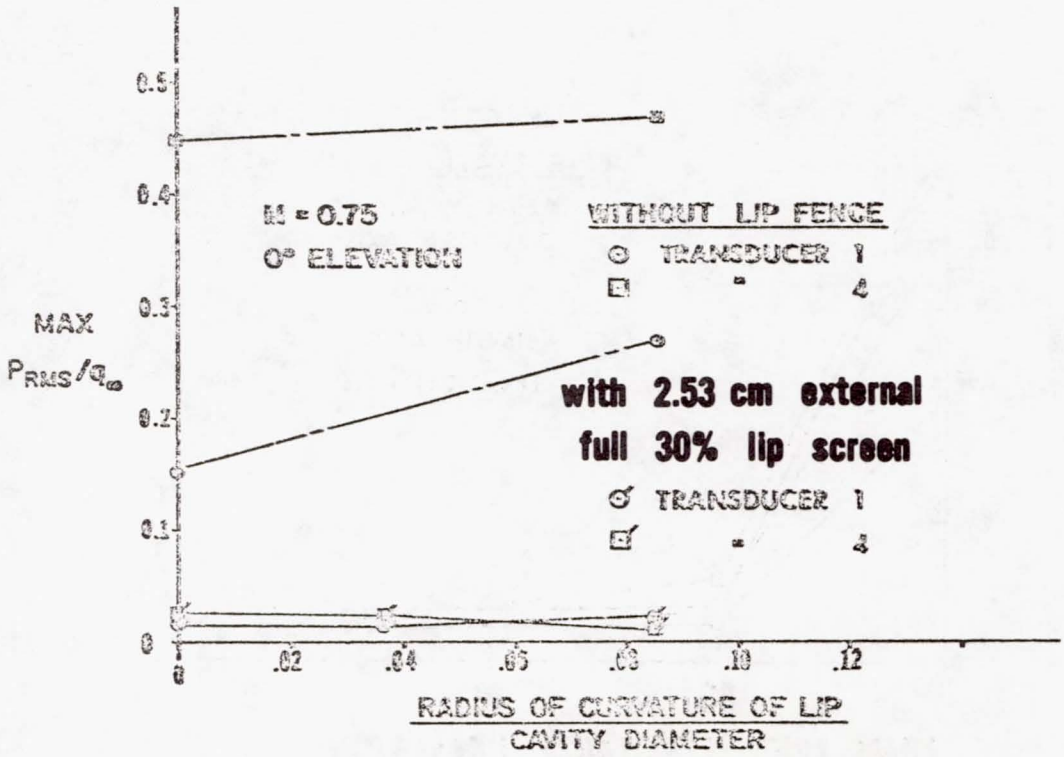

FIGURE 13. CAVITY LIP RADIUS VS CAVITY UNSTEADY PRESSURES.

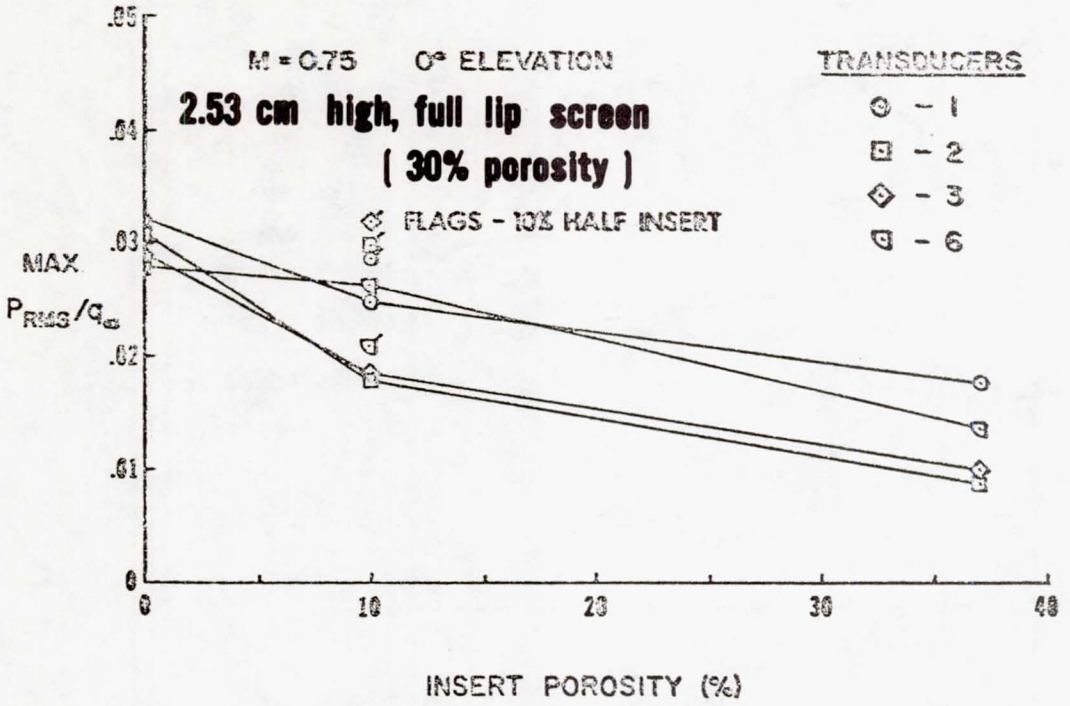

FIGURE 14. INSERT POROSITY VS CAVITY UNSTEADY PRESSURES.

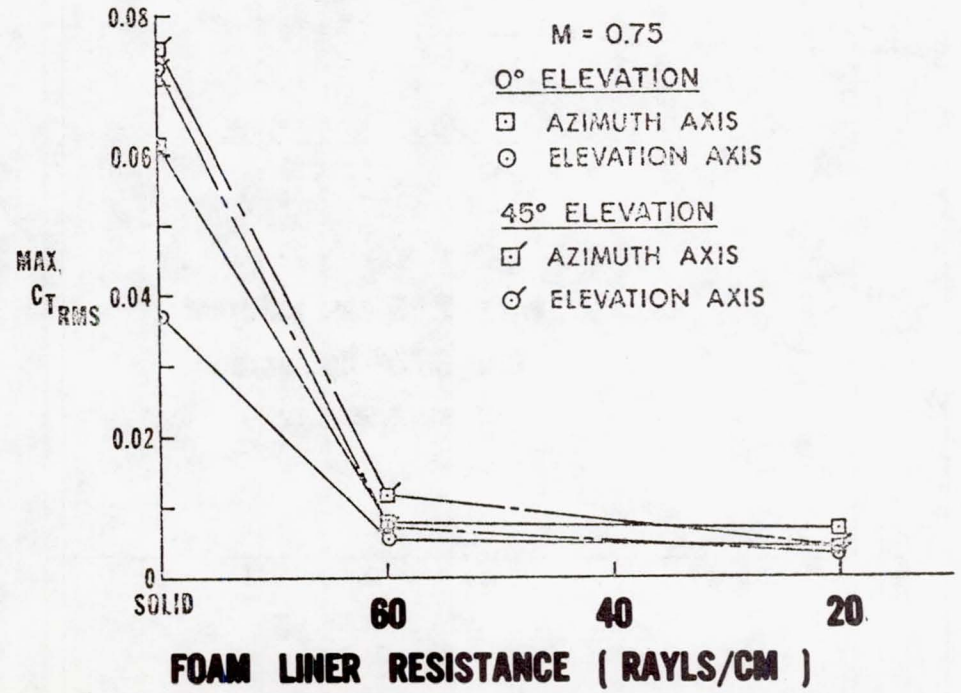

FIGURE 15. INSERT POROSITY VS UNSTEADY AZIMUTH TORQUES.

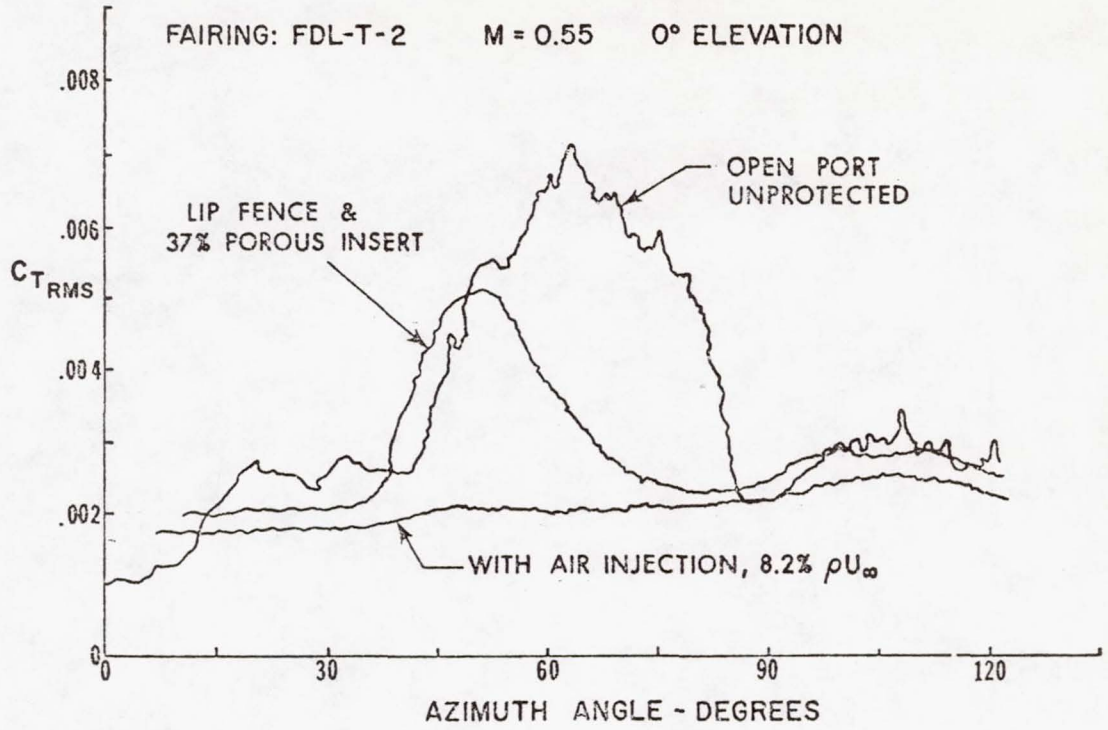

FIGURE 16. UNSTEADY AZIMUTH TORQUE COMPARISONS.

Measurement of External Forces and Torques on a Large Pointing System

R. C. Morenus

Ford Aerospace & Communications Corporation

MEASUREMENT OF EXTERNAL FORCES AND TORQUES ON A LARGE POINTING SYSTEM

ABSTRACT

Methods of measuring external forces and torques are discussed, in general and as applied to the Large Pointing System (LPS) wind tunnel tests.

The LPS tests were in two phases. The first test was a preliminary test of three models representing coelostat, heliostat, and on-gimbal telescope configurations. The second test explored the coelostat configuration in more detail. The second test used a different setup for measuring external loads.

Some results are given from both tests.

GENERAL

This paper is concerned with what can be done to measure external aerodynamic forces and moments during a wind tunnel test of an airborne telescope system. It is assumed that the primary test objective is high response measurements within the telescope.

It would clearly be desirable to measure both static and dynamic loads, but dynamic response of the model to tunnel vibration and flow fluctuations will tend to swamp readings. It is very difficult to pick out what's happening at frequencies above the model-balance frequency, which tends to be low. By careful, light weight, statically balanced construction, perhaps with isolation mounts to attenuate base motion, and with careful analysis of the data, it would be possible to obtain useful information, but success would not be assured the first try. This would require a dedicated test, as the weight, friction, and damping of pressure tubes, transducers, and cables would be intolerable.

For these reasons, only static external loads should be considered in a test of this type.

With this restriction, the following points should be kept in mind during test planning.

- Priority: It is assured that external loads will be only part of the total data to be gathered during the test, but what is the relative importance? Will the test be a failure if the external loads data are not usable?

- Cost: How much budget is available for special instrumentation or precision model work?

- Schedule: How much time is available? Schedule and cost considerations make the use of existing, checked-out instrumentation very deisrable.

- Resolution: Will the selected set-up be able to separate the wheat from the chaff?

- Load Capacity: The loads will often be acting some distance from the geometric center of the balance, so the effective force capacity of the balance may be much smaller than its nominal value. If the balance is greatly over-strength the resolution will suffer, but deflections will be smaller.

- Deflection: Balance and support system deflections are very difficult to calculate, and are almost invariably underestimated. Even where empirical data are available on balance deflections, the compliance of the various joints involved prevents an accurate estimate.

- Dynamics: Where there is deflection and there is mass (and large telescope models tend to be heavy) the model-balance system will have a tendency to oscillate. If there is enough component of the aerodynamic load at or below the model-balance resonant frequencies, oscillations will develop which will increase the total deflection.

- Space Available: The volume and location of the space that is available for the balance may have a strong influence on the design.

Two Examples

Keeping these guidelines in mind, here are a pair of examples of at least partially successful attempts to measure external loads on telescope systems in the Ames 14 foot transonic wind tunnel.

Large Pointing System Phase I Tests

Both tests were conducted during the Large Pointing System (LPS) study. The first test was an exploratory one to obtain preliminary data on three quite different pointing system concepts. The first model, shown in Figure 1, was a coelostat system. It had a fixed horizontal telescope and used two mirrors arranged like a periscope in a large sphere to direct the beam. The outer gimbal was rotation of the sphere about the telescope centerline; the inner was rotation of about one third of the sphere relative to the rest. Only a third of the sphere was exposed to the air flow.

The second model, shown in Figure 2, was a heliostat system, also with a fixed horizontal telescope but with only one mirror mounted in a horizontal drum to point the beam. The outer gimbal is rotation of the drum about the telescope centerline and the inner gimbal is rotation of the mirror about an axis perpendicular to the drum axis. This had very low aerodynamic drag but a somewhat limited field of view.

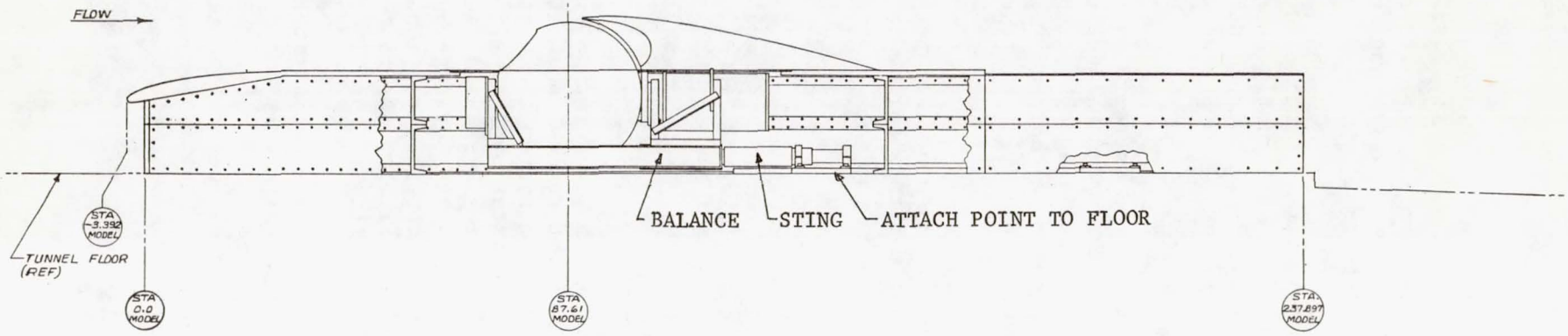

Figure 1. Coelostat Model, Phase I Installation - Side View.

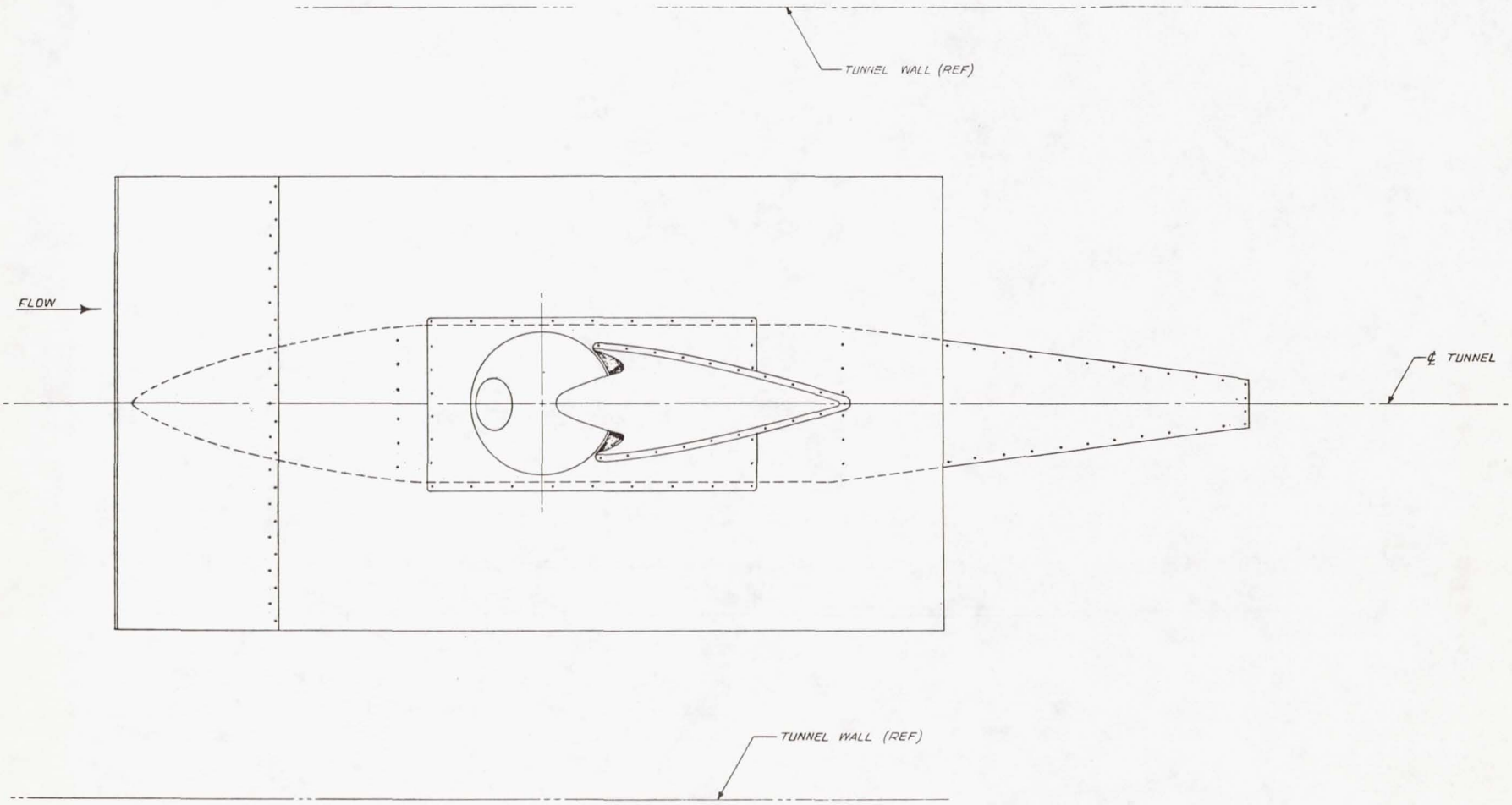

Figure 1. (concluded) Coelostat Model, Phase I Installation - Top View.

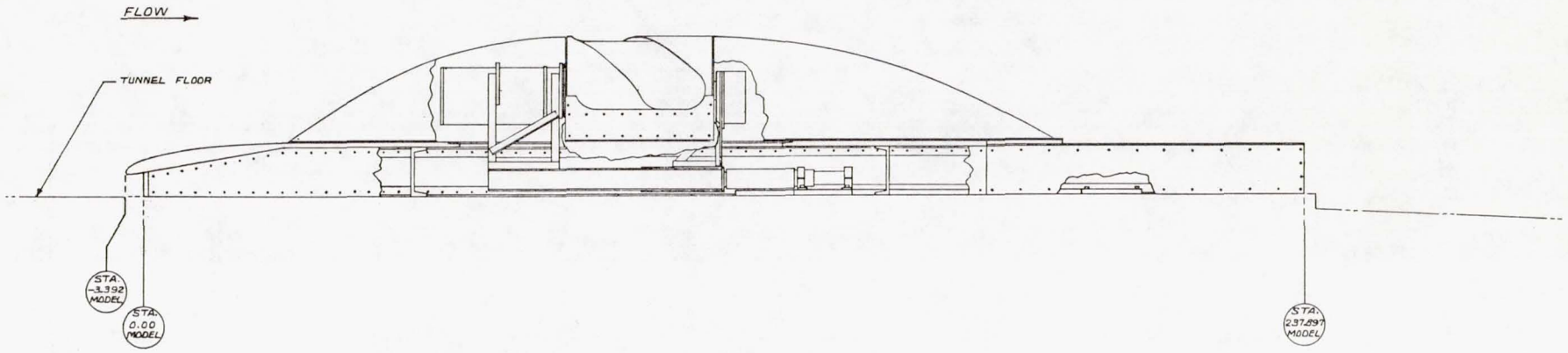

Figure 2. Heliostat Model, Phase I Installation.

The third model, shown in Figure 3, was an on-gimbal telescope resembling the system used on the Airborne Laser Laboratory. The entire telescope was rotated in azimuth and elevation.

All three models used a common support structure and boundary layer splitter plate. Because the tunnel construction precluded removing large portions of the tunnel walls, the entire large sphere of the first model had to be inside the tunnel. This was done by raising the boundary layer splitter plate and having a large fairing underneath. The other two models used the same arrangement but with the splitter plate lowered to reduce the total frontal area of the model and support assembly.

This would have been an ideal application for an old fashioned external balance found under the floor of most large low speed tunnels, but the 14 foot transonic tunnel did not have one. As a substitute, the largest sting balance available (a 4 inch Task balance) was mounted in a steel platform just above the floor and supported by a stub sting attached to the tunnel floor. In each case the entire telescope system was mounted to the metric platform to avoid the problem of attempting to separate metric and non-metric portions of the optical system.

This was a satisfactory arrangement except for one very important respect: deflection. Both the coelstat and the on-gimbal telescope models developed enough lift to rise into the floor plate and aft fairing, both statically and dynamically. By grinding extra clearance and shimming the sting/floor interface, the coelostat model could be tested, but the extra drag and higher load center of the on-gimbal telescope caused such large deflections that the metric platform had to be bolted to the floor to complete the test program. No problems were encountered with the heliostat because of the much lower load level.

In conclusion, this load measurement scheme provided data which was useful in the LPS study, even though it was never analyzed systematically. Data for the coelostat and on-gimbal telescope are definitely contaminated by unknown magnitudes of contact, or fouling, between the metric and nonmetric portions of the model, but there is no doubt that the measured values are approximately correct and good enough for sizing structure. The deflection problems slowed down the test program but did not prevent it from being completed.

Large Pointing System Phase II Tests

After the phase I tests a study was made using the phase I data to select one configuration for more detailed study. The configuration selected was a modification of the coelostat, adding a limited travel of the upper turning mirror to improve high

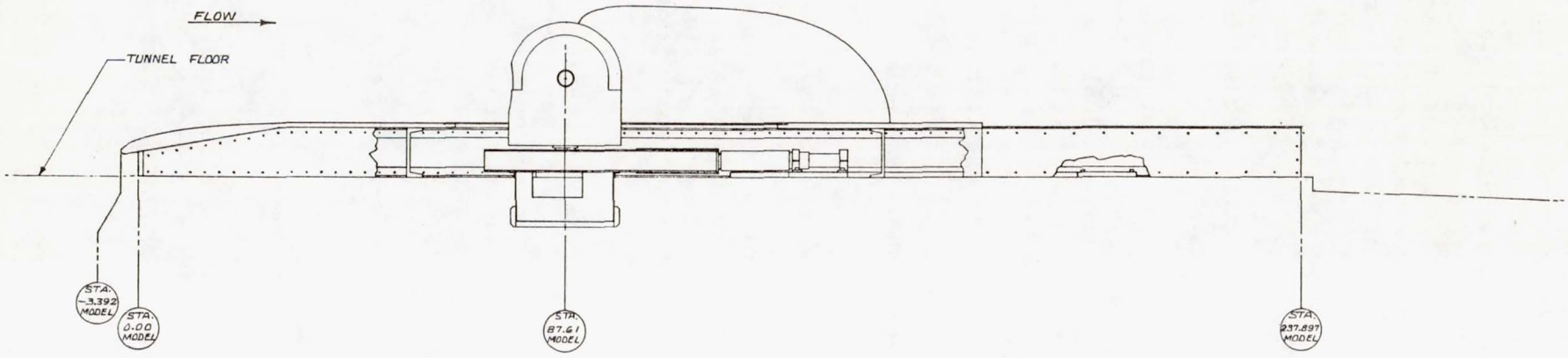

Figure 3. On Gimbal Telescope Model, Phase I Installation.

frequency response. This did not change the model, except that it was now called a coelostat/heliostat, and what was inner gimbal on the coelostat became middle gimbal on the coelostat/heliostat.

During the roughly 9 months between the two tests an important change was made to the 14 foot tunnel, however. A large balance was installed below the floor for testing semispan models. This was not perfectly suited for the LPS test because it was only 5 component (lift force, which would be side force on a semispan model, was left out) but it was quite rigid and had ample load capacity. A simple lift link was incorporated in the adaptor which bridged the space between the balance and the metric platform of the model. This is shown in Figure 4.

Several photographs of the phase II model during installation are shown in Figure 5. This is typical of phase I, also. Figure 6 shows several of the configuration changes; the external wind screens (EWS) tested in phase I were similar to the phase II screens pictured here.

The new balance arrangement eliminated the deflection problems that had plagued the phase I tests. The results were marred by greater than desired zero shifts, but these were not large enough to render the data useless. After the test, NASA characterized the zero shift problem as temperature related, but it was probably exacerbated by the newness of the balance and installation and the relatively low level of the loads being measured.

TEST RESULTS

In the following pages some sample results are given. In each case the reference area and length are the crossection area and diameter, respectively, of the sphere or the cylindrical portion of the housing that is exposed to the airstream. Moments referenced about the intersection of the outer and inner (middle, for phase II) gimbal axes.

In all the plots which follow Delta 1 is the inner (or middle for phase II) gimbal deflection, and Delta 2 is the outer gimbal deflection.

Figures 7 and 8 are force and moment data, respectively, for the on-gimbal telescope model, showing the effect of a one inch high 45 percent porosity wind screen. The apparent reduction in drag due to the screen is probably due to small changes in the non-metric fairing; the effect of the screen on yawing moment looks reasonable.

Figures 9 and 10 are force and moment data for the heliostat model, showing the effect of 1 inch and 1.8 inch high wind screens at Mach .7. Figures 11 and 12 are similar data at Mach .85. The forces and moments are predictably small, with the screens showing clearly on drag.

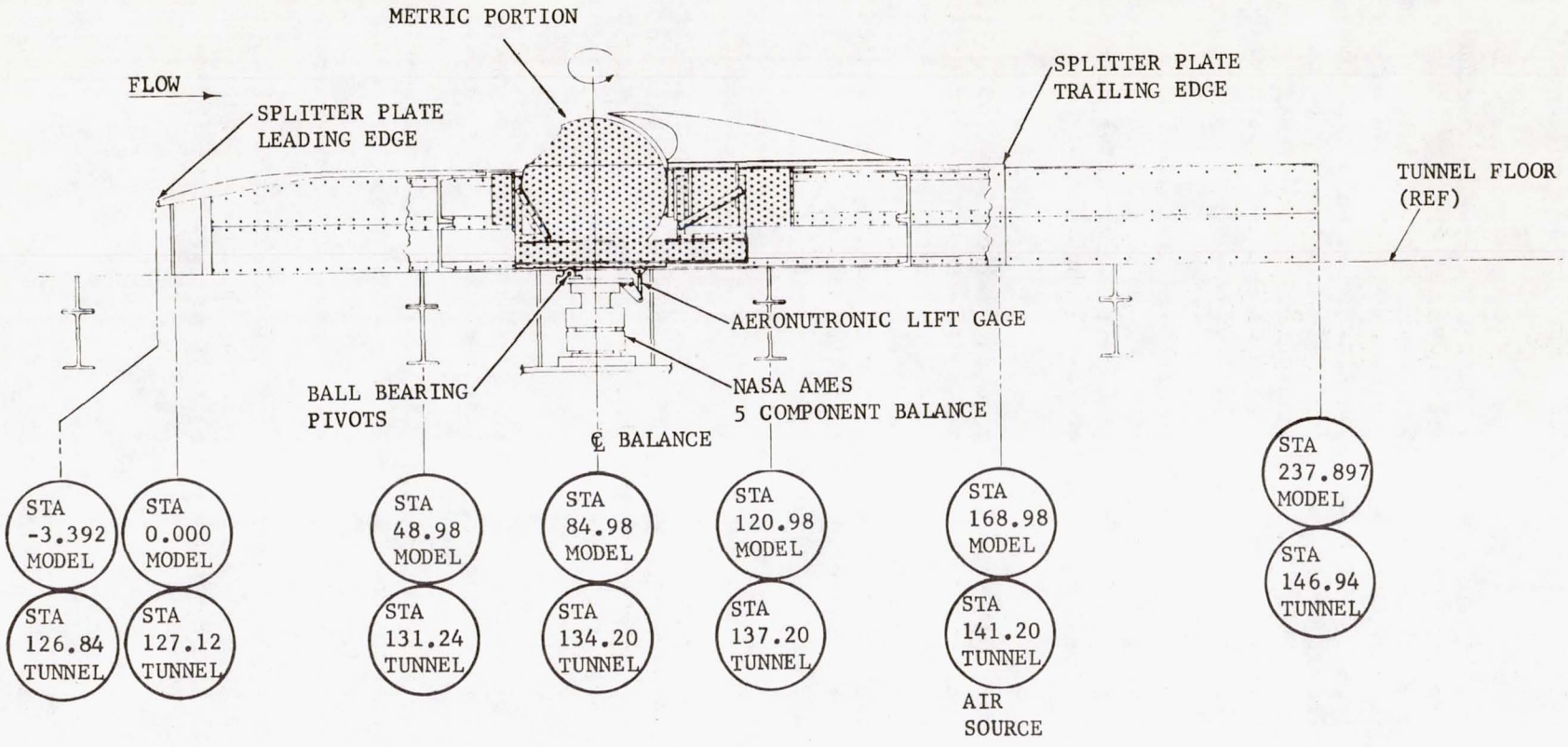

NOTE: TUNNEL STATIONS ARE FEET
MODEL STATIONS ARE INCHES

Figure 4. Phase II Model Installation.

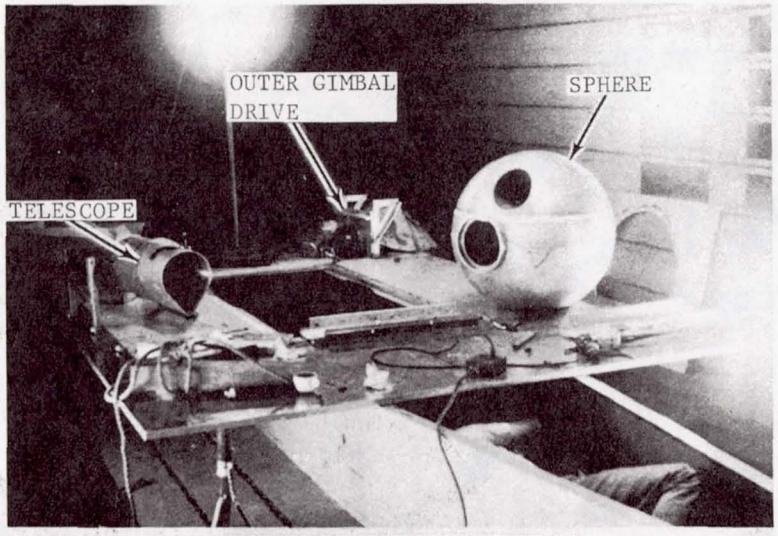

MODEL DURING INSTALLATION

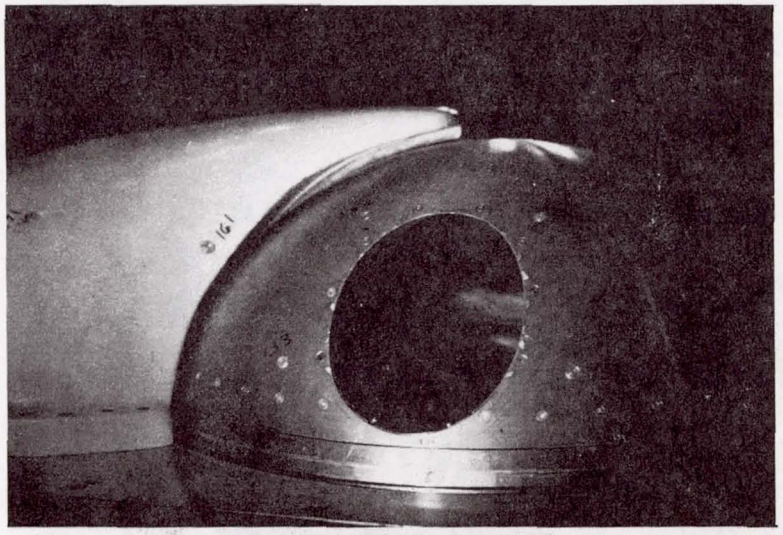

CONFIGURATION 1

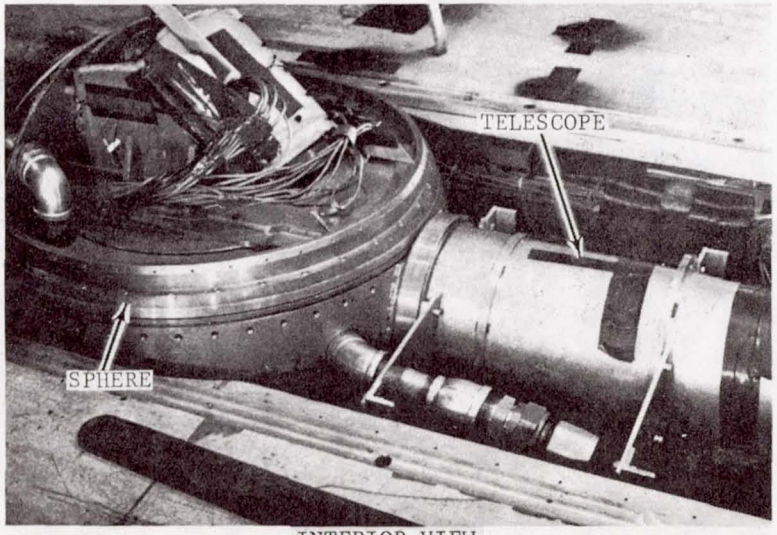

INTERIOR VIEW

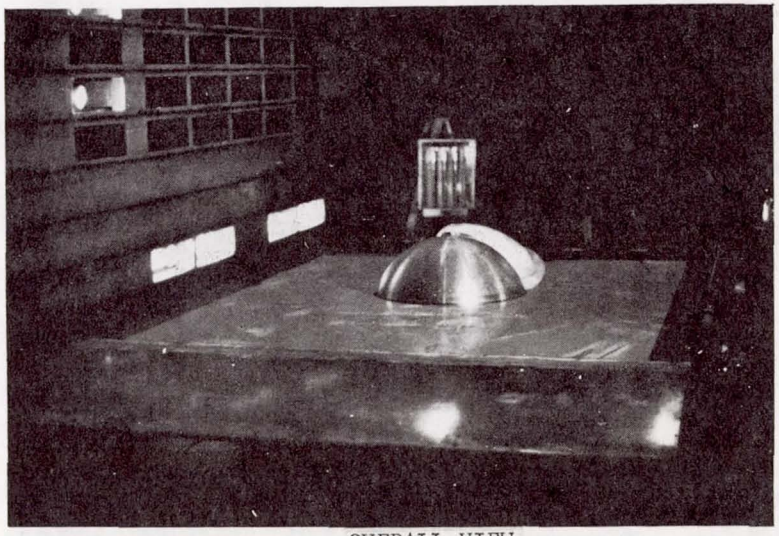

OVERALL VIEW

Figure 5. Photographs of Phase II Installation.

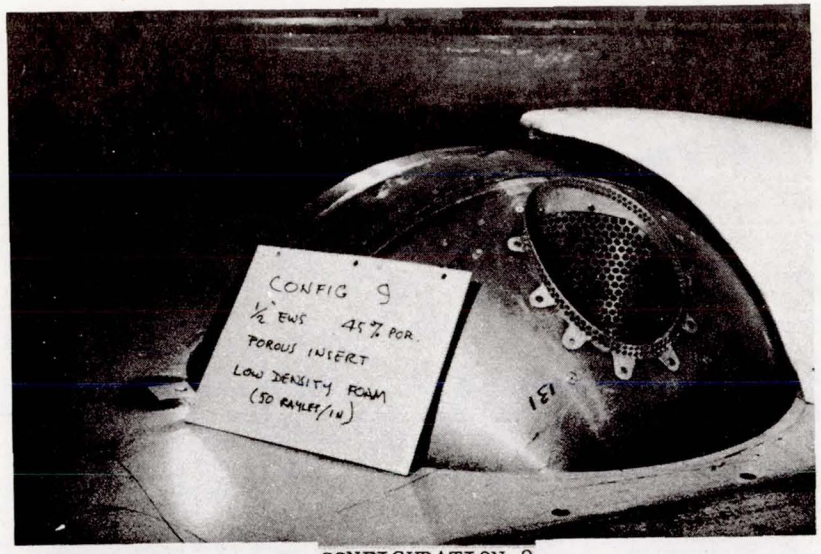

CONFIGURATION 9

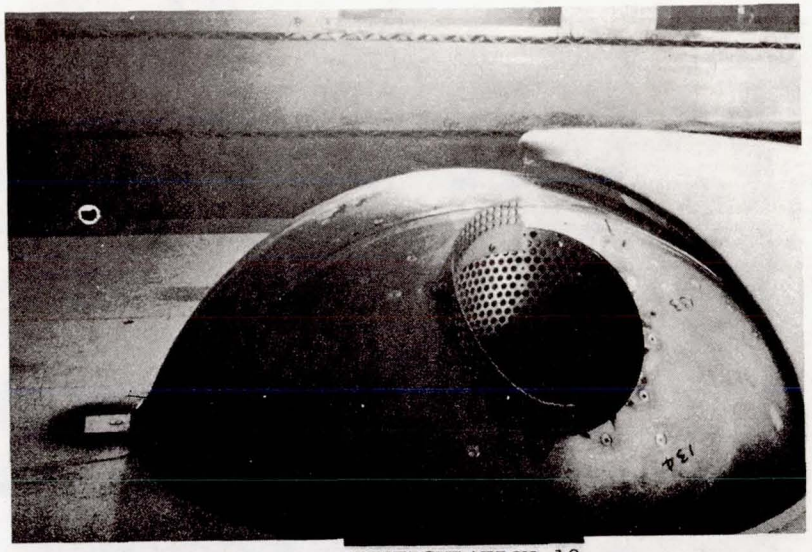

CONFIGURATION 10

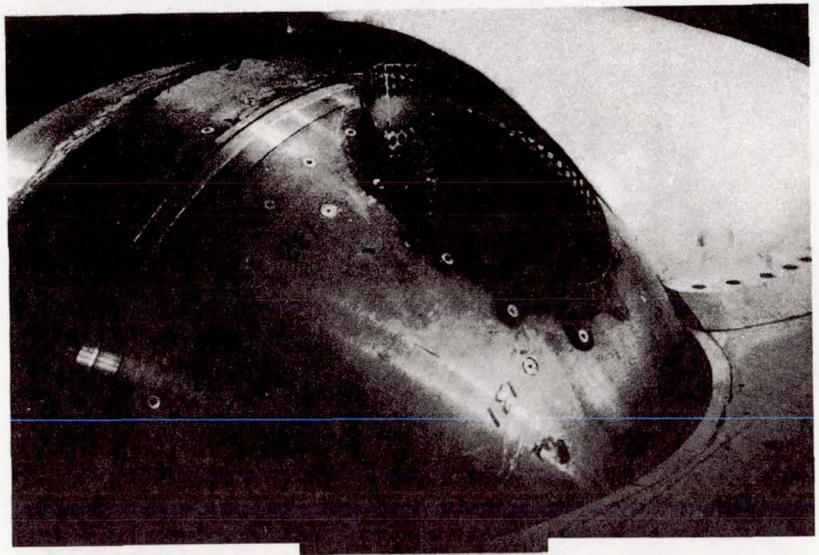

CONFIGURATION 13

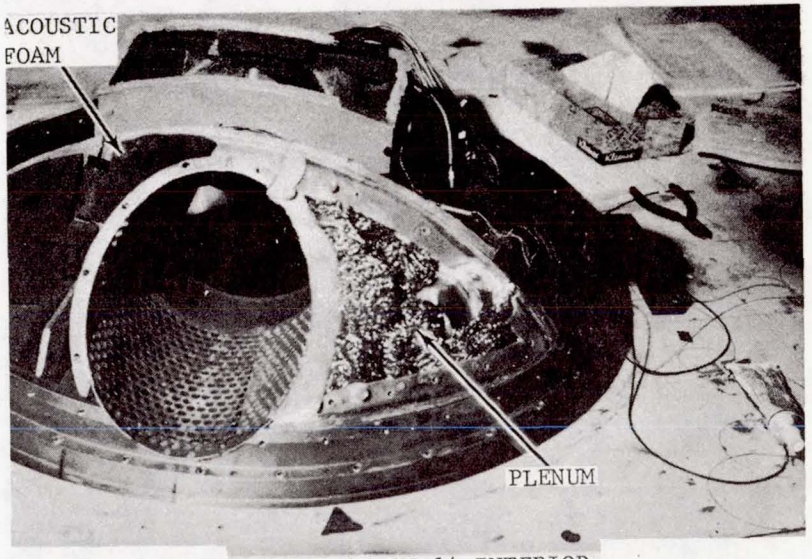

CONFIGURATION 14 INTERIOR

Figure 6. Photographs of Phase II Configurations.

Figure 7.

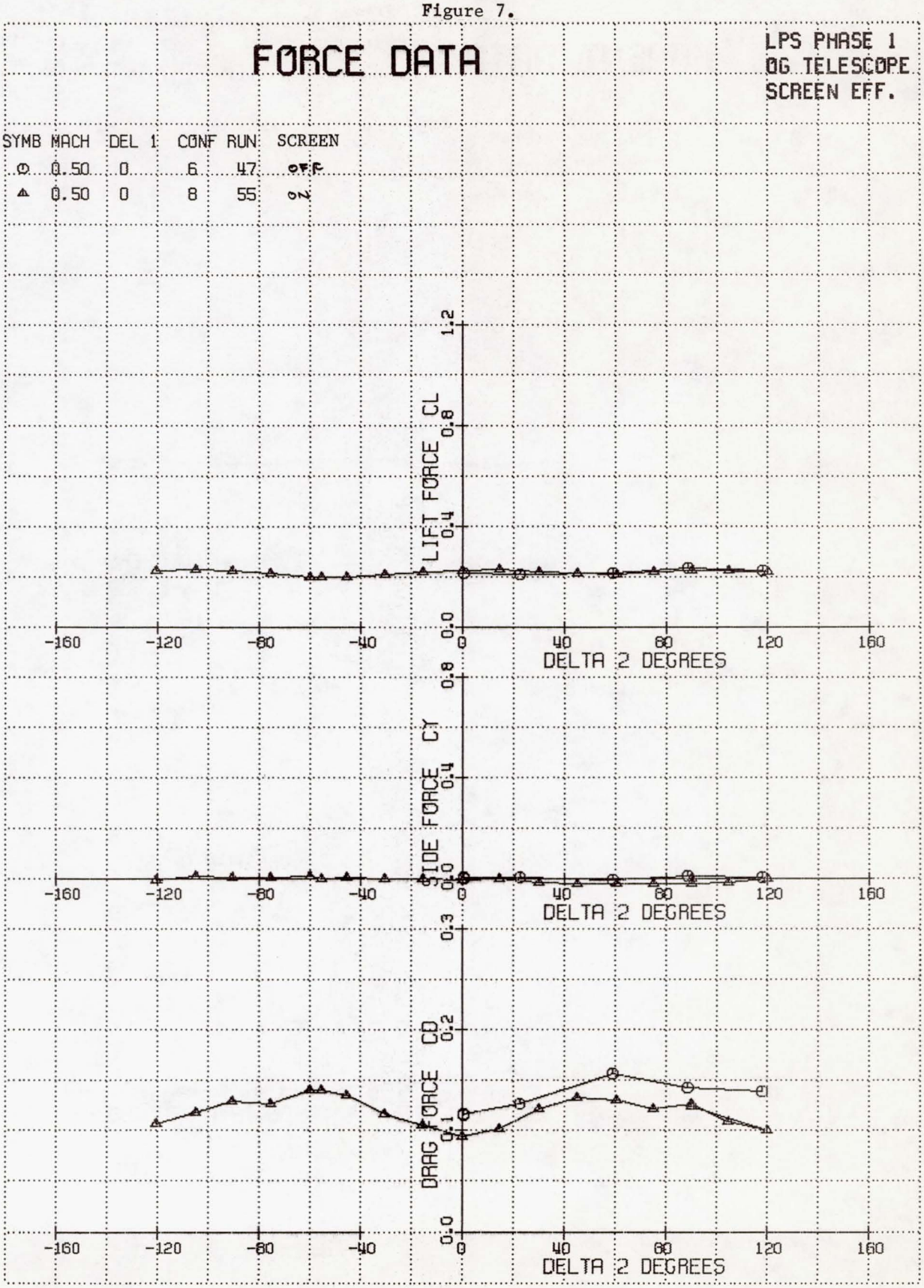

DATE=8-10-1979 AT 12:46:26

Figure 8.

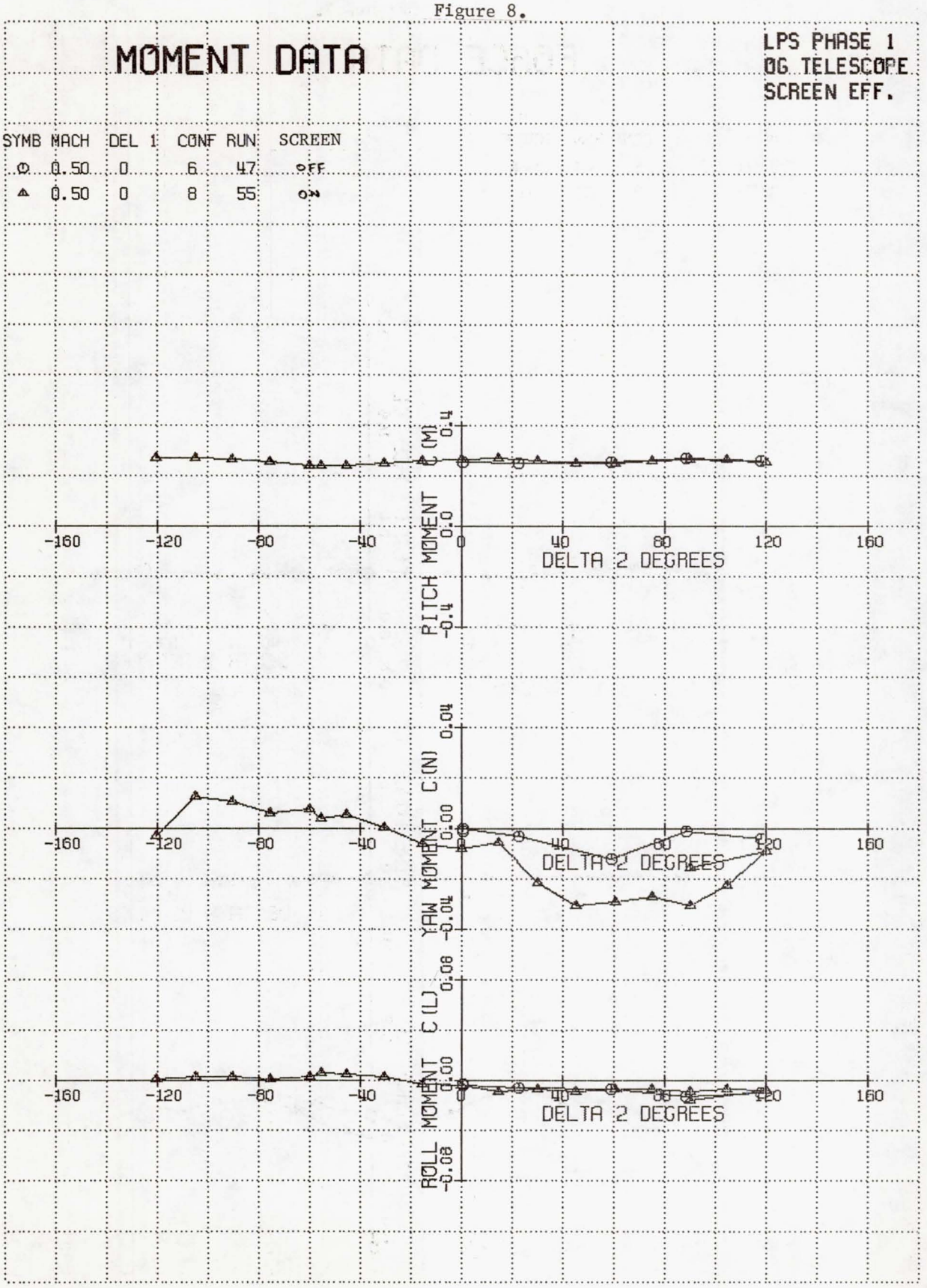

DATE=8-10-1979 AT 12:46:35

Figure 9.

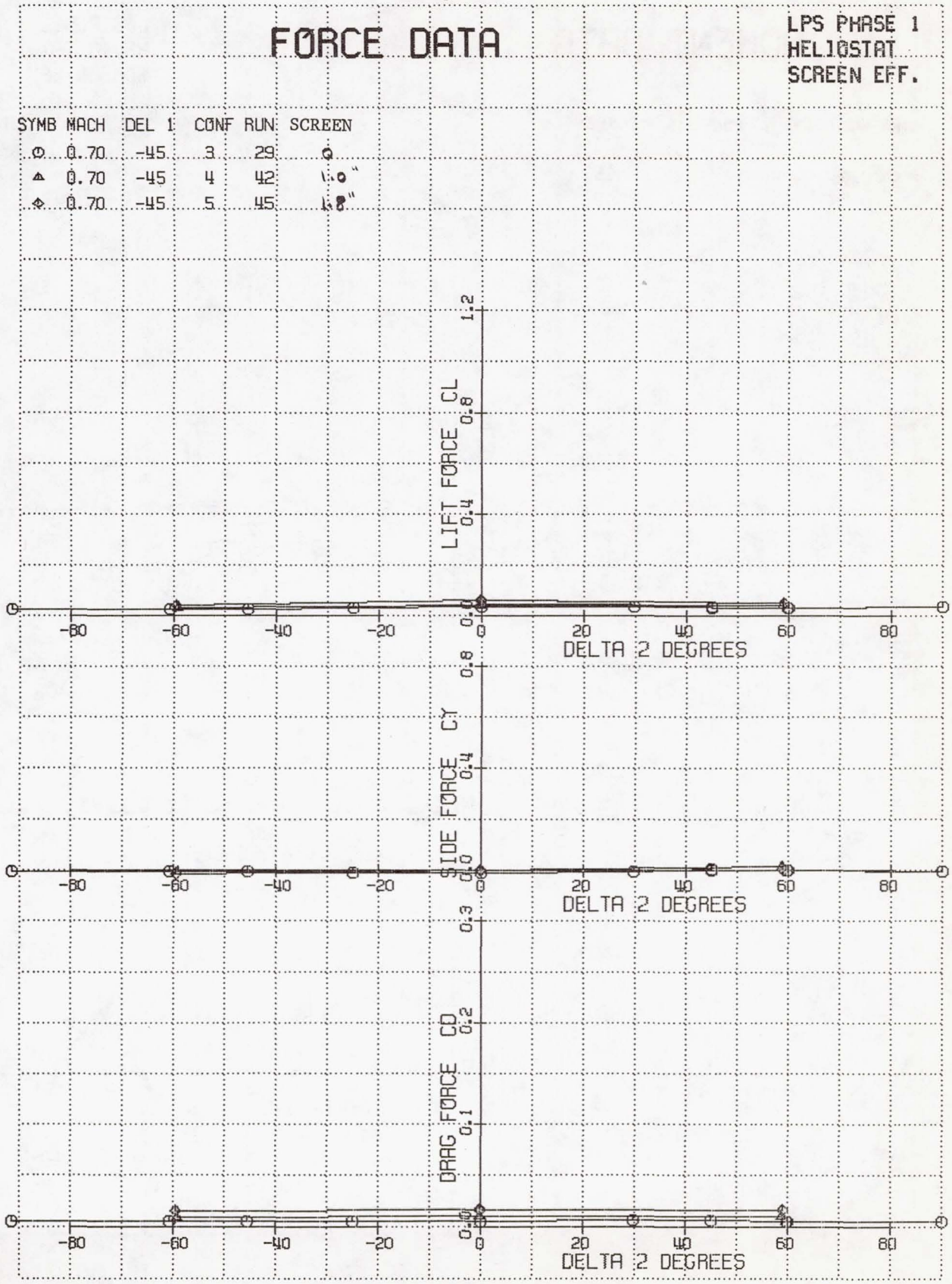

Figure 10.

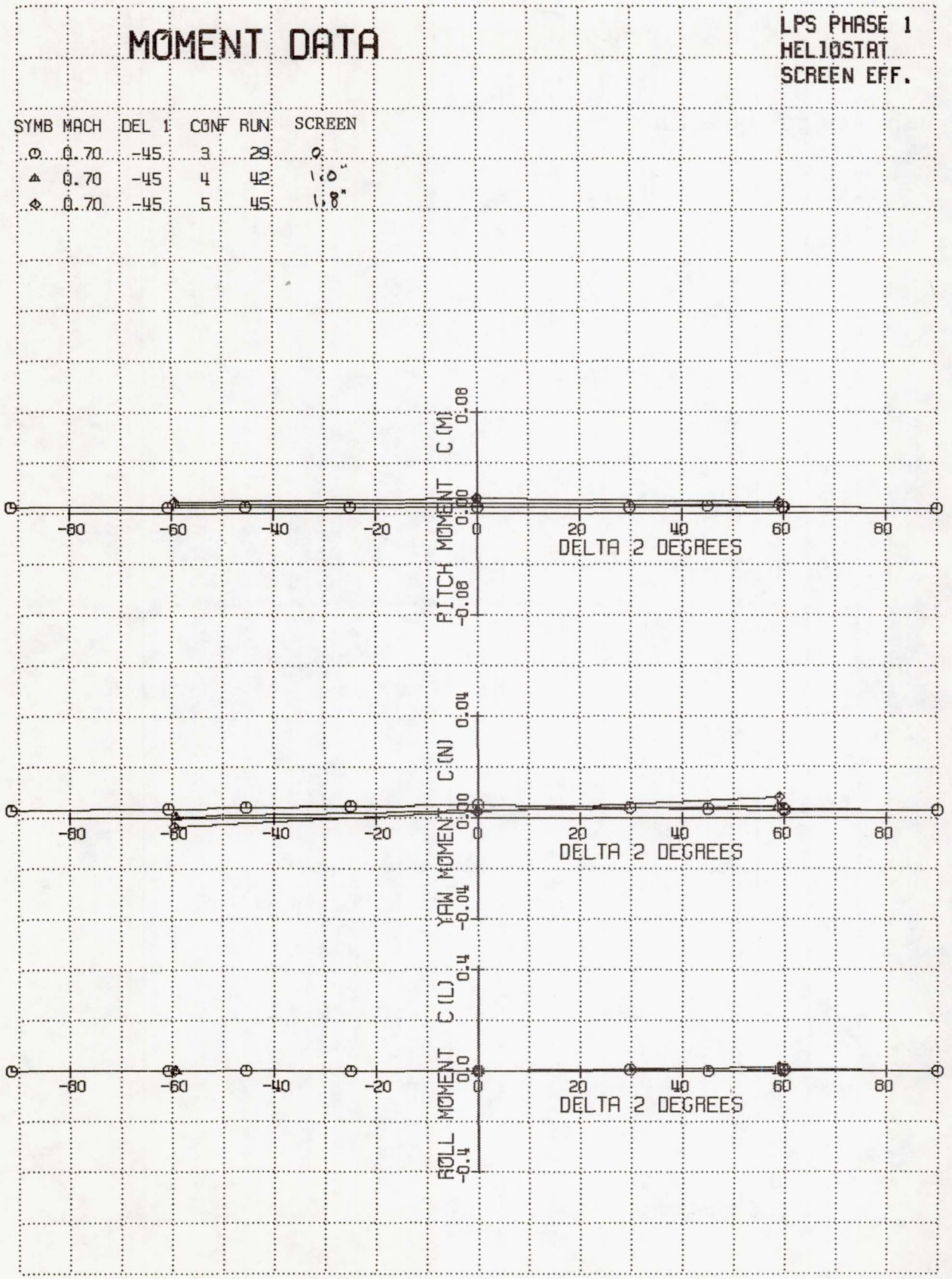

DATE=8-10-1979 AT 12:26:27

Figures 13 and 14 show force and moment data for the phase I coelostat model, showing the effect of a 1 inch high screen at Mach numbers of .7 and .85. Figure 15 is the moment about the inner gimbal axis.

The second phase was conducted with the coelostat model from phase I, modified not only with respect to external torque measurement, but also with remote control added to the inner gimbal rotation - which became the middle gimbal because analysis showed that small motions of the upper turning mirror were desirable. This change from coelostat to coelostat-heliostat was only a matter of nomenclature as far as the model was concerned, because the angular deflection of the new inner gimbal was too small to be of significance aerodynamically.

The addition of remote control to the middle gimbal allowed much more data to be taken per tunnel hour, and also allowed the change to middle gimbal angle as the parameter varied during each run. This change prevents comparing runs directly, but there was ample coverage of the same angles to allow some comparisons to be made.

Figures 16, 17, and 18 show force, moment, and middle gimbal moment for the phase II model with various screen heights at an outer gimbal angle of -90 degrees (with the middle gimbal axis vertical) and Figures 19, 20, and 21 show the same data at an outer gimbal angle of zero (middle gimbal axis horizontal). Some idea of the magnitude of the zero shifts can be obtained from the fact that side force, yawing moment, rolling moment, and middle gimbal moment should all be zero (except for configuration 10, which has an asymmetric screen) at Delta 2 = 90 degrees and Delta 1 = -90 degrees.

Figures 22, 23, and 24 show one configuration tested at Mach numbers ranging from 0.3 to 0.92. The data for Mach 0.3 and 0.5 look particularly erratic, suggesting that the balance is too big to measure small loads accurately.

In conclusion, the balance setup used for phase II was much more satisfactory because it allowed the primary test objectives to be met without delays caused by excessive deflections, but much crossplotting and shifting would be required to use the data for other than approximate loads estimation.

Figure 11.

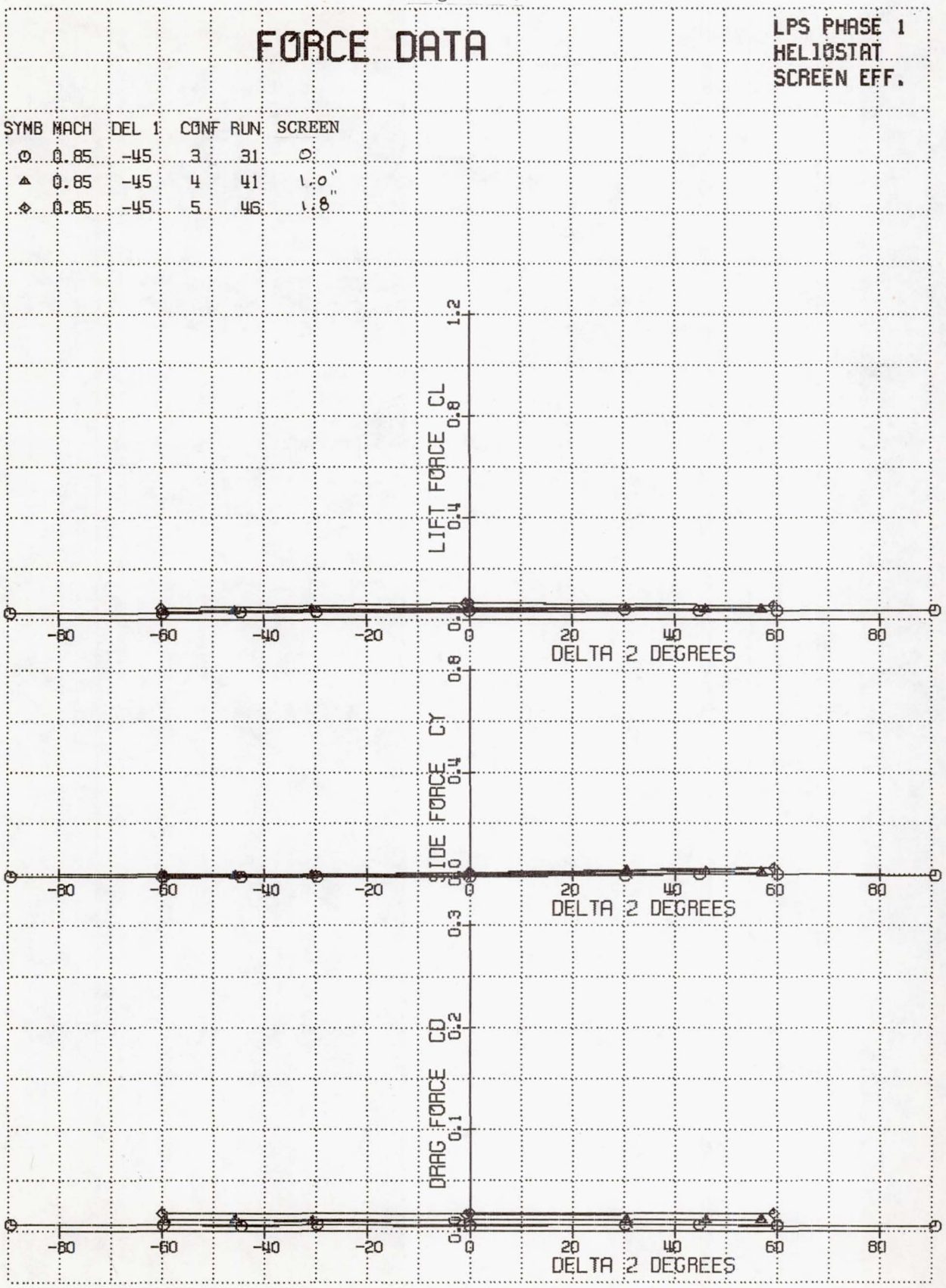

DATE=8-10-1979 AT 12:26:36

Figure 12.

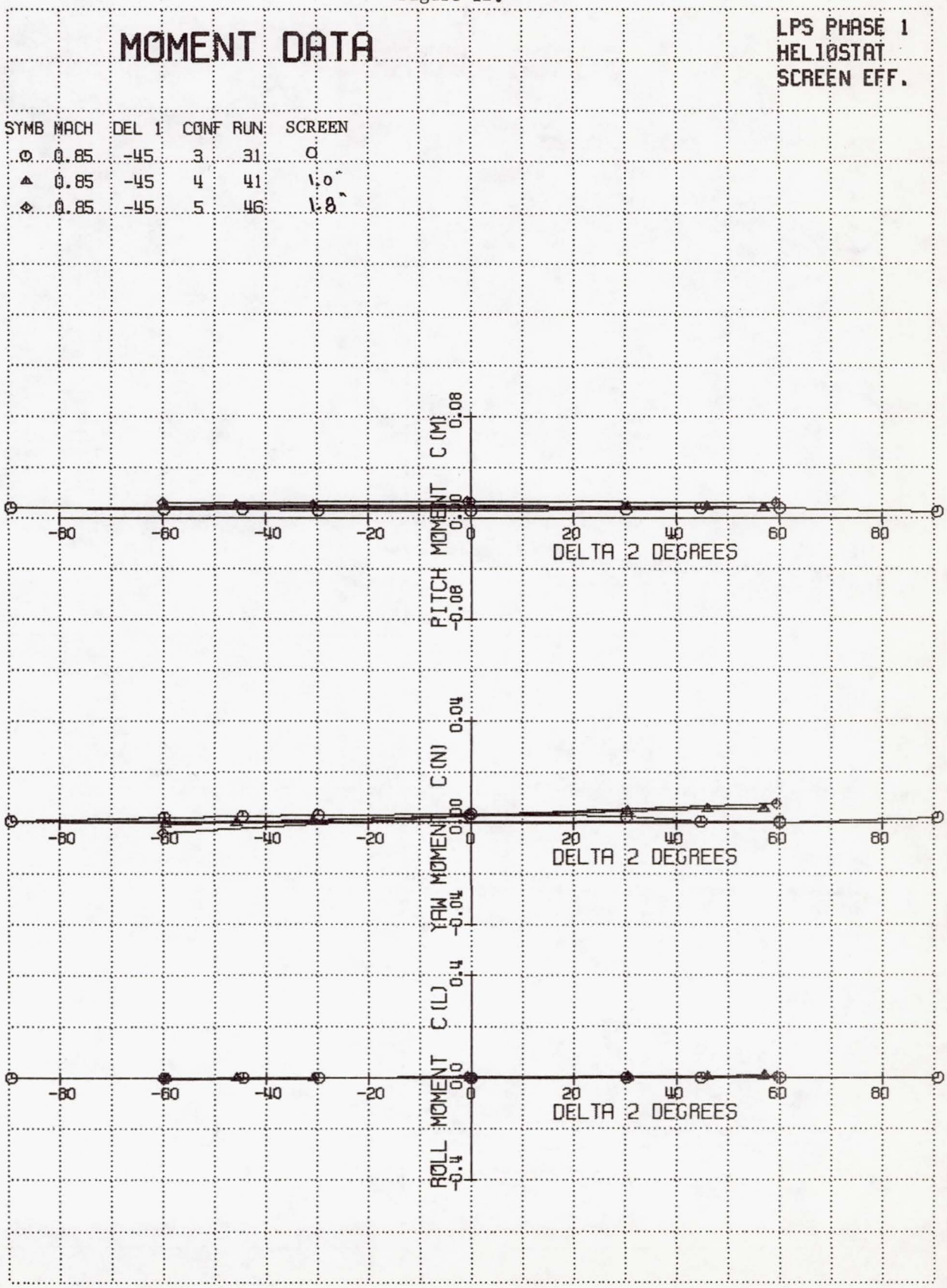

DATE=8-10-1979 AT 12:26:45

Figure 13.

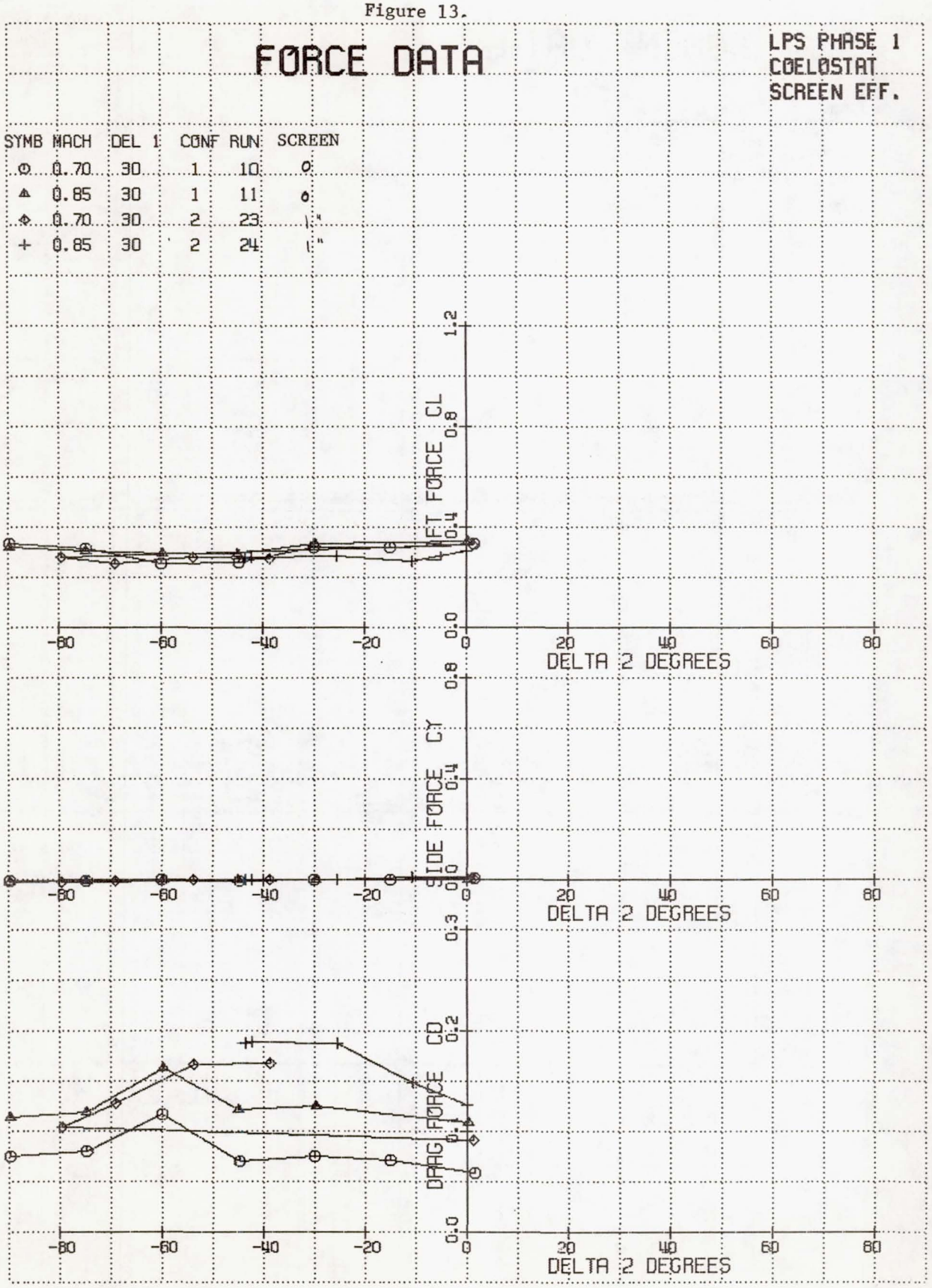

DATE=8-13-1979 AT 8:37:04

Figure 14.

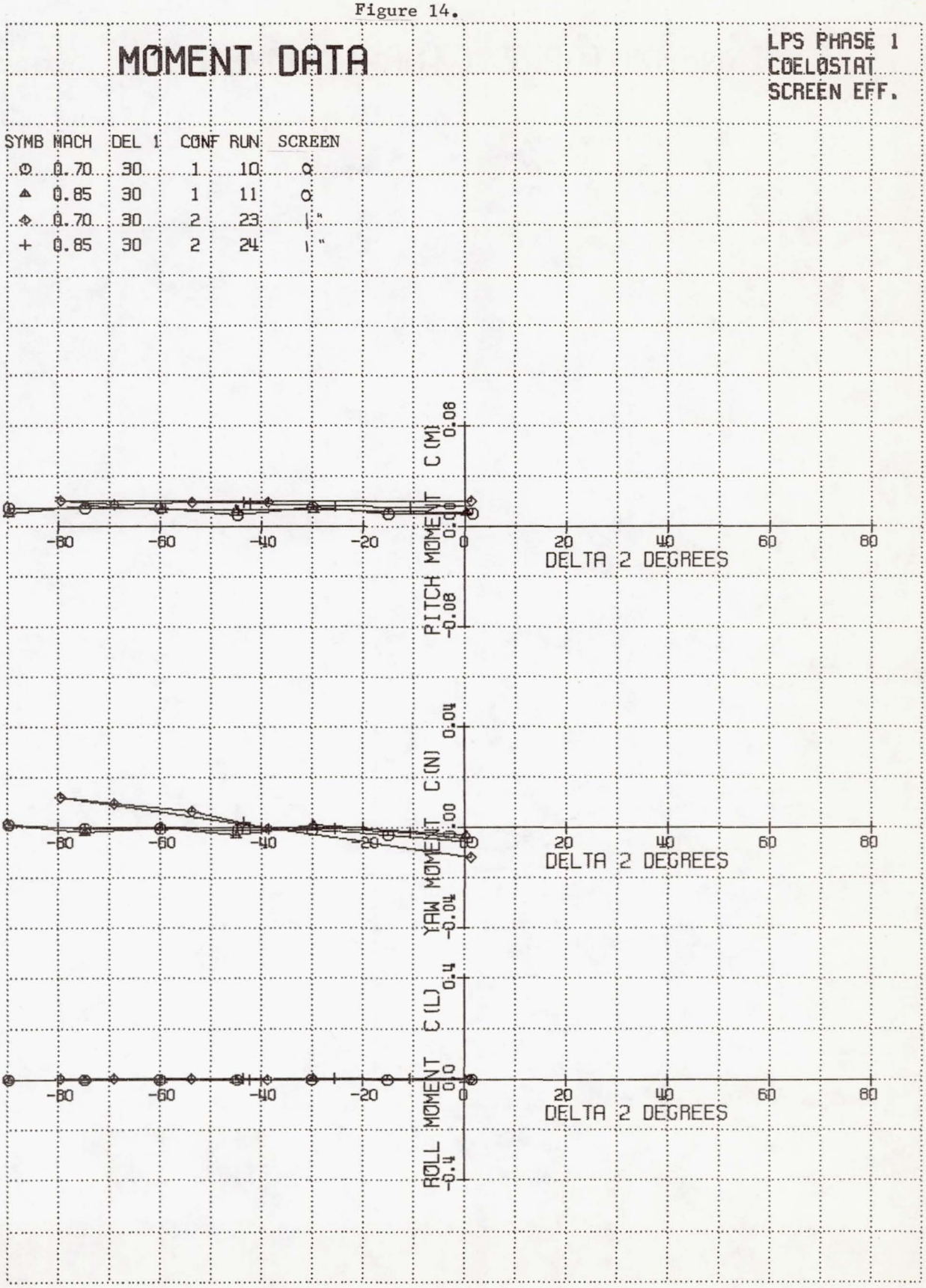

DATE=8-13-1979 AT 8:37:14

Figure 15.

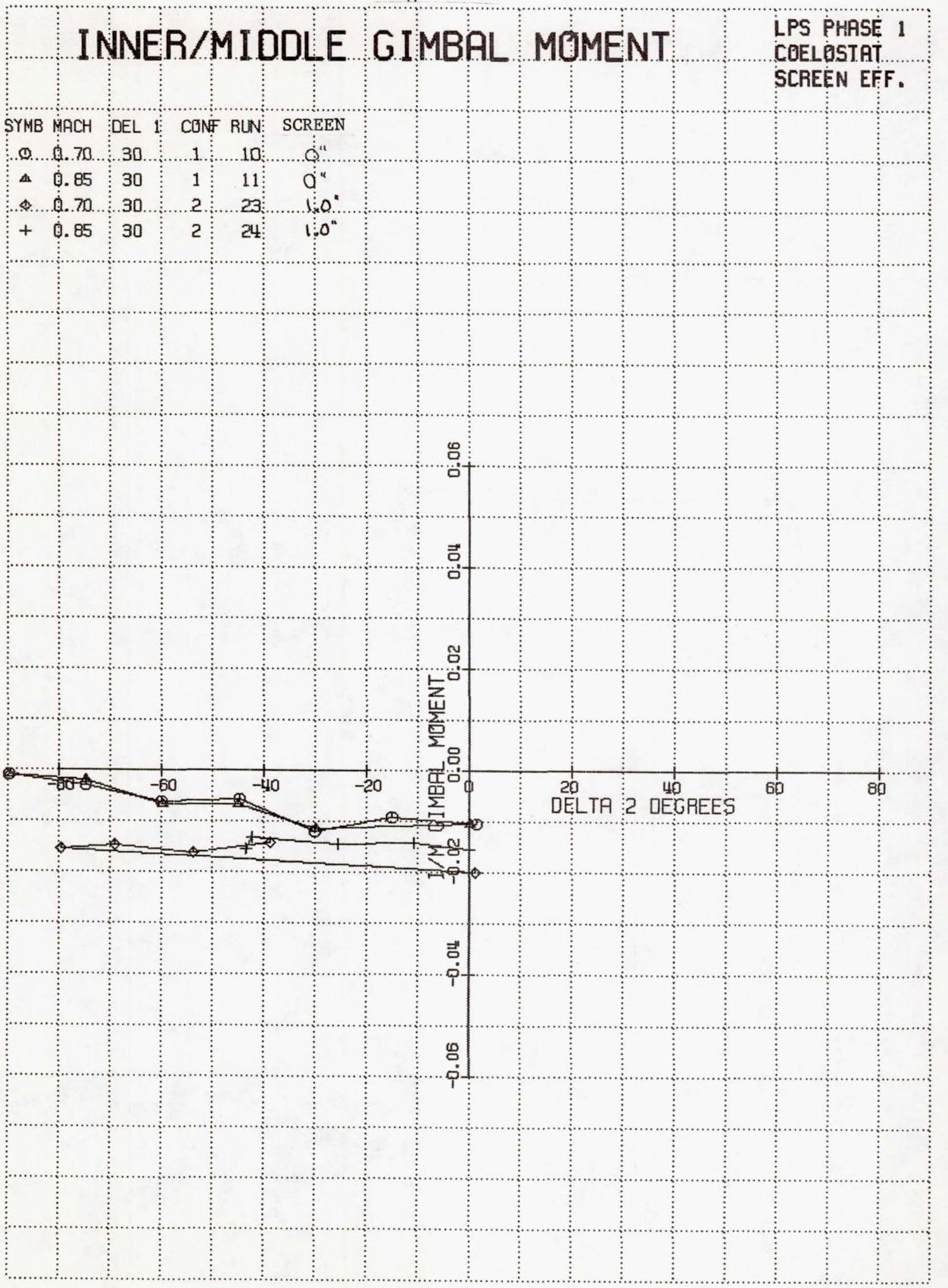

DATE=8-16-1979 AT 9:50:30

Figure 16.

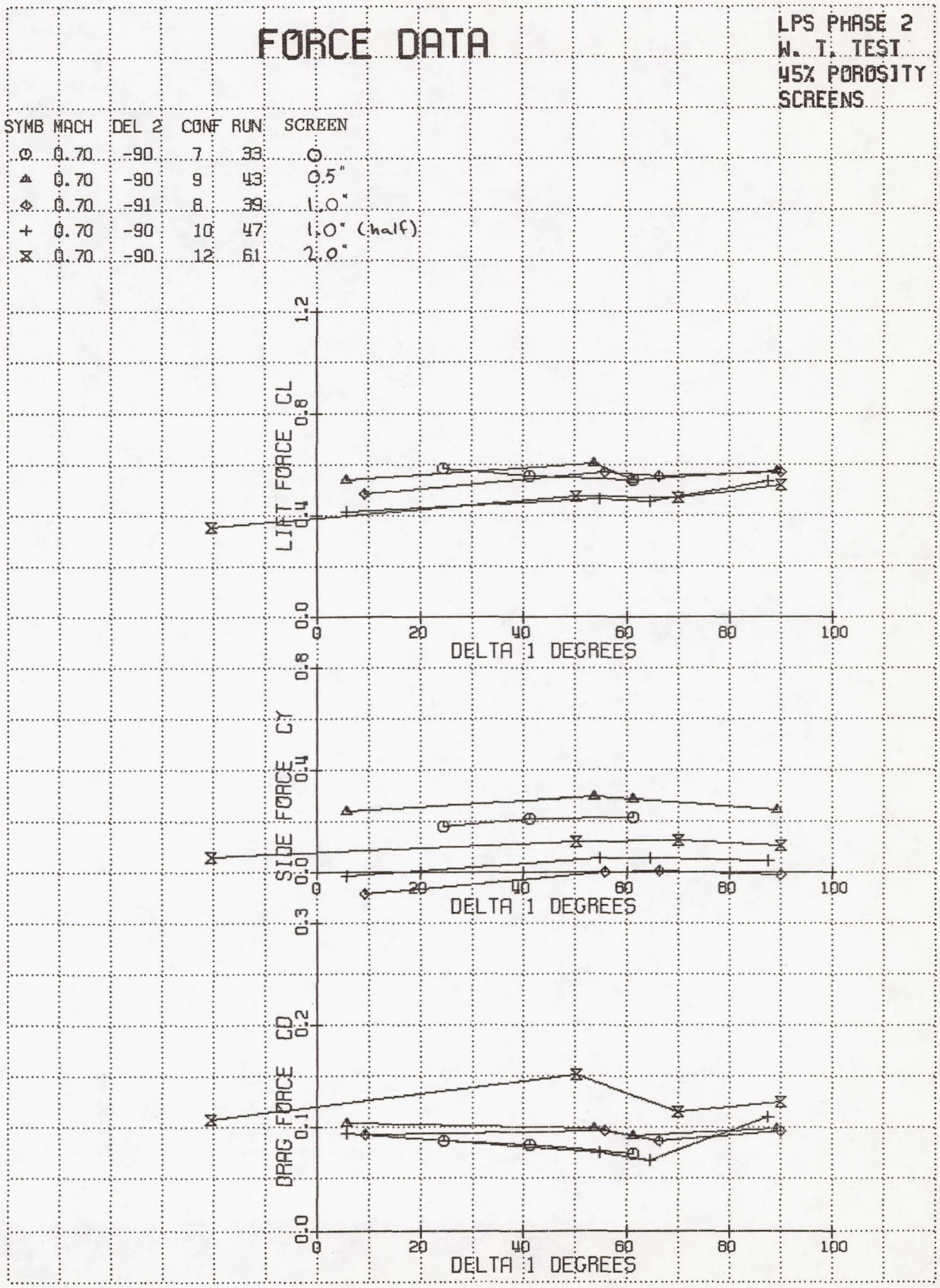

DATE=8-13-1979 AT 8:32:04

Figure 17.

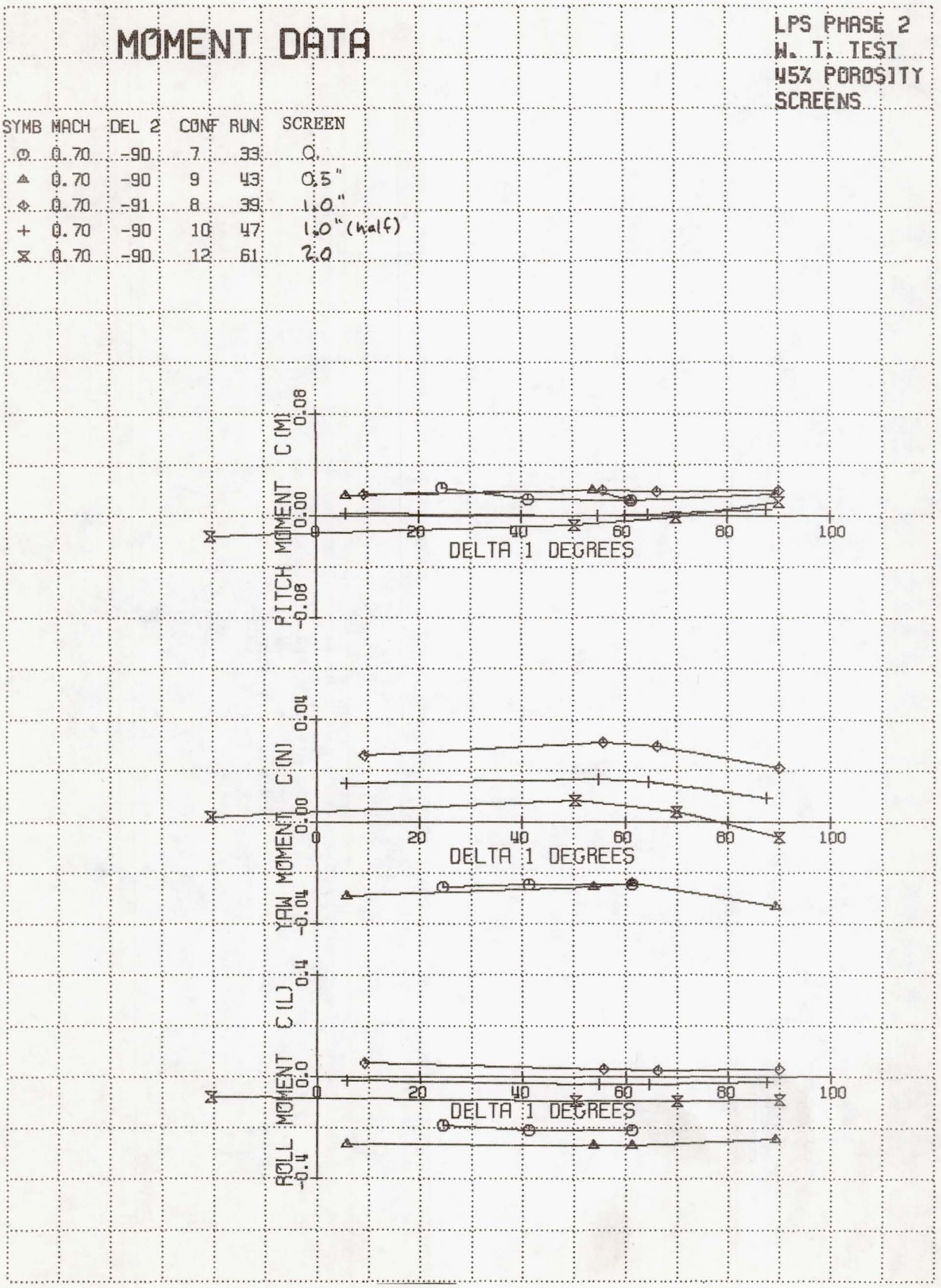

Figure 18.

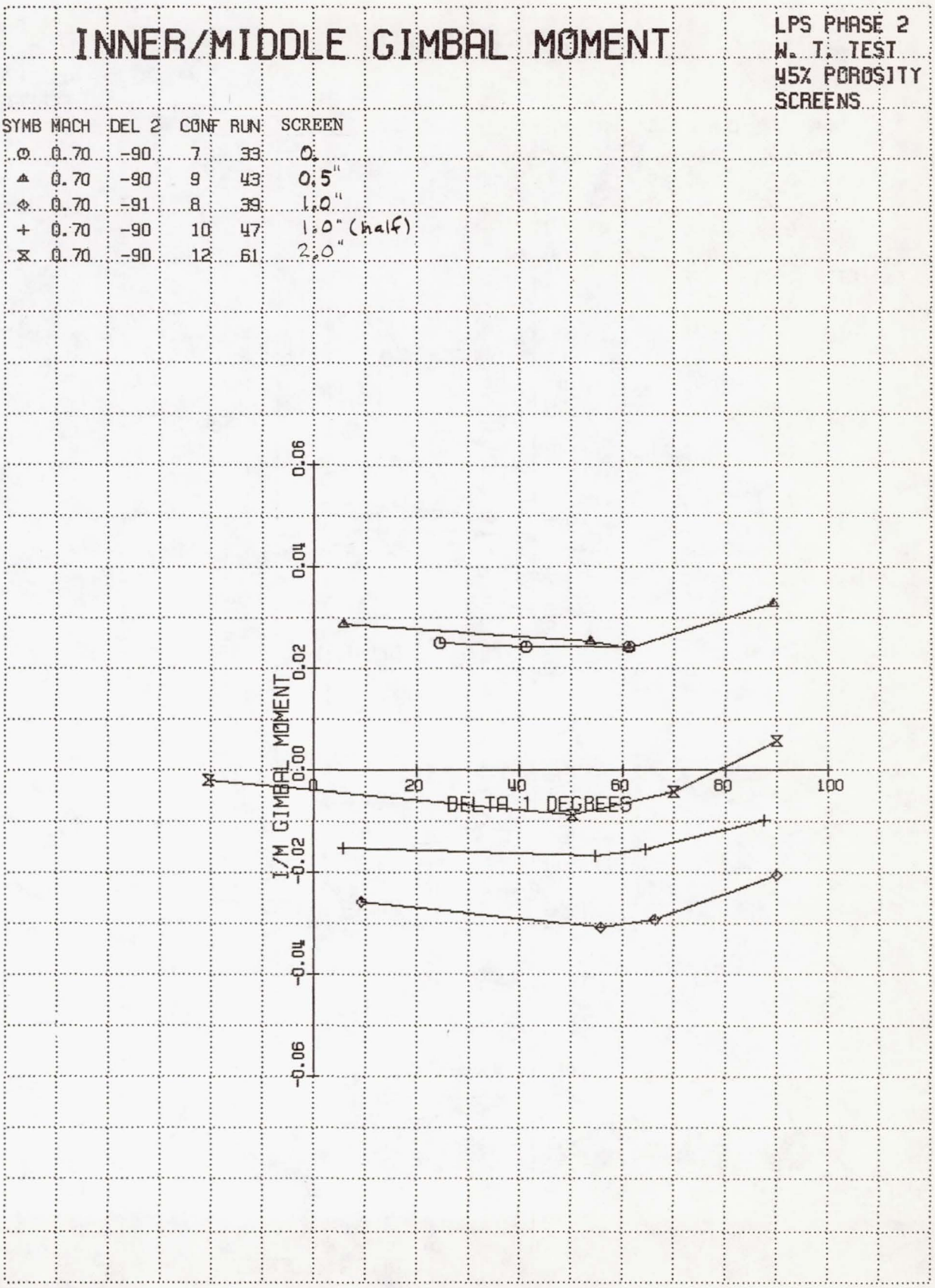

DATE=8-13-1979 AT 8:32:21

Figure 19.

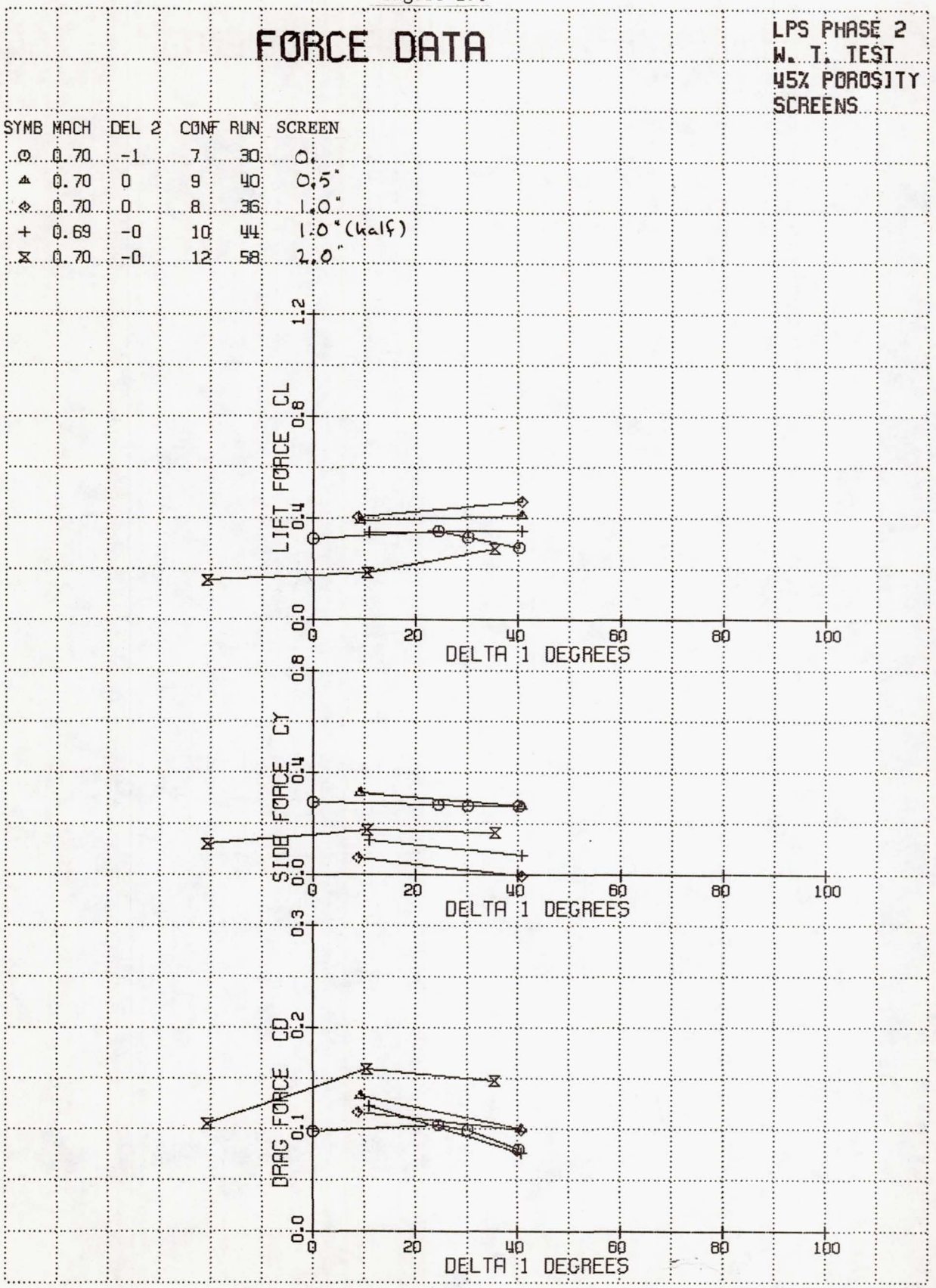

DATE=8-13-1979 AT 8:31:43

Figure 20.

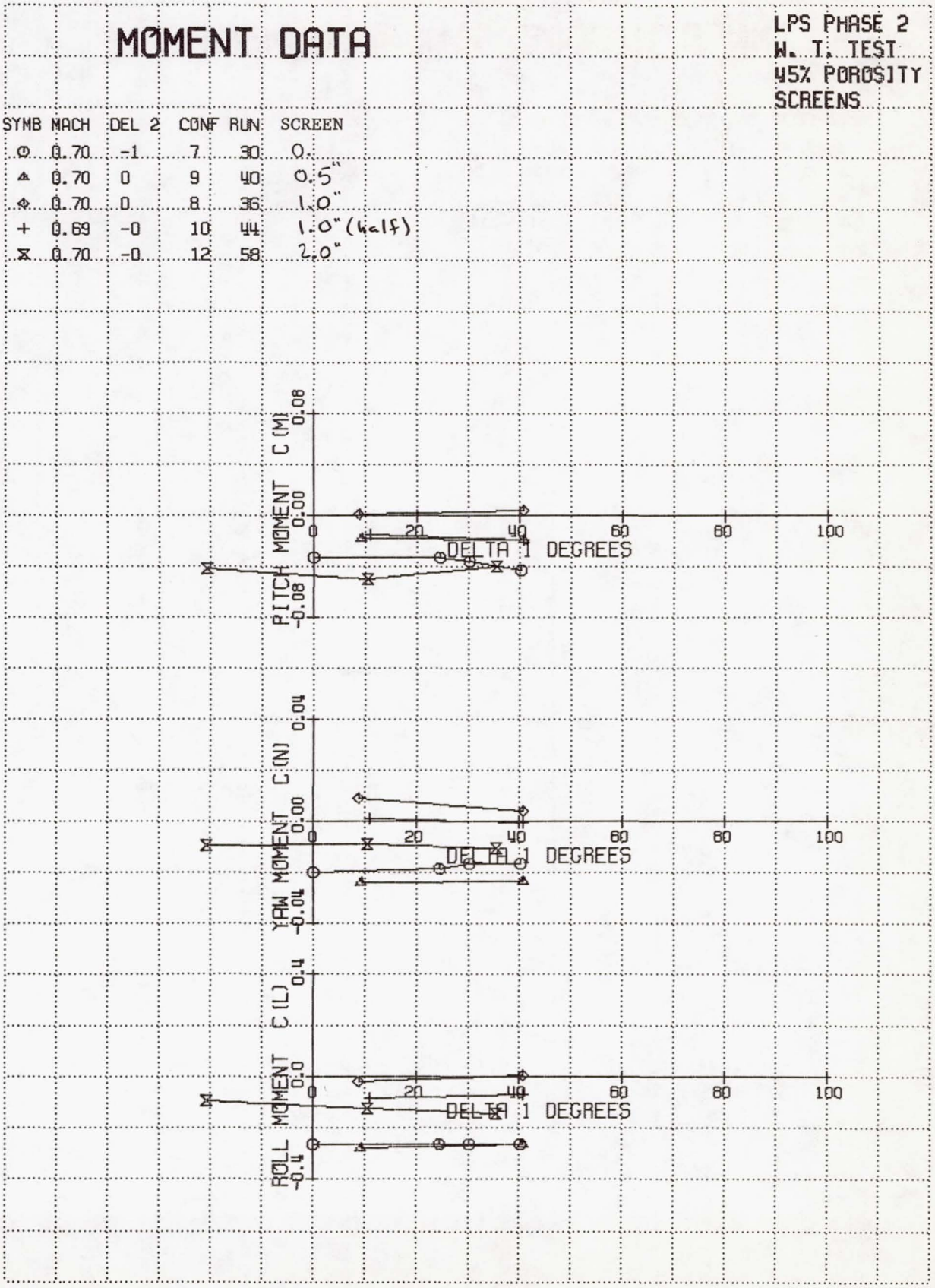

Figure 21.

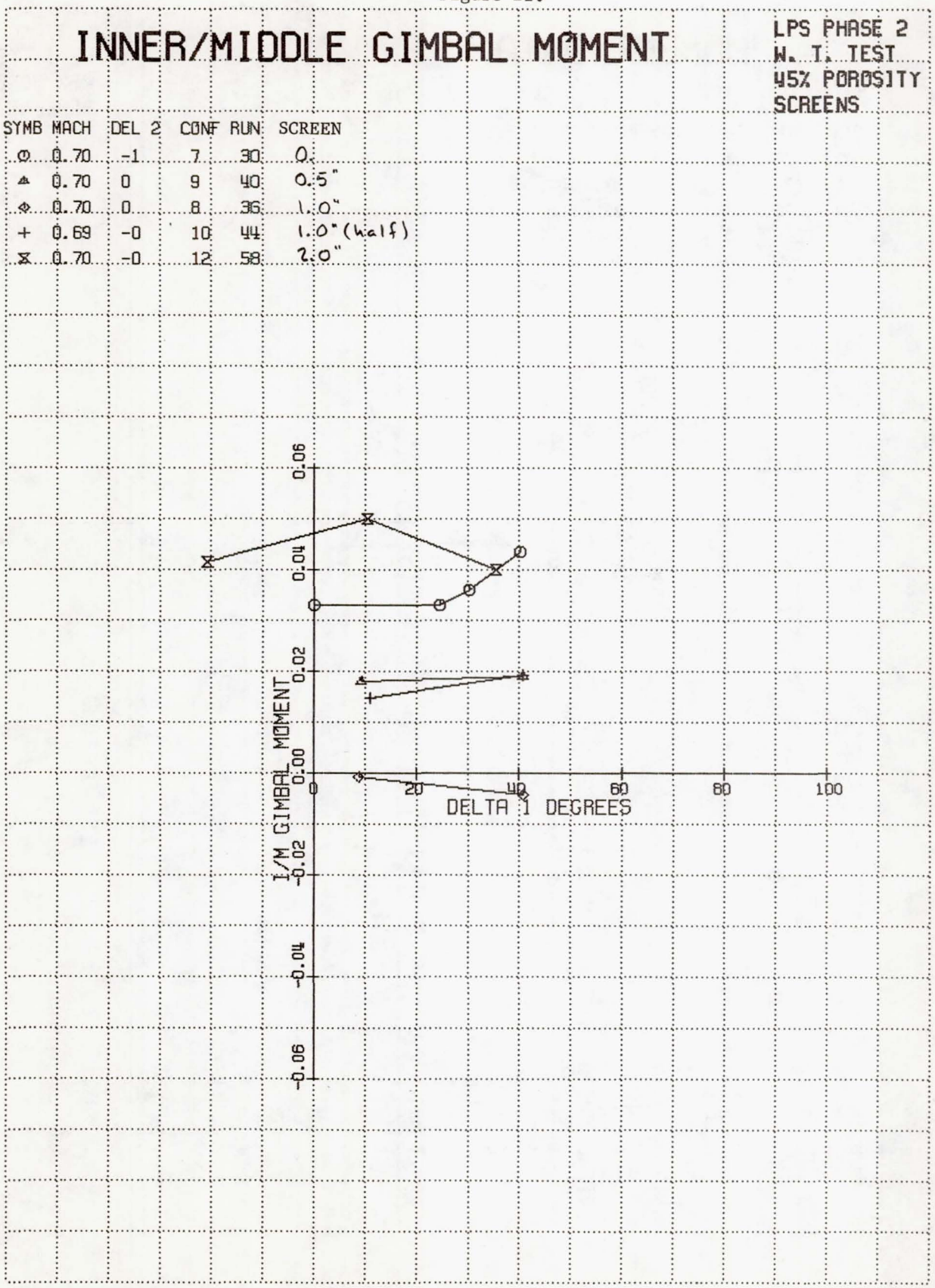

DATE=8-13-1979 AT 8:31:58

Figure 22.

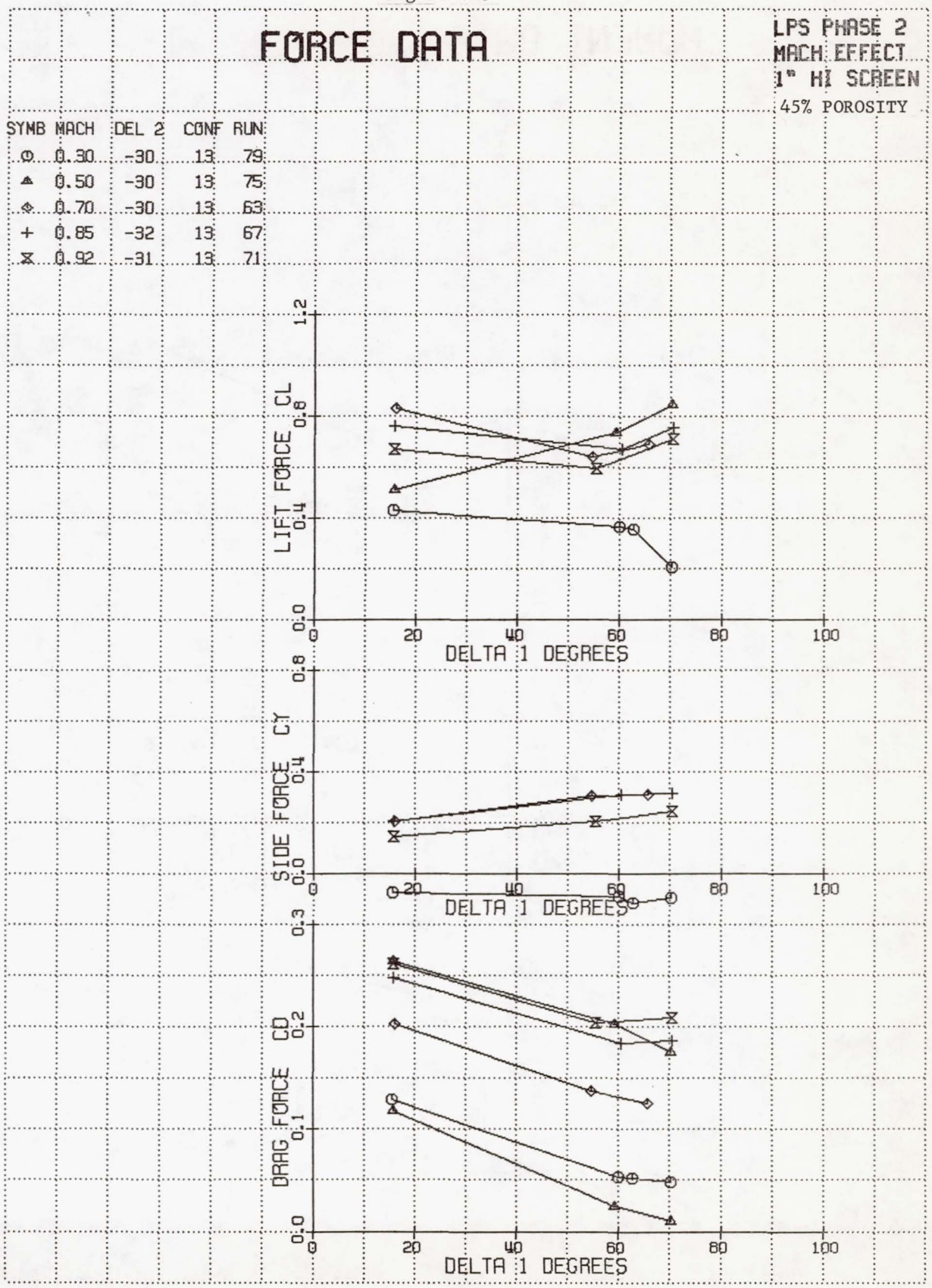

DATE=8-1-1979 AT 17:49:42

Figure 23.

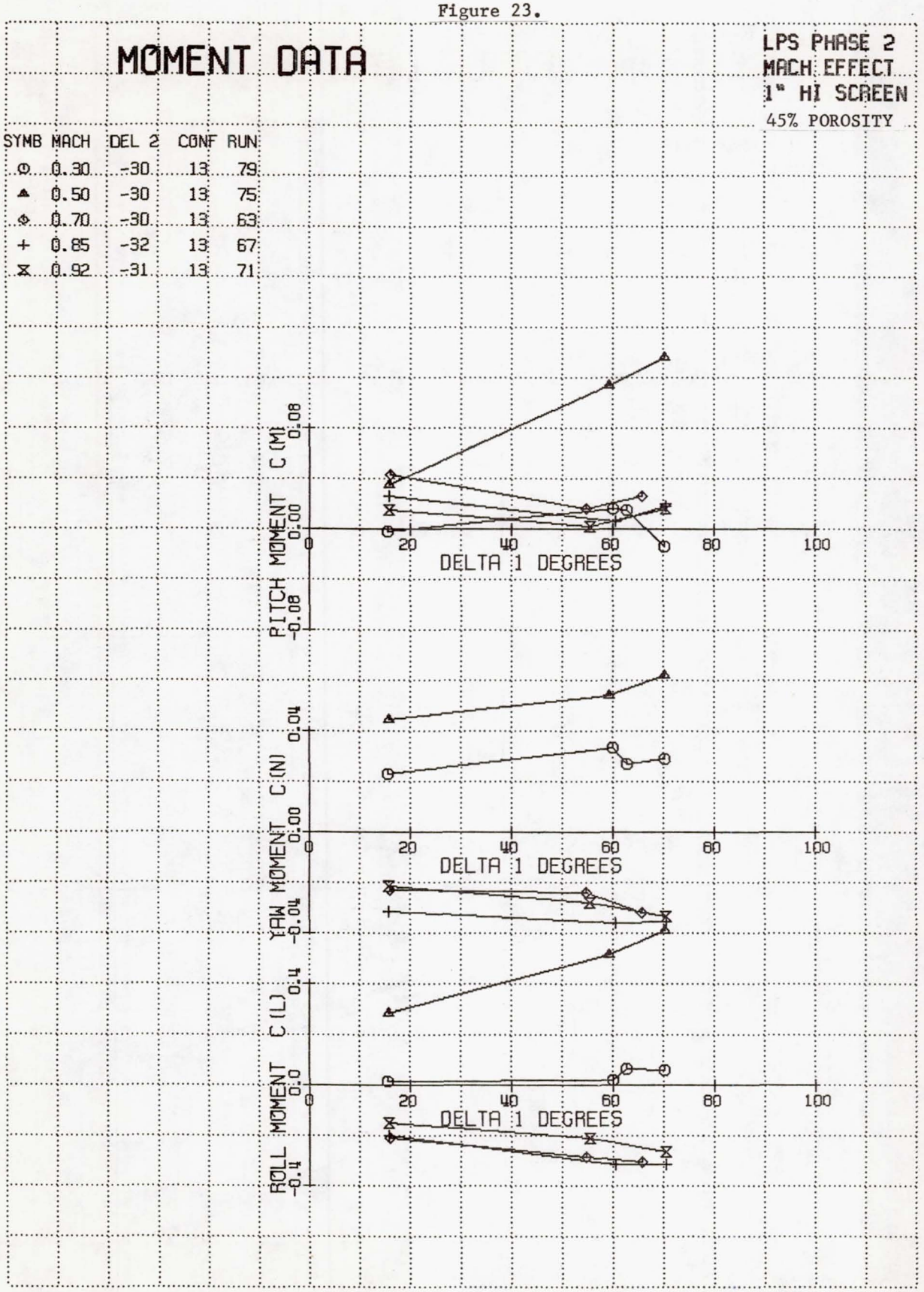

DATE=8-1-1979 AT 17:49:50

Figure 24.

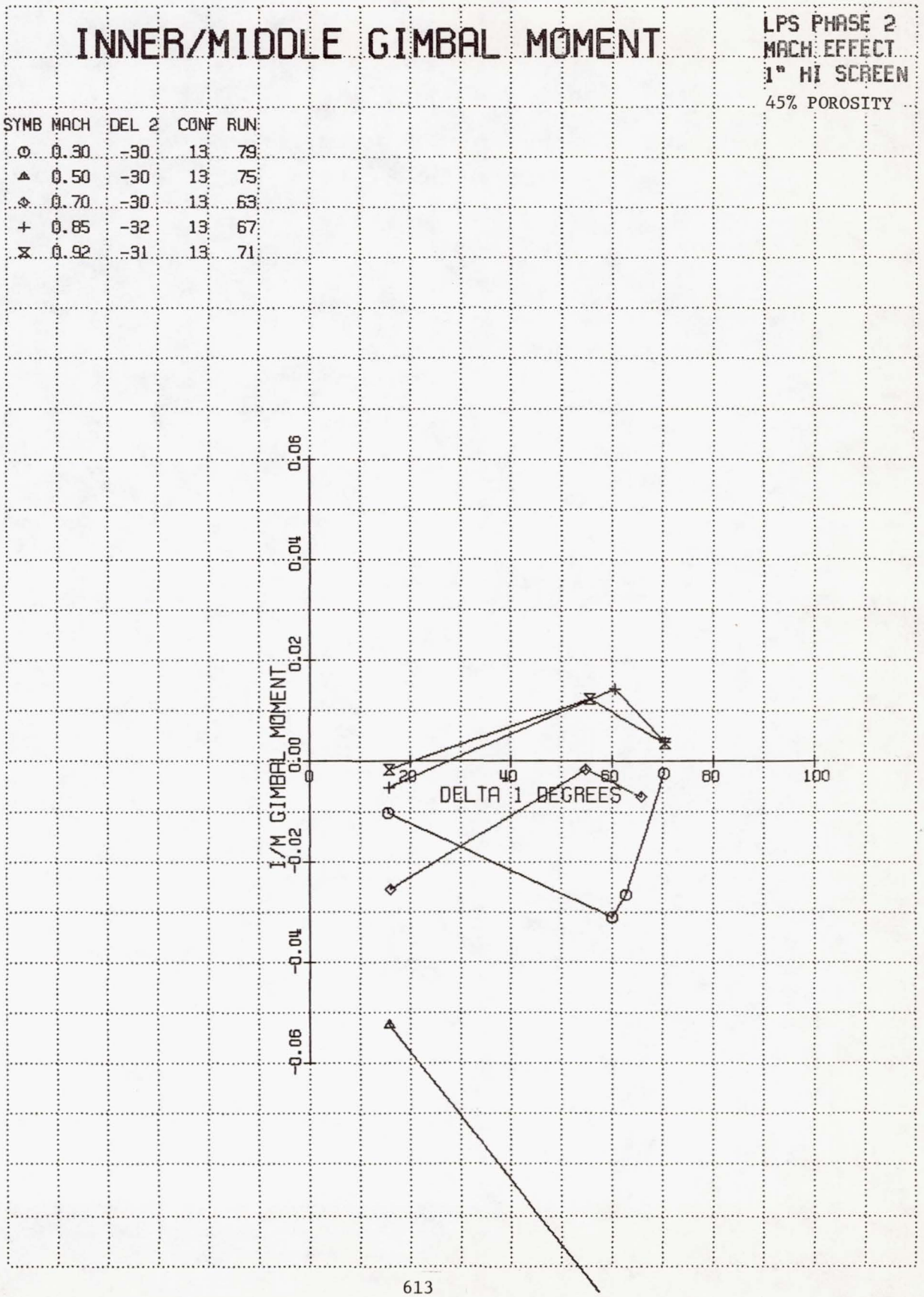

DATE=8-1-1979 AT 17:49:58

VALIDITY OF SMALL SCALE TESTS FOR TURRET/FAIRING LOADS AND CAVITY EFFECTS

BY

Daniel J. McDermott
James T. Van Kuren

Aeromechanics Division
Air Force Flight Dynamics Laboratory
Wright-Patterson Air Force Base, Ohio 45433

ABSTRACT

Numerous wind tunnel tests have been conducted by the Air Force and NASA to investigate the aerodynamic/airframe integration of an airborne optical pointing and tracking system. A common feature of the various systems tested is the use of a fuselage mounted open-port turret to house the optics. The suppression of undesirable aerodynamic phenomena within the open port cavity together with the development of aerodynamic fairings for the reduction of base pressure drag behind the turret has received special attention. In this paper, data from several wind tunnel experiments along with available flight test data are used to discuss the validity of these small scale tests and their inherent limitations. Tests were performed at transonic speeds to measure the turbulence levels in a cavity with and without a forward porous fence, turret drag with and without an aerodynamic fairing, and turret/fairing unsteady pressures.

LIST OF SYMBOLS

A_T	Turret Forward Projected Area
d	Cavity Width
D	Turret Diameter
f	Frequency, Hz
F	Friction force
h	Fence Height
Hz	Hertz, One Cycle per Second
k	Ratio of Specific Heats
kHz	Kilohertz = 1000 Hz
ℓ	Distance from Plate Leading Edge or Characteristic Length
m	Integer That Defines Mode Number
M	Mach Number
P	Pressure Force
P_{rms}	Root Mean Square Pressure
q	Free Stream Dynamic Pressure
R_D	Reynolds Number Based on Turret Diameter D
$R_D(M)$	Reynolds Number Based on Turret Diameter D as a Function of Mach Number M
R_ℓ	Reynolds Number Based on Distance ℓ
S	Strouhal Number = fd/V_∞ or fD/V_∞
u	Velocity Anywhere in the Boundary Layer in the x Direction
V_∞	Free Stream Velocity
x	Distance Along the Model Centerline in the Free Stream Direction. Measured from Plate or Cavity Leading Edge
y	Distance From the Model Centerline Normal to the Free Stream

LIST OF SYMBOLS (CONT'D)

δ	Boundary Layer Disturbance Thickness
δ_1	Boundary Layer Displacement Thickness
δ_2	Boundary Layer Momentum Thickness
$\delta_\ell(x)$	Laminar Boundary Layer Disturbance Thickness as a Function of x
$\delta_t(x)$	Turbulent Boundary Layer Disturbance Thickness as a Function of x
ΔC_D	Incremental Drag Coefficient = $\frac{\text{Drag Force}}{\frac{1}{2}\rho_\infty V_\infty^2 \; A_T}$
ε_t	Turbulent Momentum Eddy Diffusivity
μ	Dynamic Viscosity
ρ	Mass Density Anywhere in the Boundary Layer
ρ_∞	Free Stream Mass Density
τ_ℓ	Laminar Shear Stress
τ_t	Turbulent Shear Stress
Φ	Power Spectral Density of Pressure, $\left[\frac{\text{Force}}{\text{Length}^2}\right]^2/\text{Hz}$

SECTION I

INTRODUCTION

BACKGROUND

During the past ten years the Air Force and NASA have conducted numerous wind tunnel tests to investigate the aerodynamic/airframe integration of an airborne optical pointing and tracking system. A common feature of the various systems tested has been the use of a fuselage mounted turret to house the optics. The light beam propagates from the optical platform through an open port in the turret and thus eliminates the losses associated with a solid material window. However, the optical beam quality and the performance of the pointing and tracking system are still very much a function of the external aerodynamic flow field. When exposed to the free stream flow the open port turret acts as a cavity, and under a resonance condition, internal unsteady pressure fluctuations become significant. These acoustical resonances create unwanted vibrations of the internal optical components and thus degrade the overall system performance. In addition, flow separation on the turret creates unsteady external torques while increasing the total aircraft drag.

In the above mentioned wind tunnel tests, the suppression of undesirable aerodynamic phenomena within these cavities together with the development of aerodynamic fairings for the reduction of base pressure drag behind the turret, has received special attention (References 1,2,3,4,5,6). Since much time has been spent in these developmental areas a data comparison of various scale wind tunnel tests is desirable. In this paper, data from several of the wind tunnel experiments along with available

flight test data are used to discuss the validity of these small scale tests and their inherent limitations.

SECTION II

FLUID FLOW CONCEPTS

Before discussing the wind tunnel results it's worthwhile to recall a few concepts governing different flow processes which have a direct affect on the comparison of large and small scale test data. The understanding of these concepts points out some inherent limitations of small scale tests and helps in the interpretation of such data.

REYNOLDS NUMBER AND DYNAMIC SIMILARITY

Approximately 100 years ago Osborne Reynolds identified the importance of the ratio of inertial to viscous forces in defining the character of fluid flows in pipes, i.e., whether the flow will be laminar or turbulent. The introduction of this ratio, $\rho_\infty V_\infty \ell/\mu$, referred to as the Reynolds number, contributed significantly to another important concept call Dynamic Similarity. Consider an experiment where a low speed fluid flows around two geometrically similar bodies. If the flow properties are measured at geometrically similar locations, and their respective Reynolds numbers are identical, then the two experiments are said to be dynamically similar. In others words, two flow systems are said to be dynamically similar if they are geometrically similar and the forces in one system are in the same ratio to each other as the forces in the second system. The practical importance of the principle of similarity is that inexpensive wind tunnel tests of scale models can be used to predict the performance of full-scale aircraft. However, in many instances several force ratios are involved and consequently it is

impossible to have complete dynamic similarity. For example, when measuring drag on an airfoil in high speed flow both compressible gas forces and viscous shear forces are important. In general, complete similarity in such cases is possible only for full scale models.

BOUNDARY LAYER CONCEPT

Since the Reynolds number is the ratio of the inertial forces to viscous forces one might expect that viscous forces would be negligible at very high Reynolds numbers. The fact is, that no matter how large the Reynolds number, viscous forces can never be completely ignored. The reason for this is that fluid particles do not slip at the surface of a solid boundary. Thus, the imposed boundary condition is that the tangential velocity at the wall is zero. Moving outward from the wall the velocity increases to a value nearly equal to that of the free stream. This region of retarded flow is called the "boundary layer".

The development of a boundary layer can best be illustrated by a study of an incompressible, uniform flow over a flat plate (see Figure 1). As the fluid particles reach the plate leading edge, large shear stresses are created at the surface which slows down the fluid. This relatively thin region close to the body surface varies in "thickness" downstream along the plate. The actual boundary layer thickness δ is usually defined as the distance from the surface to the point where the local velocity u equals ninety-nine percent of the free stream velocity V_∞. Since the term boundary layer thickness is somewhat ambiguously defined, more useful terms such as displacement thickness δ_1 and momentum thickness δ_2 are often used. The displacement thickness δ_1 is a measure of the displacement of the free stream flow away from the plate and is defined as:

$$\delta_1 = \int_0^\infty \left[1 - \frac{\rho u}{\rho_\infty V_\infty}\right] dy$$

where ρ and ρ_∞ are the local and free stream mass densities respectively. The momentum thickness δ_2 is a measure of the deficit of momentum flux caused by the boundary layer and is proportional to the drag on the plate. The momentum thickness δ_2 is defined as:

$$\delta_2 = \int_0^\infty \frac{\rho u}{\rho_\infty V_\infty}\left[1 - \frac{u}{V_\infty}\right] dy$$

The boundary layer along the plate is separated into a laminar, transitional and turbulent region. Depending mostly on the local Reynolds number the boundary layer remains laminar for some distance along the plate. In this region the viscous shear stress τ_ℓ is proportional to the velocity gradient, that is:

$$\tau_\ell \sim \frac{du}{dy}$$

In laminar flow the transport of momentum is molecular in nature. The transport coefficient is called the dynamic viscosity μ and is a function only of the fluid properties. Thus the laminar shear stress can be expressed as:

$$\tau_\ell = \mu \frac{du}{dy}$$

The layer remains truly laminar up to the transition point but after this "critical point" (more usually defined by a "critical Reynolds

number") small disturbances or fluctuations are amplified in magnitude, eventually becoming so large as to disrupt the laminar flow pattern which then breaks up into large eddies. Such disturbances are introduced from the free stream or by surface irregularities, both of which are always present to some degree. Once the turbulent mixing process starts, some distance is required for an equilibrium mixing process to be established. Hence, transition requires a "zone" rather than suddenly occurring at a point. Thereafter, the characteristics of the layer are essentially turbulent in nature.

In turbulent flow the transport of momentum is greatly enhanced. Consequently the shear stress is higher than in the laminar flow case (see Figure 1). Expressions for the viscous shear stress have been developed which are similar to the laminar equation. However, the turbulent momentum transport coefficient is by no means a constant but rather a function of the dynamics of the flow. This turbulent coefficient, ε_t, is both a function of the magnitude of the velocity fluctuations and eddy scale size. Thus the turbulent shear stress can be expressed as:

$$\tau_t = \varepsilon_t \frac{du}{dy}$$

The above description of a boundary layer has indeed been a simplified one. Many aspects of boundary layers such as effects of compressibility, pressure gradient, wall shape and wall temperature were not addressed. However, it is found that drag due to viscous shear stresses is higher when the flow is completely turbulent.

DRAG FORCES FOR BLUNT AND STREAMLINED BODIES

Newton's law of motion states, that for a constant mass, the sum of the external forces on a body is equal to the product of its mass and acceleration. In fluid aerodynamics,the two surface forces which are of particular importance are friction forces and pressure forces. The relative importance of these two forces play a significant role in the drag of blunt and streamlined bodies such as a fuselage mounted turret/ fairing (see Figure 2). As was previously discussed, the magnitude of the viscous drag depends on whether the surface boundary layer is laminar or turbulent. For high Reynolds number flows the boundary layer is mostly turbulent and the viscous drag is higher than for low Reynolds number flows where the boundary layer is laminar. Therefore, it is important to maintain a laminar boundary layer on a streamlined body where the pressure drag is small. In contrast, and for a different reason, turbulent flow is also of importance on a blunt shaped body. When a fluid flows around a blunt body,the boundary layer starts out laminar and tends to separate from the surface creating a low pressure wake. This low pressure region acts as a drag force on the body and its magnitude is a function of the location on the body where the flow separates. For such cases, early transition from laminar to turbulent flow would have the effect of reducing the size of the wake and thus reducing the pressure drag. Drag reduction of this form is therefore very much a function of Reynolds number. Recall that transition can also be a function of free stream turbulence and surface roughness. A high free stream turbulence could cause earlier transition which would help reduce the pressure drag. Surface roughness could also cause a drag reduction but is very dependent on Reynolds number.

WIND TUNNEL TESTING

The wind tunnel is probably the aeronautical engineer's most important design and development tool. Excellent agreement between small and full scale tests can be obtained when the various force systems involved are properly modeled. Indeed, proper modeling is implied by the principles of similarity discussed earlier. Generally speaking this statement is true. However, it's true only if *all* the pertinent parameters are the same. For example, the drag force on a blunt body could be a function of Mach number, Reynolds number, geometry, and free stream turbulence. Matching the Mach number, Reynolds number and geometry may not be sufficient. Since boundary layer transition and separation are affected by the free stream turbulence level, the drag force measured in two different wind tunnel tests may not be the same. In addition, local steady and unsteady pressure measurements can be significantly influenced by the degree of free stream turbulence, the location of transition and local separated flow regions. Spatial resolution of local instrumentation on a small scale model should also be considered. The measurement may really be an integrated effect over a relatively large surface area!

All things considered, the wind tunnel testing of small scale models has proven very useful to the aeronautical engineer. The principles of dynamic similarity and an understanding of the basic fluid flow concepts help the engineer to interpret such data. When dynamic similarity is incomplete the data trends are still very important results. Much of the data presented in this paper shows good correlation between tests. Some of the anomalies that are present can be attributed to one or more of the reasons discussed in this section.

SECTION III

CAVITY AND FENCE TESTS

MODELS AND TEST FACILITIES

Two separate models of a 15.2 cm (6 in.) cube shaped cavity mounted on a flat plate were tested in the Air Force Flight Dynamics (AFFDL) 0.61 m by 0.61 m (2 ft by 2 ft) and NASA-Ames 1.83 m by 1.83 m (6 ft by 6 ft) transonic wind tunnels. The dimensions of these two models are shown in Figures 3a and 3b. Several porous fences which were designed to reduce the turbulence levels in the cavity could be mounted upstream of the cavity in one of three different locations. The results from two of these fence configurations are presented in this paper. Their dimensions and location upstream of the cavity are given in Table 1.

The NASA-Ames flat plate model was mounted in the tunnel on a center pylon sufficiently far from the wall to assure that the plate was not immersed in the tunnel boundary layer (Ref. 7). An elliptic leading edge of major axis four times the minor axis was used to preclude separation and to reduce the mass flow and blockage beneath the plate. The AFFDL flat plate model was mounted on the side wall of the 0.38 m by 0.38 m (1.25 ft by 1.25 ft) transonic test section. This particular test section has slotted walls and a removable section sidewall which protrudes 3.81 cm (1.5 in.) into the flow, thus bleeding off the boundary layer.

TYPES OF MEASUREMENTS AND TEST CONDITIONS

Data recorded during the cavity tests included both mean and unsteady pressure measurements. Dynamic pressure transducers were located at key

positions inside the cavity and on the flat plate forward and aft of the cavity. Total pressure probes were also used to measure the velocity profiles at the leading edge of the cavity with and without a porous fence. Only a portion of the unsteady pressure measurements are presented in this paper. The discussion is limited to two fence configurations, a Mach number range of 0.60 to 0.89, and one fence location.

UNSTEADY PRESSURE RESULTS - PLAIN CAVITY

Overall root mean square (rms) pressure levels for the plain cavity configurations are presented in Figures 4a and 4b. The data are normalized by the free stream dynamic pressure and represent an averaging over a frequency range from 1 to approximately 50 kHz.

For a free stream Mach number of 0.60 the rms pressure data from the AFFDL test are in good agreement with the Ames data. However, significant differences occur at Mach 0.89 for measurements made inside the cavity and on the flat plate at the cavity leading edge. It is not suggested that such an effect is primarily due to the change in Mach number. In fact, trends in the data for both Mach numbers show that the unsteady pressure levels increase with decreasing local Reynolds number R_ℓ. This decrease with Reynolds number suggests that transitional instabilities in the approaching boundary layer radiate energy which generate more intense fluctuations within the cavity. Since the free stream flow is subsonic, the cavity pressure fluctuations also radiate forward and increase the pressure levels on the plate at the cavity leading edge. Similar findings have been found by previous investigators (Reference 8). They conclude that in comparison to a fully turbulent boundary layer, the laminar portion of a boundary layer "produces more intense fluctuations despite its own lower noise levels".

From the AFFDL and Ames tests its evident that the scaling of cavity unsteady pressure data should include boundary layer parameters. More experimental work needs to be done before all the important parameters can be defined. However, it appears that transitional effects from the upstream boundary layer can significantly affect the magnitude of cavity resonance.

UNSTEADY PRESSURE RESULTS - CAVITY WITH FENCE

Normalized unsteady pressure data for two fence configurations are presented in Figures 5a and 5b. Comparison of the data along the centerline of the flat plate and cavity floor shows that the AFFDL and Ames tests results are in excellent agreement for both fence configurations. No effect of Reynolds number on cavity resonance or fence effectiveness was found. Both the AFFDL and Ames fences were equally effective in significantly reducing the cavity dynamic pressure levels as compared to the plain cavity. This is probably due to the fact that the fence height h was greater than the local boundary layer thickness δ for both tests. Ratios of $h/\delta_\ell > 1$ were considered to be an important design parameter in order to prevent the shear layer from entering the cavity. Notice that for $h/\delta_\ell = 1.2$, the Ames fence 2 (58% porosity and thus less drag) was equally effective as the Ames fence 1 (38% porosity). Of course, this neglects the differences in free stream Mach number.

UNSTEADY PRESSURE SPECTRA RESULTS - PLAN CAVITY AND CAVITY WITH FENCE

Nondimensional resonant frequency data or Strouhal numbers ($S = fd/V_\infty$) for both the Ames and AFFDL cavity tests are presented as a function of free stream Mach number in Figures 6a and 6b. Frequency data from the Ames test were obtained from a varying bandwidth analysis between 2 and 800 Hz. The AFFDL data were obtained from a narrow bandwidth analysis with

a frequency resolution of ± 20 Hz. The solid curves represent calculated values of Strouhal number for various cavity resonance modes m. These curves were calculated from the following modified Rossiter equation obtained from Reference 1:

$$m = 1,2,3,4$$

$$S = \frac{m - 0.25}{\frac{M}{\left[1 + \frac{k-1}{2} M^2\right]^{\frac{1}{2}}} + 1.75}$$

where M is the free stream Mach number and k is the ratio of specific heats.

For the first fundamental mode and the second harmonic both the Ames and AFFDL frequency data are in excellent agreement for the plain cavity case (Figure 6a). In addition, predicted values using the Rossiter equation are in good agreement with the measured data, especially for the first mode. Significant differences are found between the two tests and also between the test and predicted values for m = 4. The differences between the experimental data are probably due to the relatively large bandwidth of the Ames data at the higher frequencies. In any case, the lower resonant modes have the highest energy content and thus are of greater importance.

Comparison of the AFFDL and Ames data for the cavity with fence configuration are shown in Figure 6b. Excellent agreement between experiments and predicted values were also obtained with results similar to the plain cavity case. It's interesting to note that, although the fences significantly reduce the cavity dynamic pressures, the same resonant

frequencies are still present but at a much lower energy level. Consequently the Rossiter equation, although not developed for the cavity with fence configuration, still successfully predicts the cavity resonant frequencies.

SECTION IV

TURRET/FAIRING TESTS

MODELS AND TEST FACILITIES

In this section, selected data from several wind tunnel and flight tests are compared. The drag data presented were obtained from experiments conducted in the Air Force Academy (AFA) and AFFDL transonic wind tunnels. Two separate 0.025 scale models of a turret with a high rise aft fairing were mounted in the wind tunnels on a hollow circular cylinder with forward and aft ramps. The cylindrical section was designed to approximate the upper forward portion of a KC-135 aircraft fuselage. A sketch of the model configuration is shown along with the drag data in Figure 7.

The unsteady pressure data presented in this section were obtained from experiments conducted in the AFFDL 0.61 m by 0.61 m (2 ft by 2 ft) and NASA-Ames 4.27 m by 4.27 m (14 ft by 14 ft) wind tunnels and from flight tests of the Airborne Laser Laboratory (ALL). The wind tunnel models were candidate configurations of the ALL cycle III/IV aft fairing with a forward ramp. A configuration sketch is shown in Figure 8. The AFFDL and NASA-Ames model scales were 0.025 and 0.30 respectively.

TYPES OF MEASUREMENTS AND TEST CONDITIONS

Data recorded during the AFA and AFFDL high rise fairing/turret tests included force measurements and oil flow visualization photography. Only the drag force data are presented in this paper for a Mach number range from 0.60 to Mach 0.90. At the AFA, the free stream unit Reynolds number varied with tunnel Mach number while at AFFDL, the free stream unit Reynolds number was a constant. The drag data ΔC_D which is presented in Figure 7 reflects drag caused by the addition of the turret

and fairing only and are based upon the forward projected area of the turret (Ref. 9). The Reynolds numbers R_D are based on the turret diameter D.

Selected unsteady pressure data from the AFFDL and NASA-Ames wind tunnels and the ALL flight tests are presented in this paper. The locations of the dynamic pressure transducers on the turret, forward ramp, and aft fairings are shown in Figure 8. Data results from these tests are presented in Figures 9a through 9d for a Mach number range from 0.50 to Mach 0.90. Turret Reynolds numbers varied from $R_D = 2.3 \times 10^5$ to $R_D = 40 \times 10^5$.

Two nondimensional power spectal density plots are also shown in Figures 10a and 10b comparing the 0.30 scale and full scale tests at Mach numbers of 0.55 and 0.75. However, these data were obtained from tests of a different fairing than that shown in Figure 8. They are presented here because they were the only wind tunnel and flight test data available and show that both power spectra data as well as root mean square pressure data can be correlated.

DRAG DATA RESULTS - AFA AND AFFDL TESTS

Several important observations can be made from the drag data results presented in Figure 7. Consider the drag versus Mach number curve for the bare turret configuration. If the two tests were dynamically similar, one would expect these curves to show much better agreement. As expected, the higher drag curve is at the lower turret Reynolds number. Differences between the two curve shapes is probably due to the variation of Reynolds number with free stream Mach number. Similar Reynolds number effects are also observed for the turret and aft fairing configuration. However, the two curve shapes are in much better agreement.

Although dynamic similarity between these two tests was incomplete, some very useful and important results exist which should not be overlooked. First, both configurations for both tests indicate an increase in drag with increasing Mach number. This, of course, was to be expected since similar results have been measured for flow around spheres and can be attributed to the appearance of unstable shock waves. A more important result, however, is found in the ranking of the drag curves. Both tests show the fairing drag to be less than the bare turret drag and for both configurations the AFA data ranks lower than the AFFDL data. The important point to be made here is that such trends in the data are useful results. Although the absolute drag coefficients cannot be compared between each test, both tests can be used to provide useful information concerning the effectiveness of one configuration over another.

UNSTEADY PRESSURE RESULTS - AFFDL, AMES, AND FLIGHT TESTS

Generally speaking, the unsteady pressure data presented in Figures 9 and 10 show good correlation between the AFFDL and NASA-Ames wind tunnel tests and the ALL flight tests. The best correlations are found in Figures 9c and 9d and in Figures 10a and 10b. First, it should be noted that the instrumentation locations for each test were substantially different in some cases. Consequently, the data comparisons would be expected to be poor especially in highly unstable flow regions. Figure 9a is such a case. Not only are the pressure transducers at very different locations but they are also located in a very turbulent flow region on the turret and aft fairing. At these locations local shock waves form, the flow separates from the turret and then reattaches to the fairing. Better agreement between tests is shown in Figure 9b although there are some discrepancies with the flight test data at the

lower Mach numbers. The reason for this is not clear, but is possibly due to a local separated flow region on the ALL fairing. The best agreement, of course, is shown in Figures 9c and 9d where the flow is attached and fairly stable. Notice that for these locations the unsteady pressure levels are much lower than those of Figures 9a and 9b. Since the flow is attached in these areas, the measurement is primarily due to boundary layer noise. Other differences between transducers such as those in Figures 9c and 9d are most likely attributed to differences in spatial resolution of the instrumentation between tests.

All in all, the unsteady pressure data show good correlation and provide a fairly accurate picture of the flow phenomena which occurs at different locations. As was the case with the drag data discussed earlier, the unsteady pressure data from each test also show similar trends. In the highly unstable regions (Figures 9a and 9b) all three tests show a decrease in the unsteady pressure levels with an increase in the free stream Mach number. In the stable flow regions (Figures 9c and 9d) all three tests show very little change in the unsteady pressure levels with Mach number.

Finally, when comparing flight and wind tunnel power spectral density data excellent correlations have been obtained (see Figures 10a and 10b). However, it should be emphasized that these data were obtained from tests of a much different configuration than the cycle III/IV configuration shown in Figure 8. The pressure transducers were at the top of the turret (same as location A in Figure 8) but were in a very protected region behind a high rise forward ramp fairing.

SECTION V

CONCLUSIONS

Data from several wind tunnel experiments along with available flight test data were used to discuss the validity of small scale tests. Tests were performed at transonic speeds to measure the turbulence levels in a cavity with and without a forward porous fence, turret drag with and without an aerodynamic fairing, and turret/fairing unsteady pressures. Analysis of the test results leads to the following conclusions:

1. Porous fences were found to be effective in reducing cavity unsteady pressure levels of small scale models. However, scaling the magnitude of unsteady pressure reduction to full scale is uncertain. The data shows that there is a fixed ratio of fence height to cavity length independent of model scale.

2. Trends and levels of unsteady pressure coefficients on turrets and fairings are predicted by small scale tests in regions of attached flow. In regions susceptible to flow separation such as on the turret itself, small scale data are not expected to scale up because of Reynolds number effects.

3. Resonant frequencies of a plain cavity and a cavity with a porous fence can be predicted for small scale tests.

4. Upstream boundary layer conditions can significantly influence the degree of correlation between different small scale cavity tests.

REFERENCES

1. Conner, W. R., Airborne Laser Laboratory Exhaust Channel Acoustic Analysis, AFFDL-TR-75-149, February 1976.

2. McDermott, D. J., Airborne Laser Laboratory Cavity and Fence Tests, AFFDL-TR to be published.

3. Buell, D. A., Aerodynamic Properties of a Flat Plate with Cavity for Optical Propagation, NASA TM 78487, January 1979.

4. Van Kuren, J. T. and Conner W. R., Fairing Design For Fuselage Mounted Turret in Transonic Flow, AFFDL-TM-73-115 FXM, September 1973.

5. Van Kuren, J. T., Walterick R. E. and McDermott, D. J., Transducer Sensitivities For Unsteady Pressure in Transonic Flow, 46th Semi-Annual Supersonic Wind Tunnel Association Meeting, October 1976.

6. Walterick R. E. and Van Kuren, J. T., Wind Tunnel Tests Of Fairings For An On-Gimbal Telescope Turret, AFFDL-TM-75-177 FXM, November 1975.

7. Van Kuren, J. T., Experiments to Develop a Thick Turbulent Boundary Layer For Optical Degradation Measurements, AFFDL-TM-75-106-FX, June 1975.

8. Heller, H. H., Holmes, D. H. and Covert E. E., Flow Induced Pressure Oscillations in Shallow Cavities, 1971 Journal of Sound and Vibration 18, pp. 565-553.

9. Shapiro, A, H., Shape and Flow - The Fluid Dynamics of Drag, 1961.

FENCE CONFIGURATIONS

TABLE 1

FENCE #	HEIGHT	WIDTH	THICKNESS	% POROSITY	REMARKS
1	0.89 cm (AFFDL) 2.29 cm (AMES)	25.40 cm	0.51 cm	38	A) ONE ROW OF HOLES 0.52 cm IN DIAMETER. FORTY-THREE HOLES PER ROW. (THREE ROWS AND 35 HOLES PER ROW FOR AMES FENCE) B) FENCE LOCATED 4.06 cm UPSTREAM OF CAVITY LEADING EDGE
2	2.29 cm (AFFDL & AMES)	25.40 cm	0.51 cm	58	A) TWO ROWS OF HOLES 0.99 cm IN DIAMETER. TWENTY-TWO HOLES PER ROW. B) FENCE LOCATED 4.06 cm UPSTREAM OF CAVITY LEADING EDGE

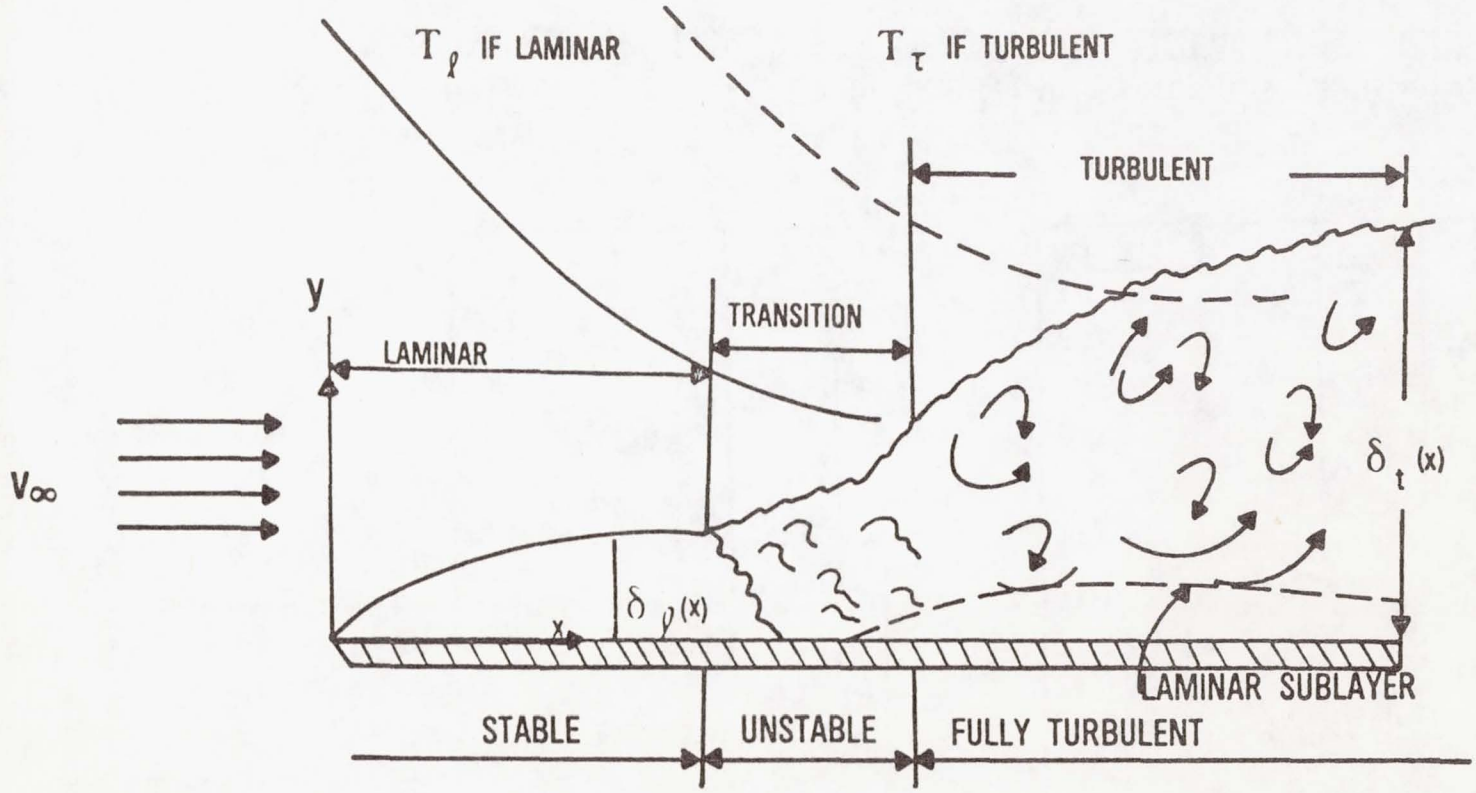

FIGURE 1

DEVELOPMENT OF A BOUNDARY LAYER ON A FLAT PLATE.

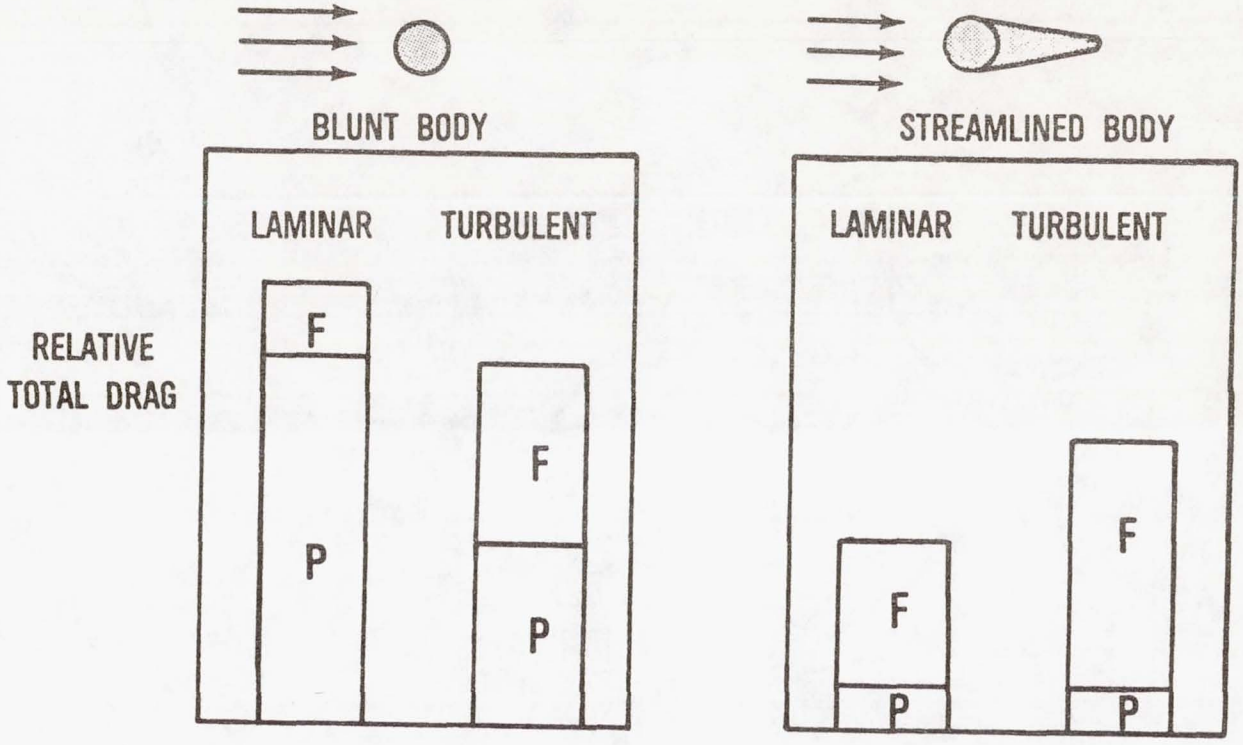

FIGURE 2

THE RELATIVE EFFECTS OF FRICTION AND PRESSURE DRAG IN LAMINAR AND TURBULENT FLOWS FOR BLUNT AND STREAMLINED BODIES.

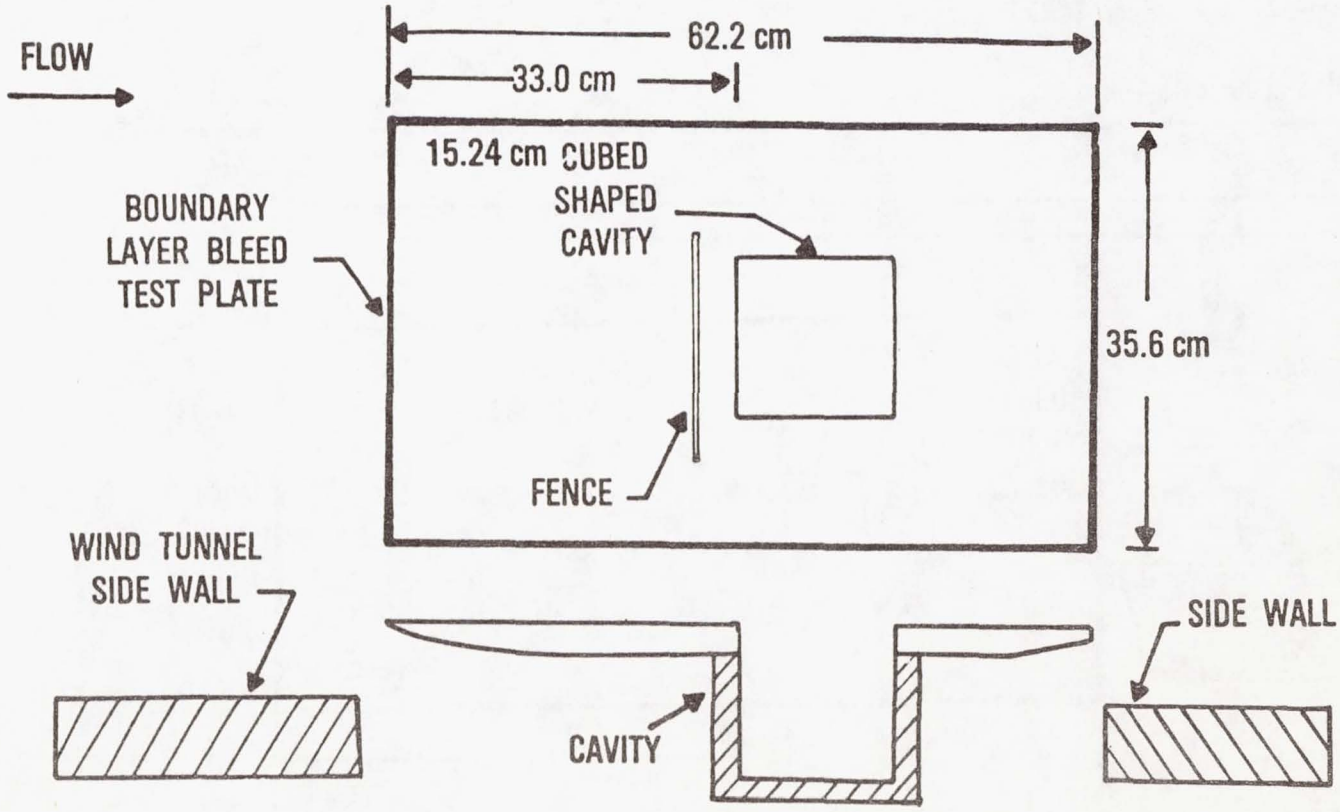

FIGURE 3a

AFFDL FLAT PLATE MODEL WITH CAVITY.

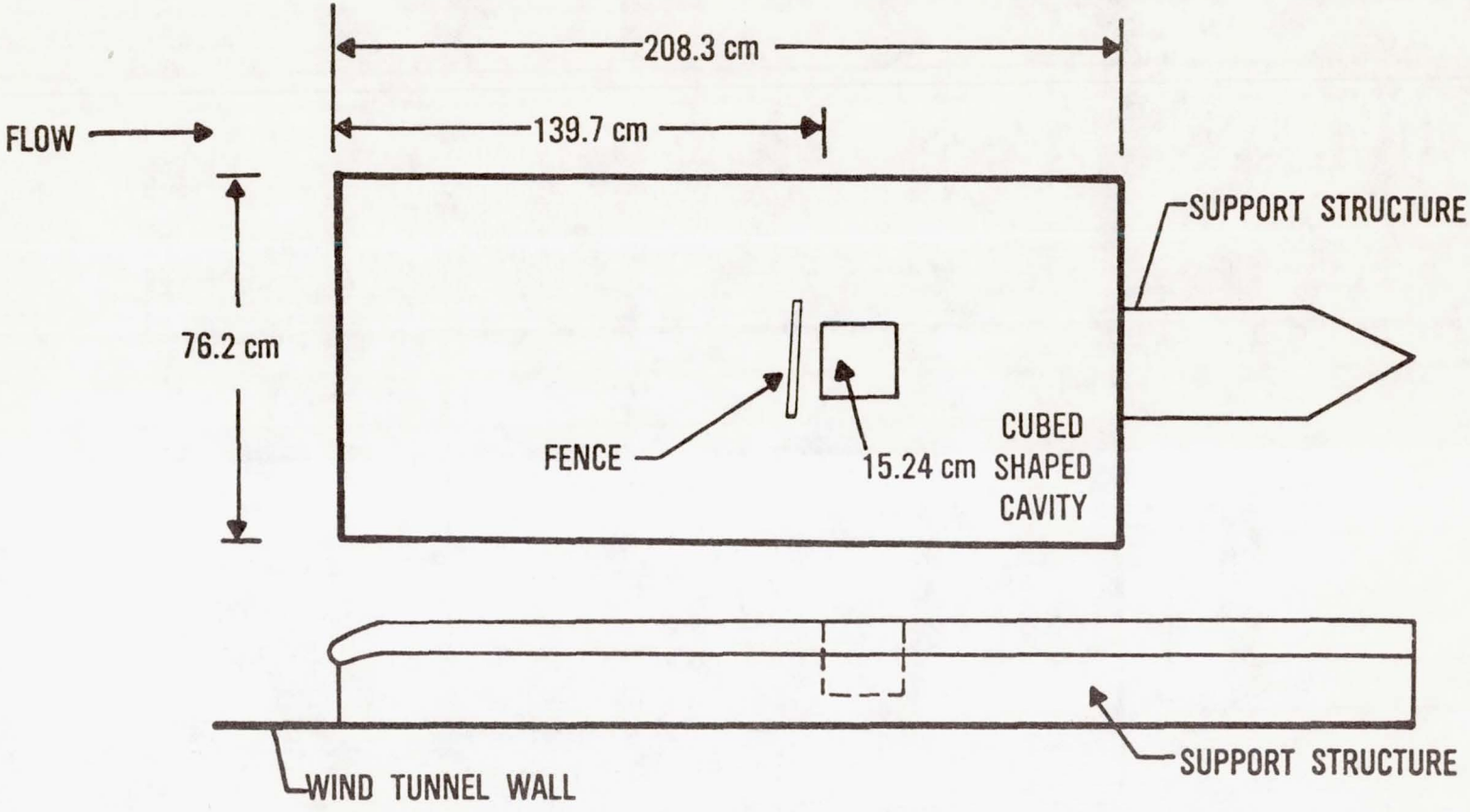

FIGURE 3b
NASA – AMES FLAT PLATE MODEL WITH CAVITY.

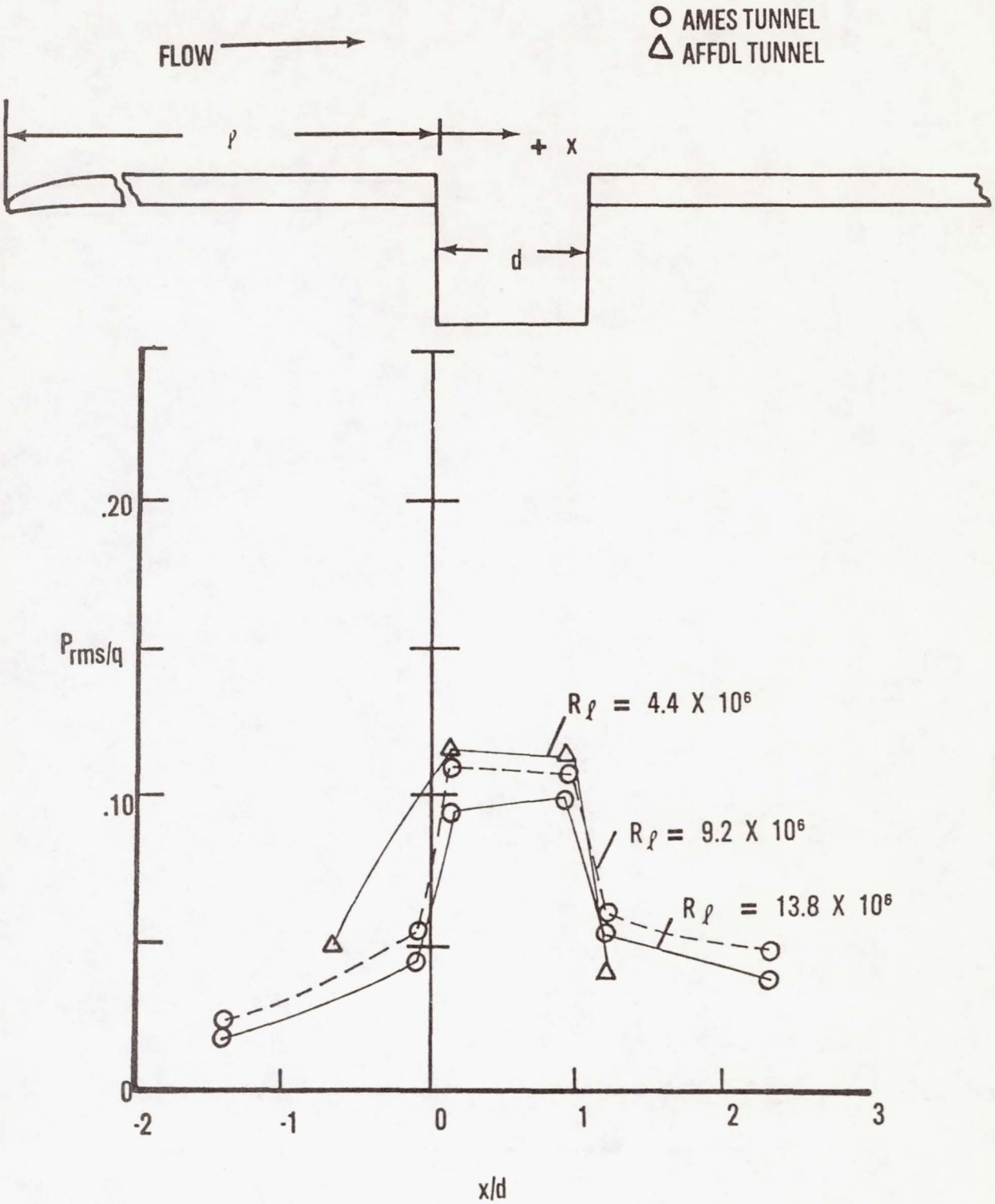

FIGURE 4a

COMPARISON OF NASA-AMES AND AFFDL DYNAMIC PRESSURE DATA ALONG THE CENTERLINE OF THE FLAT PLATE AND CAVITY FLOOR. PLAIN CAVITY, M = 0.60.

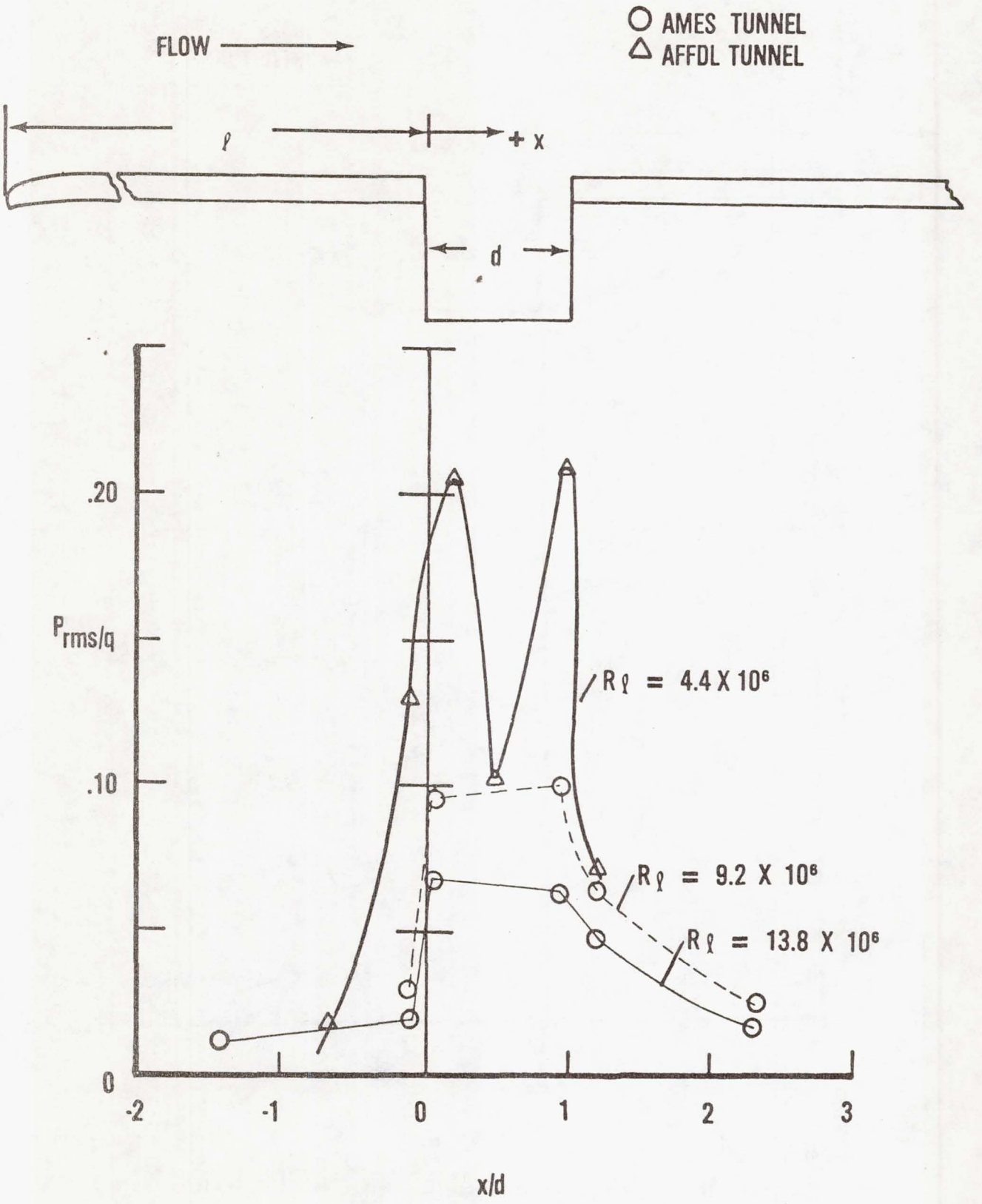

FIGURE 4b

COMPARISON OF NASA–AMES AND AFFDL DYNAMIC PRESSURE DATA ALONG THE CENTERLINE OF THE FLAT PLATE AND CAVITY FLOOR. PLAIN CAVITY, M = 0.89.

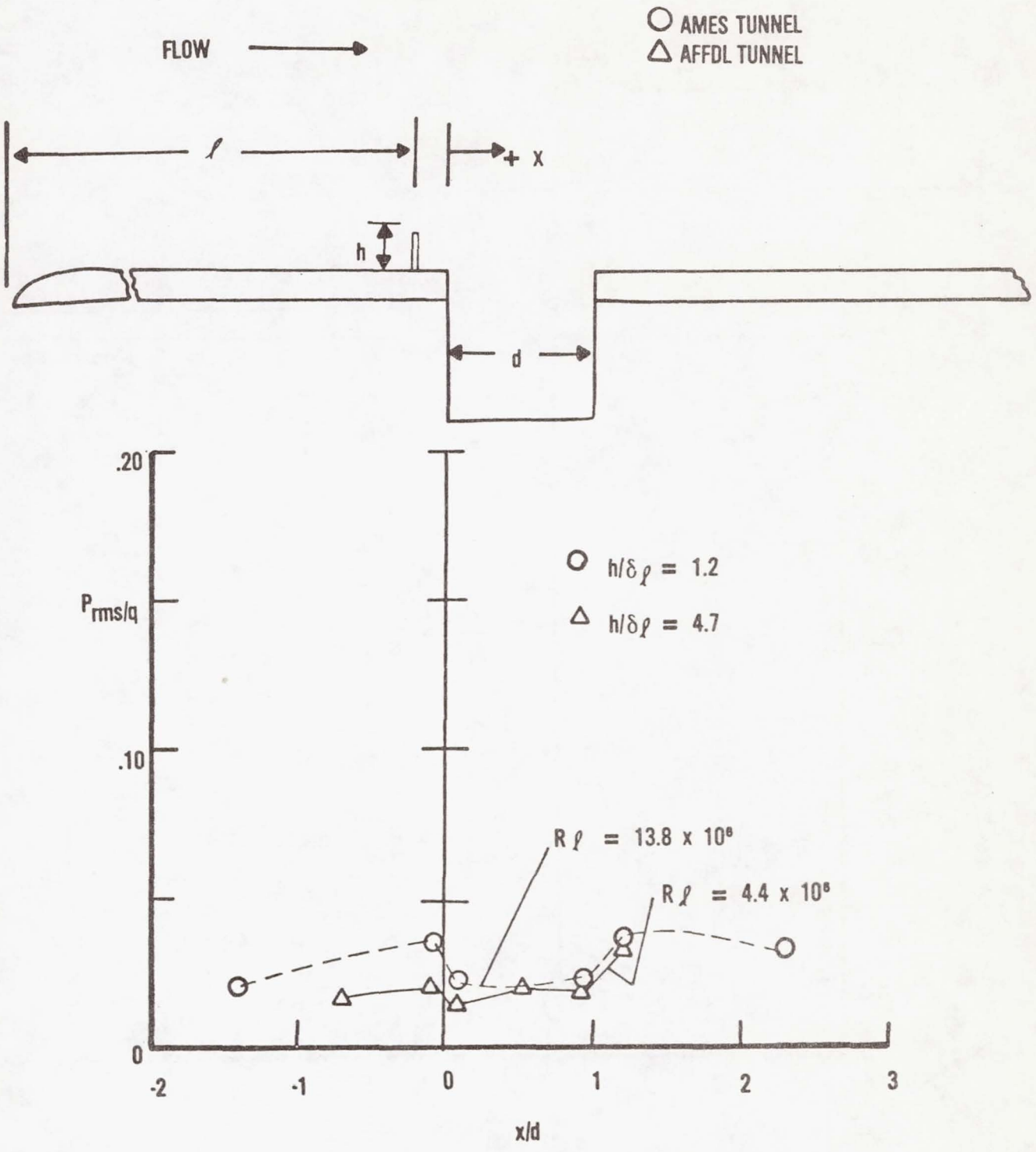

FIGURE 5a

COMPARISON OF NASA-AMES AND AFFDL DYNAMIC PRESSURE DATA ALONG THE CENTERLINE OF THE FLAT PLATE AND CAVITY FLOOR. CAVITY WITH FENCE 1, M = 0.60.

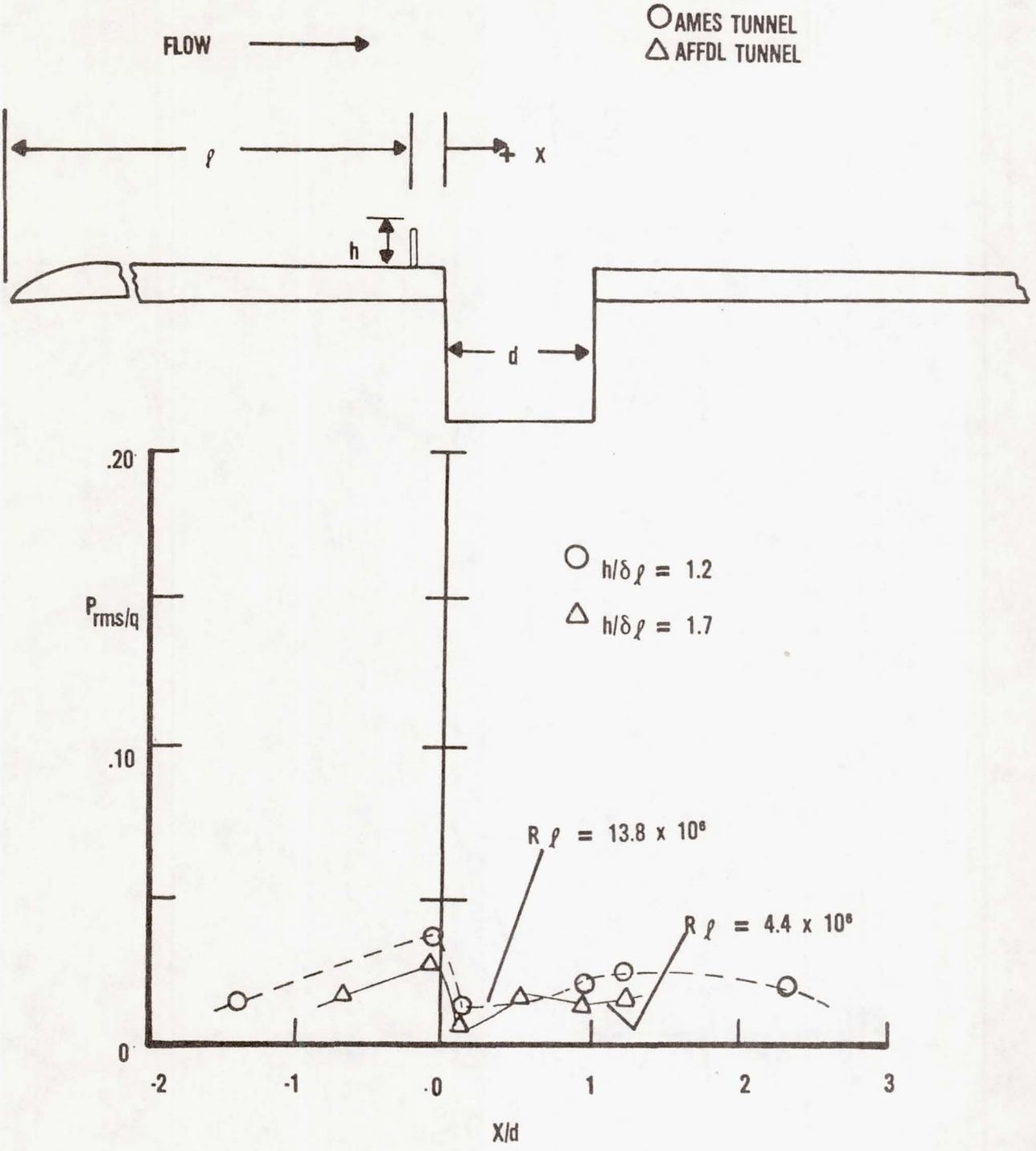

FIGURE 5b

COMPARISON OF NASA–AMES AND AFFDL DYNAMIC PRESSURE DATA ALONG THE CENTERLINE OF THE FLAT PLATE AND CAVITY FLOOR. CAVITY WITH FENCE 2, M = 0.89.

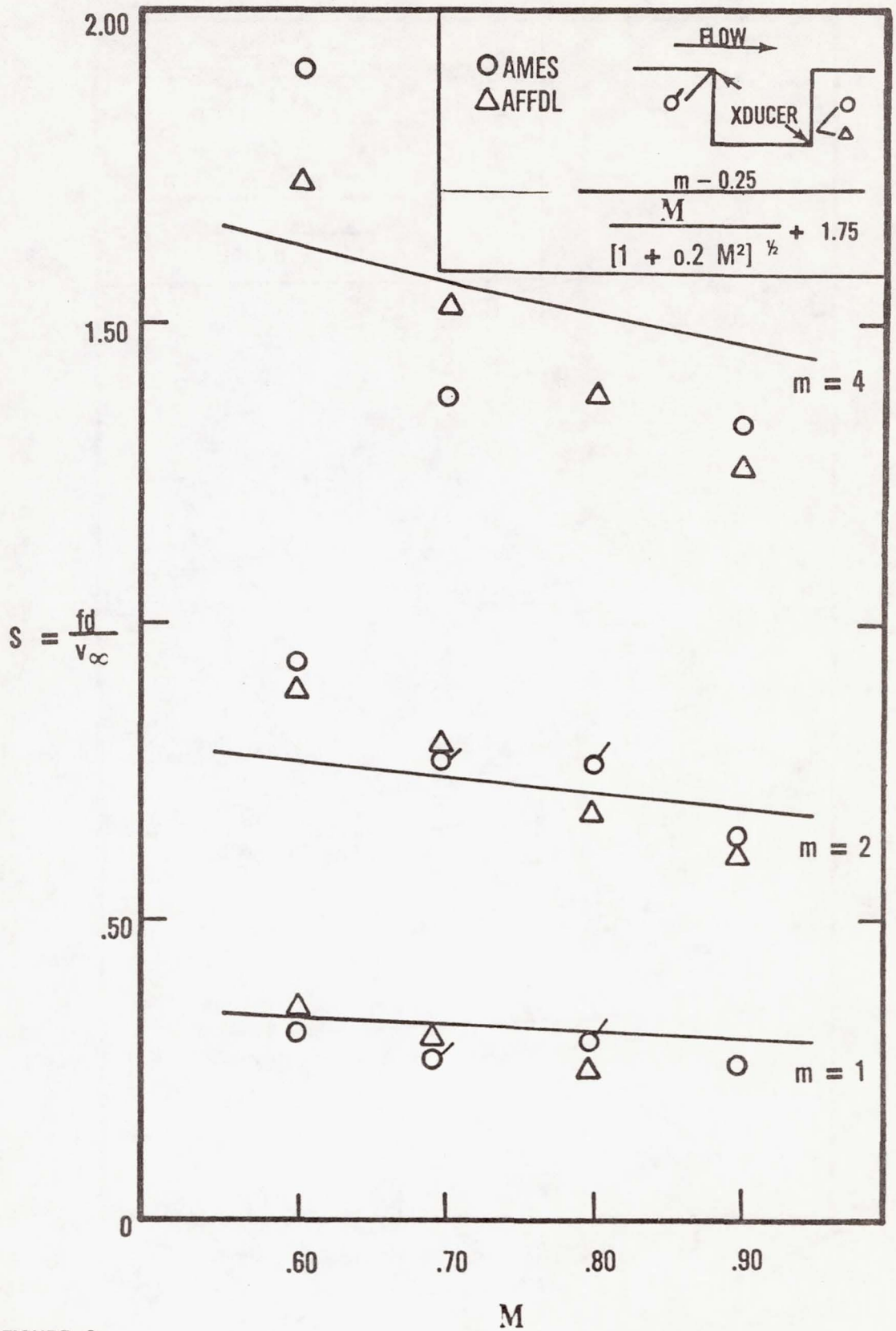

FIGURE 6a

COMPARISON OF NASA–AMES AND AFFDL NONDIMENSIONAL RESONANT FREQUENCY DATA AS A FUNCTION OF MACH NUMBER. PLAIN CAVITY.

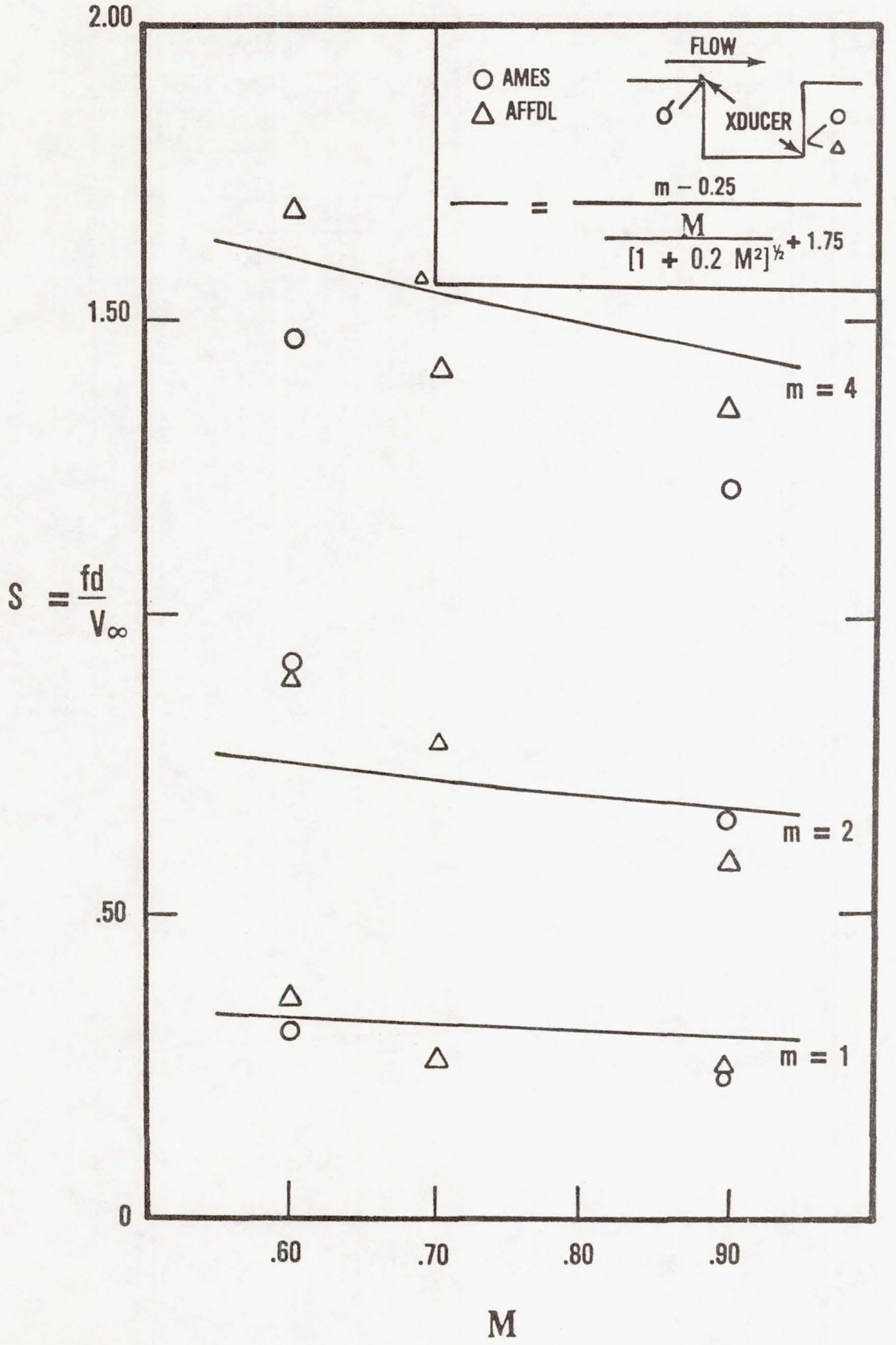

FIGURE 6b

COMPARISON OF NASA–AMES AND AFFDL NONDIMENSIONAL RESONANT FREQUENCY DATA AS A FUNCTION OF MACH NUMBER. CAVITY WITH FENCE 2.

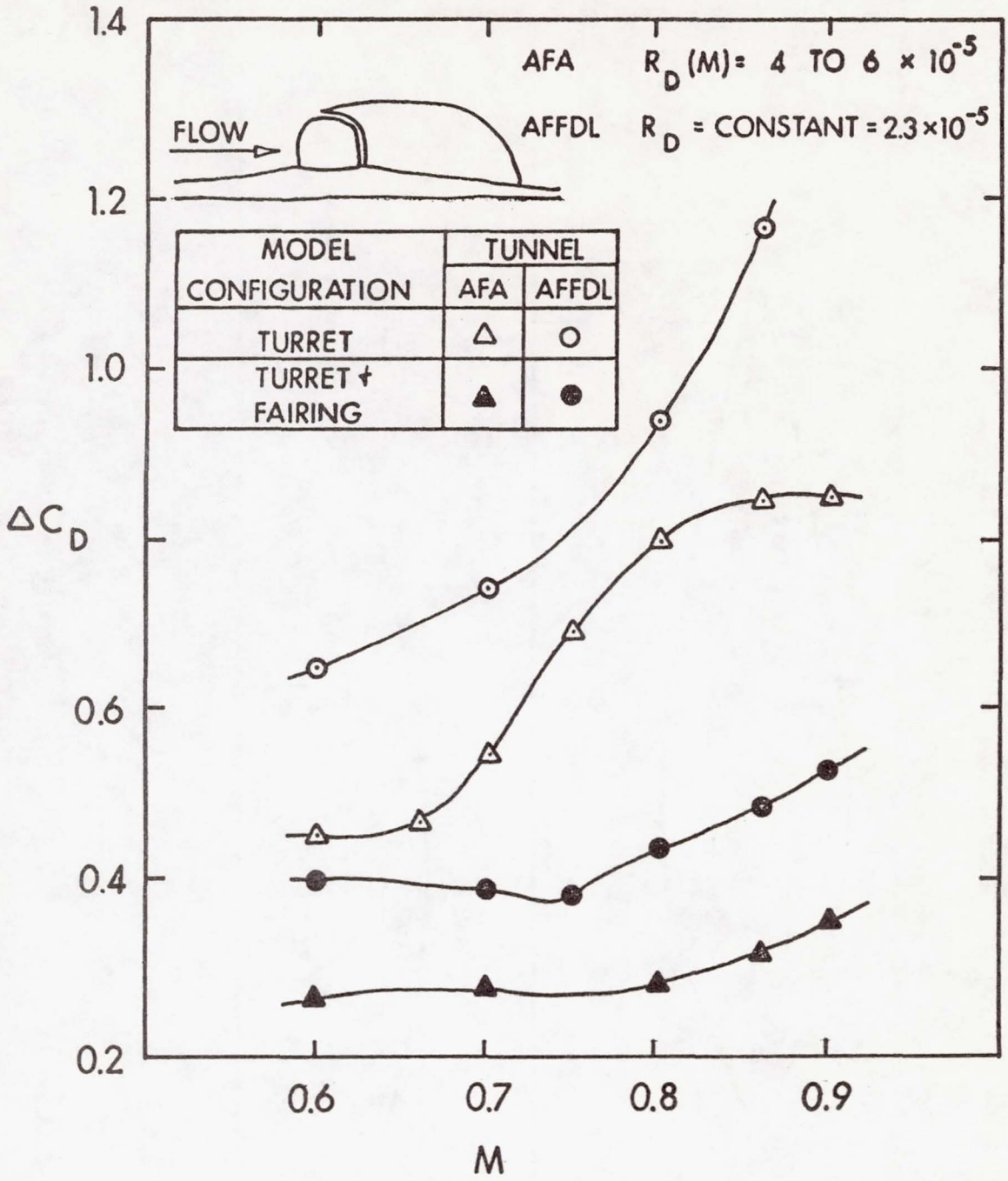

Figure 7

COMPARISON OF AIR FORCE ACADEMY AND AFFDL FAIRING AND TURRET DRAG DATA AS A FUNCTION OF MACH NUMBER.

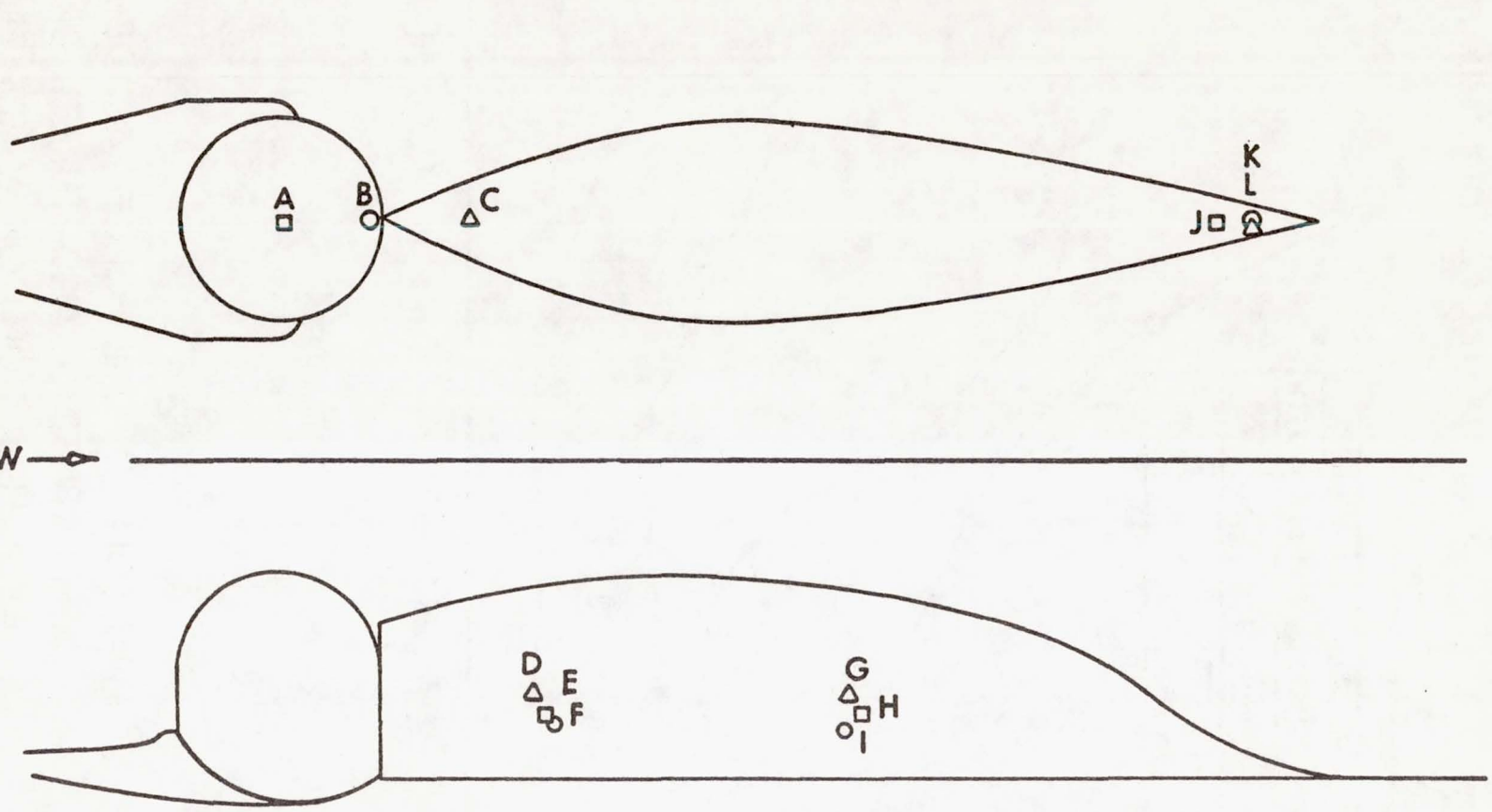

650

Figure 8 PRESSURE TRANSDUCER LOCATIONS ON ALL CYCLE III/IV TURRET AND FAIRING.

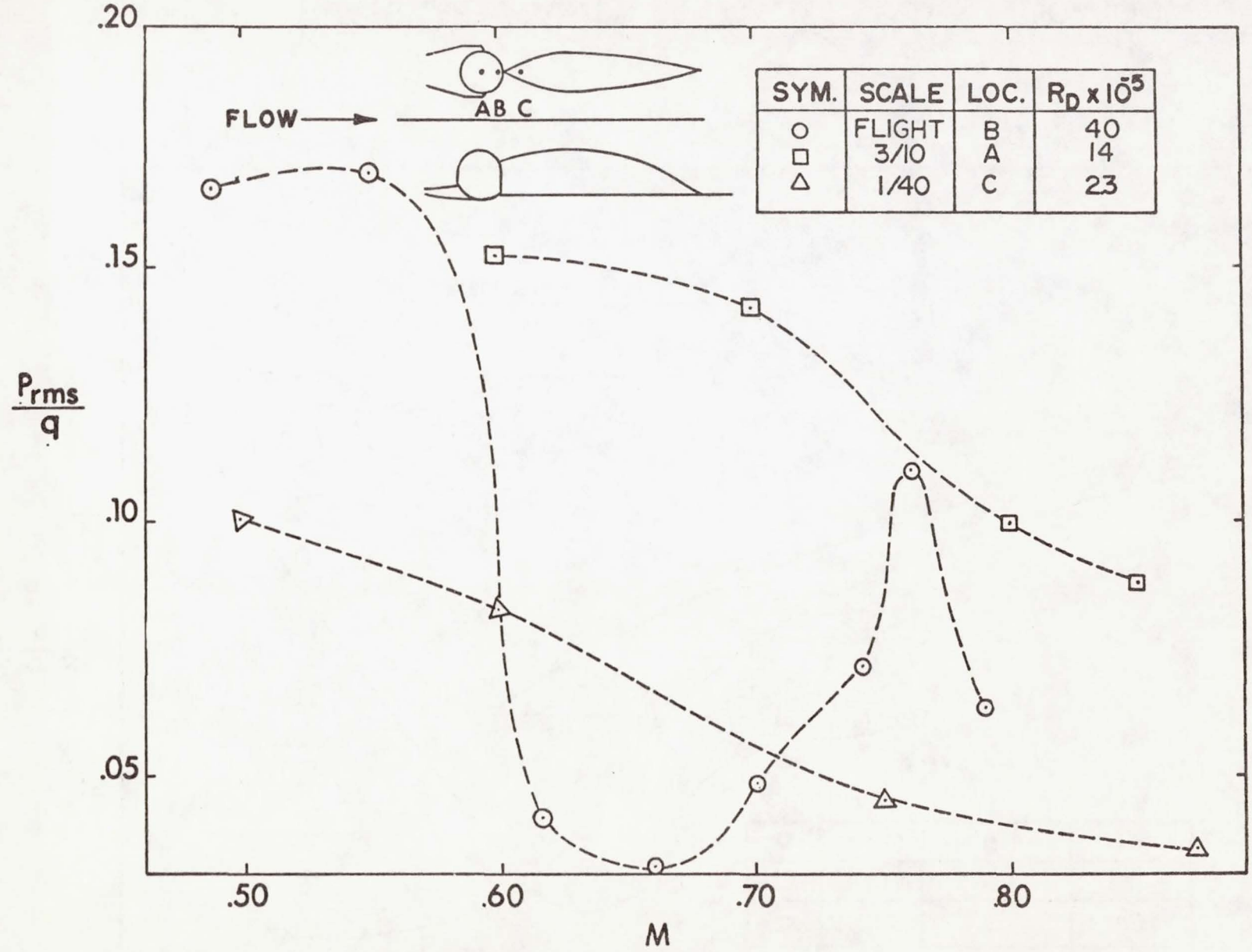

Figure 9a : COMPARISON OF THE CYCLE III/IV TURRET-FAIRING DYNAMIC PRESSURE DATA FROM AFFDL AND NASA AMES WIND TUNNEL AND ALL FLIGHT TEST. PRESSURE.

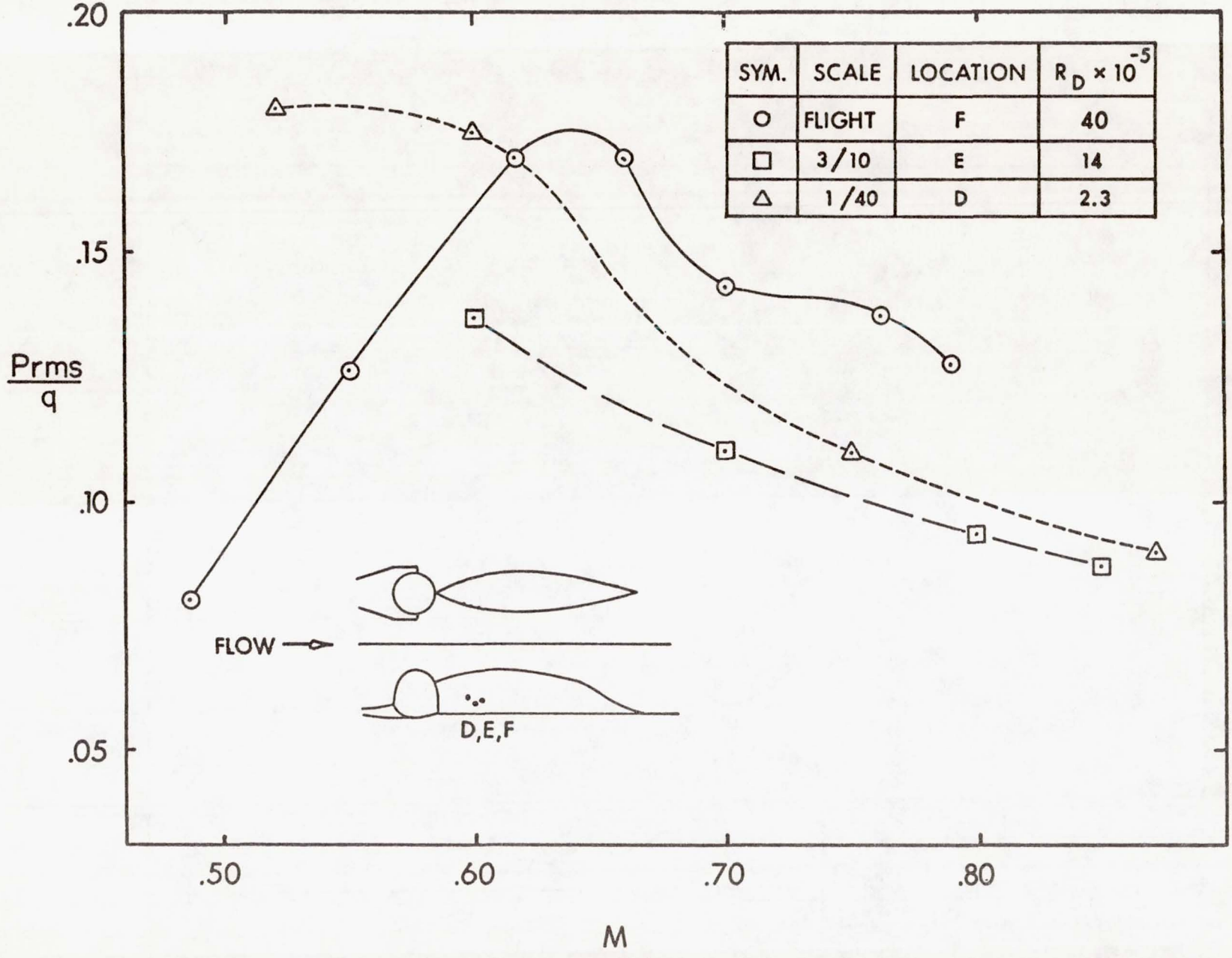

Figure 9b PRESSURE TRANSDUCER AT D,E, AND F, LOCATIONS.

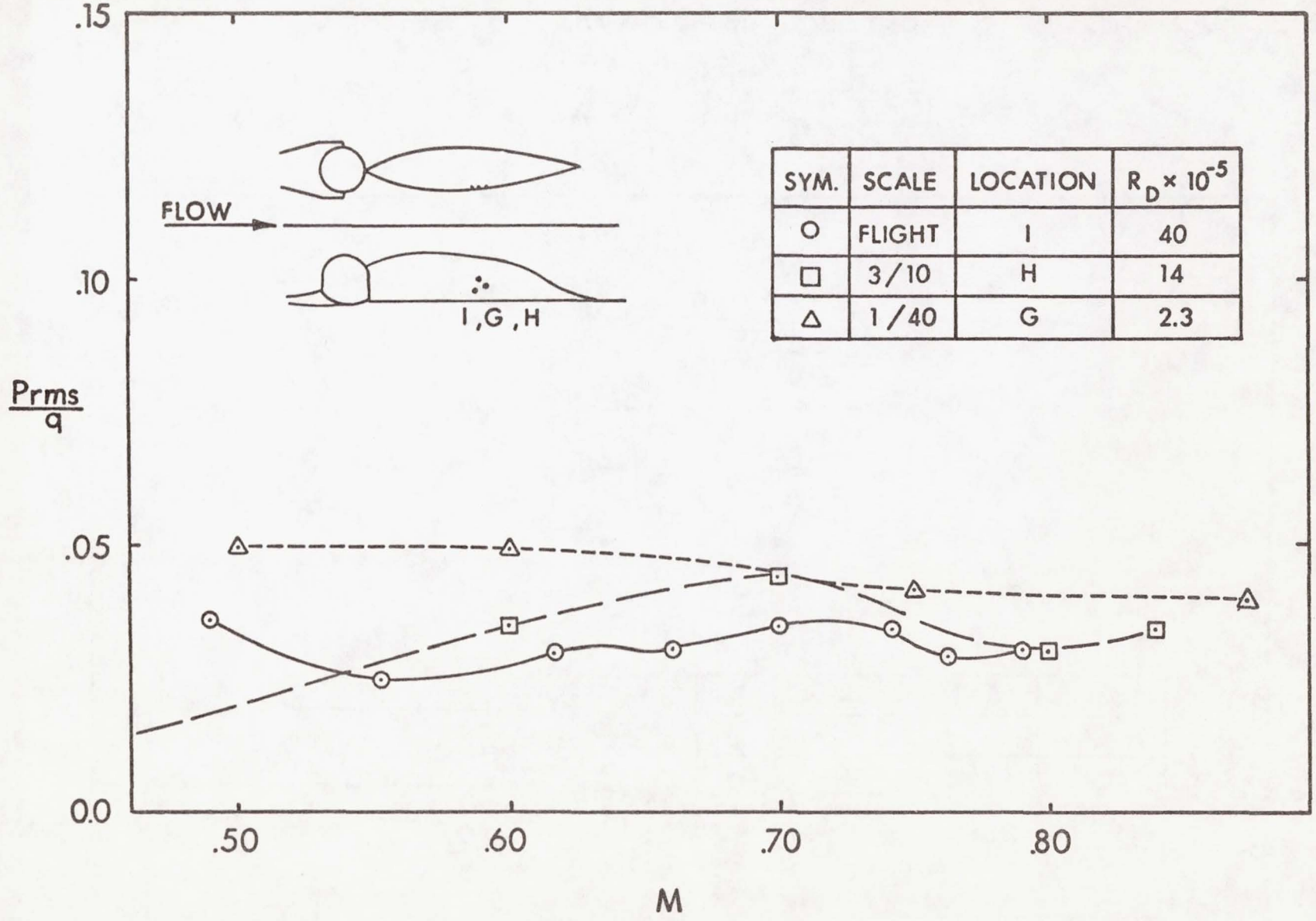

Figure 9c PRESSURE TRANSDUCER AT I, H, AND G LOCATIONS.

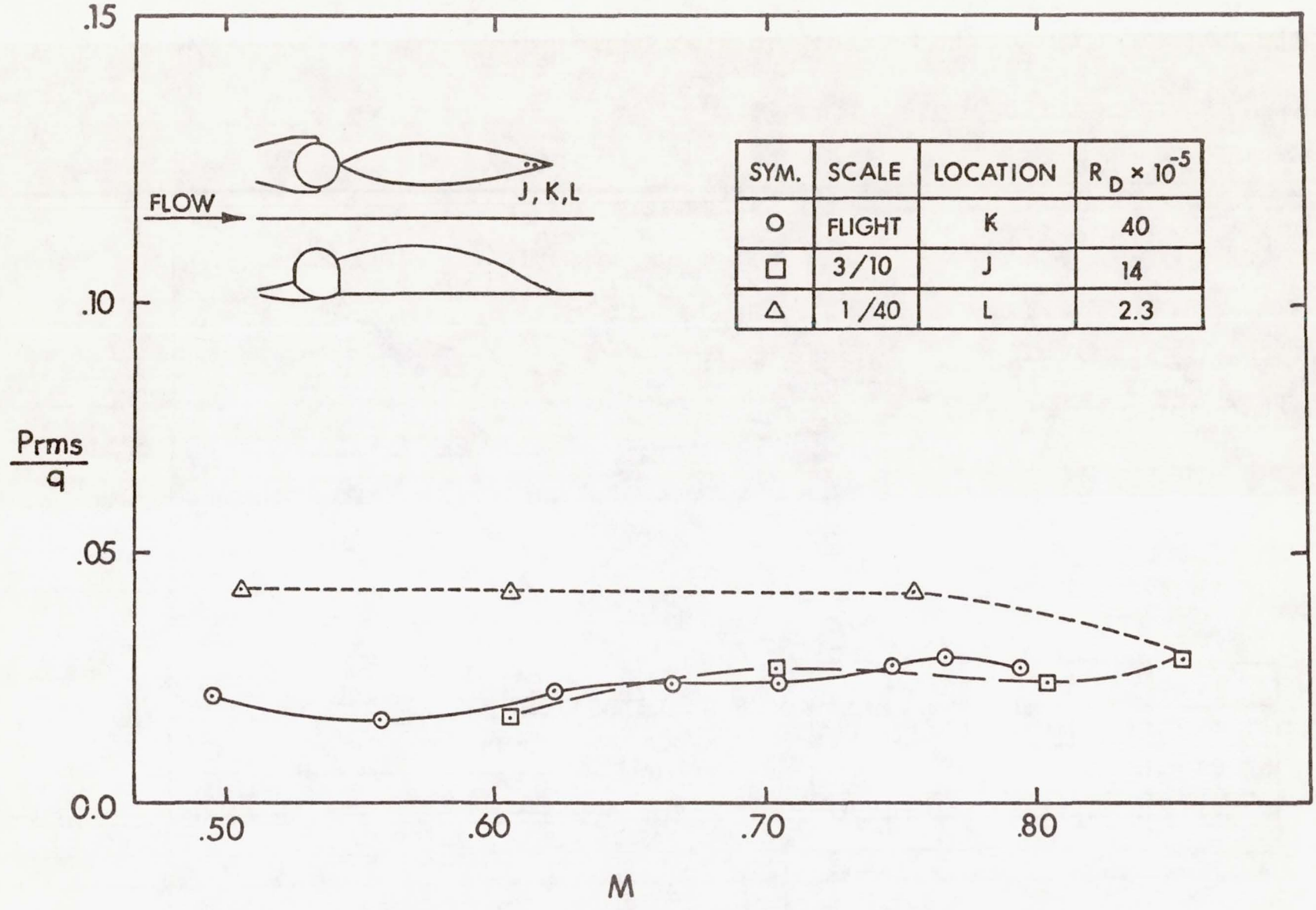

Figure 9d PRESSURE TRANSDUCER AT K, J, AND L LOCATIONS

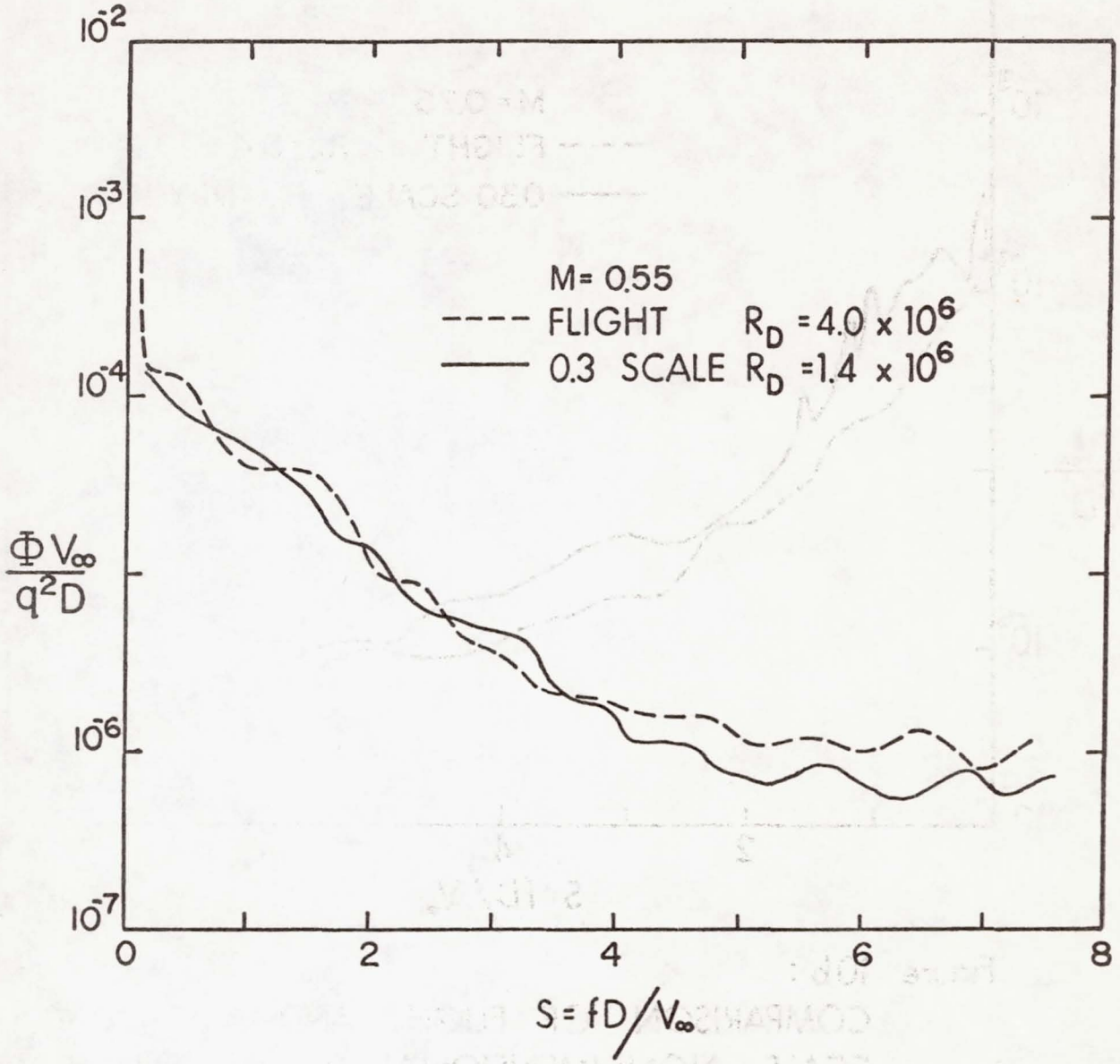

Figure 10a:
COMPARISON OF FLIGHT AND AMES 0.30 SCALE NONDIMENSIONAL POWER SPECTRAL DENSITIES. TRANSDUCERS ON TOP OF TURRET, M=0.55.

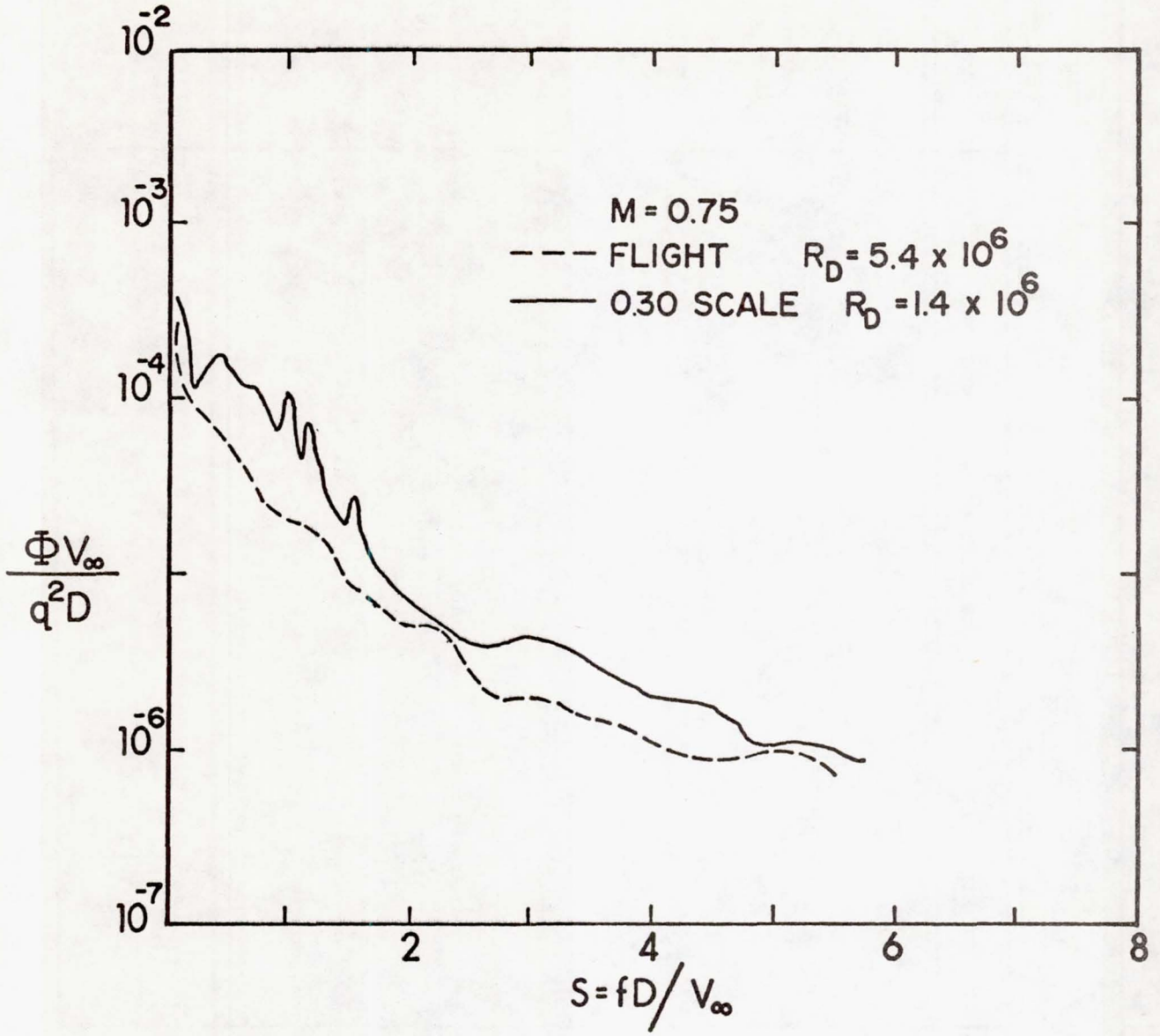

Figure 10b :
COMPARISON OF FLIGHT AND AMES 0.30 SCALE NONDIMENSIONAL POWER SPECTRAL DENSITIES. TRANSDUCER ON TOP OF TURRET, M = 0.75.

AERO-OPTICS OVERVIEW

KEITH G. GILBERT, LT COL, USAF

Introduction

The advent of the laser in 1960 brought with it the revolutionary concept of a radiation transport weapon system. Advantages of this novel system vis-a-vis conventional momentum transport weaponry (e.g., bullets, missiles, etc.) include:

(1) Zero time-of-flight

(2) Large angular coverage (i.e., lasers are low inertia systems)

(3) Meticulous, not mass destruction

Disadvantages of laser weapons, shared to some extent by their more traditional counterparts, include:

(1) Weather constraints - lasers are sometimes dubbed "fair weather friends."

(2) Range limitation - system lethality scales at least as the inverse square of the range.

(3) Countermeasure susceptibility. Lasers generally affect a kill by melting or vaporizing into the target. Sometimes relatively simple, lightweight target alterations (e.g., paint removal, insulation of vulnerable innards, etc.) can dramatically harden them to laser radiation. Laser weapon systems have been proposed for a plethora of military applications covering land to sea to air. Each system has its unique set of advantages and constraints.

All laser weapon systems have these basic components:

- Photon source
- Beam transport system - means to get energy from device to telescope

- Pointing and tracking system
- Environmental factors - the particular milieu through which the energy must propagate.
- Target

Figure 1 depicts this photon odyssey and the effect it can have on far field beam quality and, hence, weapon system lethality. The challenge to the optical engineer is to ferret out the various error sources and to quantify their contributions to overall system performance.

Aero-optics is that portion of the error budget due to interaction of the airborne platform and the atmosphere. These effects manifest themselves both as mirror vibration and optical path phase distortions. Jitter arises from buffetting effects on the aircraft and its laser turret assembly. This same interaction with the surrounding flow field produces boundary layers, shear layers and separated flow regimes as well as potential flow and local shocks. Optical losses from these latter phenomena are due to index of refraction fluctuations within the flow field. In general, the convolution of the above aero-optical effects produces a reduction in far field intensity, or power in the bucket. Understanding these various aero-optical effects, and how each is effected by aircraft performance parameters for a particular laser turret geometry, is the central challenge of aero-optics.

The field of aero-optics has experienced dramatic growth in the last several years. Early flying observers performing "ocular" imaging experiments through aircraft boundary layers saw negligible degradation due to the small apertures involved (pupil diameter is of order 2 millimeters). The first known quantitative observation of aero-optical degradations was Project

Press, a mid-1960's test series which involved a star-imaging shearing interferometer mounted onboard an Air Force KC-135 aircraft. The perplexing discovery was that celestial images observed in clear air at 30-40 KFT altitudes and high subsonic Mach numbers frequently had blurring or image spreads of 5 to 15 microradians, levels frequently exceeding ground observations! Lincoln Laboratory, the principal investigator, attributed this inflight degradation to the aircraft turbulent boundary layer.

Lethality of a laser system is proportional to the amount of energy one can deliver within a given bucket size at some specified range. Two common lethality figures of merit are peak and average intensity, the latter being defined as the power delivered within some bucket of area A,

$$(1) \qquad \bar{I} = \frac{P}{A}$$

Diffraction theory limits the peak intensity deliverable by a perfect laser device and beam control system (sans atmosphere) to

$$(2) \qquad I_p = \frac{K\ P_o\ D^2}{\lambda^2\ R^2}$$

With P_o = laser power output

D = diameter of telescope primary optic

λ = laser wavelength

R = range

K = dependent on laser beam mode and limiting apertures, but having order unity.

This equation provides a first-order prescription for increasing system lethality; the lure of a shorter wavelength system is obvious. Actually, however, nature combines risk with reward. As the wavelength decreases, turbulence and optical train degradations generally grow to partially offset this advantage. A more accurate description of the important physics is:

$$(3)\quad I_p = \frac{P_o}{R^2} \cdot \frac{1}{\left(\frac{\lambda}{D}\right) + \theta_j^2 + \theta_{Bw}^2 + \theta_{Bs}^2} \cdot \gamma e^{-\frac{4\pi^2}{\lambda^2}\left(\sigma_{opt}^2 + \sigma_F^2\right)}$$

With θ_j = System mechanical jitter

θ_{Bw} = Atmospheric beam jitter

θ_{Bs} = Atmospheric beam wander

σ_{opt} = rms phase variance of optics

σ_F = rms phase variance of platform-induced atmospherics

γ = Everything else

The form of this relationship is sketched in figure 2, showing there is an optimal wavelength for system lethality which depends primarily on the degree of system phase aberrations. In the absence of the thermal blooming, this optical wavelenth for propagation is

$$(4)\quad \lambda^* = 2\sqrt{\pi\left(\sigma_{opt}^2 + \sigma_F^2\right)}$$

Description of Aero-Optical Phenomena

The prospect of airborne high energy laser weapons poses a really scintillating challenge. In general, a laser beam must be generated within the aircraft, propagated efficiently to the exit telescope, and then through the aircraft-induced and natural turbulence fields. Such is a veritable photon odyssey. Aero-optics is the study of laser optical degradations

accruing from aircraft-induced flow fields. Figure 3 depicts a high energy laser error budget, showing at each stop the parameters implicit in determining far-field intensity, or system lethality.

A laser beam exiting from a fast-moving aircraft is susceptible to several compressibility effects induced in the surrounding flow field. These losses are due to changes in index of refraction directly related to density fluctuations via the Gladstone-Dale relationship

$$n' = G\rho' \tag{4}$$

Where n' = Index of refraction fluctuations

ρ' = Density fluctuations

G = Gladstone-Dale constant

Viscous effects manifest themselves as aircraft boundary layers or shear layers which exist near the aircraft surface. These viscous layers are typically fully turbulent with randomly fluctuating air density, and scale sizes of order 10 percent of the thickness of the layer. Because the boundary-layer scale sizes are typically small compared with the laser beam diameter, energy is scattered at wide angles. This leads to a decrease in far-field peak intensity. When these random flows depart the fuselage they become separated flow regions. Because they can present long optical paths for certain aft look angles, these can be the source of severe optical degradations.

The second aero-optical source of loss is inviscid flow fields surrounding the aircraft due to airflow around protuberances such as laser turret

assemblies. These flow fields yield spatially steady density variations which act effectively as an aberrated lens to the beam.

The final aero-optical loss mechanisms are shocks, established whenever local flow exceeds Mach one. For typical cylindrical turret geometries these conditions exist for aircraft Mach numbers in the 0.5 to 0.6 regime. The strong density gradients associated with these shocks generally both refract and disperse the laser beam. The convolution of these effects imposes a near-field phase aberration on the beam with a concomitant reduction in lethality or far-field intensity. The challenge of aero-optics is to quantify this far-field degradation for a particular airborne laser system.

Interaction of a laser beam with a turbulent boundary layer is described in figure 4. The important physical parameters describing the interaction are the unsteady density fluctuations ρ', the propagation direction coherence length ℓ_z associated with the turbules, and the total path length through the disturbance.

In general, the system far-field performance is limited by the telescope diffraction angle

$$\theta_D \approx \lambda/D \tag{5}$$

With λ = laser wavelength

D = telescope diameter

The turbs, on the other hand, scatter radiation at a relative wide angle,

$$\theta_\ell = \frac{\lambda}{\ell} \tag{6}$$

The net far-field pattern is a central spot reduced in intensity but having a spot size defined only by the laser and beam transfer optics convoluted

with a turbulence-generated halo. If the beam diameter is large compared with the turbulence coherence length ($D>>\ell$), then the reduction in on-axis intensity (Strehl ratio) is approximately

$$I/I_0 = e^{-K^2 \sigma^2} \tag{7}$$

Where K = wavevector ($2\pi/\lambda$)

σ = rms phase variance

The phase variance can be calculated by integrating through the disturbance along the optical axis

$$\sigma^2 = 2 G^2 \int_0^L \langle \rho' \rangle^2 \ell_z \, dz \tag{8}$$

With G = Gladstone-Dale constant

ρ' = Unsteady density

Armed with these tools one can make an aerodynamic estimate of the Strehl ratio I/I_0 via equations (7) and (8). Then an integrated path optical technique such as a Modulation Transfer Function or a Line Spread Function measurement provides a comparison measurement. Recent experiments on relatively thick (L 30 cm) aircraft boundary layers have produced good correlations between these aerodynamic and optical measurements.

Separated flow is established behind aerodynamic bodies such as wings or turrets or aircraft themselves. The aircraft boundary layer separates from the surface at some point and spreads to form a turbulent wake. This flow is generally fully turbulent, and has scale sizes of the order of the body itself. The total optical degradation through such a disturbance can

also be estimated from equations (7) and (8). Even though the unsteady density fluctuations are usually smaller than those associated with fuselage boundary layers and shear layers, the larger coherence lengths and longer paths for aft look angles more than compensate. In short, aircraft separated flows can act as a major constraint to airborne laser weapon systems.

Potential flow regions are established outside the boundary layer, and occur due to flow around aerodynamic postuberances. The flow in these regions is both inviscid and approximately incompressible. The rudiments of a potential flow field are depicted in figure 5. The density changes through this regime are estimated by using compressibility corrections to the potential flow. This region acts as an aberrated lens with approximate focal length

$$f = R \frac{\rho_1}{\rho_1 - \rho_0} \tag{9}$$

With R = radius of curvature of flow

ρ_1 = characteristic density within flow

ρ_0 = free-stream density

The potential flow field of a one meter diameter hemispherically capped circular cylinder has been calculated numerically for a range of high subsonic Mach numbers. The density variations in the flow were inferred from compressibility corrections applied to the potential flow model. The optical effects of this flow field were found to produce primarily a defocus, with

secondary astigmatic effects. The effective focal length of this negative aerodynamic lens was a few kilometers. Though the dominant effect of the flow field was defocusing, which is correctable via the system telescope, there is no reason to believe that higher-order aberrations will be negligible for different laser turret geometries.

A shock wave is formed whenever local flow velocities around turrets exceed Mach one. This can occur for common geometries at relatively low aircraft Mach numbers (e.g., cylinder turret $M \gtrsim 0.55$). A laser beam traversing this shock will generally be both refracted and dispersed (the reflected component at the shock interface is negligible). Maximum refractive angles are typically of order one milliradian, when dispersion depends on details of the shock geometry. Because optical refraction is essentially wavelength independent, if the high energy laser tracker shares the optical axis then shock-induced beam deflection will not be a source of optical degradation.

Aerodynamic-induced beam jitter is generally a major source of airborne laser degradation. This jitter arises from an interaction of aerodynamic structures with the natural turbulent medium through which it is flying. The aerodynamic buffeting manifests itself as optical train mechanical jitter; the far-field result is an increased effective spot size on target with a concomitant reduction in system lethality.

Figure 6 depicts the aero-loading problem. This aerodynamic-induced jitter spectrum has two major components. Energy coupled into the airframe and laser turret assembly causes the whole structure to respond, with a resultant (indirect) response of the optics. These components have characteristic frequencies

$$\nu_o \sim V/d$$

With V = aircraft velocity relative to airstream

d = size of protuberance

Too, in the event of a windowless turret, the telescope can be loaded directly. These unsteady pressures produce both a jitter and a torque. Both these phenomena tax the ability of the beam control system to hold the spot on the target.

Aerodynamic-induced jitter is a primary source of far field degradation for today's 10.6μm airborne high energy laser (HEL) systems. Moreover, as shorter wavelength HEL airborne systems emerge, enabling one presumably to engage harder target at longer ranges, the premier challenge for beam control will be to keep net system jitter less than or of the order of the intrinsic diffraction angle; i.e.,

$$\theta_j \lesssim \frac{\lambda}{D}$$

To date little has been done to aerodynamically ameliorate turret buffeting. Fairing assemblies offer some relief, as they offer a degree of insulation against the mainflow. However, these ploys generally limit the laser field of view. Aerodynamic flow control is another possiblity, as by suctioning or diverting. Future wind-tunnel efforts should plumb the efficiency of these techniques. Most of the investments to date have been toward measuring the torque and bandwidth capabilities of trackers to compensate for aero-loading. Clearly a combination of techniques is needed to meet and solve the general problem.

The field of aero-optics has matured dramatically over the past half-decade. This monograph hopefully describes this maturation.

Early experiments were conducted in wind tunnels, which provided a cost-effective simulation tool for some airborne aero-optical phenomena as well as a development laboratory for essential aerodynamic and optical instrumentation. In spite of spiraling operation costs, wind tunnels are a much more benign and efficient laboratory for research than are airborne platforms. Large wind-tunnel tests mainly broached the aero-loading problem. As we shall see, these experiments found great success in simulating airborne unsteady pressure fields (i.e., the driving function) but less success in simulating the vehicle response (i.e., jitter) to this forcing function.

Similarly, techniques to infer unsteady density and correlation lengths within boundary layers and shear layers were developed in Air Force sponsored wind-tunnel experiments. Corresponding nascent optical techniques yielded corroborative integrated path measurements of optical degradation. A recent airborne flight test program plumbed aircraft turbulent boundary layer/shear layer degradations via both aerodynamic and optical instrumentation. Good correlations were shown between these two independent techniques of inferring optical Strehl loss I/I_0.

Little definitive work has been done on laser propagation through separated flows, though the investigative techniques are similar to those developed for boundary layers and shear layers. The importance of understanding separated flow effects for rear-looking laser missions cannot be overstressed.

One article describes a wind-tunnel investigation of laser potential flow-induced degradation. Though these effects have a frequency bandwidth of only a few hertz, the potential laser optical degradation is significant. No

known work has been done on the effect of aircraft-induced shocks on airborne laser systems.

Flight tests are clearly essential as a "proof of principle." Only via flying laboratory experiments can one examine real world random flows, potential flows and aero-loading effects essential to an evaluation of airborne high energy laser weapon potential.

Though the consensus status of aero-optics has reached an impressive quantum level of maturity, eminent challenges remain. These include (1) aero-optical design optimization of laser turret systems, or, turretology. As shorter wavelength laser systems emerge, the contributions of turret-induced jitter and optical degradation to the system error budget will grow. Techniques such as flow separation control, potential flow tailoring, and unsteady pressure amelioration must be nurtured in wind tunnels and brought to airborne testing fruition over the next decade.

(2) Adaptive optic system development. Residual aero-optical degradations may be amenable to advanced beam control techniques. In particular, several of the low bandwidth phenomena such as potential flow, shocks, and certain aspects of wake turbulence effects may be correctable via adaptive optic technology.

(3) Generalized analyses of aero-optical degradations must be developed. The majority of experiments accomplished to date have examined only beam propagation normal to relatively simple shear layers or boundary layers. Furthermore, laser turret geometries have generally been rudimentary. Certainly some experiments with more interesting configurations must be accomplished. Analytical techniques must be developed to extrapolate these results to more generalized aircraft turret configurations. Included should

be the ability to handle the observed inhomogenious, anisotropic random flow density fluctuations.

The generalized challenge to laser turret optimization can be sketched as follows. First a mission profile is defined, which sets a Mach number regime, field of view requirements and a laser telescope diameter. A useful aero-optical figure of merit is then:

$$\gamma_i = \frac{e^{-\phi_i^2}}{(\lambda/D)^2 + \theta_i^2}$$

Where ϕi = optical phase variance associated with the 1^{th} set of mission parameters

θ_i = aero-optical jitter associated with i^{th} mission point

The objective then is to design a turret which maximizes the various γ_i subject, of course, to the condition that aircraft performance must be preserved!

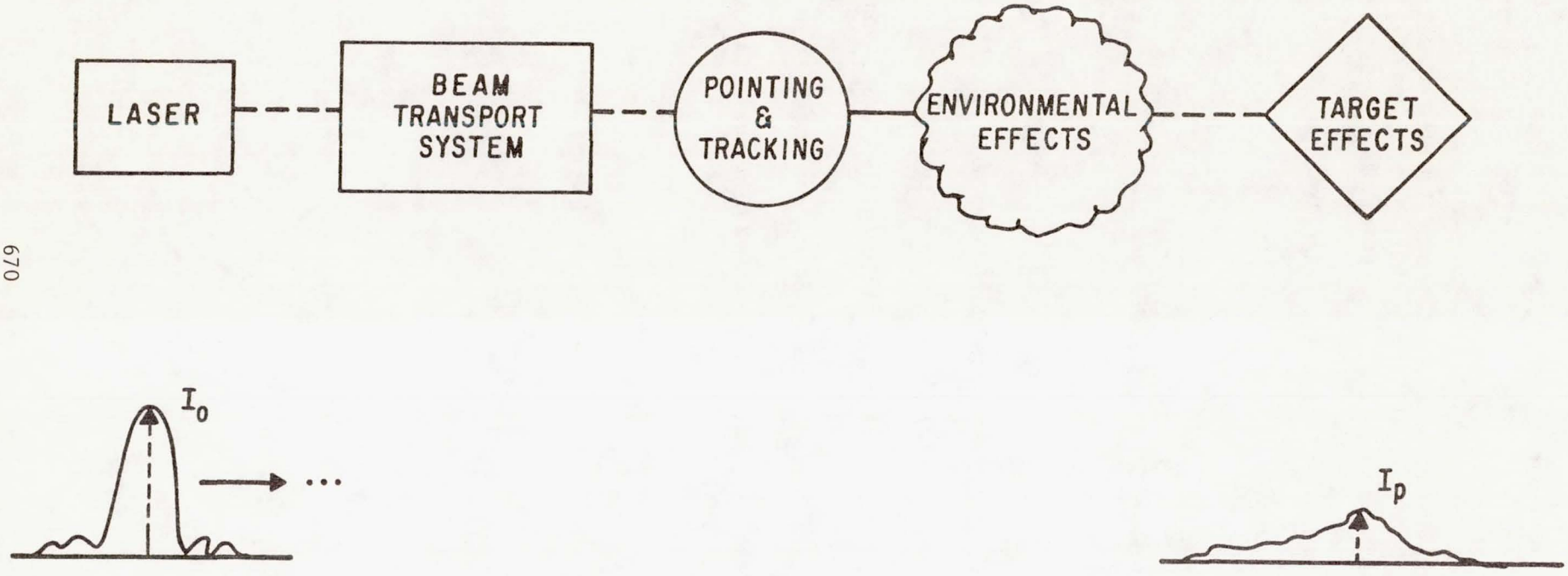

Fig. 1. Elements of Laser Weapon System.

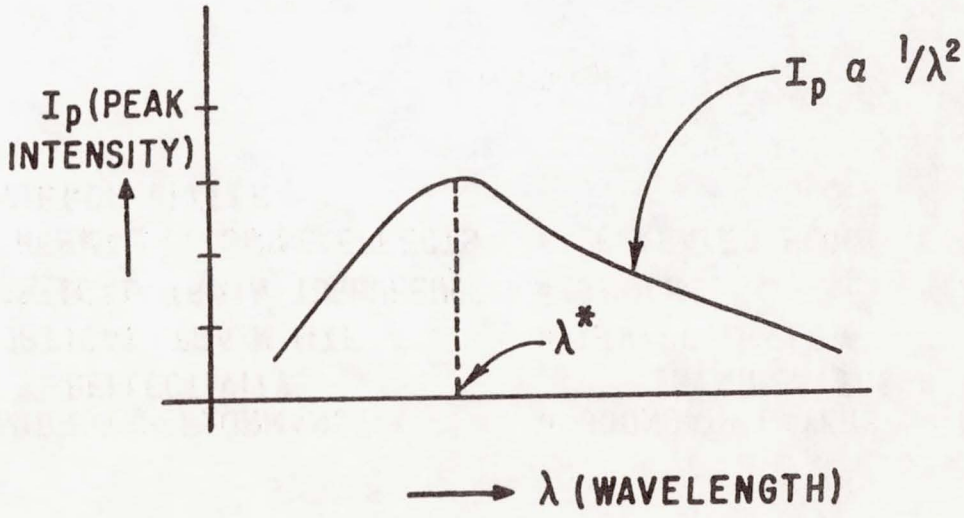

Fig. 2. Wavelength Scaling of Laser System Lethality.

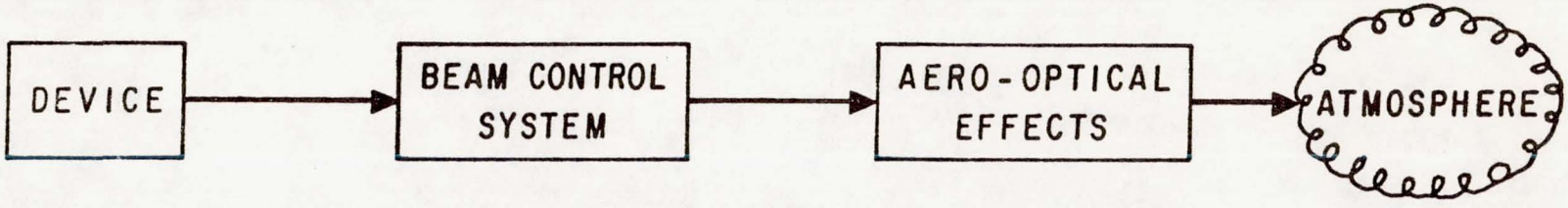

- POWER
- BEAM QUANTITY
- JITTER

- MIRROR PERFORMANCE REFLECTIVITY
- OPTICAL TRAIN MTF
- OPTICAL TRAIN TURBULENCE
- THERMAL BLOOMING EFFECTS
- MIRROR JITTER

- BOUNDARY LAYERS/ SHEAR LAYERS
- INVISCID FLOW
- SHOCKS
- SEPARATED FLOW

- NATURAL TURBULENCE JITTER SPREAD
- ABSORPTION
- AEROSOL SCATTER
- THERMAL BLOOMING

Fig. 3 Error Budget.

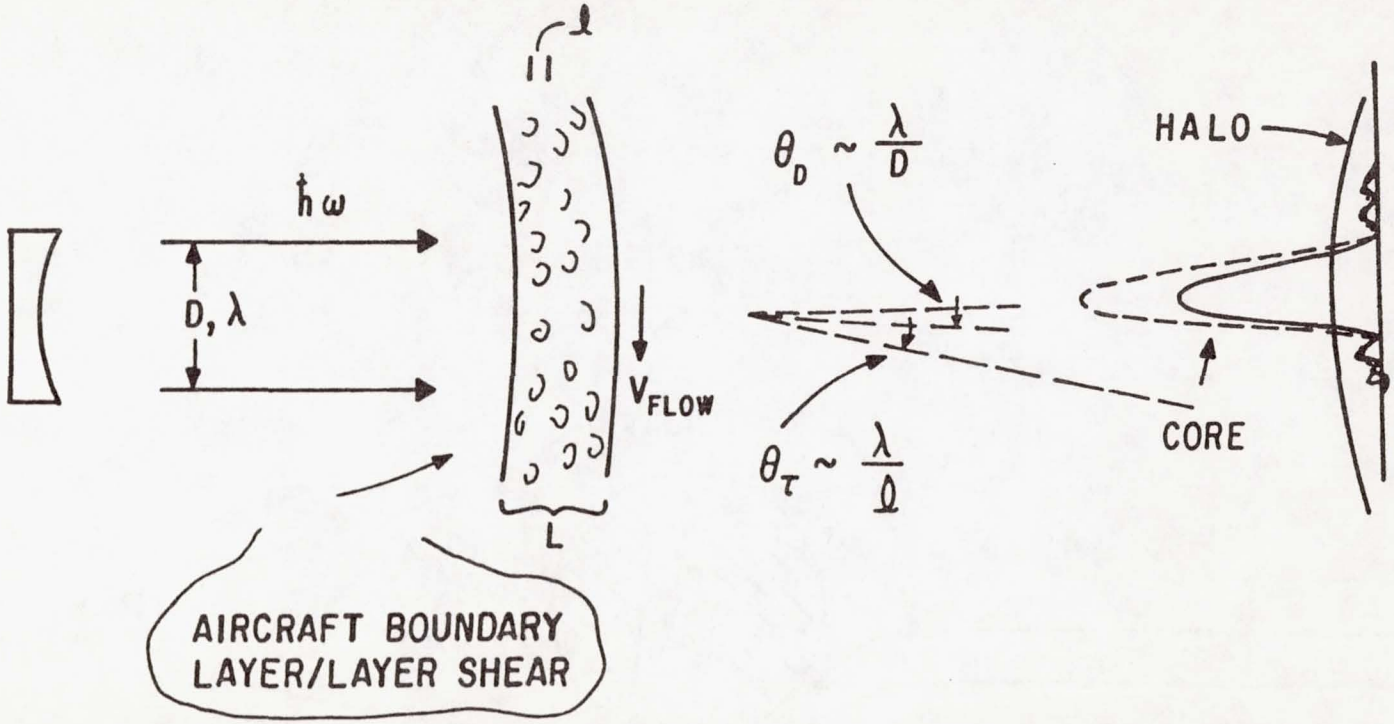

- SYSTEM DIFFRACTION ANGLE — $\theta_D \sim \frac{\lambda}{D}$, D = TELESCOPE DIAMETER
- TURBULENCE SCATTER ANGLE — $\theta_T \sim \frac{\lambda}{\ell}$, ℓ = TURBULENCE SCALE
- BOUNDARY LAYER-INDUCED STREHL LOSS

$$I/I_0 \sim e^{-k^2\sigma^2} \quad (D/\ell \gtrsim 5)$$

$$K = 2\pi/\lambda$$

$$\sigma^2 = 2G^2 \int_0^L \langle \rho' \rangle^2 \ell_z \, dz$$

Fig. 4 Interaction of Laser Beam with Aircraft Random Flow Regions.

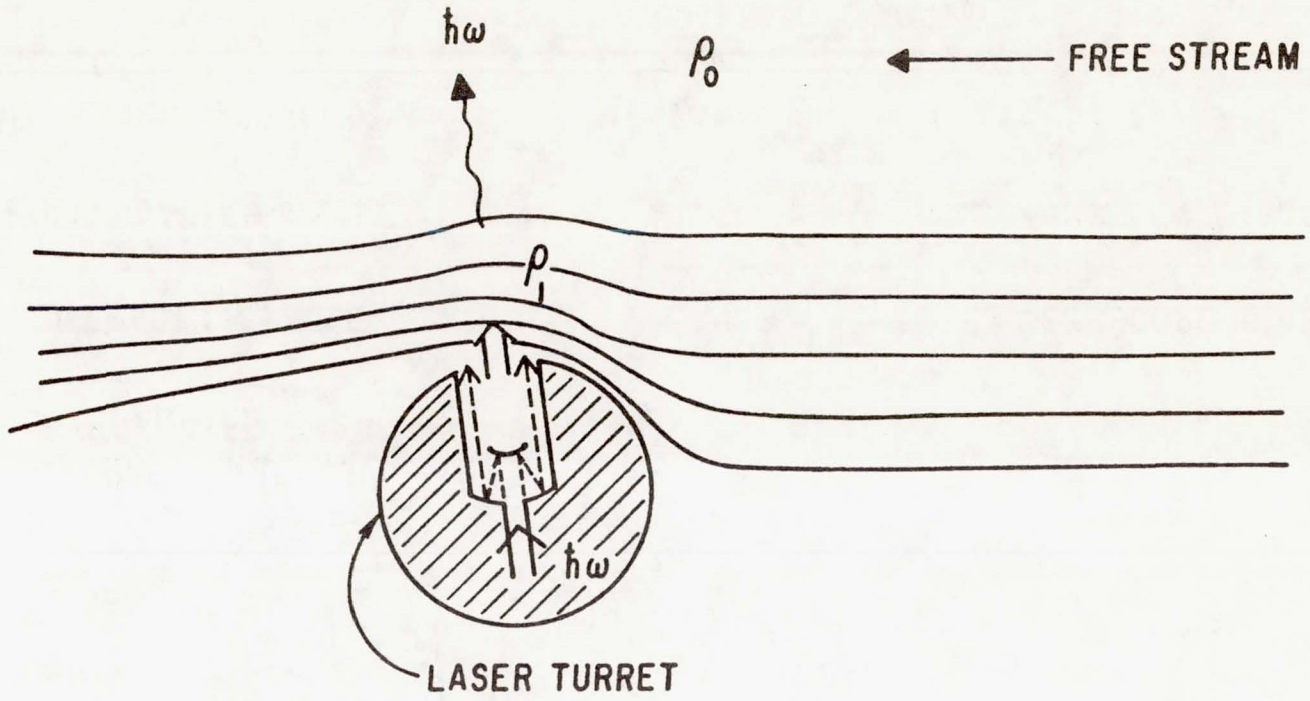

Fig. 5 Interaction of Laser Beam with Aircraft Potential Flow Field.

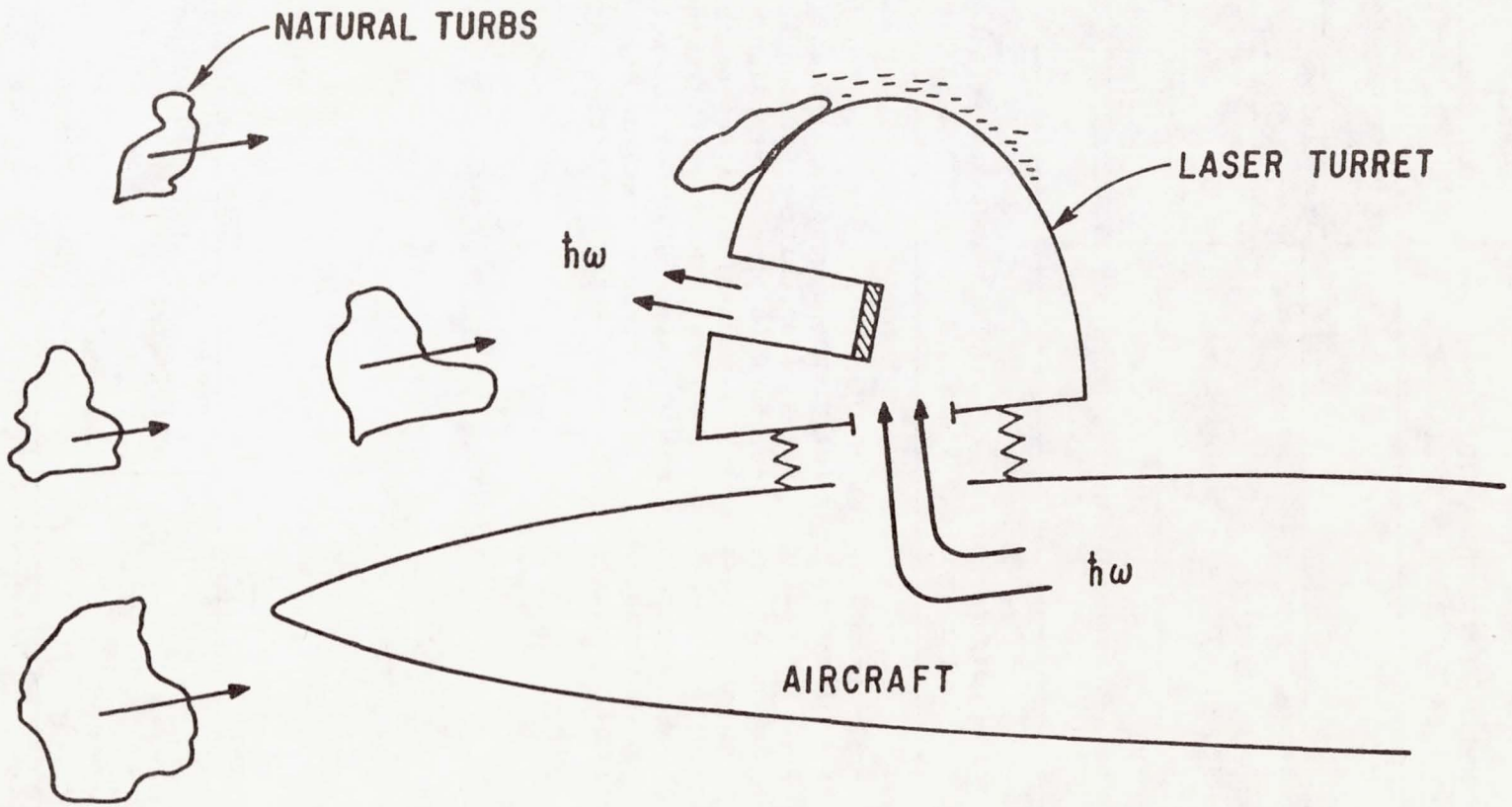

Fig. 6 Aerodynamic Loading Phenomena.

1. Report No.	2. Government Accession No.	3. Recipient's Catalog No.
NASA CP-2121		

4. Title and Subtitle	5. Report Date
PROCEEDINGS OF THE AERO-OPTICS SYMPOSIUM ON ELECTROMAGNETIC WAVE PROPAGATION FROM AIRCRAFT*	6. Performing Organization Code
7. Author(s)	8. Performing Organization Report No. A-8090
9. Performing Organization Name and Address Ames Research Center, NASA Moffett Field, Calif. 94035	10. Work Unit No. 505-31-21 11. Contract or Grant No.
12. Sponsoring Agency Name and Address National Aeronautics and Space Administration Washington, D.C. 20546	13. Type of Report and Period Covered Conference Publication 14. Sponsoring Agency Code

15. Supplementary Notes

*Sponsored by Air Force Weapons Laboratory and NASA-Ames Research Center; held at Ames Research Center, Moffett Field, CA on August 14-15, 1979.

16. Abstract

Data are presented from a series of wind-tunnel and flight experiments concerning natural and induced turbulence around an airplane, and the effects on propagation characteristics of an emitter mounted in the airplane. Some of the papers are concerned with phase distortion of the propagating radiation, and others deal with mechanical jitter of the optical elements when exposed to open-cavity turbulence. The results include both aerodynamic and optical measurements and a consideration of the relationship between the two. Primary emphasis is on the dynamic disturbances, but theoretical and experimental evaluations of steady-state distortions are also presented.

17. Key Words (Suggested by Author(s))	18. Distribution Statement
Aerodynamics of bodies Boundary layers Measuring instruments Holography Light phenomena	Unlimited Star Category - 34

19. Security Classif. (of this report)	20. Security Classif. (of this page)	21. No. of Pages	22. Price*
Unclassified	Unclassified	681	$19.00

*For sale by the National Technical Information Service, Springfield, Virginia 22161

GPO 695-346/225